Tourmalinisation of perigranitic hydrothermal systems : experimental approach to the stability field and dynamics of metasomatic processes in borosilicate systems

Julien Fort

To cite this version:

Julien Fort. Tourmalinisation of perigranitic hydrothermal systems : experimental approach to the stability field and dynamics of metasomatic processes in borosilicate systems. Earth Sciences. Université d'Orléans, 2023. English. NNT : 2023ORLE1065 . tel-04562395

HAL Id: tel-04562395
https://theses.hal.science/tel-04562395v1

Submitted on 29 Apr 2024

UNIVERSITÉ D’ORLÉANS

ÉCOLE DOCTORALE
ENERGIE, MATERIAUX, SCIENCES DE LA TERRE ET DE L’UNIVERS
Institut des Sciences de la Terre d’Orléans

THÈSE présentée par :

Julien FORT

soutenue le : **12 Septembre 2023**

pour obtenir le grade de : **Docteur de l’Université d’Orléans**

Discipline/ Spécialité : Sciences de la Terre / Métallogénie

Tourmalinisation of perigranitic hydrothermal systems: experimental approach to the stability field and dynamics of metasomatic processes in borosilicate systems

THÈSE dirigée par :

M. Stanislas SIZARET	Professeur, ISTO, Orléans (Directeur de thèse)
M. Johann TUDURI	Ingénieur de recherche, BRGM, Orléans (Co-encadrant de thèse)
M. Olivier BLEIN	Ingénieur de recherche, BRGM, Orléans (Co-encadrant de thèse)

RAPPORTEURS :

M. Larryn W. DIAMOND	Professeur, University of Bern
M. Vincent VAN HINSBERG	Associate Professor, University of McGill

JURY :

Mme Caroline MARTEL	Professeur, ISTO, Orléans, **Présidente du jury**
M. David DOLEJŠ	Professeur, University of Freiburg
M. Alexander GYSI	Assistant Professeur, New Mexico Institute of Mining and Technology
M. Larryn W. DIAMOND	Professeur, University of Bern
M. Vincent VAN HINSBERG	Associate Professor, University of McGill
M. Stanislas SIZARET	Professeur, ISTO, Orléans
M. Johann TUDURI	Ingénieur de recherche, BRGM, Orléans

INVITES :

M. Olivier BLEIN	Ingénieur de recherche, BRGM, Orléans

UNIVERSITÉ D'ORLÉANS

ÉCOLE DOCTORALE
ENERGIE, MATERIAUX, SCIENCES DE LA TERRE ET DE L'UNIVERS

Institut des Sciences de la Terre d'Orléans

THÈSE présentée par :

Julien FORT

soutenue le : **12 Septembre 2023**

pour obtenir le grade de : **Docteur de l'Université d'Orléans**

Discipline/ Spécialité : Sciences de la Terre/ Métallogénie

Tourmalinisation des systèmes hydrothermaux périgranitiques : approche expérimentale du champ de stabilité et des dynamiques des processus métasomatiques dans les systèmes borosilicatés

THÈSE dirigée par :

M. Stanislas SIZARET	Professeur, ISTO, Orléans (Directeur de thèse)
M. Johann TUDURI	Ingénieur de recherche, BRGM, Orléans (Co-encadrant de thèse)
M. Olivier BLEIN	Ingénieur de recherche, BRGM, Orléans (Co-encadrant de thèse)

RAPPORTEURS :

M. Larryn W. DIAMOND	Professeur, University of Bern
M. Vincent VAN HINSBERG	Associate Professor, University of McGill

JURY :

Mme Caroline MARTEL	Professeur, ISTO, Orléans, Président du jury
M. David DOLEJŠ	Professeur, University of Freiburg
M. Alexander GYSI	Assistant Professeur, New Mexico Institute of Mining and Technology
M. Larryn W. DIAMOND	Professeur, University of Bern
M. Vincent VAN HINSBERG	Associate Professor, University of McGill
M. Stanislas SIZARET	Professeur, ISTO, Orléans
M. Johann TUDURI	Ingénieur de recherche, BRGM, Orléans

INVITES :

M. Olivier BLEIN	Ingénieur de recherche, BRGM, Orléans

"*on the whole, the chemistry of* [the tourmaline] *is more like a medieval doctor's prescription, than the making of a respectable mineral* […]*, but it may, perhaps, be owing to the strange complexity of its make, that it has notable habit which makes it, to me, one of the most interesting minerals*"

Ruskin J (1894) The Ethics of the Dust: Ten Lectures to Little Housewives on the Elements of Crystallisation. Henry Altemus, Philadelphia, pp 1–180

Remerciements

Lorsque j'ai franchi les portes de l'OSUC pour la première fois il y a 9 ans, j'étais loin, très loin, de me douter que j'y resterais aussi longtemps et que je conclurais mes études à l'Université par une thèse. Cette thèse c'est 4 années de ma vie passées à travailler sur un sujet scientifique. Quatre années qui ont été ponctuées de hauts et de bas, de moments où je sentais que je n'étais à rien d'une découverte scientifique majeure et d'autres où ma seule motivation à me lever le matin était la potentielle présence de pizzas à la cantine. J'y ai appris ce qu'est la recherche scientifique, l'expérimentation en sciences de la Terre et j'ai découvert des sujets de recherche et des disciplines dont je ne soupçonnais même pas l'existence. J'ai appris à aimer la tourmaline mais aussi à la détester, puis à la re-aimer et à la re-détester ; aujourd'hui je dirais que je la « détaime ». Mais j'ai surtout appris qu'une thèse c'est le résultat de mes interactions avec les autres. Que ce soit pour m'aider dans les calculs thermo, m'expliquer comment fonctionne un appareil ou pour boire un coup le soir, ce sont toutes les personnes avec qui j'ai interagi pendant ces 4 ans (et même avant) qui m'ont permis de construire et d'aller au bout de ce travail. Cette section est donc là pour remercier toutes ces personnes et je croise les doigts pour ne pas oublier quelqu'un.

Je tiens tout d'abord à remercier Vincent van Hinsberg et Larryn W. Diamond pour avoir accepté d'évaluer ce manuscrit, ainsi que Caroline Martel, David Dolejš et Alexander Gysi pour avoir accepté de faire partie de mon jury.

Je souhaite ensuite remercier mon directeur de thèse Stanislas Sizaret pour m'avoir fait confiance et m'avoir offert cette formidable opportunité. J'ai pu bénéficier d'une très grande liberté de recherche pendant ces trois ans, mais tu as su aussi me guider pour refocaliser mon travail quand cela se montrait nécessaire. Depuis le M2 sur les kaolins de Ploemeur jusqu'au derniers instants de la thèse, merci pour la pédagogie, la patience et la bienveillance dont tu as fait preuve à mon égard.

Je tiens également à remercier Johann Tuduri et Olivier Blein mes encadrants au BRGM, qui ont participé au montage de la thèse. Merci à vous pour avoir permis de lancer ce projet, ainsi que pour m'avoir permis l'accès aux outils analytiques du BRGM. Bien que le sujet de thèse ait évolué par rapport à la maquette initiale, vos conseils et les discussions que nous avons pu avoir ont contribué à l'ouverture de ma recherche sur des domaines géologiques plus variés.

Merci à Michel Pichavant pour m'avoir appris à faire de la géologie expérimentale. Du choix des produits de départ jusqu'à l'interprétation des résultats, en passant par le principe d'un sensor, j'ai énormément appris grâce à toi. Merci aussi de m'avoir formé à l'art de la rédaction scientifique en m'apportant de nombreux conseils et corrections lors de la rédaction de mon premier article.

Merci à Florian Osselin pour m'avoir fait découvrir les expériences en bancs de transfert réactifs. Quel bonheur que de rester de 7h du matin à 1h du matin (le lendemain) devant une machine capricieuse qui sent le fer chaud. Tout ça pour découvrir 6h plus tard qu'un capillaire s'est cassé et qu'il va me falloir passer 12h à attendre que l'autoclave refroidisse tout en subissant ton sarcasme. Malgré cela, cette partie de ma thèse m'a vraiment passionné et je tenais à te remercier pour m'avoir fait découvrir l'infinie richesse des expériences en transport-réactif.

Merci à Arnault Lassin pour m'avoir énormément appris sur l'utilisation de PHREEQC et sur la thermodynamique en général. Je suis très heureux que cette collaboration ait pu être mise en avant dans une publication.

Il y a deux autres personnes que je souhaite vraiment remercier et qui ont été essentielles à la réalisation de ce travail. Rémi Champallier, pour son aide technique sur les appareils expérimentaux et pour avoir lancé ma première manip pendant le confinement de 2020. Et Ida Di Carlo pour son aide à la microsonde, au MEB et pour ses conseils quant à la thèse. Je me réengage ici à te remettre un petit pot de K1C, le kaolin ultrapur de Ploemeur (c'est de la bonne) sur ton bureau en guise de remerciement.

Merci à l'ISTO-OSUC d'être un labo où il fait bon vivre et où la bonne ambiance, nécessaire pour conserver le moral, règne.

Merci à l'équipe de l'administration pour leur aide tout au long de ces années : Marie-France R., Olivier G., Martine B., Fabienne G., Virginie L., Carole R. ; le staff informatique : Julien C. et Yohann B., ainsi que Nathalie P. pour sa capacité à trouver de sombres articles russes et Ferly C. pour son aide lors des évènements et pour ses nombreuses réparations de la porte du bureau.

Merci aux techniciens et ingénieurs sans qui la recherche expérimentale serait impossible : les « *gars de l'atelier* », Esteban M., Fred S. et Rémy P., Didier B. pour la partie electronique, Sylvain J. pour la réalisation de plots et lames minces sur mes produits toujours plus incongrus, Patricia B-J. pour le MEB et sa bonne humeur constante, Marielle H. (BONJOUR MARIELLE !!!!) pour son aide en salle de chimie et Philipe P. pour les DRX et les tests au microtomo. Merci à Nicolas M. pour les DRX au BRGM. Merci aux différents gardiens que j'ai pu croiser lors de mes surveillances de manip nocturnes. C'était toujours des discussions très sympathiques et bienvenues.

Merci à tous les doctorants, post-doctorants et chercheurs du labo avec qui j'ai pu échanger sur tout et n'importe quoi : Aneta S. (merci pour ton aide au RAMAN et avec l'administration de l'ED), Ary B., Romain A., Austin G., Anaëlle S., Mathieu S., Guillaume R., Cyprien S., Yan C., Eric M., Nicole LB. (merci de m'avoir fait confiance pour les TP de minéralogie aux L1), Claude LM., Nicolas F., Giada I. M. (qui a permis aux nouveaux arrivants de m'identifier comme « le type avec une blouse dégueulasse »), Fabrice G., Gaëlle P., Lionel M., Jonas B., Federica F., Laurent A., Hela B. Z. et Yannick B.

Merci à Armin M. avec qui j'aurais partagé mon bureau pendant 3 ans, tu as permis à ce bureau d'avoir l'air organisé, au moins sur une moitié.

Une pensée toute particulière va aux membres du groupe Trahison-ISTO dont l'ambiance est toujours délétère : Bryan, F-X, François, Amélie, Hector, Khadija, Imad, Mohamadou, Nathan, Ismael et Juliette. Je reviens très vite manger avec vous tous afin de répandre ma mauvaise humeur et bon courage à ceux d'entre vous qui commencent à rédiger leur thèse.

Hors labo, je tenais à remercier aussi les amis qui ont rendu ces années plus agréables. Barnabé et Isabelle avec leur innombrables soirées jeux, Clément, Sylvie, les gens du bar « Le Roi Hérisson » sur Blois, Magali et Gaby pour notre passion commune la sangri… la peinture de figurine.

Un grand merci à Vals (oui, je mets un « s » en l'honneur de tes ambitions politiques) pour tous ces merveilleux débats scientifico-politique et pour m'avoir fait découvrir tant de choses, allant de jeux de sociétés (p'tit Root ?) à la rando itinérante, en passant par le Hellfest et les catas de Paris. Merci à Franck qui m'a tant appris (l'ouverture facile d'une cannette, la différence entre le poids et la masse et j'en passe) et à Alex pour toutes ces années à être le major de promo et le premier d'entre nous à avoir fini sa thèse.

Merci aux potes de Châteauroux pour ces merveilleux échanges. Pendant que certains font des thèses, d'autres mènent une vie d'adulte avec de vrais métiers, des maisons et mêmes des enfants…Mais je serais le seul à avoir le titre de Docteur et ça, je saurais vous le rappeler.

« *Fabulous Fab* ». 9 ans que l'on se connait, on aura fait la thèse ensemble dans le même labo et on va la finir pratiquement en même temps. Un immense merci pour ton humour aux petits oignons (il nous reste près de 150 blagues à lire d'ailleurs), tes rapports de passage au bureau au moins une fois par jour et pour toutes les discussions que nous avons pu avoir et qui ont su me redonner du courage quand j'en avais besoin.

Je conclus ces remerciements par ma famille qui m'a toujours soutenu de près ou de loin durant ces quatre dernières années. Merci à mes parents pour m'avoir permis de me lancer dans les études universitaires et m'avoir accompagné dans mes différents choix d'orientation. Merci à ma sœur pour toutes les discussions que nous avons pu avoir et à mon frère pour ses quelques visites impromptues dans mon appartement pour prendre de mes nouvelles.

Le merci de la fin te revient Lise, toi qui a toujours cru en moi et à su me supporter et m'accompagner lors de cette épreuve qu'a été la rédaction. Malgré la présence de l'insupportable Thertone (c'est un chat, vous avez le jeu de mots ?), cela m'a fait beaucoup de bien de bosser à tes côtés.

Abstract

The formation of hydrothermal deposits depends essentially on the physico-chemical properties of the fluid and the surrounding rocks. Hydrothermal dynamics are strongly linked to thermal, hydraulic, mechanical and chemical couplings and feedback. The observation of the alterations associated with mineralisation only gives a static and fragmented overview of these complex phenomena. Numerical simulations are therefore extremely useful for assessing these couplings, either by modelling fluid flow and heat transfer, or by modelling thermodynamic equilibria between fluid and minerals. Recent advances allowed the combination of those two kinds of simulations and the results highlight that by modifying the petrophysics properties of the host rock, alteration constitute both a physical and chemical driving force during the ore deposit formation. Such development requires (i) a good implementation of the alteration in the batch equilibrium simulation and (ii) quantitative laws describing the effect of the alteration on the permeability of the rock.

This PhD focus on tourmaline, an emblematic ubiquitous mineral of the magmatic/hydrothermal transition, present in the alterations from the late stage of magmatic crystallisation to the low temperature metasomatism. However, the lack of calibrating data on tourmaline stability is a barrier to its use in thermodynamic modelling. Thus, the objectives are (i) to provide new experimental constraints on $[B_2O_3]_{fluid\_EQ}$, the boron concentration of the fluid at equilibrium with tourmaline, (ii) to assess the actual quality of tourmaline implementation in thermodynamic models, and (iii) to study the dynamic of boron metasomatism in perigranitic environment, through reactive percolation experiment.

The results obtained by batch experimentation at 600, 500 and 400°C (200 MPa, under moderately oxidising conditions) show that the tourmaline-cordierite and tourmaline-biotite equilibriums require a $[B_2O_3]_{fluid}$ ranging between 8 and 1 wt%. Experiments performed on the same assemblages but with varying fluid chemistry (pH and alkali chloride concentration) show a reduction of the $[B_2O_3]_{fluid\_EQ}$ along with important textural and compositional modifications. Those boron concentration ranges required to form tourmaline are consistent with compositional constraints from natural hydrothermal fluids and peraluminous melts. Comparison between experimental results and thermodynamic calculations of $[B_2O_3]_{fluid\_EQ}$ highlights the limitations of numerical simulations, due to the lack of a solid solution model for chemically complex tourmalines. The reactive percolation experiment was performed by infiltrating a $B(OH)_3$ brine into a spotted micaschist at 300°C and 30 MPa for 6 weeks. The global organisation of the alterations is interpreted as the result of an interplay between the local mineralogy and the fluid velocity ranging from intense leaching in the high-flow zones to pseudomorphism in low-flow zones.

Résumé

La formation des gisements hydrothermaux dépend essentiellement des propriétés physico-chimiques du fluide et de la roche encaissante. La dynamique hydrothermale est fortement liée aux couplages et rétroactions thermiques, hydrauliques, mécaniques et chimiques. L'observation des altérations associées aux minéralisations ne donne qu'un aperçu statique et parcellaire de ces phénomènes complexes. Les simulations numériques sont donc extrêmement utiles pour évaluer ces couplages, soit en modélisant l'écoulement des fluides et le transfert de chaleur, soit en modélisant les équilibres thermodynamiques entre les fluides et les minéraux. Des progrès récents ont permis de combiner ces deux types de simulations et les résultats soulignent qu'en modifiant les propriétés pétrophysiques de la roche hôte, l'altération constitue une force motrice à la fois physique et chimique lors de la formation des gisements. Un tel développement nécessite (i) une bonne implémentation de l'altération dans les simulations d'équilibre en batch et (ii) des lois quantitatives décrivant l'effet de l'altération sur la perméabilité de la roche.

Cette thèse se concentre sur la tourmaline, un minéral emblématique et omniprésent de la transition magmatique/hydrothermale, présent dans les altérations depuis le stade tardif de la cristallisation magmatique jusqu'au métasomatisme à basse température. Cependant, le manque de données calibrant la stabilité de la tourmaline est un obstacle à son utilisation dans la modélisation thermodynamique. Les objectifs sont donc (i) de fournir de nouvelles contraintes expérimentales sur $[B_2O_3]_{fluid\_EQ}$, la concentration en bore du fluide à l'équilibre avec la tourmaline, (ii) d'évaluer la qualité actuelle de l'implémentation de la tourmaline dans les modèles thermodynamiques, et (iii) d'étudier les dynamiques du métasomatisme du bore dans un environnement périgranitique, via une expérience de percolation réactive.

Les résultats obtenus par expérimentation en batch à 600, 500 et 400°C (200 MPa, en condition modérément oxydante) montrent que les équilibres tourmaline-cordiérite et tourmaline-biotite nécessitent une $[B_2O_3]_{fluid}$ compris entre 8 et 1 wt%. Les expériences réalisées sur les mêmes assemblages mais avec une chimie des fluides variable (pH et concentration en chlorure alcalin) montrent une réduction du $[B_2O_3]_{fluid\_EQ}$ ainsi que d'importantes modifications de texture et de composition. Ces gammes de concentrations en bore sont cohérentes avec les contraintes de composition des fluides hydrothermaux naturels et des magmas peralumineux. La comparaison entre les résultats expérimentaux et les calculs thermodynamiques du $[B_2O_3]_{fluid\_EQ}$ soulignent les limitations des simulations numériques, liées à l'absence de modèle de solution solide pour les tourmalines complexes. L'expérience de percolation réactive a été réalisée en infiltrant une saumure de $B(OH)_3$ dans un micaschiste tacheté à 300°C et 30 MPa pendant 6 semaines. L'organisation globale des altérations est interprétée comme le résultat d'une interaction entre la minéralogie locale et la vitesse du fluide, allant d'un lessivage intense dans les zones à fort débit à des pseudomorphoses dans les zones à faible débit.

Contents

Remerciements vii

Abstract x

Résumé xi

Contents..1

Résumé étendu 5

Introduction 7
L'équilibre tourmaline-cordiérite 8
Estimation thermodynamique de $[B_2O_3]_{fluid\_EQ}$ 10
L'équilibre tourmaline-biotite 11
Visualisation des dynamiques des processus métasomatiques 12

Chapter I: Introduction 15

I- Hydrothermal alteration: impacts and modelling 17
  A) The conceptual model of a hydrothermal deposit 17
  B) Understanding the circulation and equilibria inside a hydrothermal deposit: the use of numerical simulations 19
    1/ Modelling the fluid flow 19
    2/ Thermodynamic modelling of fluid-rock equilibria 21
    3/ Integrating alterations through dynamic permeability: the case study of Panasqueira 23
II- Tourmaline, a useful mineral in borosilicated system 25
  A) An ubiquitous complex mineral 25
  B) A petrogenetic indicator 26
  C) An indicator of fluid flow, source and composition 27
  D) An indicator of pressure and temperature conditions 30
III- Tourmaline stability in natural systems 32
  A) The boron concentration at equilibrium with tourmaline 33

B) Boron in hydrothermal fluids 35
    1/ Range of concentration 35
    2/ Speciation in fluids 38
C) An extensive P-T stability range 39
IV- Thesis outline and aims 41
References: 43

Chapter II: Tourmaline-cordierite equilibrium constraints on the boron concentration of hydrothermal fluids. 55

Introduction 57
I- Tourmaline forming reactions and end-members 58
II- Experimental and analytical methods 59
    A) Starting products 59
A) Experimental procedure 60
    B) Analytical procedures 61
    C) Choice of P-T-fO_2 conditions 62
III- Results 64
    A) Redox conditions 65
    B) Experimental products and textures 65
    C) Evolution of phase assemblages and tourmaline textures 68
        1/ Effect of $[B_2O_3]_{fluid}$ 68
        2/ Effect of temperature. 70
        3/ Effect of fO_2. 71
    D) Tourmaline compositions 71
        1/ Effect of texture 71
        2/ Effect of temperature and $[B_2O_3]_{fluid}$ 73
        3/ Effect of fO_2 75
        4/ MAS NMR results 75
IV- Discussion 76
    A) Experimental reaction mechanisms 76
    B) Thermodynamic estimation of the $[B_2O_3]_{fluid\_EQ}$ 78
        1/ Calculation 78
        2/ $B(OH)_{3(aq)}$ HKF parameters 79
        3/ Calculation of $[B_2O_3]_{fluid\_EQ}$ 80
        4/ Attempt of ideal solid solution modelling 81

C) Tourmaline textural evolution ... 84
D) Control on tourmaline composition ... 85
E) Tourmaline stability and boron fluid concentration ... 86
V- Geological implications ... 88
References ... 89

Chapter III: Experimental investigation of the tourmaline-biotite equilibrium: implication for tourmalinisation in hydrothermal perigranitic environment...95

Introduction ... 97
I- Materials and methodology ... 97
A) Tourmaline forming reactions and endmembers ... 97
B) Starting products ... 99
C) Experimental and analytical procedure ... 100
D) Choice of P-T-fO_2 conditions ... 100
II- Results ... 101
A) Redox conditions ... 101
B) Experimental products and textures ... 103
C) Evolution of phases assemblages and tourmaline textures ... 105
1/ Effect of B_2O_3 ... 106
2/ Effect of temperature ... 108
D) Tourmaline composition ... 109
1/ Effect of the textures ... 109
2/ Effect of B_2O_3 ... 109
3/ Effect of temperature ... 112
III- Discussion ... 113
A) Experimental reaction mechanism ... 113
B) Control on the composition and texture of tourmaline: comparison to tourmaline-cordierite equilibrium experiments ... 114
C) Tourmaline stability and boron fluid concentration in natural systems ... 115
References ... 117

Chapter IV: Dynamic visualisation of fluid-rock interaction in a perigranitic environment: reactive transport experiments on boron metasomatism...121

Introduction 123
- I- Material and methods 124
  - A) Starting material 124
    - 1/ Petrology 124
    - 2/ Petrophysical properties 125
  - B) Reactive percolation experiments 126
    - 1/ Experimental setup 126
    - 2/ Geochemical relevance of the condition 127
    - 3/ Fluid and mineral analysis 128
- II- Results 129
  - A) Panasqueira spotted schist 129
    - 1/ Petrography 129
    - 2/ Chemical composition 131
    - 3/ Petrophysical properties 135
  - B) Reactive percolation experiment 135
    - 1/ Permeability evolution 136
    - 2/ Macroscopic observations 137
    - 3/ General organisation of the alteration 137
  - 1/ Mineralogical evolution 139
  - 2/ Chemical evolution 142
- III- Discussion 144
  - A) Permeability evolution 144
    - 1/ A highly impermeable schist 144
    - 2/ Vein opening through hydraulic fracturing 145
  - B) Mineralogical evolution and alteration pattern 146
    - 1/ Alteration reactions 146
    - 2/ Longitudinal Vs Radial alteration fronts 148

Conclusion 149

References: 150

General conclusions 155

Appendix 159

Résumé étendu

Introduction

Les connaissances actuelles sur la tourmaline indiquent que ce minéral possède toutes les caractéristiques requises pour en faire un outil pétrologique puissant. Elle est répandue, présente dans la plupart des environnements géologiques, stable sur une partie importante de l'espace P-T-X de la croûte, présente une diffusion intracristalline négligeable, est réfractaire et accueille une large gamme d'éléments différents (Dutrow & Henry 2011 ; Marschall et Jiang 2011 ; van Hinsberg et al. 2011b). Ces propriétés lui permettent d'enregistrer des preuves de son histoire géologique dans sa composition et sa texture. De multiples études ont été réalisées afin de déchiffrer comment la composition majeure et mineure de la tourmaline (ainsi que ses isotopes) répond aux conditions P-T, à la pétrologie et à la composition des fluides de son environnement de cristallisation. Les résultats qualitatifs et/ou quantitatifs, notamment sur les coefficients de partage, permettent à des études récentes d'utiliser ce minéral accessoire comme traceur de l'évolution des fluides dans les systèmes hydrothermaux et même de reconstruire la composition des fluides (Berryman et al. 2017 ; Codeço et al. 2017 ; Harlaux et al. 2020). Cependant, ces mêmes propriétés font de la tourmaline un minéral difficile à manipuler et des utilisations plus avancées, comme en géothermobarométrie ou dans la modélisation thermodynamique, manquent encore de calibration.

Les progrès récents dans le domaine de la métallogénie des gisements hydrothermaux impliquent la combinaison des simulations multiphysiques (écoulement de chaleur et de fluides) avec la modélisation thermodynamique. Cette méthodologie, appliquée par Launay et al. (2023), souligne qu'en modifiant les propriétés pétrophysiques de la roche hôte, l'altération constitue une force motrice à la fois physique et chimique pendant la formation du gisement de minerai. La tourmaline est un minéral emblématique de la transition magmatique/hydrothermale, présent depuis le stade tardif de la cristallisation magmatique jusqu'au métasomatisme à basse température. L'application de la méthodologie de Launay et al. (2023) à la tourmalinisation permettrait de comprendre l'impact de cette altération sur son environnement hydrothermal. Ainsi, la tourmaline fournirait plus non seulement des informations sur les conditions physico-chimiques de son environnement, mais aussi sur les phénomènes de rétroaction contrôlant l'écoulement des fluides et la localisation de la minéralisation. Un tel développement nécessite (i) **une bonne implémentation de l'altération dans les modèles thermodynamiques en batch** (fonctionnement en système fermé) et (ii) des **lois quantitatives décrivant l'effet de l'altération sur la perméabilité de la roche**. Les recherches sur ce dernier point sont assez récentes et restent encore à explorer pleinement, à travers des expériences de percolation réactive à "haute température", jusqu'à 400°C (Launay et al. 2019 ; Osselin et al. 2022). Mais, dans le cas de la tourmaline, même la première condition est loin d'être remplie. Comme expliqué précédemment, le manque de données de calibration sur la stabilité de la tourmaline, notamment concernant la concentration en bore dans le système, est un obstacle à son utilisation dans la modélisation thermodynamique. Les quelques contraintes expérimentales déjà existantes sur le sujet se concentrent principalement sur des systèmes sans Fe à haute température (> 500°C) et présentent quelques incohérences en fonction de la composition du fluide utilisé.

Cette thèse vise, dans une première partie, à compléter et à fournir de nouvelles contraintes expérimentales sur $[B_2O_3]_{fluid\_EQ}$, la concentration en bore du fluide à l'équilibre avec la tourmaline. Des expériences en batch dans des cuves sous pression chauffées intérieurement ont été menées entre 400 et 600°C à 200 MPa et dans des conditions de fO_2 contrôlées, afin de suivre l'évolution de la stabilité de la tourmaline. Bien qu'elle soit relativement rare dans les systèmes naturels, la tourmalinisation de la cordiérite est étudiée depuis longtemps et est la seule réaction pour laquelle la $[B_2O_3]_{fluid\_EQ}$ a été mesurée (Weisbrod et al. 1986 ; von Goerne et al. 1999b). Le système minéralogique représenté a l'avantage d'être exempt de Fe, limitant ainsi l'effet du fO_2, et d'être bien corrélé avec les systèmes magmatiques et les fusions peralumineuses. Afin de constituer une base de référence solide, le **Chapitre II** fournit de nouvelles contraintes expérimentales sur les équilibres tourmaline + cordiérite + albite + quartz + andalousite + fluide (H_2O +$B(OH)_3$). Les évolutions texturales et compositionnelles sont interprétées comme une fonction du niveau de sursaturation du fluide et de l'effet des conditions T- fO_2. Les valeurs de la $[B_2O_3]_{fluid\_EQ}$ estimées sont directement comparables aux études précédentes sur la stabilité des tourmalines et soulignent le besoin de données sur des systèmes plus proches de ce qui peut être observé dans la nature. Ce chapitre est également l'occasion d'examiner l'ensemble des propriétés thermodynamiques standard de la tourmaline et de voir dans quelle mesure les calculs basés sur ces propriétés sont capables de reproduire les données expérimentales. Le **Chapitre III** aborde la question de la stabilité de la tourmaline dans un système plus naturel, en suivant la même méthodologie qu'au chapitre II. La $[B_2O_3]_{fluid\_EQ}$ est estimé expérimentalement pour les équilibres entre la biotite et la tourmaline, la forme la plus courante de tourmalinisation dans les systèmes périgranitiques (e.g. Lecumberri-Sanchez et al. 2017 ; Orlando et al. 2017 ; Harlaux et al. 2020).

Le **Chapitre IV** traite d'une approche dynamique du métasomatisme du bore en milieu périgranitique. L'étude rapporte les résultats d'une expérience de percolation réactive sur un micaschiste tacheté de Panasqueira, infiltré avec une saumure de B(OH)3 à 300°C pendant 5 semaines. Les changements de perméabilité ont été suivis et l'évolution pétrographique, texturale et chimique des carottes après l'expérience, ainsi que la composition des fluides de sortie ont été analysées. Bien que la variation de la perméabilité ne réponde pas à une circulation généralisée du fluide dans la roche, l'expérience reproduit l'ouverture d'une veine par fracturation hydraulique. Les caractéristiques de l'évolution des fronts d'altération de la paroi sont décryptées afin d'explorer les interactions entre la chimie du système, la cinétique de réaction et la circulation locale des fluides.

L'équilibre tourmaline-cordiérite

Des assemblages de tourmaline naturelle et de cordiérite ont été équilibrés expérimentalement en présence d'albite, d'andalousite, de quartz et de solutions H_2O-B_2O_3 afin de contraindre la concentration en bore des fluides hydrothermaux. Les expériences ont été réalisées à pression constante (200 MPa) et à 400, 500 et 600°C, dans des conditions contrôlées de fO_2 allant de NNO+0,8 à NNO+5,3 et pour des durées allant de 2 à 8 semaines. Des expériences forward et reverse, à partir d'assemblages sans tourmaline et avec tourmaline respectivement, ont été réalisées. Dans des conditions modérément oxydantes (NNO+0.8 à NNO+1.9), la cordiérite plus l'albite et l'andalousite réagissent en tourmaline plus quartz pour $[B_2O_3]_{fluide}$ > 3.4 wt% à 600°C et pour $[B_2O_3]_{fluide}$ > 2.1 wt% à 500°C (Fig. RE.1). L'augmentation de $[B_2O_3]_{fluide}$ au-dessus de ~5 wt% stabilise la tourmaline et le quartz. A 400°C, la tourmaline apparaît pour $[B_2O_3]_{fluide}$ > 2.0 wt% mais la smectite remplace la cordiérite dans l'assemblage réagissant. Des expériences dans des conditions fortement oxydantes

(NNO+5.3) montrent que la $[B_2O_3]_{fluide}$ nécessaire à l'apparition de la tourmaline ne varie pas de manière significative avec la fO_2. Les expériences reverses n'ont pas été concluantes car la réaction inverse de la tourmaline à la cordiérite n'a pas pu être démontrée. Les tourmalines expérimentales présentent différents types de textures : gerbes de fines tiges de tourmaline (Groupe I), grands cristaux allongés (Groupe II), agrégats fibro-radiés (Groupe IIIa), longues fibres (Groupe IIIb) et excroissances (Groupe IV). La nucléation hétérogène sur les grains de cordiérite et/ou d'albite est observée à faible $[B_2O_3]_{fluide}$ et la nucléation homogène dans le fluide à $[B_2O_3]_{fluide}$ plus élevée. La croissance de la tourmaline suit deux régimes de sursaturation (locale et globale) des composants formant la tourmaline dans le fluide.

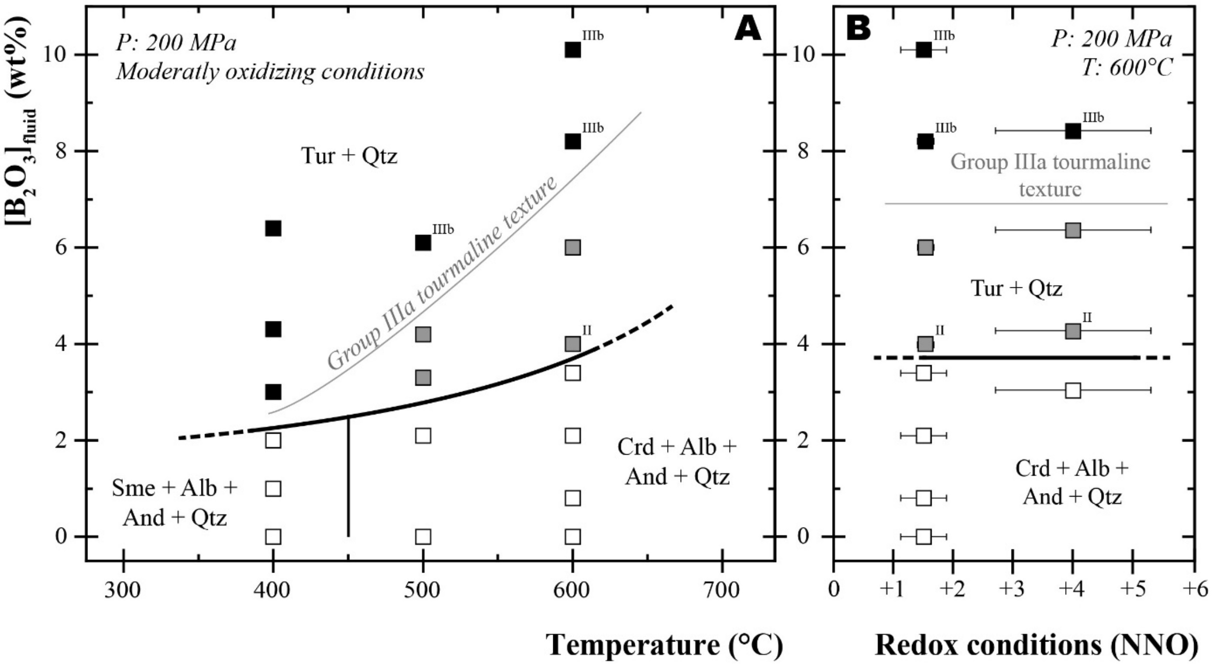

Figure RE. 1: Evolution des assemblages de phases et des textures de tourmaline dans les expériences. (A) Diagramme $[B_2O_3]_{fluide}$ vs. Température montrant les résultats expérimentaux dans des conditions modérément oxydantes. (B) Diagramme $[B_2O_3]_{fluide}$ vs. fO_2 (NNO représente l'écart par rapport au tampon Ni-NiO à la même T et P) montrant les résultats expérimentaux à 600°C. Les symboles pleins et ouverts indiquent respectivement la présence et l'absence de tourmaline dans les produits expérimentaux. La tourmaline du Groupe I est présente dans toutes les charges contenant de la tourmaline. Les symboles noirs et gris indiquent respectivement la présence et l'absence de tourmaline du Groupe IIIa. La présence de tourmaline des Groupes II et IIIb est indiquée par des exposants au-dessus du symbole correspondant. Les lignes épaisses représentent les limites de stabilité et les lignes fines délimitent les conditions d'apparition des tourmalines du Groupe IIIa. Abréviations : Alb = albite ; And = andalousite ; Crd = cordiérite ; FK = feldspath K ; Qtz = quartz ; Sme = smectite ; Tur = tourmaline.

Les analyses à la microsonde électronique montrent que les tourmalines expérimentales sont des solutions solides entre principalement la dravite ($NaMg_3Al_6Si_6O_{18}(BO_3)_3(OH)_4$), magnesiofoitite ($[]_X(Mg_2Al)Al_6Si_6O_{18}(BO_3)_3(OH)_4$) et schorl ($NaFe_3Al_6Si_6O_{18}(BO_3)_3(OH)_4$). Le rapport atomique (at.) Fe/(Fe+Mg) est proche de celui de la cordiérite de départ, malgré des variations significatives dans une charge donnée et du noyau au bord (noyau riche en Fe et Ca allant vers des bords riches en Mg et Na), affectant également le at. Ca/(Ca+Na). Ceci reflète les changements dans les mécanismes de nucléation et de croissance de la tourmaline au cours des expériences, contrôlés par l'évolution de la composition du fluide et le niveau de sursaturation des composants formant la tourmaline. La diminution de la température de 500 à

400°C est marquée par la substitution alcaline déficiente NaMg → $[]_X$Al, tandis que l'augmentation de la condition d'oxydation à 600°C diminue légèrement la teneur en Ca et Al de la tourmaline.

Nos déterminations de la $[B_2O_3]_{\text{fluide}}$ à l'équilibre avec la tourmaline et la cordiérite sont globalement en bon accord avec les études expérimentales antérieures de tourmalinisation, mais la comparaison met également en évidence l'effet potentiel d'autres variables telles que la chimie des fluides (pH et concentration de chlorure alcalin) sur la stabilité de la tourmaline. La faible concentration en bore nécessaire pour former de la tourmaline à partir de la cordiérite est cohérente avec les contraintes de composition des fluides hydrothermaux naturels et des magmas peralumineux.

Estimation thermodynamique de $[B_2O_3]_{\text{fluid\_EQ}}$

En se basant sur l'écriture de la constante d'équilibre des réactions formant la tourmaline à partir de cordiérite, la $[B_2O_3]_{\text{fluid}}$ à l'équilibre peut être calculé. Les calculs se sont basés sur différents sets de données thermodynamiques, notamment concernant les paramètres HKF de l'espèce aqueuse $B(OH)_3$ et les propriétés thermodynamiques standard de la tourmaline (mesure par calorimétrie d'Ogorodova et al. (2012) ou estimation par le modèle des polyèdres de van Hinsberg & Schumacher (2007)).

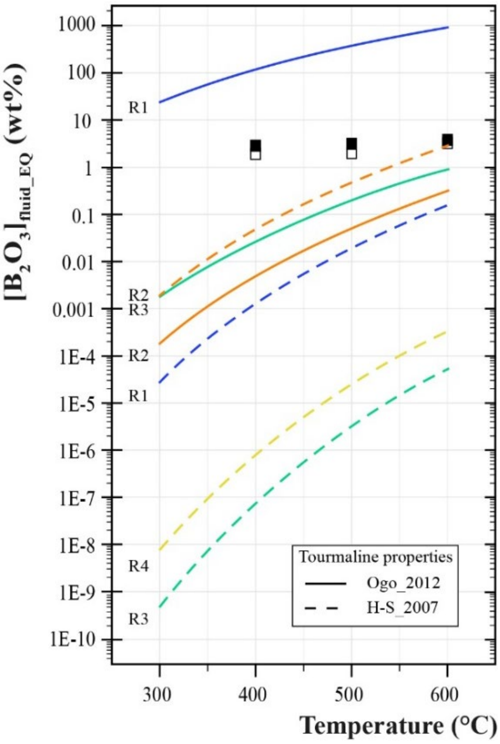

Figure RE. 2: $[B_2O_3]_{\text{fluide\_EQ}}$ calculée en fonction de la température pour les quatre réactions de formation de tourmaline considérées (R1, R2, R3, R4) et les deux ensembles de données thermodynamiques de tourmaline utilisés dans les calculs (lignes pleines pour Ogorodova et al., 2012 (Ogo_2012) et lignes pointillées pour van Hinsberg & Schumacher, 2007b (H-S_2007)). Les contraintes expérimentales sur $[B_2O_3]_{\text{fluide\_EQ}}$ issues de cette étude sont représentées par des symboles pleins (tourmaline présente) et ouverts (tourmaline absente).

Tous les calculs montrent une corrélation positive entre la $[B_2O_3]_{\text{fluid\_EQ}}$ et la température, comme observé expérimentalement, mais diffèrent de plusieurs ordres de grandeur par rapport aux points expérimentaux (Fig. RE.2). Des différences importantes dans l'estimation de la $[B_2O_3]_{\text{fluid\_EQ}}$ apparaissent en fonction des propriétés thermodynamiques utilisées pour la tourmaline, alors que les deux sets ne présentent que peu de différence. Par conséquent, les résultats expérimentaux fournis par cette étude peuvent apporter de nouvelles contraintes plus précises sur les propriétés thermodynamiques de la tourmaline. Cependant, le calcul effectué concerne uniquement des compositions de pôles pures, alors que les tourmalines expérimentales sont des solutions solides dont la composition varie avec T. Lorsque les $[B_2O_3]_{fluid\_EQ}$ sont calculées à partir des propriétés d'Ogorodova et al. (2012), les réactions de formation de la tourmaline peuvent être divisées en deux groupes (Fig. RE.2): celles qui déstabilise la tourmaline expérimentale (surestimation de $[B_2O_3]_{fluid\_EQ}$ par rapport aux expériences; R1) et celles qui la stabilise (sous-estimation du $[B_2O_3]_{fluid\_EQ}$; R2 et R3). En utilisant un modèle de solution solide idéal très simplifié entre ces pôles purs, les calculs thermodynamiques arrivent à coïncider avec les données expérimentales. Bien qu'encourageant, ces résultats soulignent le besoin d'avoir des données thermodynamiques sur les propriétés de mélange des pôles purs de la tourmaline afin de pouvoir l'incorporer dans des modèles prédictifs plus complexes.

L'équilibre tourmaline-biotite

Des assemblages de tourmaline naturelle et de biotite ont été équilibrés expérimentalement en présence d'albite, d'andalousite, de quartz, de feldspath potassique et de solutions H_2O-B_2O_3 afin de contraindre la concentration en bore des fluides hydrothermaux. Contrairement à la cordiérite qui limitait les applications aux systèmes peralumineux, la tourmalinisation de la biotite est une réaction d'altération courante dans de nombreux contextes géologiques différents.

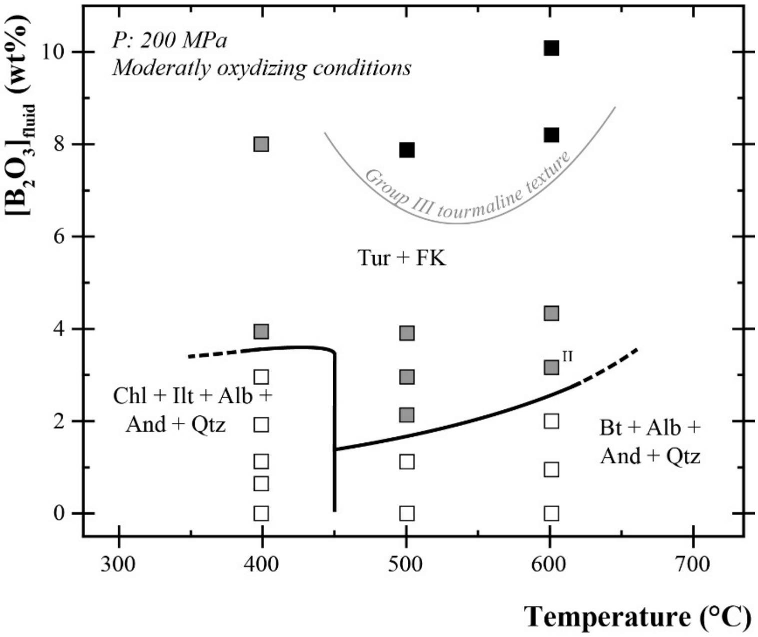

Figure RE. 3: Évolution des assemblages de phases et des textures de tourmaline dans les expériences, représenté dans un diagramme $[B_2O_3]_{fluid}$ en fonction de la température. Abréviations : Alb = albite ; And = andalousite ; Bt = biotite ; Chl = chlorite ; FK = feldspath K ; Ilt = illite ; Qtz = quartz ; Tur = tourmaline.

Les expériences ont été réalisées à pression constante (200 MPa) et à 400, 500 et 600°C, dans des conditions contrôlées de fO_2 allant de NNO+0,8 à NNO+5,3 et pour des durées allant de 2 à 8 semaines. Des expériences forward et reverse, à partir d'assemblages sans tourmaline et avec tourmaline respectivement, ont été réalisées. Dans des conditions modérément oxydantes (NNO+1.0 à NNO+2.6), la biotite plus l'albite, le quartz et l'andalousite réagissent en tourmaline plus feldspath potassique pour $[B_2O_3]_{fluide} > 2.0$ wt% à 600°C et pour $[B_2O_3]_{fluide} > 1.1$ wt% à 500°C (Fig. RE.3). A 400°C, la tourmaline apparaît pour $[B_2O_3]_{fluide} > 2.9$ wt% à cause de la déstabilisation de la biotite en chlorite + illite. Les expériences reverses n'ont pas été concluantes, sauf lorsqu'elles contenaient des tourmalines expérimentales des expériences forward. La tourmaline présente alors des figures de dissolution sur ses arêtes, tandis que la biotite devient automorphe, attestant donc de la réversibilité de l'équilibre. Les contrôles sur la texture et la chimie des tourmalines sont identiques à ce qui a pu être décrit pour l'équilibre tourmaline-cordiérite, à la seule différence que seul le at. Ca/(Ca+Na) est impacté.

La gamme de $[B_2O_3]_{fluide}$ déterminée pour ce nouvel équilibre est très similaire à celle reportée pour la cordiérite. L'association fréquente entre tourmaline et biotite/chlorite à des températures ≤ 400°C requiert, si l'on se fie aux seules données expérimentales, des concentrations en bore dans le fluide trop important pour la plupart des systèmes hydrothermaux. La comparaison avec des systèmes naturels met en avant, encore une fois, un fort effet de la chimie des fluides sur la stabilité de la tourmaline.

Visualisation des dynamiques des processus métasomatiques

Cette étude présente les résultats d'une expérience de percolation réactive d'une saumure de $B(OH)_3$ à 300°C et 300 bars dans un schiste tacheté naturel afin d'étudier la dynamique des réactions métasomatiques dans un environnement riche en bore. En raison de la très faible perméabilité de la roche et de la faible pression effective fixée dans les premiers jours, le fluide a pu créer et se concentrer dans un canal entre l'enveloppe Au et la carotte. Ainsi, la perméabilité mesurée dans cette expérience ne reflète pas les variations des propriétés pétrophysiques de la roche, mais reproduit plutôt l'ouverture d'un filon par fracturation hydraulique avec l'altération de la paroi rocheuse associée. Les observations générales et l'analyse de la carotte et du fluide de sortie après l'expérience montrent une forte augmentation de la porosité le long des canaux due à la dissolution du quartz (Fig. RE 4). Causée par la présence de $B(OH)_3$ dans le fluide, cette altération est la seule qui affecte à la fois la composition de l'ensemble de la roche et le fluide de sortie.

La localisation de l'altération est contrôlée localement par la relation entre la vitesse de réaction et la vitesse du fluide. Les zones à fort débit, comme le chenal, forment un front d'altération longitudinal où la lixiviation du quartz est prédominante. Dans cet environnement où la réaction est limitée, les solutés sont mobilisés par advection et quittent le noyau sans pouvoir précipiter plus bas. L'altération de la matrice schisteuse correspond à des zones de faible débit où le transport, par diffusion, permet la formation d'un front d'altération radial net. L'altération des minéraux primaires se produit plus localement, formant une interface couplant dissolution-précipitation (par exemple la pseudomorphose de la sidérite en fayalite). Les différents régimes décrits dans cette expérience (zone de haut débit dominée par des processus advectifs Vs zone de bas débit dominée par des processus de diffusion) correspondent bien à l'altération des veines et des parois rocheuses décrite dans l'environnement naturel.

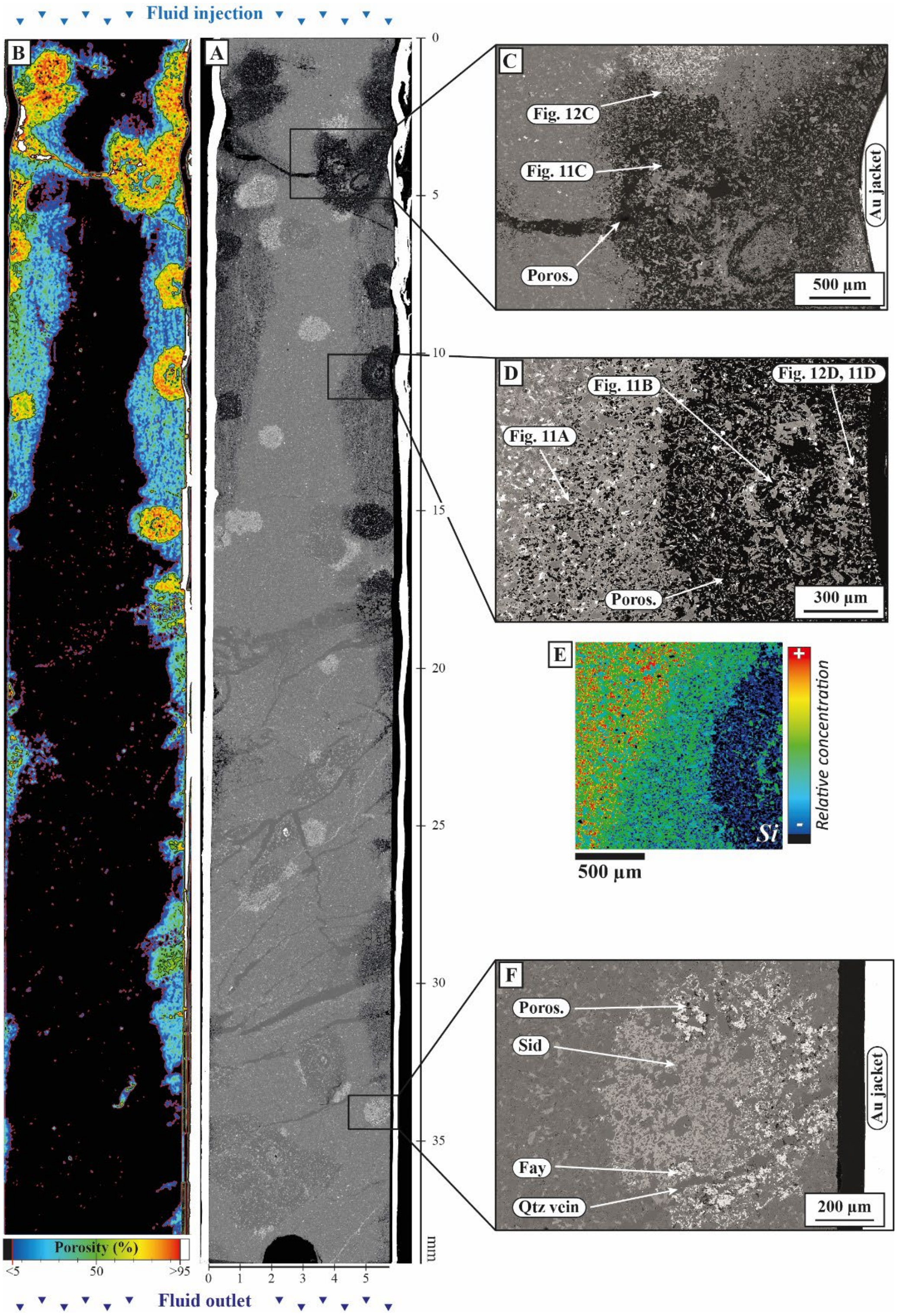

Figure RE. 4: (A) Panorama MEB de la carotte ayant réagi. (B) Cartographie de la porosité de la carotte, calculée par analyse d'images. (C) Image MEB d'une grande zone de haute porosité (en noir) située près de la section d'injection. (D) Image MEB d'une zone de haute porosité et de la matrice qui l'entoure. (E) Cartographie élémentaire du Si acquise sur (D). (F) Image MEB d'une tache de carbonate près de la section de sortie de la carotte, présentant des changements minéralogiques sur son bord droit. Toutes les images sont orientées de la même manière, avec l'injection du fluide expérimental du haut vers le bas.

Chapter I: Introduction

I- Hydrothermal alteration: impacts and modelling

A) The conceptual model of a hydrothermal deposit

Based on the description of the physical and compositional attributes of numerous deposits, explorer and researcher have been led to recognise those unusual geological occurrences as potentially belonging to diverse types of ore deposits. Beyond the work of description, these classifications have allowed to put forward genetic processes on these objects. Heinrich & Candela (2014), rationalised those processes by three factors: the global-scale tectonic settings, the interactions of endogenous processes with the atmosphere and the type of medium allowing selective components transport. The nature of the mobile phase yields to a global subdivision between the magmatic, hydrothermal and surface ore deposits (Table 1). Among the different hydrothermal ore deposits, an important part of them is linked to magmatic processes either genetically, in the case of magmatic-hydrothermal deposits (e.g. Porphyry deposits, Sn-W veins and greisens, Skarns), or as an external energy source (e.g. VMS, IOCG, orogenic gold deposits). Those magmatic-related deposits are strategic mineralised systems that can host important resources of W, Sn, Cu, Mo, Au, Ag, Zn, Pb (Table 1).

Process, transport medium	***Ore deposit type***	***Key source for***	***Important regions***
A. Orthomagmatic ore deposits: Element enrichment from melts at high T, without essential involvement of aqueous fluids			
B. Hydrothermal ore deposits: Enrichment by selective dissolution, transport and precipitation from aqueous fluids of different sources			
Fluid-saturation of H_2O-bearing magmas: Magmatic-hydrothermal	**Porphyry deposits** ('Cu-Mo-Au porphyries')	**Cu**; **Mo** Au	Chile, USA
	Sn-W-veins and replacement deposits	**Sn**, W (Cu, Pb, Ag)	Russia, China, Bolivia
	Skarn-deposits (calc-silicate replacement)	**W**, Cu, Au	China (W – scheelite)
Continental geothermal systems (± shallow magmatic fluids)	**Epithermal veins** und hydrothermal breccias	**Au, Hg** (Ag, Pb, Zn)	Circumpacific rim
Continental evaporite brines heated by magmatism ± magmatic fluids	**Iron Oxide Cu-Au (-U-REE) deposits** ('IOCG') deposits	Cu, Au, U, Fe, REE	Aus, Brazil, Chile
Seawater ± magmatic fluid convection through oceanic crust and submarine volcanoes	**Volcanogenic massive sulfide deposits** 'black smoker' systems and older equivalents	Cu, Zn (Pb, Au, Sn)	Can, Iberia, Aus Cyprus Kuroko; Kermadec
Metamorphic dehydration ± deep magmatic fluids ± basin fluid interaction	**Orogenic ('metamorphogenic') gold deposits** in Archean greenstones & young orogens	**Au**	Can, Aus, Brazil USA, Uzbekistan
	Carlin-type gold deposits in sediments	Au	USA, China
Connate or evaporite-derived basin brines flowing through sedimentary ± underlying basement rocks	**Sediment-hosted Cu ± Co deposits**	Cu, **Co**, Ag	Central Africa, Poland
	Stratiform Pb-Zn-Ag-deposits ('sedex' = sedimentary-exhalative, early-diagenetic)	**Pb**, Zn, **Ag**	Can, Aus, Ireland
	Mississippi Valley-type (MVT) Pb-Zn epigenetic replacement in carbonates ± sandstones	Pb, **Zn**, **Cd**; F	USA, Can
	Five-Element Silver Veins	Ag, Ni, Co As, Bi	N-Europe, Can
Deep infiltration of oxygenated surface waters	**Sandstone uranium deposits**	**U**, V	USA, Khazakstan
	Vein- and **unconformity-related U deposits**	**U** (Au, Pd, Pt)	Can, Aus
C. Surface ore deposits, forming at the interface between solid Earth and hydrosphere + atmosphere			

Table 1: Major ore deposit types of elemental resources (modified from Heinrich & Candela (2014)).

The objective of many studies in economic geology is the creation of genetic models explaining and connecting the various processes leading to the formation of deposits. In the case of hydrothermal deposits, they can be summarised in a general conceptual model based on the variations of concentrations in a flow (Pélissonier 1965; Heinrich and Candela 2014). It is divided into 3 stages separated in space and time: (1) a source for metals, (2) a transport and (3) a deposition zone (Fig. 1). In addition, a fourth phase can be considered, involving a zone and/or an age of modification (dismantling of the deposit by remobilisation, alteration or metamorphism).

- The source area is defined by the notion of fertility. Metals must be available either in already enriched zones or in low concentration but in a large volume of rocks. These elements are leached and mobilised by ligand-rich aqueous fluids (e.g. Cl^-, F^-, H_2S, OH^-), serving as transport agents. In perigranitic deposits (deposits located near plutonic intrusions and sharing a genetic link with the said intrusion), metals may be derived from the enclosing rocks or from residual enriched magmatic fluids. The fluid usually comes from several sources at the same time (meteoric, exsolution from the melt, etc.), which can also contribute to the supply of metallic elements.
- The metal-bearing fluid circulates within the rocks through structures of enhanced permeability (lithological facies, faults, facies transitions, etc.). In addition to allowing large-scale fluid migration, these structures drain a large volume of mineralising fluid. This focus leads to a local increase in metal flow within a small volume of rock (Fig. 1), an essential condition for the formation of a large deposit.

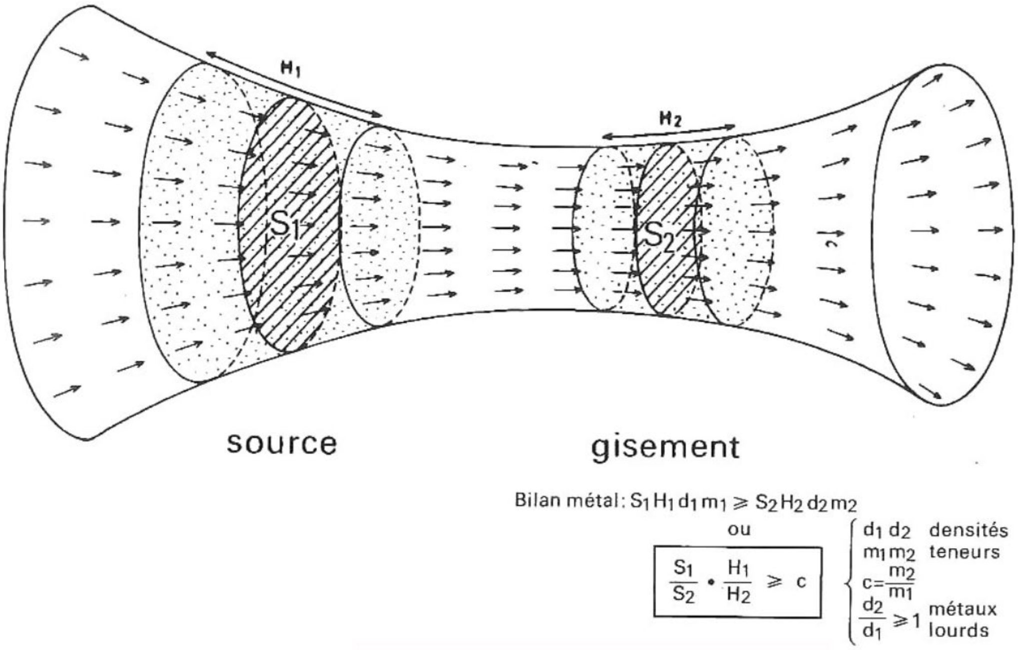

Figure 1: Conceptual genetic model for hydrothermal deposits (Pélissonier, 1965)

- These focus zones may be subject to changes in their physico-chemical conditions such as variations in temperature (T), pressure (P), pH, redox conditions(fO_2) and/or fluid composition. These changes are generally induced by boiling of the mineralising fluid, by its mixing with a fluid from another reservoir or by important fluid-rock interactions. These various processes lead to the destabilisation of the

> fluids and the precipitation of metal-rich minerals in the primary or secondary porosity of the host rock. It is this phase or this cycle of phases, in the case of juxtaposition of hydrothermal cycles, which forms the hydrothermal deposits as observed on the field.

The large scale of ore-forming systems requires a physical driving force for advective material transport by flowing fluids, and chemical driving forces for reactions between minerals and the transporting phases, i.e. a solubility gradient along the flow path of the fluids (Heinrich & Candela 2014). Those solubility gradients are responsible for metal enrichment as well as for the development of alteration along the transport path. Hydrothermal alteration is defined as a chemical replacement or modification of the original minerals in a rock by new minerals or composition. The hydrothermal fluid delivers the chemical reactants and removes the aqueous reaction products (Reed 1997).Tracking those specific relative enrichment or depletion of elements, or changes to elements speciation or mineralogical associations, are a common prospecting technique allowing deposit reconnaissance at regional scale.

An understanding of hydrothermal alteration is of value because it provides insights into the physico-chemical attributes and origin of the fluid and serves as an exploration guide. However, those systems are particularly complex, involving thermal, hydraulic, mechanic and chemical (THMC) coupling and feedback. Those relations are difficult to evaluate, due to the fact that practically all ore deposits are fossil system. Thus, numerical simulations, are of great help to assess those coupling, either by modelling the fluid flow and heat transfer or by modelling the thermodynamics of fluid-mineral equilibria.

B) Understanding the circulation and equilibria inside a hydrothermal deposit: the use of numerical simulations

1/ Modelling the fluid flow

As explained previously, the formation of a hydrothermal deposit requires the transport and focus of the metal-bearing fluids. In magmatic-hydrothermal systems, fluid flow can be described with a continuum, porous medium approach according to Darcy’s law. This law describes a non-turbulent and incompressible fluid flow through a porous medium at medium and large scale:

$$\vec{\boldsymbol{q}} = -\frac{\boldsymbol{k}}{\mu_{\boldsymbol{f}}}\left(\vec{\boldsymbol{\nabla}}\boldsymbol{P} - \boldsymbol{\rho}_{\boldsymbol{f}}\vec{\boldsymbol{g}}\right) \qquad \boldsymbol{Eq}\,(1)$$

The Darcy velocity $\vec{q}$ (volumetric flow rate, in m/s) is proportional to the pressure gradient $\vec{\nabla}P$ (Pa/m, along the x, y and z spatial axes) minus the hydrostatic pressure differential caused by the weight of the fluid $\rho_f\vec{g}$ (ρ_f in kg/m^{3}and $\vec{g}$ = 9,81 m/s^2). The flux rate is also dependent on the properties of the fluid through its dynamic viscosity μ_f (Pa/s) and the properties of the host medium/rock through its intrinsic permeability k (in m^2). Permeability expresses the ease with which the fluid can flow through the porous and/or fractured medium considered. It is interesting to note that it is the only parameter in Darcy's law that depends on the properties of the surrounding rock.

By coupling this law with heat transfer and state equation driving the density variation, one can numerically simulate the functioning of a hydrothermal circulation as a heat (and sometimes also chemical) flows through the crust (Ague 2014; Ingebritsen & Gleeson 2015). For example, Weis (2015) achieve to simulate a multiphase flow of a H_2O-NaCl fluid in a perigranitic environment, in order to reproduce the characteristics of porphyry copper and epithermal systems and locate the high-flow areas (Fig. 2).

His models are based on a dynamic value of the permeability, incorporating (i) depth-dependent permeability profile characteristics for tectonically active crust, (ii) pressure- and temperature-dependent relationship describing hydraulic fracturing and (iii) the transition from brittle to ductile rock behaviour. Another specificity is the implementation of a thermodynamic model that can accurately describe the phase relation and fluid properties of a variably miscible H_2O-NaCl fluid (based on Haar et al. 1984; Driesner 2007; Driesner & Heinrich 2007). The initial geometry considers a magma chamber that conductively heats the surrounding homogeneous host rock and serves as the driving force for the convection of ambient fluids. The simulation demonstrates that porphyry systems are constructed through repeated events of hydraulic fracturing, allowing magmatic fluid pulses toward the surface. It also highlights the preponderant effect of the saline fluid buoyancy on the dynamic of the systems, resulting in the physical separation between the porphyry deposit (dominated by ascending magmatic fluids under near-lithostatic pressure) and the related epithermal deposits (dominated by convection of colder meteoric fluids under near-hydrostatic pressure).

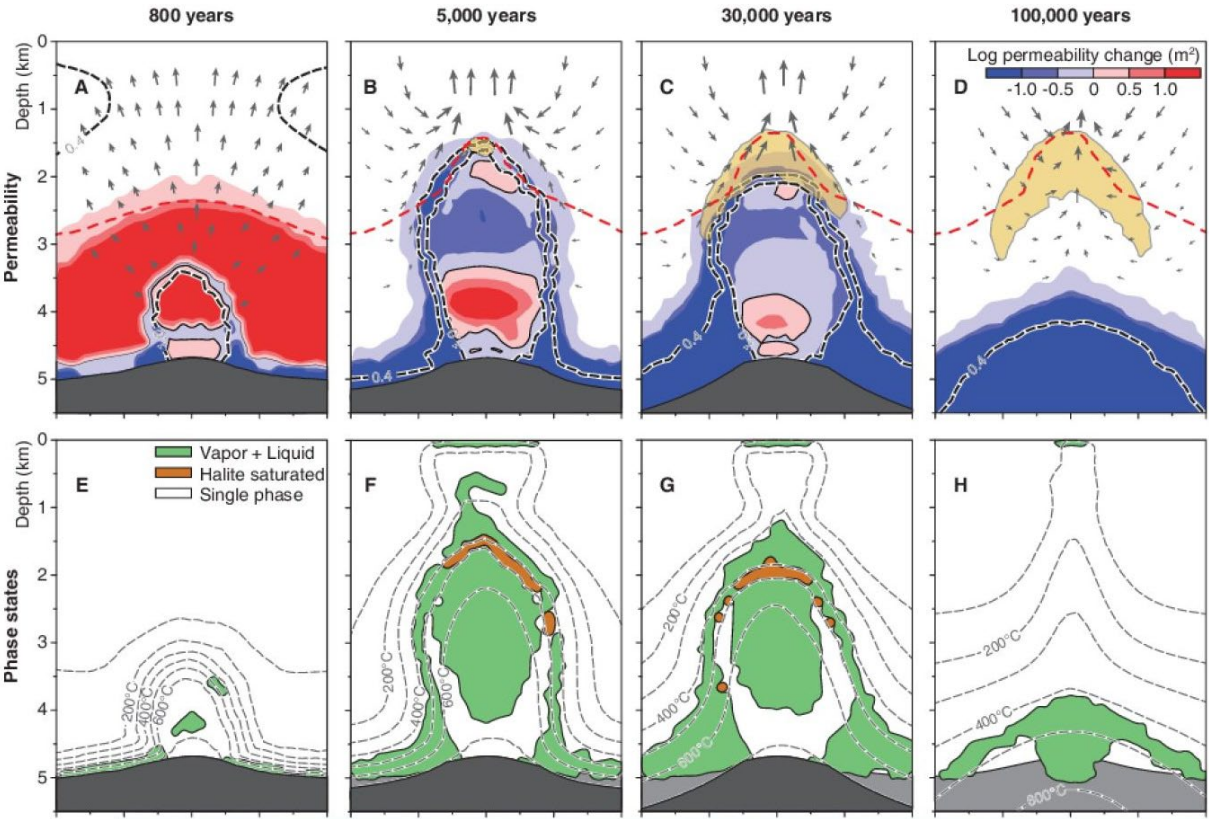

Figure 2: Temporal and spatial evolution of the hydrology of porphyry copper systems. A-D: Dynamic permeability changes in reference to the background value after 800, 5 000, 30 000 and 100 000 years of simulation time. E-H: Temperature distribution and multiphase fluid states. The black area represents the magma chamber and the light grey area the solidified pluton. (From Weis, 2015)

2/ Thermodynamic modelling of fluid-rock equilibria

Physical transport by a flow of heat and matter systematically leads to chemical interactions between the transporting fluid and the mineral composing the host rocks. Those interactions, coupled with P, T, pH and fO_2 conditions control the solubility gradient along the fluid transport path. Thermodynamic modelling of fluid-rock equilibria deals with various aspects of these chemically complex systems (e.g. Reed 1997; Anderson 1998; Halter et al. 1998; Tagirov & Schott 2001; Heinrich 2005; Dolejš & Wagner 2008; Liu & Xiao 2020; Hurtig et al. 2021). Those simulations predict the chemistry of the fluids and the stable mineral assemblages between evolving equilibrium states. To calculate accurately the stability of these minerals, aqueous species, minerals and gases requires the development of adequate activity models, equation of state and underlying robust thermodynamic databases to correct for P, T and nonideality of solutions (Gysi et al. 2020; e.g. Johnson et al. 1992; Holland and Powell 2011; Blanc et al. 2012; Wagner et al. 2012; Reed and Palandri 2014).

By using different kinds of models depending on the system and variable of interest, researchers have been able to describe the equilibrium controlling the hydrothermal system chemistry. The Fig. 3, from Hurtig et al. (2021), represent the simplified description of porphyry and epithermal ore deposits through various thermodynamic models, focusing on metal

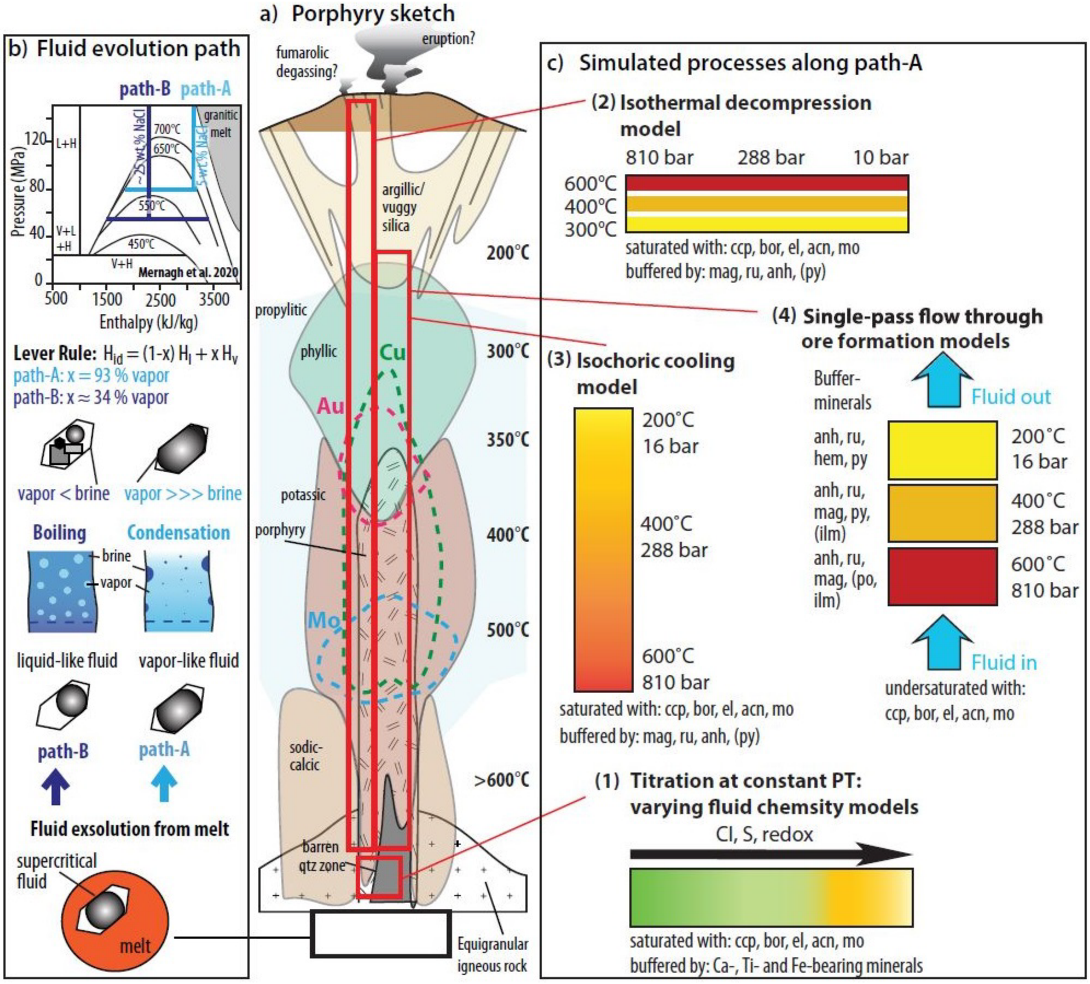

Figure 3: (A.) Schematic sketch of a porphyry ore deposit, showing the overlapping alteration and ore zones. (B.) Illustration of the fluid evolution along path A for an intermediate-density vapour-dominated pathway and along path B for liquid-dominated pathways. (C.) Schematic sketches of simulated processes. (From Hurtig et al., 2021)

transport. With regards to the results of fluid inclusion study and phase separation mechanism occurring in those systems, only the gas phase was simulated (no vapour-liquid partitioning). Four numerical setups (Fig. 3) were employed to understand (1) the effect of fluid chemistry on metal solubility and ratios at high temperature (through titration of Cl, S and O in the vapour-like fluid), (2) the effect of isothermal decompression and (3) isochoric cooling on metal mobility and metal ratios, and (4) single-pass flow-through ore formation and metal zoning models. The models predict that vapour-like fluids may transport and efficiently precipitate metals in concentrations sufficient to form porphyry ore deposits. The fluid composition and P-T-fO_2 evolution paths of vapour-like and intermediate-density fluids have a strong effect on metal solubility and, thus, exert an important control on their metal ratios and zoning.

Reed et al. (2013) also work on porphyry system through thermodynamic simulations. They didn't focus their work on metal mobility but rather on the alteration types caused by this interaction. Through modelling the titration of the granite into a finite volume of magmatic fluid (i.e. batch equilibrium modelling) between 600 and 200°C at 100 MPa, they obtain a petrographic diagram (Fig. 4) showing the absence or presence of minerals as a function of the water/rock (W/R) ratio. W/R ratio can be used as a proxy to describe the spatial and temporal evolution of alteration patterns in hydrothermal systems (Reed 1997). From the high-T biotite-feldspar-andalusite to the low-T sericite-pyrite-quartz and main argillic and propylitic stage, all the minerals composing the alteration sequence in porphyry deposits are present in the diagram. This study demonstrates that the full array of alteration observed on the field can be formed from a single initial fluid composition as it cooled and reacted with the wall rock.

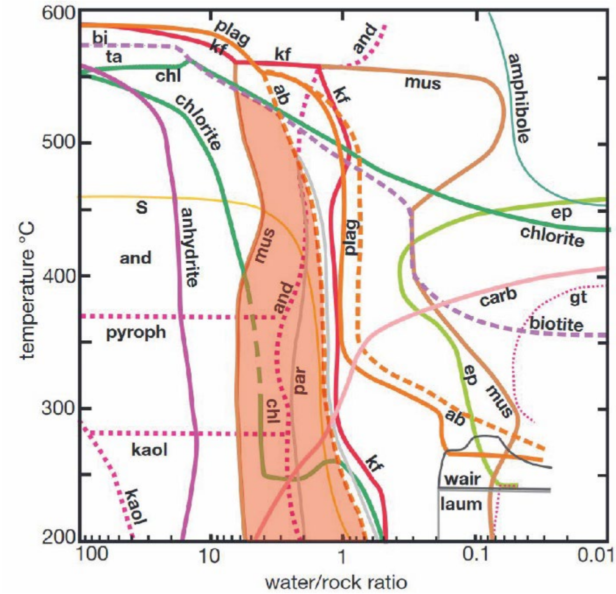

Figure 4: Alteration phase diagram showing the conditions of temperature and reaction ratio of magmatic fluid to the Butte granite that controls the presence or absence of minerals. Each curve on the diagram is labelled on the side of the curve where the relevant mineral exists; the mineral is absent on the opposite side of the curve. Quartz is present throughout the diagram. The red space corresponds to the optimum condition for greisenisation. (Diagram from Reed et al. (2013), greisen space from Launay et al. (2023))

The approach used by Hurtig et al. (2021) can be easily related to the work of Weis (2015). Indeed, the thermodynamic properties of hypersaline brine show that it contributes significantly to the metal budget, depending on the proportion of vapour to liquid, the relative mobility of the hypersaline liquid in the magmatic hydrothermal plume and the efficiency of cooling. Those parameters can be inferred by numerical simulations of fluid flow. Linking the two kinds of models by the P, T and proportion of vapour, would allow the quantification of the metal transported in the plume and the localisation of precipitation sites inside the considered geometry. In contrast, incorporating alteration patterns deduced from batch equilibrium modelling to fluid flow modelling is not straightforward and need to be done through k, the permeability of the host rock.

3/ Integrating alterations through dynamic permeability: the case study of Panasqueira

The notion of dynamic permeability used in Weis (2015) can be further developed with regards to the alteration. Indeed, fluid flow models do not explicitly account for geochemical feedback on porosity and permeability, caused by the mineralogical change in the rock. The volume change ΔV between the product and reactant minerals can be responsible for the closing or opening of the permeability along the fluid path (Jamtveit et al. 2008; Booden et al. 2011; Pollok et al. 2011; Jonas et al. 2014; Putnis 2015; Hoover et al. 2022). Those modification of permeability can greatly affect the localisation and duration of the hydraulic fracturing responsible for the various hydrothermal pulses composing the deposits (Scott & Driesner 2018; Launay et al. 2023).

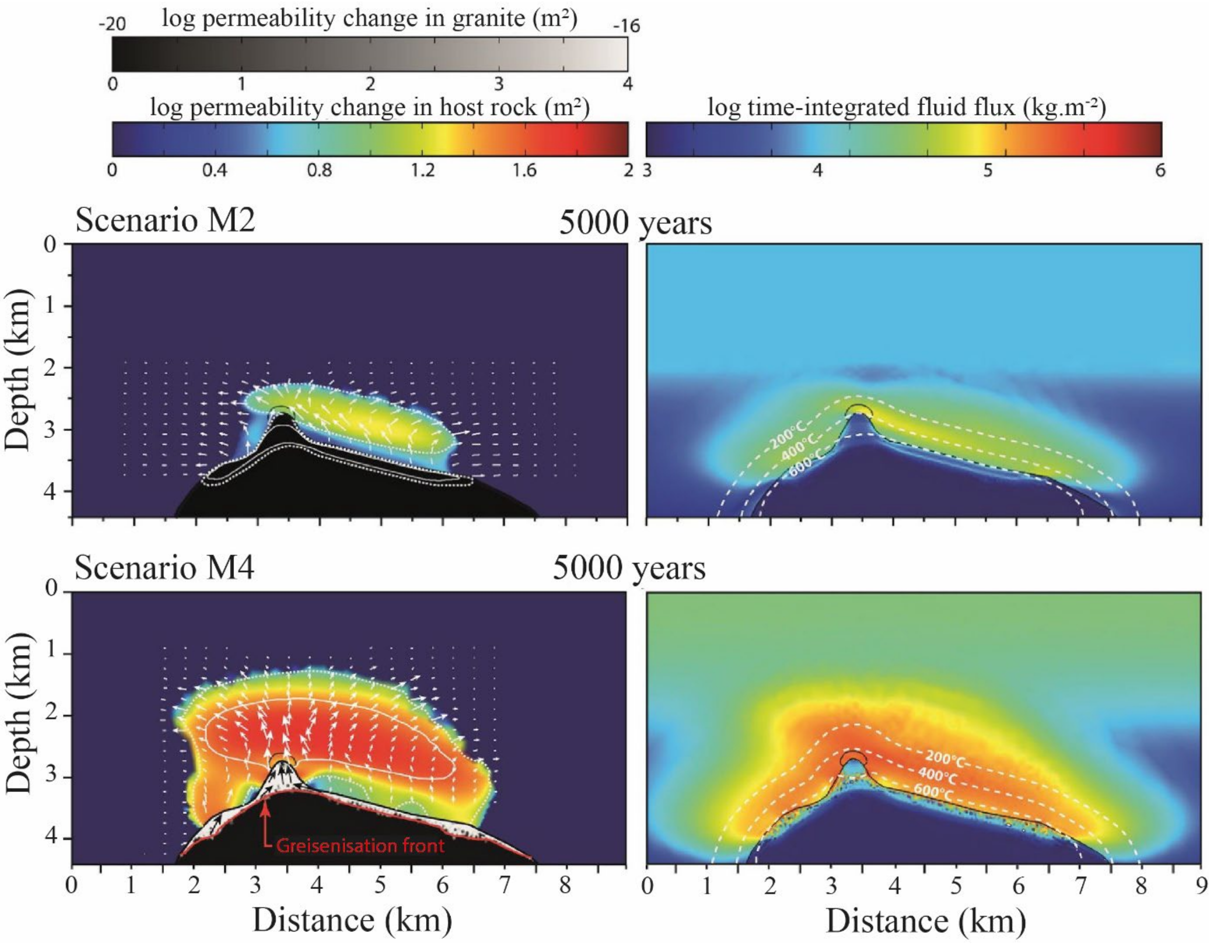

Figure 5: Results of the time evolution of the fluid flow patterns and the time-integrated fluid flux, considering the production of magmatic fluid during the granite crystallisation. Scenario M2: static granite permeability. Scenario M4: reaction-enhanced permeability (effect of greisenisation of the granite). (Modified from Launay et al. 2023).

Working on Panasqueira (Portugal), Sn-W deposits, Launay et al. (2019) studied the petrophysics properties of the greisen present in the granite roof. This alteration results from the metasomatic reaction between the granitic rock and an acidic fluid at 250-450°C and forms a coarse-grained assemblage composed mainly of quartz and muscovite (Harlov & Austrheim 2013). They measure the permeability and porosity on samples representative of incremental degrees of greisenisation, quantified through the use of an Alteration Index (AI). The measurements show that permeability increase progressively with the level of alteration, from 10^{-20} m^2 in the fresh granite to 10^{-17} m^2 in the greisen. This permeability increase was also monitored during a reactive percolation experiment, reproducing the greisenisation of the granite. The study allowed to quantify the positive correlation between porosity evolution and AI through an exponential law.

In order to include this new relationship into a fluid flow simulation, Launay et al. (2023) converted the AI as a W/R ratio according to the batch equilibrium result of Reed et al. (2013). Greisenisation is simplified as the stability field where muscovite is stable without recrystallising feldspar. An optimum for the alteration is found around W/R = 2 (Fig. 4). Thus, by calculating a time integrated W/R ratio (Schardt & Large 2009) in the fluid flow simulation, the porosity of the granite can be calculated through a function based on the exponential law between porosity and AI. Figure 5, displays the result of a fluid flow simulation around the Panasqueira pluton, considering a fixed permeability value (Scenario M2) or a greisen-enhanced permeability (Scenario M4). The comparison between both models emphasises that the permeability change induced by the greisenisation of the granite roof enhance and facilitate the expulsion of the magmatic fluids by building up more important fluid overpressure in the host rock domain. Consequently, greisenisation can constitute an important mechanism in the formation of large deposits. By locating zones of higher permeability, which determines the locus of focused fluid expulsion, the alteration enhances mass transfer within and above granitic intrusion.

Those examples on Sn-W and porphyry deposits highlight that by modifying the petrophysics properties of the host rock, alteration constitute both a physical and chemical driving force during the ore deposit formation. Considering the interplays between permeability and hydrothermal alteration means integrating feedback phenomena. Those feedback impact the focalisation and intensity of hydrothermal flows and the evolution of the W/R, an important trigger for ore deposition. Indeed, the efficiency of the ore metal deposition is limited by the mass balance between the reactive components in the advected fluid and the local rock. Therefore, final ore grade depends not only on a thermodynamic driving force, but also on the quantities of fluid and rocks interacting together (Heinrich & Candela 2014). For example, wolframite precipitation in Panasqueira is triggered by the release of Fe in the fluid due to the tourmalinisation of the host rock (Lecumberri-Sanchez et al. 2017). The iron mobility, and so, its availability, depends on the permeability of the rock being altered. If Fe is the limiting factor for wolframite precipitation, then permeability is a first order parameter on the W-ore grade. For example, if tourmalinisation close the permeability of the system, ore deposition will be limited by the amount of Fe contained in the vein-wall surface. But if it opens the permeability, the fluid is able to interact with a greater volume of fresh host-rock, triggering more wolframite deposition.

The methodology was followed by Launay et al. (2023) is based on good implementation of the alteration through batch equilibrium simulation and knowledge about its effect on the permeability/porosity. Both requirements that are completely missing in the case of tourmalinisation, an alteration caused by B-bearing fluids and present in many hydrothermal contexts.

II-Tourmaline, a useful mineral in borosilicate system

A) A ubiquitous complex mineral

Tourmaline comes from the Sinhalese word “thuramali” which means “stone with mixed colours” and was used to designate all unknown coloured stones. In geology, the term tourmaline refers to a mineralogical supergroup that encompass 38 endmembers recognised by the IMA (Warr 2021, tourmaline classification in Appendix A1) and constitute the most widespread borosilicate in the earth’s crust (Grew et al. 2017). It belongs to the cyclosilicate family and has a rhombohedral lattice within the R3m space group. Tourmaline present a morphology in rods with various textures and sizes ranging from 5 m long single crystal to sheaves of micrometric fibbers. This highly anisotropic structure with no center of symmetry gives its characteristic polar properties related to the position of its <c+> axis (morphology, growth rate, piezoelectricity, pyroelectricity; reviewed in Henry & Dutrow (1996). The general structural formula of tourmaline is $X\ Y_3\ Z_6\ (T_6O_{18})\ (BO_3)_3\ V_3\ W$, with X a nine-coordinated site, Y and Z two octahedral site, T a tetrahedral site and W and V, two anionic sites (Henry et al. 2011). This variety of site not only allows it to incorporate a large number of chemical elements as major components (Table 2), but make many substitutions possible, particularly between the two octahedral sites. This complex chemical composition, together with its crystallographic structural properties, makes tourmaline a chemically and mechanically stable refractory mineral with negligible intracristalline diffusion processes (Büttner 2005; Büttner and Kasemann 2007; van Hinsberg and Schumacher 2007).

Site name	Coordination	Commons elements
X	[IX]	Na, $[]_X$, Ca, K
Y	Octahedral [VI]	Fe^{2+}, Mg, Mn, Al, Fe^{3+}, Li, Ti, Zn, Ni, Co, Cu, Cr, V
Z	Octahedral [VI]	Al, Fe^{3+}, Mg, Fe^{2+}, Cr, V
T	Tetrahedral [IV]	Si, Al, B
(BO_3)	Trigonal [III]	B
V	Anions	OH, O
W	Anions	OH, O, F

Table 2: Description of the coordination level and elemental occupancy of various tourmaline sites (after Hawthorne & Dirlam, 2011; Henry et al., 2011). $[]_X$ = X site vacant

As reported by Slack & Trumbull (2011), tourmaline is a ubiquitous accessory mineral in hydrothermal veins and in metasomatized rocks from alteration aureoles developed around and within granitic plutons. Hence, it has been described in many deposits (Fig. 6) such as Sn-W granitoids and/or veins (Williamson et al. 2000; Codeço et al. 2017; Broska and Kubiš 2018; Harlaux et al. 2020), porphyry Cu-(Mo-)Au and the epithermal system associated (Lynch and Ortega 1997; Garwin 2002; Tuduri et al. 2018; Li et al. 2022) , orogenic Au (Garofalo et al. 2002; Hazarika et al. 2015; Kalliomäki et al. 2017; Sciuba et al. 2021), IOCG (Dreher et al. 2008; Su et al. 2016; Kelly et al. 2020), VMS and SEDEX (Slack et al. 1993; Hellingwerf et al. 1994; Deb et al. 1997; Taylor et al. 1999; Slack 2022) and skarn (Hellingwerf et al. 1994; Baskina et al. 2009; Yu et al. 2017; Zhao et al. 2021). Independently of magmatic/hydrothermal contexts, tourmaline is also commonly found in metamorphic rocks from the sub-greenschist to the amphibolite facies (Henry and Guidotti 1985; Marsala et al. 2013; Dutrow and Henry 2022), in subduction zones (Ota et al. 2008b; Marschall et al. 2009; van Hinsberg et al. 2017) and even in sediments undergoing diagenesis (Henry et al. 1999; Henry and Dutrow 2012).

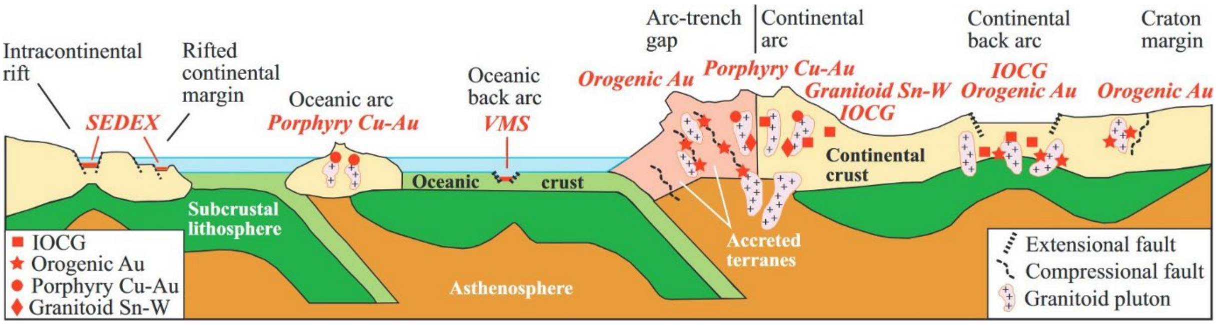

Figure 6: Schematic diagram showing tectonic settings of tourmaline-bearing hydrothermal ore deposits (from Slack & Trumbull 2011).

The common occurrence of tourmaline in those contexts indicates that it is a phase stable under a wide range of P-T conditions (van Hinsberg et al. 2011a). This property is partly due to the ability of tourmaline to adjust its composition by selectively incorporating a large number of major and trace elements (Table 2). Consequently, tourmaline is considered as a "*geologic DVD*" (Dutrow and Henry 2011), whose chemistry is commonly used as a probe of its crystallisation environments. The major element composition of tourmaline is correlated with the typology of its host-rock (Henry and Guidotti 1985; Henry and Dutrow 1996; Slack and Trumbull 2011; Sciuba et al. 2021), whereas the incorporation of trace elements accounts for more local phenomena including fluid-rock interaction, element partitioning between phases and/or crystallochemical effects (Marks et al. 2013; Hazarika et al. 2015; Yang et al. 2015; Kalliomäki et al. 2017; Harlaux et al. 2020; Sciuba et al. 2021). As a suitable recorder of the physicochemical conditions of its environment, many studies have tried to use tourmaline as a petrologic indicator, as a fluid composition and flow recorder and as a geothermobarometer.

B) A petrogenetic indicator

The type of host rock can affect the chemical composition and morphology of the tourmalines it contains (Trumbull & Chaussidon 1999; van Hinsberg et al. 2011a, 2011b). This influence is difficult to determine in the case of natural tourmaline, as temperature, pressure and fluid composition effects on the tourmaline chemistry are superimposed. However, some characteristics and evolution are systematically associated with certain contexts. For example, lithiniferous tourmalines are generally specific to pegmatites (London 2011; van Hinsberg et al. 2011a; Marks et al. 2013), whereas high concentrations of Ni, V and/or Cr are only found in metabasites, metabauxites and metamorphosed anoxic sediments (Henry & Dutrow 2001; Bačík et al. 2011). Finally, diagenetic tourmalines are easily recognised by the formation of asymmetric comb-like overgrowth along the <c+> axe of detrital grains (van Hinsberg et al. 2011b).

Henry & Guidotti (1985), highlighted some generalisations between tourmaline composition and the nature of the host rocks which they used to construct a classification on AFM and CFM diagrams (Fig. 7). While this classification has proven useful for determining the original casings of tourmaline clasts in detrital sediments (Walden 2016), its application to hydrothermal systems remains debatable (Henry & Dutrow 1996; Walden 2016). The diagrams provide relevant information in the case of pegmatites (Lensing-Burgdorf et al. 2017), but in cases where the W/R ratio is important, the chemistry of the mineral depends too little on the chemistry of the host rock for this classification to work (Henry & Guidotti 1985; Tuduri 2005; Slack & Trumbull 2011).

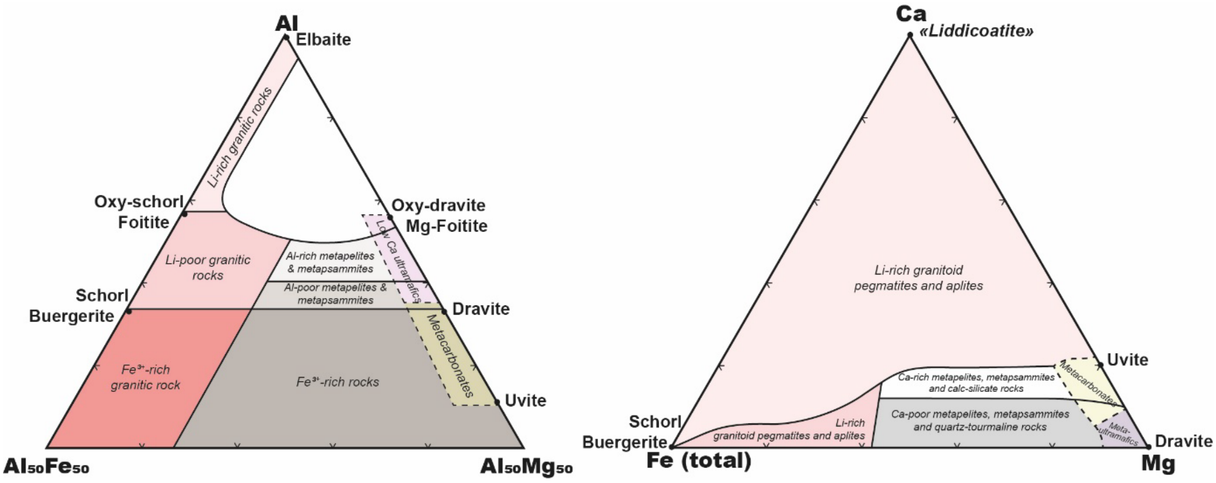

Figure 7: Petrogenetic classification of tourmaline by Henry & Guidotti and van Hinsberg et al. (2011b). The domains delimited by dotted lines are superimposed on the others, delimited by solid lines.

C) An indicator of fluid flow, source and composition

In hydrothermal systems, fluids interacting with tourmaline can come from one of two different sources. Either the fluid comes from an internal source, therefore in equilibrium with the surrounding rock (rock-buffered system). Or the fluid come from an external source, therefore in disequilibrium with the tourmaline-bearing mineralogical assemblage and resulting in fluid-rock interactions (fluid-buffered system). The tourmaline is able to distinctly record the opening and/or closing phases throughout the hydrothermal history of its environment. These different growth episodes provides a wealth of information such as the fluid phase availability, hydrodynamic (direction and velocity of the fluid flow) and composition (Dutrow & Henry 2016, 2018). Tourmaline occurs mainly as an accessory phase in hydrothermal systems and as such it passively responds to fluid compositions. Its presence indicates by itself the availability of B in the system, either directly in the fluid or through the breakdown of B-bearing minerals. Tourmaline growth is only favourable in aqueous fluid with neutral-to-acidic conditions, where B is predominantly in triangular coordination in the fluid (Morgan & London 1989; Henry & Dutrow 1996; Leeman & Sisson 1996). Thus, tourmaline is a direct proxy of $B(OH)_3$ activity in the fluid phase. A large number of studies have investigated the chemistry of tourmaline within a same system to derive information about the evolution of hydrothermal fluids (e.g. Lynch & Ortega 1997; Tuduri 2005; Baksheev et al. 2009; Yang et al. 2015; Harlaux et al. 2020). Those studies, coupled with experimental data, have recurring conclusions regarding particular chemical trends. The transition from oxy-dravite to povondraite (O-P trend), marked by the substitutions $[]_X$ Al → Na Fe and Al → Fe^{3+}, indicate the evolution of a highly saline fluid (low H_2O activity) under oxidising conditions and low T (150 to 400°C) (Henry & Dutrow 2012; Dutrow & Henry 2018). NaMg → $[]_X$Al (alkali-deficient) and MgOH → AlO (deprotonation) substitutions correlate with a change in fluid salinity, with the former being prevalent in low to moderately saline solutions while deprotonation of the W site is more prominent in highly saline fluids (von Goerne et al. 2001, 2011; Dutrow and Henry 2018).

Based on the experimental data of Orlando et al. (2017), the transition from Mg-rich to Fe-rich tourmaline, often observed in magmatic-hydrothermal systems (e.g. Mlynarczyk & Williams-Jones 2006; Li et al. 2022), can be explained by a decreased in fluid salinity.

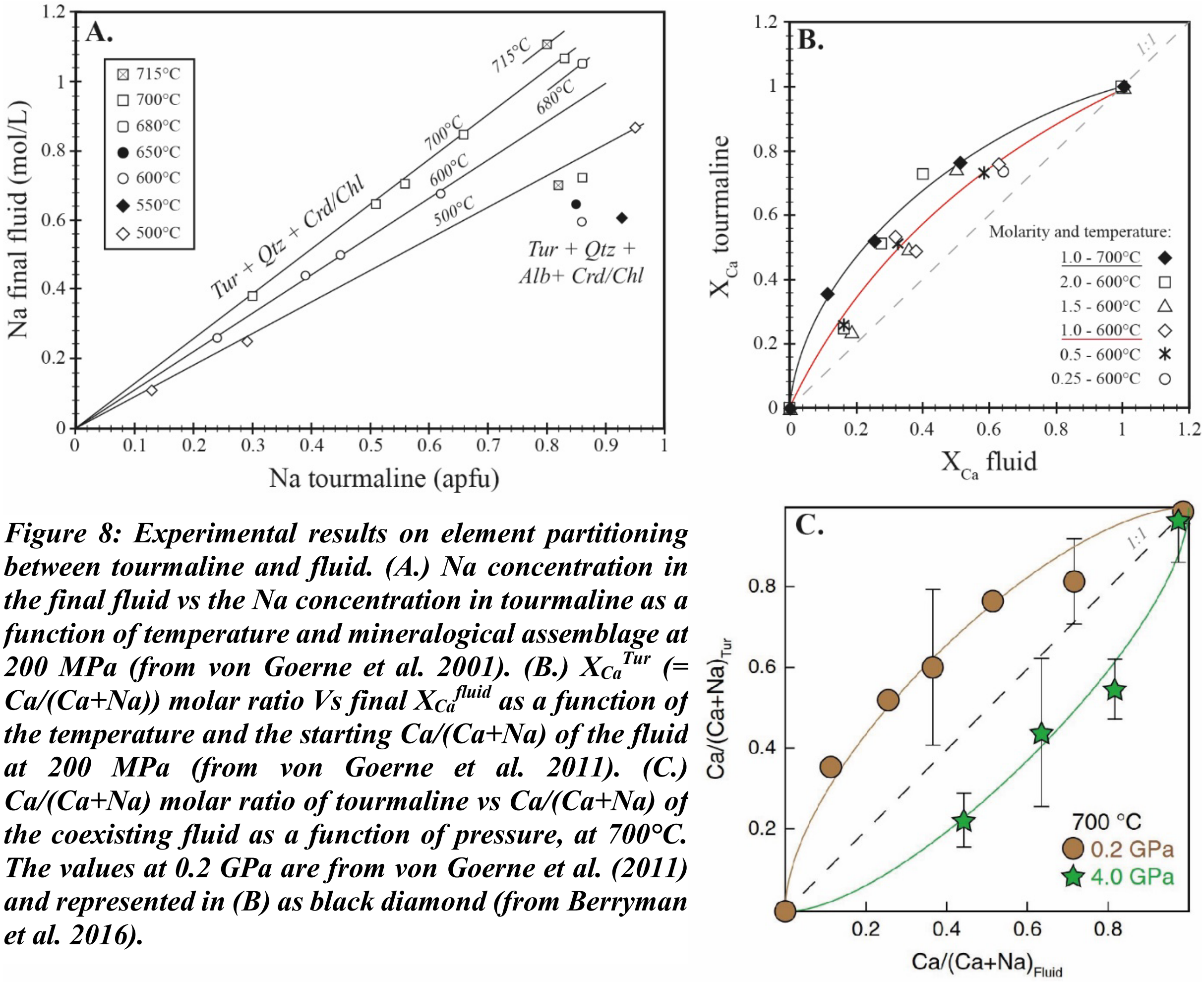

Figure 8: Experimental results on element partitioning between tourmaline and fluid. (A.) Na concentration in the final fluid vs the Na concentration in tourmaline as a function of temperature and mineralogical assemblage at 200 MPa (from von Goerne et al. 2001). (B.) X_{Ca}^{Tur} (= Ca/(Ca+Na)) molar ratio Vs final X_{Ca}^{fluid} as a function of the temperature and the starting Ca/(Ca+Na) of the fluid at 200 MPa (from von Goerne et al. 2011). (C.) Ca/(Ca+Na) molar ratio of tourmaline vs Ca/(Ca+Na) of the coexisting fluid as a function of pressure, at 700°C. The values at 0.2 GPa are from von Goerne et al. (2011) and represented in (B) as black diamond (from Berryman et al. 2016).

Experimental studies of element partitioning between tourmaline and fluid have focused on the relation between the X-site composition of tourmaline (Fig. 8) and the composition of the fluid phase to quantitatively estimate the concentration of those elements in the fluid phase (von Goerne & Franz 2000; von Goerne et al. 2001, 2011; Berryman et al. 2015, 2016). These experiments were realised in Fe-free systems with temperatures between 500 and 700°C and pressure between 0.2 to 4 GPa. At a given Na concentration in the fluid, the Na content in tourmaline decreases with increasing temperature (Fig. 8A). If the system contains albite, the concentration of Na in the final fluid is buffered and show little variation with temperature. By adding Ca in the fluid, von Goerne et al. (2011) demonstrate that Ca partitions preferentially in the tourmaline over the fluid, an effect amplified by the temperature.(Fig. 8B). However, at higher P (> 1 GPa), Ca preferentially partitions into the fluid, regardless of the temperature (Fig. 8C). Those relations give interesting insights for the use of tourmaline as a geothermobarometer (see below), but, as presented in Figure 8, those relations depend primarily on the bulk (fluid + rock) composition. Consequently, the application of those relations on natural systems is still a difficult task requiring more information, especially on Fe-rich systems.

Boron isotope signature ($\delta^{11}B$) of fluids and melts provide important evidence for understanding the generation, transport and recrystallisation of slab-derived melts and fluids in subduction zones. As a borosilicate minerals frequently found in such contexts, tourmaline is considered as a useful tracer of multiple melt/fluid-rock interaction and of boron cycling in continental subduction zones (Chen et al. 2023). Other than boron, the chemical complexity of tourmaline allows the application of a wide range of isotopic systems, such as O, H, Si, Mg, Li, Sr, Nd, Pb, K(Ar) and Cu (Marschall & Jiang 2011; Henry & Dutrow 2018). Information about the physicochemical condition associated with fluid-rock interaction, the fluid origin and evolution, the timing of magmatic, metamorphic and hydrothermal events that produce tourmaline can be inferred. Recent studies on the San Rafael tin deposit (Peru) have applied isotopy in order to trace fluid processes during the magmatic-hydrothermal transition leading to the mineralisation (Harlaux et al. 2019, 2020). The initial radiogenic Sr and Nd isotope compositions of different tourmaline generations support a dominantly magmatic origin of the hydrothermal fluids and is similar to the values found in Bolivian tin porphyry. Combined $\delta^{18}O$ and $\delta^{11}B$ measurement coupled with quantitative fluid modelling shows that magmatic and pre-

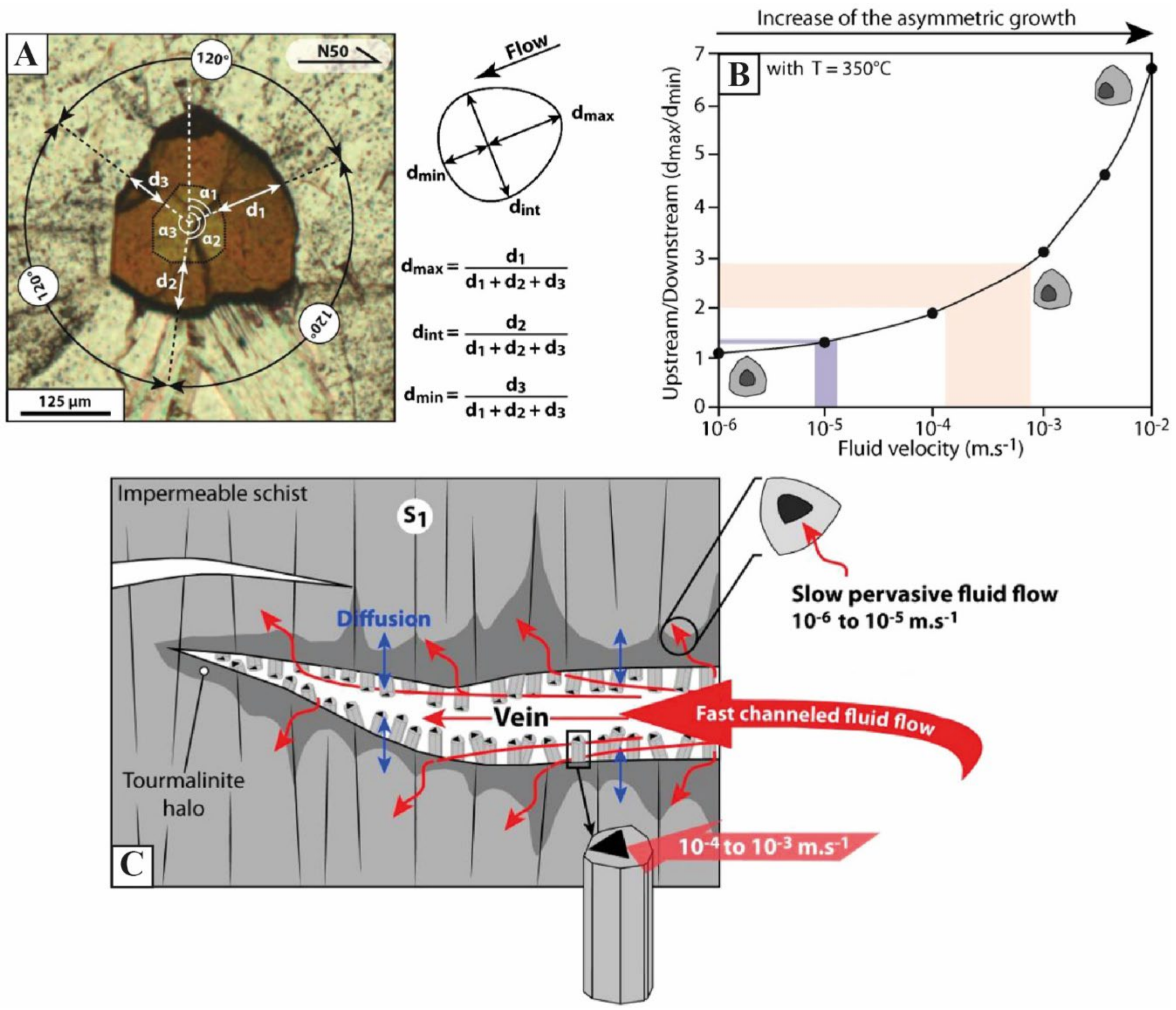

Figure 9: Fluid flow reconstruction through tourmaline growth band analysis applied in Panasqueira (from Launay et al., 2018). (A.) Measurements of growth bands thickness and orientation on a basal section of tourmaline. (B.) Curve deduced from numerical modelling showing relationship between fluid velocity and flux ratio. The filled boxes indicate the range of averages of fluid velocities derived from d_{max}/d_{min} ratio measured on tourmalines from altered wall-rocks (blue) and veins (red). (C.) Hydrodynamic model of fluid flow in and around the veins.

hydrothermal tourmaline were formed in continuously evolving magmatic-hydrothermal closed system. In contrast, the $\delta^{18}O$-$\delta^{11}B$ composition of syn-ore tourmaline can only be explained by the mixing of a hot and saline tin-rich magmatic fluid with a heated meteoric fluid.

Tourmaline growth bands can be used to track both the flow and chemical composition of the fluid involved during the formation of hydrothermal ore deposits (Sizaret et al. 2009; Mahjoubi et al. 2016; Launay et al. 2018). In hydrothermal systems, a crystal's shape is controlled by its intrinsic symmetry and the effects of external forces, such as fluid flow, that induce anisotropic growth (Fig. 9A). The faces exposed to the chemical flux, the upstream faces, grow faster than the downstream faces (Kesler et al. 1972; Sizaret et al. 2009; Sizaret 2011). The relationship between flow velocity and the relative growth rate of upstream and downstream faces can be modelled and quantified by solving the coupled Navier-Stokes and chemical transport equation (Sizaret et al. 2006, 2009). Thus, the growth band thicknesses measured on hydrothermal crystals can be considered as chemical fluxes integrated over a given period of time. The fluid velocity can be determined by plotting the measured d_{max}/d_{min} of the crystal vs the velocity curve (Fig. 9B). This methodology was applied at Panasqueira (tungsten deposit, Portugal) to decipher fluid flow from tourmaline in veins and altered wall-rocks (Launay et al. 2018). Velocity values highlights a transport of metals in veins, largely dominated by advective processes (10^{-4} to 10^{-3} m/s). However, fluid flow in the altered wall-rocks is slow and pervasive (10^{-6} to 10^{-5} m/s), suggesting that element transport through the metasedimentary host rock was low and limited to the alteration haloes (Fig. 9C).

D) An indicator of pressure and temperature conditions

Regardless of its composition or its crystallographic specificity, tourmaline can provide useful information about the temperature and, to a lesser extent, pressure of its environment. This can be acquired through microthermometry on fluid inclusions host directly in tourmaline (Thomas & Spooner 1988; Ootes et al. 2010). However, these fluid inclusions are often too small to allow satisfactory analyses (Slack & Trumbull 2011). Another possible thermometer is based on the oxygen isotope partitioning between quartz and tourmaline at equilibrium (Taylor et al. 1999; Lerouge and Bouchot 2009). A similar method with ^{11}B partitioning between tourmaline and B-rich mineral, such as biotite, white micas or amphibole, remains to be experimentally calibrated (Slack & Trumbull 2011).

In natural environments, chemical variations of tourmaline are frequently look in order to highlight relationships with the P-T evolution deduced from other analyses. Relationship between T-P and the $Na/(Na+[]_X)$ and $Mg/(Fe+Mg)$ ratio, as well with the K, Ti, F and ^{IV}B content in tourmaline, are often described (Henry and Dutrow 1996; Nakano and Nakamura 2001; Tuduri 2005; Mlynarczyk and Williams-Jones 2006; Ertl et al. 2008, 2010; Wadoski et al. 2011; Berryman et al. 2015; Bačík et al. 2017). However, these changes may be due to controls others than the P-T conditions, making it difficult to create generalisable thermobarometric laws. The Na incorporation in tourmaline has been experimentally studied by von Goerne et al. (2001, 2011), between 700 and 500°C, 200 MPa and for various concentrations of NaCl and $CaCl_2$ in the fluid. Their results, represented in Fig. 10, show that for a weakly to moderately saline solution, the decrease of temperature induces an alkali-deficient substitution $Na\ Y^{2+} \rightarrow {}^{VI}Al\ []_X$ (with Y^{2+} a divalent cation from the Y-site). But for more enriched solution, this correlation is no longer observed. This change of relationship shows that the concentration of Na in tourmaline is controlled first by the fluid composition and then by the temperature (von Goerne et al. 1999b, 2001; Berryman et al. 2016; Bosi et al. 2016). In contrast, synthesis experiments at ultra-high pressure, show that the incorporation of K in tourmaline (in the X-site) is primarily dependent on pressure and temperature rather than on fluid composition (Berryman et al. 2015). The Mg/(Fe+Mg) ratio is more related to the chemistry of the surrounding rocks. Its correlation with metamorphic grade can be either positive (e.g. Nakano & Nakamura 2001) or negative (e.g. (Kawakami & Ikeda 2003) depending on the geological context. At high temperature (≥ 700°C), the pressure negatively affects the Ti incorporation into the tourmaline structure. But, at relatively low pressures, the Ti incorporation in tourmaline structure is governed by the Ti content in the mineral-forming medium (Vereshchagin et al. 2022). F content is directly dependent on X-site occupancy for crystallographic reasons (Henry & Dutrow 1996, 2011). Ertl et al. (2008) demonstrated that the amount of ^{IV}B (tetrahedral boron substituting Si in T-site) is greater at low temperature and increase with the pressure until 1 GPa. However, crystallographic controls interfere with this relationship. The substitution Si → ^{IV}B requires a low <T-O> bond length that can only be achieve with a high-Al content in the Z-site (Lussier et al. 2009; Bosi et al. 2010).

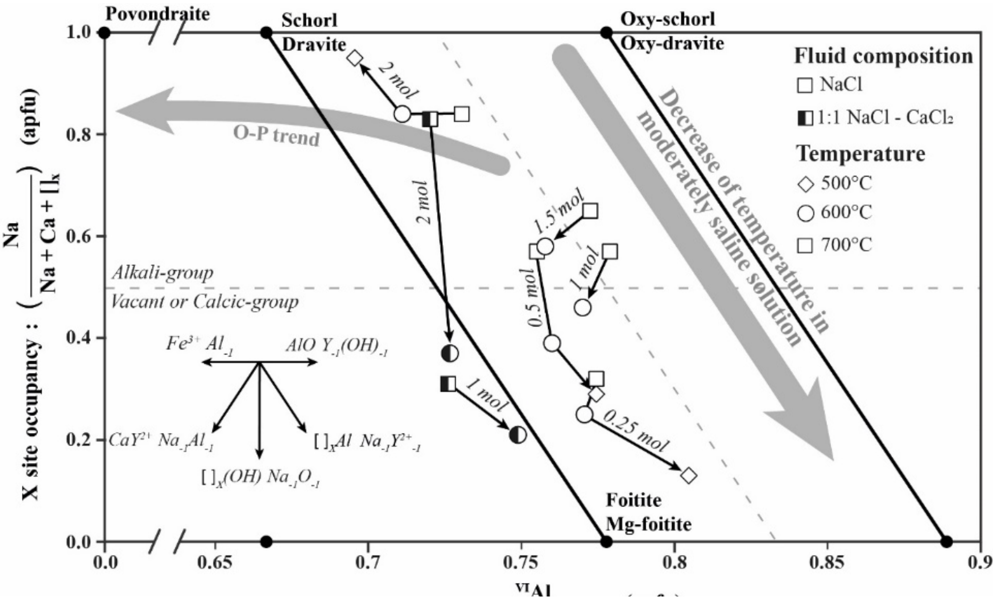

Figure 10: Compositional variability of free-Fe synthetic tourmaline as a function of temperature and fluid composition (data from von Goerne et al., 2001, 2011). The O-P trend shows the transition from oxy-dravite to povondraite, signing retrograde evolution in porphyry systems (Beckett-Brown et al. 2023).

Other thermometers rely on the crystallographic order of atoms within the Y- and Z-site. Al-Mg disorder was first proposed to be indirectly temperature dependent by Ertl et al. (2010). This hypothesis was based on natural and experimental observations showing a correlation between the decrease of temperature below 400°C and the transition from Mg-rich (dravite) to Al-rich (magnesiofoitite) tourmaline (Dutrow & Henry 2016; Bosi et al. 2018). However, due to multiple crystallographic constraints (mentioned thereafter) the calibration of a proper thermometer was not possible (Bačík 2015; Bosi et al. 2016). Bosi et al. (2016) proposed a thermometer based on Fe-Mg disorder, applicable for Fe-rich tourmalines. Indeed, with increasing temperature, the disordering of Fe between the Y- and Z-sites, is balanced by ordering of Mg at Y sites, according to the order-disorder reaction $^{Y}Fe + {}^{Z}Mg \rightarrow {}^{Z}Fe + {}^{Y}Mg$.

Several attempts to calibrate geothermobarometric relationships between tourmaline and various metapelitic minerals have been tested (Kawakami & Ikeda 2003; van Hinsberg & Schumacher 2007, 2009). Currently, thermobarometers based on Fe-Mg exchange between tourmaline and ferromagnesian minerals (garnet, staurolite, biotite, muscovite and chlorite) are not yet applicable, due to the problem of elemental partitioning between the two octahedral sites Y and Z (predicted by Henry & Dutrow (1996) and verified by van Hinsberg & Schumacher (2009)). Variations in the element distribution over these sites, their relative participation in the exchange and differences in temperature dependence of exchange with each site, strongly affects the K_D vs T relation. On the other hand, the Ca-Na exchange between tourmaline and plagioclase is weakly impacted by intracrystalline substitution phenomena and constitutes the only potentially applicable thermobarometer today (van Hinsberg & Schumacher 2009).

Finally, an alternative thermometric approach has been proposed by Henry & Dutrow (1996) and van Hinsberg & Schumacher (2007), based on the temperature dependence of Ca and Ti partitioning along opposite crystallographic sectors in tourmalines with hourglass zonations (example of an application in Berryman et al. 2017). The strong anisotropy within the tourmaline structure produces charge differences on the surface of the <a>, <c+> and <c-> faces, resulting in morphological and compositional differences. The composition of the various crystallographic sectors tends to converge with temperature, according to a law determined empirically by van Hinsberg & Schumacher 2007. However, this method can only be applied to tourmalines with hourglass zonations, which are particularly rare in hydrothermal contexts, and only for temperatures above 350°C (Slack & Trumbull 2011).

III- Tourmaline stability in natural systems

Natural observations and experimentations highlight the capacity of tourmaline to react to how hydrothermal systems evolve both chemically and physically. Applying the relations found experimentally between tourmaline composition and its environment to natural system is still a difficult task. Furthermore, despite its common occurrence as an accessory phase, tourmaline is totally absent from thermodynamic modelling (e.g. Halter et al. 1998). Hence, tourmaline is generally only studied for its composition and isotopy in order to distinct the various stages of an environment. However, quantitative reconstructions of its crystallising environment conditions are within reach in particular with the development of tourmaline/fluid ($D^{Tur}/_{fluid}$) and tourmaline/mineral ($D^{Tur}/_{min}$) partitioning studies. Such reconstruction was conducted by van Hinsberg et al. (2017) on a subduction-zone fluid. Based on equilibrium evidences between tourmaline and phengite, they estimate the $D^{Tur}/_{fluid}$ for various elements by combining $D^{Phg}/_{Tur}$ data from subduction-zone rocks (Klemme et al. 2011) with experimentally determined $D^{Phg}/_{fluid}$ (Green & Adam 2003). This methodology yield to robust reconstruction of the crystallising environment conditions of tourmaline. But it also highlights the lack of calibrating experimental information on essential properties. Among them, are those concerning tourmaline stability (Hinsberg & Schumacher 2007; Dutrow & Henry 2011).

A) The boron concentration at equilibrium with tourmaline

The general stability of tourmaline regarding the bulk composition of its crystallising environment is also wide. Thanks to the diversity of crystalline sites and the variety of elements able to be incorporated, a wide range of common igneous, metamorphic and even sedimentary rocks may contain the necessary structural components to form tourmaline. Thus, the only real chemical limiting factor for tourmaline formation is the boron concentration (expressed as wt% of B_2O_3 thereafter and noted $[B_2O_3]$).

Natural observation of silicate melts demonstrates that during the crystallisation of peraluminous magma, biotite and cordierite are the first ferromagnesian minerals to crystallise. Magmatic tourmaline crystallises in the late stage of the fractionation when the boron content reaches tourmaline saturation. Through a series of crystallisation and dissolution experiments, Wolf & London (1997) investigated the $[B_2O_3]_{melt}$ in peraluminous granitic magma required to reach tourmaline saturation. At 750°C and 200 MPa H_2O, with an Aluminium Saturation Index (ASI) of the melt around 1.35, the stability of tourmaline, in the presence of cordierite and/or biotite, is achieved for $[B_2O_3]_{melt} = 2$wt%. The stability decreases with the value of the ASI: the tourmaline saturation for the same experiment with an ASI of 1.27 is reached at $[B_2O_3]_{melt} = 6.99$ wt%. At a constant Al content, the amount of B needed to maintain tourmaline saturation in the melt decrease with falling temperature. For example, a tourmaline-saturated melt at about 13.25 wt% Al_2O_3 contain 2.98 wt% B_2O_3 at 650°C and only 2.22 wt% B_2O_3 at 500°C. This behaviour was confirmed later by the study of Acosta-Vigil et al. (2003).

In hydrothermal environments the boron concentration in the fluid required to reach tourmaline saturation ($[B_2O_3]_{fluid\_EQ}$) has been poorly investigated. Most of the experimental studies have been tourmaline synthesis (Rosenberg et al. 1986; von Goerne et al. 1999a; Wodara & Schreyer 2001; Setkova et al. 2015, 2019; Berryman et al. 2016) or tourmalinisation experiments (von Goerne et al. 1999b; Orlando et al. 2017; Cheng et al. 2019) which has the disadvantage that tourmaline stability limit as a function of $[B_2O_3]_{fluid}$ is poorly defined. Only the study of Weisbrod et al. (1986) has been fully dedicated to constrain $[B_2O_3]_{fluid\_EQ}$, however, their results have only been published in abstract form. Nonetheless, an estimation can be made by using the results of the tourmalinisation experiments (Fig. 11).

Weisbrod et al. (1986) measured the $[B_2O_3]_{fluid\_EQ}$ required to equilibrate the assemblage tourmaline + cordierite + albite + andalusite + quartz + saline aqueous fluid (3 wt% NaCl) between 300 and 730°C (solidus condition) at 100 MPa. $[B_2O_3]_{fluid\_EQ}$ remain ≤ 0.3 wt% from 300 to 500°C, with an optimum around 375°C. Over 500°C, increasing temperature leads to a strong increase of the $[B_2O_3]_{fluid\_EQ}$, from ~0.2 wt% at 500°C to 2.4 wt% at 700°C (Fig. 11).

Between 475 and 600°C, at 200 MPa, Morgan & London (1989) performed metasomatic reaction experiments between an amphibolite (hornblende + plagioclase) and acidic or alkaline boron-bearing fluids. They found that Al-poor rocks may give relatively Al-rich tourmalinite through the reaction hornblende + Ca-plagioclase → tourmaline + danburite + clinopyroxene + quartz in acidic fluid with a $[B_2O_3]_{fluid} > 2.1$ wt% at 600°C (referred to as Serie 2, unseeded runs in the paper). Increasing the pH of the solution up to 6.5, by adding B as borate species ($Na_2B_4O_7$), result in higher $[B_2O_3]_{fluid}$ required to stabilise tourmaline. By adding boron only as alkaline borate species, tourmaline is destabilised and/or failed to precipitate, regardless of the concentration. This study indicates that tourmaline is stable in acid-to-neutral aqueous solution, where $B(OH)_3$ is dominant. The boron concentration of their equilibrated product was not measured, and only the $[B_2O_3]_{fluid}$ initial is given. Thus, as tourmaline was not observed as a product of the experimental charge with $[B_2O_3]_{fluid} = 2.1$ wt%, this concentration is considered as a minimal threshold for the equilibrated value ($[B_2O_3]_{fluid} < [B_2O_3]_{fluid\_EQ}$). The concentrations of the charges where tourmaline appear are considered as a maximal threshold, as they contain enough boron to form tourmaline ($[B_2O_3]_{fluid} > [B_2O_3]_{fluid\_EQ}$, see Fig. 11).

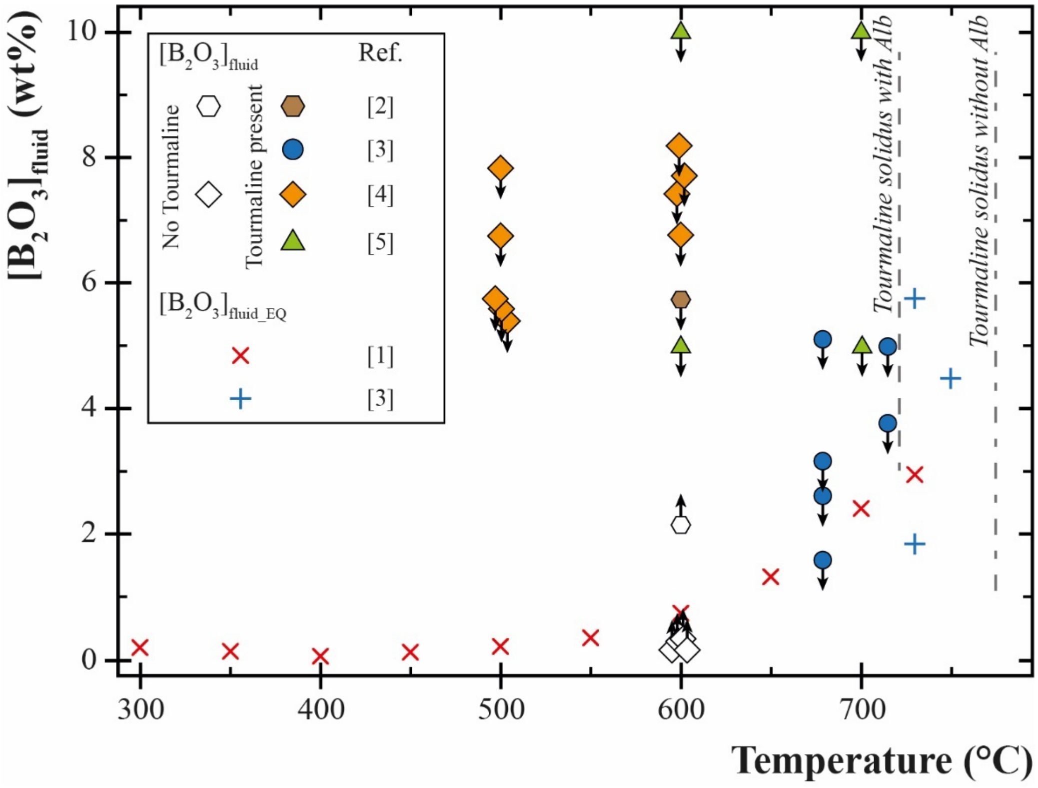

Figure 11: Compilation of tourmalinisation experiments results in a $[B_2O_3]_{fluid}$ vs Temperature diagram. Cross symbols represent experiments where the final boron concentration at equilibrium with tourmaline ($[B_2O_3]_{fluid\_EQ}$) has been measured. Other symbols represent experiments where the boron concentration reported is not equilibrated with tourmaline ($[B_2O_3]_{fluid}$). If tourmaline was not present in the products phases (open symbols), the symbol is accompanied by an upward arrow. If tourmaline was present (solid symbols) but a reactant was missing in the product phase, or if only the initial $[B_2O_3]_{fluid}$ is reported, the symbol is accompanied by a downward arrow. References: [1] Weisbrod et al. (1986); [2] Morgan and London (1989); [3] von Goerne et al. (1999b); [4] Orlando et al. (2017); [5] Cheng et al. (2019).

Von Goerne et al. (1999b) studied the stability of tourmaline between 680 and 850°C, at 200 MPa, for the following two metasomatic equilibria: tourmaline + quartz = cordierite + sillimanite + fluid (Na-free system) and tourmaline + quartz = cordierite + albite + saline fluid (Na-bearing system). For each system, the $[B_2O_3]_{fluid}$ varied between [0.6; 10] wt% and HCl was introduced in some charge to reduce the pH from 4.3 (fluid nearly saturated with $B(OH)_3$ only) to 2. Their results, in agreement with those of Wolf & London (1997), indicate that tourmaline saturation is reached for $[B_2O_3]_{melt} = 2.3$ wt%. In experiments below the solidus, the final boron content in the fluid has been analysed. But due to the total consumption of sillimanite or albite in the experiment below 730°C, only three measurements in the Na-free system can be considered as $[B_2O_3]_{fluid\_EQ}$ (Fig.11). At 730°C the same charge with or without HCl in the fluid yield to very different results: with the $H_2O\text{-}B(OH)_3$ fluid $[B_2O_3]_{fluid\_EQ} = 5.76$ wt%, while, the $H_2O\text{-}HCl\text{-}B(OH)_3$ fluid result in a $[B_2O_3]_{fluid\_EQ} = 1.83$ wt%. The non-equilibrated experiments reported correspond all to maximum threshold to $[B_2O_3]_{fluid\_EQ}$ and display an important disparity due to the use of different fluid compositions. Those results highlight an effect of the fluid composition on the tourmaline stability, that is not fully explored yet.

Orlando et al. (2017) and Cheng et al. (2019) tourmalinisation experiments were conducted in order to study the effect of tourmalinisation on natural rocks, respectively a biotite-rich schist and a two-mica granite. As the tourmaline stability was not studied, the $[B_2O_3]_{fluid}$ reported are mainly non-equilibrated and serves either as minimal or maximal limit to tourmaline stability, depending on tourmaline presence in the product phases (Fig. 11).

Figure 11 presents the various experiments in a $[B_2O_3]_{fluid}$ vs temperature space. The $[B_2O_3]_{fluid\_EQ}$ appears to be in the order of the wt% and evolves positively with the temperature. This compilation also highlights a few inconsistencies. At 730°C, the equilibrated data from von Goerne et al. (1999b) does not match those of Weisbrod et al. (1986), being twice higher in the case of a pure H_2O fluid or lower with a HCl fluid. At 600°C, non-equilibrated data brackets a $[B_2O_3]_{fluid\_EQ}$ between 2.1 and 5 wt%, while Weisbrod et al. (1986) measured a lower value, around 0.75 wt%, incompatible with the results of Morgan & London (1989). Below 600°C, the data are poorly constraints. Those inconsistencies and lack of data on stability in hydrothermal systems compromise the calibration of tourmaline as a proper “petrologic forensic mineral” tool (van Hinsberg et al. 2011b).

B) Boron in hydrothermal fluids

1/ Range of concentration

Boron is a widespread constituent of crustal rocks, being found in sedimentary, volcanic, plutonic and metamorphic environments. The Earth’s upper continental crust contained between 15 and 36 ppm, which made it the 27th element in abundance (Wedepohl 1995; Henry & Dutrow 1996; Rudnick & Gao 2003). Researchers in earth sciences have given it less attention than other minor elements in the Earth’s crust,because there are numerous analytical difficulties of working with boron (Anovitz & Grew 1996). Common occurrences of borosilicate minerals (tourmaline, grandidierite, dumortierite, danburite, etc…) in magmatic environment leads to characterise the behaviour of boron in igneous system. Experimental studies highlight the fact that boron is an important flux for silicate melts. It lowers solidus and liquidus temperature for silicate systems, and it also reduces the viscosity of their melts (Pichavant 1987; Dingwell et al. 1996; London et al. 1996). Furthermore, boron behaves as an incompatible element. As such, it tends to be concentrated in felsic and silicic differentiates magmas. During volatile exsolution, triggered by crystallisation and/or decompression, boron partitions preferentially in the aqueous vapour phase (Pichavant 1981; Schatz et al. 2004). Consequently, hydrothermal fluids of magmatic origin can contain really high boron concentration, as demonstrated by the occurrence of sassoline ($B(OH)_{3(s)}$) in fluid inclusion (Fig. 12A) from various localities and contexts (Peretyazhko et al. 2000; Prokof’ev et al. 2002; Thomas et al. 2003). The solubility of sassoline at room temperature is 35 g/kg of water, corresponding to a boron concentration of 6 g/kg of water. Consequently, the boron concentration in hydrothermal systems can possibly reach some weight percentage. Prokof’ev et al. (2002) investigated the boron concentration of 11 deposits of various genesis and geochemical profile. The compiled database of fluid inclusions (n=81) covers a wide range of temperature (175-550°C) and salinities (0.6-67 wt% NaCl eq.). The boron concentration varies widely from 1 to 8000 ppm and shows no regular relation to chlorine and CO_2 in analysed samples.

For the past 20 years, laser ablation coupled to inductively coupled plasma mass spectrometry (LA-ICP-MS) has been the technique of choice for analysing fluid inclusions. This method allows rapid and precise acquisition of data from individual inclusions, a significant benefit compared to bulk sample leaching. By using the salinity measured by microthermometry as an internal calibration standard for Na, the data are converted into absolute element concentration. Numerous studies have used this method in order to characterise the average composition and evolution of paleo-fluids in hydrothermal systems. Boron has long been overlooked in those studies, and thus rarely quantified. However, Sirbescu et al. (2013) highlight the fact that, whether included in salt correction or not, high boron concentration in fluid inclusion can yield large errors in the internal standardisation of Na, leading to a miscalculation of all elements concentrations. This impact was first characterised for pegmatites and it is only recently that it was discussed in hydrothermal systems (Pan et al. 2019). This has led to more systematic boron analyses in recent fluid inclusions study and even to the quantification of the effect of boron concentration on salinity measurement by microthermometry (Legros et al. 2022).

The results of 29 fluid inclusion studies were compiled in order to assess the boron concentration in perigranitic systems (Source details in Appendix A2). Data are LA-ICP-MS analyses performed on quartz fluid inclusion and represent either a single analysis or an average composition, depending on the data availability. This compilation (n=2458) covers a wide range of temperature (homogenisation temperature), from 90 to 650°C and salinity, from 0.3 to 57.1 wt% NaCl eq. (Fig. 12B). As observed by Prokof’ev et al. (2002), there is no clear relation between temperature or salinity with the boron content of the fluid. Boron concentration ranges from 12 ppm to 18.6 wt% (186,000 ppm) with a mean value of 3684 ppm (Fig. 12C). The concentrations are bimodally distributed, with a first group around 500 ppm and a second, more concentrated, around 8000 ppm. In Figure 12C, the boxplot shows the range of boron concentration reported in various hydrothermal ore deposit (Sn-W, skarn, Sb, Carlin-type, Orogenic gold , porphyry and epithermal; see Table 1) and barren plutonic (pegmatites, miarolitic cavities, barren greisen and (F-)granite), metamorphic (mainly green-schist and amphibolite facies) and volcanic (carbonatite, caldera) systems. The boron concentration in seawater (Millero et al. 2008) and in the upper crust (Wedepohl 1995; Rudnick & Gao 2003) are also represented. Illustrating the incompatible behaviour of boron, the fluids in every system are enriched compared to the upper crust. Metamorphic systems are characterised by a median (Q2) concentration of 500 ppm, whereas volcanic environments present relatively low content (Q2 < 500 ppm). The highest concentrations (Q2 > 1000 ppm) are found in more differentiated magmatic systems such as Sn-W deposits, skarn and peraluminous plutonic settings. Some of the fluid inclusions concentration in boron even exceeds the sassoline saturation level (60,000 ppm). The presence of borosilicate (mainly tourmaline) reported in those three systems is common and generally associated with high value of boron in fluid inclusions (> 1000 ppm). However, in other systems, especially those associated with metaluminous magmas, this association borosilicate–high-boron content is more difficult to observe, as accessory phases may be overlooked (Qiu et al. 2021; Beckett-Brown et al. 2023).

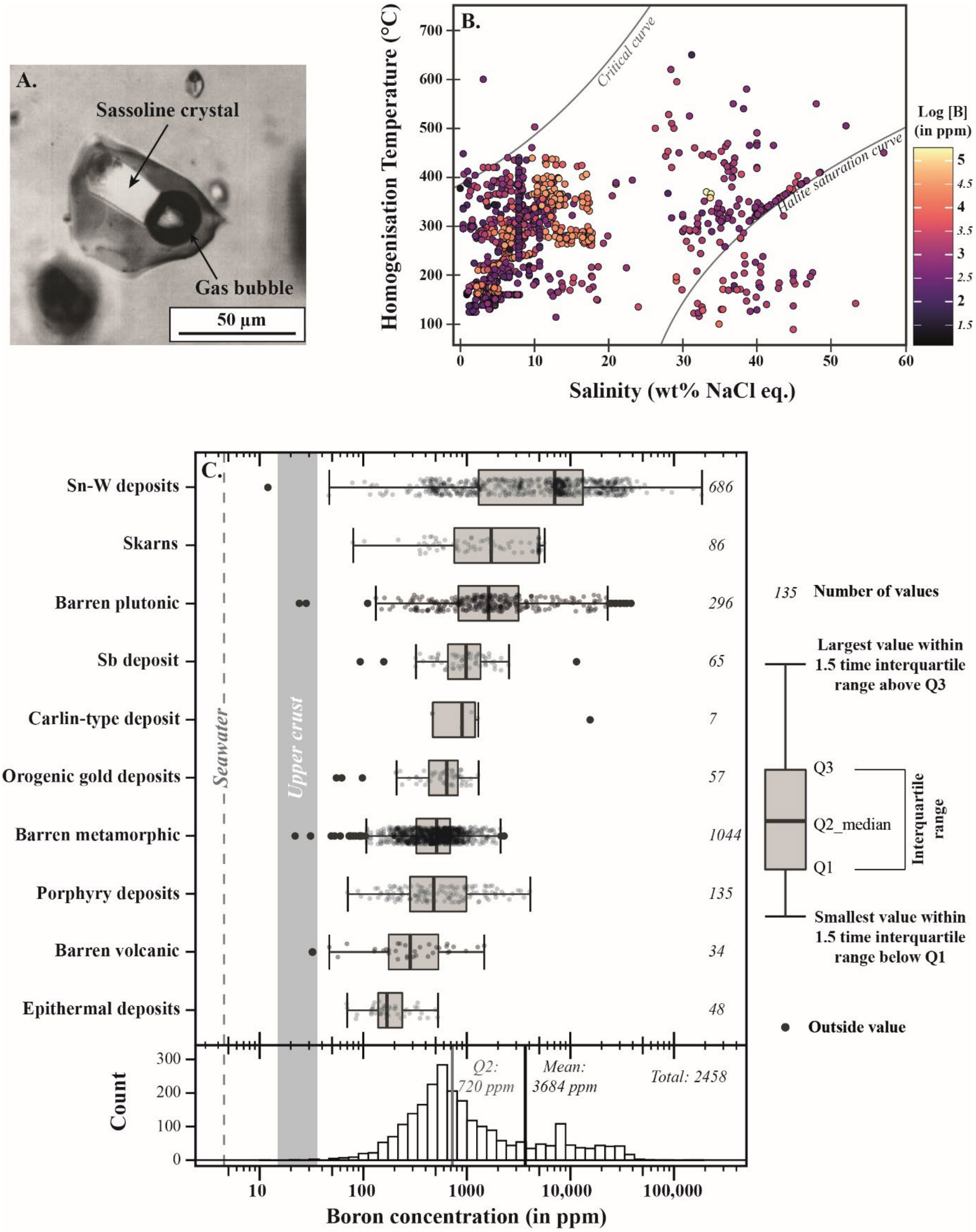

Figure 12: (A.) Fluid inclusion of B(OH)3 brine from the pegmatite veins Mika (Pamir; Prokof'ev et al. (2002)). (B.) Homogenisation temperature vs salinity as a function of the boron concentration for all fluid inclusions compiled. (C.) Box plot displaying the boron concentration (in ppm) of the fluid inclusions of the compiled database, as a function of their hydrothermal environment. Below the boxplot, a histogram of boron concentration in the entirety of the compiled database with the global mean and median value indicated by vertical lines. Seawater boron concentration from Millero et al. (2008) and upper crust range from Wedepohl (1995) and Rudnick & Gao (2003).

2/ Speciation in fluids

The presence of sassoline in fluid inclusions not only provides insights into the boron concentration of hydrothermal fluids, but also gives information about its speciation. Boron speciation has been largely investigated at low temperature thanks to the role of boric acid ($B(OH)_3$) as a neutron absorber in the primary coolant of pressurised water nuclear reactors (Schott et al. 2014; Ferguson et al. 2019). Extensive data on the T-P evolution of the $B(OH)_3$ + H_2O systems were obtained through solubility, potentiometric and in-situ experiments (Ingri 1962, 1963; Mesmer et al. 1972; Pokrovski et al. 1995; Schmidt et al. 2005; Smirnov et al. 2005; Akinfiev et al. 2006).

At 25°C, 1 bar (Fig. 13A), the major boron solute in acid to neutral fluids is the ^{III}B weak Lewis acid $B(OH)_3$. Boric acid interacts with water to form the borate (^{IV}B) hydroxy complex $B(OH)_4^-$, which become predominant only under strongly alkalic conditions, at pH > 9 (Akinfiev et al. 2006; Schott et al. 2014). The transition between $B(OH)_3$ and $B(OH)_4^-$ involves the formation of various polyborate anions. In natural systems, four of them have been recognised: $B_3O_3(OH)_4^-$, $B_4O_5(OH)_4^{2-}$, $B_5O_6(OH)_6^{3-}$ and, depending on the study, $B_3O_3(OH)_5^{2-}$ (Schott et al. 2014; Zhang et al. 2021) or $B_2O(OH)_5^-$ (Akinfiev et al. 2006; Wang et al. 2013). In NaCl-bearing fluids (Fig. 13B), $B(OH)_4^-$ proportion is reduced in alkali solution, giving way to the neutral complex $NaB(OH)_4$. Under acid condition, however, boric acid remains the principal constituent of the fluid, with $B(OH)_3Cl^-$ being the second most abundant boron species.

Experiments investigating higher temperature (up to 300°C, saturated vapour pressure (Fig. 13C) shows that the predominance field for $B(OH)_3$ expands with increasing temperature

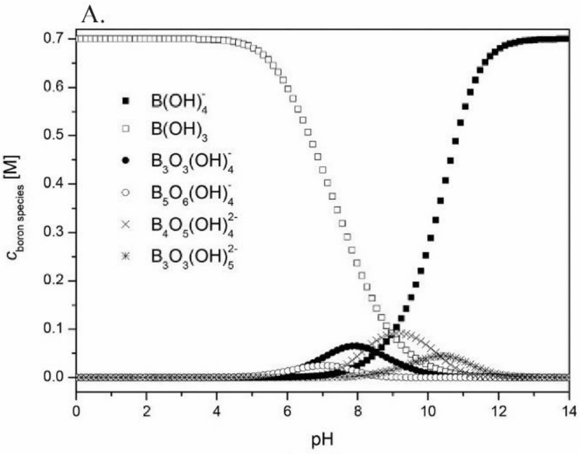

Figure 13: Speciation of aqueous boron-bearing species as a function of pH. (A.) B-O-H system at 25°C, 1 bar for a total boron concentration of 0.7 M (from Schott et al., 2014). (B.) Na-B-Cl-O-H system at 25°C, 1 bar and (C.) at 300°C and water vapour pressure. In both diagrams, the total boron concentration and NaCl are 1 mol/kg. The vertical dashed lines indicate the position of the neutral pH at the corresponding temperature (from Akinfiev et al., 2006).

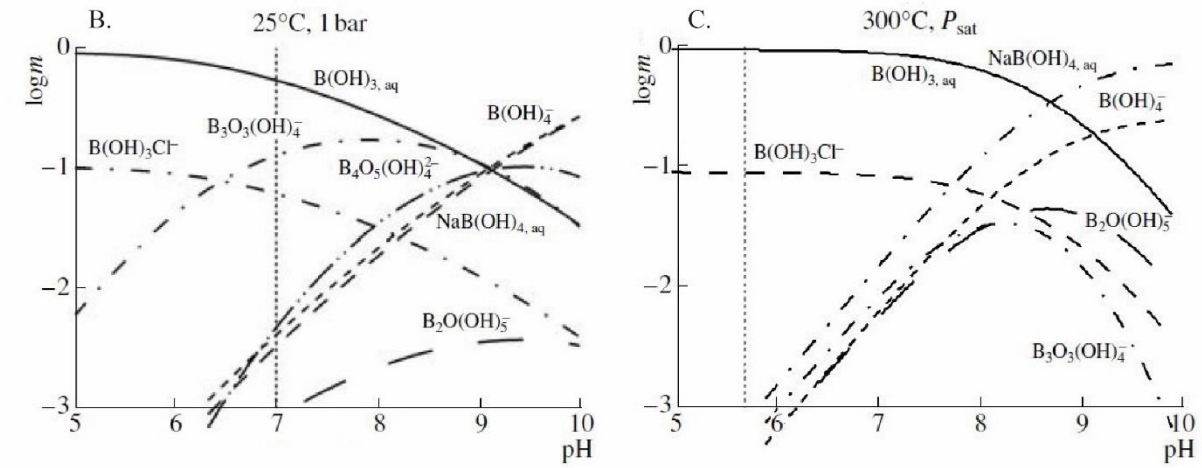

toward more alkaline condition. High temperature also favours $NaB(OH)_4$ as the major specie under highly alkaline condition and polyborate complexes tend to depolymerise, favouring the simpler molecules. Schmidt et al. (2005) used in-situ Raman spectroscopy in order to study the evolution of the speciation toward higher temperature (up to 600°C) and pressure (up to 2 GPa). Their observations confirmed the evolution described under 300°C, and show the total disappearance of the polyborate at $T > 350°C$. At $T \geq 200°C$ in highly concentrated H_2O + $B(OH)_3$ solution (> 37 wt% $B(OH)_3$), dehydration of boric acid lead to the formation of a small proportion of $HBO_{2(aq)}$: ($B(OH)_{3(aq)} \rightarrow HBO_{2(aq)} + H_2O$). In NaCl + H_2O + $B(OH)_3$ solutions, however, the amount of $HBO_{2(aq)}$ is decreased, implying that the addition of NaCl stabilise $B(OH)_3$. High pressure tends to expand the stability of $B(OH)_4^-$ toward less alkaline condition, but it is largely compensated by the temperature effect. Consequently, boric acid is recognised as the principal boron form in hydrothermal fluids.

Formation of boron complexes with elements other than Na and Cl have been barely studied in geology. Fluoroborate species are described in boron-rich geothermal water (e.g. Liu et al. 2020). Smirnov et al. (2005) studied the boron speciation in the system Na_2O–B_2O_3–SiO_2–H_2O. They reported an increase solubility of quartz in $B(OH)_3$ solution, which is consistent with the observations of Pichavant (1983) and Mar'ina et al. (1999). Unfortunately, the RAMAN spectra of the solutions did not allow the identification of any B-Si aqueous complexes, probably due to a too weak signal. Except for those studies, other complex aqueous polyborate are rarely mentioned. However, complexes with Li, K, Rb, Cs and/or Mg might exist in geological environment as they have been reported and studied in the nuclear engineering literature (Zhang et al. 2021).

C) An extensive P-T stability range

As mentioned before, the common occurrence of tourmaline as an accessory phase in many geological contexts is an indicator of a wide P-T stability range. The upper P-T stability has been largely investigated in order to understand the behaviour of boron and its isotopic fractionation during melting / crystallisation in the context of a subduction (e.g. Nakano and Nakamura 2001; Ota et al. 2008). Van Hinsberg et al. (2011a) compiled the estimated P-T stability for tourmaline (Fig. 14). The incongruent melting of tourmaline has been observed in experiments between 725 and 1000°C, depending on pressure and composition. The dravite exhibits one of the largest stability fields, with an upper thermal limit at 875°C at 500 MPa, which decreases to 775°C at 200 MPa (Robbins & Yoder 1962; Ota et al. 2008). The presence of albite lowers this stability to 730°C at 200 MPa (Weisbrod et al. 1986; von Goerne et al. 1999b). Recent in situ and ex situ high-T experiments on the breakdown of Li-tourmaline (elbaite) of particular composition such as Mn-elbaite or Fe-rich fluor-elbaite are within the range of upper thermal limits determined on more "classic" tourmaline composition (Celata et al. 2021; Ballirano et al. 2022). Boron released during tourmaline breakdown does not necessarily produce B-rich melt. Instead, breakdown product such as dumortierite, grandidierite, B-mullite or other borosilicate minerals are often observed (Dingwell et al. 1996; von Goerne et al. 1999b; Ballirano et al. 2022). Upper pressure stability reported for dravite (up to 8 GPa at 900°C, Krosse 1995; Werding & Schreyer 1996) suggests that tourmaline is stable up to subarc conditions. High-pressure tourmalines are generally dravitic, but, K-tourmaline occurrences in ultra-high P rocks have frequently been described (Shimizu & Ogasawara 2005, 2013; Ota et al. 2008a; Marschall et al. 2009). Those compositions reflect a K-rich system, in which tourmaline is the only mineral able to incorporate K at elevated pressure (Berryman et al. 2015). Experiments on natural uvite sample implied that tourmaline may be stable under even higher pressures, up to ~ 18 GPa at 450°C, corresponding to old and rapidly subducting slabs (Xu et al. 2016).

The lower P-T limits of stability are not well defined, but tourmaline has been found in diverse low P-T environments such as calcitic cap rocks associated with salt domes (Henry et al. 1999), archean stromatolites (Henry & Dutrow 1996) and gas fields in Wyoming where tourmaline is a pore-filling authigenic mineral (Henry & Dutrow 2012). Consequently, it is believed that the tourmaline stability is lower than 150°C and 1 MPa (Henry & Dutrow 2018).

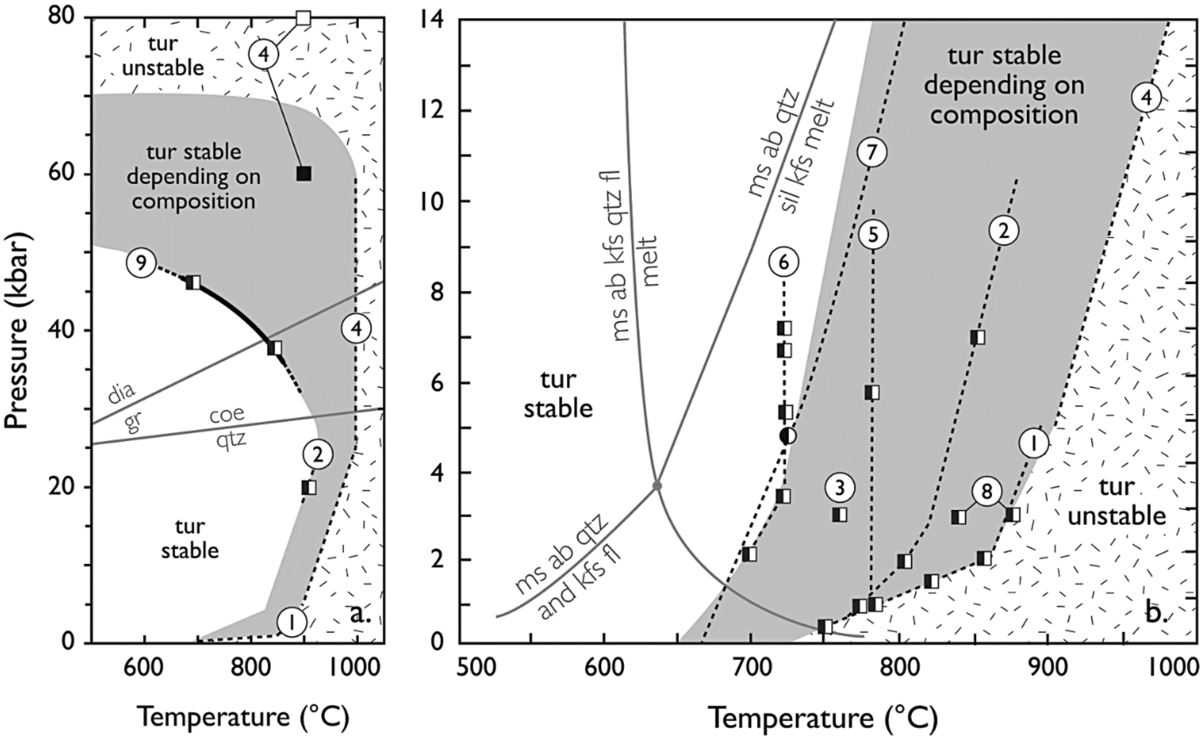

Figure 14:Compilation of P-T stability estimates for tourmaline of varying composition (from van Hinsberg et al., 2011a). Circles represent constraints from natural examples, square are experimental data, and dashed lines, the extrapolations presented by the original authors.

IV- Thesis outline and aims

Current knowledge of tourmaline indicates that this mineral has all the characteristics required to make it a powerful petrological tool. It is widespread, occurs in most geological environment, stables over a significant portion of the P-T-X space of the crust, shows negligible intracristalline diffusion, is refractory and it accommodates a large range of different elements (Dutrow & Henry 2011; Marschall and Jiang 2011; van Hinsberg et al. 2011b). Those properties allow it to record evidence of its geologic history in its composition and texture. Multiple studies have been realised in order to decipher how tourmaline major and minor composition (as well as its isotopes) respond to the P-T conditions, petrology and fluid composition of its crystallising environment. The qualitative and/or quantitative results, notably on partition coefficients, allow recent study to use this accessory mineral as a tracer of the fluid evolution in hydrothermal systems and even to reconstruct the fluid composition (Berryman et al. 2017; Codeço et al. 2017; Harlaux et al. 2020). However, those same properties make tourmaline a difficult mineral to deal with and more advanced use, such as a geothermobarometer or in thermodynamic modelling, are still lacking calibration.

Recent advances in the metallogeny of hydrothermal ore deposits implies the combination of fluid flow simulations with thermodynamic modelling. This methodology, applied by Launay et al. (2023) highlight that by modifying the petrophysics properties of the host rock, alteration constitute both a physical and chemical driving force during the ore deposit formation. Tourmaline is an emblematic mineral of the magmatic/hydrothermal transition, present from the late stage of magmatic crystallisation to the low temperature metasomatism. Applying the methodology of Launay et al. (2023) on tourmalinisation would allow us to understand how this alteration impact its hydrothermal environment. Thus, the tourmaline would provide not only information on the physico-chemical conditions of its environment, but also on the feedback phenomena controlling the fluid flow and the location of mineralisation. Such development requires (i) a good implementation of the alteration in batch equilibrium simulation and (ii) quantitative laws describing the effect of the alteration on the permeability of the rock. Research on this last point is quite recent and remains to be fully explored, through reactive percolation experiments at “high temperature”, up to 400°C (Launay et al. 2019; Osselin et al. 2022). But, in the case of tourmaline, even the first condition is far from being completed. As explained previously, the lack of calibrating data on tourmaline stability, notably concerning the boron concentration in the system, is a barrier to its use in thermodynamic modelling. The few experimental constraints already existing on the subject are mainly focusing on Fe-free systems at high temperature (> 500°C) and present some inconsistencies depending of the fluid composition used.

This thesis aim, in a first part, to complement and provide new experimental constraints on $[B_2O_3]_{fluid\_EQ}$, the boron concentration of the fluid at equilibrium with tourmaline. Batch experiments in internally heated pressure vessels were conducted between 400 and 600°C at 200 MPa and under fO_2 controlled conditions, in order to bracket the evolution of tourmaline stability. Although it is relatively rare in natural systems, tourmalinisation of cordierite has long been studied and is the only reaction for which $[B_2O_3]_{fluid\_EQ}$ has been measured (Weisbrod et al. 1986; von Goerne et al. 1999b). The mineralogical system represented has the advantages to be Fe-free, thus limiting the effect of the fO_2, and of being well correlated with magmatic systems and peraluminous melts. In order to form a solid base of reference, **Chapter II** provides new experimental constraints on the equilibria tourmaline + cordierite + albite + quartz + andalusite + fluid (H_2O +$B(OH)_3$). Textural and compositional evolution are interpreted as a function of the supersaturation level of the fluid and effect of the T-fO_2 conditions. The value of $[B_2O_3]_{fluid\_EQ}$ estimated is directly comparable to previous studies on tourmaline stability and highlights the need for data on systems that are closer to what can be observed in nature. This chapter is also the occasion to look at the actual set of standard thermodynamic properties for tourmaline and look at how well calculations based on them are able to reproduce experimental data. In **Chapter III**, the question concerning tourmaline stability in a more natural-like system is addressed, following the same methodology as in Chapter II. The $[B_2O_3]_{fluid\_EQ}$ is experimentally estimated for the equilibria between biotite and tourmaline, the most common form of tourmalinisation in perigranitic systems (e.g. Lecumberri-Sanchez et al. 2017; Orlando et al. 2017; Harlaux et al. 2020).

Chapter IV deals with a dynamic approach of boron metasomatism in perigranitic environment. The study reports the result of a reactive percolation experiment on a spotted micaschist from Panasqueira, infiltrated with a $B(OH)_3$ brine at 300°C for 5 weeks. Permeability changes were monitored and the petrographic, textural and chemical evolution of the post-experiment cores, as well as outlet fluids composition were analysed. Although permeability variation does not respond to a pervasive circulation of the fluid through the rock, the experiment reproduces a vein opening through hydraulic fracturing. The characteristics of the evolution of the wall alteration fronts are deciphered in order to explore the interactions between the chemistry of the system, the reaction kinetics and the local fluid flow.

Finally, **Chapter V** ties together the conclusion of the two experimental parts, batch and transport reaction and highlights the consequences of this thesis on the understating of the stability and dynamics of boron metasomatism in hydrothermal systems.

References:

Acosta-Vigil, A., London, D., Morgan, G.B., and Dewers, T.A. (2003) Solubility of excess alumina in hydrous granitic melts in equilibrium with peraluminous minerals at 700–800 °C and 200 MPa, and applications of the aluminum saturation index. Contributions to Mineralogy and Petrology, 146, 100–119.

Ague, J.J. (2014) Fluid Flow in the Deep Crust. In Treatise on Geochemistry Vols. 1-15, Vol. 4, pp. 203–247. Elsevier.

Akinfiev, N.N., Voronin, M.V., Zotov, A.V., and Prokof'ev, V.Yu. (2006) Experimental investigation of the stability of a chloroborate complex and thermodynamic description of aqueous species in the B-Na-Cl-O-H system up to 350°C. Geochemistry International, 44, 867–878.

Anderson, G.M. (1998) The Thermodynamics of Hydrothermal Systems. In Techniques in Hydrothermal Ore Deposits Geology pp. 1–31. The Society of Economic Geologists.

Anovitz, L.M., and Grew, E.S. (1996) Chapter 1. Mineralogy, Petrology and Geochemistry of Boron: an Introduction. In Boron _ Mineralogy, Petrology and Geochemistry Vol. 33, pp. 1–40. De Gruyter, Berlin, Boston.

Bačík, P. (2015) Cation ordering at octahedral sites in schorl-dravite series tourmalines. The Canadian Mineralogist, 53, 571–590.

Bačík, P., Meres, S., and Uher, P. (2011) Vanadium-bearing tourmaline in metacherts from Chvojnica, Slovak Republic: crystal chemistry and multistage evolution. The Canadian Mineralogist, 49, 195–206.

Bačík, P., Dikej, J., Fridrichová, J., Miglierini, M., and Števko, M. (2017) Chemical composition and evolution of tourmaline-supergroup minerals from the Sb hydrothermal veins in Rožňava area, Western Carpathians, Slovakia. Mineralogy and Petrology, 111, 609–624.

Baksheev, I.A., Tikhomirov, P.L., Yapaskurt, V.O., Vigasina, M.F., Prokof'ev, V.Yu., and Ustinov, V.I. (2009) Tourmaline of the Mramorny tin cluster, Chukotia peninsula, Russia. The Canadian Mineralogist, 47, 1177–1194.

Ballirano, P., Celata, B., Skogby, Hk., Andreozzi, G.B., and Bosi, F. (2022) HT breakdown of Mn-bearing elbaite from the Anjanabonoina pegmatite, Madagascar. Journal of Geosciences, 151–161.

Baskina, V.A., Prokof'ev, V.Yu., Lebedev, V.A., Borisovsky, S.E., Dobrovol'skaya, M.G., Yakushev, A.I., and Gorbacheva, S.A. (2009) The Dal'negorsk borosilicate skarn deposit, primorye, Russia: Composition of ore-bearing solutions and boron sources. Geology of Ore Deposits, 51, 179–196.

Beckett-Brown, C.E., McDonald, A.M., and McClenaghan, M.B. (2023) Recognizing Tourmaline in Mineralized Porphyry Cu Systems: Textures and Major-Element Chemistry. The Canadian Journal of Mineralogy and Petrology, 61, 3–29.

Berryman, E.J., Wunder, B., Wirth, R., Rhede, D., Schettler, G., Franz, G., and Heinrich, W. (2015) An experimental study on K and Na incorporation in dravitic tourmaline and insight into the origin of diamondiferous tourmaline from the Kokchetav Massif, Kazakhstan. Contributions to Mineralogy and Petrology, 169, 28.

Berryman, E.J., Wunder, B., Rhede, D., Schettler, G., Franz, G., and Heinrich, W. (2016) P–T–X controls on Ca and Na distribution between Mg–Al tourmaline and fluid. Contributions to Mineralogy and Petrology, 171, 31.

Berryman, E.J., Kutzschbach, M., Trumbull, R.B., Meixner, A., van Hinsberg, V.J., Kasemann, S.A., and Franz, G. (2017) Tourmaline as a petrogenetic indicator in the Pfitsch Formation, Western Tauern Window, Eastern Alps. Lithos, 284–285, 138–155.

Blanc, Ph., Lassin, A., Piantone, P., Azaroual, M., Jacquemet, N., Fabbri, A., and Gaucher, E.C. (2012) Thermoddem: A geochemical database focused on low temperature water/rock interactions and waste materials. Applied Geochemistry, 27, 2107–2116.

Booden, M.A., Mauk, J.L., and Simpson, M.P. (2011) Quantifying Metasomatism in Epithermal Au-Ag Deposits: A Case Study from the Waitekauri Area, New Zealand. Economic Geology, 106, 999–1030.

Bosi, F., Balic-Zunic, T., and Surour, A.A. (2010) Crystal structure analyses of four tourmaline specimens from the Cleopatra's Mines (Egypt) and Jabal Zalm (Saudi Arabia), and the role of Al in the tourmaline group. American Mineralogist, 95, 510–518.

Bosi, F., Skogby, H., and Hålenius, U. (2016) Thermally induced cation redistribution in Fe-bearing oxy-dravite and potential geothermometric implications. Contributions to Mineralogy and Petrology, 171, 47.

Bosi, F., Naitza, S., Skogby, H., Secchi, F., Conte, A.M., Cuccuru, S., Hålenius, U., De La Rosa, N., Kristiansson, P., Charlotta Nilsson, E.J., and others (2018) Late magmatic controls on the origin of schorlitic and foititic tourmalines from late-Variscan peraluminous granites of the Arbus pluton (SW Sardinia, Italy): Crystal-chemical study and petrological constraints. Lithos, 308–309, 395–411.

Broska, I., and Kubiš, M. (2018) Accessory minerals and evolution of tin-bearing S-type granites in the western segment of the Gemeric Unit (Western Carpathians). Geologica Carpathica, 69, 483–497.

Büttner, S.H. (2005) Deformation-controlled cation diffusion in compositionally zoned tourmaline. Mineralogical Magazine, 69, 471–489.

Büttner, S.H., and Kasemann, S.A. (2007) Deformation-controlled cation diffusion in tourmaline: A microanalytical study on trace elements and boron isotopes. American Mineralogist, 92, 1862–1874.

Celata, B., Ballirano, P., Andreozzi, G.B., and Bosi, F. (2021) In situ high-temperature behaviour of fluor-elbaite: breakdown conditions and products. Physics and Chemistry of Minerals, 48, 24.

Chen, X., Jiang, S., R.Palmer, M., Schertl, H.-P., Cambeses, A., Hernández-Uribe, D., Zhao, K., Lin, C., and Zheng, Y. (2023) Tourmaline chemistry, boron, and strontium isotope systematics trace multiple melt–fluid–rock interaction stages in deeply subducted continental crust. Geochimica et Cosmochimica Acta, 340, 120–140.

Cheng, L., Zhang, C., Yang, X., Qi, D., Zhou, Y., and Holtz, F. (2019) Experimental investigation of reactions between two-mica granite and boron-rich fluids: Implications for the formation of tourmaline granite. Science China Earth Sciences, 62, 1630–1644.

Codeço, M.S., Weis, P., Trumbull, R.B., Pinto, F., Lecumberri-Sanchez, P., and Wilke, F.D.H. (2017) Chemical and boron isotopic composition of hydrothermal tourmaline from the Panasqueira W-Sn-Cu deposit, Portugal. Chemical Geology, 468, 1–16.

Deb, M., Tiwary, A., and Palmer, M.R. (1997) Tourmaline in Proterozoic Massive Sulfide Deposits from Rajasthan, India. Mineralium Deposita, 32, 94–99.

Dingwell, D.B., Pichavant, M., and Holtz, F. (1996) Chapter 8. Experimental Studies of Boron in Granitic Melts. In L.M. Anovitz and E.S. Grew, Eds., Boron _ Mineralogy, Petrology and Geochemistry Vol. 33, pp. 331–386. De Gruyter, Berlin, Boston.

Dolejš, D., and Wagner, T. (2008) Thermodynamic modelling of non-ideal mineral–fluid equilibria in the system Si–Al–Fe–Mg–Ca–Na–K–H–O–Cl at elevated temperatures and pressures: Implications for hydrothermal mass transfer in granitic rocks. Geochimica et Cosmochimica Acta, 72, 526–553.

Dreher, A.M., Xavier, R.P., Taylor, B.E., and Martini, S.L. (2008) New geologic, fluid inclusion and stable isotope studies on the controversial Igarapé Bahia Cu–Au deposit, Carajás Province, Brazil. Mineralium Deposita, 43, 161–184.

Driesner, T. (2007) The system H2O–NaCl. Part II: Correlations for molar volume, enthalpy, and isobaric heat capacity from 0 to 1000°C, 1 to 5000bar, and 0 to 1 XNaCl. Geochimica et Cosmochimica Acta, 71, 4902–4919.

Driesner, T., and Heinrich, C.A. (2007) The system H2O–NaCl. Part I: Correlation formulae for phase relations in temperature–pressure–composition space from 0 to 1000°C, 0 to 5000bar, and 0 to 1 XNaCl. Geochimica et Cosmochimica Acta, 71, 4880–4901.

Dutrow, B., and Henry, D. (2022) Calcium-rich dravite from the Arignac Gypsum Mine, France: Implications for tourmaline development in a sulfate-rich, highly magnesian meta-evaporite. Journal of Geosciences, 191–207.

Dutrow, B.L., and Henry, D.J. (2011) Tourmaline: A Geologic DVD. Elements, 7, 301–306.

Dutrow, B.L., and Henry, D.J. (2016) Fibrous Tourmaline: A Sensitive Probe of Fluid Compositions and Petrologic Environments. The Canadian Mineralogist, 54, 311–335.

Dutrow, B.L., and Henry, D.J. (2018) Tourmaline compositions and textures: reflections of the fluid phase. Journal of Geosciences, 99–110.

Ertl, A., Tillmanns, E., Ntaflos, T., Francis, C., Giester, G., Körner, W., Hughes, J.M., Lengauer, C., and Prem, M. (2008) Tetrahedrally coordinated boron in Al-rich tourmaline and its relationship to the pressure-temperature conditions of formation. European Journal of Mineralogy, 20, 881–888.

Ertl, A., Marschall, H.R., Giester, G., Henry, D.J., Schertl, HP., Ntaflos, T., Luvizotto, G.L., Nasdala, L., and Tillmanns, E. (2010) Metamorphic ultrahigh-pressure tourmaline: Structure, chemistry, and correlations to P-T conditions. American Mineralogist, 95, 1–10.

Ferguson, J.P., Arcis, H., and Tremaine, P.R. (2019) Thermodynamics of Polyborates under Hydrothermal Conditions: Formation Constants and Limiting Conductivities of Triborate and Diborate. Journal of Chemical & Engineering Data, 64, 4430–4443.

Garofalo, P., Matthai, S.K., and Heinrich, C.A. (2002) Three-dimensional geometry, ore distribution and time-integrated mass transfer through the quartz-tourmaline-gold vein network of the Sigma deposit (Abitibi belt, Canada). Geofluids, 2, 217–232.

Garwin, S. (2002) The Geologic Setting of Intrusion-Related Hydrothermal Systems near the Batu Hijau Porphyry Copper-Gold Deposit, Sumbawa, Indonesia. In Integrated Methods for Discovery: Global Exploration in the Twenty-First Century Vol. 9. Society of Economic Geologists.

Goerne, G.V., and Franz, G. (2000) Synthesis of Ca-tourmaline in the system CaO-MgO-Al 2 O 3 -SiO 2 -B 2 O 3 -H 2 O-HCl. Mineralogy and Petrology, 69, 161–182.

Green, T.H., and Adam, J. (2003) Experimentally-determined trace element characteristics of aqueous fluid from partially dehydrated mafic oceanic crust at 3.0 GPa, 650-700C. European Journal of Mineralogy, 15, 815–830.

Grew, E.S., Hystad, G., Hazen, R.M., Krivovichev, S.V., and Gorelova, L.A. (2017) How many boron minerals occur in Earth's upper crust? American Mineralogist, 102, 1573–1587.

Gysi, A., Mei, Y., and Driesner, T. (2020) Advances in Numerical Simulations of Hydrothermal Ore Forming Processes. Geofluids, 2020, 1–4.

Haar, L., Gallagher, J.S., and Kell, G.S. (1984) NBS/NRC Steam Tables: Thermodynamic and Transport Properties and Computer Programs for Vapor and Liquid States of Water in SI Units, 320 p. Hemisphere Publishing Corp, Washington, D.C.

Halter, W.E., Williams-Jones, A.E., and Kontak, D.J. (1998) Modeling fluid–rock interaction during greisenization at the East Kemptville tin deposit: implications for mineralisation. Chemical Geology, 150, 1–17.

Harlaux, M., Kouzmanov, K., Gialli, S., Fontboté, L., Marger, K., Bouvier, A.-S., Baumgartner, L., Dini, A., Chauvet, A., and Kalinaj, M. (2019) Cassiterite deposition triggered by fluid mixing : Evidence from in-situ δ18O-δ11B analysis of tourmaline from the San Rafael tin deposit, Peru p. 4. Presented at the 15th Biennial SGA Meeting., Glasgow (Scotland).

Harlaux, M., Kouzmanov, K., Gialli, S., Laurent, O., Rielli, A., Dini, A., Chauvet, A., Menzies, A., Kalinaj, M., and Fontboté, L. (2020) Tourmaline as a Tracer of Late-Magmatic to Hydrothermal Fluid Evolution: The World-Class San Rafael Tin (-Copper) Deposit, Peru. Economic Geology.

Harlov, D.E., and Austrheim, H. (2013) Metasomatism and the Chemical Transformation of Rock: The Role of Fluids in Terrestrial and Extraterrestrial Processes. Springer Berlin Heidelberg, Berlin, Heidelberg.

Hawthorne, F.C., and Dirlam, D.M. (2011) Tourmaline the Indicator Mineral: From Atomic Arrangement to Viking Navigation. Elements, 7, 307–312.

Hazarika, P., Mishra, B., and Pruseth, K.L. (2015) Diverse Tourmaline Compositions from Orogenic Gold Deposits in the Hutti-Maski Greenstone Belt, India: Implications for Sources of Ore-Forming Fluids. Economic Geology, 110, 337–353.

Heinrich, C.A. (2005) The physical and chemical evolution of low-salinity magmatic fluids at the porphyry to epithermal transition: a thermodynamic study. Mineralium Deposita, 39, 864–889.

Heinrich, C.A., and Candela, P.A. (2014) Fluids and Ore Formation in the Earth's Crust. In Treatise on Geochemistry Vols. 1-15, Vol. 13, pp. 1–28. Elsevier.

Hellingwerf, R.H., Gatedal, K., Gallagher, V., and Baker, J.H. (1994) Tourmaline in the central Swedish ore district. Mineralium Deposita, 29.

Henry, D.. J., and Dutrow, B.L. (2012) Tourmaline at diagenetic to low-grade metamorphic conditions: Its petrologic applicability. Lithos, 154, 16–32.

Henry, D.J., and Dutrow, B.L. (1996) Chapter 10. Metamorphic Tourmaline and its Petrologic Applications. In E.S. Grew and L.M. Anovitz, Eds., Boron _ Mineralogy, Petrology and Geochemistry Vol. 33, pp. 503–558. De Gruyter, Berlin, Boston.

——— (2001) Compositional zoning and element partitioning in nickeloan tourmaline from a metamorphosed karstbauxite from Samos, Greece. American Mineralogist, 86, 1130–1142.

——— (2011) The incorporation of fluorine in tourmaline: internal crystallographic controls or external environmental influences? The Canadian Mineralogist, 49, 41–56.

——— (2018) Tourmaline studies through time: contributions to scientific advancements. Journal of Geosciences, 63, 77–98.

Henry, D.J., and Guidotti, C.V. (1985) Tourmaline as a petrogenetic indicator mineral: an example from the staurolite-grade metapelites of NW Maine. American Mineralogist, 70, 1–15.

Henry, D.J., Kirkland, B.L., and Kirkland, D.W. (1999) Sector-zoned tourmaline from the cap rock of a salt dome. European Journal of Mineralogy, 11, 263–280.

Henry, D.J., Novak, M., Hawthorne, F.C., Ertl, A., Dutrow, B.L., Uher, P., and Pezzotta, F. (2011) Nomenclature of the tourmaline-supergroup minerals. American Mineralogist, 96, 895–913.

Hinsberg, V.J.V., and Schumacher, J.C. (2007) Intersector element partitioning in tourmaline: a potentially powerful single crystal thermometer. Contributions to Mineralogy and Petrology, 153, 289–301.

Hinsberg, V.J.V., and Schumacher, J.C. (2009) The geothermobarometric potential of tourmaline, based on experimental and natural data. American Mineralogist, 94, 761–770.

Holland, T.J.B., and Powell, R. (2011) An improved and extended internally consistent thermodynamic dataset for phases of petrological interest, involving a new equation of state for solids: THERMODYNAMIC DATASET FOR PHASES OF PETROLOGICAL INTEREST. Journal of Metamorphic Geology, 29, 333–383.

Hoover, W.F., Penniston-Dorland, S., Piccoli, P., and Kylander-Clark, A. (2022) Reaction-induced porosity in an eclogite-facies vein selvage (Monviso Ophiolite, W. Alps): Textural evidence and in situ trace elements and Sr isotopes in apatite. Journal of Petrology.

Hurtig, N.C., Migdisov, A.A., and Williams-Jones, A.E. (2021) Are Vapor-Like Fluids Viable Ore Fluids for Cu-Au-Mo Porphyry Ore Formation? Economic Geology, 116, 1599–1624.

Ingebritsen, S.E., and Gleeson, T. (2015) Crustal permeability: Introduction to the special issue. Geofluids, 15, 1–10.

Ingri, N. (1962) Equilibrium Studies of Polyanions 8. On the First Equilibrium Steps in the Hydrolysis of Boric Acid, a Comparison between Equilibira in 0.1 M and 3.0 M NaClO4. Acta Chemica Scandinavica, 16, 439–448.

——— (1963) Equilibrium Studies of Polyanions. 10. On the First Equilibrium Steps in the Acidification of B(OH)4-, an Application of the Self-Medium Method. Acta Chemica Scandinavica, 17, 573–580.

Jamtveit, B., Malthesorenssen, A., and Kostenko, O. (2008) Reaction enhanced permeability during retrogressive metamorphism. Earth and Planetary Science Letters, 267, 620–627.

Johnson, J.W., Oelkers, E.H., and Helgeson, H.C. (1992) SUPCRT92: A software package for calculating the standard molal thermodynamic properties of minerals, gases, aqueous species, and reactions from 1 to 5000 bar and 0 to 1000°C. Computers & Geosciences, 18, 899–947.

Jonas, L., John, T., King, H.E., Geisler, T., and Putnis, A. (2014) The role of grain boundaries and transient porosity in rocks as fluid pathways for reaction front propagation. Earth and Planetary Science Letters, 386, 64–74.

Kalliomäki, H., Wagner, T., Fusswinkel, T., and Sakellaris, G. (2017) Major and trace element geochemistry of tourmalines from Archean orogenic gold deposits: Proxies for the origin of gold mineralising fluids? Ore Geology Reviews, 91, 906–927.

Kawakami, T., and Ikeda, T. (2003) Boron in metapelites controlled by the breakdown of tourmaline and retrograde formation of borosilicates in the Yanai area, Ryoke metamorphic belt, SW Japan. Contributions to Mineralogy and Petrology, 145, 131–150.

Kelly, C.J., Davis, W.J., Potter, E.G., and Corriveau, L. (2020) Geochemistry of hydrothermal tourmaline from IOCG occurrences in the Great Bear magmatic zone: Implications for fluid source(s) and fluid composition evolution. Ore Geology Reviews, 118, 103329.

Kesler, S.E., Stoiber, R.E., and Billings, G.K. (1972) Direction of Flow of Mineralizing Solutions at Pine Point, N.W.T. Economic Geology, 67, 19–24.

Klemme, S., Marschall, H.R., Jacob, D.E., Prowatke, S., and Ludwig, T. (2011) Trace-element partitioning and boron isotope fractionation between white mica and tourmaline. The Canadian Mineralogist, 49, 165–176.

Krosse, S. (1995) Hochdrucksynthese, stabilität und eigenschaften der borsilikate dravit und kornerupin sowie darstellung und stabilitätsverhalten eines neuen Mg-Al-borates. Earth Sciences, Ruhr-University, Bochum.

Launay, G., Sizaret, S., Guillou-Frottier, L., Gloaguen, E., and Pinto, F. (2018) Deciphering fluid flow at the magmatic-hydrothermal transition: A case study from the world-class Panasqueira W–Sn–(Cu) ore deposit (Portugal). Earth and Planetary Science Letters, 499, 1–12.

Launay, G., Sizaret, S., Guillou-Frottier, L., Fauguerolles, C., Champallier, R., and Gloaguen, E. (2019) Dynamic Permeability Related to Greisenization Reactions in Sn-W Ore Deposits: Quantitative Petrophysical and Experimental Evidence. Geofluids, 2019, 1–23.

Launay, G., Branquet, Y., Sizaret, S., Guillou-Frottier, L., and Gloaguen, E. (2023) How greisenization could trigger the formation of large vein-and-greisen Sn-W deposits: A numerical investigation applied to the Panasqueira deposit. Ore Geology Reviews, 153, 105299.

Lecumberri-Sanchez, P., Vieira, R., Heinrich, C.A., Pinto, F., and Wälle, M. (2017) Fluid-rock interaction is decisive for the formation of tungsten deposits. Geology, 45, 579–582.

Leeman, W.P., and Sisson, V.B. (1996) Chapter 12. Geochemistry of Boron and its Implications for Crustal and Mantle Processes. In L.M. Anovitz and E.S. Grew, Eds., Boron _ Mineralogy, Petrology and Geochemistry Vol. 33, pp. 645–708. De Gruyter, Berlin, Boston.

Legros, H., Elongo, V., Laurent, O., Adlakha, E., Chelle-Michou, C., Falck, H., and Lecumberri-Sanchez, P. (2022) Formation of the Lened W-(Be) Skarn Deposit by Neutralization of a Magmatic Fluid—Evidence from H3BO3-Rich Fluids. Geosciences, 12, 236.

Lensing-Burgdorf, M., Watenphul, A., Schlüter, J., and Mihailova, B. (2017) Crystal chemistry of tourmalines from the Erongo Mountains, Namibia, studied by Raman spectroscopy. European Journal of Mineralogy, 29, 257–267.

Lerouge, C., and Bouchot, V. (2009) Conditions of formation and origin of fluids of quartz-tourmaline veins in the La Châtaigneraie tungstiferous district (Massif Central, France): fluid inclusions and stable isotopes. Bulletin de la Société Géologique de France, 180, 263–270.

Li, W., Qiao, X., Zhang, F., and Zhang, L. (2022) Tourmaline as a potential mineral for exploring porphyry deposits: a case study of the Bilihe gold deposit in Inner Mongolia, China. Mineralium Deposita, 57, 61–82.

Liu, M., Guo, Q., Luo, L., and He, T. (2020) Environmental impacts of geothermal waters with extremely high boron concentrations: Insight from a case study in Tibet, China. Journal of Volcanology and Geothermal Research, 397, 106887.

Liu, X., and Xiao, C. (2020) Wolframite solubility and precipitation in hydrothermal fluids: Insight from thermodynamic modelling. Ore Geology Reviews, 117, 103289.

London, D. (2011) Experimental synthesis and stability of tourmaline: a historical overview. The Canadian Mineralogist, 49, 117–136.

London, D., Morgan, G.B., and Wolf, M.B. (1996) Chapter 7. Boron in granitic rocks and their contact aureoles. In L.M. Anovitz and E.S. Grew, Eds., Boron _ Mineralogy, Petrology and Geochemistry Vol. 33, pp. 299–330. De Gruyter, Berlin, Boston.

Lussier, A.J., Aguiar, P.M., Michaelis, V.K., Kroeker, S., and Hawthorne, F.C. (2009) The occurrence of tetrahedrally coordinated Al and B in tourmaline: An 11B and 27Al MAS NMR study. American Mineralogist, 94, 785–792.

Lynch, G., and Ortega, J. (1997) Hydrothermal alteration and tourmaline-albite equilibria at the Coxheath porphyry Cu-Mo-Au deposit, Nova Scotia. The Canadian Mineralogist, 35, 79–94.

Mahjoubi, E.M., Chauvet, A., Badra, L., Sizaret, S., Barbanson, L., El Maz, A., Chen, Y., and Amann, M. (2016) Structural, mineralogical, and paleoflow velocity constraints on Hercynian tin mineralisation: the Achmmach prospect of the Moroccan Central Massif. Mineralium Deposita, 51, 431–451.

Mar'ina, E.A., Balitskii, V.S., Balittskaya, L.V., Urusov, V.S., and Rossman, J.R. (1999) Solubility and growth of quartz crystals in aqueous-borate solutions. Doklady Earth Sciences, 369(A), 1285–1287.

Marks, M.A.W., Marschall, H.R., Schühle, P., Guth, A., Wenzel, T., Jacob, D.E., Barth, M., and Markl, G. (2013) Trace element systematics of tourmaline in pegmatitic and hydrothermal systems from the Variscan Schwarzwald (Germany): The importance of major element composition, sector zoning, and fluid or melt composition. Chemical Geology, 344, 73–90.

Marsala, A., Wagner, T., and Wälle, M. (2013) Late-metamorphic veins record deep ingression of meteoric water: A LA-ICPMS fluid inclusion study from the fold-and-thrust belt of the Rhenish Massif, Germany. Chemical Geology, 351, 134–153.

Marschall, H.R., and Jiang, S.-Y. (2011) Tourmaline Isotopes: No Element Left Behind. Elements, 7, 313–319.

Marschall, H.R., Korsakov, A.V., Luvizotto, G.L., Nasdala, L., and Ludwig, T. (2009) On the occurrence and boron isotopic composition of tourmaline in (ultra)high-pressure metamorphic rocks. Journal of the Geological Society, 166, 811–823.

Mesmer, R.E., Baes, C.F., and Sweeton, F.H. (1972) Acidity Measurements at Elevated Temperatures. VI. Boric Acid Equilibria. Inorganic Chemistry, 11, 537–543.

Millero, F.J., Feistel, R., Wright, D.G., and McDougall, T.J. (2008) The composition of Standard Seawater and the definition of the Reference-Composition Salinity Scale. Deep Sea Research Part I: Oceanographic Research Papers, 55, 50–72.

Mlynarczyk, M.S.J., and Williams-Jones, A.E. (2006) Zoned tourmaline associated with cassiterite : implications for fluid evolution and tin mineralisation in the San Rafael Sn-Cu deposit, Southeastern Peru. The Canadian Mineralogist, 44, 347–365.

Morgan, G.B., and London, D. (1989) Experimental reactions of amphibolite with boron-bearing aqueous fluids at 200 MPa: implications for tourmaline stability and partial melting in mafic rocks. Contributions to Mineralogy and Petrology, 102, 281–297.

Nakano, T., and Nakamura, E. (2001) Boron isotope geochemistry of metasedimentary rocks and tourmalines in a subduction zone metamorphic suite. Physics of the Earth and Planetary Interiors, 127, 233–252.

Ootes, L., Goff, S., Jackson, V.A., Gleeson, S.A., Creaser, R.A., Samson, I.M., Evensen, N., Corriveau, L., and Mumin, A.H. (2010) Timing and thermochemical constraints on multi-element mineralisation at the Nori/RA Cu–Mo–U prospect, Great Bear magmatic zone, Northwest Territories, Canada. Mineralium Deposita, 45, 549–566.

Orlando, A., Ruggieri, G., Chiarantini, L., Montegrossi, G., and Rimondi, V. (2017) Experimental Investigation of Biotite-Rich Schist Reacting with B-Bearing Fluids at Upper Crustal Conditions and Correlated Tourmaline Formation. Minerals, 7, 23.

Osselin, F., Pichavant, M., Champallier, R., Ulrich, M., and Raimbourg, H. (2022) Reactive transport experiments of coupled carbonation and serpentinization in a natural serpentinite. Implication for hydrogen production and carbon geological storage. Geochimica et Cosmochimica Acta, 318, 165–189.

Ota, T., Kobayashi, K., Kunihiro, T., and Nakamura, E. (2008a) Boron cycling by subducted lithosphere; insights from diamondiferous tourmaline from the Kokchetav ultrahigh-pressure metamorphic belt. Geochimica et Cosmochimica Acta, 72, 3531–3541.

Ota, T., Kobayashi, K., Katsura, T., and Nakamura, E. (2008b) Tourmaline breakdown in a pelitic system: implications for boron cycling through subduction zones. Contributions to Mineralogy and Petrology, 155, 19–32.

Pan, J.-Y., Ni, P., and Wang, R.-C. (2019) Comparison of fluid processes in coexisting wolframite and quartz from a giant vein-type tungsten deposit, South China: Insights from detailed petrography and LA-ICP-MS analysis of fluid inclusions. American Mineralogist, 104, 1092–1116.

Pélissonier, H. (1965) Le problème de la concentration naturelle des substances minérales. Ann. des Mines, 889–924.

Peretyazhko, I.S., Prokofiev, V.Y., Zagorsky, V.Y., and Smirnov, S.Z. (2000) Role of Boric Acids in the Formation of Pegmatite and Hydrothermal Minerals: Petrologic Consequences of Sassolite (H3BO3) Discovery in Fluid Inclusions. (MAIK "Nauka/Interperiodica," Trans.)Petrology, 8, 214–237.

Pichavant, M. (1981) An experimental study of the effect of boron on a water saturated haplogranite at 1 Kbar vapour pressure: Geological applications. Contributions to Mineralogy and Petrology, 76, 430–439.

——— (1983) Melt-fluid interaction deduced from studies of silicate-B2O3-H2O systems at 1 kbar. Bulletin de Minéralogie, 106, 201–211.

Pichavant, M. (1987) Effects of B and H2O on liquidus phase relations in the haplogranite system at 1 kbar. American Mineralogist, 72, 1056–1070.

Pokrovski, G.S., Schott, J., and Sergeyev, A.S. (1995) Experimental determination of the stability constants of NaSO4− and NaB (OH)40 in hydrothermal solutions using a new high-temperature sodium-selective glass electrode — Implications for boron isotopic fractionation. Chemical Geology, 124, 253–265.

Pollok, K., Putnis, C.V., and Putnis, A. (2011) Mineral replacement reactions in solid solution-aqueous solution systems: Volume changes, reactions paths and end-points using the example of model salt systems. American Journal of Science, 311, 211–236.

Prokof'ev, V.Y., Akinfiev, N.N., and Groznova, E.O. (2002) On the Boron Concentration and Forms of Its Occurrence in Hydrothermal Ore-Forming Fluids. Geology of Ore Deposits, 44, 386–397.

Putnis, A. (2015) Transient Porosity Resulting from Fluid–Mineral Interaction and its Consequences. Reviews in Mineralogy and Geochemistry, 80, 1–23.

Qiu, Y., Zhang, R., Chou, I.-M., Wang, X., Hu, W., Zhang, W., Lu, J., Li, G., and Li, Z. (2021) Boron-rich ore-forming fluids in hydrothermal W-Sn deposits from South China: Insights from in situ Raman spectroscopic characterisation of fluid inclusions. Ore Geology Reviews, 132, 104048.

Reed, M., Rusk, B., and Palandri, J. (2013) The Butte Magmatic-Hydrothermal System: One Fluid Yields All Alteration and Veins. Economic Geology, 108, 1379–1396.

Reed, M.H. (1997) Hydrothermal alteration and its relationship to ore fluid composition. In Geochemistry of hydrothermal ore deposits _ 3rd Edition pp. 303–366. New-York.

Reed, M.H., and Palandri, J. (2014) SOLTHERM-XPT: Data Base of Equilibrium Constants for Aqueous-Mineral-Gas Equilibria.

Robbins, C.R., and Yoder, H.S.J. (1962) Stability relations of dravite, a tourmaline, 106–108 p. Yearbook 61, Carnegie Inst. Wash.

Rosenberg, P.E., Foit, F.F.J., and Ekambaram, V. (1986) Synthesis and characterisation of tourmaline in the system Na2O-Al2O3-SiO2-B2O3-H2O. American Mineralogist, 71, 971–976.

Rudnick, R.L., and Gao, S. (2003) Composition of the Continental Crust. In R.L. Rudnick, Ed., The Crust Vol. 3, pp. 1–64. Amsterdam.

Schardt, C., and Large, R.R. (2009) New insights into the genesis of volcanic-hosted massive sulfide deposits on the seafloor from numerical modelling studies. Ore Geology Reviews, 35, 333–351.

Schatz, O.J., Dolejš, D., Stix, J., Williams-Jones, A.E., and Layne, G.D. (2004) Partitioning of boron among melt, brine and vapour in the system haplogranite–H2O–NaCl at 800 °C and 100 MPa. Chemical Geology, 210, 135–147.

Schmidt, C., Thomas, R., and Heinrich, W. (2005) Boron speciation in aqueous fluids at 22 to 600°C and 0.1 MPa to 2 GPa. Geochimica et Cosmochimica Acta, 69, 275–281.

Schott, J., Kretzschmar, J., Acker, M., Eidner, S., Kumke, M.U., Drobot, B., Barkleit, A., Taut, S., Brendler, V., and Stumpf, T. (2014) Formation of a Eu(III) borate solid species from a weak Eu(III) borate complex in aqueous solution. Dalton Trans., 43, 11516–11528.

Sciuba, M., Beaudoin, G., and Makvandi, S. (2021) Chemical composition of tourmaline in orogenic gold deposits. Mineralium Deposita, 56, 537–560.

Scott, S.W., and Driesner, T. (2018) Permeability Changes Resulting from Quartz Precipitation and Dissolution around Upper Crustal Intrusions. Geofluids, 2018, 1–19.

Setkova, T.V., Balitsky, V.S., and Shapovalov, Yu.B. (2015) Synthesis of fine-crystalline tourmaline in hydrothermal solutions. Doklady Earth Sciences, 462, 468–471.

——— (2019) Experimental Study of the Stability and Synthesis of the Tourmaline Supergroup Minerals. Geochemistry International, 57, 1082–1094.

Shimizu, R., and Ogasawara, Y. (2005) Discovery of K-tourmaline in diamond-bearing quartz-rich rock from the Kokchetav Massif, Kazakhstan. Mitteilungen der Osterreichischen Mineralogischen Gesellschaft, 150, 141.

Shimizu, R., and Ogasawara, Y. (2013) Diversity of potassium-bearing tourmalines in diamondiferous Kokchetav UHP metamorphic rocks: A geochemical recorder from peak to retrograde metamorphic stages. Journal of Asian Earth Sciences, 63, 39–55.

Sirbescu, M.-L.C., Krukowski, E.G., Schmidt, C., Thomas, R., Samson, I.M., and Bodnar, R.J. (2013) Analysis of boron in fluid inclusions by microthermometry, laser ablation ICP-MS, and Raman spectroscopy: Application to the Cryo-Genie Pegmatite, San Diego County, California, USA. Chemical Geology, 342, 138–150.

Sizaret, S. (2011) La reconstruction de l’hydrodynamique des paléocirculations. Mémoire pour l’obtention de l’Habilitation à Diriger les Recherches, Orléans.

Sizaret, S., Fedioun, I., Barbanson, L., and Chen, Y. (2006) Crystallisation in flow - II. Modelling crystal growth kinetics controlled by boundary layer thickness. Geophysical Journal International, 167, 1027–1034.

Sizaret, S., Branquet, Y., Gloaguen, E., Chauvet, A., Barbanson, L., Arbaret, L., and Chen, Y. (2009) Estimating the local paleo-fluid flow velocity: New textural method and application to metasomatism. Earth and Planetary Science Letters, 280, 71–82.

Slack, J.F. (2022) Perspectives on premetamorphic stratabound tourmalinites. Journal of Geosciences, 73–102.

Slack, J.F., and Trumbull, R.B. (2011) Tourmaline as a Recorder of Ore-Forming Processes. Elements, 7, 321–326.

Slack, J.F., Palmer, M.R., Stevens, B.P.J., and Barnes, R.G. (1993) Origin and significance of tourmaline-rich rocks in the Broken Hill District, Australia. Economic Geology, 88, 505–541.

Smirnov, S.Z., Thomas, V.G., Demin, S.P., and Drebushchak, V.A. (2005) Experimental study of boron solubility and speciation in the Na2O–B2O3–SiO2–H2O system. Chemical Geology, 223, 16–34.

Su, Z.-K., Zhao, X.-F., Li, X.-C., and Zhou, M.-F. (2016) Using elemental and boron isotopic compositions of tourmaline to trace fluid evolutions of IOCG systems: The worldclass Dahongshan Fe Cu deposit in SW China. Chemical Geology, 441, 265–279.

Tagirov, B., and Schott, J. (2001) Aluminum speciation in crustal fluids revisited. Geochimica et Cosmochimica Acta, 65, 3965–3992.

Taylor, B.E., Palmer, M.R., and Slack, J.F. (1999) Mineralizing Fluids in the Kidd Creek Massive Sulfide Deposit, Ontario: Evidence from Oxygen, Hydrogen, and Boron Isotopes in Tourmaline*. In M.D. Hannington and C.T. Barrie, Eds., The Giant Kidd Creek Volcanogenic Massive Sulfide Deposit, Western Abitibi Subprovince, Canada Vol. 10, p. 0. Society of Economic Geologists.

Thomas, A.V., and Spooner, E.T.C. (1988) Fluid inclusions in the system H2O-CH4-NaCl-CO2 from metasomatic tourmaline within the border unit of the Tanco zoned granitic pegmatite, S.E. Manitoba. Geochimica et Cosmochimica Acta, 52, 1065–1075.

Thomas, R., Förster, H.-J., and Heinrich, W. (2003) The behaviour of boron in a peraluminous granite-pegmatite system and associated hydrothermal solutions: a melt and fluid-inclusion study. Contributions to Mineralogy and Petrology, 144, 457–472.

Trumbull, R.B., and Chaussidon, M. (1999) Chemical and boron isotopic composition of magmatic and hydrothermal tourmalines from the Sinceni granite–pegmatite system in Swaziland. Chemical Geology, 153, 125–137.

Tuduri, J. (2005) Processus de formation et relations spatio-temporelles des minéralisations à or et argent en contexte volcanique Précambrien (Jbel Saghro, Anti-Atlas, Maroc). Implications sur les relations déformation-magmatisme-volcanisme-hydrothermalisme. Sciences de la Terre et de l'Atmosphère : Métallogénie et Géologie structurale, Université d'Olréans, Orléans.

Tuduri, J., Chauvet, A., Barbanson, L., Bourdier, J.-L., Labriki, M., Ennaciri, A., Badra, L., Dubois, M., Ennaciri-Leloix, C., Sizaret, S., and others (2018) The Jbel Saghro Au(–Ag, Cu) and Ag–Hg Metallogenetic Province: Product of a Long-Lived Ediacaran Tectono-Magmatic Evolution in the Moroccan Anti-Atlas. Minerals, 8, 592.

van Hinsberg, V.J., and Schumacher, J.C. (2007) Intersector element partitioning in tourmaline: a potentially powerful single crystal thermometer. Contributions to Mineralogy and Petrology, 153, 289–301.

van Hinsberg, V.J., Henry, D.J., and Marschall, H.R. (2011a) Tourmaline: an ideal indicator of its host environment. The Canadian Mineralogist, 49, 1–16.

van Hinsberg, V.J., Henry, D.J., and Dutrow, B.L. (2011b) Tourmaline as a Petrologic Forensic Mineral: A Unique Recorder of Its Geologic Past. Elements, 7, 327–332.

van Hinsberg, V.J., Franz, G., and Wood, B.J. (2017) Determining subduction-zone fluid composition using a tourmaline mineral probe. Geochemical Perspectives Letters, 160–169.

Vereshchagin, O.S., Wunder, B., Baksheev, I.A., Wilke, F.D.H., Vlasenko, N.S., and Frank-Kamenetskaya, O.V. (2022) Ti4+ and Sn4+-bearing tourmalines - pressure control and comparison of synthetic and natural counterparts. Journal of Geosciences, 163–171.

von Goerne, G., Franz, G., and Wirth, R. (1999a) Hydrothermal synthesis of large dravite crystals by the chamber method. European Journal of Mineralogy, 11, 1061–1078.

von Goerne, G., Franz, G., and Robert, J.L. (1999b) Upper thermal stability of tourmaline + quartz in the system MgO-Al2O3-SiO2-B2O3-H2O and Na2O-MgO-Al2O3-SiO2-B2O3-H2O-HCl in hydrothermal solutions and siliceous melts. The Canadian Mineralogist, 37, 1025–1039.

von Goerne, G., Franz, G., and Heinrich, W. (2001) Synthesis of tourmaline solid solutions in the system Na2O–MgO–Al2O3–SiO2–B2O3–H2O–HCl and the distribution of Na between tourmaline and fluid at 300 to 700 °C and 200 MPa. Contributions to Mineralogy and Petrology, 141, 160–173.

von Goerne, G., Franz, G., and van Hinsberg, V.J. (2011) Experimental determination of Na-Ca distribution between tourmaline and fluid in the system CaO-Na2O-MgO-Al2O3-SiO2-B2O3-H2O. The Canadian Mineralogist, 49, 137–152.

Wadoski, E.R., Grew, E.S., and Yates, M.G. (2011) Compositional evolution of tourmaline-supergroup minerals from granitic pegmatites in the Larsemann Hills, East Antarctica. The Canadian Mineralogist, 49, 381–405.

Wagner, T., Kulik, D.A., Hingerl, F.F., and Dmytrieva, S.V. (2012) GEM-Selektor Geochemical Package: TSolMod Library and Data Interface for Multicomponent Phase Models. The Canadian Mineralogist, 50, 1173–1195.

Walden, E.L. (2016) Using Tourmaline As An Indicator Of Provenance: Development And Application Of A Statistical Approach Using Random Forests. Master's Theses, Louisiana State University and Agricultural and Mechanical College, Baton Rouge.

Wang, P., Kosinski, J.J., Lencka, M.M., Anderko, A., and Springer, R.D. (2013) Thermodynamic modelling of boric acid and selected metal borate systems. Pure and Applied Chemistry, 85, 2117–2144.

Warr, L.N. (2021) IMA–CNMNC approved mineral symbols. Mineralogical Magazine, 85, 291–320.

Wedepohl, K.H. (1995) The composition of the continental crust. Geochimica et Cosmochimica Acta, 59, 1217–1232.

Weis, P. (2015) The dynamic interplay between saline fluid flow and rock permeability in magmatic-hydrothermal systems. Geofluids, 15, 350–371.

Weisbrod, A., Polak, C., and Roy, D. (1986) Experimental study of tourmaline solubility in the system Na-Mg-Al-Si-B-O-H. Applications to the boron content of natural hydrothermal fluids and tourmalinization processes. pp. 140–141. Nancy - France.

Werding, G., and Schreyer, W. (1996) Chapter 3. Experimental studies on borosilicates and selected borates. In L.M. Anovitz and E.S. Grew, Eds., Boron _ Mineralogy, Petrology and Geochemistry Vol. 33, pp. 117–163. De Gruyter, Berlin, Boston.

Williamson, B.J., Spratt, J., Adams, J.T., Tindle, A.G., and Stanley, C.J. (2000) Geochemical Constraints from Zoned Hydrothermal Tourmalines on Fluid Evolution and Sn Mineralization: an Example from Fault Breccias at Roche, SW England. Journal of Petrology, 41, 1439–1453.

Wodara, U., and Schreyer, W. (2001) X-site vacant Al-tourmaline: a new synthetic end-member. European Journal of Mineralogy, 13, 521–532.

Wolf, M.B., and London, D. (1997) Boron in granitic magmas: stability of tourmaline in equilibrium with biotite and cordierite. Contributions to Mineralogy and Petrology, 130, 12–30.

Xu, J., Kuang, Y., Zhang, B., Liu, Y., Fan, D., Li, X., and Xie, H. (2016) Thermal equation of state of natural tourmaline at high pressure and temperature. Physics and Chemistry of Minerals, 43, 315–326.

Yang, S.-Y., Jiang, S.-Y., Zhao, K.-D., Dai, B.-Z., and Yang, T. (2015) Tourmaline as a recorder of magmatic–hydrothermal evolution: an in situ major and trace element analysis of tourmaline from the Qitianling batholith, South China. Contributions to Mineralogy and Petrology, 170, 42.

Yu, M., Feng, C.Y., Mao, J.W., Zhao, Y.M., Li, D.X., and Zhu, Y.F. (2017) Multistage Skarn-Related Tourmaline From the Galinge Deposit, Qiman Tagh, Western China: A Fluid Evolution Perspective. The Canadian Mineralogist, 55, 3–19.

Zhang, T., Li, D., and Meng, L. (2021) Recent progresses on the boron species in aqueous solution: structure, phase equilibria, metastable zone width (MZW) and thermodynamic model. Reviews in Inorganic Chemistry, 41, 49–60.

Zhao, K.-D., Zhang, L.-H., Palmer, M.R., Jiang, S.-Y., Xu, C., Zhao, H.-D., and Chen, W. (2021) Chemical and boron isotopic compositions of tourmaline at the Dachang Sn-polymetallic ore district in South China: Constraints on the origin and evolution of hydrothermal fluids. Mineralium Deposita, 56, 1589–1608.

Chapter II: Tourmaline-cordierite equilibrium constraints on the boron concentration of hydrothermal fluids.

Part of this chapter have been submitted for publication in "American Mineralogist" on June 14, 2023:

Tourmaline-cordierite equilibrium constraints on the boron concentration of hydrothermal fluids.

Julien Fort[1*], Stanislas Sizaret[1], Michel Pichavant[1], Arnault Lassin[2], Johann Tuduri[1,2], Olivier Blein[2]

[1] Institut des Sciences de la Terre d'Orléans (ISTO), UMR 7327, Université d'Orléans, CNRS, BRGM, F-45071 Orléans, France.

[2] Bureau de Recherches Géologiques et Minières (BRGM), F-45060 Orléans, France

Introduction

Tourmaline is a common accessory mineral of magmatic-hydrothermal environments from diverse tectonic settings (Slack and Trumbull 2011). It is ubiquitous in hydrothermal veins and metasomatized rocks from alteration aureoles developed around and within granitic plutons, such as greisens (Williamson et al. 2000; Codeço et al. 2017) and potassic alteration and advanced argillic zones (Lynch & Ortega 1997; Tuduri et al. 2018; Beckett-Brown et al. 2023).

The common occurrence of tourmaline in various contexts indicates that it is a phase stable under a wide range of pressure (P) and temperature (T) conditions (Henry & Dutrow 1996; van Hinsberg et al. 2011a). This property is partly due to the ability of tourmaline to adjust its composition by selectively incorporating a large number of major and trace elements (Dutrow & Henry 2011; van Hinsberg et al. 2011b) and, so, tourmaline chemistry has been commonly used as a probe of crystallisation environments. Thus, the major element composition of tourmaline is correlated with the typology of its host-rock (Henry & Guidotti 1985; Henry & Dutrow 1996; Slack & Trumbull 2011; Sciuba et al. 2021). Tourmaline also retains information on P-T and fO_2 conditions (Fuchs et al. 1998; von Goerne et al. 2011; van Hinsberg et al. 2011a; Berryman et al. 2016; Dutrow & Henry 2016). Element partitioning between tourmaline sectors has been used for thermometric purposes (van Hinsberg & Schumacher 2009). Tourmaline reacts to both chemical and physical evolution of hydrothermal systems, for example fluid flux, composition, mixing, and boiling. In combination with stable isotope (H, B, O) data, tourmaline composition can provide information on the origin of fluids (e.g. Nakano & Nakamura 2001; Slack & Trumbull 2011; Kelly et al. 2020; Sciuba et al. 2021). Quantitative reconstruction of the element contents of the fluid is within reach with the development of tourmaline/fluid partitioning studies (von Goerne et al. 2001, 2011; Williamson et al. 2010; van Hinsberg et al. 2017). Hence, tourmaline is assumed to be a proxy for fluid characterisation and a recorder of ore forming processes. However, presently, its use is limited by the lack of calibrating experimental information on essential properties such as those concerning tourmaline stability (see van Hinsberg & Schumacher 2007; Dutrow & Henry

2011). This issue is addressed in this study with new experimental data constraining tourmaline stability in the presence of aqueous hydrothermal fluids.

Tourmaline is chemically a highly complex mineral whose stability is influenced by numerous chemical variables, in addition to P and T (Dutrow & Henry 2011; London 2011). Information on tourmaline stability has come both from natural occurrences and experimental studies. However, most of the latter have been tourmaline synthesis or tourmalinisation experiments (von Goerne et al. 1999b; Orlando et al. 2017) using high boron concentration to ensure tourmaline formation. The disadvantage of such studies is that tourmaline stability limits as a function of chemical variables are poorly defined. In particular, for tourmaline in the presence of aqueous fluids, the determination of the boron concentration in the fluid at equilibrium ($[B_2O_3]_{fluid\_EQ}$) with tourmaline is essential. Information on this point would place strong constraints on the boron concentration of natural hydrothermal fluids , on conditions of boron metasomatism in and around granitic plutons (Drivenes et al. 2015; Codeço et al. 2017; Hong et al. 2017; Cheng et al. 2019; Harlaux et al. 2020) and also on the boron concentration of silicic magmas (Pichavant & Manning 1984; Dingwell et al. 1996; London 2011). Previous experimental work on this topic is almost non-existent, including in part Morgan & London (1989) and Cheng et al. (2019) and only one fully dedicated study has been published in abstract form (Weisbrod et al., 1986). In the present work, new experiments have been conducted at 200 MPa from 400 to 600°C and under fO_2-controlled conditions to define the boron content of the fluid at equilibrium with tourmaline. Experimental methods and results are detailed and interpreted according to thermodynamic considerations. Their implications for the boron content of natural systems and for the actual incorporation of tourmaline in thermodynamic modelling are discussed.

I- Tourmaline forming reactions and end-members

Equilibrium between quartz, albite, andalusite, cordierite, and tourmaline buffers the boron concentration of the hydrothermal fluid (Weisbrod et al. 1986; von Goerne et al. 1999b) according to reaction R1, written below for the pure Mg components (at. Fe/(Mg+Fe) = 0) in cordierite and tourmaline. The tourmaline end-member involved is dravite (Table 2.1).

$$3Mg_2Al_4Si_5O_{18} + 2NaAlSi_3O_8 + 6B(OH)_3 = 2NaMg_3Al_6Si_6O_{18}(BO_3)_3(OH)_4 + 8SiO_2 + Al_2SiO_5 + 5H_2O \qquad \text{(R1)}$$

cordierite albite fluid tourmaline (dravite) quartz andalusite fluid

For the pure Fe components (at. Fe/(Mg+Fe) = 1), the reaction equivalent to R1 (R2 below) involves the schorl end-member (Table 2.1).

$$3Fe_2Al_4Si_5O_{18} + 2NaAlSi_3O_8 + 6B(OH)_3 = 2NaFe_3Al_6Si_6O_{18}(BO_3)_3(OH)_4 + 8SiO_2 + Al_2SiO_5 + 5H_2O \qquad \text{(R2)}$$

Fe -cordierite albite fluid tourmaline (schorl) quartz andalusite fluid

For an albite-free assemblage, reaction R3, again written below for at. Mg/(Mg+Fe) = 1, buffers $[B_2O_3]_{fluid}$ and involves the magnesiofoitite tourmaline end-member (Table 2.1).

$$2Mg_2Al_4Si_5O_{18} + 3Al_2SiO_5 + 6B(OH)_3 = 2\,\square\,Mg_2Al_7Si_6O_{18}(BO_3)_3(OH)_4 + SiO_2 + 5H_2O \qquad \text{(R3)}$$

cordierite andalusite fluid tourmaline (magnesiofoitite) quartz fluid

For the pure Fe components, reaction R4 equivalent to R3 (not written) would involve the foitite end-member (Table 2.1).

The four tourmaline-forming reactions above have been considered in this study. They are all mica-free but the minerals and phase assemblage involved are representative of common pelitic metamorphic rocks. These are typical country rock lithologies for the emplacement of granitic magmas and the development of B metasomatism and tourmalinisation (Drivenes et al., 2015; Codeço et al. 2017). The four tourmaline end-members involved in the reactions (dravite, magnesiofoitite, schorl, and foitite) cover an important fraction of compositions of natural tourmalines in perigranitic environments. Their chemical formula as well as their Gibbs free energy of formation at 25°C, 1 atm are given in Table 1. A fifth tourmaline end-member (uvite) relevant to this study has been added to Table 1.

	Formula	$\Delta_f G°_m$ (kJ/mol)	
End-member	$X Y_3 Z_6 T_6 O_{18} (BO_3)_3 V_3 W$	Ogorodova et al. (2012)	van Hinsberg and Schumacher (2007)
Dravite	$Na (Mg)_3 Al_6 Si_6O_{18} (BO_3)_3 (OH)_4$	-14,397	-14,600.68 ± 3.3
Schorl	$Na (Fe)_3 Al_6 Si_6O_{18} (BO_3)_3 (OH)_4$	-13,513	-13,494.46 ± 3.5
Mg-foitite	$[\ ] (Mg_2Al) Al_6 Si_6O_{18} (BO_3)_3 (OH)_4$	-14,341	-14,564.86 ± 3.1
Foitite	$[\ ] (Fe_2Al) Al_6 Si_6O_{18} (BO_3)_3 (OH)_4$		-13,827.38 ± 3.2
Uvite	$Ca (Mg)_3 (MgAl_5) Si_6O_{18} (BO_3)_3 (OH)_4$	-14,594	-14,697.55 ± 3.2

Table 2. 1: Chemical formula and estimated thermodynamic properties of tourmaline endmembers of relevance in this study.

II-Experimental and analytical methods

A) Starting products

The forward experiments started from tourmaline-free mixtures of natural minerals, cordierite, albite, quartz, and andalusite (compositions in Appendix A3). The cordierite single crystal used (of unknown provenance) is relatively magnesian (at. Fe/(Fe+Mg) = 0.14 ± 0.01). The plagioclase of unknown provenance is albitic (An03Or04Ab93, at. Ca/Na+Ca = 0.03 ±0.015) and contains K-feldspar and quartz inclusions. Quartz and andalusite come respectively from the exploited quarries of Ploemeur and Glomel (France), and they contain apatite, ilmenite, and chlorite inclusions. Some forward experiments were seeded with 3 to 5 large (~1 mm) natural tourmaline crystals (collected from quartz veins in the Huelgoat granite, France) which served to test for tourmaline stability and for the observation of tourmaline overgrowth. These tourmalines are mainly Fe-rich and zoned (Appendix A4) and they contain quartz and zircon inclusions. A few reversal experiments were performed to check for equilibrium by using starting mineral mixtures containing tourmaline (the natural mineral) plus quartz, andalusite, and albite. All minerals were crushed in an agate mortar and then sieved. Only the [40-80] µm granulometric fractions were retained. For the forward experiments, mixtures were prepared in 61.6/18.4/14.9/5.1 wt% proportions for cordierite, albite, quartz, and andalusite. Amounts of quartz and andalusite are relatively low (20 wt%) since both should crystallise as products together with tourmaline according to reactions R1 and R2 (in contrast, andalusite is a reactant in R3 and R4). For the reversal experiments, the starting mixtures contained 64.6/10.2/5.2/20 wt% tourmaline, quartz, andalusite, and albite.

Mineral mixtures were reacted with an aqueous fluid phase of varying composition in the system H_2O-B_2O_3 obtained by dissolving boric acid ($B(OH)_3$) crystals in distilled water. Initial boron contents of the fluid ranged from 0 to 10 wt% $[B_2O_3]_{fluid}$. With the use of $B(OH)_3$, the fluid is slightly acidic (pH = 7 to 4.3 from simulations using PHREEQC (Parkhurst & Appelo 2013) with the Thermoddem database (V1.10, Blanc et al. 2012), at 25°C, 1 atm) and representative of conditions of tourmaline crystallisation (Morgan & London 1989).

A) Experimental procedure

All experiments used Au or Pt capsules as containers, approximately 35 mm long with 5.4 mm outer diameters and a wall thickness of 0.2 mm. The motivation for using Pt instead of Au capsules was its high H_2 permeability at low temperatures (Gunter et al. 1987) which initially appeared as a key advantage for our redox-buffered 500 and 400°C experiments. However, later on, Fe loss problems were identified in charges contained in Pt capsules, and duplicate experiments were performed in Au at 500 and 400°C (and also in Pt at 600°C) to fully evaluate the influence of capsule material. Charges consisting of 100 mg of fluid and 50 mg of the powdered mineral mixture were loaded into the capsules. These were then welded, plunged into boiling oil to check for leaks, and then kept in an oven for at least 12 hours at 120°C to homogenise the fluid inside the capsules. Before and after each of those steps, capsules were weighed to check for the absence of fluid loss.

Experiments were performed in an internally heated pressure vessel (ISTO, Institut des Sciences de la Terre d'Orléans) operating vertically and pressurised with Ar-H_2 gas mixtures. Up to 7 capsules were loaded into the vessel and run simultaneously under the same P, T, and fH_2 conditions. A total of 6 individual experiments were completed in this study. The pressure was recorded by a transducer calibrated against a Heise Bourdon tube gauge (uncertainty ±2 MPa). A Kanthal furnace was used and the temperature was continuously controlled by two type K thermocouples located respectively at the base and the top of the furnace hot spot (uncertainty ±5°C). At the end of the experiments, the power of the furnace was turned off, resulting in a rapid cooling (~ 5 min) of the vessel to room temperature. Capsules were removed from the vessel and weighted to check for leaks. They were then opened and their content was rinsed with pure H_2O in a Büchner filter system equipped with a nylon membrane. Solids > 0.45 µm in size were recovered, dried in an oven at 120°C for 20 min and then prepared for analysis. In this study, the fluid phases were not recovered and thus not analysed.

Previous time series experiments (Morgan & London 1989) have shown that tourmaline crystallisation is rapid, reaching near completion in less than 160-240 h at 600°C. In several previous tourmalinisation studies, experimental durations have lasted generally between 144 to 240 hours at 600°C (von Goerne et al. 1999; Orlando et al. 2017; Cheng et al. 2019). However, Orlando et al. (2017) noted some discrepancies between their results and those of von Goerne et al. (2001), obtained after 14 days at 600°C, and questioned the attainment of chemical equilibrium in tourmalinisation experiments of 168 h at 500 and 600°C. Thus, in this study, the experimental duration was increased to between 336 and 361 h at 600°C. At 500°C, the experiments lasted for approximately one month (666 h for Run 3 and 694 h for Run 4, Table 2.2) and two months (1379 h) at 400°C.

Control of redox conditions was achieved by adjusting the proportion of H_2 in the pressurising Ar-H_2 gas (Scaillet et al. 1992). H_2 was first introduced to a specific PH_2 (generally 0.2 MPa, 0.0 MPa in one case) at room temperature followed by Ar. In the 600 and 500°C experiments, experimental fH_2 and fO_2 were measured with the solid sensor technique (Taylor et al. 1992). The NiO-NiPd sensors were first contained in Au capsules in Run 1, but later on Pt was preferred because of its higher H_2 permeability compared to Au (Gunter et al. 1987). Each sensor comprised two NiO-NiPd pellets, both made of NiPd and NiO powders in 4:1 wt proportion. One pellet had an atomic fraction of Ni in NiPd alloy (X_{Ni}) of 0.15 initially whereas the other had a X_{Ni} of 0.5. After the experiment, X_{Ni} were measured and the fO_2 of the solid sensor was determined using the Pownceby &O'Neill (1994) calibration which needed to be extrapolated down the temperature for the 500°C runs. The fO_2 of the solid sensor should be equal to the fO_2 of experimental charges since fH_2 is the same in all capsules (if H_2 permeabilities are high enough) and fH_2O in solid sensor and experimental capsules are assumed equal to $fH_2O°$ (the fugacity of pure water at experimental P and T) despite the presence of B_2O_3 in experimental fluids. At 400°C, H_2 permeabilities in Pt and Au capsules decrease markedly which would imply very long timescales for NiPd alloys to equilibrate. 400°C is also a temperature 200°C lower than the lower limit of the NiO-NiPd sensor calibration (Pownceby and O'Neill 1994). For those reasons, no solid sensors were used at 400°C although the initial PH_2 (0.2 MPa) was adjusted to yield the same fO_2 range as in the higher temperature experiments.

B) Analytical procedures

All experimental run products were examined with an optical microscope after immersion in oil of a 1.4912 refractive index. The starting and experimentally reacted powders were mounted, both unpolished and polished. Mounts were imaged with a Merlin compact ZEISS scanning electron microscope (SEM, ISTO, Orléans) working under an acceleration voltage of 15 kV and equipped with a Bruker EDS (Energy Dispersive Spectrum) detector (QUANTAX-Xflash6). An Everhart-Thornley detector and a high resolution InLens detector were used to perform secondary electron imaging (SEI) and observe in particular the morphological aspect of the grains. Phases present were identified and their mutual textural relationships were investigated using backscattered electron imaging (BSE) combined with the EDS.

X-ray diffraction (XRD) characterisation of starting and experimental powders was carried out on an INEL transmission diffractometer with a Debye-Scherrer geometry (ISTO, Orléans). The instrument is equipped with an INEL CPS 120 curved detector and a Co*Kα*1 monochromator ($\lambda_{K\alpha1Co}$ = 1.78897 Å) allowing acquisition of the diffractogram between 3 and 90° 2θ with a resolution of 0.03°. Powders were reground in an agate mortar and placed in a Mark capillary (050 glass) with a diameter of 0.3 mm. The standard ICDD PDF 2004 database was used to identify mineral phases and to qualitatively estimate their relative proportions.

Mineral phases were analysed for major and minor elements using a CAMECA SX Five electron microprobe (ISTO-BRGM, Orléans) operated under an acceleration voltage of 15 kV and a beam current of 7 nA. Each element on each point was analysed for 10 s with a focused beam (≈ 2 µm), starting with Na to avoid any migration problems. Standards included albite (SiKα and Na*Kα*), synthetic $MnTiO_3$ (Mn*Kα* and Ti*Kα*), andalusite (Al*Kα*), Fe_2O_3 (Fe*Kα*), MgO (Mg*Kα*), andradite (Ca*Kα*), orthoclase (K*Kα*). As the microprobe cannot measure boron and hydrogen in minerals, a range of analytical totals between 85.0 and 88.2 wt% is expected for Li-free tourmalines. Considering the uncertainties associated with the microprobe itself, tourmaline analyses with totals between 84 and 89 wt% were considered satisfactory (see below). Others were rejected. Structural formulae of tourmaline were calculated via the method described in Morgan (2016), assuming 4 atoms per formula unit (apfu) OH and 3 apfu ^{III}B.

Difficulties were encountered with the electron microprobe analysis of tourmalines because of their textures and morphologies. Experimental tourmalines rarely exceeded 2 µm widths. Thus, isolated tourmaline fibers proved impossible to analyse correctly, although an analysis became possible when several fibers were present, intersecting each other. Consequently, not all tourmalines from tourmaline-bearing charges could be analysed and only tourmaline with specific favourable textures (see below) were correctly probed.

^{11}B MAS NMR analyses were performed at the CEMHTI laboratory (Orléans, France) in order to check the presence of ^{IV}B in our experimental tourmaline. ^{IV}B occurs as a substitution for Si in the tourmaline T-site. Standard thermodynamic properties of tourmaline estimated by polyhedron model does not account for the effect of the presence of ^{IV}B polyhedron (Garofalo et al. 2000; van Hinsberg & Schumacher 2007). Thus, if ^{IV}B is detected in the experimental tourmaline, the thermodynamic standard properties sets obtain by polyhedral model must be considered cautiously. Every charge containing tourmaline were investigated. Because of the low amount of powder (50 mg instead of the 200 mg generally used) and low boron content of the solid (especially in charges with low amount of tourmaline), the 11B analyses were carried out on a high field Bruker AVANCE III spectrometer (850 MHz-19.9T). This instrument allows for a complete resolution of the BO_3 and BO_4 contributions. Moreover, the use of a specially designed Doty probe optimised for ^{11}B signal observation and equipped with a 'boron-free" stator ensures the acquisition of spectra completely representative of the sample and free from probe signals. All the experimental powder (50 mg) was packed in 3 mm rotors allowing magic angle rotation conditions of 30 kHz. The spectra were acquired at an observation frequency of 272.8 MHz for ^{11}B after a short excitation pulse to ensure homogeneous irradiation of boron species. The recycling delay was fixed at 3 s and the number of accumulated scans was adjusted accordingly to the boron content of the sample. The use of a boron-free probe and multiple scans allow the acquisition of reliable spectra for solids with B concentrations as low as 10 ppm (Mavromatis et al. 2015).

C) Choice of P-T-fO_2 conditions

Our experiments aim at simulating conditions of boron metasomatism and tourmalinisation that occur within granitic bodies and in their country rock aureoles (Drivenes et al. 2015; Lecumberri-Sanchez et al. 2017; Cheng et al. 2019; Harlaux et al. 2020). Granitic rocks are generally emplaced in mid to shallow crustal conditions, i.e., in a range between 100 and 500 MPa (e.g. Kontak & Clark 2002; Drivenes et al. 2016; Launay et al. 2018; Korges et al. 2020; Legros et al. 2022). Hydrothermal systems developed in perigranitic contexts have temperatures generally in the 300 to 600°C range (Charoy 1979; Kontak and Clark 2002; Frikken et al. 2005; Codeço et al. 2017; Orlando et al. 2017; Legros et al. 2022). Therefore, in this study, experiments were performed at a constant pressure of 200 MPa and between 400 and 600°C. Redox conditions are rarely precisely defined and, moreover, highly variable between granitic rocks and series, in a range typically between the fayalite-magnetite-quartz (FMQ) and magnetite-hematite (MH) oxygen buffers (Frikken et al. 2005; Li et al. 2017). Thus, the fO_2 in this study was set to moderately oxidising conditions in the average of this range. Most 500 and 600°C experiments were made with an initial PH_2 of 0.2 MPa corresponding to fO_2 in the Nickel-Nickel Oxide (NNO) + 0.5 to NNO + 2 range except one slightly more oxidising (Table 2.2). They will be designated thereafter as “moderately oxidising” (Table 2.2). The one performed without H_2 added (PH_2 = 0 MPa) yielded more oxidising conditions and will be designated below as “highly oxidising” (Table 2.2).

III- Results

Charge	Capsule	T (°C)	fO_2	$[B_2O_3]_{fl}$ wt%	Reaction products[d]	Texture grou
Moderately oxidizing conditions						
			Run 1 : 361h			
S600-0[a]	Au	600	NNO + [1.12 ; 1.90]	0.0	Crd + Alb + Qtz + And	-
S600-1	Au	600	NNO + [1.12 ; 1.90]	0.8	Crd + Alb + Qtz + And	-
S600-2	Au	600	NNO + [1.12 ; 1.90]	2.1	Crd + Alb + Qtz + And	-
S600-3	Au	600	NNO + [1.12 ; 1.90]	3.4	Crd + Alb + Qtz + And	-
S600-10	Au	600	NNO + [1.12 ; 1.90]	10.1	Tur + Qtz * *Crd*	I; IIIa; IIIb
S600-10G[b]	Au	600	NNO + [1.12 ; 1.90]	10.1	Tur + Qtz * *Crd*	I; IIIa; IIIb; IV
			Run 2 : 336h			
S600-4	Au	600	NNO + [1.42 ; 1.69]	4.0	Crd + Alb + Qtz + And * *Tur + qch*	I; II
S600-6	Au	600	NNO + [1.42 ; 1.69]	6.0	Crd + Qtz + Alb + And * *Tur + FK + qch*	I
S600-6Pt	Pt	600	NNO + [1.42 ; 1.69]	6.1	Crd + Qtz + Alb + And * *Tur + FK + qch*	I
S600-8	Au	600	NNO + [1.42 ; 1.69]	8.2	Tur + Qtz + Crd * *FK + Alb*	I; IIIa; IIIb
S600-Rev[c]	Au	600	NNO + [1.42 ; 1.69]	Reverse _ 0	Tur + Qtz + Alb + And	No etching
			Run 3 : 666h			
S500-0Pt	Pt	500	NNO + [0.78 ; 1.73]	0.0	Crd + Alb + Qtz + And	-
S500-2Pt	Pt	500	NNO + [0.78 ; 1.73]	2.1	Crd + Alb + Qtz + And * *FK*	-
S500-3Pt	Pt	500	NNO + [0.78 ; 1.73]	3.3	Crd + Qtz + Alb + And * *Tur + FK + qch*	I
S500-4Pt	Pt	500	NNO + [0.78 ; 1.73]	4.2	Crd + Qtz + Alb + And * *Tur + FK + qch*	I
S500-4	Au	500	NNO + [0.78 ; 1.73]	4.1	Crd + Qtz + Alb + And * *Tur + FK + qch*	I
S500-6PtG[b]	Pt	500	NNO + [0.78 ; 1.73]	6.1	Tur + Qtz +Crd * *Alb*	I; IIIa; IIIb; IV
S500-Rev[c]	Pt	500	NNO + [0.78 ; 1.73]	Reverse _ 0	Tur + Qtz + Alb + And	No etching
			Run 4 : 694h			
S500-6	Au	500	NNO + [1.7 ; 2.75]	6.3	Tur + Qtz +Crd * *Alb*	I; IIIa; IIIb
			Run 5 : 1379h			
S400-0Pt	Pt	400	~ NNO + [0 ; 2]	0.0	Crd + Sme + Alb + Qtz + And	-
S400-1Pt	Pt	400	~ NNO + [0 ; 2]	1.0	Crd + Sme + Alb + Qtz + And	-
S400-2Pt	Pt	400	~ NNO + [0 ; 2]	2.0	Crd + Sme + Alb + Qtz + And	-
S400-3Pt	Pt	400	~ NNO + [0 ; 2]	3.0	Crd + Sme + Qtz + Alb + And * *Tur*	I; IIIa
S400-4Pt	Pt	400	~ NNO + [0 ; 2]	4.3	Tur + Qtz + Alb * *Crd + Sme*	I; IIIa
S400-6PtG[b]	Pt	400	~ NNO + [0 ; 2]	6.4	Tur + Qtz * *Crd + Sme + Alb + FK*	I; IIIa; IV
S400-6G	Au	400	~ NNO + [0 ; 2]	6.3	Tur + Qtz * *Crd + Sme + Alb + FK*	I; IIIa; IV
Highly oxidizing conditions						
			Run 6 : 337h			
SOX-3	Au	600	NNO + [2.71 ; 5.32]	3.0	Crd + Alb + Qtz + And * *FK + FeTi ox*	-
SOX-4	Au	600	NNO + [2.71 ; 5.32]	4.2	Crd + Qtz + Alb + And * *Tur + FK + FeTi ox*	I; II
SOX-6	Au	600	NNO + [2.71 ; 5.32]	6.3	Crd + Qtz + Tur + Alb + And * *FK + qch*	I
SOX-8	Au	600	NNO + [2.71 ; 5.32]	8.3	Tur + Qtz + Crd * *Alb + FK*	I; IIIa; IIIb
SOX-8G[b]	Au	600	NNO + [2.71 ; 5.32]	8.1	Tur + Qtz + Crd * *Alb + FK*	I; IIIa; IIIb; IV

(a) Forward experiment performed with a starting tourmaline-free mixture except when otherwise noted. (b) Forward experiment with tourmaline seeds added. (c) Reversal experiment performed with a tourmaline-bearing starting mixture (see text). (d) The asterisk separate the phases confirmed by XRD (left side, ordered by proportion) from the others, identified by SEM and EDS (right side, in italic). Mineral abbreviation: Alb = albite; And = andalusite; Crd = cordierite; FeTi ox = Fe Ti oxydes; FK = potassium feldspar; Qtz = quartz; Sme = smectite; Tur = tourmaline. qch = quench phases.

Table 2. 2: Experimental conditions and results

A) Redox conditions

The evolution of the alloy phase of the NiO-NiPd sensor is illustrated in the example of Run 2 (Table 2.2), a moderately oxidising experiment at 600°C (Fig. 2.1).

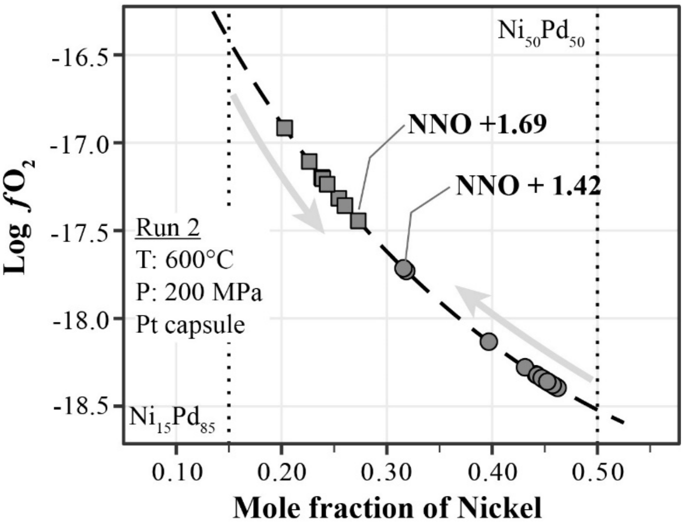

Figure 2. 1: Evolution of the alloy phase of the NiO-NiPd sensor as a function of log fO_2 in Run 2 (Table 2). The dashed line gives the relation between the mole fraction of Ni in the alloy phase (X_{Ni}) and fO_2 at 600°C and 200 MPa using the calibration of Pownceby and O'Neill (1994). The initial X_{Ni} of the two pellets is represented by the dotted vertical lines and their final compositions by squares and circles on the dashed line. Directions of evolution of alloys in each pellet are indicated by arrows.

The two analysed pellets display a range of X_{Ni}, respectively from 0.32 to 0.46 for one and from 0.2 to 0.27 for the other (Fig. 2.1). We note the decrease in X_{Ni} for the pellet with initial X_{Ni} = 0.5 and the increase in X_{Ni} for the pellet with initial X_{Ni} = 0.15 and the convergence toward X_{Ni} ~0.3 from both sides. This indicates that the sensor approached equilibrium even if it was not completely attained. Using the calibration of Pownceby & O'Neill (1994), we use the minimum X_{Ni} of the reduced pellet (0.32) and the maximum X_{Ni} of the oxidised pellet (0.27) to bracket the fO_2 in this experiment (Fig. 2.1), yielding NNO + 1.42 to NNO + 1.69 (abbreviated below as NNO +[1.42 ; 1.69]). For the same temperature and targeted fO_2, the sensor contained in Run 1 (Au capsule) yielded a slightly wider fO_2 range (NNO +[1.12 ; 1.9]) than in Run 2. In the 500°C moderately oxidising experiments (Run 3), the sensor returned a fO_2 interval (NNO +[0.78 ; 1.73]) larger than 600°C indicating less well equilibrated conditions despite the experimental duration being longer than 600°C. Experiment S500-6 (Run 4) equilibrated at NNO +[1.77 ; 2.64], hence under a more oxidising fO_2 range than in Run 3. In the strongly oxidising experiment at 600°C (Run 6), both pellets had experimental $X_{Ni} \leq 0.15$ thus implying a minimum fO_2 of NNO + 2.71, the lowest X_{Ni} analysed corresponding to a fO_2 of NNO + 5.32 (Table 2.2). Details of the compositional data for the NiPd alloys are summarised in Appendix A5. For the 400°C experiment (Run 5), the fO_2 was estimated to NNO +[0 ; 2] from the results of sensors in the other 600 and 500°C experiments performed with a 0.2 MPa initial PH_2.

B) Experimental products and textures

Upon opening the capsules, all experimental products comprised a solid powder and a free fluid. The more boron in the charge, the more agglomerated is the solid powder. In some charges, part of the solid products was found to float, forming a thin film at the surface of the fluid phase. Cordierite, albite, andalusite, quartz, and tourmaline are the major mineral phases, appearing in the XRD spectra of experimental products at 600 and 500°C (see Appendix A6 for a compiled figure and Appendix A7 for the detail of all diffractograms) and also identified from SEM imaging (Table 2.2). These are accompanied by several accessory minerals only detected by SEM. K-feldspar appears in the proximity of plagioclase undergoing dissolution. It is commonly euhedral and can contain cores of relictual albite indicating that the source of K is the starting feldspar mineral. Under highly oxidising conditions (Run 6, Table 2.2), Fe-Ti oxides, generally < 10µm in size, occur in experimental products. SEM imaging and EDS analyses show that they are made up of a small anhedral Ti-rich core (interpreted as ilmenite coming from starting materials, see above) surrounded by a euhedral Fe-rich rim corresponding to recrystallisation under high experimental fO_2. A first-order difference in phase assemblage appears upon decreasing temperature from 500°C to 400°C. In Run 5 (Table 2.2), cordierite is destabilised and forms sheeted minerals (Fig. 2.2), identified by XRD as belonging to the smectite group (Appendix A6). However, the 060 peak is not visible and so, precise identification of the mineral species within the smectite group is impossible.

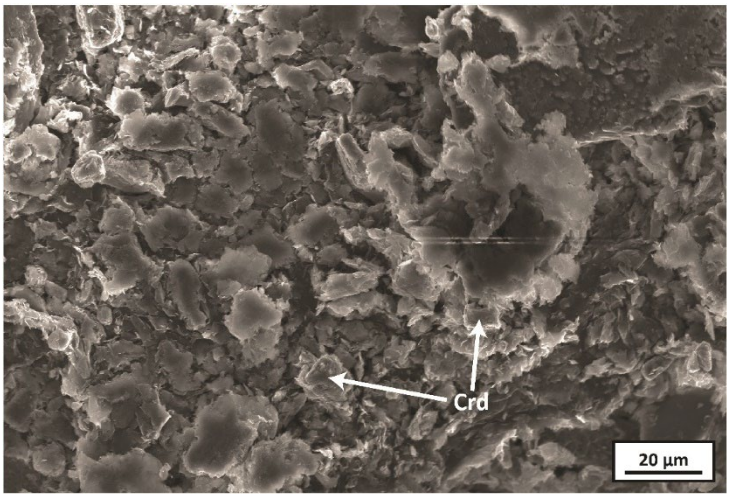

Figure 2. 2: SEM (InLens) image of the charge S400-0Pt. The cordierite is destabilised, forming sheeted minerals belonging to the smectite group.

Experimental assemblages split into two types: tourmaline-free and tourmaline-bearing. Charges, where tourmaline is absent, are characterised by a general reduction of grain sizes and the development of dissolution textures on cordierite, andalusite and albite (Fig. 2.3A). In tourmaline-bearing charges, tourmaline textures can be subdivided into four groups (Table 2.3): sheaves (group I), large crystals (group II), clusters (group III) and overgrowth (group IV).

Group	Description	Figure
I	Sheaves composed of multiple thin rods up to 200µm long.	2B
II	Large elongated crystal forming a tight sheaf on one end.	2C
IIIa	Radiating clusters of fibrous crystals.	2D
IIIb	Clusters of single long fibers intersecting each other.	2E
IV	Experimental overgrowth on natural tourmaline seed.	2F

Table 2. 3: Experimental tourmaline textures

Group I tourmalines always occur as sheaves made of rods up to 200µm long and generally less than 1µm large (Fig. 2.3B). These textures are characteristic of charges where tourmaline is the most (or one of the most) abundant phase. At the base of the sheaves, crystals of albite and/or cordierite can be found, sometimes with euhedral K-feldspar crystals. Small quartz beads (less than 2µm diameter) crystallise on tourmaline rods. Unidentified sub-micrometric materials, appearing as rings on tourmaline sheaves, are also present in some charges and interpreted as quench phases. Among the phases spatially associated with

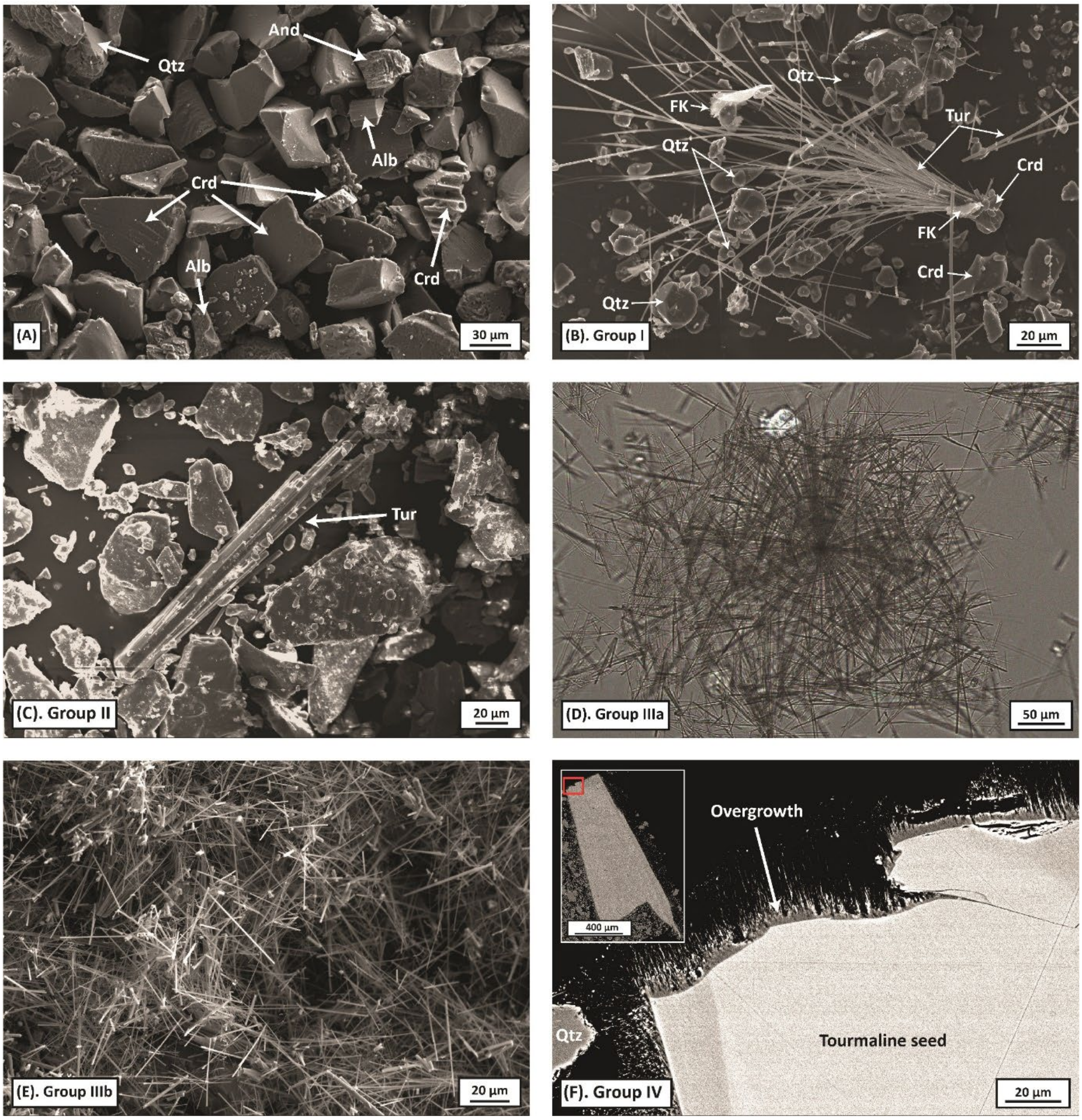

Figure 2. 3: SEM (InLens and BSE) and optical microscopic images of the experimental products. See Table 2.2 for the experimental conditions. (A) Charge S600-0, all starting products are present and show limited dissolution. (B) Charge S600-6, Group I tourmaline nucleated on cordierite grains. The sheaf is associated with platy FK crystals and small Qtz beads. The starting Qtz grains have euhedral edges. (C) Charge SOX-4, Group II tourmaline. (D) Charge S600-10, Group IIIa tourmaline found part of the solid powder in the charge. (E) Charge S600-10, Group IIIb tourmaline found to float, forming a thin film at the surface of the fluid in the charge. (F) Charge S500-6PtG, Group IV tourmaline overgrowth forming a hairy texture parallel to the long axis of the seed. On other faces of the seed, tourmaline overgrowth has a different texture, less developed. Abbreviations: Alb = albite; And = andalusite; Crd = cordierite; FK = K-feldspar; Qtz = quartz; Tur = tourmaline.

tourmaline, quartz grains show euhedral edges and the reactant minerals have dissolution textures developed on their surface. Those whose size has decreased to < 20µm tend to form agglomerates with tourmaline sheaves inside and around. Individual reactant minerals > 40µm support tourmaline fibers larger than those grown from agglomerates. Group II tourmalines form large (10 to 20 µm wide) elongated tourmaline crystals found crystallised alongside the sheaves (Fig. 2.3C). At their extremities, those crystals can divide into a tight sheaf (about 4-5 µm large). This textural group was only found in 2 charges and fewer than 5 specimens per charge were observed. Group III tourmalines refer to radiating clusters of fibrous tourmaline crystals (Fig. 2.3D), named fibro-radiated aggregates below. They are only present in charges where tourmaline is the most (or one of the most) abundant phase and occur either as associated with (Group IIIa) or separate from (Group IIIb) the solid powder in the charge. In Group IIIa, all associated quartz grains are euhedral and often intergrown with tourmaline and small quartz beads develop euhedral edges. Cordierite and albite are generally still visible despite being strongly reacted, sometimes appearing as inclusions near the center of fibro-radiated aggregates or, for albite, as inclusions in K-feldspar. The Group IIIb tourmalines are found inside the thin film floating in the fluid. Upon drying, they form single long fibers intersecting each other (Fig. 2.3E), globally thinner than the Group I and IIIa sheaves. Group IV tourmalines are restricted to the seeded charges where a thin layer of experimentally formed tourmalines grows around the natural tourmaline crystals. This tourmaline overgrowth develops on specific crystallographic faces, allowing the growth to be parallel to the long axis of the seed. It forms a hairy texture, with thin fibers growing parallel and in the same direction (Fig. 2.3F).

C) Evolution of phase assemblages and tourmaline textures

Experimental mineral assemblages and textures of tourmaline (when present) are detailed in Table 2.2. No difference is observed between identical charges ran in Au and Pt capsules. The effects of the initial $[B_2O_3]_{fluid}$, temperature and fO_2 are detailed in the following sections.

1/ Effect of $[B_2O_3]_{fluid}$.

At 600°C in the moderately oxidising Run 1 (Table 2.2), tourmaline is absent (undetected by SEM) at low $[B_2O_3]_{fluid}$ concentrations (0, 0.8, 2.1, 3.4 wt%) and the starting assemblage cordierite + albite + andalusite + quartz remains stable (Table 2.2, Fig. 2.4A). Upon increasing $[B_2O_3]_{fluid}$, reactant phases progressively reduce in size and dissolution textures appear more marked. Tourmaline is detected by XRD in the S600-10 and S600-10G charges (both having very high $[B_2O_3]_{fluid}$, 10.1 wt%, Table 2.2) where it forms Group I and III crystals. In Run 2 designed to more precisely locate the appearance of tourmaline between 3.4 and 10.1 wt% $[B_2O_3]_{fluid}$, the SEM observations show that tourmaline is present for the lowest boron concentration ($[B_2O_3]_{fluid} = 4$ wt%, S600-4 charge, Run 2, Table 2.2). It occurs mainly with the Group I texture and coexist with a few large elongated Group II crystals. Therefore, the two 600°C moderately oxidising experiments consistently find tourmaline to appear for an initial boron fluid concentration ≥ 4 wt%. For higher $[B_2O_3]_{fluid}$ concentrations, the proportion, length, and width of Group I tourmalines increase and large Group II crystals are no longer present (S600-6 charge, $[B_2O_3]_{fluid} = 6$ wt%, Run 2, Table 2.2). Cordierite remains as the main reactant phase, but the proportion of albite and andalusite decreases sharply. At the highest boron concentration in Run 2 ($[B_2O_3]_{fluid} = 8.2$ wt%), Group III tourmalines are found to occur both

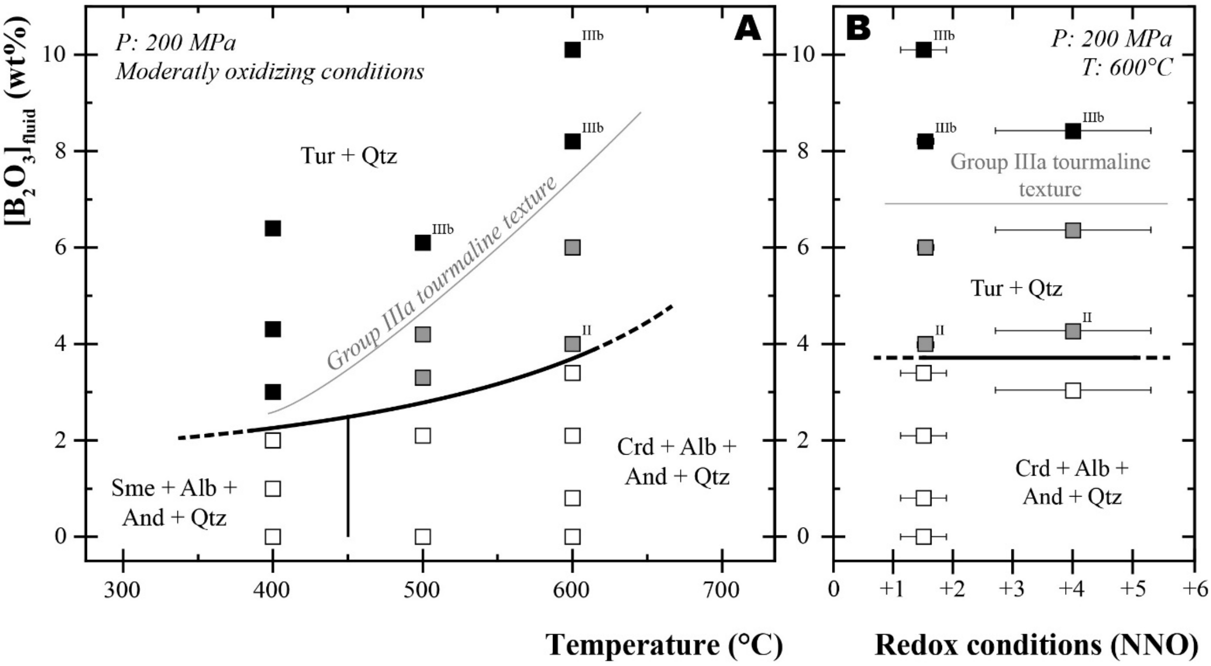

Figure 2. 4: Evolution of phase assemblages and tourmaline textures in the experiments. (A) $[B_2O_3]_{fluid}$ vs. Temperature diagram showing experimental results under moderately oxidising conditions (Table 2). (B) $[B_2O_3]_{fluid}$ vs. fO_2 diagram (NNO represents the deviation from the Ni-NiO buffer at the same T and P, see text for the notation) showing experimental results at 600°C (Table 2). Solid and open symbols denote respectively the presence and absence of tourmaline in experimental products. Group I tourmaline is present in all tourmaline-bearing charges. Black and grey-filled symbols indicate respectively the presence and absence of Group IIIa tourmaline. The presence of Group II and IIIb tourmaline is indicated by superscripts above the corresponding symbol. Thick lines represent stability limits and thin lines delimits conditions of appearance of Group IIIa tourmalines. Abbreviations: Alb = albite; And = andalusite; Crd = cordierite; FK = K-feldspar; Qtz = quartz; Sme = smectite; Tur = tourmaline.

in the reacted solid powder (IIIa) and as particles floating in the fluid (IIIb), the same as in the 10.1 wt% $[B_2O_3]_{fluid}$ charges in Run 1 (Table 2.2). In both experiments, at high $[B_2O_3]_{fluid}$ concentrations, the tourmaline + quartz assemblage becomes predominant in experimental products.

Two reversal experiments were performed at 600°C and 500°C (charges S600-Rev, Run 2 and S500-Rev, Run 3, Table 2.2) to test tourmaline destabilisation and the formation of cordierite, albite and andalusite for fluids with boron concentrations lower than required for tourmaline to appear, according to the forward experiments. The two charges (with $[B_2O_3]_{fluid}$ = 0 wt%) yielded phase assemblages unchanged compared to the starting mixture. Tourmalines in the reacted assemblage were carefully checked for the presence of etching textures on their edges and surfaces but none was recognised. Only sharp edges and fractures, probably formed during crushing, were found (Fig. 2.5). Yet, quartz, albite, and andalusite showed dissolution textures on their surfaces and they experienced an overall grain size reduction. Therefore, the reversibility of tourmaline formation according to reactions R1 to R4 is not demonstrated and the two reversal experiments suggest that tourmaline behaves as a refractory phase, once formed (Henry & Dutrow 1996; von Goerne et al. 1999b; van Hinsberg et al. 2011a).

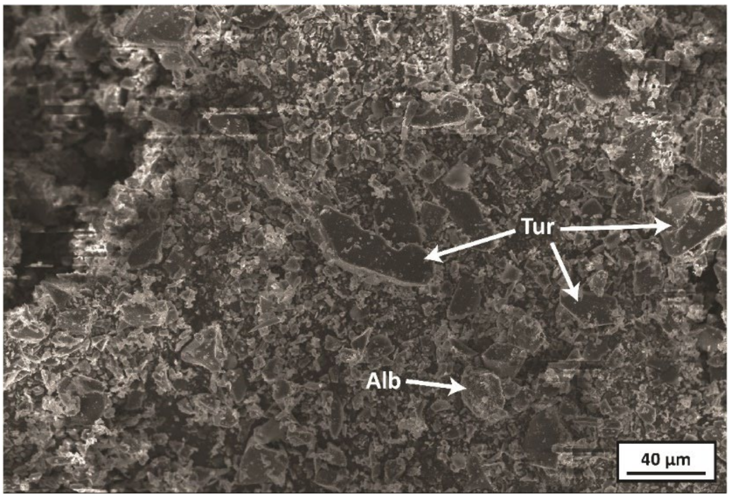

Figure 2. 5: SEM (InLens) image of the charge S600-Rev. In this reversal experiment, tourmaline remain stable, displaying sharp edges and fractures and no etching textures.

2/ Effect of temperature.

In the 500°C and 400°C experiments, the same evolution of phase assemblages than at 600°C is observed. Experimental charges evolve from tourmaline-free to tourmaline-bearing assemblages when the boron fluid concentration is increased. However, decreasing temperature leads to a reduction of the $[B_2O_3]_{fluid}$ required for tourmaline to appear. The transition from tourmaline-free to tourmaline-bearing assemblages occurs for $[B_2O_3]_{fluid} \geq 3$ wt% at 500 and 400°C vs. ≥ 4 wt% at 600°C (Fig. 2.4A). As at 600°C, tourmaline and quartz become the two most abundant phases at 500°C in the charge with the highest $[B_2O_3]_{fluid}$ (6.1 wt%, S500-6PtG, Run 3, Table 2.2). The textural evolution from Group I to Group IIIa tourmalines with increasing $[B_2O_3]_{fluid}$ is similar at 500°C and 600°C and a limit for the appearance of tourmaline aggregates (IIIa) can be drawn (Fig. 2.4A). Tourmaline fibers in Group I, III and IV become more numerous and thinner at a lower temperature (Fig. 2.6A). The large Group II tourmaline crystals only occur in the 600°C charges (S600-4, Run 2, SOX-4, Run 6, Table 2.2).

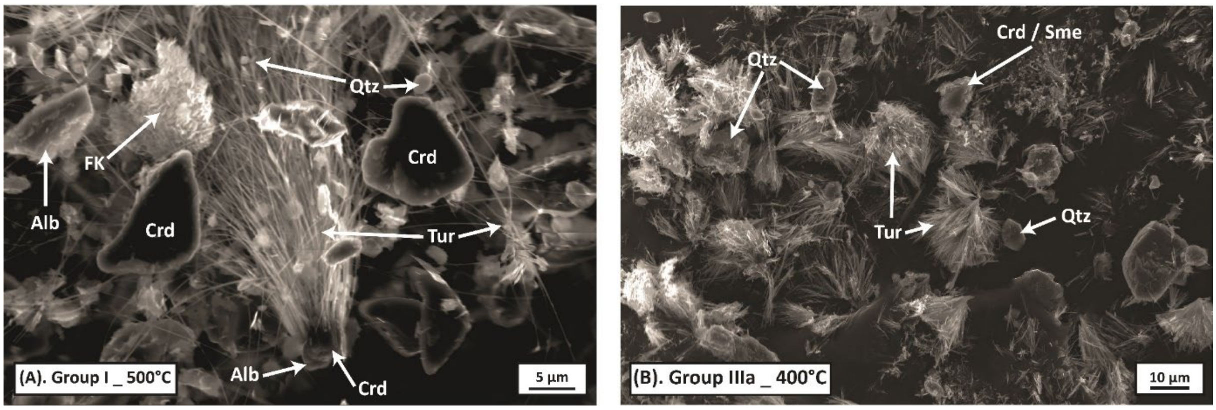

Figure 2. 6: SEM (InLens) image showing the evolution of the textural group with temperature. (A) Charge S500-4. Group I tourmaline at 500°C displaying the exact same feature than Fig. 2.3B at 600°C: the tourmaline nucleates on cordierite and albite grains and the sheaf is associated with platy K-feldspar and quartz beads. However, the rods formed at 500°C are thinner and more numerous than at 600°C. (B) Charge S400-4Pt. Group IIIa tourmaline equivalent to Fig. 2.3D, but the radius of the acicular aggregate is greatly reduced at 400°C compared to 600°C.

At 400°C, tourmaline and smectite are intergrown, the sheaves being more or less organised along sheet planes. Another specificity of the 400°C run is that tourmaline directly crystallises with the Group IIIa texture (Fig. 2.6B) at low $[B_2O_3]_{fluid}$ (3 wt%, charge S400-3Pt, Table 2, Fig. 2.4A). Group IIIb is also absent and tourmaline plus quartz become the most abundant phases for initial boron concentrations in fluid lower than at 500 and 600°C.

3/ *Effect of fO_2.*

The highly oxidising 600°C charges present no particular difference in terms of phase assemblage compared to their moderately oxidising equivalents. There is no influence of fO_2 on the $[B_2O_3]_{fluid}$ required for tourmaline to appear (Fig. 2.4B). Charge SOX-4 (highly oxidising) contains a higher proportion of group II tourmaline than S600-4 (moderately oxidising, Table 2.2). Globally, tourmaline fibers in Group I, III, and IV are slightly larger (> 1 μm) under highly than moderately oxidising conditions.

D) Tourmaline compositions

Analyses of group IIIa and IV tourmalines, which form relatively coarse aggregates, yielded satisfactory chemical data. Analysis of the group I and IIIb crystals were only possible in the case of multiple fibers intersecting each other. Because of textural constraints imposed by the crystal for obtaining a satisfactory analysis, it was not possible to choose the zone (i.e., core or rim, base or end of the sheaf) to be probed. No Group II tourmaline was found in our polished sections and so their chemistry is unknown. All experimental tourmaline analyses are detailed in Appendix A6.

1/ *Effect of texture*

Representative compositions of tourmaline crystallised in experimental charges are given in Table 4. S600-10(G) is used to regroup data for charge S600-10 and its seeded duplicate S600-10G and SOX-8(G) to regroup data for SOX-8 and SOX-8G (Table 2.2). For S400-6G, S600-10(G), and SOX-8(G), compositional data are available for different tourmaline textural groups (Table 4) and the influence of textures on tourmaline composition is illustrated in Figure 2.7. In the 600°C charges (S600-10(G) and SOX-8(G)), tourmaline compositions from Groups IIIa, IIIb and IV overlap. However, at 400°C (S400-6G charge), the Group IIIa has lower Al and lower at. (atomic ratio) Ca / (Na + Ca) than the Group IV tourmalines. It should be noted that only three analyses of Group I tourmalines are available in SOX6 (Table 2.4), corresponding to zones where sheaves were covering each other. All other attempts to analyse Group I tourmalines proved unsuccessful due to their small width ($\leq$ 1 μm).

Charge	**S600-8**	**S600-10(G)**			**S500-6**	**S400-6G**		**SOX-6**	**SOX-8(G)**		
Textural group	*IIIa*	*IIIa*	*IIIb*	*IV*	*IIIa*	*IIIa*	*IV*	*I*[a]	*IIIa*	*IIIb*	*IV*
n	12	21	11	16	17	21	15	3	28	3	25
SiO_2	36.30 (1.15)	35.54 (1.25)	36.35 (0.85)	35.57 (0.85)	36.99 (0.54)	36.95 (0.91)	36.28 (0.37)	36.69 (1.69)	35.93 (0.9)	36.49 (1.6)	35.54 (0.56)
TiO_2	0.27 (0.07)	0.32 (0.34)	0.26 (0.09)	0.21 (0.07)	0.11 (0.04)	0.12 (0.02)	0.13 (0.03)	0.28 (0.08)	0.26 (0.07)	0.37 (0.04)	0.27 (0.08)
Al_2O_3	38.73 (0.88)	37.55 (0.53)	38.12 (1.08)	37.35 (0.66)	36.23 (0.55)	36.78 (0.77)	37.89 (0.56)	34.92 (0.58)	36.91 (0.65)	34.73 (0.9)	36.75 (0.46)
FeO	2.24 (0.19)	2.81 (0.87)	2.20 (0.51)	2.43 (0.27)	2.43 (0.29)	1.97 (0.11)	2.05 (0.13)	4.63 (0.58)	3.27 (0.82)	3.32 (0.78)	3.88 (1.03)
MgO	6.35 (0.74)	6.58 (0.71)	7.17 (0.82)	6.91 (0.42)	7.57 (0.37)	7.12 (0.29)	6.56 (0.24)	6.34 (0.75)	6.96 (0.46)	7.59 (0.1)	6.68 (0.58)
MnO	0.11 (0.02)	*b.d.l.*	*b.d.l.*	*b.d.l.*	0.15 (0.02)	*0.16* (0.02)	*b.d.l.*	b.d.l.	*0.00*	*b.d.l.*	*b.d.l.*
CaO	0.75 (0.2)	0.67 (0.3)	0.63 (0.36)	0.51 (0.2)	0.50 (0.24)	0.67 (0.26)	1.10 (0.16)	0.94 (0.05)	0.66 (0.2)	0.71 (0.32)	0.71 (0.18)
Na_2O	1.67 (0.2)	1.80 (0.18)	1.94 (0.3)	1.95 (0.17)	1.95 (0.16)	1.43 (0.07)	1.30 (0.09)	1.57 (0.22)	1.90 (0.18)	2.00 (0.15)	1.85 (0.17)
K_2O	0.10 (0.02)	0.09 (0.02)	*b.d.l.*	0.09 (0.02)	0.06 (0.02)	0.06 (0.02)	0.10 (0.01)	0.11 (0.01)	0.09 (0.01)	*b.d.l.*	0.08 (0.02)
B_2O_3[b]	11.02	10.83	*11.04*	10.81	10.93	10.90	10.91	10.74	10.88	*10.76*	10.80
H_2O[c]	3.80	3.73	*3.80*	3.72	3.77	3.76	3.76	3.70	3.75	*3.71*	3.72
Total	101.34	99.92	101.51	99.55	100.69	99.92	100.08	99.92	100.75	99.68	100.28
Site T											
Si	5.73 (0.14)	5.71 (0.14)	5.73 (0.11)	5.73 (0.1)	5.89 (0.06)	5.90 (0.11)	5.79 (0.04)	5.93 (0.18)	5.75 (0.1)	5.90 (0.18)	5.72 (0.07)
Al	0.27 (0.14)	0.29 (0.14)	0.27 (0.11)	0.27 (0.1)	0.11 (0.06)	0.11 (0.1)	0.21 (0.04)	0.09 (0.14)	0.25 (0.1)	0.13 (0.13)	0.28 (0.07)
Site Z											
Al	6.00	6.00	6.00	6.00	6.00	6.00	6.00	6.00	6.00	6.00	6.00
Site Y											
Al	0.93 (0.12)	0.82 (0.05)	0.81 (0.11)	0.81 (0.08)	0.68 (0.04)	0.82 (0.06)	0.92 (0.04)	0.57 (0.14)	0.71 (0.06)	0.48 (0.07)	0.70 (0.04)
Ti	0.03 (0.01)	0.03 (0.04)	0.02 (0.02)	0.02 (0.01)	0.01 (0.01)	0.00 (0.01)	0.00 (0.01)	0.03 (0.01)	0.03 (0.01)	0.03 (0.03)	0.03 (0.01)
Fe	0.30 (0.02)	0.38 (0.12)	0.29 (0.07)	0.33 (0.04)	0.32 (0.04)	0.26 (0.01)	0.27 (0.02)	0.63 (0.09)	0.44 (0.11)	0.45 (0.11)	0.52 (0.14)
Mg	1.50 (0.18)	1.57 (0.16)	1.69 (0.19)	1.66 (0.1)	1.80 (0.09)	1.70 (0.06)	1.56 (0.06)	1.53 (0.15)	1.66 (0.1)	1.83 (0.02)	1.60 (0.13)
Mn	0.00	0.00	0.00	0.00	0.00 (0.01)	0.00 (0.01)	0.00	0.00	0.00	0.00	0.00
Site X											
Ca	0.13 (0.03)	0.12 (0.05)	0.11 (0.06)	0.09 (0.03)	0.08 (0.04)	0.11 (0.05)	0.19 (0.03)	0.16 (0.01)	0.11 (0.04)	0.12 (0.06)	0.12 (0.03)
Na	0.51 (0.06)	0.56 (0.05)	0.59 (0.09)	0.61 (0.05)	0.60 (0.05)	0.44 (0.02)	0.40 (0.03)	0.49 (0.07)	0.59 (0.05)	0.63 (0.04)	0.58 (0.05)
K	0.00 (0.01)	0.00	0.00	0.00	0.01 (0.01)	0.00	0.00 (0.01)	0.02 (0.02)	0.00 (0.01)	0.00	0.00 (0.01)
[]x	0.36 (0.06)	0.32 (0.03)	0.30 (0.05)	0.30 (0.04)	0.31 (0.02)	0.44 (0.04)	0.41 (0.02)	0.32 (0.06)	0.29 (0.04)	0.25 (0.02)	0.30 (0.04)
B	3.00	3.00	3.00	3.00	3.00	3.00	3.00	3.00	3.00	3.00	3.00
OH-	4.00	4.00	4.00	4.00	4.00	4.00	4.00	4.00	4.00	4.00	4.00
Total Al	7.20 (0.12)	7.11 (0.15)	7.08 (0.18)	7.09 (0.11)	6.80 (0.08)	6.93 (0.15)	7.13 (0.04)	6.66 (0.23)	6.96 (0.12)	6.62 (0.16)	6.97 (0.08)
Fe/(Fe+Mg)	0.17 (0.02)	0.19 (0.06)	0.15 (0.04)	0.17 (0.02)	0.15 (0.02)	0.13 (0.01)	0.15 (0.01)	0.29 (0.04)	0.21 (0.05)	0.20 (0.04)	0.25 (0.06)
Ca/(Ca+Na)	0.20 (0.05)	0.18 (0.07)	0.16 (0.09)	0.13 (0.07)	0.12 (0.06)	0.20 (0.08)	0.32 (0.05)	0.25 (0.03)	0.16 (0.06)	0.16 (0.07)	0.17 (0.05)

(a) The Group I tourmaline analyzed in SOX-6 corresponds to a zone where sheaves were covering each other, allowing correct analyses to be obtained. (b) B_2O_3 calculated assuming 3 apfu. (c) H_2O calculated assuming 4 apfu of OH^-. n = number of analyses. b.d.l. = below detection limit.

Table 2. 4: Average composition of experimental tourmaline

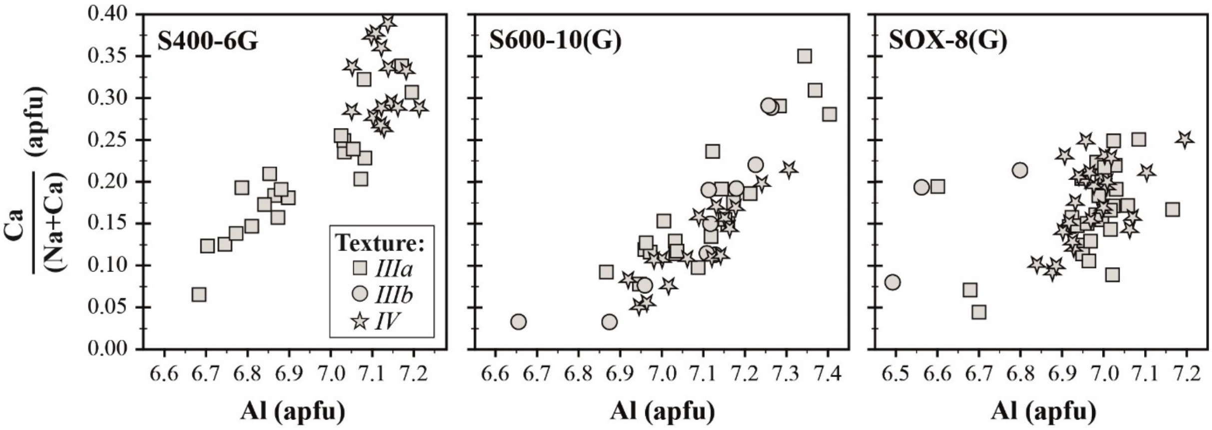

Figure 2. 7: Compositions of tourmaline textural groups (IIIa, IV and IIIb if present) in charges S400-6G, S600-10(G) and SOX-8(G), plotted in at. Na/(Na+Ca) Vs at. Al diagram. See Table 2.2 and text for experimental conditions.

2/ Effect of temperature and [B_2O_3]$_{fluid}$

All experimental tourmalines are solid solutions between magnesio-foitite and dravite with small amounts of foitite, schorl, and uvite (Fig. 2.8A-F, see Table 2.1 for structural formulae of end-members). Most compositions have a at. Fe/(Fe+Mg) slightly higher than the starting cordierite (vertical grey bands in Fig. 2.8A; B; D and E). All tourmaline compositions have an at. Ca/(Ca+Na) higher than the starting plagioclase (horizontal grey bands in Fig. 2.8B and E), which is the main source of Ca in our experiments. Influences of [B_2O_3]$_{fluid}$ and temperature on tourmaline composition are represented in Figure 2.8 where the different tourmaline domains (magnesio-foitite, dravite, foitite, schorl, uvite, Fe-uvite) are shown. At 600°C, increasing the fluid boron content generates tourmalines closer to the dravite endmember although the data for 8 and 10 wt% [B_2O_3]$_{fluid}$ overlap (Fig. 2.8A). Important variations in the Na proportion in X site are observed at 600°C, decreasing progressively with temperature (Fig. 2.8A). These variations are accompanied by large changes in at. Ca/(Ca+Na) at the three temperatures investigated (Fig. 2.8B). In comparison, at. Fe/(Fe+Mg) are less variable with the exception of the 600°C, [B_2O_3]$_{fluid}$ = 10 wt% compositions which show a large spread (Fig. 2.8A; B). In those charges, five compositions (labelled with “c”) come from analyses at the center of an exceptionally large Group IIIa tourmaline aggregate, whose elemental mapping is presented in Fig. 2.9. Additional analyses away from the center yielded more Mg-, Na-rich and Fe-, Ca-poor compositions plotting together with the others (Fig. 2.8A; B and Fig. 2.9). Variations in Al content are also observed with temperature: the 500°C (charge S500-6 contained in Au, Table 2.2) tourmalines being less Al-rich than the 600°C (Fig. 2.8C). The 400°C compositions are distinctive with their low and grouped Na proportions in the X site, positioned at the limit of the dravite and magnesio-foitite domains (Fig. 2.8A) and their at. Fe/(Fe+Mg) = 0.13, constant and identical to the starting cordierite (Fig. 2.8A; B).

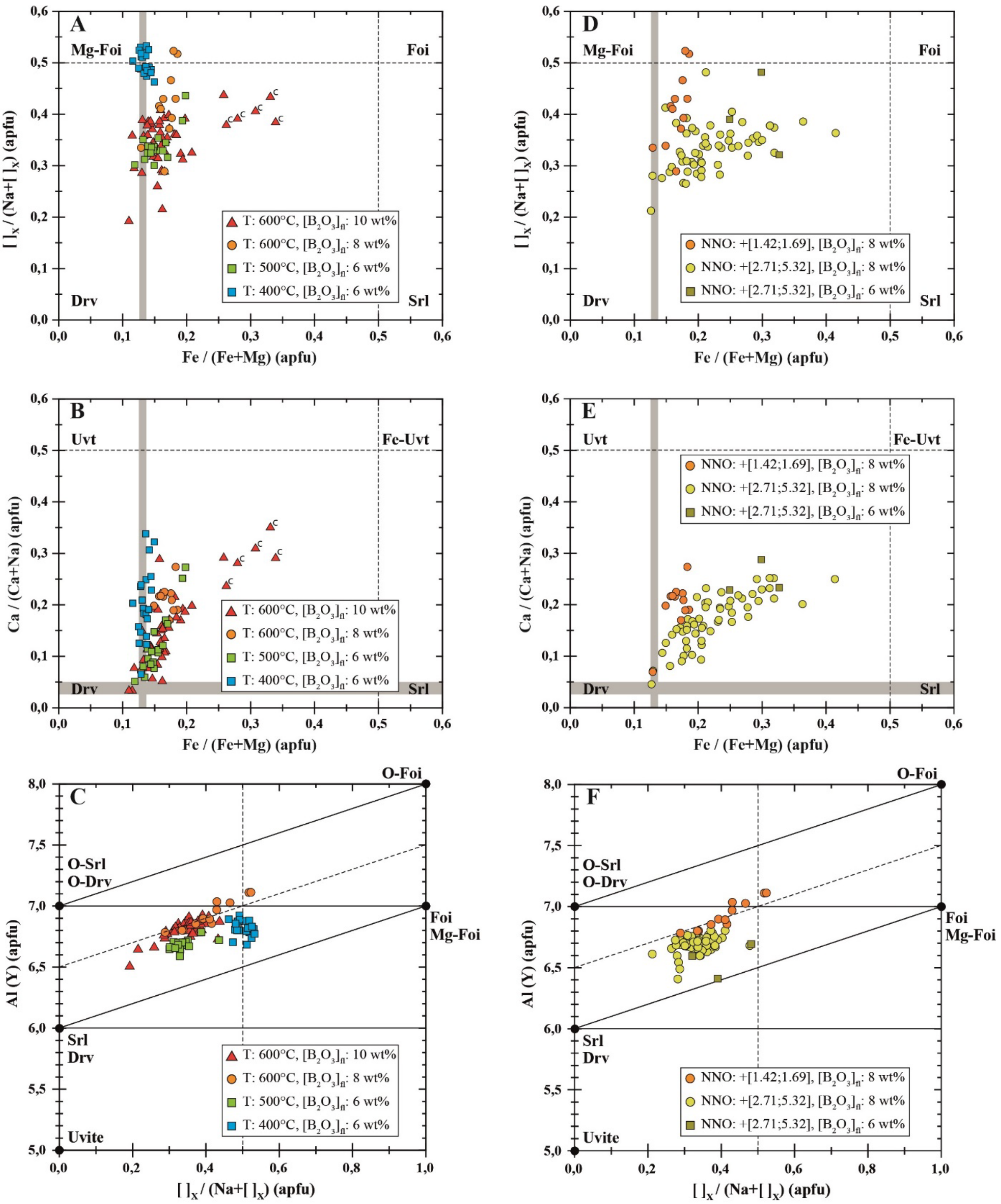

Figure 2. 8: Compositions of experimental tourmalines as a function of temperature (A; B; C) and of fO$_2$ (NNO represents the deviation from the Ni-NiO buffer at the same T and P, see text for the notation) at 600°C (D; E; F). The grey vertical band represents the at. Fe/(Fe+Mg) of the starting cordierite and the horizontal grey band the at. Ca/(Ca+Na) of the starting plagioclase. In temperature diagrams (A; B; C), the data come from the charges S600-10(G) (all textures), S600-8, S500-6 and S400-6G (group IIIa only). In fO$_2$ diagrams (D; E; F), the data come from the charges S600-8, SOX-8(G) (all textures) and SOX-6. See Table 2.2 and text for experimental conditions. Diagrams A to E from Hawthorne and Henry (1999) and C and F from Bačík et al. (2017).

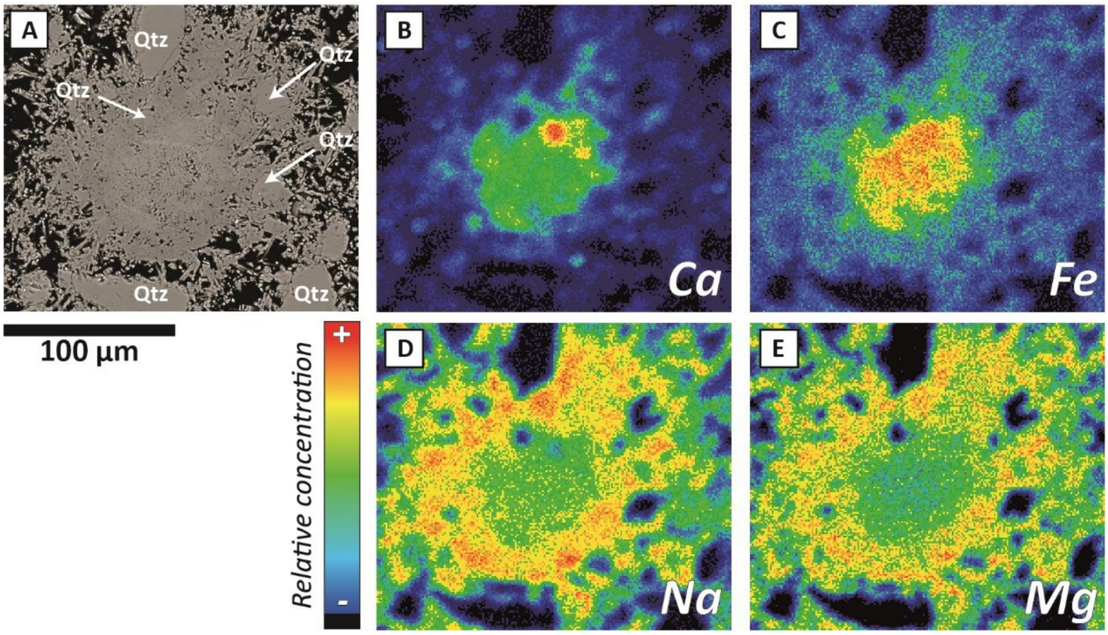

Figure 2. 9: BSE image (A) and Ca, Fe, Na, Mg X-ray elemental maps of a large Group IIIa tourmaline aggregate in S600-10 charge (Table 2.2). In each map, the relative abundance of the respective element is represented by the color scale, whereby dark blue corresponds to the lowest abundance and red to the highest. Abbreviations as in Fig. 2.3.

3/ *Effect of fO_2*

The influence of fO_2 on tourmaline composition at 600°C is illustrated in Fig. 2.8D; E; F. Generally, compositional trends are identical under moderately and highly oxidising fO_2. In both cases, important changes in the Na proportion in X site and in at. Ca/(Ca+Na) are observed (Fig. 2.8D; E). However, the at. Fe/(Fe+Mg) dispersion is larger (from 0.13 to 0.41) in highly oxidising than in moderately oxidising charges. Comparing charges with the same $[B_2O_3]_{fluid}$ (8 wt%), the highly oxidising have tourmaline compositions with higher Na in X site and at. Fe/(Fe+Mg) and lower at. Ca/(Ca+Na) (for Fe/(Fe+Mg) constant) and Al than the moderately oxidising (Fig. 2.8D; E; F). The correlation between at. Ca/(Ca+Na) and at. Fe/(Fe+Mg) seen in the moderately oxidising compositions (Fig. 2.8B) is confirmed and strengthened by the highly oxidising data so that the more Fe-rich, the more Ca-rich the tourmaline (Fig. 2.8E). The three Group I tourmalines analysed in the highly oxidising $[B_2O_3]_{fluid} = 6$ wt% charge generally follow the trends for the $[B_2O_3]_{fluid} = 8$ wt% compositions (Fig. 2.8E) although for lower Al contents (Fig. 2.8F).

4/ *MAS NMR results*

The MAS NMR analysis allowed the acquisition of a total of 5 spectra, corresponding to the experimental products where tourmaline was dominant (S600-10, S600-8, S500-6Pt, S400-6, and S400-4Pt, see Table 2). All the spectra show a unique pic between 20 and 10 ppm, corresponding to BO_3 liaisons (Fig. 2.10). No BO_4 at 0 ppm was observed. Plan spectra were obtained for all the other charges, indicating a material with less than 10 ppm of boron. Considering the phase assemblages characterisation and the $[B_2O_3]_{fluid}$ used in the starting fluid, such low concentration are unlikely to occur in our experiment. The non-obtention of a spectra may be caused by the low-crystallinity of the B-bearing phase and / or by a relatively high proportion of paramagnetic mineral compared to the B-bearing phase.

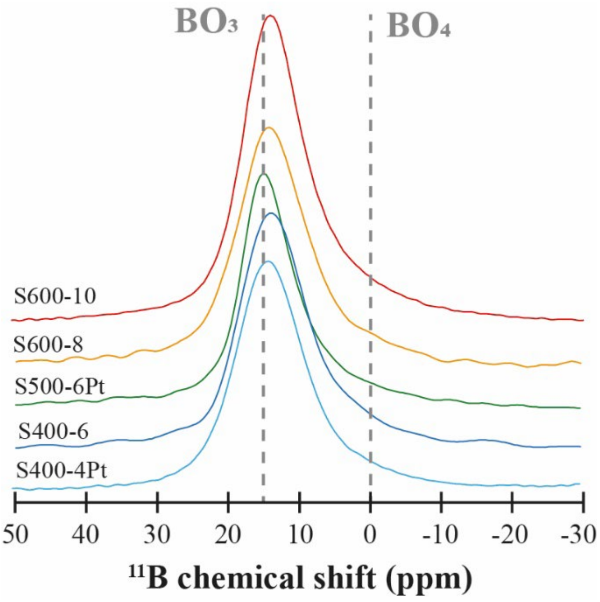

Figure 2. 10: 11B MAS NMR spectra of experimental tourmalines. All spectra are scaled to the same height.

IV- Discussion

A) Experimental reaction mechanisms

The four model tourmalinization reactions R1 to R4 involve pure phases (quartz, andalusite), solid solutions (plagioclase, cordierite, tourmaline), and fluid. The corresponding equilibrium constants are of the same form, e.g., for R1:

$$K_{R1} = \frac{\left(a_{DRV}^{Tur}\right)^2 . \left(a_{H_2O_{(g)}}\right)^5}{\left(a_{MgCRD}^{Crd}\right)^3 . \left(a_{ALB}^{Pl}\right)^2 . \left(a_{B(OH)_3\,(aq)}\right)^6} \qquad \text{(Eq. 1)}$$

where $a_{DRV}^{Tur}, a_{MgCRD}^{Crd}$ and a_{ALB}^{Pl} are the activities of the dravite, Mg-cordierite and albite end-members in tourmaline, cordierite and plagioclase solid solutions, respectively. $a_{H_2O_{(g)}}$ is the activity of water (gas) and, in the range of temperature investigated, $a_{H_2O_{(g)}} \approx f_{H_2O}$. $a_{B(OH)_3\,(aq)}$ represents the activity of boric acid in the fluid, which, for a neutral aqueous specie, can be simplified as equivalent to $B(OH)_3$ molality. This molality can easily be expressed as $[B_2O_3]_{fluid}$. If, in Equation (1), tourmaline, cordierite and plagioclase compositions are identical to their respective end-member components, the equilibrium constant reduces to:

$$K_{R1} \approx \frac{\left(f_{H_2O}\right)^5}{\left(2[B_2O_3]_{fluid}\right)^6} \qquad \text{(Eq. 2)}$$

which shows that, for a given P-T condition, the equilibrium constant only depends on the fluid composition although it can vary between reactions because different tourmaline end-members are involved. If the components of the fluid other than H_2O and B_2O_3 are neglected, Eq. 2 implies that, at equilibrium, the boron content of the fluid ($[B_2O_3]_{fluidEQ}$) is uniquely determined ($[B_2O_3]_{fluid} = [B_2O_3]_{fluidEQ}$). For variable temperatures, $[B_2O_3]_{fluidEQ}$ would follow an univariant curve in T-$[B_2O_3]_{fluid}$ space. Experimentally, equilibrium along R1 (or the other tourmaline-forming reactions) implies that increasing the boron fluid concentration above $[B_2O_3]_{fluidEQ}$ would shift the reaction toward the right, thus producing tourmaline and consuming the reactants in R1-R4. Conversely, lowering the boron fluid concentration below $[B_2O_3]_{fluidEQ}$ should lead to the reaction being shifted to the left, thus consuming tourmaline and producing B-free phases.

Our forward experiments are generally consistent with this theoretical framework. Focusing on results at 600°C and 500°C since smectite takes the place of cordierite at 400°C and so reactions R1 to R4 are no longer valid, the experiments demonstrate the appearance of tourmaline in phase assemblages for boron contents in the fluid above a minimum value. Tourmaline formation thus follows an evolution toward the right as expected from reactions R1 to R4. $[B_2O_3]_{fluidEQ}$ is experimentally bracketed by charges without tourmaline and others with tourmaline present and it weakly varies with temperature between 500 and 600°C, being also independent of fO_2 (Fig. 2.4). Our determinations are reproducible and mutually consistent, i.e., at 600°C the brackets on $[B_2O_3]_{fluidEQ}$ in Run 1 (3.4-10.1 wt%), Run 2 (< 4 wt%) and Run 6 (3-4.2 wt%) overlap (Table 2.2). For charges near $[B_2O_3]_{fluidEQ}$, experimental phase assemblages include the five major phases involved in reactions R1-R4 (e.g., charges S600-4, SOX-4, SOX-6, Table 2.2). They evolve in a systematic way upon increasing the initial boron content of the fluid above $[B_2O_3]_{fluidEQ}$. Cordierite, andalusite, and albite progressively disappear and tourmaline and quartz proportions increase in experimental products. These changes in phase assemblage are consistent with the tourmaline-forming reactions becoming progressively more advanced and evolving away from equilibrium conditions as $[B_2O_3]_{fluid}$ is increased. Last, compositions of experimental tourmalines (solid solutions between magnesio-foitite and dravite with small amounts of foitite, schorl, and uvite, see above, Fig.2.7, 2.8) are consistent with tourmaline formation along with reactions R1 to R4. Uvite is the only component that would require a fifth model reaction to be written to fully account for the range of our experimental tourmalines. The chemical variability of experimental tourmaline reflects complex nucleation and growth mechanisms instead of disequilibrium, as discussed in detail below.

Although the forward experiments have closely simulated the theoretical tourmaline-forming reactions, no tourmaline consumption and production of B-free phases could be demonstrated in the two reversal experiments. Phase assemblages in these two experiments were unchanged compared to the starting mixture, a result attributed to the refractory behaviour of tourmaline (Henry & Dutrow 1996; von Goerne et al. 1999; van Hinsberg et al. 2011b). The refractory character of tourmaline has been attributed to different factors such as extremely slow kinetics of element exchange with fluids (Zimmermann et al. 1996). It has been proposed that the destabilisation of tourmaline requires alkaline fluids (Morgan and London 1989; Henry and Dutrow 1996; 2018). However, the reaction of tourmaline plus quartz to form cordierite was successfully obtained under acidic fluid (pH = 3.2) conditions but at a temperature (680°C) higher than in this study (von Goerne et al., 1999b). Our inability to demonstrate the reversibility of the tourmaline-forming reactions implies that equilibrium cannot be claimed in our experiments. Therefore, the boron fluid concentration brackets defined from the forward experiments represent the maximum (upper bounds) and minimum limits (lower bounds) on $[B_2O_3]_{fluidEQ}$.

B) Thermodynamic estimation of the $[B_2O_3]_{\text{fluid\_EQ}}$

1/ Calculation

Experimental uncertainties on $[B_2O_3]_{\text{fluid\_EQ}}$ (e.g., unsuccessful reversals) and the possibility that Na and alkali-deficient Fe-Mg tourmalines are stable for different $[B_2O_3]_{\text{fluid}}$ have prompted us to constrain $[B_2O_3]_{\text{fluid\_EQ}}$ thermodynamically for the four tourmaline-forming reactions considered in this study. On the example of reaction R1, $[B_2O_3]_{\text{fluid\_EQ}}$ can be expressed from Eq. 2:

$$[B_2O_3]_{fluid\_Eq\,R1} \approx 0.5 \times 10^{\frac{5\log\left(f_{H_2O}\right)-\log(K_{R1})}{6}} \qquad \text{(Eq.3)}$$

Values for f_{H_2O} come from (Burnham et al. 1969; see Appendix A9). As all four tourmaline-forming reactions contain the same amount of H_2O and $B(OH)_3$, the Eq.3, expressed for R1, applies equally to R2, R3, and R4. At given T and P, the log K of the tourmaline-forming reactions are calculated from:

$$Log(K_{R\,T,P}) = \frac{-\Delta_r G°_{T,P}}{RTln(10)} \qquad \text{(Eq 4)}$$

where R is the ideal gas constant (= 8,3144 J/mol.K) and $\Delta_r G°_{T,P}$ is the Gibbs free energy change associated with the reaction considered. Based on the revised-HKF model (Tanger & Helgeson 1988), standard reaction properties can be calculated from the apparent standard thermodynamic properties of the components involved in the reaction (Helgeson et al. 1981a). For reaction R1:

$$\Delta_r G°_{T,P\,R1} = 2\Delta_{app} G°_{T,P,Drv} + 8\Delta_{app} G°_{T,P,Qtz} + \Delta_{app} G°_{T,P,And} + 5\Delta_{app} G°_{T,P,H_2O_{(g)}} - \left(3\Delta_{app} G°_{T,P,Mg-Crd} + 2\Delta_{app} G°_{T,P,Alb} + 6\Delta_{app} G°_{T,P,B(OH)_3}\right) \qquad \text{(Eq.5)}$$

where Drv, Qtz, And, Mg-Crd, and Alb refer to the pure mineral components dravite, quartz, andalusite, cordierite, and albite respectively in reaction R1. The apparent standard Gibbs free energy at T and P for the component X is given by the equation:

$$\Delta_{app} G°_{T,P,X} = \Delta_f G°_{T°,P°,X} - (T - T°)S°_{T°,P°,X} + \int_{T°}^{T} Cp°_{P°,X}.dT - T\int_{T°}^{T} \frac{Cp°_{P°,X}}{T}.dT + \int_{P°}^{P} V°_{T°,X}.dP \qquad \text{(Eq.6)}$$

where T° and P° are the reference temperature (298.15°K) and pressure (1 bar), respectively. The thermodynamic properties of the component X in Eq.6 are the standard Gibbs free energy of formation ($\Delta_f G°_{T°,P°,X}$), the standard entropy, ($S°_{T°,P°,X}$), the standard heat capacity ($Cp°_{P°,X}$) and the molar volume ($V°_{T°,X}$). The expression of the heat capacity as a function of T can be written for every phase as:

$$Cp°\,(T) = a + bT + cT^{-2} + dT^{-0.5} \qquad \text{(Eq. 7)}$$

By considering Eq. 7 and the volume of solid phases as a constant, independent of P, Eq. 6 can be rewritten, for the phase X, as:

$$\Delta_{app} G°_{T,P,X} = \Delta_f G°_{T°,P°,X} - (T - T°)S°_{T°,P°,X} + a\left((T - T°) - T * ln\left(\frac{T}{T°}\right)\right) + b\left(\frac{-(T-T°)^2}{2}\right) - c\left(\frac{(T-T°)^2}{2TT°^2}\right) + 2d\left(\sqrt{T} - \sqrt{T°} + \frac{T}{\sqrt{T}} - \frac{T}{\sqrt{T°}}\right) + (P - P°)V°_{T°,X} \qquad \text{(Eq.8)}$$

This allows calculating the log K at T, P for the chosen reaction using Eq. 5 and 4.

2/ $B(OH)_{3(aq)}$ HKF parameters

In the present work, the HKF theory (Helgeson et al. 1981b; Tanger and Helgeson 1988) is applied to calculate the standard thermodynamic properties of aqueous species as a function of temperature and pressure. In thermodynamic databases that are compatible with the HKF theory, the thermodynamic properties and HKF parameters for the $B(OH)_3$ aqueous species come from either Shock et al. (1989), used in SUPCRTBL (Zimmer et al. 2016a) or Pokrovski et al. (1995), used in Thermoddem (Blanc et al. 2012b). To take account of the amphoteric behaviour of aqueous boron, Shock et al. (1989) introduced the BO_2^- species, while Pokrovski et al. (1995) replaced BO_2^- by $B(OH)_4^-$ and added $NaB(OH)_4$. Aside from those studies, two other teams propose new $B(OH)_3$ HKF parameters, based on the Pokrovski et al. (1995) experimental data. Akinfiev et al. (2006), reassessed those parameters with regards to polyborate species and experiments on NaCl-$B(OH)_3$ fluids, between 0 and 300°C. Wang et al. (2013) realised the same work for more B aqueous species through bibliographic compilation, in order to construct a mixed-solvent electrolyte model, mainly calibrated up to 100°C. Using the PHREEQC software, those four sets of parameters were tested in combination with the Thermoddem database by reproducing experiments between 0 and 300°C (Fig. 2.11).

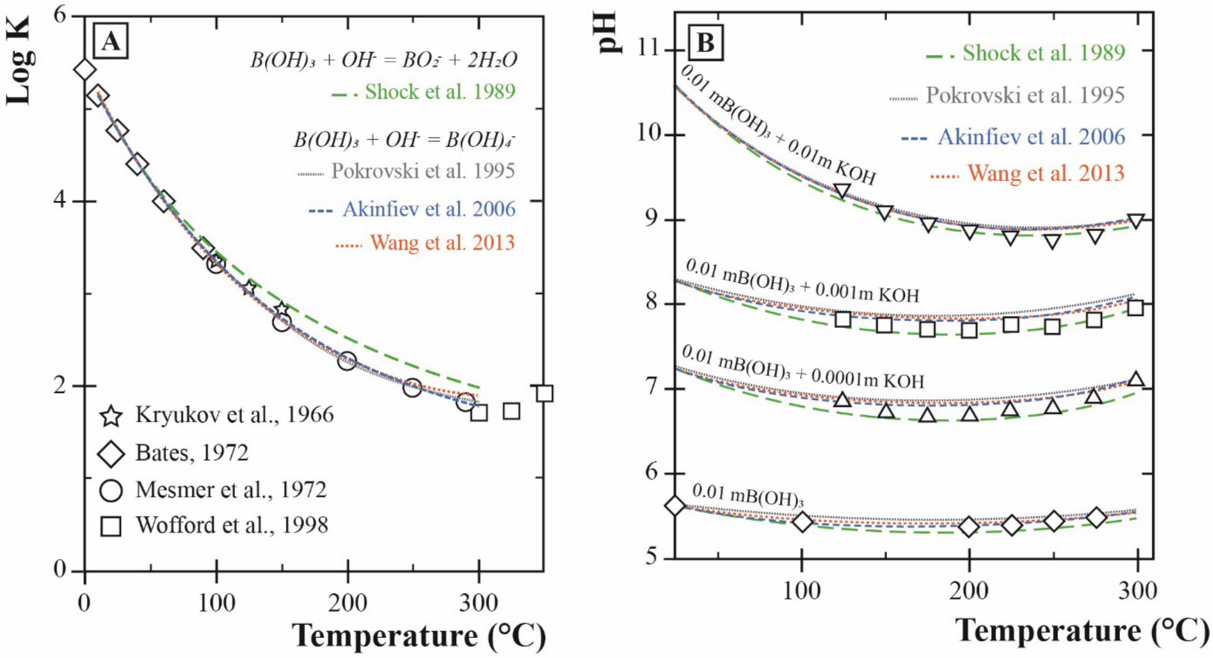

Figure 2. 11: (A) Temperature dependence of the equilibrium constant of the reaction $B(OH)_3 + OH^- \rightarrow B(OH)_4^-$ or its equivalent $B(OH)_3 + OH^- \rightarrow BO_2^- + 2H_2O$ between 10 and 300°C at saturated water vapour pressure. Experimental points interpreted as Log K by Akinfiev et al. (2006), based on the data from Kryukov et al. (1966), Bates (1972), Mesmer et al. (1972) and Wofford et al. (1998). The lines represent the pH calculated by PHREEQC of each solution, for four different data sources of HKF parameters for $B(OH)_3$. (B) pH evolution of various $B(OH)_3$ / $K(OH)$ solutions with temperature. Experimental points are from Macdonald et al. (1992), except for the pure $B(OH)_3$ solution which come from Macdonald et al. (1980). The lines represent the pH calculated by PHREEQC of each solution, for four different data sources of HKF parameters for $B(OH)_3$.

Shock et al. (1989) parameters show the largest deviation with respect to other simulations and experimental results at T > 50°C. The three others display similar results, in accordance with the experimental points. However, in Figure 2.11A at high temperature, the simulation using Wang et al. (2013) parameters begin to deviate from the other two. Akinfiev et al. (2006) parameters show the best overall reproduction and thus were considered as the best to use in our calculations. Results for the calculations realised with the others $B(OH)_3$ HKF parameters are presented in Appendix A10. The apparent standard Gibbs free energy at our experimental T and P conditions calculated with the Thermo-ZNS computer-code (Lassin et al. 2005) are given in Appendix A9.

3/ Calculation of $[B_2O_3]_{fluid\_EQ}$

The $\Delta_{app}G°_{T,P}$ of the minerals and $H_2O_{(g)}$ were calculated from the thermodynamic database Thermoddem (Blanc et al. 2012a), except for Fe-cordierite, whose properties came from SUPCRTBL (Zimmer et al. 2016b), and tourmaline. For the tourmaline components, the thermodynamic properties come from polyhedron models (van Hinsberg & Schumacher, 2007b) and calorimetric measurements (Ogorodova et al., 2012; n.b. this dataset does not include the foitite end-member for R4) (Table 2.1) and the calculations have been performed in parallel with these two latter datasets. The absence of ^{IV}B in the experimental tourmaline allow the use of the polyhedron model without to have to consider an effect of ^{IV}B polyhedra on the standards properties. The properties used are listed in Appendix A9 and A11. Results, using $B(OH)_3$ HKF parameters from Akinfiev et al. (2006), are plotted in Figure 2.12 where they are compared with the $[B_2O_3]_{fluid\_EQ}$ brackets from this study.

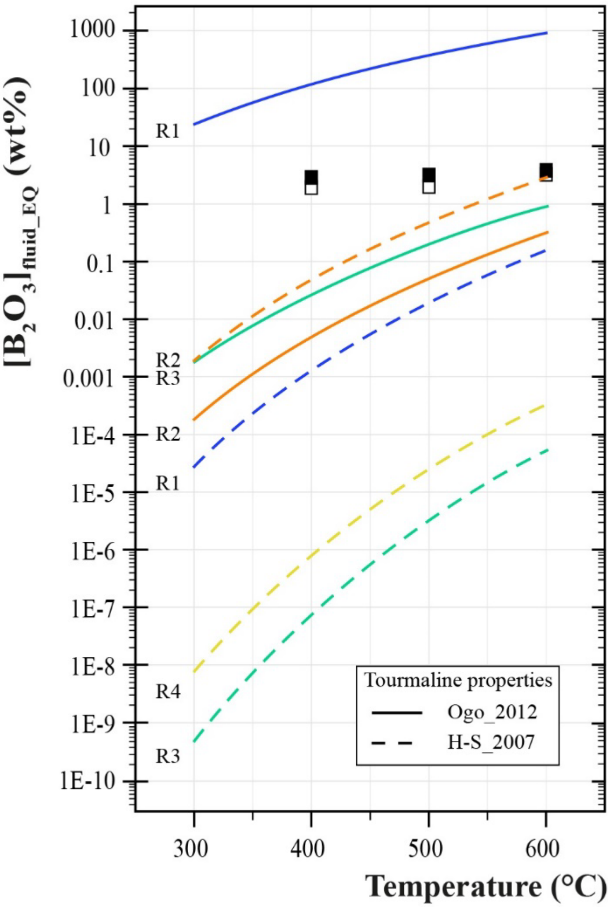

Figure 2. 12: Calculated $[B_2O_3]_{fluid\_EQ}$ as a function of temperature for the four tourmaline-forming reactions considered (R1, R2, R3, R4, see text) and the two tourmaline thermodynamic datasets used in the calculations (solid lines for Ogorodova et al., 2012 (Ogo_2012) and dashed lines for van Hinsberg & Schumacher, 2007b (H-S_2007)). Experimental brackets of $[B_2O_3]_{fluid\_EQ}$ from this study are shown by solid (tourmaline present) and open (tourmaline absent) symbols.

All calculations show a positive correlation between $[B_2O_3]_{fluid\_EQ}$ and temperature, as experimentally observed. However, important differences in $[B_2O_3]_{fluid\_EQ}$ appear depending on the thermodynamic properties used for tourmaline. Using values from Ogorodova et al. (2012) yields $[B_2O_3]_{fluid\_EQ}$ values higher than those obtained when considering tourmaline properties from van Hinsberg & Schumacher (2007b) for reactions R1, R2 and R3. The mismatch between calculations and experiments is large, of several orders of magnitude on $[B_2O_3]_{fluid\_EQ}$, and calculations with the Ogorodova et al. (2012) data frame the experimental brackets (reaction R1, Fig. 2.12). Yet, both thermodynamic datasets suggest that alkali tourmaline equilibration according to reaction R1 (dravite) needs higher $[B_2O_3]_{fluid}$ than alkali-deficient tourmaline equilibration according to R3 (Mg-foitite). To equilibrate, Schorl (R2) requires a lower $[B_2O_3]_{fluid}$ than dravite (R1) when calculated with the Ogorodova et al. (2012) data whereas the opposite is observed with van Hinsberg & Schumacher (2007b) (Fig. 2.12). These results stress the uncertainties on the thermodynamic properties of tourmaline. The data from Ogorodova et al. (2012) are in a good agreement with the estimated properties, within errors, given by van Hinsberg & Schumacher (2007). Yet, those small differences between the two sets at 25°C, 1 bar, imply large differences in the $[B_2O_3]_{fluid\_EQ}$ calculated at higher temperature. Therefore, the experimental results provided by this study can provide new, more refined constraints on the thermodynamic properties of tourmaline. However, the calculation is pertained to end-members, whereas experimental tourmalines are solid solutions whose composition varies with T. When the $[B_2O_3]_{fluid\_EQ}$ are calculated from Ogorodova et al. (2012) properties, the tourmaline-forming reactions can be divided into two group (Fig. 2.12): the one destabilising the experimental tourmaline (overestimation of $[B_2O_3]_{fluid\_EQ}$ compared to the experimental bracket; R1) and the one stabilizing it (underestimating $[B_2O_3]_{fluid\_EQ}$; R2 and R3). Using those properties, calculation of the $[B_2O_3]_{fluid\_EQ}$ for ideal solid solution between those three end-members should approach the experimental brackets. An attempt of such calculation is presented thereafter.

4/ Attempt of ideal solid solution modelling

Using those properties, calculation of the $[B_2O_3]_{fluid\_EQ}$ for ideal solid solution between those three end-members should approach the experimental brackets. The solid solution modelled is controlled by the two substitutions $Na^XMg^Y \rightarrow []_XAl^Y$ (dravite to magnesiofoitite) and $Mg_3^Y \rightarrow Fe_3^Y$ (dravite to schorl). Foitite could not be added to the solid solution as its properties have not been estimated by (Ogorodova et al. 2012). Group IIIa tourmaline from charge S600-10(G), S500-6 and S400-6G were selected as representative of the experimental solid solution at 600, 500 and 400°C, respectively. Their composition (Table 2.4) were simplified by removing elements other than Fe, Mg, Al in the site Y and other than Na, $[]_X$ in the site X, and considering only Al in site Z and Si in site T (Table 2.1). The amount of Na and $[]_X$ was recalculated with respect to their original proportion so that Na + $[]_X$ = 1. Based on the alkali-deficient substitution, $Al^Y = []_X$ and so, Mg and Fe were recalculated with respect to their original proportion so that Mg + Fe = 3 – Al^Y. Based on this new composition the proportion of each end-member was calculated with: $X_{Mg-Fo} = [\,]_X$, $X_{Drv} = \frac{Mg-2*[\,]_X}{Fe+Mg-2*[\,]_X} * Na$ and $X_{Srl} = \frac{Fe}{Fe+Mg-2*[\,]_X} * Na$. Foitite being left aside, the proportions of magnesiofoitite and schorl are overestimated in regards to dravite. This induces an underestimation of $[B_2O_3]_{fluid\_EQ}$, especially for tourmaline where dravite is not the main end-member. The simplified composition of the experimental tourmalines and their end-members proportions are presented in Table 2.5.

T°C (charge)	Average composition		Simplified composition		Solid solution			$[B_2O_3]_{fluid\_EQ}$
Reaction	X	Y	X	Y	X_{Drv}	$X_{Mg\text{-}Fo}$	X_{Srl}	calculated
600°C (S600-10(G))	$Na_{0.56}\,Ca_{0.12}\,[]_{X\,0.32}$	$Mg_{1.57}\,Fe_{0.38}\,Al_{0.82}$	$Na_{0.64}\,[]_{X\,0.36}$	$Mg_{2.12}\,Fe_{0.52}\,Al_{0.36}$	0.47	0.36	0.17	6.79
500°C (S500-6)	$Na_{0.60}\,Ca_{0.08}\,[]_{X\,0.31}$	$Mg_{1.80}\,Fe_{0.32}\,Al_{0.68}$	$Na_{0.66}\,[]_{X\,0.34}$	$Mg_{2.26}\,Fe_{0.4}\,Al_{0.34}$	0.53	0.34	0.13	3.26
400°C (S400-6G)	$Na_{0.44}\,Ca_{0.11}\,[]_{X\,0.44}$	$Mg_{1.70}\,Fe_{0.26}\,Al_{0.82}$	$Na_{0.5}\,[]_{X\,0.5}$	$Mg_{2.17}\,Fe_{0.33}\,Al_{0.5}$	0.39	0.50	0.11	0.22

Table 2. 5: Simplified average composition of experimental tourmaline (see Table 2.4).

The apparent standard Gibbs free energy at T and P for the tourmaline solid solution is given by the equation:

$$\Delta_{app}G^{\circ}{}_{T,P,sol} = \sum_i X_i * \Delta_{app}G^{\circ}{}_{T,P,i} + TR\nu \sum_i X_i \ln(X_i) \qquad \text{(Eq. 9)}$$

With $\Delta_{app}G^{\circ}{}_{T,P,i}$ the apparent standard Gibbs free energy at T, P of the end-member i, X_i its molar fraction, R the ideal gas constant and ν the number of sites concerned by the mixing in 1 mol of the mineral. In our case, the solid solution impacts the site X and the three sites Y. However, the alkali-deficient substitution is a bi-site substitution induced by a charge compensation: the incorporation of Al^{3+} instead of Mg^{2+} in the site Y requires losing a charge in the site X. As such, this substitution can be considered as impacting only one site, reducing the total number of sites impacted by the solid solution to 3. The calculated values of $[B_2O_3]_{fluid\_EQ}$ are given in Table 2.5 and are compared with the experimental brackets and values for pure end-members in Figure. 2.13. The error bars associated to each point correspond to the $[B_2O_3]_{fluid\_EQ}$ calculated for the most dravitic (high) and schorlitic (low) possible compositions regarding the standard deviation on the average composition (Table 2.4). $[B_2O_3]_{fluid\_EQ}$ values for simplified experimental tourmaline compositions at 600 and 500°C fit, with respect to the error bar, the bracket determined in this study. However, at 400°C the $[B_2O_3]_{fluid\_EQ}$ determined is too low by one order of magnitude compared to the bracket. This may be caused by the overestimated magnesiofoitite proportion, especially for those compositions with low amount of Na. Tourmaline formed at 400°C presents also the highest at. Ca/(Ca+Na). The non-incorporation of uvite in the modelled solid solution induces larger differences between the simplified and experimental compositions at 400°C. By applying the same methodology used for R1-R4, the $[B_2O_3]_{fluid\_EQ}$ deduced from a uvite-forming reaction (involving anorthite instead of albite) is always higher than the experimental bracket. Thus, the reaction with uvite is a destabilising reaction. Its incorporation in a ideal solid solution would affect the values presented in Figure. 2.13 by increasing the $[B_2O_3]_{fluid\_EQ}$ calculated.

The non-integration of Ca end-member is not the only important simplification. The experimental tourmalines also contain a large amount of Al in the Y-site (Table 2.5), more than what can be explain with the alkali-deficient tourmalines. Two endmembers can be used to reproduce this high Al content: the olenite ($NaAl_3Al_6Si_6O_{18}(BO_3)_3O_3(OH)$) and/or the oxy-dravite ($NaAl_3(Al_4Mg_2)Si_6O_{18}(BO_3)_3(OH)_3O$) (Henry et al. 2011). The thermodynamic properties of those compositions have not been investigated by Ogorodova et al. (2012) and only the olenite have been estimated in the study of van Hinsberg & Schumacher (2007). Furthermore, the analysis carried out in this study does not make it possible to observe the content of the anionic sites V and W (OH^- or O^{2-}). Usually realised through RAMAN analysis, investigating the [3400 ; 3800]cm^{-1} section (e.g. Watenphul et al. 2016; Lensing-Burgdorf et

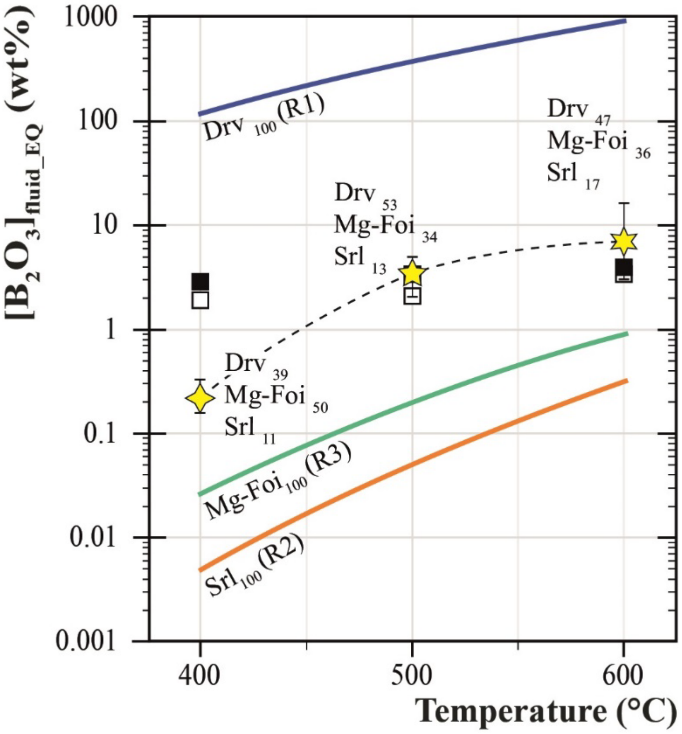

Figure 2. 13: Calculated $[B_2O_3]_{fluid\_EQ}$ for simplified solid solution (stars) representative of the experimental tourmaline composition at the corresponding temperature. Experimental brackets of $[B_2O_3]_{fluid\_EQ}$ from this study are shown by solid (tourmaline present) and open (tourmaline absent) symbols. The three curves R1, R2 R3 are from Fig. 2.12.

al. 2017), those analyses require to align the cartesian coordinate axe z to the crystallographic <c> axis of the tourmaline. This could not be done due to the very fine texture of the experimental products. Spectra acquired on disoriented or approximately oriented fibers, using a 532 nm laser (ISTO, Orléans, France), showed significant fluorescence in the spectral range above 800 cm^{-1}. Another approximation to the composition of the experimental tourmaline is to consider that the Fe content measured by the electron microprobe corresponds only to Fe^{2+}. Tourmaline with Fe^{3+} like the buergerite ($NaFe^{3+}_3Al_6Si_6O_{18}(BO_3)_3O_3(OH)$) and povondraite ($NaFe^{3+}_3(Fe^{3+}_4Mg_2)Si_6O_{18}(BO_3)_3(OH)_3O$) may also have an impact in the real composition of the experimental tourmaline, and thus, shift the result of the ideal solid-solution. Again, these end-members were not considered by Ogorodova et al. (2012) but are present in van Hinsberg & Schumacher (2007). The determination of the Fe^{2+}/Fe^{3+} ratio in our experimental tourmaline could not be performed through Mössbauer spectroscopy (Fuchs et al. 1998; Baksheev et al. 2020) due to our inability to extract tourmaline solely from the experimental products. Recently, Mrkusová & Škoda (2021) presented advancement on the calibration of Fe^{2+}/Fe^{3+} measurement for tourmaline by the flank method (Höfer & Brey 2007). Using an electron microprobe, this technic does not have the disadvantages of the bulk analysis and could be applied directly to our experimental tourmaline.

The conception of a complete multicomponent ideal solid solution from the experimental tourmalines in this study is out of reach due to the many uncertainties in their composition. The refinement of the thermodynamic properties of tourmaline requires a precise characterisation of their composition. This work is actually in progress for Li-free tourmaline (Roozen et al. 2021). Nevertheless, despite all the estimates made regarding the composition of our experimental tourmalines, the results obtained with the ideal 3 end-members solid solution model are very encouraging.

C) Tourmaline textural evolution

As reported by London (2011), all experimental studies on tourmaline have described their products as consisting of exceedingly fine-grained tourmaline (Frondel et al. 1947; Morgan & London 1989; von Goerne et al. 1999; Berryman et al. 2015, 2016), except in the case where diffusion-limited growth methods were used . Tourmaline textures in this study are in accordance with this observation. They show fibrous morphologies with strongly marked growth along the <c> axis while growth along the <a> axis is inhibited (Dutrow & Henry 2016). Nevertheless, in detail, tourmalines in our experiments show different textural types. These are interpreted to indicate different growth mechanisms under two end-member regimes of supersaturation of tourmaline-forming components in the fluid.

For fluid boron concentrations near equilibrium ($[B_2O_3]_{fluid} \approx [B_2O_3]_{fluid\_EQ}$), the dissolution of reactant minerals is limited and so, fluids are weakly supersaturated with respect to the tourmaline-forming components. Under these conditions, growth is controlled by a local balance between elements from the reactant minerals and from the fluid. Tourmaline forms Group I crystals commonly found heterogeneously nucleated on albite or cordierite grains, and also a few coarser crystals of Group II (Fig. 2.3). These latter indicate that, at low fluid supersaturation levels, growth on already formed tourmaline crystals is favoured as the potential energy (i.e., the energy barrier for nucleation) necessary to form a new crystal is high. Upon increasing the fluid saturation level ($[B_2O_3]_{fluid} > [B_2O_3]_{fluid\_EQ}$) at 600°C, more Group I tourmaline forms and Group II crystals disappear (Table 2.2). At lower temperatures (500 and 400°C), the absence of Group II textures indicates that the formation of multiple Group I tourmalines is favoured over growth on a few preexisting crystals.

In contrast, the development of acicular fibers (Group IIIa), texturally similar to "luxullianites" from Cornwall (Lister 1981), reflects rapid heterogeneous tourmaline nucleation in a solution strongly supersaturated with respect to the tourmaline-forming components ($[B_2O_3]_{fluid} >> [B_2O_3]_{fluid\_EQ}$). At 600 and 500°C, the formation of Group IIIa is accompanied by long tourmaline fibers isolated in the fluid (Group IIIb) suggesting homogeneous nucleation. This indicates rapid dissipation of the excess potential energy so that equilibrium between the fluid and the minerals is quickly established globally at the scale of the charge (Lasaga 1998). At 400°C, homogeneous nucleation is not observed and tourmaline appears directly and uniquely as Group IIIa. This difference may be explained by the presence of smectite instead of cordierite which has an impact on the global distribution of elements in the fluid. Supersaturation under these conditions is considered to be only local as suggested by the composition of the 400°C tourmalines which have grouped at. Fe/(Fe+Mg) identical to the composition of the starting cordierite (Fig. 2.8A).

Crystallisation of the Group IV tourmalines is specific. At all temperatures, the Group IV crystals are mainly located at one end of the <c> axis of the seed (Fig. 2.3F), probably the <c+> pole. This kind of overgrowth, both observed in experiments and natural rocks (van Hinsberg et al. 2011b; Dutrow & Henry 2016, 2018), is an indication of very fast nucleation processes. For a given fluid saturation level, heterogeneous nucleation on a surface sharing the same crystallographic configuration requires less potential energy than nucleation on a surface with the different crystallographic arrangement. Therefore, Group IV can be considered as the most rapidly formed tourmaline in the charge, crystallising earlier than Group IIIa crystals. This has implications for Group IV and Group IIIa tourmaline compositions at 400°C (Fig. 2.7; see below).

D) Control on tourmaline composition

Chemical compositions of experimental tourmalines, especially at. Ca/(Ca+Na) and at. Fe/(Fe+Mg), are shown to vary significantly within several charges (Fig. 2.8B; E). Tourmaline compositional data were not reported in previous experimental cordierite-tourmaline equilibrium studies (Weisbrod et al. 1986; von Goerne et al. 1999b). However, tourmalines in experiments are frequently zoned chemically and/or compositionally variable (Morgan & London 1989; von Goerne et al. 2011; Berryman et al. 2015; Orlando et al. 2017; Cheng et al. 2019). For example, von Goerne et al. (2011) obtained zoned tourmaline with an Al, Ca-rich core and a Mg-, Na-rich rim through synthesis experiments in a Fe-free system at 600°C and 200 MPa. In a Fe-bearing system, Morgan & London (1989) observed that experimental overgrowth of tourmaline over a natural seed also yields to zonation, with Mg-, Ca-rich intern parts and Fe-, Na-rich rims.

Compositionally variable products are usually taken as an indication of disequilibrium in the charge. However, we have shown above that phase assemblages in the forward experiments evolve conformably with what is expected from tourmaline-forming equilibrium reactions. The various charges yield the same range of $[B_2O_3]_{fluidEQ}$ at 600°C, further indicating a reasonably close approach toward equilibrium in our experiments. Besides, there is possibly no influence of fO_2 on tourmaline compositions since the same type of variability is observed in the moderately and strongly oxidising charges (Fig. 2.8D; E). Contrasted diffusivities of elements in tourmaline could possibly generate chemical variability although our relatively short experimental durations and specific experimental tourmaline morphologies (thin sheaves and rods) make volume diffusion negligible (van Hinsberg et al. 2011a). Natural observations have shown that the fluid exerts a first order control on tourmaline compositions (Henry & Dutrow 1996; Williamson et al. 2000; Dutrow & Henry 2011, 2016; van Hinsberg et al. 2011b, 2011a; Harlaux et al. 2020). Morgan and London (1989) explained chemical zonation in their experimental tourmalines by an evolution of the fluid composition. However, the same type of variations in tourmaline compositions are observed in charges with different $[B_2O_3]_{fluid}$ (Fig. 2.8). The effect of temperature appears more marked than the fluid composition as shown by tourmalines with at. Fe/(Fe+Mg) more grouped at 400°C than at 500 and 600°C (Fig. 2.8A; B). Below, we propose that the chemical dispersion in our experimental tourmalines is controlled by nucleation and growth mechanisms.

Chemical zonation (from core to rim, from the base to end of the sheaf) has not been documented on single tourmaline crystals due to their small widths and specific morphologies. However, analysis of an exceptionally coarse and dense Group IIIa tourmaline aggregate from a 600°C boron-rich charge reveals a systematic compositional evolution from a Fe-, Ca-rich core to a Mg-, Na-rich rim (Fig. 62.9. This trend is identical to the one marked by compositions of individual tourmaline crystals analysed within a given charge (Fig. 2.8B; E). We note that these Fe-, Ca-rich individual crystals and the aggregate core markedly differ chemically from starting materials which are Mg-rich for cordierite and Ca-poor for albite (grey bands in Fig. 2.8). Their location in the aggregate (Fig. 2.9) demonstrates that they correspond to an early stage of tourmaline growth in the experiments and that the Mg-, Na-rich compositions come later. This indicates a relation between tourmaline composition and its onset of appearance during the experiment, the crystallisation of Fe-, Ca-rich tourmalines being kinetically favoured compared to the Mg-, Na-rich.

Most tourmaline analyses in Fig. 2.8 correspond to Group III crystals which, from the preceding section, crystallised under conditions of strong supersaturation of components in the fluid with the exception of the 400°C compositions where local supersaturation effects are more important. Thus, at 500 and 600°C, tourmalines grow rapidly by heterogeneous and homogeneous nucleation in a fluid of globally constant composition at the scale of the charge. It is worth noting that the supersaturation level (deviation of $[B_2O_3]_{fluid}$ from $[B_2O_3]_{fluid\_EQ}$) varies during the experiment, being maximum during the early stages and then gradually decreasing as more tourmaline is formed and boron is removed from the fluid. These early stages are the situation envisioned for rapid preferential nucleation of the Fe-, and Ca-rich compositions found in the aggregate core (Fig. 2.9) and individual crystals (Fig. 2.8A-D). Later in the experiment, tourmalines evolve progressively toward more Mg- and Na-rich chemistry (Fig. 2.8A-D; 2.6) as a result of gradual changes of the fluid composition and supersaturation level. At 400°C, tourmaline growth is controlled mostly locally by heterogeneous nucleation on reactants. Contrasted dissolution kinetics of components from starting products (e.g., Ca being released faster to the fluid than Na) also seems possible. The tourmaline compositions at 400°C have at. Fe/(Fe+Mg) suggesting local control of the fluid Fe/Mg by cordierite (Fig. 2.8A). Their variable at. Ca/(Ca+Na) (Fig. 2.8B) reflects fast preferential nucleation of Ca-rich tourmalines or, alternatively, a faster dissolution of the anorthite component to the fluid. It is interesting to note that differences between Group IV and Group IIIa tourmalines (the former being more Ca-rich than the latter, Fig. 2.7) show up at 400°C, being absent at higher temperatures. This can be explained by the Group IV growing significantly faster and earlier than the Group III crystals at 400°C because of different growth mechanisms (see above). Thus, the 400°C compositions confirm the preferential nucleation of Fe-, and Ca-rich compositions because of kinetic reasons. We conclude to a close relationship between growth mechanisms and tourmaline compositions in our experiments and stress the importance of the fluid composition in the control of supersaturation levels.

E) Tourmaline stability and boron fluid concentration

The $[B_2O_3]_{fluid\_EQ}$ brackets from this study can be compared with previous results (Weisbrod et al., 1986; Morgan & London, 1989; von Goerne et al., 1999b; Orlando et al., 2017; Cheng et al., 2019) (Fig. 2.14). Those include equilibrium studies where the final boron concentration in the fluid has been measured and which directly constrains $[B_2O_3]_{fluid\_EQ}$ (Weisbrod et al., 1986; von Goerne et al., 1999b). Other studies only provide information on either the upper or the lower bound of $[B_2O_3]_{fluid\_EQ}$. Tourmaline-bearing charges where only initial $[B_2O_3]_{fluid}$ are known (as in the present study) give upper bounds and tourmaline-free charges lower bounds on $[B_2O_3]_{fluid\_EQ}$. If tourmaline is present but one reactant limiting the advancement of the reaction is missing in the final assemblage, an upper bound on $[B_2O_3]_{fluid\_EQ}$ is obtained. Applying those criteria shows that our 500 and 600°C brackets on $[B_2O_3]_{fluid\_EQ}$ are in agreement with the other experimental studies with the exception of those of Weisbrod et al. (1986) where $[B_2O_3]_{fluid\_EQ}$ are much lower, ≈ 0.75 wt% at 600°C and ≈ 0.21 wt% at 500°C. At temperatures > 600°C, the $[B_2O_3]_{fluid\_EQ}$ data of von Goerne et al. (1999b) are in general (but not always) higher than those of Weisbrod et al. (1986) and the highest values correlate well with the extrapolation of our results (Fig. 2.14).

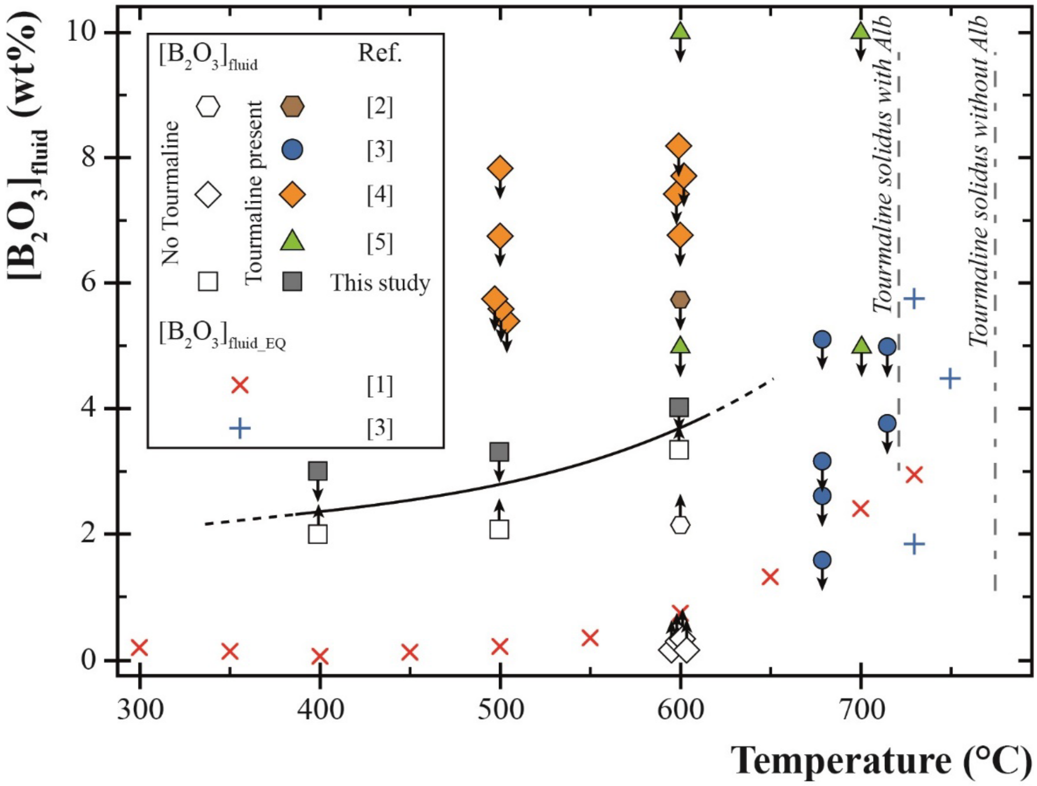

Figure 2. 14: Compilation of experimental results on tourmaline stability in a $[B_2O_3]_{fluid}$ vs. Temperature diagram. Crosses are for experiments where the final boron concentration at equilibrium with tourmaline ($[B_2O_3]_{fluidEQ}$) has been measured. Other symbols represent experiments where $[B_2O_3]_{fluidEQ}$ has not been determined. If tourmaline is not present (open symbols), an upward-pointing arrow is indicated. If tourmaline is present (solid symbols) but a reactant is missing in the final phase assemblage, or if only the initial $[B_2O_3]_{fluid}$ is reported, a downward-pointing arrow is indicated. References: [1] Weisbrod et al. (1986); [2] Morgan and London (1989); [3] von Goerne et al. (1999b); [4] Orlando et al. (2017); [5] Cheng et al. (2019).

We stress that the same system (tourmaline + Mg-cordierite + quartz + fluid ± albite ± andalusite) was investigated in Weisbrod et al. (1986), von Goerne et al. (1999b) and this study, the main points of difference concerning compositions of starting products and the fluid chemistry. Differences in pressure and fO_2 probably have a minor influence on $[B_2O_3]_{fluidEQ}$ (Ota et al. 2008; Berryman et al. 2016; Fig. 2.4B). Weisbrod et al. (1986) and von Goerne et al. (1999b) started from pure Mg-cordierite and albite synthetic phases whereas, in this study, natural Fe-bearing cordierite and albite with some Ca were used. Fluid compositions also differed, Weisbrod et al. (1986) employing a 3 wt% NaCl fluid and von Goerne et al. (1999b) various fluid compositions with or without NaCl and/or HCl. Overall, these starting materials would favor the crystallisation of the dravite end-member in the Weisbrod et al. (1986) and von Goerne et al. (1999b) experiments. Based on the previous thermodynamic calculations, the dravite-forming reaction tends to destabilize experimental tourmaline, increasing the $[B_2O_3]_{fluid\_EQ}$. As such, the $[B_2O_3]_{fluid\_EQ}$ reported by Weisbrod et al. (1986) should be higher than ours, for the same reaction. The presence of NaCl in the fluid should prevent to form highly alkali-deficient tourmaline, which could lower the $[B_2O_3]_{fluid\_EQ}$, but it may induce a new tourmaline-forming reactions that require less $[B_2O_3]_{fluid}$. The comparison between the studies highlights the potential importance of fluid composition (NaCl, HCl) on $[B_2O_3]_{fluidEQ}$.

V- Geological implications

Our experimental determinations of $[B_2O_3]_{fluid\_EQ}$ at equilibrium with tourmaline + cordierite + albite + quartz + andalusite provides insights on the boron concentration in natural hydrothermal and magmatic-hydrothermal systems. According to our data, tourmaline would begin to appear for $[B_2O_3]_{fluid}$ concentrations of a few wt% in the fluid (Fig. 2.4; 2.14). We stress that these concentrations are minimum values and that higher $[B_2O_3]_{fluid}$ are possible in natural hydrothermal systems such as those characterised by the association tourmaline + quartz (e.g. Baksheev et al. 2009; Fusswinkel et al. 2016; Lecumberri-Sanchez et al. 2017; Legros et al. 2020), which is the phase assemblage encountered for the highest $[B_2O_3]_{fluid}$ in the experiments (Table 2.2; Fig. 3). Compilation of boron concentrations of fluid inclusions from various ore deposits yields a wide range of $[B_2O_3]_{fluid}$, from 3.10^{-5} to 2.5 wt% (Prokof'ev et al., 2002). In general, hydrothermal systems developing extensive tourmalinisation phenomena have $[B_2O_3]_{fluid}$ in the high end of the range above. $[B_2O_3]_{fluid}$ concentrations of fluid inclusions in mineralised veins from Cornwall are between 0.2 and 0.63 wt% (Smith et al., 1996). At Panasqueira, the fluids in the W-mineralised veins, which are associated with an early tourmalinisation episode, have $[B_2O_3]_{fluid}$ ranging from 0.09 to 2.3 wt% (Lecumberri-Sanchez et al. 2017). These values are globally lower than in our experiments, although the highest natural concentrations approach the experimental values. It is likely that temperature plays a role since perigranitic hydrothermal systems are mostly colder than 400-500°C (Audétat et al. 2000; Gleeson et al. 2000; Korges et al. 2020) and, so, the influence of temperature on $[B_2O_3]_{fluid\_EQ}$ needs to be taken into account in the comparison (Fig. 2.4; 2.14). Another factor is that tourmalinisation processes are often developed on mica-bearing assemblages as shown for example at Panasqueira (Portugal) where tourmaline and muscovite coexist in the W-mineralised veins (Codeço et al. 2017; Launay et al. 2018). In the Sur-Sur breccia of the Río Blanco-Los Bronces Cu-Mo porphyry deposit (Chile), the mineralised breccia is cemented by tourmaline, formed by the alteration of the original biotite cement (Frikken et al. 2005). In the Sn-lode deposit of San Rafael (SE Peru), intensive tourmalinisation of the cordierite-bearing granite affects primarily the biotite (Harlaux et al. 2020). Therefore, experimental results on tourmalinisation of mica-bearing assemblages are needed for a more direct comparison with natural $[B_2O_3]_{fluid}$ concentrations (Chapter III). Last, hydrothermal fluids are chemically more complex than in experiments from this study, containing various additional anions such as chlorides and cations such as H, K, Ca, and Li (Audétat et al. 2008). The role of these fluid components on $[B_2O_3]_{fluid\_EQ}$ must be determined for the precise evaluation of the boron content of natural hydrothermal fluids.

Knowing the boron concentration of natural hydrothermal systems brings useful constraints on the boron concentration of late-stage silicic melts crystallising in the presence of a fluid phase. Boron is known to partition in favour of the fluid rather than of the melt (Pichavant 1981; London et al. 1988; Schatz et al. 2004; Pokrovski et al. 2013). With the $[B_2O_3]_{fluid\_EQ}$ values determined in this study and summarised in Figure 2.14 (~4 wt% at 650°C), one obtains a boron concentration ($[B_2O_3]_{melt}$) of ~1.3 wt% in the melt with the fluid/melt partition coefficient (3.0) of Pichavant (1981) for peraluminous systems. Previous studies have found

$[B_2O_3]_{melt} \approx 2$ wt% for peraluminous melts saturated in tourmaline at 750°C, 200 MPa (Wolf & London 1997; Acosta-Vigil et al. 2003). Pichavant and Manning (1984) and Dingwell et al. (1996) considered that melt boron concentrations up to ~1 wt% are possible in natural magmatic-hydrothermal systems. Therefore, the $[B_2O_3]_{fluid\_EQ}$ determined in this study lead to $[B_2O_3]_{melt}$ in reasonable agreement with previous values, which gives confidence in our ability to estimate the boron concentrations of natural systems.

References

Acosta-Vigil, A., London, D., Morgan, G.B., and Dewers, T.A. (2003) Solubility of excess alumina in hydrous granitic melts in equilibrium with peraluminous minerals at 700–800 °C and 200 MPa, and applications of the aluminum saturation index. Contributions to Mineralogy and Petrology, 146, 100–119.

Akinfiev, N.N., Voronin, M.V., Zotov, A.V., and Prokof'ev, V.Yu. (2006a) Experimental investigation of the stability of a chloroborate complex and thermodynamic description of aqueous species in the B-Na-Cl-O-H system up to 350°C. Geochemistry International, 44, 867–878.

——— (2006b) Experimental investigation of the stability of a chloroborate complex and thermodynamic description of aqueous species in the B-Na-Cl-O-H system up to 350°C. Geochemistry International, 44, 867–878.

Audétat, A., Günther, D., and Heinrich, C.A. (2000) Causes for Large-Scale Metal Zonation around Mineralized Plutons: Fluid Inclusion LA-ICP-MS Evidence from the Mole Granite, Australia. Economic Geology, 95, 1563–1581.

Audétat, A., Pettke, T., Heinrich, C.A., and Bodnar, R.J. (2008) Special Paper: The Composition of Magmatic-Hydrothermal Fluids in Barren and Mineralized Intrusions. Economic Geology, 103, 877–908.

Baksheev, I.A., Tikhomirov, P.L., Yapaskurt, V.O., Vigasina, M.F., Prokof'ev, V.Yu., and Ustinov, V.I. (2009) Tourmaline of the Mramorny tin cluster, Chukotia peninsula, Russia. The Canadian Mineralogist, 47, 1177–1194.

Bates, R. (1972) Determination of pH: Theory and Practice, Khimiya. Leningrad.

Beckett-Brown, C.E., McDonald, A.M., and McClenaghan, M.B. (2023) Recognizing Tourmaline in Mineralized Porphyry Cu Systems: Textures and Major-Element Chemistry. The Canadian Journal of Mineralogy and Petrology, 61, 3–29.

Berryman, E.J., Wunder, B., Wirth, R., Rhede, D., Schettler, G., Franz, G., and Heinrich, W. (2015) An experimental study on K and Na incorporation in dravitic tourmaline and insight into the origin of diamondiferous tourmaline from the Kokchetav Massif, Kazakhstan. Contributions to Mineralogy and Petrology, 169, 28.

Berryman, E.J., Wunder, B., Rhede, D., Schettler, G., Franz, G., and Heinrich, W. (2016) P–T–X controls on Ca and Na distribution between Mg–Al tourmaline and fluid. Contributions to Mineralogy and Petrology, 171, 31.

Blanc, Ph., Lassin, A., Piantone, P., Azaroual, M., Jacquemet, N., Fabbri, A., and Gaucher, E.C. (2012a) Thermoddem: A geochemical database focused on low temperature water/rock interactions and waste materials. Applied Geochemistry, 27, 2107–2116.

——— (2012b) Thermoddem: A geochemical database focused on low temperature water/rock interactions and waste materials. Applied Geochemistry, 27, 2107–2116.

Burnham, C.W., Holloway, J.R., and Davis, N.F. (1969) Thermodynamic Properties of Water to 1,000° C and 10,000 Bars, Geological Society of America. Vol. 132.

Charoy, B. (1979) Greisenisation, minéralisation et fluides associés à Cligga Head, Cornwall (sud-ouest de l'Angleterre). Bulletin de Minéralogie, 102, 633–641.

Cheng, L., Zhang, C., Yang, X., Qi, D., Zhou, Y., and Holtz, F. (2019) Experimental investigation of reactions between two-mica granite and boron-rich fluids: Implications for the formation of tourmaline granite. Science China Earth Sciences, 62, 1630–1644.

Codeço, M.S., Weis, P., Trumbull, R.B., Pinto, F., Lecumberri-Sanchez, P., and Wilke, F.D.H. (2017) Chemical and boron isotopic composition of hydrothermal tourmaline from the Panasqueira W-Sn-Cu deposit, Portugal. Chemical Geology, 468, 1–16.

Dingwell, D.B., Pichavant, M., and Holtz, F. (1996) Chapter 8. Experimental Studies of Boron in Granitic Melts. In L.M. Anovitz and E.S. Grew, Eds., Boron _ Mineralogy, Petrology and Geochemistry Vol. 33, pp. 331–386. De Gruyter, Berlin, Boston.

Drivenes, K., Larsen, R.B., Müller, A., Sørensen, B.E., Wiedenbeck, M., and Raanes, M.P. (2015) Late-magmatic immiscibility during batholith formation: assessment of B isotopes and trace elements in tourmaline from the Land's End granite, SW England. Contributions to Mineralogy and Petrology, 169, 56.

Drivenes, K., Larsen, R.B., Müller, A., and Sørensen, B.E. (2016) Crystallisation and uplift path of late Variscan granites evidenced by quartz chemistry and fluid inclusions: Example from the Land's End granite, SW England. Lithos, 252–253, 57–75.

Dutrow, B.L., and Henry, D.J. (2011) Tourmaline: A Geologic DVD. Elements, 7, 301–306.

Dutrow, B.L., and Henry, D.J. (2016) Fibrous Tourmaline: A Sensitive Probe of Fluid Compositions and Petrologic Environments. The Canadian Mineralogist, 54, 311–335.

Dutrow, B.L., and Henry, D.J. (2018) Tourmaline compositions and textures: reflections of the fluid phase. Journal of Geosciences, 99–110.

Frikken, P.H., Cooke, D.R., Walshe, J.L., Archibald, D., Skarmeta, J., Serrano, L., and Vargas, R. (2005) Mineralogical and Isotopic Zonation in the Sur-Sur Tourmaline Breccia, Río Blanco-Los Bronces Cu-Mo Deposit, Chile: Implications for Ore Genesis. Economic Geology, 100, 935–961.

Frondel, C., Hurlbut, C.S.J., and Colette, R.C. (1947) Synthesis of Tourmaline. American Mineralogist, 32, 680–681.

Fuchs, Y., Lagache, M., and Linares, J. (1998) Fe-tourmaline synthesis under different T and fO2 conditions. American Mineralogist, 83, 525–534.

Fusswinkel, T., Wagner, T., and Sakellaris, G. (2016) Fluid evolution of the Neoarchean Pampalo orogenic gold deposit (E Finland): Constraints from LA-ICPMS fluid inclusion microanalysis. Chemical Geology, 450, 96–121.

Garofalo, P., Audétat, A., Günther, D., Heinrich, C.A., and Ridley, J. (2000) Estimation and testing of standard molar thermodynamic properties of tourmaline end-members using data of natural samples. American Mineralogist, 85, 78–88.

Gleeson, S.A., Wilkinson, J.J., Shaw, H.F., and Herrington, R.J. (2000) Post-magmatic hydrothermal circulation and the origin of base metal mineralisation, Cornwall, UK. Journal of the Geological Society, 157, 589–600.

Gunter, W.D., Myers, J., and Girsperger, S. (1987) Hydrogen: Metal Membranes. In Hydrothermal Experimental Techniques pp. 100–120. John Wiley & Sons, New-York.

Harlaux, M., Kouzmanov, K., Gialli, S., Laurent, O., Rielli, A., Dini, A., Chauvet, A., Menzies, A., Kalinaj, M., and Fontboté, L. (2020) Tourmaline as a Tracer of Late-Magmatic to Hydrothermal Fluid Evolution: The World-Class San Rafael Tin (-Copper) Deposit, Peru. Economic Geology.

Helgeson, H.C., Kirkham, D.H., and Flowers, G.C. (1981a) Theoretical prediction of the thermodynamic behaviour of aqueous electrolytes at high pressures and temperatures : IV Calculation of activity coefficients, osmotic coefficients, and apparent molal and standard and relative partial molal properties to 600°C and 5kb. American Journal of Science, 28, 1249–1516.

——— (1981b) Theoretical prediction of the thermodynamic behaviour of aqueous electrolytes at high pressures and temperatures : IV Calculation of activity coefficients, osmotic coefficients, and apparent molal and standard and relative partial molal properties to 600°C and 5kb. American Journal of Science, 28, 1249–1516.

Henry, D.J., and Dutrow, B.L. (1996) Chapter 10. Metamorphic Tourmaline and its Petrologic Applications. In E.S. Grew and L.M. Anovitz, Eds., Boron _ Mineralogy, Petrology and Geochemistry Vol. 33, pp. 503–558. De Gruyter, Berlin, Boston.

Henry, D.J., and Guidotti, C.V. (1985) Tourmaline as a petrogenetic indicator mineral: an example from the staurolite-grade metapelites of NW Maine. American Mineralogist, 70, 1–15.

Hong, W., Cooke, D.R., Zhang, L., Fox, N., and Thompson, J. (2017) Tourmaline-rich features in the Heemskirk and Pieman Heads granites from western Tasmania, Australia: Characteristics, origins, and implications for tin mineralisation. American Mineralogist, 102, 876–899.

Kelly, C.J., Davis, W.J., Potter, E.G., and Corriveau, L. (2020) Geochemistry of hydrothermal tourmaline from IOCG occurrences in the Great Bear magmatic zone: Implications for fluid source(s) and fluid composition evolution. Ore Geology Reviews, 118, 103329.

Kontak, D.J., and Clark, A.H. (2002) Genesis of the Giant, Bonanza San Rafael Lode Tin Deposit, Peru: Origin and Significance of Pervasive Alteration. Economic Geology, 97, 1741–1777.

Korges, M., Weis, P., Lüders, V., and Laurent, O. (2020) Sequential evolution of Sn–Zn–In mineralisation at the skarn-hosted Hämmerlein deposit, Erzgebirge, Germany, from fluid inclusions in ore and gangue minerals. Mineralium Deposita, 55, 937–952.

Kryukov, P.A., Perkovets, V.D., Starostina, L.I., and Smolyakov, B.S. (1966) Standardization of the pH values of Buffer Solutions at Temperatures of up to 150 C. Izv. Sib. Otd. Akad. Nauk SSSR, 29–34.

Lasaga, A.C. (1998) Kinetic Theory in the Earth Sciences, 811 p. Princeton university press, Princeton.

Lassin, A., Azaroual, M., and Mercury, L. (2005) Geochemistry of unsaturated soil systems: Aqueous speciation and solubility of minerals and gases in capillary solutions. Geochimica et Cosmochimica Acta, 69, 5187–5201.

Launay, G., Sizaret, S., Guillou-Frottier, L., Gloaguen, E., and Pinto, F. (2018) Deciphering fluid flow at the magmatic-hydrothermal transition: A case study from the world-class Panasqueira W–Sn–(Cu) ore deposit (Portugal). Earth and Planetary Science Letters, 499, 1–12.

Lecumberri-Sanchez, P., Vieira, R., Heinrich, C.A., Pinto, F., and Wälle, M. (2017) Fluid-rock interaction is decisive for the formation of tungsten deposits. Geology, 45, 579–582.

Legros, H., Lecumberri-Sanchez, P., Elongo, V., Laurent, O., Falck, H., Adlakha, E., and Chelle-Michou, C. (2020) Fluid evolution of the Cantung tungsten skarn, Northwest Territories, Canada: Differentiation and fluid-rock interaction. Ore Geology Reviews, 127, 103866.

Legros, H., Elongo, V., Laurent, O., Adlakha, E., Chelle-Michou, C., Falck, H., and Lecumberri-Sanchez, P. (2022) Formation of the Lened W-(Be) Skarn Deposit by Neutralization of a Magmatic Fluid—Evidence from H3BO3-Rich Fluids. Geosciences, 12, 236.

Li, X., Chi, G., Zhou, Y., Deng, T., and Zhang, J. (2017) Oxygen fugacity of Yanshanian granites in South China and implications for metallogeny. Ore Geology Reviews, 88, 690–701.

Lister, C.Z. (1981) Studies of the Mineralogy and Geochemistry of Progressive Tourmalinisation at selected-localities in southwest England. University of London, London.

London, D. (2011) Experimental synthesis and stability of tourmaline: a historical overview. The Canadian Mineralogist, 49, 117–136.

London, D., Hervig, R.L., and Morgan, G.B. (1988) Melt-vapour solubilities and elemental partitioning in peraluminous granite-pegmatite systems: experimental results with Macusani glass at 200 MPa. Contributions to Mineralogy and Petrology, 99, 360–373.

Lynch, G., and Ortega, J. (1997) Hydrothermal alteration and tourmaline-albite equilibria at the Coxheath porphyry Cu-Mo-Au deposit, Nova Scotia. The Canadian Mineralogist, 35, 79–94.

Macdonald, D.D., Wentrcek, P.R., and Scott, A.C. (1980) The Measurement of pH in Aqueous Systems at Elevated Temperatures Using Palladium Hydride Electrodes. Journal of The Electrochemical Society, 127, 1745–1751.

Mavromatis, V., Montouillout, V., Noireaux, J., Gaillardet, J., and Schott, J. (2015) Characterization of boron incorporation and speciation in calcite and aragonite from co-precipitation experiments under controlled pH, temperature and precipitation rate. Geochimica et Cosmochimica Acta, 150, 299–313.

Mesmer, R.E., Baes, C.F., and Sweeton, F.H. (1972) Acidity Measurements at Elevated Temperatures. VI. Boric Acid Equilibria. Inorganic Chemistry, 11, 537–543.

Morgan, G.B. (2016) A spreadsheet for calculating normative mole fractions of end-member species for Na-Ca-Li-Fe2+-Mg-Al tourmalines from electron microprobe data. American Mineralogist, 101, 111–119.

Morgan, G.B., and London, D. (1989) Experimental reactions of amphibolite with boron-bearing aqueous fluids at 200 MPa: implications for tourmaline stability and partial melting in mafic rocks. Contributions to Mineralogy and Petrology, 102, 281–297.

Nakano, T., and Nakamura, E. (2001) Boron isotope geochemistry of metasedimentary rocks and tourmalines in a subduction zone metamorphic suite. Physics of the Earth and Planetary Interiors, 127, 233–252.

Ogorodova, L.P., Melchakova, L.V., Kiseleva, I.A., and Peretyazhko, I.S. (2012) Thermodynamics of natural tourmalines—Dravite and schorl. Thermochimica Acta, 539, 1–6.

Orlando, A., Ruggieri, G., Chiarantini, L., Montegrossi, G., and Rimondi, V. (2017) Experimental Investigation of Biotite-Rich Schist Reacting with B-Bearing Fluids at Upper Crustal Conditions and Correlated Tourmaline Formation. Minerals, 7, 23.

Ota, T., Kobayashi, K., Katsura, T., and Nakamura, E. (2008) Tourmaline breakdown in a pelitic system: implications for boron cycling through subduction zones. Contributions to Mineralogy and Petrology, 155, 19–32.

Parkhurst, D.L., and Appelo, C.A.J. (2013) Description of input and examples for PHREEQC Version 3 _ A computer program for speciation, batch-reaction, one-dimensional transport and inverse geochemical calculations. U.S. Department of the Interior U.S. Geological Survey.

Pichavant, M. (1981) An experimental study of the effect of boron on a water saturated haplogranite at 1 Kbar vapour pressure: Geological applications. Contributions to Mineralogy and Petrology, 76, 430–439.

Pichavant, M., and Manning, D. (1984) Petrogenesis of tourmaline granites and topaz granites; the contribution of experimental data. Physics of the Earth and Planetary Interiors, 35, 31–50.

Pokrovski, G.S., Schott, J., and Sergeyev, A.S. (1995) Experimental determination of the stability constants of NaSO4− and NaB (OH)40 in hydrothermal solutions using a new high-temperature sodium-selective glass electrode — Implications for boron isotopic fractionation. Chemical Geology, 124, 253–265.

Pokrovski, G.S., Borisova, A.Y., and Bychkov, A.Y. (2013) Speciation and Transport of Metals and Metalloids in Geological Vapors. Reviews in Mineralogy and Geochemistry, 76, 165–218.

Pownceby, M.I., and O'Neill, H.St.C. (1994) Thermodynamic data from redox reactions at high temperatures. III. Activity-composition relations in Ni-Pd alloys from EMF measurements at 850-1250 K, and calibration of the NiO+Ni-Pd assemblage as a redox sensor. Contributions to Mineralogy and Petrology, 116, 327–339.

Prokof'ev, V.Y., Akinfiev, N.N., and Groznova, E.O. (2002) On the Boron Concentration and Forms of Its Occurrence in Hydrothermal Ore-Forming Fluids. Geology of Ore Deposits, 44, 386–397.

Scaillet, B., Pichavant, M., Roux, J., Humbert, G., and Lefèvre, A. (1992) Improvements of the Shaw membrane technique for measurement and control of fH2 at high temperatures and pressures. American Mineralogist, 77, 647–655.

Schatz, O.J., Dolejš, D., Stix, J., Williams-Jones, A.E., and Layne, G.D. (2004) Partitioning of boron among melt, brine and vapour in the system haplogranite–H2O–NaCl at 800 °C and 100 MPa. Chemical Geology, 210, 135–147.

Sciuba, M., Beaudoin, G., and Makvandi, S. (2021) Chemical composition of tourmaline in orogenic gold deposits. Mineralium Deposita, 56, 537–560.

Shock, E.L., Helgeson, H.C., and Sverjensky, D.A. (1989) Calculation of the thermodynamic and transport properties of aqueous species at high pressures and temperatures: Standard partial molal properties of inorganic neutral species. Geochimica et Cosmochimica Acta, 53, 2157–2183.

Slack, J.F., and Trumbull, R.B. (2011) Tourmaline as a Recorder of Ore-Forming Processes. Elements, 7, 321–326.

Smith, M., Banks, D.A., Yardley, B.W.D., and Boyce, A. (1996) Fluid inclusion and stable isotope constraints on the genesis of the Cligga Head Sn-W deposit, S.W. England. European Journal of Mineralogy, 8, 961–974.

Tanger, J.C., and Helgeson, H.C. (1988) Calculation of the thermodynamic and transport properties of aqueous species at high pressures and temperatures; revised equations of state for the standard partial molal properties of ions and electrolytes. American Journal of Science, 288, 19–98.

Taylor, J.R., Wall, V.J., and Pownceby, M.I. (1992) The calibration and application of accurate redox sensors. American Mineralogist, 77, 284–295.

Tuduri, J., Chauvet, A., Barbanson, L., Bourdier, J.-L., Labriki, M., Ennaciri, A., Badra, L., Dubois, M., Ennaciri-Leloix, C., Sizaret, S., and others (2018) The Jbel Saghro Au(–Ag, Cu) and Ag–Hg Metallogenetic Province: Product of a Long-Lived Ediacaran Tectono-Magmatic Evolution in the Moroccan Anti-Atlas. Minerals, 8, 592.

van Hinsberg, V.J., and Schumacher, J.C. (2007) Using estimated thermodynamic properties to model accessory phases: the case of tourmaline. Journal of Metamorphic Geology, 25, 769–779.

——— (2009) The geothermobarometric potential of tourmaline, based on experimental and natural data. American Mineralogist, 94, 761–770.

van Hinsberg, V.J., Henry, D.J., and Marschall, H.R. (2011a) Tourmaline: an ideal indicator of its host environment. The Canadian Mineralogist, 49, 1–16.

van Hinsberg, V.J., Henry, D.J., and Dutrow, B.L. (2011b) Tourmaline as a Petrologic Forensic Mineral: A Unique Recorder of Its Geologic Past. Elements, 7, 327–332.

van Hinsberg, V.J., Franz, G., and Wood, B.J. (2017) Determining subduction-zone fluid composition using a tourmaline mineral probe. Geochemical Perspectives Letters, 160–169.

von Goerne, G., Franz, G., and Robert, J.L. (1999) Upper thermal stability of tourmaline + quartz in the system MgO-Al2O3-SiO2-B2O3-H2O and Na2O-MgO-Al2O3-SiO2-B2O3-H2O-HCl in hydrothermal solutions and siliceous melts. The Canadian Mineralogist, 37, 1025–1039.

von Goerne, G., Franz, G., and Heinrich, W. (2001) Synthesis of tourmaline solid solutions in the system Na2O–MgO–Al2O3–SiO2–B2O3–H2O–HCl and the distribution of Na between tourmaline and fluid at 300 to 700 °C and 200 MPa. Contributions to Mineralogy and Petrology, 141, 160–173.

von Goerne, G., Franz, G., and van Hinsberg, V.J. (2011) Experimental determination of Na-Ca distribution between tourmaline and fluid in the system CaO-Na2O-MgO-Al2O3-SiO2-B2O3-H2O. The Canadian Mineralogist, 49, 137–152.

Wang, P., Kosinski, J.J., Lencka, M.M., Anderko, A., and Springer, R.D. (2013) Thermodynamic modelling of boric acid and selected metal borate systems. Pure and Applied Chemistry, 85, 2117–2144.

Weisbrod, A., Polak, C., and Roy, D. (1986) Experimental study of tourmaline solubility in the system Na-Mg-Al-Si-B-O-H. Applications to the boron content of natural hydrothermal fluids and tourmalinization processes. pp. 140–141. Presented at the Experimental Mineralogy and Geochemistry, Nancy - France.

Williamson, B.J., Spratt, J., Adams, J.T., Tindle, A.G., and Stanley, C.J. (2000) Geochemical Constraints from Zoned Hydrothermal Tourmalines on Fluid Evolution and Sn Mineralization: an Example from Fault Breccias at Roche, SW England. Journal of Petrology, 41, 1439–1453.

Williamson, B.J., Müller, A., and Shail, R.K. (2010) Source and partitioning of B and Sn in the Cornubian batholith of southwest England. Ore Geology Reviews, 38, 1–8.

Wofford, W.T., Gloyna, E.F., and Johnston, K.P. (1998) Boric Acid Equilibria in Near-Critical and Supercritical Water. Industrial & Engineering Chemistry Research, 37, 2045–2051.

Wolf, M.B., and London, D. (1997) Boron in granitic magmas: stability of tourmaline in equilibrium with biotite and cordierite. Contributions to Mineralogy and Petrology, 130, 12–30.

Zimmer, K., Zhang, Y., Lu, P., Chen, Y., Zhang, G., Dalkilic, M., and Zhu, C. (2016a) SUPCRTBL: A revised and extended thermodynamic dataset and software package of SUPCRT92. Computers & Geosciences, 90, 97–111.

——— (2016b) SUPCRTBL: A revised and extended thermodynamic dataset and software package of SUPCRT92. Computers & Geosciences, 90, 97–111.

Zimmermann, R., Knop, E., Heinrich, W., Pehlke, I., and Franz, G. (1996) Disequilibrium in cation exchange experiments between Na-K-Ca amphiboles and aqueous Na-K-Ca chloride solutions: effects of fractional crystallisation. European Journal of Mineralogy, 97–114.

Chapter III: Experimental investigation of the tourmaline-biotite equilibrium: implication for tourmalinisation in hydrothermal perigranitic environment.

Introduction

Chapter II has been focused on constraining the boron concentration required to reach the equilibrium between tourmaline, cordierite, albite, quartz and andalusite. This assemblage reproduces a simplified composition of a silicic and peraluminous environment where tourmaline has long been recognised as a ubiquitous accessory mineral (Benard et al. 1985; Dutrow et al. 1999; Mlynarczyk & Williams-Jones 2006; Lecumberri-Sanchez et al. 2017). Indeed, boron is known to behave as an incompatible element and igneous rocks that have undergone significant chemical fractionation are more likely susceptible to form tourmaline (Pichavant 1981; London et al. 1988; Schatz et al. 2004; Pokrovski et al. 2013). However, tourmaline is described in multiple tectonic settings (Slack and Trumbull 2011) and can be related to intermediate igneous rocks or moderately fractionated granitic rocks (Lynch and Ortega 1997; Tuduri 2005; LeFort et al. 2011; Beckett-Brown et al. 2023). Thus, the use of cordierite-based reaction to study tourmaline stability limits the application of the experimental results to such environments. Furthermore, tourmalinisation processes are often developed on mica-bearing assemblages, such as schist hosting Sn-W deposits (e.g. Pirajno and Jacob 1987; Mahjoubi et al. 2016; Launay et al. 2018) or biotite-rich vein cement in porphyry deposits (Frikken et al. 2005) but more rarely on cordierite-bearing rocks (Bosi et al. 2018; Harlaux et al. 2020).

Experiments on biotite-bearing assemblages have been realised in order to assess the mineralogical and chemical variations caused by tourmalinisation (Orlando et al. 2017; Cheng et al. 2019). Those studies use high $[B_2O_3]_{fluid}$ to ensure tourmaline formation, and as such, they can be only used to constrain $[B_2O_3]_{fluid\_EQ}$ as < 5.3 wt% at 500°C and between 0.35 and 5 wt% at 600°C. This chapter presents new experiments at 200 MPa from 400 to 600°C and under fO2-controlled conditions to refine the actual constraints on the boron content of the fluid at equilibrium with biotite and tourmaline. Based on the same experimental methods that in Chapter II, the results are interpreted with regards to their implications for the boron content of natural systems.

I- Materials and methodology

A) Tourmaline forming reactions and end-members

Equilibrium between quartz, albite, andalusite, biotite and tourmaline buffers the boron concentration of the hydrothermal fluid according to multiple reactions involving different end-members for biotite and tourmaline. The eight different reactions considered in this study are written in Table 3.1. The reaction R1 to R4, are written for the pure Fe components (at. Fe/(Fe+Mg) = 1) in biotite and tourmaline and R5 to R8 for the pure Mg components (at. Fe/(Fe+Mg) = 0). Reactions R2, R4, R6 and R8 consider an albite-free assemblage, forming alkali-deficient tourmaline, and R3, R4, R7 and R8 consider Al-rich biotite. All the mineralogical assemblages involved in those reactions are representative of common pelitic metamorphic rocks such as schists. These are typical country rock lithologies for the emplacement of granitic magmas and the development of B metasomatism and tourmalinisation

Reactions															
R1	2 $KFe_3AlSi_3O_{10}(OH)_2$ *biotite (annite)*	+	2 $NaAlSi_3O_8$ *albite*	+	6 $B(OH)_3$ *fluid*	+	5 Al_2SiO_5 *andalusite*	+	SiO_2 *quartz*	=	2 $NaFe_3Al_6Si_6O_{18}(BO_3)_3(OH)_4$ *tourmaline (schorl)*	+	2 $KAlSi_3O_8$ *K-feldspar*	+	7 H_2O *fluid*
R2	4 $KFe_3AlSi_3O_{10}(OH)_2$ *biotite (annite)*	+	21 Al_2SiO_5 *andalusite*	+	18 $B(OH)_3$ *fluid*	+	15 SiO_2 *quartz*			=	6 $[\ ](Fe_2Al)Al_6Si_6O_{18}(BO_3)_3(OH)_4$ *tourmaline (foitite)*	+	4 $KAlSi_3O_8$ *K-feldspar*	+	19 H_2O *fluid*
R3	3 $KFe_2Al_3Si_2O_{10}(OH)_2$ *biotite (siderophyllite)*	+	2 $NaAlSi_3O_8$ *albite*	+	6 $B(OH)_3$ *fluid*	+	2 Al_2SiO_5 *andalusite*	+	7 SiO_2 *quartz*	=	2 $NaFe_3Al_6Si_6O_{18}(BO_3)_3(OH)_4$ *tourmaline (schorl)*	+	3 $KAlSi_3O_8$ *K-feldspar*	+	8 H_2O *fluid*
R4	2 $KFe_2Al_3Si_2O_{10}(OH)_2$ *biotite (siderophyllite)*	+	5 Al_2SiO_5 *andalusite*	+	6 $B(OH)_3$ *fluid*	+	9 SiO_2 *quartz*			=	2 $[\ ](Fe_2Al)Al_6Si_6O_{18}(BO_3)_3(OH)_4$ *tourmaline (foitite)*	+	2 $KAlSi_3O_8$ *K-feldspar*	+	7 H_2O *fluid*
R5	2 $KMg_3AlSi_3O_{10}(OH)_2$ *biotite (phlogopite)*	+	2 $NaAlSi_3O_8$ *albite*	+	6 $B(OH)_3$ *fluid*	+	5 Al_2SiO_5 *andalusite*	+	SiO_2 *quartz*	=	2 $NaMg_3Al_6Si_6O_{18}(BO_3)_3(OH)_4$ *tourmaline (dravite)*	+	2 $KAlSi_3O_8$ *K-feldspar*	+	7 H_2O *fluid*
R6	4 $KMg_3AlSi_3O_{10}(OH)_2$ *biotite (phlogopite)*	+	21 Al_2SiO_5 *andalusite*	+	18 $B(OH)_3$ *fluid*	+	15 SiO_2 *quartz*			=	6 $[\ ](Mg_2Al)Al_6Si_6O_{18}(BO_3)_3(OH)_4$ *tourmaline (magnesiofoitite)*	+	4 $KAlSi_3O_8$ *K-feldspar*	+	19 H_2O *fluid*
R7	3 $KMg_2Al_3Si_2O_{10}(OH)_2$ *biotite (eastonite)*	+	2 $NaAlSi_3O_8$ *albite*	+	6 $B(OH)_3$ *fluid*	+	2 Al_2SiO_5 *andalusite*	+	7 SiO_2 *quartz*	=	2 $NaMg_3Al_6Si_6O_{18}(BO_3)_3(OH)_4$ *tourmaline (dravite)*	+	3 $KAlSi_3O_8$ *K-feldspar*	+	8 H_2O *fluid*
R8	2 $KMg_2Al_3Si_2O_{10}(OH)_2$ *biotite (eastonite)*	+	5 Al_2SiO_5 *andalusite*	+	6 $B(OH)_3$ *fluid*	+	9 SiO_2 *quartz*			=	2 $[\ ](Mg_2Al)Al_6Si_6O_{18}(BO_3)_3(OH)_4$ *tourmaline (magnesiofoitite)*	+	2 $KAlSi_3O_8$ *K-feldspar*	+	7 H_2O *fluid*

Table 3.1: List of the different equilibriums involved in the tourmaline-biotite experiments.

(Drivenes et al., 2015; Codeço et al. 2017). The four tourmaline end-members involved in the reactions (dravite, magnesiofoitite, schorl, and foitite) cover an important fraction of compositions of natural tourmalines in perigranitic environments. Not considered in the tourmaline-forming reaction, the tourmaline end-members hydroxy-uvite ($Ca\ Mg_3\ (MgAl_5)\ Si_6O_{18}\ (BO_3)_3\ (OH)_4$) and hydroxy-feruvite ($Ca\ Fe_3\ (MgAl_5)\ Si_6O_{18}\ (BO_3)_3\ (OH)_4$) (Henry et al. 2011) must be mentioned due to their relevance in the experiments.

B) Starting products

The forward experiments started from tourmaline-free mixtures of natural minerals, biotite, albite, quartz, and andalusite (biotite composition in Appendix A12, other minerals in A3). The biotite used (of unknown provenance) is zoned, with a core relatively magnesian (at. Fe/(Fe+Mg) = 0.43 ± 0.01) and rim composition slightly more enriched in Fe (at. Fe/(Fe+Mg) = 0.56 ± 0.01). Solid inclusions of rutile and zircon were observed along with slight chlorite alteration. The plagioclase, quartz, andalusite and natural tourmaline crystal used are the same as in Chapter II. The plagioclase of unknown provenance is albitic (An03Or04Ab93, at. Ca/Na+Ca = 0.03 ±0.015) and contains K-feldspar and quartz inclusions. Quartz and andalusite come respectively from the exploited quarries of Ploemeur and Glomel (France), and they contain apatite, ilmenite, and chlorite inclusions. Some forward experiments were seeded with 3 to 5 large (~1 mm) natural tourmaline crystals (collected from quartz veins in the Huelgoat granite, France) which served to test for tourmaline stability and for the observation of tourmaline overgrowth. These tourmalines are mainly Fe-rich and zoned (Appendix A4) and they contain quartz and zircon inclusions. A few reversal experiments were performed to check for equilibrium by using starting mineral mixtures containing tourmaline (the natural mineral) plus K-feldspar, albite, andalusite and quartz. The K-feldspar crystal of unknown provenance is mainly composed of orthoclase (An0.5Or78Ab21.5) (Appendix A12) and contains inclusion of albite, quartz and zircon. All minerals were crushed in an agate mortar and then sieved. Only the [40-80] µm granulometric fractions were retained, except for biotite, where the [40-120] fraction was retained, due to the difficulty to reduce its size. For the forward experiments, mixtures were prepared in 54.9/30.4/11.2/3.5 wt% proportions for biotite, albite, andalusite, and quartz. For the reversal experiments, the starting mixtures contained 62.7/17.3/13.5/5/1.5 wt% tourmaline, K-feldspar, albite, andalusite, and quartz. Amounts of albite, quartz and andalusite are relatively low (20 wt%) since they should crystallise as products together with biotite, according to the reactions (Table 3.1). In Chapter II, we fail to demonstrate the reversibility of the tourmaline-forming reactions due to the refractory behaviour of the natural crystal of tourmaline. Furthermore, this natural tourmaline was not formed at equilibrium with the assemblage cordierite + albite. Hence, in this study we seeded one of the reversal experiments at 600°C (B600-RevTurExp) with experimental products obtained in B600-8G. By using tourmaline formed by the reaction investigated, we expect to be able to observe etching texture attesting equilibrium in our experiments.

Mineral mixtures were reacted with an aqueous fluid phase of varying composition in the system H_2O-B_2O_3 obtained by dissolving boric acid ($B(OH)_3$) crystals in distilled water. Initial boron contents of the fluid ranged from 0 to 10 wt% $[B_2O_3]_{fluid}$. With the use of $B(OH)_3$, the fluid is slightly acidic (pH = 7 to 4.3 from simulations using PHREEQC (Parkhurst and Appelo 2013) with the Thermoddem database (V1.10, Blanc et al. 2012), at 25°C, 1 atm) and representative of conditions of tourmaline crystallisation (Morgan and London 1989).

C) Experimental and analytical procedure

The experimental and analytical procedure applied in this study are identical to what has been presented in Chapter II. The few variations are listed below:

- Due to the Fe loss problems caused by the use of Pt as capsule material, all experiments were performed using Au capsule, except for one duplicate charge at 400°C.
- Based on previous experimental study (Morgan & London 1989; von Goerne et al. 1999; Orlando et al. 2017; Cheng et al. 2019) experimental duration was fixed around 336 h at 600°C. At 500°C, the experiments lasted for approximately one month (694 h) and two months (1488 h) at 400°C (Table 3.2).
- All NiO-NiPd sensors were contained in Pt capsule because of its higher H_2 permeability compared to Au (Gunter et al. 1987).
- X-ray diffraction (XRD) characterisation of starting and experimental powders was carried out on a Bruker AXS D8 Advance diffractometer (BRGM, Orléans, France). The instrument uses a Bragg-Brentano geometry and is equipped with a Cu-Kα1 monochromator ($\lambda_{K\alpha 1Cu}$ = 1.54059Å) allowing the acquisition of the diffractogram between 4 and 84° with a resolution of 0.03°. Powders were reground in an agate mortar and placed in a silicon crystal sample holder with a 0.5 mm deep hole. The standard ICDD PDF 2004 database was used to identify mineral phases and to qualitatively estimate their relative proportions.

D) Choice of P-T-fO_2 conditions

Our experiments aim to simulate the conditions of boron metasomatism and tourmalinisation that occur within granitic bodies and in their country rock aureoles (Drivenes et al. 2015; Lecumberri-Sanchez et al. 2017; Cheng et al. 2019; Harlaux et al. 2020). Granitic rocks are generally emplaced in mid to shallow crustal conditions, i.e. in a range between 100 and 500 MPa (Kontak and Clark 2002; Drivenes et al. 2016; Launay et al. 2018; Korges et al. 2020; Legros et al. 2022). Hydrothermal systems developed in perigranitic contexts have temperatures generally in the 300 to 600°C range (Charoy 1979; Kontak and Clark 2002; Frikken et al. 2005; Codeço et al. 2017; Orlando et al. 2017; Legros et al. 2022). Therefore, in this study, experiments were performed at a constant pressure of 200 MPa and between 400 and 600°C. Redox conditions are rarely precisely defined and, moreover, highly variable between granitic rocks and series, in a range typically between the fayalite-magnetite-quartz (FMQ) and magnetite-hematite (MH) oxygen buffers (Frikken et al. 2005; Li et al. 2017). Another constraint on fO_2 conditions is the biotite stability. The phase diagram of annite-phlogopite solid solution as a function of its at. Fe/(Fe+Mg) ratio, T and fO_2 determined by Wones & Eugster (1965) is represented in Figure 3.1A. Considering that the Fe/(Fe+Mg) ratio of the starting material is nearly 0.5 (Fig. 3.1B), biotite stability under oxidising conditions is limited by the MH oxygen buffer and its upper thermal stability is around 800°C. Thus, the fO_2 in this study was set to moderately oxidising conditions in the average of the range between FMQ and MH oxygen buffer. Based on the fO_2 conditions measured in the Chapter II experiments, the use of an initial PH_2 of 0.2 MPa corresponds, at 600 and 500°C, to a fO_2 in the Nickel-Nickel Oxide (NNO) + 0.5 to NNO + 2.5 range.

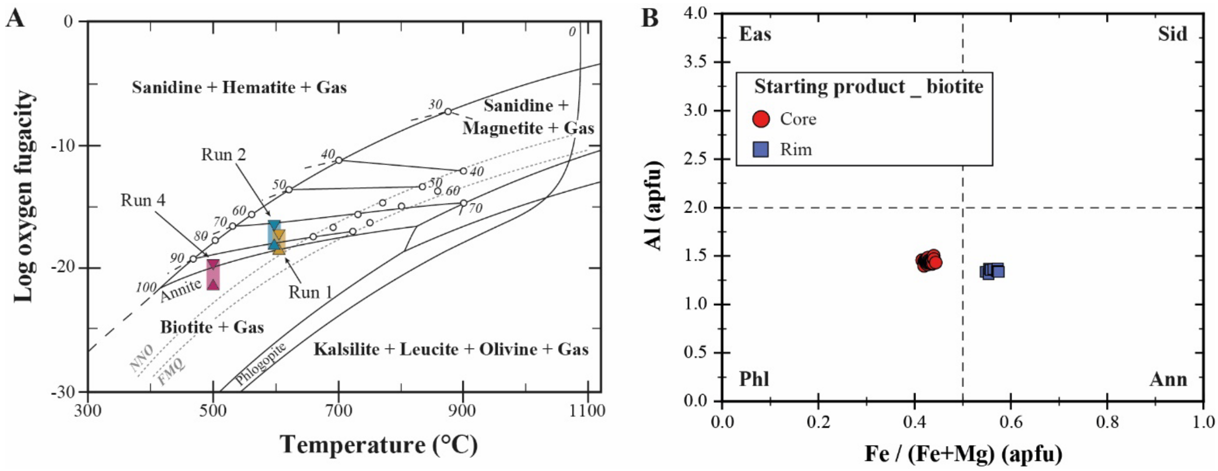

Figure 3.1: (A) Projection from the Fe/(Fe+Mg) axis of the biotite equilibria onto the log fO_2-T plane at 200 MPa total pressure, from Wones & Eugster (1965). The fO_2 intervals determined by the sensor in Run 1, 2 and 4 are represented. (B) Starting biotite composition.

II-Results

A) Redox conditions

The evolution of the alloy phase of the NiO-NiPd sensor of Run 1 (600°C, see Table 2) is illustrated in Fig. 2. The oxidised and reduced pellets bracket the fO_2 condition of this run between NNO + 1.01 and NNO + 1.51. For the same conditions, the sensor contained in Run 2 yielded a wider and higher fO_2 range (NNO +[1.36 ; 2.24]) than in Run 1, indicating less well equilibrated conditions despite the similar experimental duration. Run 3 sensors have yet to be analysed. In the 500°C experiment (Run 4), the sensor returned a fO_2 interval (NNO +[1.77; 2.64]) larger than Run 1. For the 400°C experiment (Run 5), the fO_2 was estimated to NNO +[0 ; 2] from the results of sensors in the other 600 and 500°C experiments performed with a 0.2 MPa initial PH_2. Details of the compositional data for the NiPd alloys are summarised in Appendix A13.

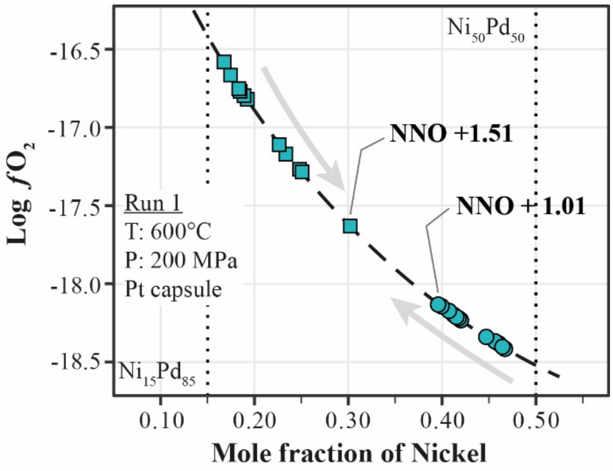

Figure 3.2: Evolution of the alloy phase of the NiO-NiPd sensor as a function of log fO_2 in Run 1 (Table 3.2). The dashed line gives the relation between the mole fraction of Ni in the alloy phase (X_{Ni}) and fO_2 at 600°C and 200 MPa using the calibration of Pownceby and O'Neill (1994). The initial X_{Ni} of the two pellets is represented by the dotted vertical lines and their final compositions by squares and circles on the dashed line. Directions of evolution of alloys in each pellet are indicated by arrows.

Charge	**Capsule**	**T (°C)**	fO_2	$[B_2O_3]_{fl}$ **wt%**	**Reaction products**[d]	**Texture group**
			Run 1 : 336 h			
B600-0[a]	Au	600	NNO + [1.01 ; 1.51]	0.0	Bt + Alb + And + Qtz	-
B600-1	Au	600	NNO + [1.01 ; 1.51]	1.0	Bt + Alb + And + Qtz	-
B600-2	Au	600	NNO + [1.01 ; 1.51]	2.0	Bt + Alb + And + Qtz	-
B600-3	Au	600	NNO + [1.01 ; 1.51]	3.2	Bt + Alb + And + Qtz * *Tur + FK + FeTi ox + qch*	IIa, IIb
B600-4	Au	600	NNO + [1.01 ; 1.51]	4.3	Bt + Alb + Qtz +And * *Tur + FK + FeTi ox + qch*	I
B600-8G[b]	Au	600	NNO + [1.01 ; 1.51]	8.2	Tur + FK + Bt + Alb + Ilm * *Qtz + qch*	I, III, IV
B600-Rev[c]	Au	600	NNO + [1.01 ; 1.51]	Reverse _ 0	Tur + FK + Alb + And + Qtz	No etching
			Run 2 : 336 h			
B600-10	Au	600	NNO + [1.36 ; 2.24]	10.1	Tur + FK + Bt + Alb + Ilm * *Qtz + qch*	I, III
			Run 3 :337 h			
B600-RevTurExp[c]	Au	600	*not analysed*	Reverse _ 0	Tur + FK + Alb + And + Qtz * *Bt*	Etching
			Run 4 : 694 h			
B500-0	Au	500	NNO + [1.77 ; 2.64]	0.0	Bt + Alb + And + Qtz	-
B500-1	Au	500	NNO + [1.77 ; 2.64]	1.1	Bt + Alb + And + Qtz	-
B500-2	Au	500	NNO + [1.77 ; 2.64]	2.1	Bt + Alb + And + Qtz * Tur + FK	I
B500-3	Au	500	NNO + [1.77 ; 2.64]	2.9	Bt + Alb + And + Qtz * *Tur + FK*	I
B500-4	Au	500	NNO + [1.77 ; 2.64]	3.9	Bt + Alb + Qtz + And * *Tur + FK*	I
B500-8G[b]	Au	500	NNO + [1.77 ; 2.64]	7.8	Tur + FK + Bt * *Qtz + Alb + FeTi ox*	I, III, IV
B500-Rev[c]	Au	500	NNO + [1.77 ; 2.64]	Reverse _ 0	Tur + FK + Alb + And + Qtz	No etching
			Run 5 : 1488 h			
B400-0	Au	400	~ NNO + [0 ; 2]	0.0	Bt + Chl + Ilt + Alb + Qtz + And	-
B400-0.5	Au	400	~ NNO + [0 ; 2]	0.6	Bt + Chl + Ilt + Alb + Qtz + And	-
B400-1	Au	400	~ NNO + [0 ; 2]	1.1	Bt + Chl + Ilt + Alb + Qtz	-
B400-2	Au	400	~ NNO + [0 ; 2]	1.9	Bt + Chl + Ilt + Alb + Qtz	-
B400-3	Au	400	~ NNO + [0 ; 2]	2.9	Bt + Chl + Ilt + Alb + Qtz	-
B400-4	Au	400	~ NNO + [0 ; 2]	3.9	Bt + Chl + Ilt + Alb + Qtz * *Tur*	I
B400-8G[b]	Au	400	~ NNO + [0 ; 2]	8.6	Bt + Chl + Ilt + Alb + Qtz * *Tur + FK*	I
B400-8Pt	Pt	400	~ NNO + [0 ; 2]	8.2	Bt + Chl + Ilt + Alb + Qtz * *Tur + FK*	I

(a) Forward experiment performed with a starting tourmaline-free mixture except when otherwise noted. (b) Forward experiment with tourmaline seeds added. (c) Reversal experiment performed with a tourmaline-bearing starting mixture (see text). (d) The asterisk separate the phases confirmed by XRD (left side, ordered by proportion) from the others, identified by SEM and EDS (right side, in italic). Mineral abbreviation: Alb = albite; And = andalusite; Bt = biotite; Chl = chlorite; FeTi ox = Fe Ti oxydes; FK = potassium feldspar; Ilm = ilmenite; Ilt = illite; Qtz = quartz; Tur = tourmaline. qch = quench phases.

Table 3.2: Experimental conditions and results

B) Experimental products and textures

Upon opening the capsules, all experimental products comprised a solid powder and a free fluid. The more boron in the charge, the more agglomerated is the solid powder. In the most boron-rich charges at 500°C, part of the solid products was found to float, forming a thin film at the surface of the fluid phase. Biotite albite, andalusite, quartz, K-feldspar and tourmaline are the major mineral phases, systematically appearing in the XRD spectra of experimental products at 600 and 500°C and also identified from SEM imaging (Table 3.2). Fe-Ti oxides, generally < 10µm in size, occur in experimental products. SEM imaging and EDS analyses show that they are made up of a small anhedral Ti-rich core (interpreted as ilmenite coming from starting materials, see above) surrounded by a euhedral Fe-rich rim corresponding to recrystallisation due to experimental fO_2. Those oxides have been characterised by XRD in the charge B600-8G and B600-10 as ilmenite. In some charges, apatite presenting strong dissolution patterns on their surface has been observed. Interpreted as being inherited from the starting mineral inclusions, they have not been reported in Table 3.2. A first-order difference in phase assemblage appears upon decreasing temperature from 500°C to 400°C. In Run 5 (Table 3.2), biotite and andalusite are destabilised and sheeted minerals grow over the starting minerals (Fig. 3.3A; B). Interpretation of the XRD diffractogram reveals the presence of chlorite (clinochlore) and illite 1M in all the charges from Run 5.

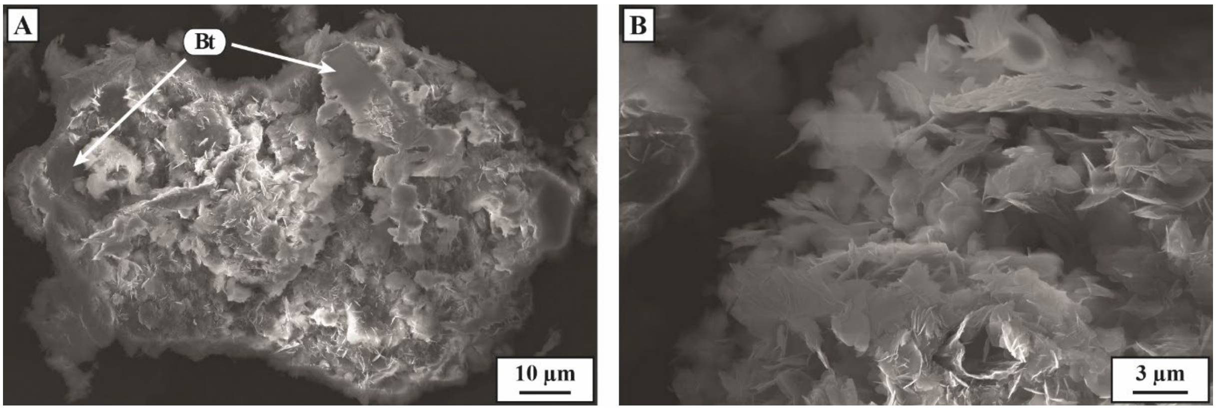

Figure 3.3: SEM (InLens) image of the charge B400-0. The biotite is destabilised, forming sheeted minerals belonging to the chlorite and illite1M group. (A) Xenomorphic biotite. (B) Zoom on the destabilisation products.

Experimental assemblages split into two types: tourmaline-free and tourmaline-bearing. Charges, where tourmaline is absent (Fig. 3.4A), are characterised by a general reduction of grain sizes and the development of dissolution textures on quartz, andalusite and albite. Small crystals of biotite tend to aggregate around other starting mineral when the fluid contains boron. In tourmaline-bearing charges, the four tourmaline texture groups defined in Chapter II (sheaves (group I), large crystals (group II), clusters (group III) and overgrowth (group IV)) are observed, except for IIIb (Table 3.3).

The first textural group to be observed is the Group IIa where tourmalines form large (10 to 40 µm wide at 600°C) elongated tourmaline crystals (Fig. 3.4B). At their extremities, those crystals can divide into a tight sheaf (about 4-5 µm large). This textural group is associated with small single euhedral rods up to 10 µm long referred to as Group IIb. They are either found among the other minerals or inside the cleavage plane of the biotite (Fig. 3.4C). Group I

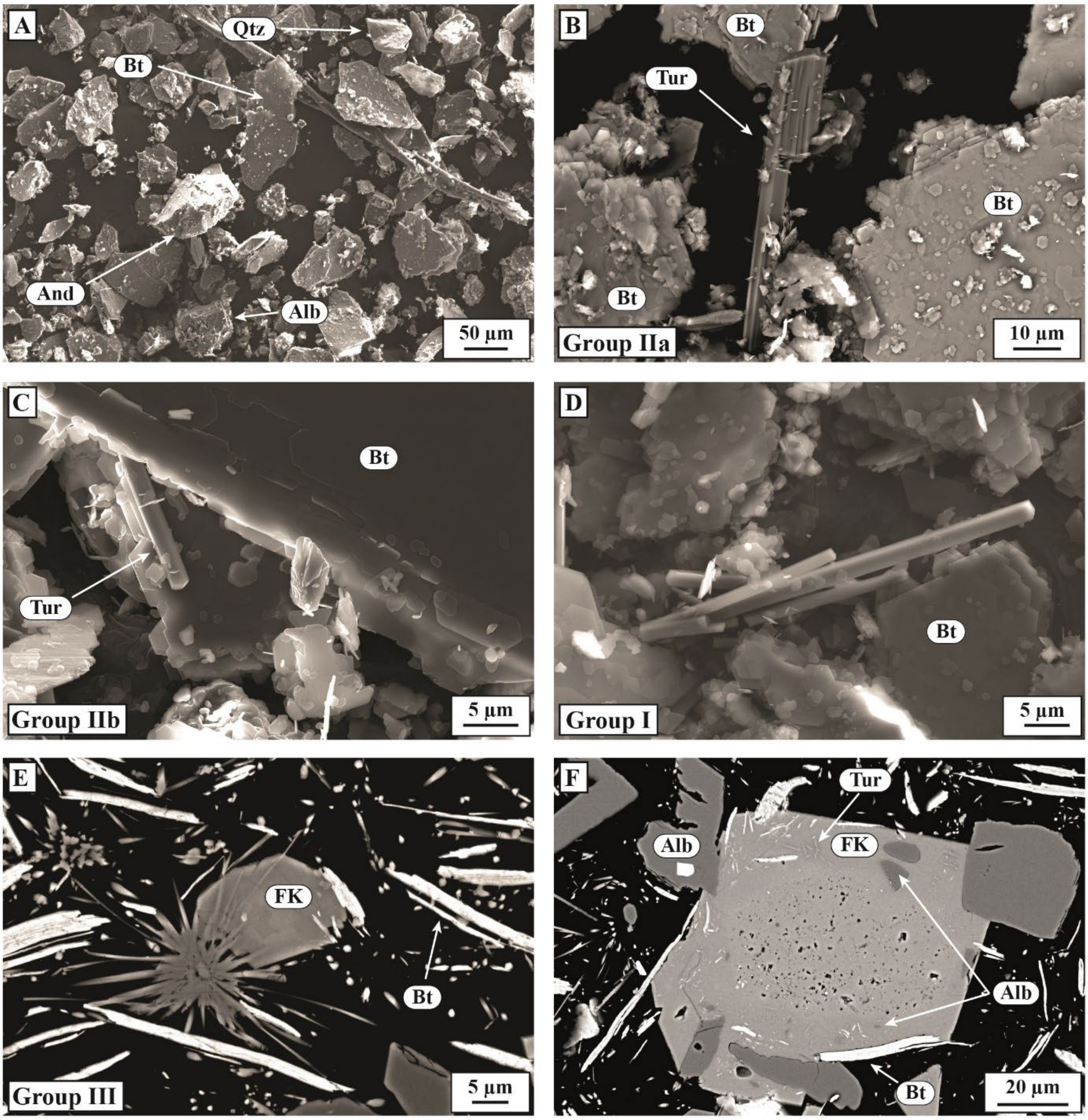

Figure 3.4: SEM (InLens and BSE) images of the experimental products. See Table 3.2 for the experimental conditions. (A) B600-0, all starting products are present and show limited dissolution. (B) B600-3, Group IIa tourmaline. (C) B600-3, Group IIb tourmaline growing inside the biotite cleavage planes. (D) B600-4, Group I tourmaline sheaf. (E) B600-8G, Group III tourmaline in intergrowth with K-feldspar. (F) B600-G, neoformed K-feldspar with a porous core containing relics of albite and euhedral rims with solid inclusions of biotite, albite, quartz and tourmaline. Abbreviations: Alb = albite; And = andalusite; Bt = biotite; FK = K-feldspar; Qtz = quartz; Tur = tourmaline.

tourmalines occur as sheaves made of rods up to 40 µm long and generally around 1µm large (Fig. 3.4D). These textures are characteristic of charges where tourmaline is the most (or one of the most) abundant phase. No mineral is specifically associated at the base of the sheaves, however small biotite crystals are generally present on the rods. Unidentified sub-micrometric materials, appearing as rings on tourmaline sheaves, are also present in some charges and interpreted as quench phases (Appendix A14). Among the phases spatially associated with tourmaline, quartz grains and andalusite have dissolution textures developed on their surface, whereas neo-formed K-feldspar precipitates as euhedral crystal or as euhedral overgrowth on starting grains of albite.

Group	Description	Figure
I	Sheaves composed of multiple thin rods up to 40 µm long.	4D; 8C
IIa	Large elongated crystal forming a tight sheaf on one end.	4B
IIb	Small single euhedral rod up to 10 µm long.	4C
III	Radiating clusters of fibrous crystals.	4E; 8A; 8B
IV	Experimental overgrowth on natural tourmaline seed.	5

Table 3.3: Experimental tourmaline texture.

Group III tourmalines refer to radiating clusters of fibrous tourmaline crystals (Fig. 3.4E), named fibro-radiated aggregates below. They are only present in charges where tourmaline is the most (or one of the most) abundant phase and occur either as associated with or separated from the solid powder in the charge (only in B500-8G). Contrary to the cordierite-tourmaline experiment, there is no textural differences caused by these associations / separations with the solid powder. All tourmalines correspond to the previously described Group IIIa. K-feldspar is euhedral, often intergrown with tourmaline (Fig. 3.4E) and contain solid inclusion of biotite and albite. Large K-feldspar crystal (up to 100 µm large) generally present a highly porous core where albite relics can be found (Fig. 3.4F). The rims are more consolidated and contain multiple solid inclusion of albite, biotite and quartz. Quartz and andalusite are rarely found in the products presenting those textures. Group IV tourmalines are restricted to the seeded charges where a thin layer of experimentally formed tourmalines grows around the natural tourmaline crystals. This tourmaline overgrowth develops on specific crystallographic faces, allowing the growth to be parallel to the long axis of the seed. It forms a hairy texture, with thin fibers growing parallel and in the same direction as the long axis (Fig. 3.5A).

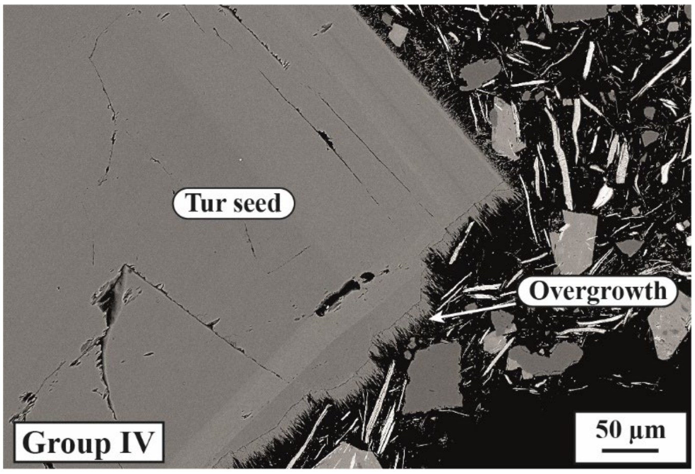

Figure 3.5: SEM image of Group IV tourmaline overgrowth forming a hairy texture parallel to the long axis of the seed. On other faces of the seed, tourmaline overgrowth has a different texture, less developed.

C) Evolution of phases assemblages and tourmaline textures

Experimental mineral assemblages and textures of tourmaline (when present) are detailed in Table 3.2. No difference is observed between identical charges ran in Au and Pt capsules. The effects of the initial $[B_2O_3]_{fluid}$, temperature and fO_2 are detailed in the following sections.

1/ Effect of B_2O_3

At 600°C in Run 1 (Table 3.2), tourmaline is absent (undetected by SEM) at low $[B_2O_3]_{fluid}$ concentrations (0, 1, and 2 wt%) and the starting assemblage biotite + albite + andalusite + quartz remains stable (Fig. 3.4A). Upon increasing $[B_2O_3]_{fluid}$, reactant phases progressively reduce in size and dissolution textures appear more marked. Tourmaline was observed in B600-3, at 3.2 wt% $[B_2O_3]_{fluid}$ (Table 3.2), allowing us to bracket the tourmaline formation for a boron content in the fluid ranging between 2 and 3.2 wt% $[B_2O_3]_{fluid}$. Tourmaline first appears as Group II, with some large elongated crystals (Group IIa; Fig. 3.4B) and little single rods located in the biotite cleavage planes (Group IIb; Fig. 3.4C). Euhedral K-feldspar is found, growing around quartz and albite staring grains. For higher $[B_2O_3]_{fluid}$ concentrations, Group II crystals are replaced by the Group I sheaves, generally composed of 4 to 6 euhedral rods of approximately 1 µm large (Fig. 3.4D). The proportion and size of the euhedral overgrowth of K-feldspar increases and quartz, andalusite and albite present important dissolution pits on their surface. At $[B_2O_3]_{fluid} \geq 8.2$ wt%, the assemblage Group III tourmaline + K-feldspar becomes the major phases in experimental products. Biotite and albite are still commonly present, despite being altered, and quartz is rarely observed, sometimes preserved in K-feldspar. Fe-Ti oxides are more frequent and form euhedral crystals up to 50 µm long. The rods composing the Group III tourmaline are more numerous and thinner (< 1 µm; Fig. 3.4E) than in the coexisting Group I tourmaline. K-feldspar crystals either contain an albitic core or a highly porous core, surrounded by a large rim with numerous solid inclusions (albite, biotite, quartz, tourmaline and Fe-Ti oxide; Fig. 3.4F).

Three reversal experiments were performed at 600°C and 500°C (charges B600-Rev, Run 2, B600-RevTurExp, Run 3 and B500-Rev, Run 3, Table 3.2) to test tourmaline destabilisation and the formation of biotite, albite and andalusite for fluids with boron

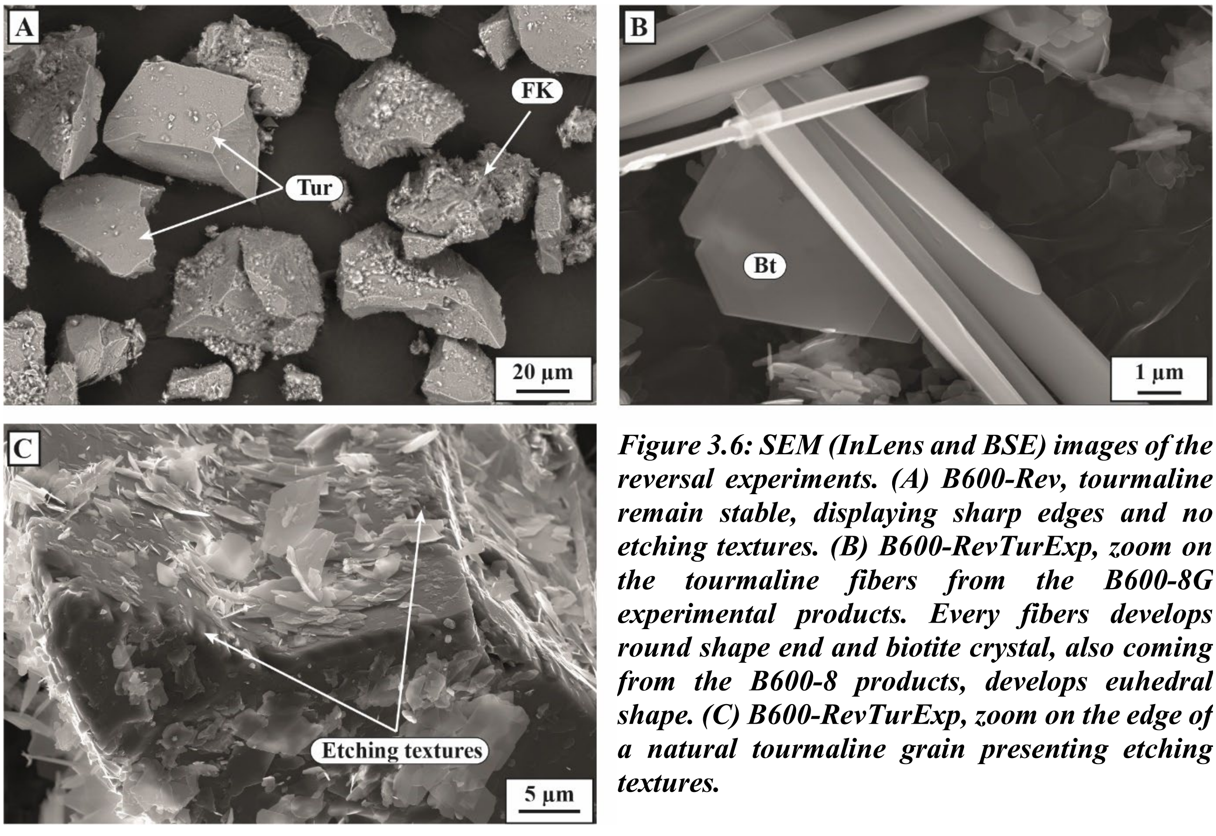

Figure 3.6: SEM (InLens and BSE) images of the reversal experiments. (A) B600-Rev, tourmaline remain stable, displaying sharp edges and no etching textures. (B) B600-RevTurExp, zoom on the tourmaline fibers from the B600-8G experimental products. Every fibers develops round shape end and biotite crystal, also coming from the B600-8 products, develops euhedral shape. (C) B600-RevTurExp, zoom on the edge of a natural tourmaline grain presenting etching textures.

concentrations lower than required for tourmaline to appear (here $[B_2O_3]_{fluid}$ = 0 wt%), according to the forward experiments. B600-Rev and B500-Rev yielded phase assemblages unchanged compared to the starting mixture and the presence of etching textures on the natural tourmaline edges and surfaces was not recognised. Only sharp edges and fractures, probably formed during crushing, were found (Fig. 3.6A). Yet, K-feldspar, albite, andalusite and quartz showed dissolution textures on their surfaces. In B600-RevTurExp, because of the addition of B600-8G experimental products in the starting assemblage, the sole presence of biotite cannot be used to determine whether the charge has reached equilibrium or not (Table 2). However, close inspection of the experimental tourmaline shows that all fibers have round-shaped extremities, not observed in B600-8G (Fig. 3.6B). Biotite, introduced by the addition of the experimental product, show euhedral edges when located near those fibers, despite originally (in B600-8G) presenting altered textures. In addition, close inspection of the natural tourmaline edges and surfaces allowed the identification of etching textures and dissolution pits (Fig. 3.6C). Thus, B600-RevTurExp demonstrates the reversibility of tourmaline formation according to the reactions R1 to R8.

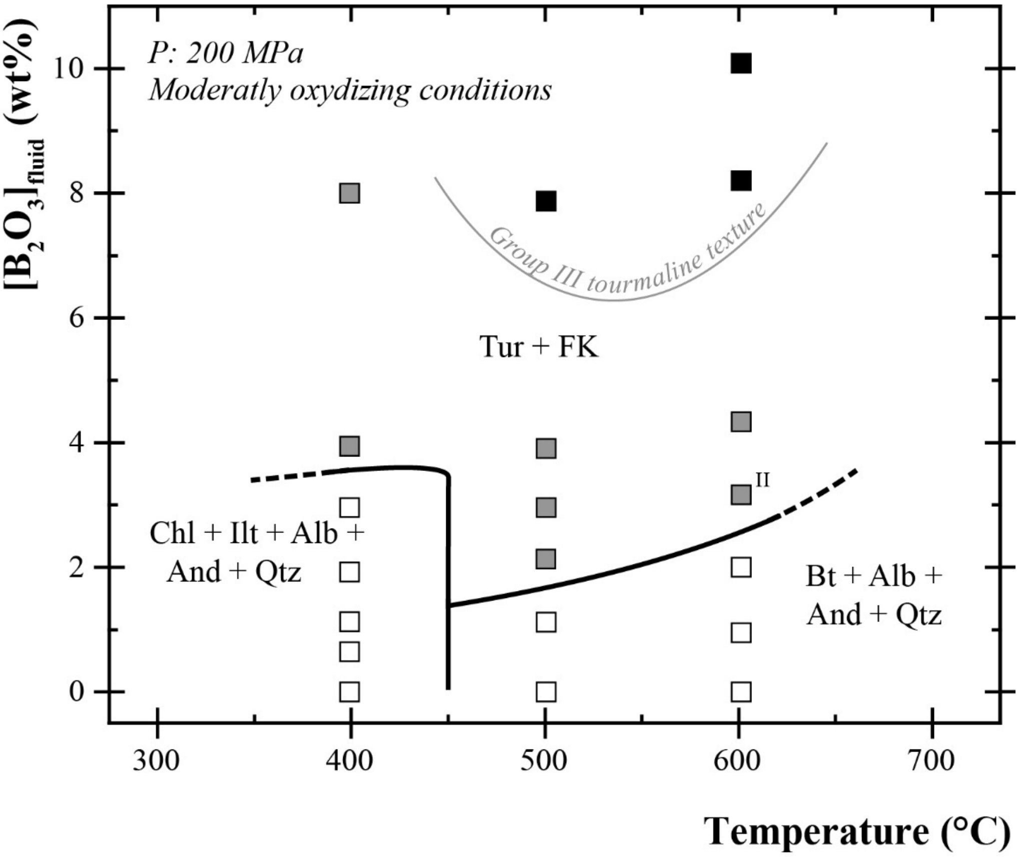

Figure 3.7: Evolution of phase assemblages and tourmaline textures in the experiments (Table 3.2), represented in a $[B_2O_3]_{fluid}$ vs. Temperature diagram. Solid and open symbols denote respectively the presence and absence of tourmaline in experimental products. Group I tourmaline is present in all tourmaline-bearing charges. Black and grey-filled symbols indicate respectively the presence and absence of Group III tourmaline. The presence of Group II tourmaline is indicated by superscripts above the corresponding symbol. Thick lines represent stability limits and thin lines delimits conditions of appearance of Group III tourmalines. Abbreviations: Alb = albite; And = andalusite; Bt = biotite; Chl = chlorite; FK = K-feldspar; Ilt = illite; Qtz = quartz; Tur = tourmaline.

2/ Effect of temperature

In the 500°C experiments, the same evolution of phase assemblages than at 600°C is observed. Experimental charges evolve from tourmaline-free to tourmaline-bearing assemblages when the boron fluid concentration is increased. However, decreasing temperature leads to a reduction of the $[B_2O_3]_{fluid}$ required for tourmaline to appear. The transition from tourmaline-free to tourmaline-bearing assemblages occurs between 1.1 and 2.1 wt% $[B_2O_3]_{fluid}$ (Fig. 3.7). As at 600°C, tourmaline and K-feldspar become the two major phases at 500°C in the charge with the highest $[B_2O_3]_{fluid}$ (7.8 wt%, B500-8G, Run 4, Table 3.2). The large Group IIa tourmaline crystals and the associated single rod only occur in the 600°C charge B600-3. At 500°C, tourmaline start to appear as Group I and evolves with increasing $[B_2O_3]_{fluid}$ toward Group III, similarly to what has been observed at 600°C and a limit for the appearance of tourmaline fibro-radiated aggregates (III) can be drawn (Fig. 3.7). At lower temperature, tourmaline fibers become more numerous, thinner and longer. In B500-8G, Group III tourmaline appears either among the grains, or in the cleavage planes of the biotite (Fig. 3.8A) or separated from the solid powder. This is the only occurrence in the tourmaline-biotite experiments, and tourmaline forms large fibro-radiated aggregates up to 100 µm long and interwove together (Fig. 3.8B). At 400°C, the biotite destabilisation seems to hinder the tourmaline-forming reaction. Tourmaline appears between 2.9 and 3.9 wt% $[B_2O_3]_{fluid}$ and only as Group I. Only three sheaves of less than 2 µm long were observed in B400-4, and in B400-8G and B400-8Pt, tourmaline sheaves occurrence remains scarce (Fig. 3.8C). Albite and quartz are heavily altered and K-feldspar is only visible as an overgrowth on a few albite crystals.

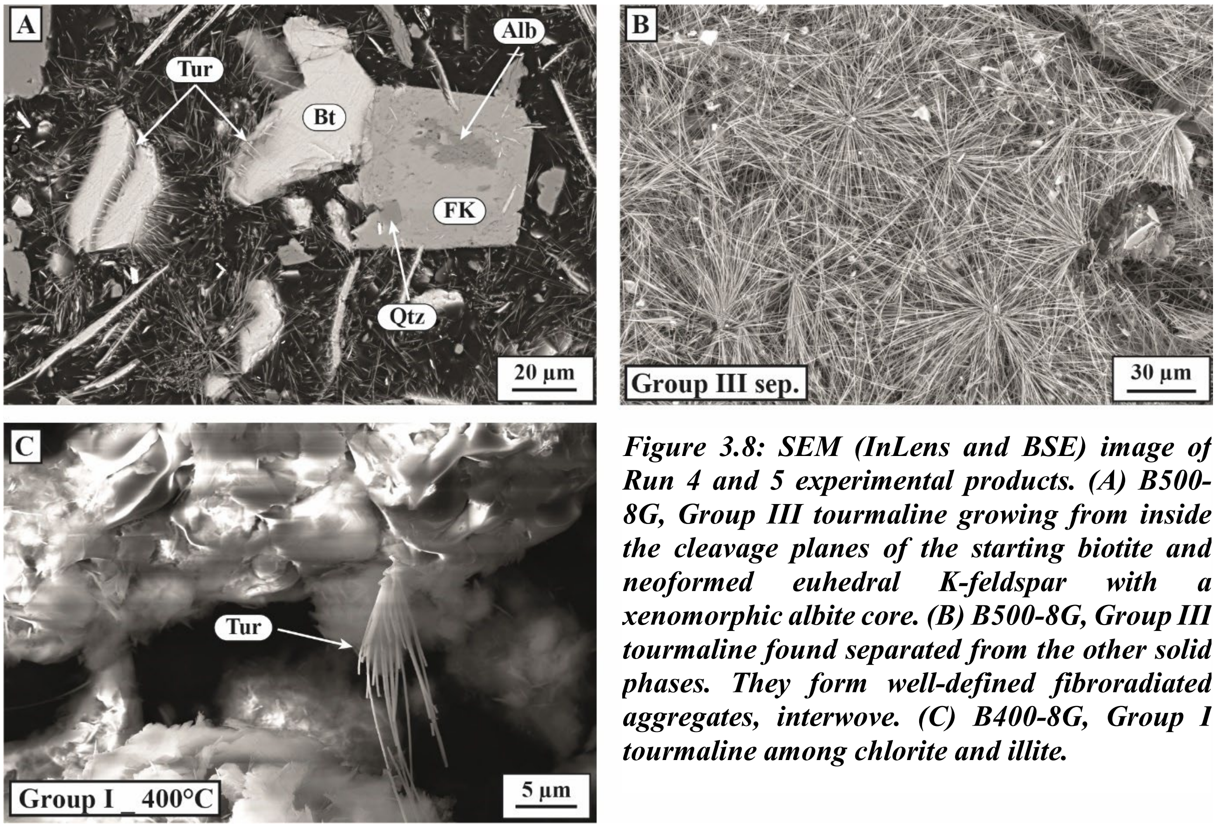

Figure 3.8: SEM (InLens and BSE) image of Run 4 and 5 experimental products. (A) B500-8G, Group III tourmaline growing from inside the cleavage planes of the starting biotite and neoformed euhedral K-feldspar with a xenomorphic albite core. (B) B500-8G, Group III tourmaline found separated from the other solid phases. They form well-defined fibroradiated aggregates, interwove. (C) B400-8G, Group 1 tourmaline among chlorite and illite.

D) Tourmaline composition

Analyses of Group IIa, III and IV tourmalines, which form relatively coarse aggregates, yielded satisfactory chemical analysis. Only one Group IIa tourmaline was found in our polished section. As it showed chemical distinction between its core and rim, we try, in other charges, to perform targeted analysis of the base (core) or the end (rim) of the sheafs. Because of textural constraints imposed by the crystal for obtaining a satisfactory analysis, it was not possible to always choose the zone to be probed. Table 3.4 shows the representative compositions of tourmaline crystallised in experimental charges. The “All” column contains all the analysis performed on a specific textural group of a same charge, core and rim include. All experimental tourmaline analyses are detailed in Appendix 15.

1/ Effect of the textures

For B600-8G and B500-8G, compositional data are available for tourmaline textural groups III and IV (Table 3.4) and the influence of these textures on the tourmaline composition is illustrated in Figure 3.9. At 600°C, tourmaline compositions from Groups III and IV overlap, with a slight enrichment in Ca for Group III (Fig. 3.9A). At 500°C, Group III was divided between the fibro-radiated aggregate found among the solid products and the ones found floating in the fluid when the capsule was opened. All Group III tourmaline share the same composition with a strong variation over their Al content. Group IV are enriched in Al compared to Group III, but present a similar at. Ca/(Ca+Na) ratio (Fig. 3.9B).

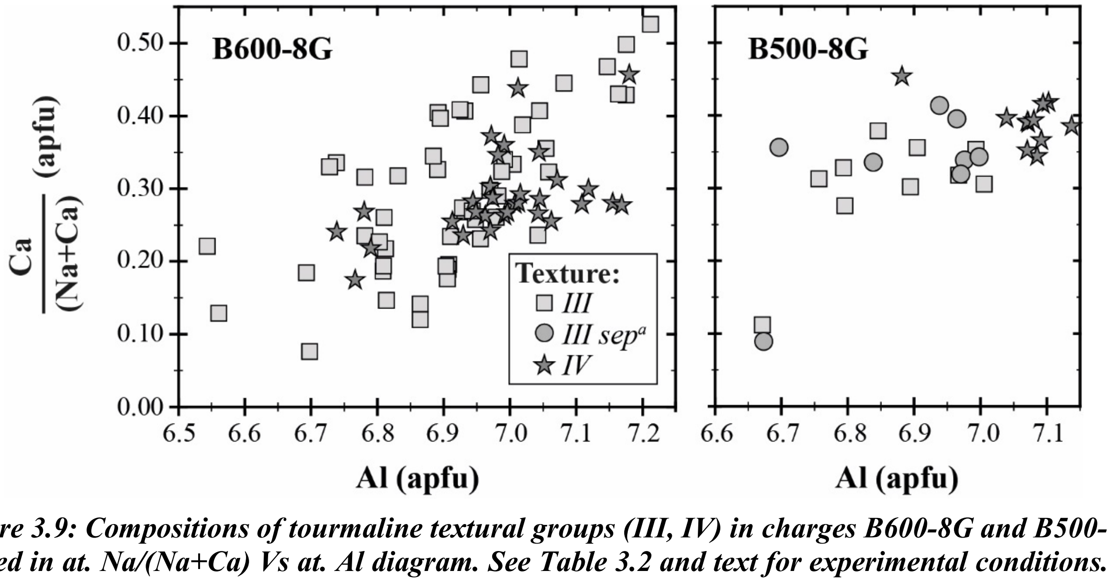

Figure 3.9: Compositions of tourmaline textural groups (III, IV) in charges B600-8G and B500-8G, plotted in at. Na/(Na+Ca) Vs at. Al diagram. See Table 3.2 and text for experimental conditions. (a) Group III found separated from the solid phases (see Fig. 3.8B).

2/ Effect of B_2O_3

All experimental tourmalines are solid solution between schorl and dravite with significant amounts of alkali-deficient (foitite, magnesiofoitite) and calcic (feruvite, uvite) tourmaline (Fig. 3.10A-F). Most composition has an at. Fe/(Fe+Mg) similar to the starting biotite (vertical grey bands in Fig. 3.10A;B;D;E). All tourmalines have an at. Ca/(Ca+Na) higher

Charge	B600-3		B600-8G				B600-10			B500-8G^a		
Textural group	*III*		*III*			*IV*	*III*			*III*		*IV*
Description	Core	Rim	All	Core	Rim		All	Core	Rim	Associated	Isolated	
n	10	18	52	15	17	31	38	11	13	10	8	11
SiO_2	36.28 (0.24)	35.55 (0.34)	33.99 (1)	33.36 (0.89)	34.75 (0.67)	33.69 (1.2)	34.71 (0.98)	33.87 (0.84)	35.29 (0.8)	35.07 (0.73)	35.25 (0.67)	35.40 (0.43)
TiO_2	0.82 (0.28)	0.61 (0.06)	0.69 (0.12)	0.70 (0.16)	0.69 (0.12)	0.63 (0.06)	0.70 (0.08)	0.66 (0.06)	0.68 (0.09)	0.40 (0.12)	0.38 (0.13)	0.28 (0.02)
Al_2O_3	33.88 (0.5)	35.68 (0.71)	35.48 (0.94)	35.95 (0.75)	35.13 (0.92)	35.69 (0.64)	35.28 (0.88)	35.93 (0.57)	34.59 (0.68)	35.37 (0.69)	35.93 (0.73)	37.39 (0.62)
FeO	8.61 (0.74)	7.59 (0.54)	8.26 (0.57)	8.58 (0.34)	7.98 (0.51)	8.18 (0.38)	8.03 (0.6)	8.39 (0.46)	7.74 (0.67)	7.97 (0.65)	8.39 (0.91)	8.11 (0.36)
MgO	4.86 (0.34)	4.84 (0.28)	4.41 (0.15)	4.38 (0.14)	4.47 (0.14)	4.29 (0.23)	4.51 (0.36)	4.50 (0.15)	4.66 (0.5)	4.15 (0.19)	4.25 (0.27)	3.95 (0.09)
MnO	0.18 (0.02)	0.22 (0.04)	0.17 (0.02)	0.21	0.16 (0.02)	0.18 (0.03)	0.19 (0.04)	0.20 (0.04)	0.15	0.18	0.15	0.17
CaO	0.33 (0.06)	0.90 (0.14)	1.20 (0.44)	1.53 (0.27)	0.85 (0.29)	1.16 (0.23)	1.14 (0.37)	1.50 (0.3)	0.83 (0.24)	1.14 (0.29)	1.27 (0.41)	1.46 (0.12)
Na_2O	1.84 (0.08)	1.69 (0.12)	1.55 (0.23)	1.41 (0.17)	1.72 (0.17)	1.56 (0.14)	1.59 (0.19)	1.45 (0.17)	1.71 (0.15)	1.43 (0.15)	1.44 (0.15)	1.25 (0.08)
K_2O	0.06 (0.01)	0.06 (0.01)	0.09 (0.05)	0.07 (0.02)	0.10 (0.06)	0.07 (0.02)	0.10 (0.03)	0.09 (0.03)	0.10 (0.03)	0.14 (0.11)	0.05 (0.01)	0.07 (0.02)
B_2O_3^{b}	10.66	10.74	10.51	10.51	10.55	10.46	10.58	10.58	10.56	10.56	10.69	10.84
H_2O^{c}	3.68	3.70	3.62	3.62	3.64	3.61	3.65	3.65	3.64	3.64	3.69	3.74
Total	101.20	101.58	99.97	100.32	100.04	99.52	100.48	100.82	99.95	100.05	101.49	102.66
Site T												
Si	5.91 (0.04)	5.75 (0.06)	5.62 (0.13)	5.52 (0.08)	5.73 (0.09)	5.60 (0.1)	5.70 (0.14)	5.56 (0.09)	5.81 (0.09)	5.77 (0.08)	5.73 (0.09)	5.68 (0.03)
Al	0.09 (0.04)	0.25 (0.06)	0.38 (0.13)	0.48 (0.08)	0.27 (0.09)	0.40 (0.1)	0.30 (0.14)	0.44 (0.09)	0.19 (0.09)	0.23 (0.08)	0.27 (0.09)	0.32 (0.03)
Site Z												
Al	6.00	6.00	6.00	6.00	6.00	6.00	6.00	6.00	6.00	6.00	6.00	6.00
Site Y												
Al	0.42 (0.07)	0.56 (0.08)	0.54 (0.07)	0.53 (0.06)	0.55 (0.05)	0.59 (0.05)	0.53 (0.07)	0.52 (0.06)	0.52 (0.05)	0.64 (0.06)	0.61 (0.05)	0.74 (0.05)
Ti	0.10 (0.03)	0.07 (0.01)	0.09 (0.01)	0.09 (0.02)	0.09 (0.01)	0.08 (0.01)	0.09 (0.01)	0.08 (0.01)	0.08 (0.01)	0.05 (0.01)	0.05 (0.02)	0.03 (0)
Fe	1.17 (0.1)	1.03 (0.08)	1.14 (0.08)	1.19 (0.06)	1.10 (0.06)	1.14 (0.06)	1.10 (0.09)	1.15 (0.07)	1.07 (0.1)	1.10 (0.08)	1.14 (0.12)	1.09 (0.05)
Mg	1.18 (0.08)	1.17 (0.06)	1.09 (0.03)	1.08 (0.03)	1.10 (0.03)	1.06 (0.05)	1.10 (0.09)	1.10 (0.04)	1.14 (0.12)	1.02 (0.04)	1.03 (0.07)	0.94 (0.03)
Mn	0.01 (0.01)	0.01 (0.01)	0.01 (0.01)	0.00 (0.01)	0.01 (0.01)	0.00 (0.01)	0.01 (0.01)	0.01 (0.01)	0.00 (0.01)	0.00 (0.01)	0.00 (0.01)	0.00 (0.01)
Site X												
Ca	0.06 (0.01)	0.16 (0.03)	0.21 (0.08)	0.27 (0.05)	0.15 (0.05)	0.21 (0.04)	0.20 (0.06)	0.26 (0.05)	0.15 (0.04)	0.20 (0.05)	0.22 (0.07)	0.25 (0.02)
Na	0.58 (0.03)	0.53 (0.04)	0.50 (0.07)	0.45 (0.05)	0.55 (0.06)	0.50 (0.04)	0.51 (0.06)	0.46 (0.05)	0.55 (0.05)	0.46 (0.05)	0.45 (0.05)	0.39 (0.02)
K	0.01 (0.01)	0.01 (0)	0.02 (0.01)	0.02 (0)	0.02 (0.01)	0.01 (0.01)	0.02 (0.01)	0.02 (0.01)	0.02 (0.01)	0.03 (0.02)	0.01 (0.01)	0.01 (0.01)
[]$_X$	0.36 (0.03)	0.30 (0.04)	0.27 (0.03)	0.26 (0.02)	0.28 (0.03)	0.28 (0.02)	0.27 (0.05)	0.26 (0.03)	0.28 (0.05)	0.31 (0.03)	0.32 (0.04)	0.35 (0.02)
B	3.00	3.00	3.00	3.00	3.00	3.00	3.00	3.00	3.00	3.00	3.00	3.00
OH-	4.00	4.00	4.00	4.00	4.00	4.00	4.00	4.00	4.00	4.00	4.00	4.00
Total Al	6.51 (0.08)	6.81 (0.12)	6.92 (0.14)	7.01 (0.11)	6.82 (0.11)	6.99 (0.11)	6.83 (0.13)	6.96 (0.08)	6.71 (0.09)	6.86 (0.11)	6.88 (0.13)	7.07 (0.07)
Fe/(Fe+Mg)	0.50 (0.04)	0.47 (0.02)	0.51 (0.02)	0.52 (0.02)	0.50 (0.01)	0.52 (0.02)	0.50 (0.03)	0.51 (0.02)	0.48 (0.04)	0.52 (0.02)	0.52 (0.04)	0.54 (0.01)
Ca/(Ca+Na)	0.09 (0.02)	0.23 (0.04)	0.30 (0.11)	0.38 (0.07)	0.22 (0.07)	0.29 (0.06)	0.28 (0.08)	0.36 (0.07)	0.21 (0.05)	0.30 (0.07)	0.32 (0.1)	0.39 (0.03)

(a) In B500-8G, distinction is made between Group III tourmaline found associated with the solid phase and Group III isolated from it. (b) B_2O_3 calculated assuming 3 apfu. (c) H_2O calculated assuming 4 apfu of OH^-. n = number of analyses. b.d.l. = below detection limit.

Table 3.4: Average composition of experimental tourmaline.

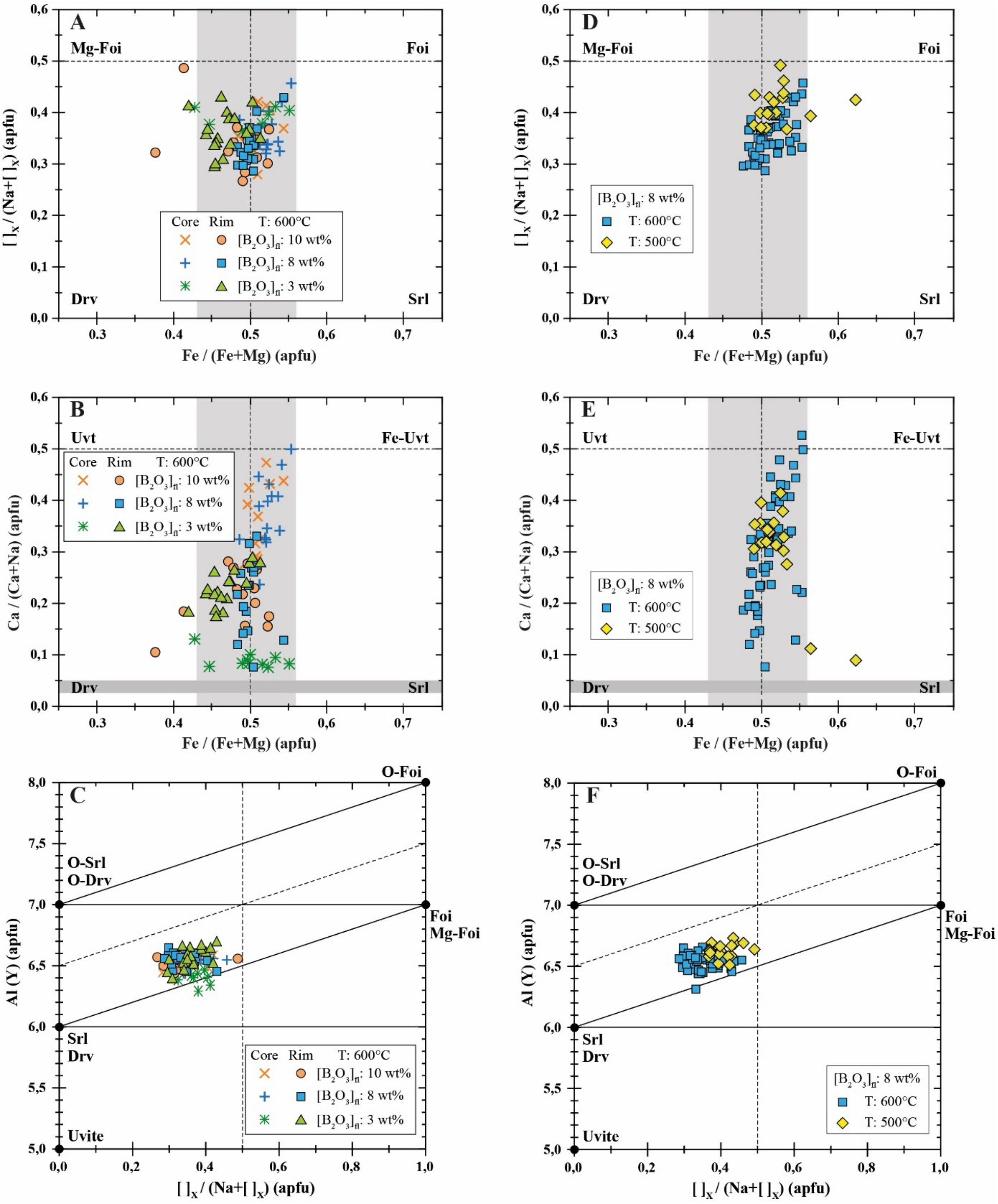

Figure 3.10: Compositions of experimental tourmalines as a function of $[B_2O_3]_{fluid}$ at 600°C (A; B; C) and of temperature at $[B_2O_3]_{fluid}$ = 8 wt%(D; E; F). The grey vertical band represents the at. Fe/(Fe+Mg) of the starting biotite and the horizontal grey band the at. Ca/(Ca+Na) of the starting plagioclase. In $[B_2O_3]_{fluid}$ diagrams (A; B; C), the data come from the charges B600-3, B600-8G and B600-10. In temperature diagrams (D; E; F), the data come from the charges B600-8G and B500-8G. See Table 3.2 and text for experimental conditions. Diagrams A to E from Hawthorne and Henry (1999) and C and F from Bačík et al. (2017).

by one order of magnitude than the starting plagioclase (horizontal grey bands in Fig. 3.10B; E), which is the main source of Ca in our experiment. Longitudinal transect performed on Group IIa tourmaline (Fig. 3.11) shows a sharp transition between the core and the rim characterised by an increase in Ca and Al and a decrease in $[\ ]_X$, Si and Fe (Table 3.4). Influence of $[B_2O_3]_{fluid}$ over the tourmaline core and rim compositions at fixed temperature is represented in Fig. 3.10 A-C. B600-8G core and rim show no to little variation in their at. Fe/(Fe+Mg), at. $[\ ]_X/([\ ]_X+Na)$ and ^{VI}Al proportion (Fig. 3.10A; C). However, the cores have a high at. Ca/(Ca+Na), near the range of the calcic tourmaline, and are relatively depleted in Si compared to the rims (Fig. 10B). The exact same relationship is observed in B600-10. Hence, the $[B_2O_3]_{fluid}$ affect the composition of the tourmaline zoning: at low $[B_2O_3]_{fluid}$ the chemistry of the tourmaline evolves by incorporating more Ca and Si whereas at high $[B_2O_3]_{fluid}$ this evolution implies a reduction of the Ca and Si budget. It is important to observe that despite those reversed evolution, all the rims fall in the same range of composition, characterised by an at. Ca/(Ca+Na) = 0.22 of chemical variations between the core and the rim of the 600°C tourmaline (Fig. 3.10B, Table 3.4).

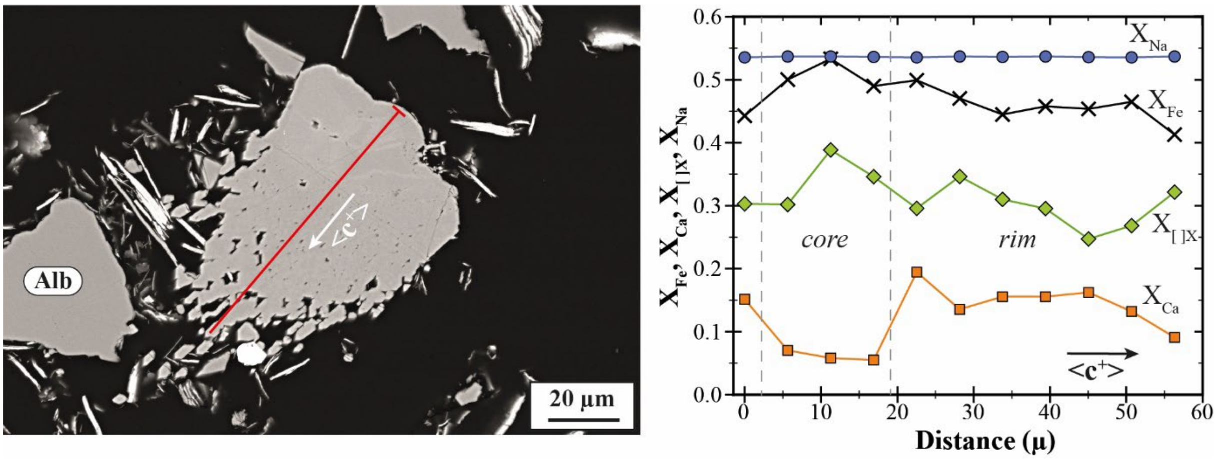

Figure 3. 11: Profil of microprobe analysis on Group II tourmaline in B600-3, plotted in terms of cation ratio. X_{Fe} : at. Fe/(Fe+Mg); X_{Ca} : at. Ca/(Ca+Na+$[\ ]_X$) ; $X_{[\ ]X}$: $[\ ]_X$/(Ca+Na+$[\ ]_X$); XNa : Na/(Ca+Na+$[\ ]_X$)

3/ Effect of temperature

The influence of temperature on tourmaline composition at fixed $[B_2O_3]_{fluid}$ is shown in Fig. 3.10D-F. The distinction between core and rim was not possible due to the small size of the tourmaline formed at 500°C, thus, all B600-8G compositions are plotted indiscriminately of their position (core or rim). The decrease of temperature do not affect the at. Fe/(Fe+Mg) ratio (Fig. 3.10D; E) nor the ^{VI}Al (Fig. 10F). Except for two analyses, the at. Ca/(Ca+Na) of the B500-8G tourmaline show little variation and correspond to the high values measured in B600-8G (rim) (Fig. 3.10E). Figure 3.10D and F show that the 500°C tourmaline has a slightly higher at. $[\ ]_X/([\ ]_X+Na)$, near the limit between alkali (schorl, dravite) and alkali-deficient (foitite, magnesiofoitite) tourmaline.

III- Discussion

A) Experimental reaction mechanism

Similarly to what has been done in Chapter II, the equilibrium constants for the eight tourmaline-forming reactions are of the same form, e.g. for R1 (considering quartz, andalusite and K-feldspar as pure phase):

$$K_{R1} = \frac{\left(a_{Srl}^{Tur}\right)^2 . \left(a_{H_2O_{(g)}}\right)^7}{\left(a_{Ann}^{Bt}\right)^2 . \left(a_{ALB}^{Pl}\right)^2 . \left(a_{B(OH)_3\,(aq)}\right)^6} \qquad \text{(Eq. 1)}$$

where a_{Srl}^{Tur}, a_{Ann}^{Bt} and a_{ALB}^{Pl} are the activities of the schorl, annite and albite end-members in tourmaline, biotite and plagioclase solid solutions, respectively. $a_{H_2O_{(g)}}$ is the activity of water (gas) and, in the range of temperature investigated, $a_{H_2O_{(g)}} \approx f_{H_2O}$. $a_{B(OH)_3\,(aq)}$ represents the activity of boric acid in the fluid, which, for a neutral aqueous specie, can be simplified as equivalent to $B(OH)_3$ molality. This molality can easily be expressed as $[B_2O_3]_{fluid}$. If, in Equation (1), tourmaline, cordierite and plagioclase compositions are identical to their respective end-member components, the equilibrium constant reduces to:

$$K_{R1} \approx \frac{\left(f_{H_2O}\right)^7}{\left(2[B_2O_3]_{fluid}\right)^6} \qquad \text{(Eq. 2)}$$

This relation is of the exact same form as what has been detailed in Chapter II discussion. By neglecting the influence of other fluid components than $B(OH)_3$ and H_2O, and with respect to the tourmaline and biotite end-members considered, this equation implies that the boron content of the fluid at equilibrium $[B_2O_3]_{fluidEQ}$ is uniquely determined. For variable temperatures, $[B_2O_3]_{fluidEQ}$ would follow an univariant curve in T-$[B_2O_3]_{fluid}$ space. Experimentally, equilibrium along R1 (or the other tourmaline-forming reactions) implies that increasing the boron fluid concentration above $[B_2O_3]_{fluidEQ}$ would shift the reaction toward the right, thus producing tourmaline and consuming the reactants in R1-R8. Conversely, lowering the boron fluid concentration below $[B_2O_3]_{fluidEQ}$ should lead to the reaction being shifted to the left, thus consuming tourmaline and producing B-free phases.

The forward experiments are generally consistent with this theoretical framework, at the exception with Run 5 at 400°C, where the destabilisation of the biotite into chlorite and illite compete with the tourmaline-forming reactions. At 600 and 500°C, tourmaline appears in phase assemblages for boron content in the fluid above a minimum value (Fig. 3.7). Tourmaline formation thus follows evolution toward the right as expected from reactions R1 to R8. $[B_2O_3]_{fluidEQ}$ is experimentally bracketed by charges without tourmaline and others with tourmaline present and it weakly varies with temperature between 500 and 600°C. Our determination are mutually consistent regarding the phase assemblage evolution. For charges near $[B_2O_3]_{fluidEQ}$ (B600-3, B600-4, B500-3, B500-4; see Table 3.2), experimental phase assemblages include the six major phases involved in reactions R1-R8. Evolving away from the equilibrium conditions with increasing $[B_2O_3]_{fluid}$ induce the progressive disappearance and / alteration of andalusite, quartz, albite and biotite and increase the tourmaline and K-feldspar proportions. This observation is consistent with the tourmaline-forming reaction becoming progressively more advanced. Tourmaline etching in reversal experiments with no $[B_2O_3]_{fluid}$ is also coherent with evolution toward the left end of the tourmaline forming reaction. Proving reversibility in our experiments at 600°C allows considering the experimental brackets on $[B_2O_3]_{\text{fluidEQ}}$ for this temperature as representative of the equilibrium of tourmaline-forming reactions. Last, tourmaline compositions are consistent with the different end-members considered in R1-R8. Hydroxy-uvite and hydroxy-feruvite are the only components that require new reactions in order to fully account for the range of our experimental tourmalines. At 600°C, although the difference in composition between the core and the rim is a feature of the chemical disequilibrium, the fact that the rim composition in different charges are almost identical (Fig. 3.10B) demonstrates that an equilibrated composition has been reached.

B) Control on the composition and texture of tourmaline: comparison to tourmaline-cordierite equilibrium experiments

Tourmaline textures in this study are in accordance with the observation of London (2011) who note that all experimental studies on tourmaline have described their products as consisting of exceedingly fine-grained tourmaline (Frondel et al. 1947; Morgan and London 1989; von Goerne et al. 1999b; Berryman et al. 2015, 2016), except in the case where diffusion-limited growth methods were used (e.g. von Goerne et al. 1999a; Setkova et al. 2019).The different defined textural group are identical to the ones previously described in Chapter II. They can be interpreted to indicate different growth mechanisms under two end-member regimes of supersaturation of tourmaline-forming components in the fluid. The only notable differences are the absence of homogeneous nucleation at 600°C in the charge with high $[B_2O_3]_{\text{fluid}}$ and the presence of only Group I tourmaline at 400°C. This last observation is related to the destabilisation of biotite into chlorite and illite which seem to hinder the tourmaline-forming reactions. By modifying the global distribution of the elements in the fluids, tourmaline growth is controlled by a local balance between the rocks and the fluid, even at high $[B_2O_3]_{\text{fluid}}$.

The composition is also controlled by processes similar to what has been described for the tourmaline-cordierite experiments. Again, tourmalines present a strong variability in their at. Ca/(Ca+Na) with Ca content in some charges high enough to be considered as calcic tourmaline (Fig. 3.10B). In Fe-free systems at 200 MPa and 600°C, Ca partition preferentially into the tourmaline compared to the fluid (von Goerne et al. 2011). However, experimental investigation in Fe-bearing systems have yet to be realised. The tourmaline-cordierite experiments showed a positive relationship between Fe and Ca, however, in the tourmaline-biotite experiments, this relationship has not been observed. The zonation of the 600°C tourmaline is mainly highlighted by variation of the at. Ca/(Ca+Na), whereas at. Fe/(Fe+Mg) remain globally constant (Fig. 10B). In highly supersaturated experiments ($[B_2O_3]_{\text{fluid}} >> [B_2O_3]_{\text{fluid\_EQ}}$, e.g. B600-8G and B600-10) the core to rim transition is marked by a decrease in the Ca content. With regards for tourmaline texture, indicating rapid growth, the high Ca-content found in the core may be due to the strong alteration of the albite during the early stages of the experiment. As more tourmaline is formed and boron removed from the fluid, the supersaturation level of the solution as well as its composition evolve toward less Ca-rich composition. This decrease in Ca is caused both by the consumption of albite by tourmaline-forming reaction and by the entrapment of solid inclusion of albite into K-feldspar. In weakly supersaturated fluid (B600-3), tourmaline growth is limited to a few crystals (group IIa) and controlled by a local balance between elements from the reactant mineral and the fluid. Under those conditions, alteration remains scarce and the fluid slowly evolved toward composition with more Ca released in the fluid by the albite dissolution (albite dissolve naturally in the fluid even if $[B_2O_3]_{fluid}$ =0wt %).

C) Tourmaline stability and boron fluid concentration in natural systems

The $[B_2O_3]_{fluid\_EQ}$ brackets from this study can be compared with previous experimental results (Weisbrod et al. 1986; Morgan and London 1989; von Goerne et al. 1999b; Orlando et al. 2017; Cheng et al. 2019), including those presented in Chapter II (Fig. 3.12). The $[B_2O_3]_{fluid\_EQ}$ for biotite is in good agreement with experimental results obtained on similar assemblages (Orlando et al. 2017; Cheng et al. 2019).Its positive evolution with temperature follow the same logic as what has been observed by Weisbrod et al. (1986), von Goerne et al. (1999b) and in Chapter II. The biotite-tourmaline equilibrium is characterised by a lower $[B_2O_3]_{fluid\_EQ}$ than equilibrium with cordierite between 500 and 600°C, although the difference is inferior to 2 wt%. This slight difference correlate well with natural observation of tourmalinisation mainly affecting biotite over cordierite in rocks containing both (Bosi et al. 2018; Harlaux et al. 2020). At 400°C, the destabilisation of biotite into chlorite and illite hinders the tourmaline formation by increasing the $[B_2O_3]_{fluidEQ}$ required, whereas destabilisation of cordierite into smectite at the same temperature do not impact the $[B_2O_3]_{fluidEQ}$. Tourmaline-chlorite assemblages are often described in hydrothermal systems related to magmatism, and

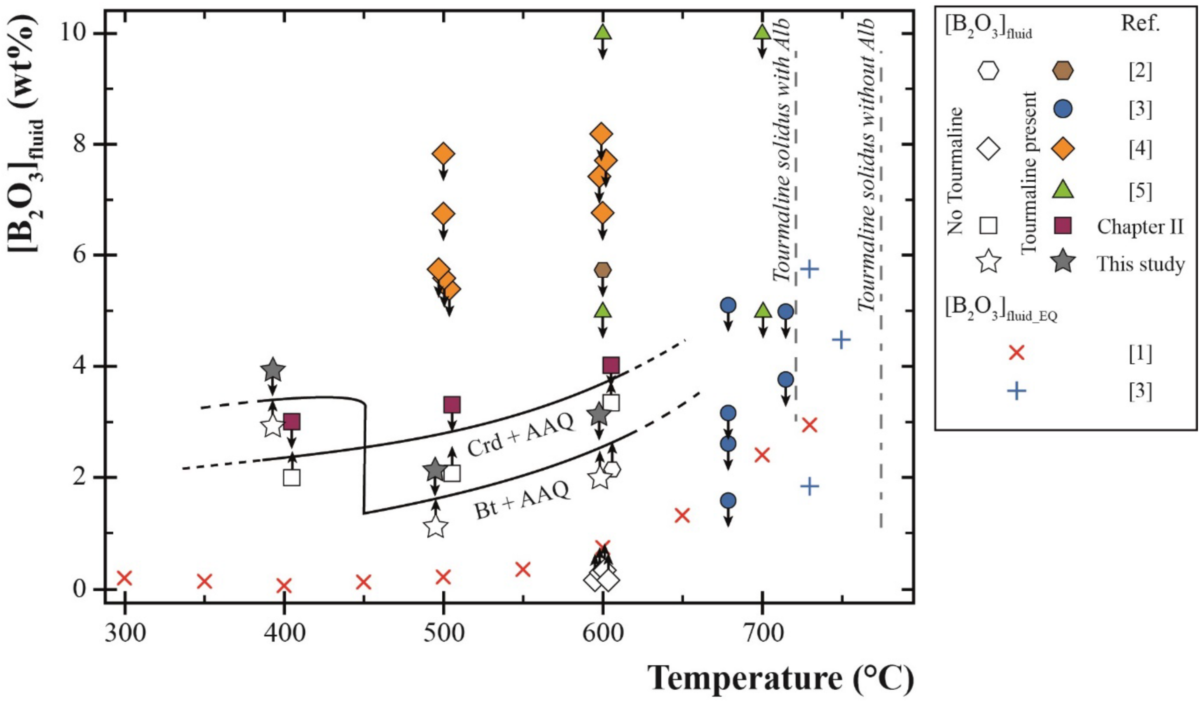

Figure 3. 12: Compilation of experimental results on tourmaline stability in a $[B_2O_3]_{fluid}$ vs. Temperature diagram. Crosses are for experiments where the final boron concentration at equilibrium with tourmaline ($[B_2O_3]_{fluidEQ}$) has been measured. Other symbols represent experiments where $[B_2O_3]_{fluidEQ}$ has not been determined. If tourmaline is not present (open symbols), an upward-pointing arrow is indicated. If tourmaline is present (solid symbols) but a reactant is missing in the final phase assemblage, or if only the initial $[B_2O_3]_{fluid}$ is reported, a downward-pointing arrow is indicated. References: [1] Weisbrod et al. (1986); [2] Morgan and London (1989); [3] von Goerne et al. (1999b); [4] Orlando et al. (2017); [5] Cheng et al. (2019).

generally occur around 400°C (e.g. Pirajno and Jacob 1987; LeFort et al. 2011; Harlaux et al. 2020). Based on our experimental results, these associations could sign a relatively high boron concentration in the fluid.

In order to assess the range of boron concentration in perigranitic hydrothermal systems, a compilation of 29 fluid inclusions studies, applied on various geological objects, was realised (see chapter I-III-B-1 for more details, and Appendix A2 for the sources). The results show that boron concentration globally ranges from 0.01 to 10 wt% $[B_2O_3]_{fluid}$, with a mean value of 1.14 wt% $[B_2O_3]_{fluid}$ (Fig. 3.13). Only three contexts present boron concentration frequently superior to 1 wt% : Sn-W deposits, skarns and barren plutonic. The different hydrothermal systems encompassed in those three categories are often related to silicic and peraluminous environments. As previously explained in the introduction, boron is known to behave as an incompatible element (Pichavant 1981; London et al. 1988; London 2011; Pokrovski et al. 2013). As such, the boron content of the melts increase during the chemical fractionation. Considering the fluid/melt coefficient = 3.0 for peraluminous systems, determined by Pichavant (1981), the hydrothermal fluid expelled by a peraluminous granite may be highly enriched in B. Experimental studies on tourmaline saturation of peraluminous melts at 750°C 200 MPa, and with an Aluminium Saturation Index (ASI) of ~1.35, have found a $[B_2O_3]_{melt} \approx 2$ wt% (Wolf & London 1997). In the hydrothermal systems related to these melts, tourmaline can appear in the early stage, either as part of the magmatic paragenesis or by self-metasomatism of the granite roof (Cheng et al. 2019). As visible in some hydrothermal Sn-W ore deposit such as San Rafael, tourmaline can be associated with every hydrothermal stage (early, syn or post-mineralisation).

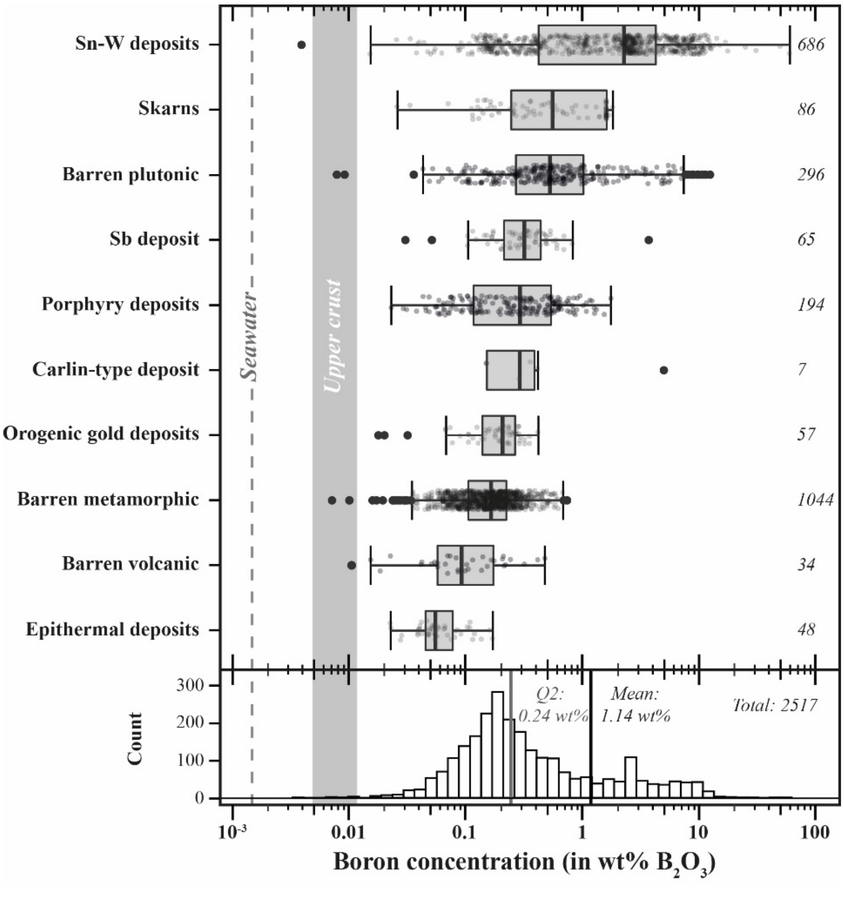

Figure 3. 13: Box plot displaying the boron concentration (in ppm) of the fluid inclusions of the compiled database, as a function of their hydrothermal environment. Below the boxplot, a histogram of boron concentration in the entirety of the compiled database with the global mean and median value indicated by vertical lines. Seawater boron concentration from Millero et al. (2008) and upper crust range from Wedepohl (1995) and Rudnick & Gao (2003).

In metaluminous environments, the reduction of the ASI makes it impossible for tourmaline to saturate in the fluid, even at high B concentration. Under H_2O-saturated conditions the saturation of the melt with respect to tourmaline at the lowest ASI possible (1.27), required 7 wt% $[B_2O_3]_{melt}$ (Wolf & London 1997). However, tourmaline is frequently described in the related hydrothermal systems, associated with the mineral assemblages characterising potassic (e.g. biotite, K-feldspar), phyllic (e.g. quartz, sericite), sodic-calcic (e.g. albite, actinolite, magnetite), propylitic (e.g. chlorite, epidote, carbonate, albite) and argillic (e.g. quartz, alunite, clays) alterations (Frikken et al. 2005; LeFort et al. 2011; Beckett-Brown et al. 2023). Unlike in Sn-W deposit, tourmaline appearance is limited and is never observed associated with all the alteration at the same time. This may imply that high-boron concentration in porphyry deposits might not be directly inherited from the magmatic source, but built up by other processes such as boiling or fluid-rock interaction. In the porphyry Cu-Au deposit of Mount Milligan, LeFort et al. (2011) measured the fluid inclusion composition before and after the formation of quartz-tourmaline-chlorite-carbonate veins. The stage before tourmaline precipitation contained approximately $[B_2O_3]_{fluid} \approx 1.2$ wt% and this concentration drop with tourmaline precipitation to $[B_2O_3]_{fluid} \approx 0.5$ wt%. Those values are lower than what has been determined experimentally and as such, tourmaline should not have been able to form. Hydrothermal fluids are chemically more complex than in experiments from this study, containing various additional anions such as chlorides and cations such as H, K, Ca, and Li (Audétat et al. 2008). The role of HCl and NaCl on the reduction of $[B_2O_3]_{fluidEQ}$ have already been questioned for the tourmaline-cordierite equilibrium and should also be addressed for the tourmaline-biotite one, as shown by the following results. Kister et al. (2005) used thermodynamic calculation in order to understand the mineralogical evolution of the Athabasca clastic sedimentary basin (Canada) where dravite, sudoite (chlorite group _ $Mg_2Al_3(Si_3Al)O_{10})(OH)_8$) and illites occur. The calculations were realised at 180°C and 1250 bars and show that the different mineral assemblages are mainly controlled by $B(OH)_3$ activity and by the activity ratio K^+/H^+ and $Mg^{2+}/(H^+)^2$. Direct transition from biotite (phlogopite) to tourmaline + K-feldspar is only possible at high boron activity, but the transition biotite→chlorite→tourmaline can be achieved by reducing the pH of the fluid. Application of their results at higher temperature might not be straightforward due to the influence of temperature on mineral stability field, but it highlights the potential effect of HCl in the reduction of the $[B_2O_3]_{fluid}$ required to form tourmaline + chlorite paragenesis.

References

Beckett-Brown, C.E., McDonald, A.M., and McClenaghan, M.B. (2023) Recognizing Tourmaline in Mineralized Porphyry Cu Systems: Textures and Major-Element Chemistry. The Canadian Journal of Mineralogy and Petrology, 61, 3–29.

Benard, F., Moutou, P., and Pichavant, M. (1985) Phase Relations of Tourmaline Leucogranites and the Significance of Tourmaline in Silicic Magmas. The Journal of Geology, 93, 271–291.

Berryman, E.J., Wunder, B., Wirth, R., Rhede, D., Schettler, G., Franz, G., and Heinrich, W. (2015) An experimental study on K and Na incorporation in dravitic tourmaline and insight into the origin of diamondiferous tourmaline from the Kokchetav Massif, Kazakhstan. Contributions to Mineralogy and Petrology, 169, 28.

Berryman, E.J., Wunder, B., Rhede, D., Schettler, G., Franz, G., and Heinrich, W. (2016) P–T–X controls on Ca and Na distribution between Mg–Al tourmaline and fluid. Contributions to Mineralogy and Petrology, 171, 31.

Blanc, Ph., Lassin, A., Piantone, P., Azaroual, M., Jacquemet, N., Fabbri, A., and Gaucher, E.C. (2012) Thermoddem: A geochemical database focused on low temperature water/rock interactions and waste materials. Applied Geochemistry, 27, 2107–2116.

Bosi, F., Naitza, S., Skogby, H., Secchi, F., Conte, A.M., Cuccuru, S., Hålenius, U., De La Rosa, N., Kristiansson, P., Charlotta Nilsson, E.J., and others (2018) Late magmatic controls on the origin of schorlitic and foititic tourmalines from late-Variscan peraluminous granites of the Arbus pluton (SW Sardinia, Italy): Crystal-chemical study and petrological constraints. Lithos, 308–309, 395–411.

Charoy, B. (1979) Greisenisation, minéralisation et fluides associés à Cligga Head, Cornwall (sud-ouest de l'Angleterre). Bulletin de Minéralogie, 102, 633–641.

Cheng, L., Zhang, C., Yang, X., Qi, D., Zhou, Y., and Holtz, F. (2019) Experimental investigation of reactions between two-mica granite and boron-rich fluids: Implications for the formation of tourmaline granite. Science China Earth Sciences, 62, 1630–1644.

Chicharro, E., Boiron, M.-C., López-García, J.Á., Barfod, D.N., and Villaseca, C. (2016) Origin, ore forming fluid evolution and timing of the Logrosán Sn–(W) ore deposits (Central Iberian Zone, Spain). Ore Geology Reviews, 72, 896–913.

Codeço, M.S., Weis, P., Trumbull, R.B., Pinto, F., Lecumberri-Sanchez, P., and Wilke, F.D.H. (2017) Chemical and boron isotopic composition of hydrothermal tourmaline from the Panasqueira W-Sn-Cu deposit, Portugal. Chemical Geology, 468, 1–16.

Drivenes, K., Larsen, R.B., Müller, A., Sørensen, B.E., Wiedenbeck, M., and Raanes, M.P. (2015) Late-magmatic immiscibility during batholith formation: assessment of B isotopes and trace elements in tourmaline from the Land's End granite, SW England. Contributions to Mineralogy and Petrology, 169, 56.

Drivenes, K., Larsen, R.B., Müller, A., and Sørensen, B.E. (2016) Crystallisation and uplift path of late Variscan granites evidenced by quartz chemistry and fluid inclusions: Example from the Land's End granite, SW England. Lithos, 252–253, 57–75.

Dutrow, B.L., Foster, C.T., and Henry, D.J. (1999) Tourmaline-rich pseudomorphs in sillimanite zone metapelites; demarcation of an infiltration front. American Mineralogist, 84, 794–805.

Frikken, P.H., Cooke, D.R., Walshe, J.L., Archibald, D., Skarmeta, J., Serrano, L., and Vargas, R. (2005) Mineralogical and Isotopic Zonation in the Sur-Sur Tourmaline Breccia, Río Blanco-Los Bronces Cu-Mo Deposit, Chile: Implications for Ore Genesis. Economic Geology, 100, 935–961.

Frondel, C., Hurlbut, C.S.J., and Colette, R.C. (1947) Synthesis of Tourmaline. American Mineralogist, 32, 680–681.

Gunter, W.D., Myers, J., and Girsperger, S. (1987) Hydrogen: Metal Membranes. In Hydrothermal Experimental Techniques pp. 100–120. John Wiley & Sons, New-York.

Harlaux, M., Kouzmanov, K., Gialli, S., Laurent, O., Rielli, A., Dini, A., Chauvet, A., Menzies, A., Kalinaj, M., and Fontboté, L. (2020) Tourmaline as a Tracer of Late-Magmatic to Hydrothermal Fluid Evolution: The World-Class San Rafael Tin (-Copper) Deposit, Peru. Economic Geology.

Henry, D.J., Novak, M., Hawthorne, F.C., Ertl, A., Dutrow, B.L., Uher, P., and Pezzotta, F. (2011) Nomenclature of the tourmaline-supergroup minerals. American Mineralogist, 96, 895–913.

Kister, P., Vieillard, P., Cuney, M., Quirt, D., and Laverret, E. (2005) Thermodynamic constraints on the mineralogical and fluid composition evolution in a clastic sedimentary basin: the Athabasca Basin (Saskatchewan, Canada). European Journal of Mineralogy, 17, 325–341.

Kontak, D.J., and Clark, A.H. (2002) Genesis of the Giant, Bonanza San Rafael Lode Tin Deposit, Peru: Origin and Significance of Pervasive Alteration. Economic Geology, 97, 1741–1777.

Korges, M., Weis, P., Lüders, V., and Laurent, O. (2020) Sequential evolution of Sn–Zn–In mineralisation at the skarn-hosted Hämmerlein deposit, Erzgebirge, Germany, from fluid inclusions in ore and gangue minerals. Mineralium Deposita, 55, 937–952.

Launay, G., Sizaret, S., Guillou-Frottier, L., Gloaguen, E., and Pinto, F. (2018) Deciphering fluid flow at the magmatic-hydrothermal transition: A case study from the world-class Panasqueira W–Sn–(Cu) ore deposit (Portugal). Earth and Planetary Science Letters, 499, 1–12.

Lecumberri-Sanchez, P., Vieira, R., Heinrich, C.A., Pinto, F., and Wälle, M. (2017) Fluid-rock interaction is decisive for the formation of tungsten deposits. Geology, 45, 579–582.

LeFort, D., Hanley, J., and Guillong, M. (2011) Subepithermal Au-Pd Mineralization Associated with an Alkalic Porphyry Cu-Au Deposit, Mount Milligan, Quesnel Terrane, British Columbia, Canada. Economic Geology, 106, 781–808.

Legros, H., Elongo, V., Laurent, O., Adlakha, E., Chelle-Michou, C., Falck, H., and Lecumberri-Sanchez, P. (2022) Formation of the Lened W-(Be) Skarn Deposit by Neutralization of a Magmatic Fluid—Evidence from H3BO3-Rich Fluids. Geosciences, 12, 236.

Li, X., Chi, G., Zhou, Y., Deng, T., and Zhang, J. (2017) Oxygen fugacity of Yanshanian granites in South China and implications for metallogeny. Ore Geology Reviews, 88, 690–701.

London, D. (2011) Experimental synthesis and stability of tourmaline: a historical overview. The Canadian Mineralogist, 49, 117–136.

London, D., Hervig, R.L., and Morgan, G.B. (1988) Melt-vapour solubilities and elemental partitioning in peraluminous granite-pegmatite systems: experimental results with Macusani glass at 200 MPa. Contributions to Mineralogy and Petrology, 99, 360–373.

Lynch, G., and Ortega, J. (1997) Hydrothermal alteration and tourmaline-albite equilibria at the Coxheath porphyry Cu-Mo-Au deposit, Nova Scotia. The Canadian Mineralogist, 35, 79–94.

Macey, P., and Harris, C. (2006) Stable isotope and fluid inclusion evidence for the origin of the Brandberg West area Sn–W vein deposits, NW Namibia. Mineralium Deposita, 41, 671–690.

Mahjoubi, E.M., Chauvet, A., Badra, L., Sizaret, S., Barbanson, L., El Maz, A., Chen, Y., and Amann, M. (2016) Structural, mineralogical, and paleoflow velocity constraints on Hercynian tin mineralisation: the Achmmach prospect of the Moroccan Central Massif. Mineralium Deposita, 51, 431–451.

Mlynarczyk, M.S.J., and Williams-Jones, A.E. (2006) Zoned tourmaline associated with cassiterite : implications for fluid evolution and tin mineralisation in the San Rafael Sn-Cu deposit, Southeastern Peru. The Canadian Mineralogist, 44, 347–365.

Morgan, G.B., and London, D. (1989) Experimental reactions of amphibolite with boron-bearing aqueous fluids at 200 MPa: implications for tourmaline stability and partial melting in mafic rocks. Contributions to Mineralogy and Petrology, 102, 281–297.

Orlando, A., Ruggieri, G., Chiarantini, L., Montegrossi, G., and Rimondi, V. (2017) Experimental Investigation of Biotite-Rich Schist Reacting with B-Bearing Fluids at Upper Crustal Conditions and Correlated Tourmaline Formation. Minerals, 7, 23.

Parkhurst, D.L., and Appelo, C.A.J. (2013) Description of input and examples for PHREEQC Version 3 _ A computer program for speciation, batch-reaction, one-dimensional transport and inverse geochemical calculations. U.S. Department of the Interior U.S. Geological Survey.

Pichavant, M. (1981) An experimental study of the effect of boron on a water saturated haplogranite at 1 Kbar vapour pressure: Geological applications. Contributions to Mineralogy and Petrology, 76, 430–439.

Pirajno, F., and Jacob, R.E. (1987) Sn-W metallogeny in the Damara orogen, South West Africa/Namibia. South African Journal of Geology, 90, 239–255.

Pokrovski, G.S., Borisova, A.Y., and Bychkov, A.Y. (2013) Speciation and Transport of Metals and Metalloids in Geological Vapors. Reviews in Mineralogy and Geochemistry, 76, 165–218.

Schatz, O.J., Dolejš, D., Stix, J., Williams-Jones, A.E., and Layne, G.D. (2004) Partitioning of boron among melt, brine and vapour in the system haplogranite–H2O–NaCl at 800 °C and 100 MPa. Chemical Geology, 210, 135–147.

Setkova, T.V., Balitsky, V.S., and Shapovalov, Yu.B. (2019) Experimental Study of the Stability and Synthesis of the Tourmaline Supergroup Minerals. Geochemistry International, 57, 1082–1094.

Slack, J.F., and Trumbull, R.B. (2011) Tourmaline as a Recorder of Ore-Forming Processes. Elements, 7, 321–326.

Tuduri, J. (2005) Processus de formation et relations spatio-temporelles des minéralisations à or et argent en contexte volcanique Précambrien (Jbel Saghro, Anti-Atlas, Maroc). Implications sur les relations déformation-magmatisme-volcanisme-hydrothermalisme. Sciences de la Terre et de l'Atmosphère : Métallogénie et Géologie structurale, Université d'Olréans, Orléans.

von Goerne, G., Franz, G., and Wirth, R. (1999a) Hydrothermal synthesis of large dravite crystals by the chamber method. European Journal of Mineralogy, 11, 1061–1078.

von Goerne, G., Franz, G., and Robert, J.L. (1999b) Upper thermal stability of tourmaline + quartz in the system MgO-Al2O3-SiO2-B2O3-H2O and Na2O-MgO-Al2O3-SiO2-B2O3-H2O-HCl in hydrothermal solutions and siliceous melts. The Canadian Mineralogist, 37, 1025–1039.

von Goerne, G., Franz, G., and van Hinsberg, V.J. (2011) Experimental determination of Na-Ca distribution between tourmaline and fluid in the system CaO-Na2O-MgO-Al2O3-SiO2-B2O3-H2O. The Canadian Mineralogist, 49, 137–152.

Weisbrod, A., Polak, C., and Roy, D. (1986) Experimental study of tourmaline solubility in the system Na-Mg-Al-Si-B-O-H. Applications to the boron content of natural hydrothermal fluids and tourmalinization processes. pp. 140–141. Presented at the Experimental Mineralogy and Geochemistry, Nancy - France.

Wolf, M.B., and London, D. (1997) Boron in granitic magmas: stability of tourmaline in equilibrium with biotite and cordierite. Contributions to Mineralogy and Petrology, 130, 12–30.

Wones, D.R., and Eugster, H.P. (1965) Stability of biotite: Experiment, Theory and Application. The American Mineralogist, 50, 1228–1272.

Chapter IV: Dynamic visualisation of fluid-rock interaction in a perigranitic environment: reactive transport experiments on boron metasomatism.

Introduction

Tourmalinisation is a metasomatic reaction, characterised by the alteration of Fe-, Mg-rich minerals such as biotite by a B-rich fluid, forming a tourmaline +/- quartz paragenesis (Schwartz 1958; Henry & Dutrow 1996; Frikken et al. 2005; Codeço et al. 2017). It was described in numerous ore deposits from different tectonic settings (Slack & Trumbull 2011), and generally predates or coexists with the mineralising stage. For example, at Mount Milligan, tourmaline marks the transition from Cu-porphyry type mineralisation to the sub-epithermal mineralisation (Au, PGE, As, Sb ; LeFort et al. 2011). In Sn-W deposits, tourmaline stages occurred at the end of greisenisation and are present within the mineralised veins (e.g. Duchoslav et al. 2017; Harlaux et al. 2020; Caldevilla et al. 2023). It is also common that the host rocks (schist, granite) of those mineralisation show more or less intense pervasive tourmalinisation (Wojdak & Sinclair 1984; Pirajno & Jacob 1987; Macey & Harris 2006; Chicharro et al. 2016; Myint et al. 2018). Some authors have investigated the potential cogenetic relationship between mineralisation and the effect of B-metasomatism on the physicochemical properties of the host rock. In the Achmmach prospect, tourmaline alterations exert a clear structural control on the mineralisation (Mahjoubi et al. 2016). By altering the mechanical behaviour of the hosted schist, tourmaline alteration has allowed a local shift from a ductile deformation to brittle fracturing, thus generating open spaces where the main Sn mineralisation was precipitated. In the Panasqueira deposit, wolframite precipitation is controlled by the release of Fe in the fluid due to the tourmalinisation of the host rock (Lecumberri-Sanchez et al. 2017). Thus, the W-ore grade can be seen as positively correlated with the quantity of magmatic fluid interacting with the schist.

The permeability has been recognised as a dynamic parameter, evolving in response to tectonism, fluid production and mineralogical reactions (Ingebritsen & Appold 2012; Ingebritsen & Gleeson 2015; Weis 2015). Depending on the reaction's stoichiometry and on P, T and water/rock ratio (W/R) conditions, alteration implies texture and volume changes (ΔV) that may significantly affect the total solid volume of the rock and thus, impact its permeability (Putnis 2002, 2015; Pollok et al. 2011; Jonas et al. 2014). Recent studies on greisenisation highlight the impact of this feedback phenomena on both the fluid flow and the location of the mineralisation (Launay et al. 2023). From the examples previously exposed, the feedback between boron alteration and permeability appear to be a key process during mineralisation stages. At Panasqueira, if the tourmalinisation decreases the permeability of the altered schist, ore deposition will be limited by the amount of Fe contained in the vein-wall surface. But, if the permeability increases, the fluid is able to interact with a greater volume of fresh Fe-rich rocks, triggering more wolframite deposition (with respect to the W concentration in the fluid).

Batch experiments on tourmalinisation reaction provide essential information on the required geochemical conditions for the alteration to develop, such as T or the boron concentration in the fluid (see chapters II to IV). However, they don't allow the quantification nor the observation of the coupling between hydrodynamics and chemistry. In open systems, the altered lithologies are controlled not only by the stability fields of the considered minerals, but also by the THMC (Thermo-Hydro-Mechano-Chemical) behaviour of the environment. Those feedback and their effect can be observed and monitored during percolating experiments. To date, only Launay et al. (2019) have realised such an experiment to reproduce a perigranitic environment, in order to study the relationship between the permeability of a granite and its greisenisation at 300°C. Other examples are focused on carbonation and serpentinisation of ultramafic core, up to 280°C (e.g. Peuble et al. 2015, 2019; Osselin et al. 2022).

In this chapter, we present the result of the first reactive percolation experiment performed on a spotted schist core. The rock, naturally tourmalinised was infiltrated with a $B(OH)_3$ brine at 300°C for 6 weeks. Permeability changes were monitored and the petrographic, textural and chemical evolution of the post-experiment cores, as well as outlet fluids composition were analysed in order to decipher the complex reactive transport couplings of the B-metasomatism.

I- Material and methods

A) Starting material

1/ Petrology

The spotted schist used as core material for this experiment was sampled at the contact of the W-mineralised veins of Panasqueira ore deposit. Here, the schist underwent important B-metasomatism resulting in the formation of tourmalinite (tourmaline + quartz) (Codeço et al. 2017; Lecumberri-Sanchez et al. 2017; Launay et al. 2018). The wall-rock is affected by the intense tourmalinisation up to 3 cm from the contact with the vein. Consequently, the core was sampled at 5 cm from the contact, where the spotted schist is only partially tourmalinised (Fig. 4.1).

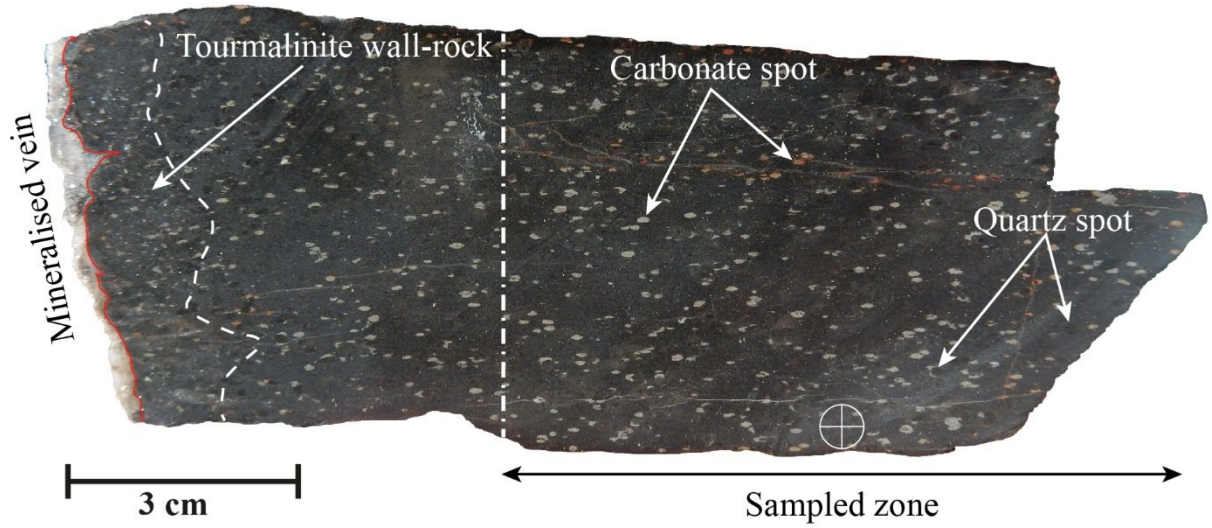

Figure 4.1: Macroscopic view of the initial spotted schist. The section is perpendicular to the foliation. On this sample, the intense tourmalinisation spreads to less than 2 cm. The round shape represents the contours of a core drilled perpendicularly to this plane.

X-ray diffraction (XRD) characterisation of the spotted schist was carried out with a Bruker AXS D8 Advance diffractometer (BRGM; Bragg-Brentano scan, Cu-Kα radiation with $\lambda = 1.54059Å$, 2θ range from 4 to 84° with 0.03° steps). Three different thin sections of the schist were realised and analysed through optical microscopy, SEM imaging (coupled with EDS analysis) and electron microprobe. Modal composition was obtained from SEM image analysis. One to three panoramas were realised at random location, on each three thin sections, using the SmartStitch software (v01.02.13). This allowed the collection of hundreds of images over a regular grid with a constant pixel resolution of approximately 0.33 µm. Then, ImageJ software was used to reconstruct the panoramas and analyse the pixel value distribution. Using optimised brightness and contrast, coupled with EDS determination, the panorama, were thresholded into 6 parts, corresponding to porosity, quartz, tourmaline, muscovite, biotite and others (siderite, oxides, apatite). This methodology was applied on the globality of the panoramas in order to obtain a global modal composition. It was also applied on distinct crop zones of 500x500 µm, representing only the schist matrix or the quartz or carbonate spot (see description thereafter). In order to ensure the accuracy of the global mineral proportion in the starting material, the modal composition deduced from the panorama was compared to a modal composition from the whole rock analysis, combined with a mean mineral formula calculated from EPMA measurements. The calculated composition differs from the image analysis by a few percent, increasing the biotite (from 18 to 21 wt%) and quartz (from 30 to 33 wt%) content and decreasing the muscovite content (from 35 to 31 wt%) (Table 4.1).

Schist texture	Matrix		Quartz spot		Carbonate spot		Global		Recalculated from whole rock composition
n	30		11		5				
	Mean	*sd*	*Mean*	*sd*	*Mean*	*sd*	*Mean*	*sd*	
Biotite	20.6	(5.3)	16.1	(2.3)	13.5	(4.5)	18.3	(4.5)	21.3
Muscovite	43.4	(2.6)	11.5	(1.8)	24.8	(5.1)	35.2	(5.1)	30.6
Siderite / Oxide	1.4	(0.7)	1.5	(0.4)	36.6	(2.5)	3.3	(2.2)	2.4
Tourmaline	15.2	(3.8)	11.2	(2)	10.9	(3)	13.5	(3)	12.7
Quartz	19.4	(2.2)	59.6	(3.8)	14.3	(5.7)	29.7	(4.7)	33

Table 4.1: Mass fractions of the minerals determined by image analysis for the spotted schist in its entirety and for specific textures in it.

2/ Petrophysical properties

In order to characterise the petrophysical properties of the spotted schist, Mercury Intrusion Porosimetry (MIP) analysis were performed on several samples of different sizes. However, these measurements did not allow the porosity of the sample to be quantified. Indeed, it appears that the porosity observed by SEM imaging is not connected by pores in the size range of those studied by MIP. In order to acquire even a vague idea of the porosity of the spotted schist, we used a batch image processing method based on the protocol of Buckman et al. (2017). SEM panoramas, acquired for modal composition determination, were thresholded to retain only pixels representing the porosity. A python code (named thereafter "*PorosCount*") was then created and applied to the obtained binary image in order to calculate the percentage of porosity on a surface defined by the user. This surface is automatically repeated over the whole image following a diamond grid. The code returns a spreadsheet containing the coordinates of the centre of each surface, as well as its porosity value. An application of this method is presented in the Appendix A16. The study of these data allows us to determine the average porosity of the sample on a 2D plane, as well as its distribution. Although this method allows for a quick and clear visualisation of the porosity, it is highly dependent on the resolution of the SEM image and does not reflect the 3D architecture (pore volume, connectivity) of the spotted schist. Micro-tomography imaging was also performed on the spotted schist in order to obtain a 3D vision of the porosity. However, this technique was unsuccessful as the biotite display important rim effect, thus blurring the neighbouring voxels representing porosity.

B) Reactive percolation experiments

1/ Experimental setup

The experiment used a core (diam. 5.6 mm, length 40.7 mm) drilled on a plane perpendicular to the foliation of the spotted schist. The first injected solution was prepared by dissolving boric acid ($B(OH)_3$) crystals in 1L of ultrapure water in order to reach a boron oxide concentration in the fluid ($[B_2O_3]_{fl}$) = 2.40 wt%. In order to reduce possible alteration of the core during heating of the autoclave, the solution was injected only after reaching the targeted temperature. As the entirety of this solution was consumed after 829 h of the experiment, a second identical solution was prepared, with a $[B_2O_3]_{fl}$ = 2.36 wt%.

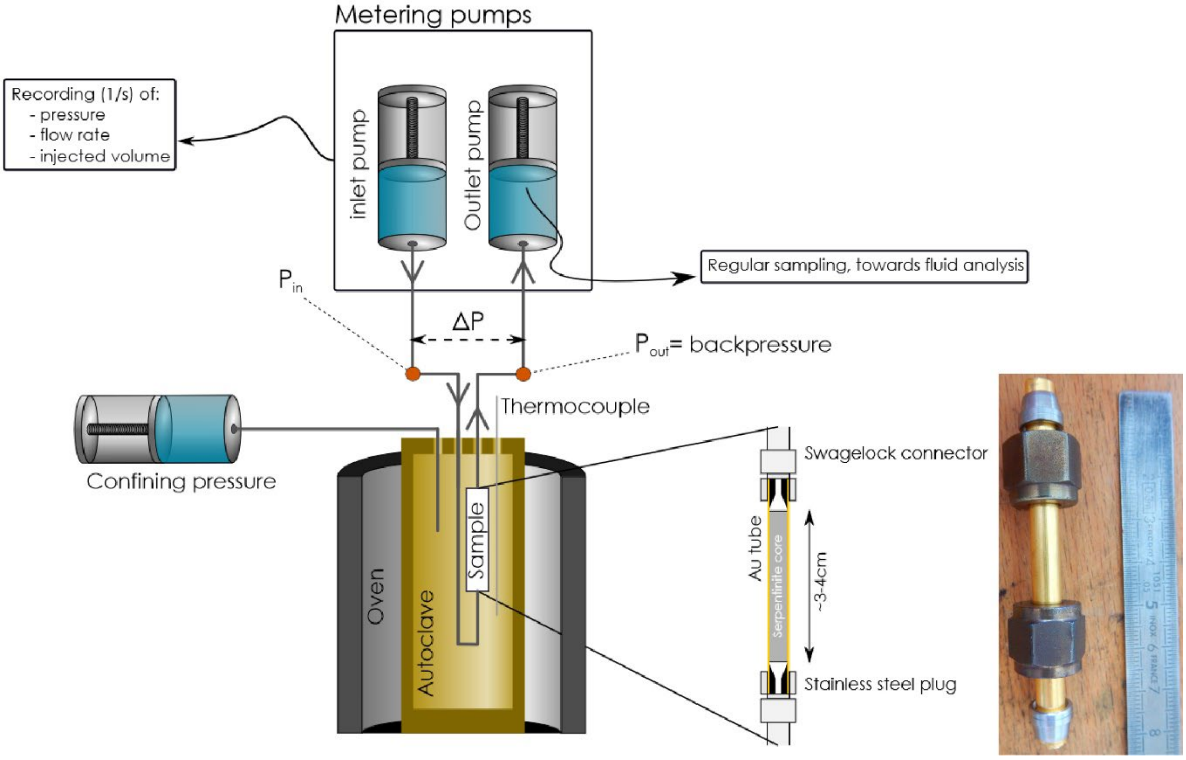

Figure 4.2: Schematics of the permeameter by Osselin et al. (2022)

The following description of the home-made permeameter used for the reactive percolation experiment, comes from Osselin et al. (2022). The complete apparatus is represented in Figure 4.2. It consists in a large volume (1 L) autoclave connected to a piston-pump (PMHP 100-500 from TOP Industry) controlling the confining pressure using deionised water as the confining fluid. The core itself is inserted in a gold tube working as a jacket which transmits the confining pressure. At both ends of the core, two stainless steel plugs are added to connect with the inlet and outlet capillaries using Swagelok tube fittings. The conical shape of the plugs allows for an even distribution of the flow at the inlet and outlet. The sample is connected to two more pumps controlling the inlet and outlet pressure and ultrapure water is injected in the circuit during heating. The autoclave is heated externally by a cylindrical oven controlled with an Eurotherm regulator. Experimental temperature is measured inside the vessel, next to the core, using an internal sheathed type K thermocouple and is known with an uncertainty < 10°C. Temperature fluctuations during the experiments were limited to 2°C.

The system works at temperature up to 400°C and confining pressure up to 500 bars. In this study, the experiment lasts nearly 37 days (877 h) with the temperature and confining pressure maintained at 300°C and 300 bars. As clogging during the experiment may occur fast (Osselin et al. 2022), the injection was controlled by imposing a constant pressure difference between the inlet and outlet of the core, in order to avoid an uncontrolled increase of pressure in the case of complete clogging when the flow rate is imposed. Thus, the outlet pressure was set at 200 bars and the inlet pressure was modified to maintain a flow rate around 8.4×10^{-3} mL/h, allowing collecting enough material to sample the fluid every 24 h. The flow rate, inlet and outlet pressure, temperature and confining pressure were recorded with a frequency of 1 data point per second for the whole duration of the experiment, by using the software Eurotherms iTools Engineering Studio (v 9.84). Those parameters were also manually read 1 to 3 time per day, the value reported corresponding to a mean over 1 to 2 h. Due to storage memory problems, the time flow rate record was not automatically saved from the hours 16 to 272 and 300 to 527. As such, the manual readings were used instead. The time-dependent permeability was calculated from Darcy's law:

$$k = \frac{Q}{S} * \frac{\Delta x}{\Delta P} * \eta \qquad \text{(Eq. 1)}$$

k the Darcy's permeability (in m^2) is determined by the dimensions of the core: S its section ($\approx 2.46\times10^{-5}$ m^2) and Δx its length (m); by ΔP, the imposed pressure difference between inlet and outlet (Pa) and Q is the corresponding flow rate (m^3/s), and by the water viscosity. This last was calculated from the IAPWS-97 equation (Huber et al. 2009) as 9.32×10^{-5} Pa.s.

2/ Geochemical relevance of the condition

This experiment aims to study the coupling between physicochemical processes, at the core scale, during boron metasomatism in a perigranitic environment. The experimental conditions were chosen in order to obtain the best compromise between reality and experimental constraint. Hydrothermal tourmalinisation occurs over a large range of P-T (summarised in van Hinsberg et al. 2011). As such, the P-T conditions were constrained by the limit of the experimental apparatus. Despite several attempts to perform reactive percolation experiments at 400°C, none have been successful. The main issue was the corrosion of the inlet capillary, at just a few centimetres from the autoclave. This may have been caused by the strong thermal gradient between the autoclave and the exterior (from 400 to 50°C in less than 6 cm), increasing drastically the reactivity of the fluid in this section. Only one attempt lasted longer than 12 h, a brief summary is presented in the Appendix A17 as it gave insights into what was observed in the successful experiment. In order to stay in a range of condition for which standard molal thermodynamic properties of charged aqueous species can be calculated using the revised HKF equations, the temperature was decreased to 300°C and the confining pressure was set to 300 bars. Those conditions can be naturally attained above the roof of a magmatic intrusion, emplaced at very shallow condition and are still within the stability domain of tourmaline, as inferred by its natural formation in low P-T environments (Henry & Dutrow 1996, 2012; Henry et al. 1999).

The $B(OH)_3$-rich fluid used in the experiment is similar to the fluid used to study tourmaline stability during batch experiments (Morgan & London 1989; von Goerne et al. 1999; Chapter II, III and IV). By using boric acid crystal to add boron in the fluid, we ensure acidic condition favourable to tourmaline formation (Morgan & London 1989). The fluid concentration was chosen to be the highest possible while staying below the saturation at 25°C. This limit is required in order to avoid any precipitation of sassolite ($B(OH)_{3(s)}$) in the inlet pump and capillary leading to a uncontrolled modification of the boron budget and a potential clogging. Compared to the stability results obtained in batch experiments (Chapters II and III), the solution concentration ($[B_2O_3]_{fl}$) = 2.40 wt%) may be too low for tourmaline to crystallise. However, by working as an open system, local high concentration can be reached and thus altered the rock. If tourmalinisation occurs, the natural presence of tourmaline in the core will promote overgrowth of experimental tourmaline rather than nucleation. This allows increasing the kinetic of the tourmaline-forming reaction (Lasaga 1998) and also to easily check if those took place. Based on natural (Baksheev et al. 2009; van Hinsberg et al. 2011b; Dutrow & Henry 2016, 2018) and experimental studies (von Goerne et al. 1999; Setkova et al. 2019; Chen et al. 2021; Chapter II, III and IV), tourmaline fibers overgrowth should be observed on the <c+> end of the natural crystals.

3/ *Fluid and mineral analysis*

As mentioned before, the outlet fluid was sampled roughly every 24 h (maximum interval ≈ 60 h) for chemical analysis and the samples were stored in a fridge at 4°C right after sampling and until analysis. After sampling the fluid, the outlet pump was emptied, cleaned with ultrapure water and then replenished with 10 mL of ultrapure water before reconnecting it with the experiment. The fluid analyses were performed after the end of the experience by the DEPA laboratory (cofrac accreditation n° 1-0251) of the BRGM (Orléans, France). Before analysis, the samples were heated at 25°C in order to dissolve crystals that precipitated due to the low temperature of the fridge and then filtrated with 0.45 µm filters in order to remove the remaining particles. The cations Al, B, Co, Mn, Ni, Zn, Ti, and Br were analysed by ICP/MS (ref. NF EN ISO 17294-2), and Ca, K, Fe, Mg, Na, and $SiO_{2(aq)}$ by sequential ICP/AES (ref. NF EN ISO 11885). Cl analysis was performed on an Ionic Chromatography with a Dionex Ionpac AS11-HS column (ref. NF EN ISO 10304-1). The dissolved inorganic carbon (DIC) was analysed with a Shimadzu TOC-L series. The obtained data are then rescaled by the dilution factor corresponding to the 10 mL of ultrapure water left in the pump after a sampling, in order to obtain the actual outlet concentrations.

After the end of the experiment, the core was retrieved and cut axially in half. A polished section was realised with one of the halves for SEM examination coupled with EDS analysis, cathodoluminescence, RAMAN spectroscopy and microprobe analysis. The other half was sent to the SARM (Service d'Analyses des Roches et des Minéraux, Nancy, France) for whole rock analysis along with the sample of the starting spotted schist.

II-Results

A) Panasqueira spotted schist

1/ Petrography

The spotted schist is a rock affected by the contact metamorphism caused by the Panasqueira magmatic intrusion. As reported by Codeço et al. (2017), it is coarser than the Beira schist from which it derives and presents porphyroblastic textures, with black quartz spots and white carbonate spots (Fig. 4.1). The spots are slightly flattened and highlight the main foliation. The sample is also crossed by quartz veins, up to a millimetre thick, and very thin (< 50 µm) carbonate veinlets. Some of the carbonate spots and veinlets are slightly oxidised, giving them a reddish colour. Microscopic and SEM observation show that the carbonate spots are frequently attached on the border of the quartz spots and sometimes overlay them (Fig. 4.3A, B). The matrix is globally homogeneous, no layering inherited from the Beira schist is observed, and the largest crystals are aligned with the foliation (Fig. 4.3). As reported in Table 4.1 and shown in Figure 4.3C, the rock is essentially composed of white mica (35 %), quartz (30 %), biotite (18 %) and tourmaline (14 %), along with minor phases (3%) including

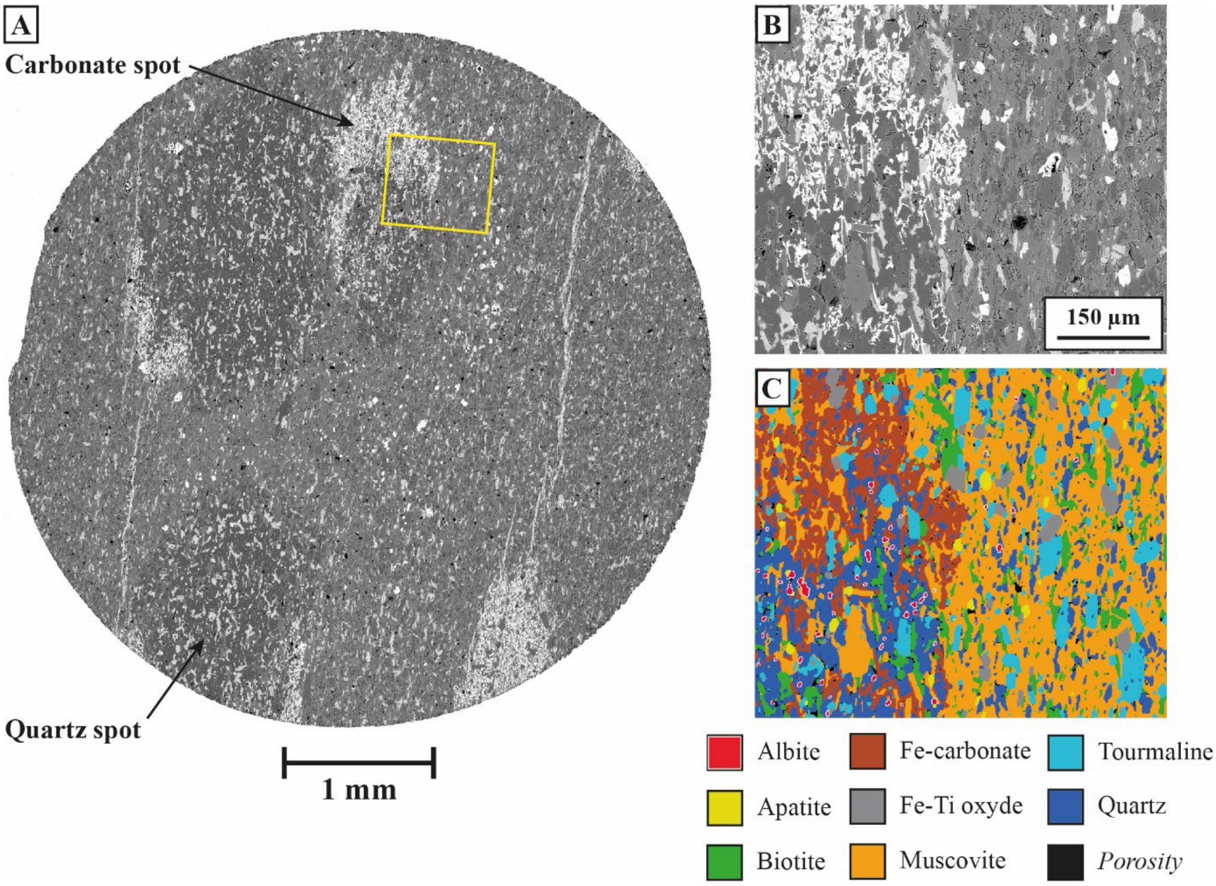

Figure 4.3: (A) General view of the spotted schist with black quartz spot and white spot and veins of carbonate. (B) Zoom on a contact between quartz spot (bottom-left side), carbonate spot (top-left side) and the matrix (right side) from the general view. (C) Mineralogical map of (B), created under ImageJ, using elemental maps. Albite, in red with white outline, are essentially located inside the quartz spot.

carbonate, apatite, Fe-Ti oxides, albite, beryl and rare sulfurs (pyrite, arsenopyrite, sphalerite, chalcopyrite).

The diffractogram analysis allowed the characterisation of the white micas as muscovite 2M1, and confirmed the presence of quartz, albite and rutile in the rock. Tourmaline could not be identified because of overlapping with the muscovite signal. Instead of biotite, characteristic peaks of chlorites are present and interpreted either as chamosite ($Fe^{2+}{}_5Al(AlSi_3O_{10})(OH)_8$) or clinochlore ($Mg_5Al(AlSi_3O_{10})(OH)_8$), depending of the database used for the identification. However, microscopic and SEM observations, as well as microprobe analyses, confirm the presence of biotite and not chlorite.

The schist matrix is essentially composed by muscovite (43 %) and biotite (21%) subhedral crystals of less than 20 µm long (Fig. 4.4A). Largest crystals (< 100 µm) are generally in the near vicinity of the quartz spot and veins. Distancing from those spots decreases the number of large crystals and increases the proportion of phyllosilicates with altered textures. Those altered crystals have xenomorph shape and microporous texture (Fig. 4.4A). For both muscovite and biotite, few subhedral crystals present a bright thin rim. Tourmaline composes approximately 15 % of the matrix minerals and this proportion is negatively correlated with the amount of biotite. Tourmaline forms prismatic subhedral to euhedral zoned crystals, with some sections > 100 µm long (Fig. 4.4A). The majority have concentric zonation with a bright core (not always visible) surrounded by darker zones and a light outer rim. Some of the crystals display a bright outer rim on the faces perpendicular to the elongation. Those bright zones can also be penetrative in the tourmaline, probably sealing fractures and are interpreted as a late tourmaline crystallisation stage. All tourmaline contains solid inclusion of quartz principally and apatite and Fe-Ti oxides more rarely (Fig. 4.4A). Modal composition obtained by image analysis on individual crop zone shows that the proportion of tourmaline is negatively correlated with the proportion of biotite. Finally, the quartz present sharp geometric texture (Fig. 4.4A), mainly due to the presence of so many subhedral mineral. It is in intergrowth with the tourmaline and frequently present xenomorphic shape at the contact with biotite. Apatite appears as round-shaped crystals with a diameter inferior to 15 µm, all over the schist matrix. Fe-Ti oxides are large euhedral crystals with a Ti-rich xenomorphic core, unevenly distributed in the matrix.

Quartz spots vary in size, with a diameter ranging from 500 µm to 2 mm. The largest ones frequently display concentric shape in their centre, formed by large xenomorph quartz crystals and large subhedral to euhedral biotite and muscovite (> 100 µm, Fig. 4.4B). Beryl is only present in those concentric shape and contains many round quartz inclusions (Fig. 4.4B). All quartz spot contains every mineral observed in the matrix, cemented by multiple quartz grains whose rims are marked by a porous trail (Fig. 4.4C). Tourmalines present the exact same texture as those observed in the matrix, but are generally smaller. As highlighted by the mineralogical map (Fig. 4.3C), the spot contains a lot of albite relics compared to the matrix. Those grains form xenomorphic inclusions in the porosity formed between the quartz grains (Fig. 4.4C).

Carbonate spots are of the same range of size as the quartz spots and overlay the muscovite, quartz and biotite present in the matrix. Carbonates are xenomorph and are formed in the space between grains, thus surrounding the original minerals (Fig. 4.4D). Tourmaline is unaffected by this transformation, and the carbonate forms straight contact with it.

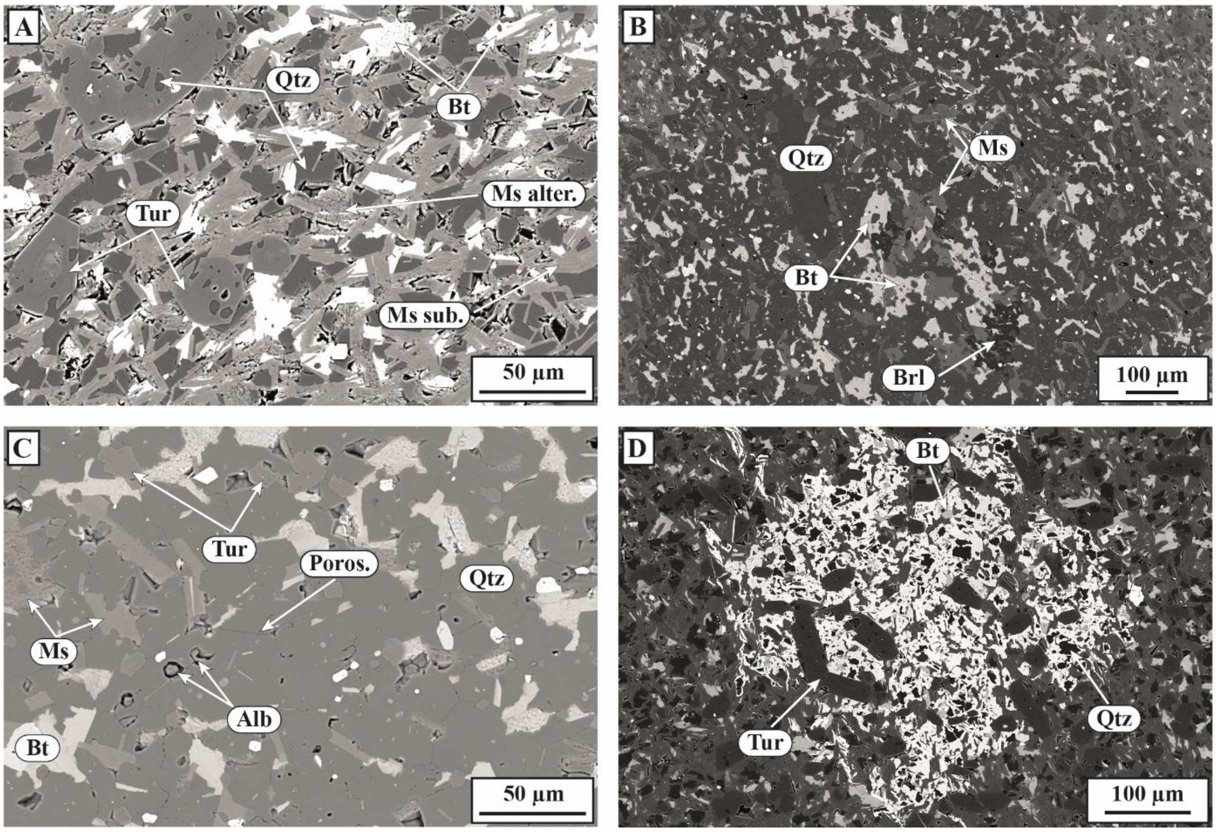

Figure 4.4:SEM images of characteristic textural features in the starting spotted schist. (A) View of the matrix. The altered white micas are identified by their xenomorphic contours and the alteration following the cleavage planes. (B) Image of the centre of a quartz spot, highlighted by the presence of large crystals of biotite, white micas and sometimes beryl (dark grey). (C) Zoomed observation in the quartz spot with some relics of albite. All the matrix minerals are present, surrounded by quartz. Porosity highlights the intergranular space between the quartz grains. (D) Image of a carbonate spot. Tourmaline are clearly visible, whereas other mineral show xenomorphic contours with the carbonate. Abbreviations: Alb = albite; Bt = biotite; Brl =beryl; Ms alter. = altered muscovite; Ms sub.= subhedral muscovite; Poros. = porosity; Qtz = quartz; Tur = tourmaline.

2/ Chemical composition

All the mean compositions tables for the spotted schist mineral are in Appendix 18 and the details of the analyses are available in Appendix A19 to A22. In order to verify the relationship between texture and chemical composition, biotite and muscovite were divided into four groups: subhedral crystals of the matrix, altered crystal of the matrix, rim and crystals in quartz spot and vein. The biotite of the spotted schist is rich in Fe and can be described as a solid solution between siderophilite ($KFe_2Al(Al_2Si_2O_{10})(OH)_4$) and annite ($KFe_3(AlSi_3O_{10})(OH)_4$) (Fig. 5A). There is no particular difference between the textures considered, except for a few rims which have a composition richer in Mg and Si (Fig. 5A, B). For the white micas, the subhedral crystals are all close to the pure muscovite pole ($KAl_2(AlSi_3O_{10})(OH)_2$), whereas the rims tend toward the celadonite pole

($K(MgFe^{3+}[])(Si_4O_{10})(OH)_2$) (Fig. 5C). Altered muscovite and those contained in quartz spots have an intermediate composition between these two end-members. These compositions are consistent with previous analyses of wall-rock samples from the Panasqueira veins (Codeço 2019), although the phengitic component is not represented in our analysis of the white micas. Thus, the composition of biotite and white micas can be considered homogeneous in the spotted schist, with some variations highlighted by an enrichment in Mg (Fig. 5A, D).

Carbonates are siderite ($FeCO_3$), with variations in Mn content depending on their origin (Fig. 5E). The carbonates in the veins contain virtually no Mn or Mg and are aligned with the siderite-magnesite joint. Most of the spots are enriched in Mn from the edge to the core. The Mg content is constant and the Mn content in the central part of the spot may account for 1/3 of the proportion of divalent cations in the carbonate.

As mentioned previously, tourmalines from the spotted schist are zoned (Fig. 6A) and those zonations can be divided into 6 subsets, shown in the diagram in Fig. 6B. Based on the content of site Y and site X, tourmalines belong to the alkali group and plot within the field of tourmaline from metasedimentary rocks (Fig. 6C, D). The ratio at. Fe/(Fe+Mg) ratio of tourmalines is stable, around 0.5, while the Na content in site X varies from 0.7 to 0.4 apfu. These characteristics mean that tourmalines can be considered as a solid solution between dravite and schorl (Fig. 6E), with variations in Na and Al related to the alkali-deficient exchange vector ($NaY^{2+} \rightarrow [\ ]_XAl$, where Y^{2+} stand for divalent cations in the Y site; Fig. 6F). All these observations are consistent with those made previously by Codeço et al. 2017 and Launay et al. 2018. Distinguishing the zonation reveals three subsets of composition. Firstly, the zonations at the core of the crystals (Core 1, Core 2 and Intermediate) and Rim 2 form a compact group characterised by an at. Fe/(Fe+Mg) =0.43 and an at. $[\ ]_X/([\ ]_X+Na)$ between 0.3 and 0.45. Rim 1 represents the compositions closest to the alkali-deficient tourmaline range (Al-rich and Na-poor), with an at. $[\ ]_X/([\ ]_X+Na) \approx 0.5$. Conversely, the compositions identified as Late are the richest in Na and their ratio at. Fe/(Fe+Mg) varies between 0.44 and 0.54.

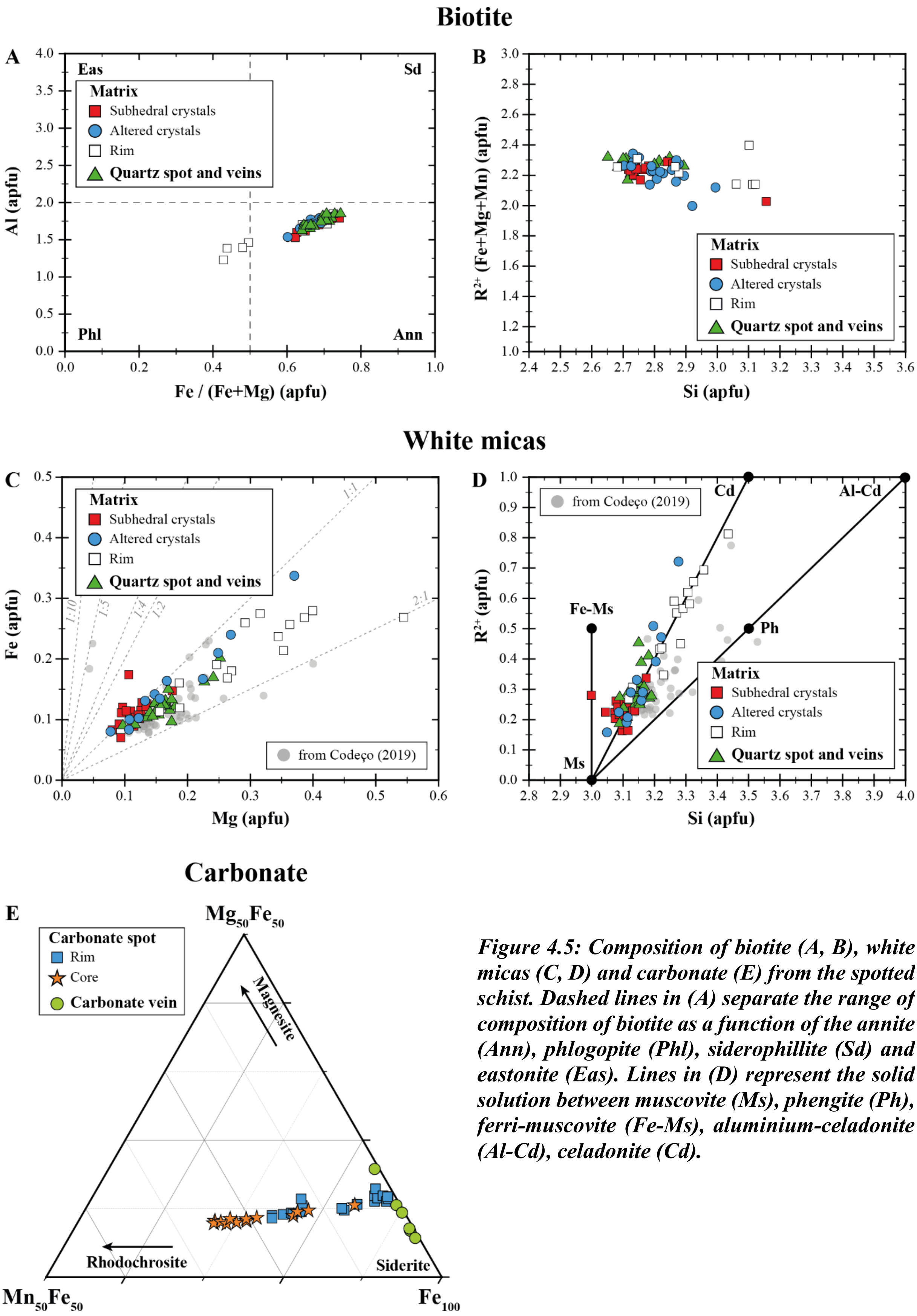

Figure 4.5: Composition of biotite (A, B), white micas (C, D) and carbonate (E) from the spotted schist. Dashed lines in (A) separate the range of composition of biotite as a function of the annite (Ann), phlogopite (Phl), siderophillite (Sd) and eastonite (Eas). Lines in (D) represent the solid solution between muscovite (Ms), phengite (Ph), ferri-muscovite (Fe-Ms), aluminium-celadonite (Al-Cd), celadonite (Cd).

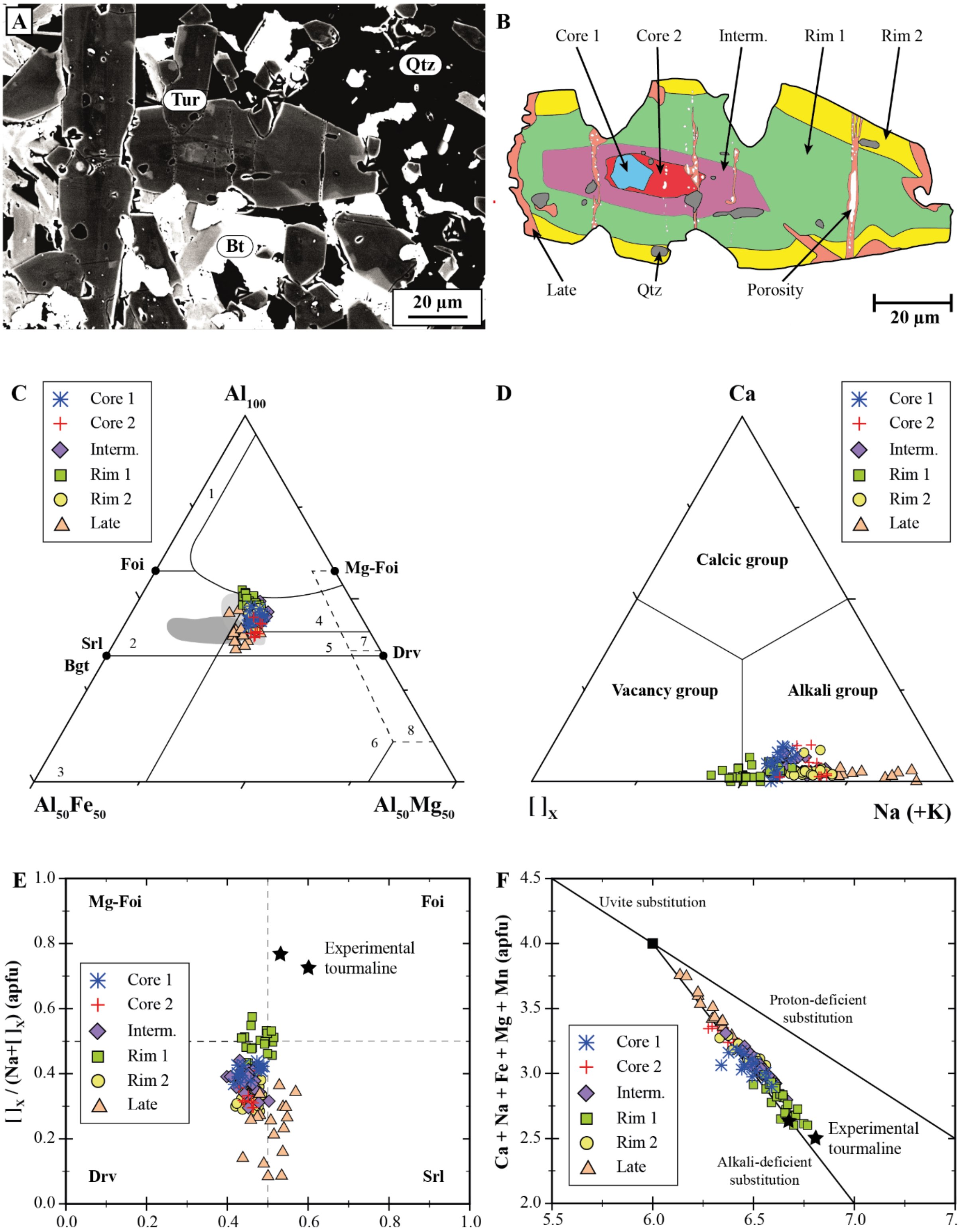

Figure 4.6: (A) SEM image of a zoned tourmaline in the spotted schist. (B) Schematic representation of the tourmaline zonation. (C to F) Composition of the different zonations in natural tourmaline and report of two experimental tourmaline compositions obtain in this study. (C) Al-$Al_{50}Fe_{50}$-$Al_{50}Mg_{50}$ ternary diagram, coupled with the petrogenetic classification (after Henry & Guidotti, 1985) Grey area represent tourmaline composition inside the Beira schist reported by Codeço (2019) and Launay et al (2017). The light grey represents rim compositions and the dark grey represent the core compositions (D) Ca-X-site vacancy-Na(+K) ternary diagram (after Hawthorne & Henry, 1999). (E) Fe-Mg Tourmaline classification. Drv = dravite, Foi = foitite, Mg-Foi = magnesiofoitite, Srl = schorl. (after Henry et al. 2011) (F) Ca+Na+Fe+Mg+Mn vs ^{VI}Al+1.33Ti representation allowing the observation of three classical tourmaline substitutions (after Trumbull & Chaussidon, 1999).

3/ Petrophysical properties

Previous MIP work on the pore characterisation of metamorphic rock reservoir highlighted the low porosity present in the schists (Bagde 2000; Zeng et al. 2022). However, none of those studies questioned their results in terms of connectivity. By performing MIP analysis on samples of different sizes, we measured a porosity 20 times greater in the sample crushed between 1 to 5 mm than in the sample with fragments > 10 mm. Consequently, not only is the schist very poorly porous, but the porosity is not connected on the scale of pore diameters investigated (here > 6 nm). Applying the Python code "*PorosCount*" on the spotted schist allowed to measure a global porosity of 2.3 %. This value must be considered as a maximum limit, since it includes the porosity resulting from the pulling out of certain minerals during the creation of the thin sections. The porosity is generally associated with the muscovite presenting altered texture or, as mentioned before, between the quartz grains (Fig. 4.7). Pore rarely exceeds 1µm of diameter and the majority is inferior to 0.33 µm, as they only represent one-pixel size.

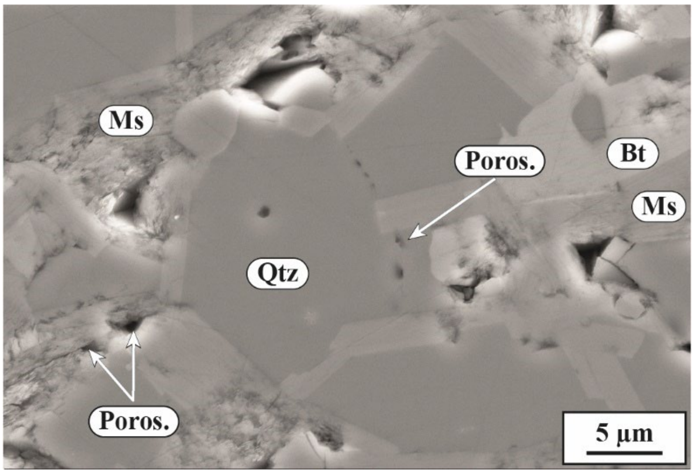

Figure 4.7: SEM (Inlens) image of the porosity inside the spotted schist matrix, generally located around and within altered phyllosilicates and between the quartz grains.

B) Reactive percolation experiment

A summary of the settings for the experiment is reported in Table 4.2. All images of the experimental product are parallel to the fluid flowing from top to bottom.

Temperature	300	
Duration (days _ hours)	37 _ 877	
Fluid composition	2.40 wt% B_2O_3	2.36 wt% B_2O_4
Core length (cm)	4.07	
Core diameter (cm)	0.56	
Flow rate (mL/h)	8.4×10^{-3}	
Water / rock (cm^3)	678.5 / 1.0	
Initial mineral composition	white micas, Qtz, Bt, Tur, Sid, Apt, Alb, Fe-Ti ox, Brl	
Identified neoformed minerals	Fay, Tur, ? (fibrous mineral)	

Table 4.2: Summary of the settings for the reactive percolation experiment.

1/ Permeability evolution

The evolution of the permeability and the inlet pressure during the experiment are reported in Fig. 6. Attempts to measure permeability before the start of the experiment were unsuccessful. Hence, we consider the sample permeability to be lower than 2×10^{-20} m^2, the lowest permeability value measured with this experimental device (Panasqueira unaltered granite by Launay et al. 2019). In order to force the fluid to circulate in the rock core, the injection pressure was set at 280 bars. This pressure not only ensures a high ΔP between the two pumps managing fluid circulation, but also reduces the effective pressure (difference between the pressure in the environment and the pressure inside the pores of the rock) received by the sample (Fig. 4.8A). However, these conditions did not allow the fluid to circulate through the sample and the permeability measurements do not reflect the petrophysical properties of the sample. After 38 hours, the fluid suddenly began to circulate through the sample. Due to this rapid increase in permeability (Fig. 4.8B) and in order to maintain a constant flow rate, the inlet pressure had to be lowered from 280 to 202 bar in the space of 24 hours (Fig. 4.8A). From hours 62 to 624 (26th day), the calculated permeability remained at a plateau value of around 1.7×10^{-16} m^2 (Fig. 4.8B). From day 26, the calculated permeability began to decrease very slightly. This decrease became increasingly significant from the 33rd day (812 h) and 2 days later (860 h) the fluid stopped circulating in the rock. The system became completely impermeable again, despite a return to the initial ΔP conditions (Fig. 4.8A). Investigation of the capillaries after the experiment revealed that this apparent drop of permeability was due to the formation of a clog inside the outlet capillary.

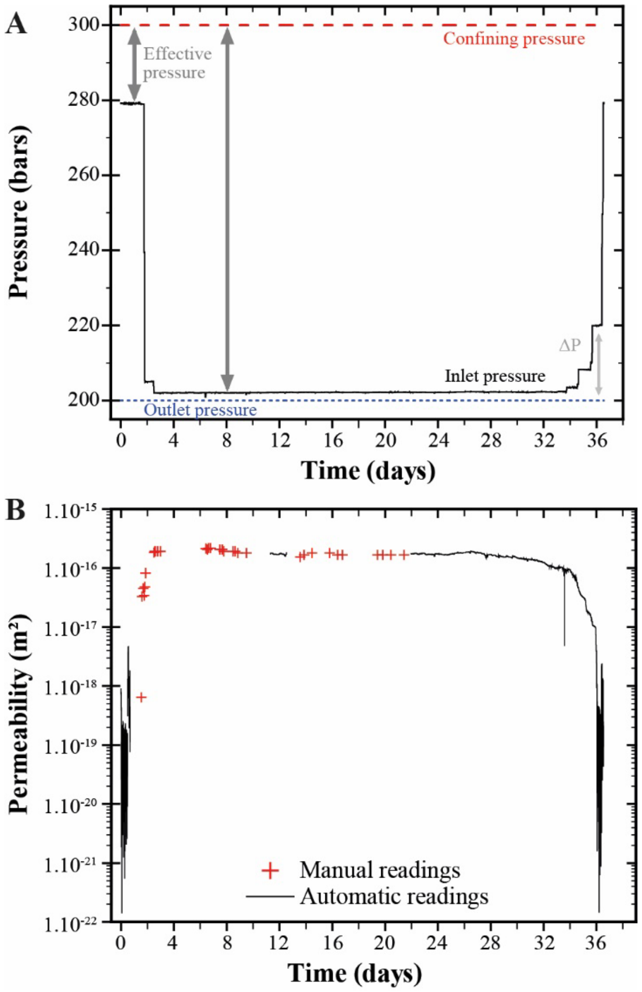

Figure 4.8: (A) Variation of the different pressures during the experiment. P_{conf} and P_{out} were maintained at 300 and 200 bars respectively and P_{in} was changed in order to maintain a constant flow. (B) Variation of the permeability as a function of time. Manual readings are reported where automatic ones failed to register.

2/ Macroscopic observations

Figure 4.9A is a photo of the inlet end of the gold capsule containing the spotted schist still installed in the experimental device. During the experiment, the gold capsule became deformed and showed numerous concave patterns all over its surface. Large depressions start at the beginning of the core and develop in the direction of fluid flow. These structures, sometimes ramified, are penetrative up to 4 mm into the sample and indicate the development of wormholes inside the core. (e.g. (Szymczak & Ladd 2009; Vialle et al. 2014). Throughout the first centimetre of the core, there are also small pits on the surface of the capsule, suggesting a negative of the original spots in the spotted schist. The inlet end of the core takes on a brick-red tone and a muddy texture, making the original textures of the spotted schist unrecognisable (Fig. 4.9B). The inlet section is uneven, deeper on the sides and particularly above the wormholes formed by the jacket. The outlet section is unaffected by these changes, with the original texture still fully visible (Fig. 4.9C). Those observations indicate significant dissolution processes at the start of the fluid circulation through the rock and a focus of those reactions on the border of the core.

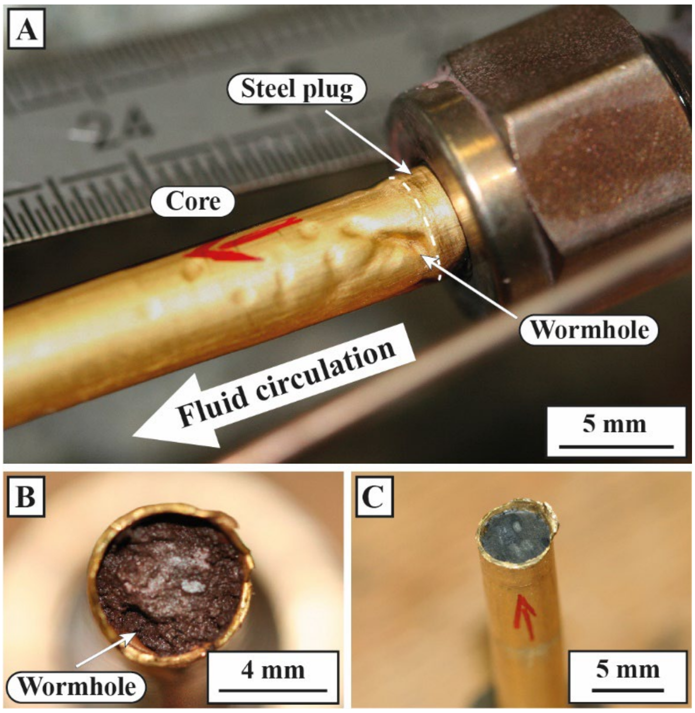

Figure 4.9: (A) Photo of the inlet end of the gold jacket containing the core after the experiment and still attached to the apparatus. At the intersection between the steel plug and the core, dissolution pits and wormholes are visible and are highlighted by the jacket deformation. (B) Photo of the inlet section of the core. (C) Photo of the outlet section of the core.

3/ General organisation of the alteration

Figure 4.10A is a reconstructed SEM view of the core of which was applied the "*PorosCount*" code in order to visualise the general organisation of the porosity (Fig. 4.10B). Zones with less than 5% porosity are considered to be no different to the original mottled shale and are shown in black. The more porous zones are concentrated at the edges of the core, particularly near the inlet. Extending up to 2 mm into the core, their surface area tends to diminish closer to the outlet. In the first 2 centimetres, porosity is organised around large rounded zones (Fig. 4.10C) between 500 µm and 2 mm in diameter and characterised by porosity ranging from 60 to 90%. Around these rounded zones, porosity drops sharply to around 25% and remains constant for several 100s of micrometres, then gradually decreases to < 5% (Fig. 4.10D).

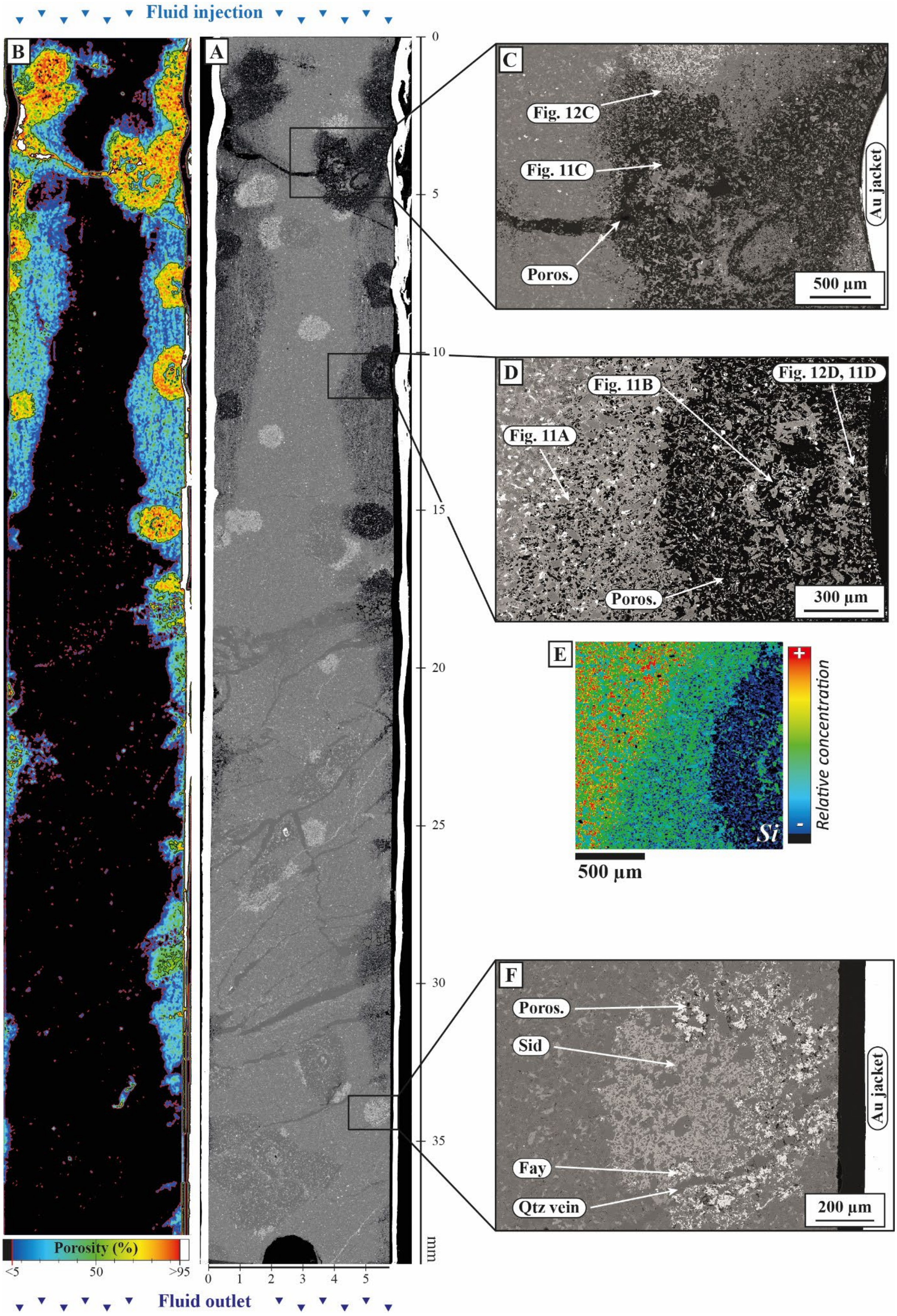
Fluid injection
B
A
0
5
10
15
20
25
30
35
mm
C
Fig. 12C
Fig. 11C
Poros.
Au jacket
500 µm
D
Fig. 11B
Fig. 12D, 11D
Fig. 11A
Poros.
300 µm
E
+
-
Relative concentration
Si
500 µm
F
Poros.
Sid
Fay
Qtz vein
Au jacket
200 µm
Porosity (%)
<5
50
>95
0
1
2
3
4
5
Fluid outlet

Figure 4.10: (A) SEM panorama of the reacted core. (B) Porosity map of the reacted core obtained through image analysis. (C) SEM image of a large high porosity (in black) zone located near the inlet of the core. (D) SEM image of a high porosity zone and the matrix around it. (E) Elemental mapping of Si acquired on (D). (F) SEM image of a carbonate spot near the outlet of the core, presenting mineralogical changes on its right border. All images are oriented in the same way, with the inlet upward and outlet downward.

In the last few centimetres of the core, porosity is more limited, appearing only around the quartz veins intersecting the edges of the core. Elemental mapping of a space containing a zone of high porosity and an unaltered zone (Fig. 4.10D) shows that porosity is directly correlated with Si concentration (Fig. 4.10E). Indeed, the areas with abnormal porosity compared with the original rock are completely depleted of quartz. The rounded areas where porosity is concentrated are therefore former quartz spots, and the surrounding areas correspond to the schist matrix initially containing around 20 wt% quartz. The carbonate spots only show alteration when they are adjacent either to the porous zones described above, or to the edge of the capsule. These alterations are generally associated with an average porosity of 8%.

1/ Mineralogical evolution

The transition from an unaltered spotted schist matrix to a quartz-free matrix takes place in less than 100µm, in which the quartz becomes increasingly rounded until it disappears completely (Fig. 4.11A). This absence of quartz also concerns solid inclusions in tourmalines, white micas, biotite and beryl. Apart from this absence of quartz, no other mineralogical or textural changes are present in the matrix located far from the border of the core. Dissolution also affects all the quartz veins intersecting the edge of the core, whose individual quartz grains become rounded and non-joining. In the innermost parts (> 1 mm from the edge of the core), dissolution is less intense and is mainly concentrated in the intergranular spaces. In areas of high porosity or close to (< 50µm) the edge of the capsule, the biotite develops xenomorphic contours and alters along its cleavage plane. In the large crystals that make up the core of the old quartz spots, the contours of the white micas begin to alter and sometimes show overgrowth appearing brighter under SEM observation (Fig. 4.11B). This overgrowth also forms around the bites and along their cleavage planes, highlighting the ghosts of fully altered crystals. Overall, the tourmaline is little affected by the alteration of the schist, and the few, limited textural variations observed are located in areas of high porosity. The smallest crystals present in the zones of high porosity close to the inlet (Fig. 4.10C) show dissolution pits that can penetrate up to 1 µm into the mineral (Fig. 4.11C). Further downstream (Fig. 4.10D), the tourmalines no longer show dissolution figures, but fibrous overgrowth of 1 to 2 µm, parallel to the elongation axis of the crystals (Fig. 4.11D). Due to the small size of the tourmaline overgrowth, only two microprobe analysis gave coherent composition. Represented in Fig. 4.6C to F, the experimental tourmaline compositions belong to the alkali-deficient group, close to the foitite end-member (see Appendix 18). From a distance of 1.5 cm from the inlet, the tourmalines no longer show any particular textures. Cathodoluminescence observations confirmed the presence of beryl in the centre of high porosity zones and kaolinite in altered quartz veins (see Appendix 23).

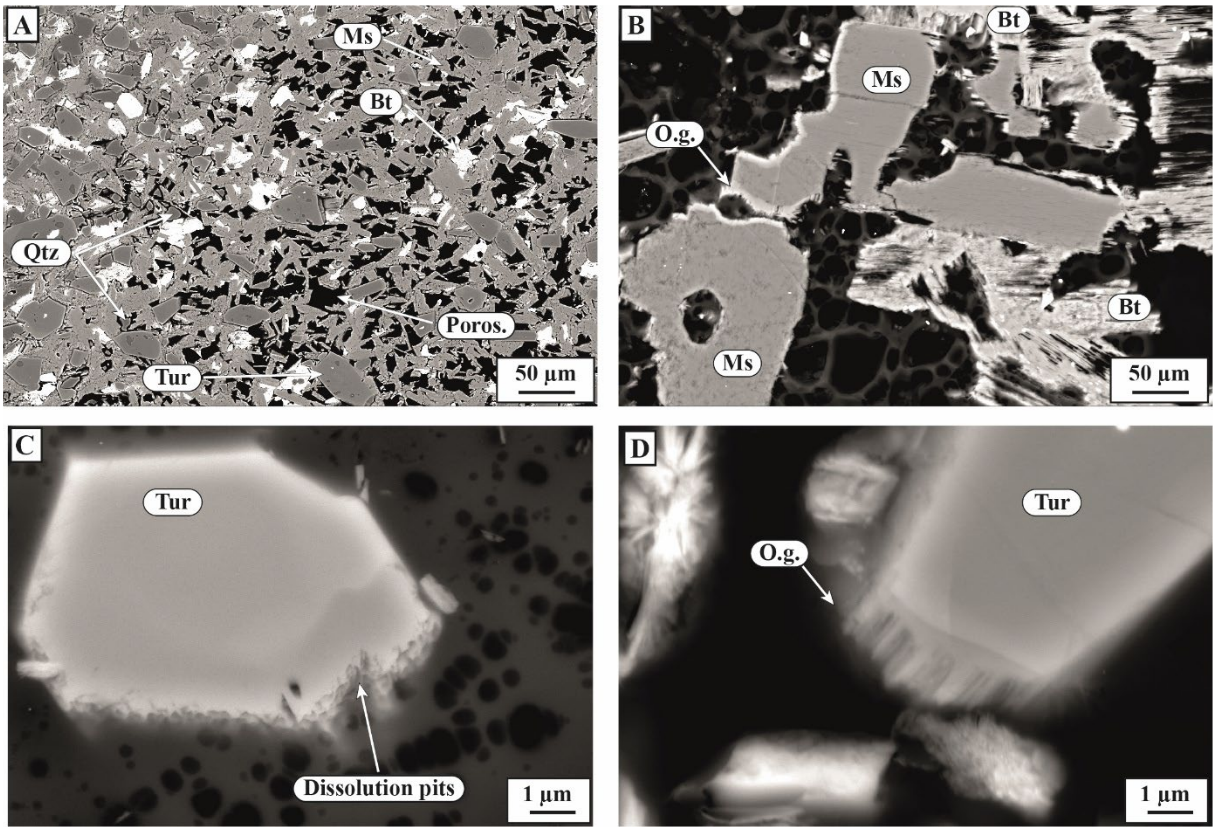

Figure 4.11: SEM images of the reacted core. Their position in the core is indicated in Figure 4.10. (A) Transition from an unaltered matrix to a porous matrix without quartz. (B) Large crystals of biotite and muscovite in a high porous zone. Biotite is altered in its centre, following the cleavage planes. Muscovite have xenomorphic contours and present a thin bright overgrowth. (C) Tourmaline crystal near the inlet end of the core presenting dissolution pits on one end. (D) Tourmaline longitudinal section in a high porous zone located further down compared to (C), with a fibrous tourmaline overgrowth developed on one end.

In order to gain a better understanding of the alteration sequence affecting the carbonate spots, we first focus on the one located furthest down the core, in the zones of weak alteration (Fig. 4.10F). Its right edge, close to the border of the core, shows the presence of brighter minerals identified as the olivine end-member fayalite (Fe_2SiO_4), and is associated with a more pronounced porosity. This mineralogical transformation also propagates along the quartz vein intersecting the spot, which is in the process of dissolution. Figure 4.12A shows that the fayalitisation of the siderite occurs by pseudomorphism and proceeds by a reaction interface moving through the parent carbonate. The composition of the fayalite (Table 4.3, Appendix A24 for detailed compositions) also contains Mn (tephroite, Mn_2SiO_4) and Mg (forsterite, Mg_2SiO_4) and the resulting solid solution can be described as a $Fa_{85}Tep_{10}Fo_5$ (Fig. 4.12B). The sum of the oxide composition of fayalite is around 95 % instead of 100%. This difference may be caused by the presence of a non-analysed element, such as boron, or by the presence of microporosity as often observed during pseudomorphism reaction (Putnis 2002, 2015; Jonas et al. 2014). We also suspect that due to the low temperature of the experiment, the crystallised olivine may contain invisible inclusions of hydrated minerals such as serpentine. In the most upstream parts, this neoformed fayalite is itself transformed into a fibrous mineral aggregate less than 0.5 µm long. This transformation is only visible when the fayalite is in contact with a zone of high porosity (Fig. 4.12C). These fibers then replace the fayalite contained in the contact zone between the two spots and crystallise around the minerals still present (tourmaline, white

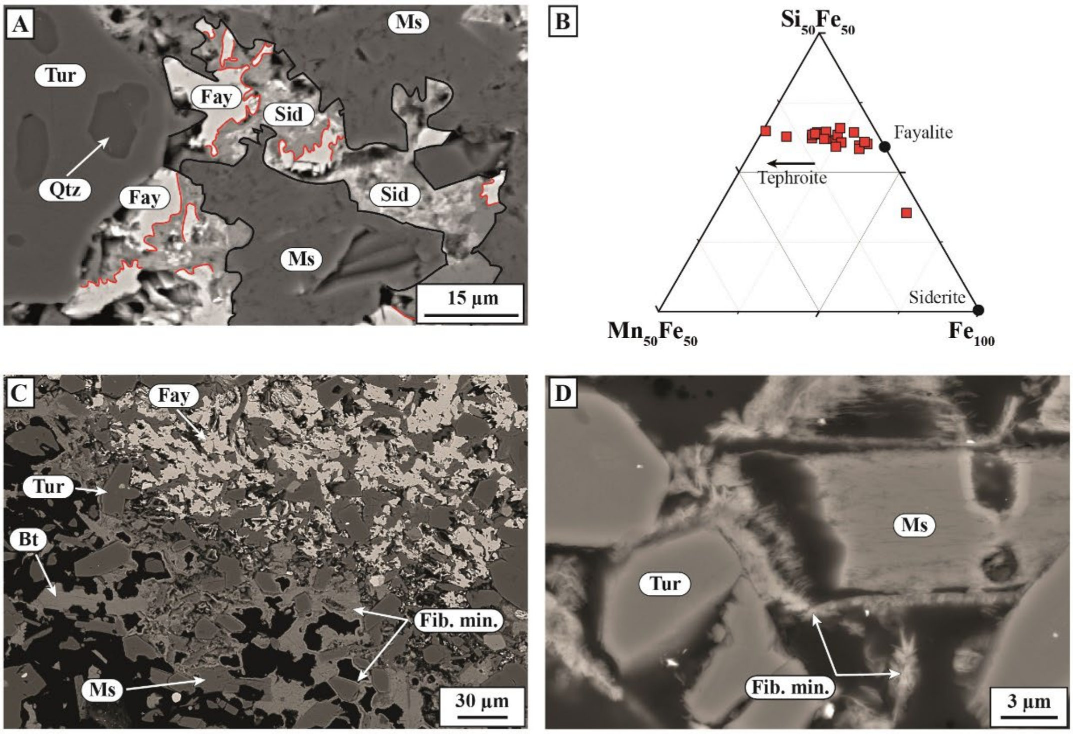

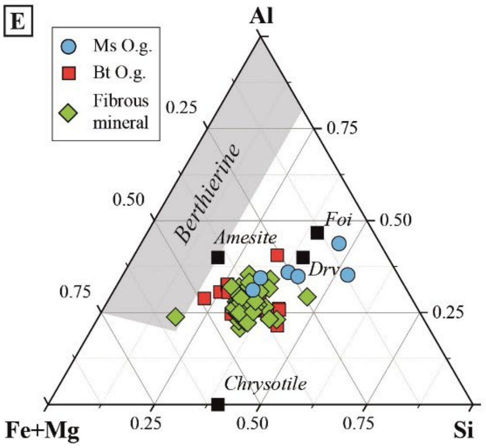

Figure 4. 12:(A) SEM image showing highlighting the presence of a dissolution-precipitation front between the original siderite and the neoformed fayalite. (B) Fayalite composition in the Fe-Mn$_{50}$Fe$_{50}$-Si$_{50}$Fe$_{50}$ ternary diagram. (C) SEM image showing the transition from fayalite to the fibrous mineral when approaching the high porosity zones. (D) SEM image showing the fibrous mineral growing around tourmaline and muscovite and filling the porosity caused by muscovite dissolution. (E) Si-Al-Fe+Mg ternary diagram showing the composition of the fibrous mineral and overgrowth over biotite and muscovite along with tourmaline and serpentine end-members. The three groups have similar proportion in Si, Al and Fe.

micas and biotite). This fibrous mineral is also found at the centre of all the areas of high porosity. For those not associated with fayalite, the fibers form small aggregates in the middle of the porosity formed by the dissolution of quartz. For those associated with fayalite, in addition to the aggregates, the fibers grow around the other minerals (Fig. 4.12D). When the mineral begins to dissolve, the fibrous mineral outlines its former contour and grow into the newly formed porosity. Microprobe analysis performed on those fibers, show the same chemical properties as in the biotite and white micas overgrowth. This mineral is characterised by approximately 30 wt% FeO, 28 wt% SiO_2, 20 wt% Al_2O_3, 6 wt% MgO and 2 wt% MnO for a total around 86 wt% (Table 4.3, Fig. 4.12E, detailed compositions in Appendix A25). RAMAN analyses carried out on these aggregates did not make it possible to identify the mineral because of its low crystallinity. Considering that the core was injected with a B-rich solution, diverse B-bearing minerals were considered as a potential candidate to match the fibers composition. However, it contains too much Fe and not enough Al to be an alkali-deficient tourmaline, there is too much Si and the sum Fe+Al is too low to be a grandidierite ((Mg, Fe)(AlFe^{3+})$_3$(SiO$_4$)(BO$_3$)O$_2$). As those fibers are an alteration product from olivine, serpentine composition, such as an amesite (Mg$_2$Al(AlSiO$_5$)(OH)$_4$), berthierine ((Fe^{2+},Fe^{3+},Al)$_3$(Si,Al)$_2$O$_5$(OH)$_4$) and chrysotile (Mg$_3$(Si$_2$O$_5$)(OH)$_4$)were also considered but are too poor in Si to explain the experimental compositions.

Mineral	Fayalite		Fibrous mineral	
n	22		57	
SiO_2	24.94	(2.69)	27.69	(4.6)
TiO_2	0.16	(0.26)	0.20	(0.3)
Al_2O_3	0.39	(0.44)	20.80	(7.96)
FeO_{total}	60.19	(5.24)	30.35	(4.88)
MgO	2.05	(1.02)	5.70	(1.93)
MnO	7.20	(3.58)	1.60	(0.74)
CaO	0.07		0.12	(0.05)
Na_2O	0.10		0.13	(0.08)
K_2O	0.13	(0.1)	0.47	(0.89)
Cl	*b.d.l*		0.08	(0.07)
F	*b.d.l*		*b.d.l*	
Total	94.70		86.29	
Si	0.91	(0.08)		
Ti	0.00	(0.01)		
Al	0.02	(0.02)		
Fe	1.84	(0.22)		
Mg	0.11	(0.06)		
Mn	0.22	(0.11)		
Ca	0.00			
Na	0.01			
K	0.01	(0)		
Cl				
F				
O	4.00			
Fay%	0.85	(0.06)		
Teph%	0.10	(0.05)		
Forst%	0.05	(0.03)		

Table 4.3: Average composition of the neo-formed fayalite and fibrous mineral.

Rock		Spotted schist	Exp. Core
SiO2	%	58.88	49.95
Al2O3	%	18.92	21.36
Fe2O3$_{tot}$	%	6.96	7.21
MnO	%	0.14	0.14
MgO	%	2.44	2.57
CaO	%	0.24	0.20
Na2O	%	0.47	0.52
K2O	%	5.24	5.53
TiO2	%	0.91	0.94
P2O5	%	0.18	0.15
PF	%	3.36	9.23
Total	%	97.72	97.80
H_2O_{tot}	%	2.21	3.6
FeO	%	4.48	4.82
S$_{tot}$	%	0.03	0.05
B	*µg/g*	4480	5230

Table 4.4: Result for the major elements of the whole rock analysis of the spotted schist and the experimental core.

2/ Chemical evolution

The whole-rock analysis of half the core shows few significant differences with the composition of the initial spotted schist (Table 4.4). Given the heterogeneity of the rock and the fact that the fluid contained only water and boron, any over-concentration of less than 5 wt% in a major element is accounted for as mineralogical differences between the two samples. The only notable differences show depletion in SiO$_2$ (49.9 instead of 58.9 in the mottled schist) and an enrichment in volatile elements (loss on ignition representing 9.2 wt% versus 3.4 wt% initially) in the core compared to the spotted schist.

Twenty-four aliquots of outlet fluid were sampled at different times over the entire experiment. The data yield the average concentration of the effluent between two sampling events. The results for B, Na, Al, SiO$_{2(aq)}$, K, Mn and Fe are presented in Figure 4.13 and take into account the dilution correction. Concentration of the first fluid sample should be considered as a minimum bracket, because of the presence of ultrapure water injected during the heating

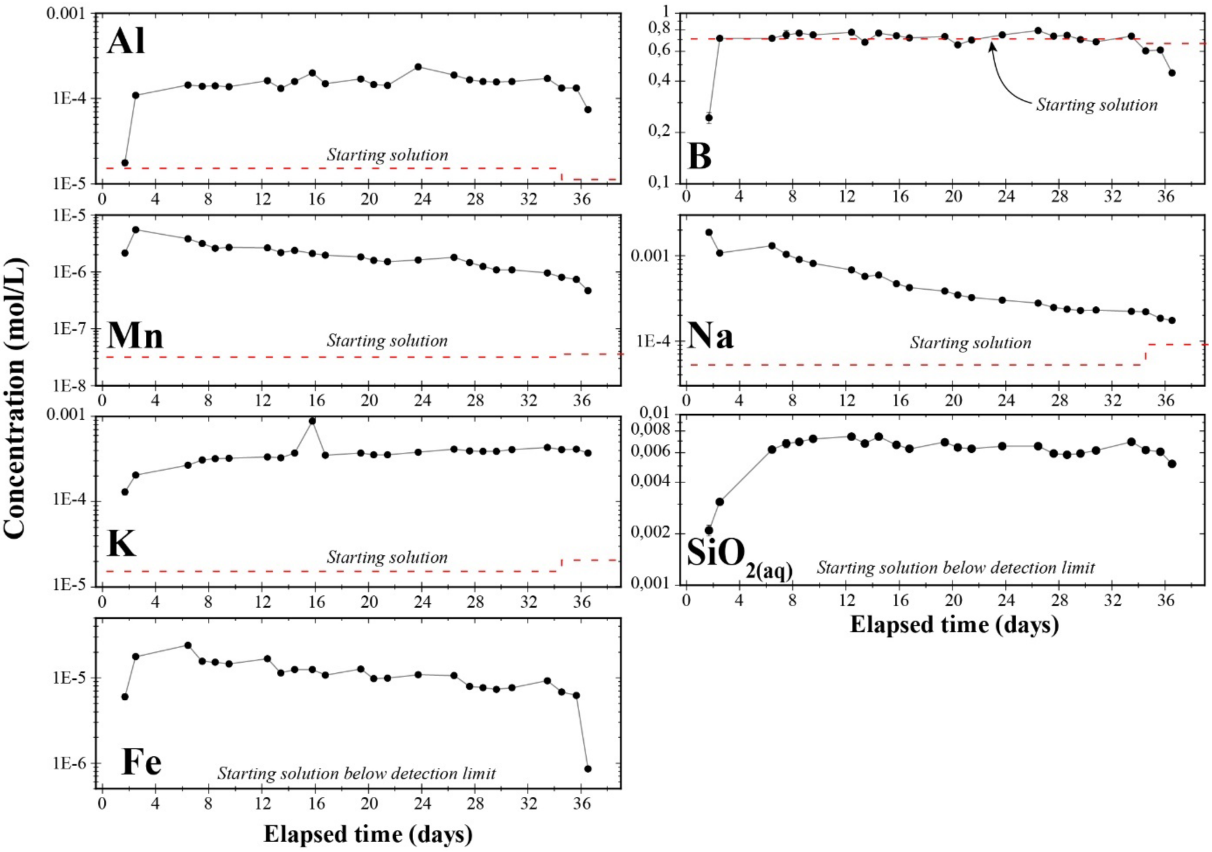

Figure 4.13:Outlet fluid composition in Al, B, Mn, Na, K, $SiO_{2(aq)}$ and Fe during the experiment, compared to the concentration measured in the two starting fluid

and remaining in the capillaries and sample before the first injection of the solution. Consequently, this sample is more diluted than the others, but as the total volume of water is unknown, it was also corrected on the basis of 10 mL. Raw concentrations and corrected ones for all elements are presented in Appendix 26. Analysis for Ti, Br and DIC concentrations were below detection limits in all the samples.

Boron concentration is mostly conserved during the totality of the experiment, reflecting no to little B-bearing mineral precipitation or dissolution. Outlet concentrations of Na, Al, K, Mn and Fe are systematically higher than the injected amount by one or two orders of magnitude. Al, K and Fe remain globally constant over the time of the experiment with the exception of the last sample showing a sharp decrease in Fe and more slightly in Al. Without any following samples, it is difficult to assess if this drop corresponds to a general tendency or an isolated value. Mn and Na concentration decrease over time and reach a total drop of nearly one order of magnitude at the end of the experiment. Finally, $SiO_{2(aq)}$ is the most concentrated element in the outlet fluid after B. Its concentration rises quickly during the first week and reaches a plateau value around 6.5×10^{-3} mol/L for the rest of the experiment.

The behaviour of those elements is directly correlated to the reactions impacting the core. All the elements are rapidly enriched in the output solution and vary little over the course of the experiment, indicating that the various forms of alteration observed have taken place throughout the experiment. The high concentration in $SiO_{2(aq)}$ is supported by the intense quartz leaching observed in the core. K reflects the biotite and muscovite dissolution, along with Al which is also impacted by the fibrous mineral precipitation. Mn is mainly concentrated in the carbonate spot, but is not entirely conserved during the fayalitisation. Consequently, Mn concentration in the fluid is dependent of the carbonate spot alteration and the slight decrease observed indicate a reduction of this alteration over time. Albite and tourmaline are the only mineral containing Na as a major element. Tourmaline remain globally stable during the experiment, whereas albite is either totally dissolved or transformed into kaolinite. As such Na concentration in the fluid is a proxy for albite alteration and indirectly for the quartz spots and veins dissolution as the albite is mainly found in those textures. The decrease of Na in the outlet fluid show that the dissolution of the spots and veins took place during the firsts weeks. After the complete leaching of the spot, only the matrix (containing very few relics of albite) and the veins were subject to quartz dissolution. This resulted in a decrease of the Na concentration in the fluid.

III- Discussion

A) Permeability evolution

1/ A highly impermeable schist

As predicted by the study of its petrophysical properties, the spotted schist is a highly impermeable rock due to its low to no porosity with a diameter superior to 6 nm (detection limit of the MIP). We can question whether those petrophysical properties are inherent to the schist or if it is the result of the B-metasomatism impacting the spotted schist. Bagde (2000) performed MIP measurement on three different schists: a quartz micaschist, a quartz micaschist with quartz veins and a biotite schist. The result shows that the porosity is ranging from 1.37 to 1.93 % in biotite schist and is lower in quartz micaschist, the minimum being in the sample with quartz veins where the porosity ranges from 0.07 to 1.4 %. Those results are confirmed by Zeng et al. (2022) study, finding an average porosity of 1.46 % in a micaschist, with a pore radius generally inferior to 0.5 µm. However, as mentioned before, none of those studies questioned their results in terms of pore connectivity. With regards with our MIP measurements, those values might be dependent of the total available surface of the sample in contact with mercury during the analysis. Nevertheless, the values are in good agreement with the ones determined by water absorption at atmospheric pressure (Barros et al. 2014; Rao et al. 2022). Thus, the schist, without hydrothermal alteration, is already a weak porous media, with a probable low permeability. In unfractured metamorphic rocks, the permeability is generally considered to be ranging from 1×10^{-21} to 1×10^{-17} m^2 (Ingebritsen & Appold 2012). Launay et al. (2019) measured the permeability of different rock samples from Panasqueira in a heated Paterson apparatus equipped with a pore-fluid pressure system enabling measurements under P-T conditions. Measurements performed on the Beira schist allowed the estimation of permeability around 1.52×10^{-20} m^2 at 400°C.

The unaltered Beira schist is a metasedimentary rock mainly composed of biotite-chlorite, quartz, sericite and albite (Launay et al. 2018). In the spotted schist near the mineralised veins, albite is only present as inclusions in the quartz spots and veins and biotite is no more the main constituent of the rock. Furthermore, in the matrix, biotite proportion tends to be lower where tourmaline is more concentrated. Those observations are in favour of replacement reactions implying the consumption of biotite and albite to form tourmaline. Lecumberri-Sanchez et al. (2017) already proposed such reactions but considered Na as provided by the fluid and not by the mineral. By considering the two end-members annite (R1) and siderophilite (R2) and a variant of R1 with no albite (R3), three tourmalinisation reactions can be written (Table 4.5). All of them implies that Al^{3+} and $B(OH)_3$ are provided by the fluid and that K^+ remains in the fluid as no potassic feldspar have been observed in the spotted schist. Based on the intergrowth between quartz and tourmaline in the rock, the Si consumed in R3 is considered as an aqueous species (H_4SiO_4). The relative volume change ΔV (%) induced by these reactions can be calculated from the stoichiometric coefficients and molar volumes of the solid phases (Pollok et al. 2011). Calculations were performed using the molar volumes of minerals in the online thermodynamic database Thermoddem (Blanc et al. 2012a), except for schorl, whose properties came from van Hinsberg & Schumacher (2007). The calculated volume changes for each tourmalinisation reactions are summarised in Table X. Reaction R1 and R3 are characterised by volume increase of 30 and 114 %, whereas R2 does not induce volume changes. This suggests that tourmalinisation reactions have impacted the petrophysical properties of the spotted schist, by closing the already low porosity.

Tourmalinisation reaction		ΔV (cm^3/mol)	ΔV (%)
(R1)	$1\ KFe_3AlSi_3O_{10}(OH)_2 + 1\ NaAlSi_3O_8 + 3\ B(OH)_{3(aq)} + 4\ Al^{3+}_{(aq)} + 2\ H_2O \rightarrow NaFe_3Al_6Si_6O_{18}(BO_3)_3(OH)_4 + K^+_{(aq)} + 11\ H^+_{(aq)}$	+ 76.3	+ 30
(R2)	$3\ KFe_2Al_3Si_2O_{10}(OH)_2 + 2\ NaAlSi_3O_8 + 6\ B(OH)_{3(aq)} + 1\ Al^{3+}_{(aq)} \rightarrow 2\ NaFe_3Al_6Si_6O_{18}(BO_3)_3(OH)_4 + 3\ K^+_{(aq)} + 8\ H_2O$	+ 9.4	+ 1
(R3)	$1\ KFe_3AlSi_3O_{10}(OH)_2 + 3\ B(OH)_{3(aq)} + 5\ Al^{3+}_{(aq)} + Na^+_{(aq)} + 3\ H_4SiO_{4(aq)} \rightarrow NaFe_3Al_6Si_6O_{18}(BO_3)_3(OH)_4 + K^+_{(aq)} + 2\ H_2O + 15\ H^+_{(aq)}$	+ 176.4	+ 114

Table 4.5: Molar volume changes (ΔV) induced by tourmaline-forming reaction. Calculated with Thermoddem and data from van Hinsberg & Schumacher (2007).

2/ Vein opening through hydraulic fracturing

Porosity mapping (Fig. 10B) in the core after the experiment shows clearly that quartz dissolution is concentrated in the edge of the sample. The center of the core remains largely intact, even in the vicinity of the injection zone. The evolution of permeability reflects an abrupt transition from a totally impermeable system to one whose high permeability remains constant for over 24 days, despite the formation of porosity in the sample. These observations suggest that permeability measurement does not correspond to a pervasive circulation of the fluid through the rock but to the channelling of the fluid between the sample and the Au-jacket. At the beginning of the experiment, in order to force the fluid to percolate into the sample, the injection pressure was set to a high ΔP between the two pumps (ΔP = 80 bar) while minimising the effective pressure ($P_{effec} = P_{in} - P_{conf}$=20 bar). The latter can have a major impact on rock permeability. For example, subjecting spillites and epidosites to effective pressures to 50 MPa at room temperature is known to reduce their permeability by up to 80% (Brett-Adams et al. 2021). However, the low P_{effec} fixed in this experiment was not sufficient enough to increase significantly the permeability of the schist. Instead, the P_{fluid} building up at the entrance of the core was high enough to overcome the difference with P_{conf}, thus, it is allowing the fluid to create a detachment between the sample and the Au jacket. Once open, this path remained unchanged for the entirety of the experiment. The permeability measured in this experiment therefore does not reflect variations in the petrophysical properties of the rock, but rather the dimensions of the detachment. Unintentionally, this experiment reproduces a vein opening through hydraulic fracturing with the associated wall-rock alteration.

In order to translate the flow rate into a fluid velocity comparable to natural data, it is necessary to estimate the surface area crossed by the fluid. In our experiment, this corresponds to the section of the channel formed between the Au tube deformed by the P_{fluid} and the core acting as an impermeable medium, i.e.:

$$S_{channel} = \pi * ((R_{core} + h)^2 - (R_{core})^2) \qquad \text{(Eq. 2)}$$

This means determining h, the gap formed between the core and the jacket. Fluid flow, under our experimental conditions, can be simplified as laminar fluid flow between two infinite parallel planes (linked to the core's cylindrical shape), caused by a pressure gradient. This configuration assumes that the gap h is constant on both sides of the core and along the entire length of the core. The flow, which can be calculated using the Couette-Poiseuille or Poiseuille plane model, is dependent on h, the distance between the two planes, such that:

$$Q = -\frac{2}{3} * \frac{l\left(\frac{1}{2}h\right)^3}{\eta} * \frac{\Delta P}{\Delta x} \qquad \text{(Eq. 3)}$$

With Q the flow rate (m^3/s), ΔP the pressure difference between outlet and inlet (Pa), η the water viscosity (9.32×10^{-5}Pa.s), Δx the length of the core (4.01×10^{-2} m) and l the width along z, considered here to be equal to the perimeter of the core (1.76×10^{-2} m). For the calculation, the flow rate corresponds to an average of the flows recorded by the pumps between days 22 and 26, and ΔP is therefore set at 2×10^{-5} Pa. This period corresponds to the permeability plateau at 1.7×10^{-16} m^2, before the effects of clogging affect the recordings. For those conditions, the space between the core and the jacket is estimated to be equal to 1.4×10^{-6} m, implying a channel section equal to 5×10^{-8} m^2. Consequently, the fluid velocity in the channel during the experiment is estimated to be around 4×10^{-3} m/s.

Zhou et al. (2007) study on the Cu-Au skarn and vein-type deposits of the Anhui Province (South China) reported that magmatic ore-forming fluids were channelled upward into faults, tiny fractures/veins and porous media with calculated velocities of 1.4 m/s, 1 to 1×10^{-6} m/s and 4×10^{-7} to 5×10^{-7} m/s, respectively. Fluid flow determined in veins in Sn-W deposits using crystal growth bands are around 1×10^{-4} m/s (Sizaret et al. 2009; Mahjoubi et al. 2016; Launay et al. 2018). Launay et al. (2018) performed a coupled textural and chemical study on tourmaline growth bands at Panasaqueira to constrain fluid flow in mineralised veins and altered wall-rock. The velocities obtained are in the same order of magnitude (10^{-4} to 10^{-3} m/s) than the calculated velocity in the channel and highlights a transport of metals in veins, largely dominated by advective processes (Dolejš 2015). Fluid flow in the altered wall-rock is slower and more pervasive (10^{-6} to 10^{-5} m/s), suggesting that element transport through the metasedimentary host rock was dominated by diffusion processes limited to the alteration halo. This distinction made in natural systems between the vein dominated by advection (high fluid velocity) and the wall-rock dominated by diffusion (low fluid velocity) is also valid in our experiment and explain the mineralogical evolution and organisation observed in the core.

B) Mineralogical evolution and alteration pattern

1/ *Alteration reactions*

The main form of alteration visible in the core is the intensive leaching of quartz by the injected solution. Experimental studies of Pichavant (1983) and Mar'ina et al. (1999) on quartz solubility indicate that the presence of, and increase in the concentration of H_3BO_3 (0 to 30 wt% B_2O_3) in solutions as well as temperature (400 to 700°C) and pressure (1 to 1.4 kbars) increase, enhance substantially the quartz solubility. Hence, at 400°C and 1.4 kbars, the quartz solubility in pure H_2O is around 2.4 g/L, whereas with 3.4 wt% B_2O_3 in the fluid the solubility ranged between 3.3 and 4.1 g/L. Study on the boron speciation in the system Na_2O–B_2O_3–SiO_2–H_2O also reports this increasing solubility of quartz in $B(OH)_3$ solution but was unable to identify any B-Si aqueous complex, probably due to a too weak RAMAN signal (Smirnov et al. 2005). Due to the quartz leaching, the outlet fluid is quickly enriched in $SiO_{2(aq)}$ and reach a plateau value. This behaviour can be explained either by a constant dissolution of the quartz during the experiment, implying that the concentration of the outlet solution is near c_{sat} the saturated concentration, or either by the constant precipitation of Si-bearing mineral. Three Si-bearing minerals were identified. (i) Among the reaction observed in the core, the fayalitisation of the siderite requires a contribution in SiO_2. The reaction is located near fluid pathways such as quartz veins or spots undergoing dissolution or near the border of the core. Siderite spots inside the core without any connection to such zones do not show any sign of alteration despite being in contact with quartz. As such, the fayalitisation is triggered by the interaction between the siderite and a $SiO_{2(aq)}$-bearing fluid, as written in the following reaction:

$$2\,FeCO_3 + H_4SiO_{4\,(aq)} \rightarrow Fe_2SiO_4 + 2\,CO_{2(aq)} + 2H_2O$$

However, the decreased of Mn in the fluid over time shows that the carbonate spot alteration is more and more limited during the experiment, an evolution that is not reported on the $SiO_{2(aq)}$ evolution. (ii) The fibrous mineral also contains Si in its composition, however, without proper identification it is hard to tell if its formation requires the consumption of $SiO_{2(aq)}$ from the fluid. (iii) Finally, as the experiment stopped due to a clog, we considered the potential precipitation of amorphous silica in the outlet capillary. PHREEQC simulations with the Thermoddem database (V1.10, Blanc et al. 2012) were run with the $SiO_{2(aq)}$ concentration measured at 200 bars, the pressure set by the outlet pump. The clog in the capillary was located outside of the autoclave, but near enough to be warmer than ambient temperature. Thus, a temperature of 40°C was set for the calculation. The saturation index curve calculated shows that amorphous silica is near equilibrium (SI ~0.4) with the outlet solution. Consequently, the precipitation of amorphous silica inside the capillary caused the concentration of the outlet fluid to be capped.

The alteration of the siderite into fayalite raises the problem of the CO_2 behaviour during the experiment. DIC measurement in outlet fluid are below the detection limit and no phases seem to incorporate carbon. It is possible that the stockage condition or/and the elapsed time between the sampling and the analysis have not allowed to preserve the DIC in the sampling tube. The DIC could also be transformed into organic molecules after the sampling. Another possibility is the formation of graphite instead of CO_2 during the fayalitisation. Indeed, fayalite formation from carbonate at a fixed temperature can be achieved either by decreasing P_{CO2} or by an important reduction of the environment (French 1971; Frost 1979). This second option implies a two-step reaction where firstly siderite reacts with quartz and vapour to form grunerite ($Fe_7Si_8O_{22}(OH)_2$), graphite and O_2 and then grunerite transformed into fayalite, quartz and vapour (Bonnichsen 1975; Frost 1979). However, the presence of grunierite, graphite or localised oxidation has not been found and, consequently, does not allow us to confirm the occurrence of those reactions.

2/ Longitudinal Vs Radial alteration fronts

The organisation of the alterations is directly dependent on the relationship between chemical reaction and mass transfer. This relationship can be visualised through the Damköhler number , $Da = \frac{k}{vc}$, with k the intrinsic reaction rate of a given reaction, v the fluid velocity from Darcy's law and c the solubility of the mineral in pure water (Osselin et al. 2016). If the reaction rate is very fast, nearly instantaneous, relative to the rate of transport (large Da), then fluid and rock are essentially in chemical equilibrium at any given point along the flow path (local equilibrium condition) (Ague 2014). In the case of a fluid flow inside a fracture, Szymczak & Ladd (2011) define the penetration length lp of the unsaturated fluid as $lp \propto \frac{Q}{2k(S)}$, with Q the flow rate, k the reaction rate and S the reactive surface area. In the case where Da is important, the unsaturated fluid is not able to penetrate deep inside the fracture because of the quick saturation in reactant near the fluid inlet. After a fast initial dissolution, the whole sample dissolves slowly, forming sharp solute and geochemical front on localised areas. On the other hand, a small Da corresponds to situations where the fluid velocity is more important than the reaction rate. As such, the system remains permanently out of equilibrium and the whole sample dissolves almost uniformly. Returning to the example of the fluid flow inside a fracture, the unsaturated fluid, in a low Da system, could penetrate deep inside the fracture (Szymczak & Ladd 2009).

At the beginning of the experiment, the fluid velocity was really low, almost nil, due to the impermeable nature of the spotted schist. The fluid reacted with the inlet section of the core in accordance to the reaction rate but quickly reached near saturation condition due to the non-renewal of the fluid. By approaching saturation, the dissolution rate of the minerals sharply drops (Szymczak & Ladd 2011) and resulted in a static system between the fluid and a barely altered rock. The channel formation drastically enhances the flow rate of the fluid and focused the majority of the flow in it, while most of the pore space is eventually bypassed. New alteration fronts are developed and can be classified into two groups with different behaviours in accordance to their Damköhler number.

In the border of the core, directly at the contact with the channel, the dissolution of quartz impacts the whole length of the core. The fluid is considered to be far-from equilibrium due to the high fluid velocity. Solutes (essentially $SiO_{2(aq)}$) are mobilised through advection and are unable to precipitate in the lower part of the sample, resulting in their exit from the system (net mass loss in SiO_2 reported in the whole rock analysis). In this reaction-limited environment (small Da), only dissolution occurs and forms a longitudinal alteration front. The fluid is gradually charged with solute as it moves through the channel toward the outlet. Its concentration slowly tends toward saturation, implying a decrease in distance to equilibrium. The result is a high level of dissolution near the inlet, which decreases the closer the fluid get to the outlet (Fig. 4.10A, B). The channel is not the only part of the core whose behaviour is explained by a small Da. Quartz spots and veins are characterised by a more important reactive surface area compared to the quartz contained in the matrix. As such the dissolution of those areas is easier and results in the creation of high flow zone inside the core. The flow rate in these zones remains slower than in the channel. Those conditions allow the other primary minerals to dissolve but also the neoformed fibrous mineral to precipitate (Fig. 4.12D). Tourmaline seems to be the only mineral whose reaction rate is fast enough to dissolve near the inlet (Fig. 4.11C) and still precipitate further down the core as an overgrowth (Fig. 4.11D).

In the matrix, the quartz dissolution allows the fluid to percolate inside the core. The fluid velocity is significantly lower, leading to a transport-limited regime and more localised reactivity. This result in the formation of sharp radial alteration front on localised areas (Fig. 4.11A). The alteration of the primary minerals occur more locally, as an interface controlled process (Ruiz-Agudo et al. 2014), close to equilibrium, with the neoformed minerals precipitating at the same location as the dissolution occurred. The fayalitisation of the siderite is a perfect example of such reaction where the synchronisation of the reaction fronts forms pseudomorphic mineral replacement. In those environments solutes are mobilised through diffusion. The development of those radial alteration fronts is facilitated by the formation of the high porous zone inside the matrix. Those zones serve as new pathways for the unsaturated fluid to percolate in the core and improve fluid flow locally resulting in the formation of an alteration front parallel to the fluid flow.

Conclusion

This study presented the result of a reactive percolation experiment of a $B(OH)_3$ brine at 300°C and 300 bars in a natural spotted schist in order to study the dynamic of the B-metasomatism. Due to the very low permeability of the rock and the low effective pressure fixed in the first days, the fluid was able to create and focus into a channel between the Au jacket and the core. Thus, the permeability measured in this experiment does not reflect variations in the petrophysical properties of the rock, but rather reproduces a vein opening through hydraulic fracturing with the associated wall-rock alteration. General observations and analysis of the core and outlet fluid after the experiment show a sharp increase in porosity along the channels due to quartz dissolution. Caused by the presence of $B(OH)_3$ in the fluid, this alteration is the only one affecting both the whole rock composition and the outlet fluid.

The localisation of the alteration is controlled locally by the relationship between the reaction rate and the fluid velocity. High flow zones, such as the channel, form a longitudinal alteration front where quartz leaching is predominant. In this reaction-limited environment, the solutes are mobilised through advection and leave the core without being able to precipitate further down. Alteration of the schist matrix corresponds to low flow zones where the limited transport by diffusion allows the formation of a sharp radial alteration front. The alteration of the primary minerals occurs more locally, forming interface coupled dissolution-precipitation (e.g. the pseudomorphism of siderite into fayalite). The different regimes described in this experiment (high flow zone dominated by advective processes Vs low flow zone dominated by diffusion processes) correlate well with the vein and wall-rock alteration described in natural environment.

References:

Ague, J.J. (2014) Fluid Flow in the Deep Crust. In Treatise on Geochemistry Vols. 1-15, Vol. 4, pp. 203–247. Elsevier.

Bagde, M.N. (2000) An investigation into strength and porous properties of metamorphic rocks in the Himalayas: A case study. Geotechnical and Geological Engineering, 18, 209–219.

Baksheev, I.A., Tikhomirov, P.L., Yapaskurt, V.O., Vigasina, M.F., Prokof'ev, V.Yu., and Ustinov, V.I. (2009) Tourmaline of the Mramorny tin cluster, Chukotia peninsula, Russia. The Canadian Mineralogist, 47, 1177–1194.

Barros, R.S., Oliveira, D.V., Varum, H., Alves, C.A.S., and Camões, A. (2014) Experimental characterisation of physical and mechanical properties of schist from Portugal. Construction and Building Materials, 50, 617–630.

Blanc, Ph., Lassin, A., Piantone, P., Azaroual, M., Jacquemet, N., Fabbri, A., and Gaucher, E.C. (2012a) Thermoddem: A geochemical database focused on low temperature water/rock interactions and waste materials. Applied Geochemistry, 27, 2107–2116.

——— (2012b) Thermoddem: A geochemical database focused on low temperature water/rock interactions and waste materials. Applied Geochemistry, 27, 2107–2116.

Bonnichsen, B. (1975) Geology of the Biwabik Iron Formation, Dunka River area, Minnesota. Economic Geology, 70, 319–340.

Brett-Adams, A.C., Diamond, L.W., Petrini, C., and Madonna, C. (2021) Influence of in-situ temperatures and pressures on the permeability of hydrothermally altered basalts in the oceanic crust. Tectonophysics, 815, 228994.

Buckman, J., Bankole, S., Zihms, S., Lewis, H., Couples, G., and Corbett, P. (2017) Quantifying Porosity through Automated Image Collection and Batch Image Processing: Case Study of Three Carbonates and an Aragonite Cemented Sandstone. Geosciences, 7, 70.

Caldevilla, P., González-Menéndez, L., Martín-Crespo, T., Vindel, E., Guedes, A., Berrezueta, E., Castañón, A.M., and Gómez-Fernández, F. (2023) The Peña do Seo W-Sn deposit, NW Iberia: Petrology, fluid inclusions and O-H-S isotopes. Ore Geology Reviews, 155, 105361.

Chen, P., Zeng, Q., Zhou, L., and Zhou, T. (2021) Fluid inclusion evidence for hydrothermal evolution of the Sadaigoumen porphyry Mo deposit on the northern margin of the north China Craton. Ore Geology Reviews, 134, 104145.

Chicharro, E., Boiron, M.-C., López-García, J.Á., Barfod, D.N., and Villaseca, C. (2016) Origin, ore forming fluid evolution and timing of the Logrosán Sn–(W) ore deposits (Central Iberian Zone, Spain). Ore Geology Reviews, 72, 896–913.

Codeço, M.S. (2019) Constraining the Hydrology at Minas da Panasqueira W-Sn-Cu, Portugal. Universität Potsdam, Postdam.

Codeço, M.S., Weis, P., Trumbull, R.B., Pinto, F., Lecumberri-Sanchez, P., and Wilke, F.D.H. (2017) Chemical and boron isotopic composition of hydrothermal tourmaline from the Panasqueira W-Sn-Cu deposit, Portugal. Chemical Geology, 468, 1–16.

Dolejš, D. (2015) Quantitative characterisation of hydrothermal systems and reconstruction of fluid fluxes: the significance of advection, disequilibrium, and dispersion p. 4. Presented at the SGA Proceedings 13th SGA Biennial Meeting.

Duchoslav, M., Marks, M.A.W., Drost, K., McCammon, C., Marschall, H.R., Wenzel, T., and Markl, G. (2017) Changes in tourmaline composition during magmatic and hydrothermal processes leading to tin-ore deposition: The Cornubian Batholith, SW England. Ore Geology Reviews, 83, 215–234.

Dutrow, B.L., and Henry, D.J. (2016) Fibrous Tourmaline: A Sensitive Probe of Fluid Compositions and Petrologic Environments. The Canadian Mineralogist, 54, 311–335.

Dutrow, B.L., and Henry, D.J. (2018) Tourmaline compositions and textures: reflections of the fluid phase. Journal of Geosciences, 99–110.

French, B.M. (1971) Stability relations of siderite (FeCO3) in the system Fe-C-O. American Journal of Science, 271, 37–78.

Frikken, P.H., Cooke, D.R., Walshe, J.L., Archibald, D., Skarmeta, J., Serrano, L., and Vargas, R. (2005) Mineralogical and Isotopic Zonation in the Sur-Sur Tourmaline Breccia, Río Blanco-Los Bronces Cu-Mo Deposit, Chile: Implications for Ore Genesis. Economic Geology, 100, 935–961.

Frost, B.R. (1979) Metamorphism of iron-formation; parageneses in the system Fe-Si-C-O-H. Economic Geology, 74, 775–785.

Harlaux, M., Kouzmanov, K., Gialli, S., Laurent, O., Rielli, A., Dini, A., Chauvet, A., Menzies, A., Kalinaj, M., and Fontboté, L. (2020) Tourmaline as a Tracer of Late-Magmatic to Hydrothermal Fluid Evolution: The World-Class San Rafael Tin (-Copper) Deposit, Peru. Economic Geology.

Hawthorne, F.C., and Henrys, D.J. (1999) Classification of the minerals of the tourmaline group. European Journal of Mineralogy, 11, 201–216.

Henry, D.. J., and Dutrow, B.L. (2012) Tourmaline at diagenetic to low-grade metamorphic conditions: Its petrologic applicability. Lithos, 154, 16–32.

Henry, D.J., and Dutrow, B.L. (1996) Chapter 10. Metamorphic Tourmaline and its Petrologic Applications. In E.S. Grew and L.M. Anovitz, Eds., Boron _ Mineralogy, Petrology and Geochemistry Vol. 33, pp. 503–558. De Gruyter, Berlin, Boston.

Henry, D.J., and Guidotti, C.V. (1985) Tourmaline as a petrogenetic indicator mineral: an example from the staurolite-grade metapelites of NW Maine. American Mineralogist, 70, 1–15.

Henry, D.J., Kirkland, B.L., and Kirkland, D.W. (1999) Sector-zoned tourmaline from the cap rock of a salt dome. European Journal of Mineralogy, 11, 263–280.

Henry, D.J., Novak, M., Hawthorne, F.C., Ertl, A., Dutrow, B.L., Uher, P., and Pezzotta, F. (2011) Nomenclature of the tourmaline-supergroup minerals. American Mineralogist, 96, 895–913.

Huber, M.L., Perkins, R.A., Laesecke, A., Friend, D.G., Sengers, J.V., Assael, M.J., Metaxa, I.N., Vogel, E., Mareš, R., and Miyagawa, K. (2009) New International Formulation for the Viscosity of H2O. Journal of Physical and Chemical Reference Data, 38, 101–125.

Ingebritsen, S.E., and Appold, M.S. (2012) The Physical Hydrogeology of Ore Deposits. Economic Geology, 107, 559–584.

Ingebritsen, S.E., and Gleeson, T. (2015) Crustal permeability: Introduction to the special issue. Geofluids, 15, 1–10.

Jonas, L., John, T., King, H.E., Geisler, T., and Putnis, A. (2014) The role of grain boundaries and transient porosity in rocks as fluid pathways for reaction front propagation. Earth and Planetary Science Letters, 386, 64–74.

Lasaga, A.C. (1998) Kinetic Theory in the Earth Sciences, 811 p. Princeton university press, Princeton.

Launay, G., Sizaret, S., Guillou-Frottier, L., Gloaguen, E., and Pinto, F. (2018) Deciphering fluid flow at the magmatic-hydrothermal transition: A case study from the world-class Panasqueira W–Sn–(Cu) ore deposit (Portugal). Earth and Planetary Science Letters, 499, 1–12.

Launay, G., Sizaret, S., Guillou-Frottier, L., Fauguerolles, C., Champallier, R., and Gloaguen, E. (2019) Dynamic Permeability Related to Greisenization Reactions in Sn-W Ore Deposits: Quantitative Petrophysical and Experimental Evidence. Geofluids, 2019, 1–23.

Launay, G., Branquet, Y., Sizaret, S., Guillou-Frottier, L., and Gloaguen, E. (2023) How greisenization could trigger the formation of large vein-and-greisen Sn-W deposits: A numerical investigation applied to the Panasqueira deposit. Ore Geology Reviews, 153, 105299.

Lecumberri-Sanchez, P., Vieira, R., Heinrich, C.A., Pinto, F., and Wälle, M. (2017) Fluid-rock interaction is decisive for the formation of tungsten deposits. Geology, 45, 579–582.

LeFort, D., Hanley, J., and Guillong, M. (2011) Subepithermal Au-Pd Mineralization Associated with an Alkalic Porphyry Cu-Au Deposit, Mount Milligan, Quesnel Terrane, British Columbia, Canada. Economic Geology, 106, 781–808.

Macey, P., and Harris, C. (2006) Stable isotope and fluid inclusion evidence for the origin of the Brandberg West area Sn–W vein deposits, NW Namibia. Mineralium Deposita, 41, 671–690.

Mahjoubi, E.M., Chauvet, A., Badra, L., Sizaret, S., Barbanson, L., El Maz, A., Chen, Y., and Amann, M. (2016) Structural, mineralogical, and paleoflow velocity constraints on Hercynian tin mineralisation: the Achmmach prospect of the Moroccan Central Massif. Mineralium Deposita, 51, 431–451.

Mar'ina, E.A., Balitskii, V.S., Balittskaya, L.V., Urusov, V.S., and Rossman, J.R. (1999) Solubility and growth of quartz crystals in aqueous-borate solutions. Doklady Earth Sciences, 369(A), 1285–1287.

Morgan, G.B., and London, D. (1989) Experimental reactions of amphibolite with boron-bearing aqueous fluids at 200 MPa: implications for tourmaline stability and partial melting in mafic rocks. Contributions to Mineralogy and Petrology, 102, 281–297.

Myint, A.Z., Yonezu, K., Boyce, A.J., Selby, D., Scherstén, A., Tindell, T., Watanabe, K., and Swe, Y.M. (2018) Stable isotope and geochronological study of the Mawchi Sn-W deposit, Myanmar: Implications for timing of mineralisation and ore genesis. Ore Geology Reviews, 95, 663–679.

Osselin, F., Kondratiuk, P., Budek, A., Cybulski, O., Garstecki, P., and Szymczak, P. (2016) Microfluidic observation of the onset of reactive-infitration instability in an analog fracture. Geophysical Research Letters, 43, 6907–6915.

Osselin, F., Pichavant, M., Champallier, R., Ulrich, M., and Raimbourg, H. (2022) Reactive transport experiments of coupled carbonation and serpentinization in a natural serpentinite. Implication for hydrogen production and carbon geological storage. Geochimica et Cosmochimica Acta, 318, 165–189.

Peuble, S., Godard, M., Luquot, L., Andreani, M., Martinez, I., and Gouze, P. (2015) CO2 geological storage in olivine rich basaltic aquifers: New insights from reactive-percolation experiments. Applied Geochemistry, 52, 174–190.

Peuble, S., Godard, M., Gouze, P., Leprovost, R., Martinez, I., and Shilobreeva, S. (2019) Control of CO2 on flow and reaction paths in olivine-dominated basements: An experimental study. Geochimica et Cosmochimica Acta, 252, 16–38.

Pichavant, M. (1983) Melt-fluid interaction deduced from studies of silicate-B2O3-H2O systems at 1 kbar. Bulletin de Minéralogie, 106, 201–211.

Pirajno, F., and Jacob, R.E. (1987) Sn-W metallogeny in the Damara orogen, South West Africa/Namibia. South African Journal of Geology, 90, 239–255.

Pollok, K., Putnis, C.V., and Putnis, A. (2011) Mineral replacement reactions in solid solution-aqueous solution systems: Volume changes, reactions paths and end-points using the example of model salt systems. American Journal of Science, 311, 211–236.

Putnis, A. (2002) Mineral replacement reactions: from macroscopic observations to microscopic mechanisms. Mineralogical Magazine, 66, 689–708.

Putnis, A. (2015) Transient Porosity Resulting from Fluid–Mineral Interaction and its Consequences. Reviews in Mineralogy and Geochemistry, 80, 1–23.

Rao, S.E., Ray, L., Khan, T., and Ravi, G. (2022) Thermal conductivity, density and porosity of sedimentary and metamorphic rocks from the Lower and Higher Himalaya, Western Himalaya, India. Geophysical Journal International, 231, 459–473.

Ruiz-Agudo, E., Putnis, C.V., and Putnis, A. (2014) Coupled dissolution and precipitation at mineral–fluid interfaces. Chemical Geology, 383, 132–146.

Schwartz, G.M. (1958) Alteration of biotite under mesothermal conditions. Economic Geology, 53, 164–177.

Setkova, T.V., Balitsky, V.S., and Shapovalov, Yu.B. (2019) Experimental Study of the Stability and Synthesis of the Tourmaline Supergroup Minerals. Geochemistry International, 57, 1082–1094.

Sizaret, S., Branquet, Y., Gloaguen, E., Chauvet, A., Barbanson, L., Arbaret, L., and Chen, Y. (2009) Estimating the local paleo-fluid flow velocity: New textural method and application to metasomatism. Earth and Planetary Science Letters, 280, 71–82.

Slack, J.F., and Trumbull, R.B. (2011) Tourmaline as a Recorder of Ore-Forming Processes. Elements, 7, 321–326.

Smirnov, S.Z., Thomas, V.G., Demin, S.P., and Drebushchak, V.A. (2005) Experimental study of boron solubility and speciation in the Na2O–B2O3–SiO2–H2O system. Chemical Geology, 223, 16–34.

Szymczak, P., and Ladd, A.J.C. (2009) Wormhole formation in dissolving fractures. Journal of Geophysical Research, 114, B06203.

Szymczak, P., and Ladd, A.J.C. (2011) The initial stages of cave formation: Beyond the one-dimensional paradigm. Earth and Planetary Science Letters, 301, 424–432.

Trumbull, R.B., and Chaussidon, M. (1999) Chemical and boron isotopic composition of magmatic and hydrothermal tourmalines from the Sinceni granite–pegmatite system in Swaziland. Chemical Geology, 153, 125–137.

van Hinsberg, V.J., and Schumacher, J.C. (2007) Using estimated thermodynamic properties to model accessory phases: the case of tourmaline. Journal of Metamorphic Geology, 25, 769–779.

van Hinsberg, V.J., Henry, D.J., and Marschall, H.R. (2011a) Tourmaline: an ideal indicator of its host environment. The Canadian Mineralogist, 49, 1–16.

van Hinsberg, V.J., Henry, D.J., and Dutrow, B.L. (2011b) Tourmaline as a Petrologic Forensic Mineral: A Unique Recorder of Its Geologic Past. Elements, 7, 327–332.

Vialle, S., Contraires, S., Zinzsner, B., Clavaud, J., Mahiouz, K., Zuddas, P., and Zamora, M. (2014) Percolation of CO_2-rich fluids in a limestone sample: Evolution of hydraulic, electrical, chemical, and structural properties. Journal of Geophysical Research: Solid Earth, 119, 2828–2847.

von Goerne, G., Franz, G., and Robert, J.L. (1999) Upper thermal stability of tourmaline + quartz in the system MgO-Al2O3-SiO2-B2O3-H2O and Na2O-MgO-Al2O3-SiO2-B2O3-H2O-HCl in hydrothermal solutions and siliceous melts. The Canadian Mineralogist, 37, 1025–1039.

Weis, P. (2015) The dynamic interplay between saline fluid flow and rock permeability in magmatic-hydrothermal systems. Geofluids, 15, 350–371.

Wojdak, P.J., and Sinclair, A.J. (1984) Equity Silver silver-copper-gold deposit; alteration and fluid inclusion studies. Economic Geology, 79, 969–990.

Zeng, Z., Shan, X., Hao, G., He, W., Zheng, C., Yi, J., and Guo, J. (2022) Semiquantitative microscopic pore characterizations of the metamorphic rock reservoir in the central paleo-uplift belt, Songliao Basin. Scientific Reports, 12, 2606.

Zhou, T., Yuan, F., Yue, S., Liu, X., Zhang, X., and Fan, Y. (2007) Geochemistry and evolution of ore-forming fluids of the Yueshan Cu–Au skarn- and vein-type deposits, Anhui Province, South China. Ore Geology Reviews, 31, 279–303.

General conclusions

Recent advances in the metallogeny of hydrothermal ore deposits implies the combination of fluid flow simulations with thermodynamic modelling. This methodology, applied by Launay et al. (2023) highlight that by modifying the petrophysics properties of the host rock, alteration constitute both a physical and chemical driving force during the ore deposit formation. Tourmaline is an emblematic mineral of the magmatic/hydrothermal transition, present from the late stage of magmatic crystallisation to the low temperature metasomatism. Applying the methodology of Launay et al. (2023) on tourmalinisation would allow us to understand how this alteration impact its hydrothermal environment. Thus, the tourmaline would provide not only information on the physico-chemical conditions of its environment, but also on the feedback phenomena controlling the fluid flow and the location of mineralisation. Such development requires **(i) a good implementation of the alteration in batch equilibrium simulation** and **(ii) quantitative laws describing the effect of the alteration on the permeability of the rock**. Research on this last point is quite recent and remains to be fully explored, through reactive percolation experiments at “high temperature”, up to 400°C. But, in the case of tourmaline, even the first condition is far from being completed. As explained previously, the lack of calibrating data on tourmaline stability, notably concerning the boron concentration in the system, is a barrier to its use in thermodynamic modelling. The few experimental constraints already existing on the subject are mainly focusing on Fe-free systems at high temperature (> 500°C) and present some inconsistencies depending of the fluid composition used.

In this PhD, we used experimental technic in order to investigate the two missing requirements for tourmalinisation to be used in coupled numerical model.

In a first time, we have complemented and provided new experimental constraints on the boron concentration of the fluid at equilibrium ($[B_2O_3]_{fluid\_EQ}$) with tourmaline and cordierite and tourmaline and biotite at 200 MPa and 400, 500 and 600°C, under fO_2 controlled conditions. The major findings are listed below:

- Under moderately oxidising conditions (NNO+0.8 to NNO+1.9), the assemblage cordierite + albite + andalusite react to tourmaline + quartz for $[B_2O_3]_{fluid} > 3.4$ wt% at 600°C and for $[B_2O_3]_{fluid} > 2.1$ wt% at 500°C. At 400°C, tourmaline appears for $[B_2O_3]_{fluid} > 2.0$ wt% but smectite replaces cordierite in the reacting assemblage. Experiments under strongly oxidising conditions (NNO+5.3) show that $[B_2O_3]_{fluid}$ necessary for tourmaline to appear does not vary significantly with fO_2.

- Under moderately oxidising conditions (NNO+1.0 to NNO+2.6), the assemblage biotite + albite + andalusite + quartz reacts to tourmaline + K-feldspar for $[B_2O_3]_{fluid} > 2.0$ wt% at 600°C and for $[B_2O_3]_{fluid} > 1.1$ wt% at 500°C. At 400°C, tourmaline appears for $[B_2O_3]_{fluid} > 2.9$ wt% but chlorite and illite replace biotite in the reacting assemblage.

- In both experiments, tourmaline growth follows two supersaturation regimes (local and bulk) of tourmaline-forming components in the fluid.

- In both experiments, tourmaline displays significant chemical variation (especially on the at. Ca/(Ca+Na) ratio) inside a same charge. This reflects changes in tourmaline nucleation and growth mechanisms during the experiments, controlled by the evolution of fluid composition and the level of supersaturation of the tourmaline-forming components.

- Our determinations of $[B_2O_3]_{fluid}$ at equilibrium with tourmaline and cordierite and tourmaline and biotite are globally in good agreement with previous experimental tourmalinisation studies but the comparison also highlights the potential effect of other variables such as the fluid chemistry (pH and alkali chloride concentration) on tourmaline stability.

- The low boron concentration range required to form tourmaline from cordierite or from biotite is consistent with compositional constraints from natural hydrothermal fluids and peraluminous melts.

- Despite being in good agreement, within errors, the two most complete and recent sets of standard thermodynamic properties for tourmaline end-members yield to large differences in the $[B_2O_3]_{fluid\_EQ}$ calculated at high temperature. Therefore, the experimental results provided by this study can provide new, more refined constraints on the thermodynamic properties of tourmaline. However, lack of solution model for chemically complex tourmalines prevent more detailed comparison with the experimental results.

In a second time, the PhD deals with a dynamical approach of boron metasomatism in perigranitic environment by performing a reactive percolation experiment on a spotted micaschist from Panasqueira, infiltrated with a $B(OH)_3$ brine at 300°C for 5 weeks. The objective was to determine quantitative laws describing the effect of the alteration on the permeability of the rock. Due to the very low permeability of the rock and the low effective pressure fixed in the first days, the fluid was able to create and focus into a channel between the Au jacket and the core. Thus, the permeability measured in this experiment does not reflect variations in the petrophysical properties of the rock, but rather reproduces a vein opening through hydraulic fracturing. Despite not answering the primary objective, this experiment allowed to reproduce in a controlled environment the dynamic of wall-rock alteration in natural environment. The localisation of the alteration is controlled locally by the relationship between the reaction rate and the fluid velocity. High flow zones, such as the channel, form reaction-limited environment where the solutes are mobilised through advection and leave the core without being able to precipitate further down. Alteration of the schist matrix corresponds to low flow zones where the limited transport by diffusion allows the formation of a sharp radial alteration front.

Appendix

Appendix A1

Tourmaline classification by Henry et al. (2011)

Name	(X)	(Y_3)	(Z_6)	T_6O_{18}	$(BO_3)_3$	V_3	W
Alkali-group							
Dravite	Na	Mg_3	Al_6	Si_6O_{18}	$(BO_3)_3$	$(OH)_3$	(OH)
Schorl	Na	Fe_3	Al_6	Si_6O_{18}	$(BO_3)_3$	$(OH)_3$	(OH)
Elbaite	Na	$Li_{1.5}Al_{1.5}$	Al_6	Si_6O_{18}	$(BO_3)_3$	$(OH)_3$	(OH)
Povondraite	Na	$Fe^{3+}{}_3$	$Fe_4{}^{3+}Mg_2$	Si_6O_{18}	$(BO_3)_3$	$(O)_3$	O
Oxy-dravite	Na	Al_3	Al_4Mg_2	Si_6O_{18}	$(BO_3)_3$	$(O)_3$	O
Oxy-schorl	Na	Al_3	$Al_4Fe_2{}^{2+}$	Si_6O_{18}	$(BO_3)_3$	$(O)_3$	O
Olenite	Na	Al_3	Al_6	Si_6O_{18}	$(BO_3)_3$	$(O)_3$	(OH)
Buergerite	Na	$Fe^{3+}{}_3$	Al_6	Si_6O_{18}	$(BO_3)_3$	$(O)_3$	(OH)
Calcic-group							
Uvite	Ca	Mg_3	$MgAl_5$	Si_6O_{18}	$(BO_3)_3$	$(OH)_3$	(OH)
Feruvite	Ca	Fe_3	$MgAl_5$	Si_6O_{18}	$(BO_3)_3$	$(OH)_3$	(OH)
Vacant-group							
Foitite	$[]_X$	Fe_2Al	Al_6	Si_6O_{18}	$(BO_3)_3$	$(OH)_3$	(OH)
Magnesio-foitite	$[]_X$	Mg_2Al	Al_6	Si_6O_{18}	$(BO_3)_3$	$(OH)_3$	(OH)

Appendix A2 : Fluid inclusion studies compilation

Context	Site (Country)	T_{homog} (°C)	NaCl (wt% equiv.)	[B] (ppm)		Tourmaline presence	Reference
				mean	range		
Barren plutonic	Cantung (Canada)	[177 ; 226]	[4.2 ; 6.7]	1600	[134 ; 5016]	Yes	*Legros et al. 2020*
	Cryo-Genie (USA)	[161 ; 180]	[2.2 ; 5.1]	17184	[2107 ; 38715]	No	*Sirbescu et al. (2013)*
	Huangshan pluton (China)	[280 ; 396]	[2.1 ; 7]	1883	[218 ; 7454]	No	*Zhang & Audetat (2018)*
	Huashan pluton (China)	[279 ; 375]	[7.4 ; 10.5]	1511	[253 ; 3750]	No	*Tang et al. (2022)*
	Kymi granite (Finland)	[149 ; 362]	[8.5 ; 20.5]	1335	[530 ; 2970]	Yes	*Berni et al. (2020)*
	Land's End (UK)	[89 ; 409]	[29.9 ; 48.4]	1784	[372 ; 4245]	Yes	*Albrecht (2017)*
	Luumäki (Finland)	[207 ; 448]	[0 ; 43.6]	1421	[24 ; 5000]	No	*Michallik et al. (2021)*
	Mole Granite (Australia)	[308 ; 620]	[2.9 ; 57.1]	1919	[370 ; 10800]	No	*Audétat et al. (2000)*
	Rito del Medio pluton	[420 ; 480]	[1.2 ; 29.6]	908	[580 ; 1200]	No	*Audétat et al. (2008)*
	Schellerhau granite (Germany)	[100 ; 226]	[3.2 ; 53.3]	3070	[299 ; 9934]	No	*Albrecht (2017)*
Barren volcanic	Brothers Volcano (New Zealand)	[301 ; 346]	[1.6 ; 7.6]	68	[33 ; 132]	No	*Lee at al. (2022)*
	Huangshui'an (China)	[279 ; 384]	[5.5 ; 35.1]	464	[130 ; 1500]	No	*Tang et al. (2021)*
Carlin-type deposit	Gold Quarry - Chukar (USA_Nevada)	[125 ; 260]	[-3.1 ; 8.8]	2889	[470 ; 15500]	No	*Large et al. (2016)*
Epithermal deposits	Dahu (China)	[202 ; 440]	[7.9 ; 10.7]	202	[70 ; 527]	No	*Jian et al. (2018)*
Metamorphic	Alpine orogenic belt (Swiss)	[138 ; 313]	[0.4 ; 10.2]	430	[22 ; 1460]	No	*Rauchenstein-Martinek et al. (2016)*
	Rhenish Massif (Germany)	[124.5 ; 224.8]	[1 ; 5.4]	634	[85 ; 2290]	No	*Marsala et al. (2013)*
Orogenic gold deposit	Pampalo (Finland)	[150 ; 160]	[0.7 ; 15.2]	616	[55 ; 1300]	Yes	*Fusswinkel et al. (2016)*
Porphyry deposits	Battle Mountain (USA_Nevada)	[160 ; 400]	[1.6 ; 40.8]	1262	[140 ; 4100]	No	*Large et al. (2016)*
	Cave Peak	[450 ; 600]	[2.7 ; 49.7]	330	[320 ; 340]	No	*Audétat et al. (2008)*
	Mount Milligan (Canada)	[117 ; 263]	[4.2 ; 24.3]	1942	[720 ; 5440]	Yes	*LeFort et al. (2011)*
	Leimengou (China)	[260 ; 384]	[6.7 ; 38.2]	519	[96 ; 3160]	No	*Tang et al. (2022)*
	Qiyugou (China)	[294 ; 362]	[8.5 ; 36.4]	464	[90 ; 1140]	No	*Tang et al. (2022)*
	Sadaigoumen (China)	[224.4 ; 502.8]	[1.9 ; 40]	624	[133 ; 1525]	No	*Chen et al. (2021)*
	Santa Rita	[650 ; 720]	[10 ; 33.1]	367	[71 ; 750]	No	*Audétat et al. (2008)*
Sb deposit	Banxi (China)			1200	[94 ; 11458]	No	*Fu et al. (2022)*
Skarns	Battle Mountain (USA_Nevada)	[195 ; 394]	[21 ; 24.7]	555	[440 ; 790]	No	*Large et al. (2016)*
	Cantung (Canada)		[2.2 ; 11.8]	1294	[80 ; 4388]	No	*Legros et al. 2020*
	Hämmerlein (Germany)	[170.9 ; 334.1]	[1.9 ; 35.4]	2403	[104 ; 5654]	No	*Korges et al. (2020)*
	Lened (Canada)	[350 ; 350]	[3.5 ; 3.5]	5000		Yes	*Legros et al. (2022)*
	Stronghold Granite	[396 ; 510]	[0.9 ; 31.6]	1881	[590 ; 4100]	No	*Audétat et al. (2008)*
Sn-W deposits	Chuankou (China)	[272 ; 298]	[2.5 ; 4.3]	4194	[895 ; 13488]	Yes	*Li et al. (2022)*
	Gottesberg (Germany)		[10 ; 43]	3146	[1046 ; 4955]	No	*Albrecht (2017)*
	Hämmerlein (Germany)	[169 ; 345.3]	[4.7 ; 37.7]	2626	[136 ; 9857]	Yes	*Korges et al. (2020)*
	Huanuni (Bolivia)	[374 ; 386]	[6 ; 21]	4528	[2230 ; 9430]	Yes	*Müller et al. (2001)*
	Mole Granite (Australia)	[172 ; 595]	[0.1 ; 48.5]	1168	[120 ; 3500]	Yes	*Audétat et al. (2000)*
	Narenwula (China)	[160 ; 440]	[0.9 ; 33.8]	19735	[12 ; 186465]	No	*Xie et al. (2022)*
	Panasqueira (Portugal)	[204 ; 313]	[6.5 ; 6.5]	2562	[270 ; 7135]	Yes	*Lecumberri et al. (2017)*
	Yaogangxian (China)	[225 ; 310]	[5.1 ; 8.7]	6857	[79 ; 17177]	Yes	*Pan et al. (2019)*
	Zinnwald-Cinovec (Germany - Czech Republic)	[183.5 ; 490.6]	[0.2 ; 42.2]	1196	[47 ; 6112]	No	*Korges et al. (2018)*

Appendix A3

Average composition of starting cordierite, plagioclase and andalusite

Starting product	Cordierite				Plagioclase				Andalusite			
n	23				32				14			
	Mean	*Sd*	*Min*	*Max*	*Mean*	*Sd*	*Min*	*Max*	*Mean*	*Sd*	*Min*	*Max*
SiO_2	49.49	(0.298)	*49.00*	*50.10*	67.91	(0.808)	*64.22*	*69.08*	36.21	(0.278)	*35.82*	*36.82*
TiO_2	0.08	(0.052)	*0.05*	*0.12*	0.02	(0.012)	*0.01*	*0.04*	0.06	(0.007)	*0.05*	*0.06*
Al_2O_3	33.45	(0.171)	*33.15*	*33.74*	19.76	(0.433)	*18.12*	*20.60*	63.38	(0.258)	*62.91*	*63.69*
FeO_{total}	3.21	(0.129)	*2.91*	*3.46*	0.10	(0.043)	*0.06*	*0.15*	0.28	(0.053)	*0.21*	*0.38*
MgO	11.06	(0.709)	*10.35*	*12.11*	*b.d.l*				0.05	(0.011)	*0.03*	*0.07*
MnO	*b.d.l*				0.05	(0.041)	*0.00*	*0.09*	*b.d.l*			
CaO	0.05	(0.021)	*0.04*	*0.08*	0.58	(0.262)	*0.24*	*1.49*	*b.d.l*			
Na_2O	0.18	(0.029)	*0.12*	*0.25*	10.79	(1.84)	*0.85*	*11.85*	*b.d.l*			
K_2O	0.06	(0)	*0.06*	*0.06*	0.67	(2.928)	*0.05*	*15.90*	*b.d.l*			
Total	97.60				99.89				99.97			
Si	5.02	(0.042)	4.95	5.08	2.98	(0.013)	2.94	3.00	0.98	(0.006)	0.97	0.99
Ti	0.01	(0.004)	0.00	0.01	0.00	(0)	0.00	0.00	0.00	(0)	0.00	0.00
Al	4.00	(0.021)	3.96	4.04	1.02	(0.015)	1.00	1.06	2.02	(0.008)	2.01	2.03
Fe	0.27	(0.011)	0.25	0.29	0.00	(0.002)	0.00	0.01	0.01	(0.001)	0.00	0.01
Mg	1.67	(0.099)	1.57	1.82	*b.d.l*				0.00	(0)	0.00	0.00
Mn	*b.d.l*				0.00	(0.002)	0.00	0.00	*b.d.l*			
Ca	0.01	(0.002)	0.00	0.01	0.03	(0.013)	0.00	0.06	*b.d.l*			
Na	0.04	(0.006)	0.02	0.05	0.93	(0.157)	0.08	1.03	*b.d.l*			
K	0.01	(0)	0.01	0.01	0.04	(0.166)	0.00	0.95	*b.d.l*			
Fe/(Fe+Mg)	0.14	(0.010)										
Ca/(Ca+Na)	0.14	(0.046)			0.03	(0.015)						

n = number of analyses. b.d.l. = below detection limit.

Appendix A4

Average composition of starting tourmaline

Starting tourmaline[a]	**Core**		**Inner rim**		**Outer rim**		**Late**	
n	41		53		55		12	
SiO_2	36.21	(0.49)	35.67	(0.6)	35.77	(0.52)	35.60	(0.29)
TiO_2	0.35	(0.15)	0.67	(0.11)	0.69	(0.11)	0.74	(0.16)
Al_2O_3	35.64	(0.43)	34.18	(0.4)	34.23	(0.3)	32.94	(0.55)
FeO	9.89	(0.7)	9.43	(0.52)	10.06	(0.49)	11.65	(0.79)
MgO	2.95	(0.3)	3.94	(0.38)	3.49	(0.21)	3.06	(0.52)
MnO	0.14	(0.01)	0.17	(0.04)	0.17	(0.03)	0.19	(0.05)
CaO	0.09	(0.07)	0.13	(0.08)	0.11	(0.03)	0.21	(0.09)
Na_2O	1.53	(0.1)	1.90	(0.1)	1.86	(0.06)	1.84	(0.08)
K_2O	0.08	(0.01)	0.07	(0.01)	0.09	(0.01)	0.11	(0.01)
B_2O_3[b]	10.65		10.55		10.56		10.42	
H_2O[c]	3.67		3.64		3.64		3.59	
Total	101.20		100.35		100.66		100.36	
Site T								
Si	5.91	(0.05)	5.88	(0.06)	5.90	(0.04)	5.94	(0.04)
Al	0.09	(0.05)	0.12	(0.06)	0.10	(0.04)	0.06	(0.04)
Site Z								
Al	6.00		6.00		6.00		6.00	
Site Y								
Al	0.76	(0.05)	0.53	(0.05)	0.54	(0.04)	0.41	(0.07)
Ti	0.04	(0.02)	0.08	(0.01)	0.09	(0.01)	0.09	(0.02)
Fe	1.35	(0.1)	1.30	(0.07)	1.39	(0.07)	1.62	(0.11)
Mg	0.72	(0.07)	0.97	(0.09)	0.86	(0.05)	0.76	(0.13)
Mn	0.00	(0.01)	0.00	(0)	0.00	(0.01)	0.00	(0.01)
Site X								
Ca	0.01	(0.01)	0.02	(0.01)	0.02	(0)	0.04	(0.02)
Na	0.48	(0.03)	0.61	(0.03)	0.59	(0.02)	0.60	(0.03)
K	0.00	(0)	0.00	(0)	0.00	(0.01)	0.01	(0.01)
$[]_X$	0.50	(0.04)	0.37	(0.03)	0.38	(0.02)	0.36	(0.04)
B	3.00		3.00		3.00		3.00	
OH-	4.00		4.00		4.00		4.00	
Total Al	6.85	(0.06)	6.64	(0.07)	6.65	(0.06)	6.47	(0.08)
Fe/(Fe+Mg)	0.65	(0.04)	0.57	(0.04)	0.62	(0.02)	0.68	(0.05)
Ca/(Ca+Na)	0.02	(0.02)	0.04	(0.02)	0.03	(0.01)	0.06	(0.02)

(a) The zonation of the starting tourmaline has been simplified into three main zones, common to all observed sections. The Late tourmalines correspond to the filling of fractures intersecting the 3 other zonations. (b) B_2O_3 calculated assuming 3 apfu. (c) H_2O calculated assuming 4 apfu of OH^-. n = number of analyses.

Appendix A5

Evolution of the alloy phase of the NiO-NiPd sensor as a function of log fO_2 for every run. The dashed line corresponds to the function of Pownceby and O'Neill (1994) linking fO_2 and the X_{Ni} of the sensors at 600°C and 200 MPa. The initial X_{Ni} of both pellets is represented by the dotted lines and their final composition by the square and circle on the dashed line. In Run 6, both pellets migrated toward high fO_2 conditions. Consequently, the bracket reported encompass every measurement.

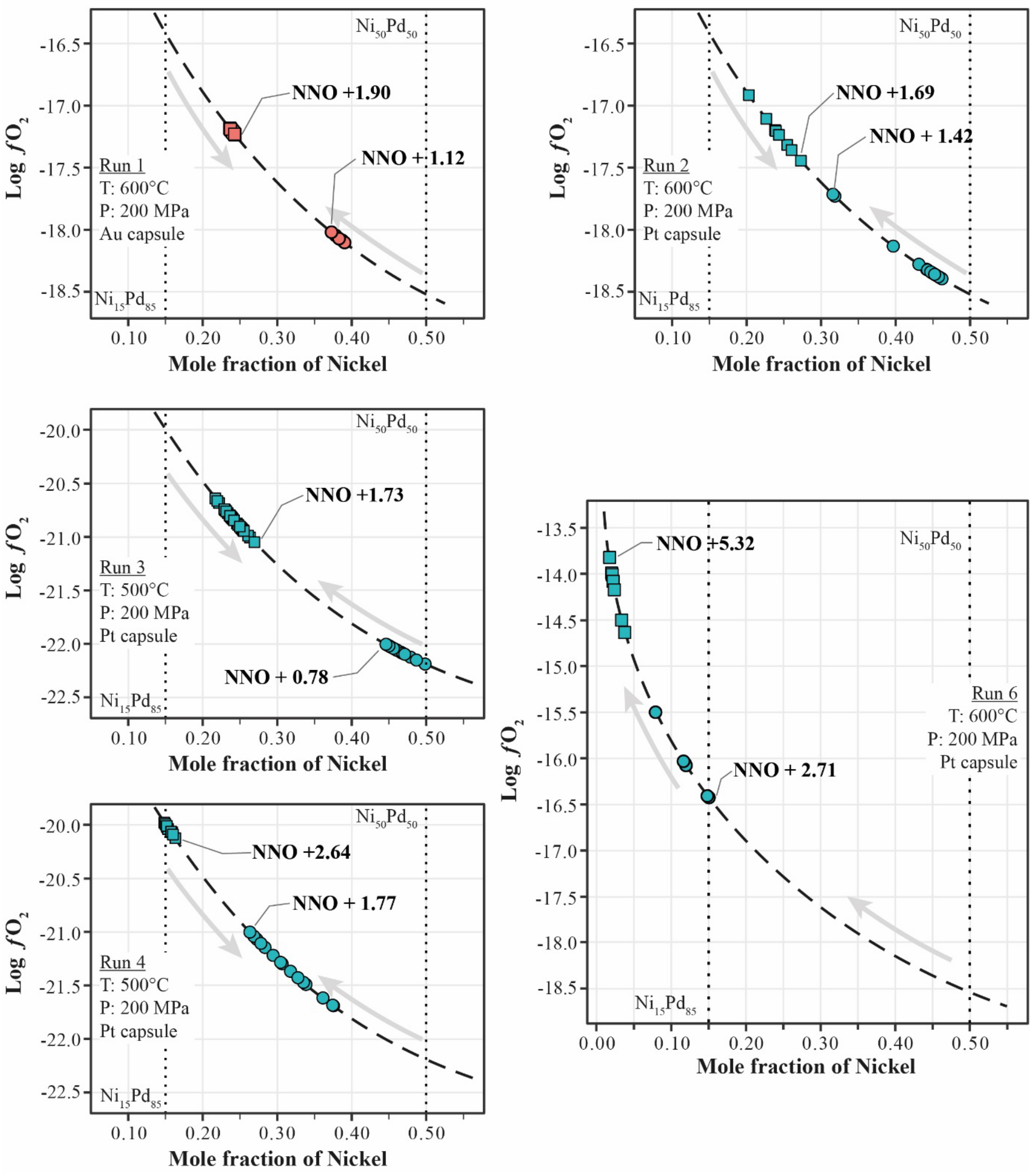

Appendix A6

Diffractograms of specific experiments representative of the different phase assemblage variation observed in the experiments. A. Total diffractogram and two different zooms (B and C) interpreted for the major peaks.

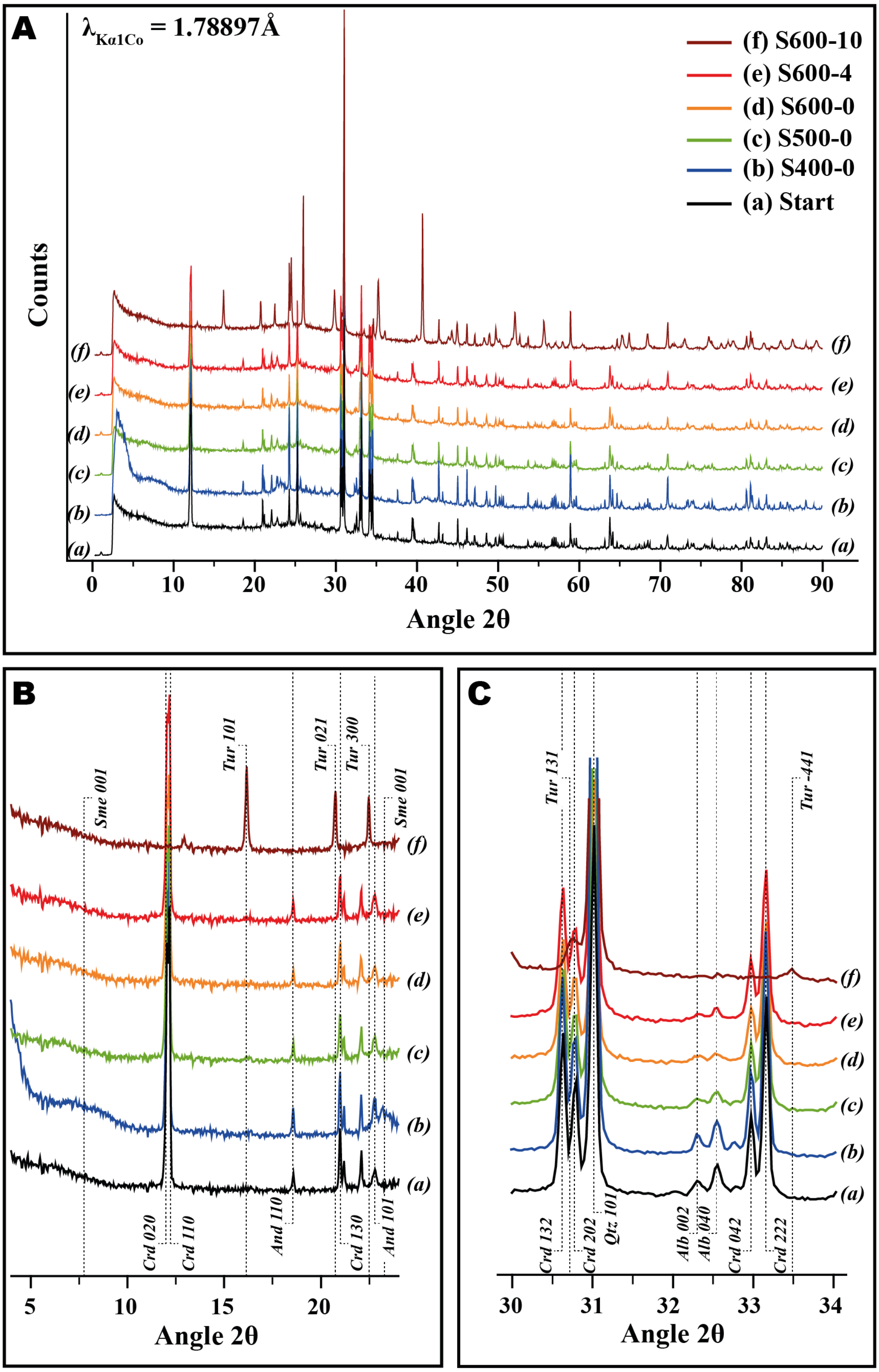

Appendix A7

All diffractograms for starting materials and experimental products.

Starting powder

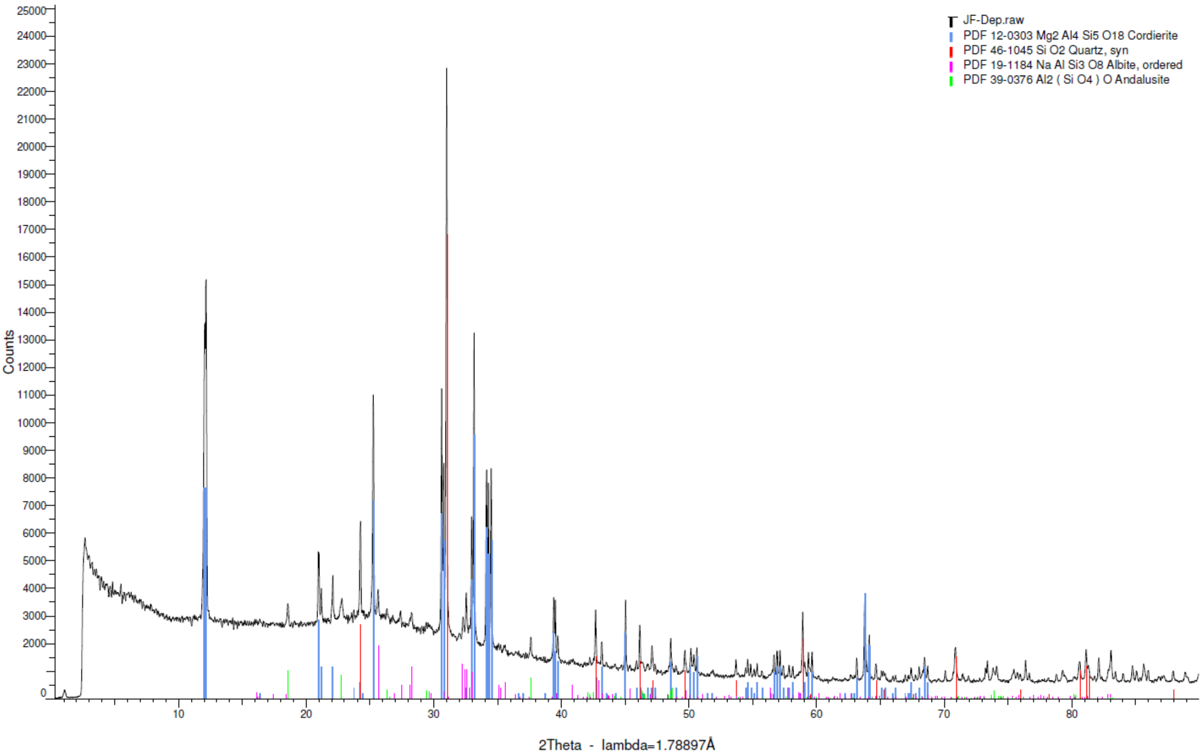

Starting powder for reverse experiments

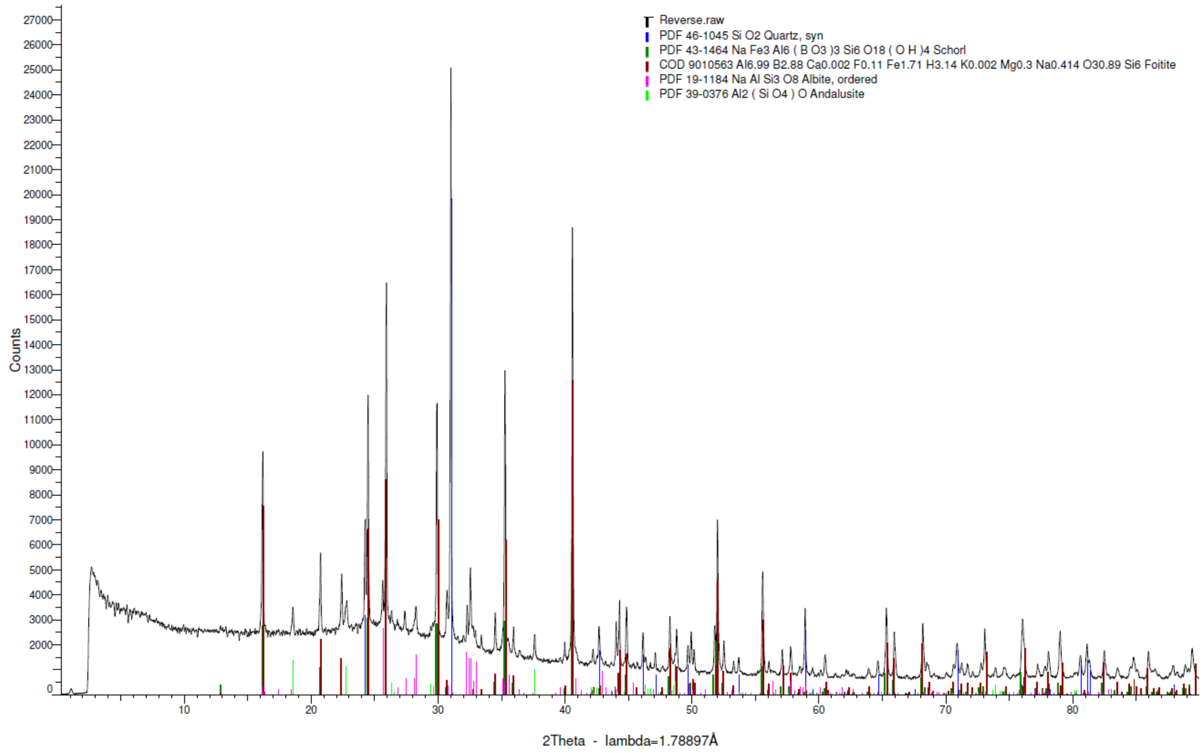

S600-0

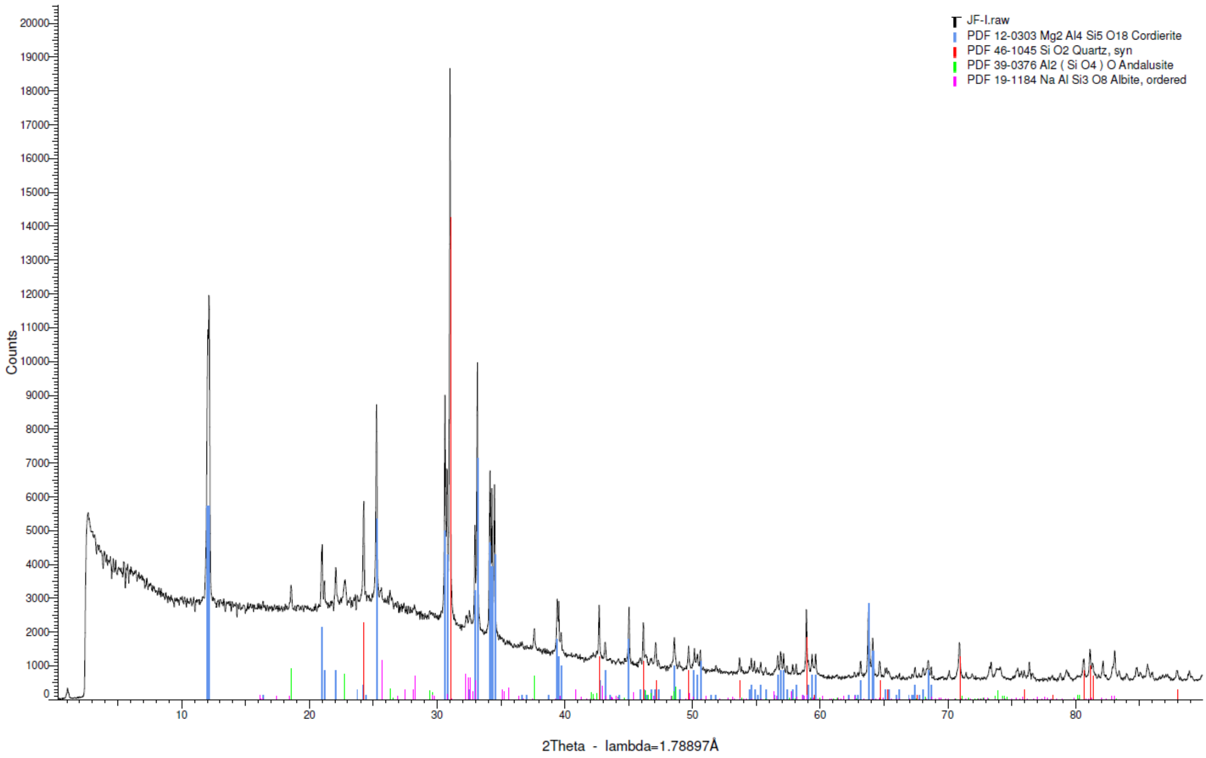
JF-I.raw
PDF 12-0303 Mg2 Al4 Si5 O18 Cordierite
PDF 46-1045 Si O2 Quartz, syn
PDF 39-0376 Al2 (Si O4) O Andalusite
PDF 19-1184 Na Al Si3 O8 Albite, ordered
Counts
20000
19000
18000
17000
16000
15000
14000
13000
12000
11000
10000
9000
8000
7000
6000
5000
4000
3000
2000
1000
0
10
20
30
40
50
60
70
80
2Theta - lambda=1.78897Å

S600-1

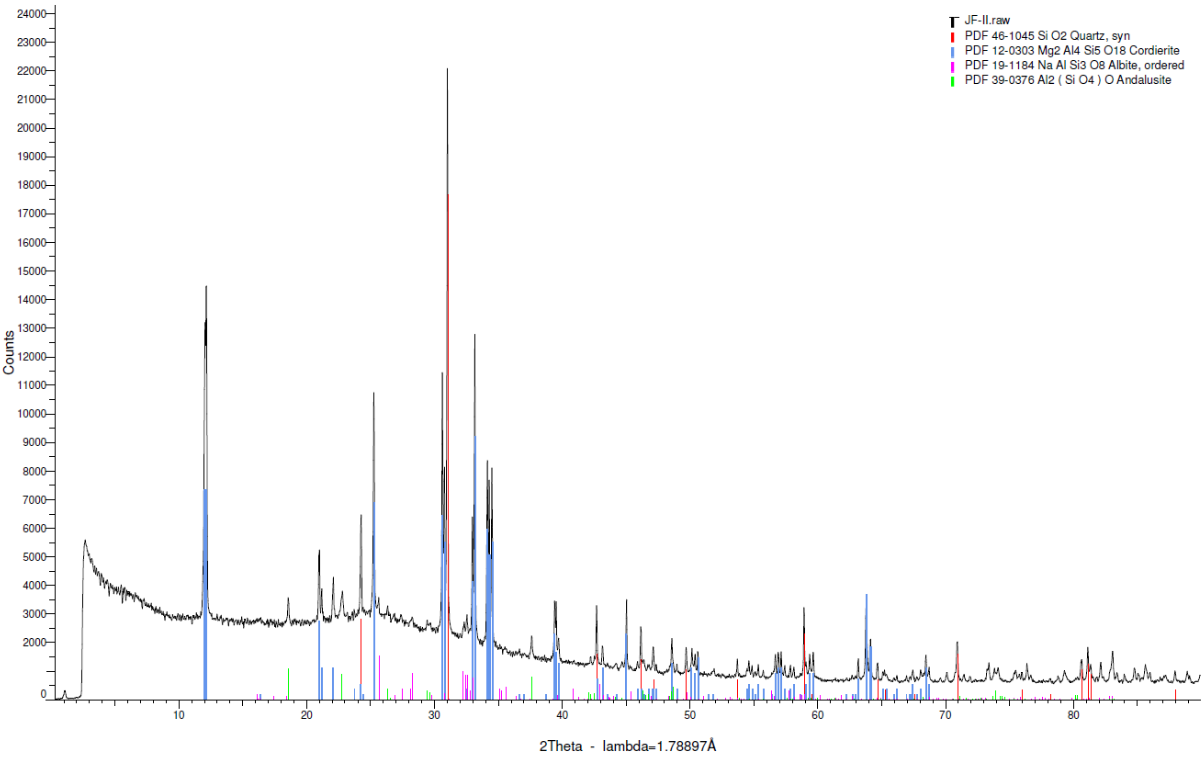
JF-II.raw
PDF 46-1045 Si O2 Quartz, syn
PDF 12-0303 Mg2 Al4 Si5 O18 Cordierite
PDF 19-1184 Na Al Si3 O8 Albite, ordered
PDF 39-0376 Al2 (Si O4) O Andalusite
Counts
24000
23000
22000
21000
20000
19000
18000
17000
16000
15000
14000
13000
12000
11000
10000
9000
8000
7000
6000
5000
4000
3000
2000
0
10
20
30
40
50
60
70
80
2Theta - lambda=1.78897Å

S600-2

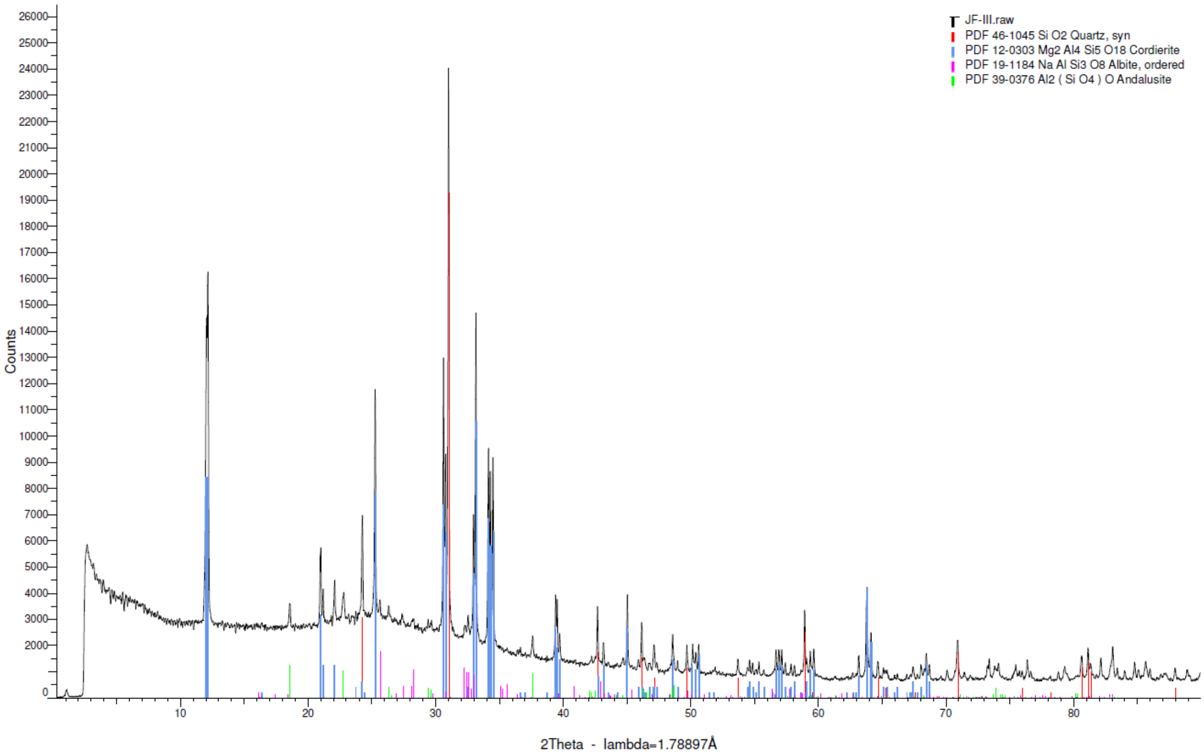
JF-III.raw
PDF 46-1045 Si O2 Quartz, syn
PDF 12-0303 Mg2 Al4 Si5 O18 Cordierite
PDF 19-1184 Na Al Si3 O8 Albite, ordered
PDF 39-0376 Al2 (Si O4) O Andalusite
Counts
0
2000
3000
4000
5000
6000
7000
8000
9000
10000
11000
12000
13000
14000
15000
16000
17000
18000
19000
20000
21000
22000
23000
24000
25000
26000
10
20
30
40
50
60
70
80
2Theta - lambda=1.78897Å

S600-3

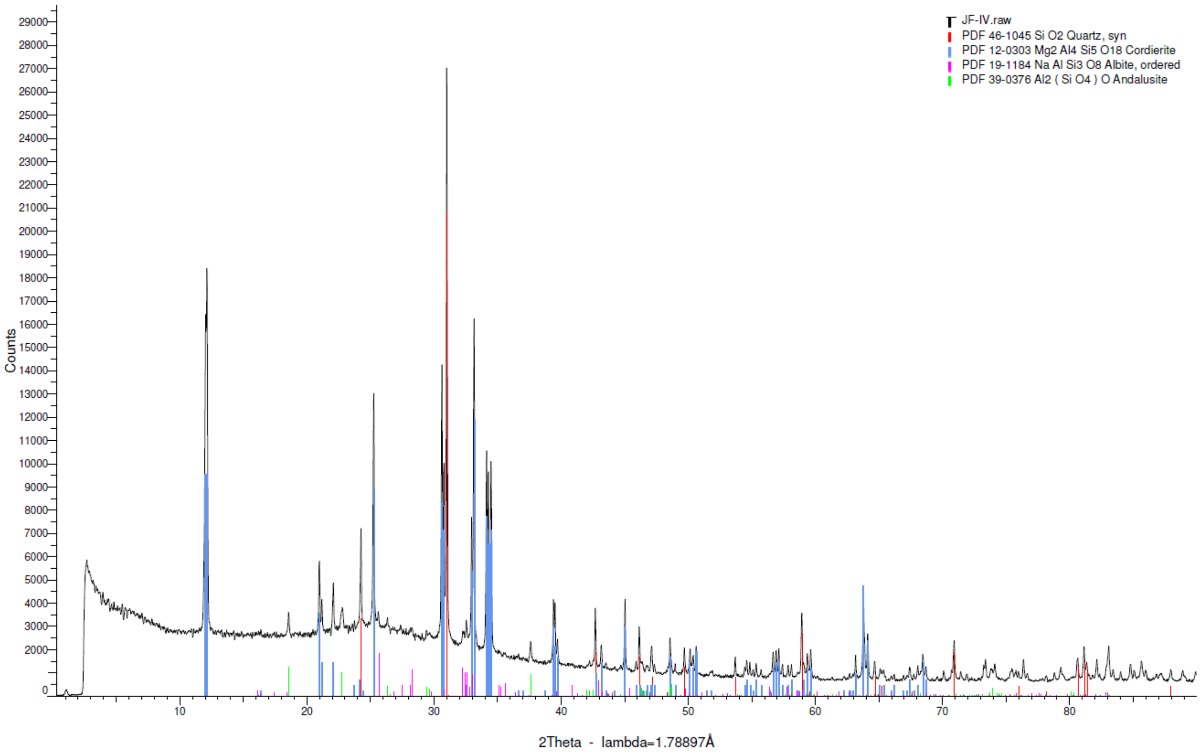
JF-IV.raw
PDF 46-1045 Si O2 Quartz, syn
PDF 12-0303 Mg2 Al4 Si5 O18 Cordierite
PDF 19-1184 Na Al Si3 O8 Albite, ordered
PDF 39-0376 Al2 (Si O4) O Andalusite
Counts
0
2000
3000
4000
5000
6000
7000
8000
9000
10000
11000
12000
13000
14000
15000
16000
17000
18000
19000
20000
21000
22000
23000
24000
25000
26000
27000
28000
29000
10
20
30
40
50
60
70
80
2Theta - lambda=1.78897Å

S600-10

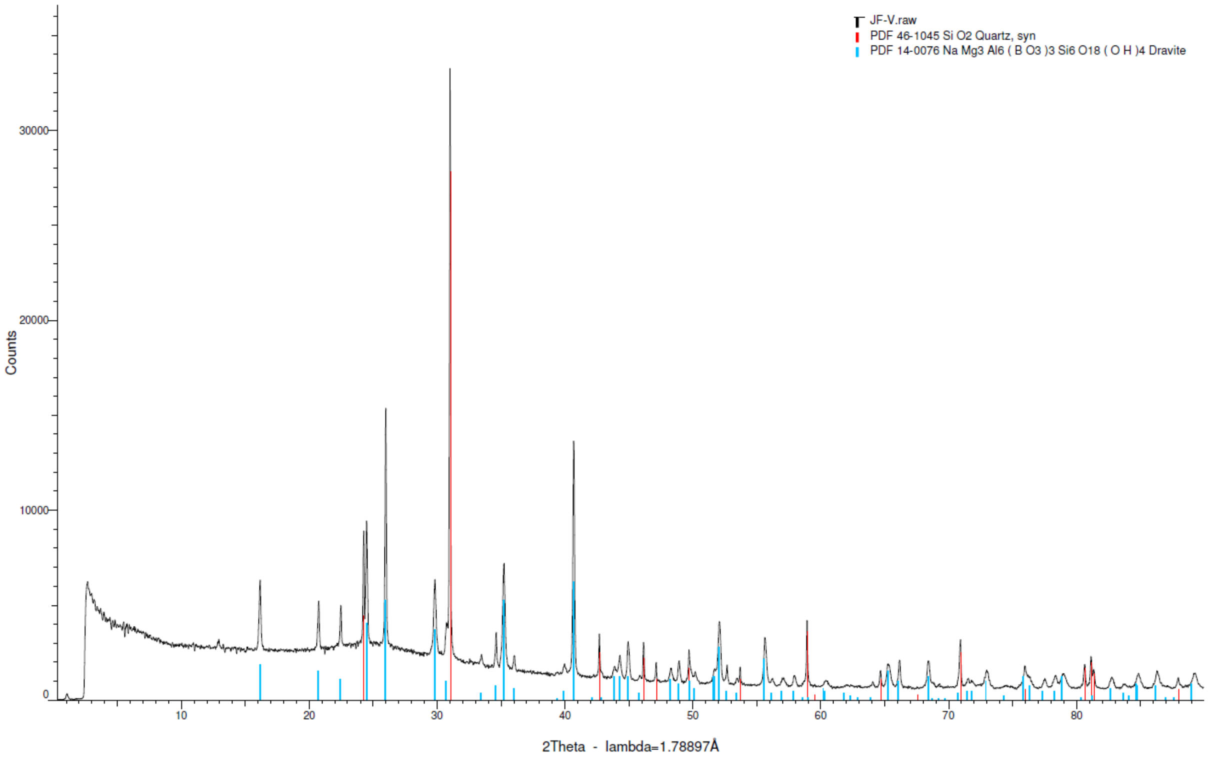

S600-10G

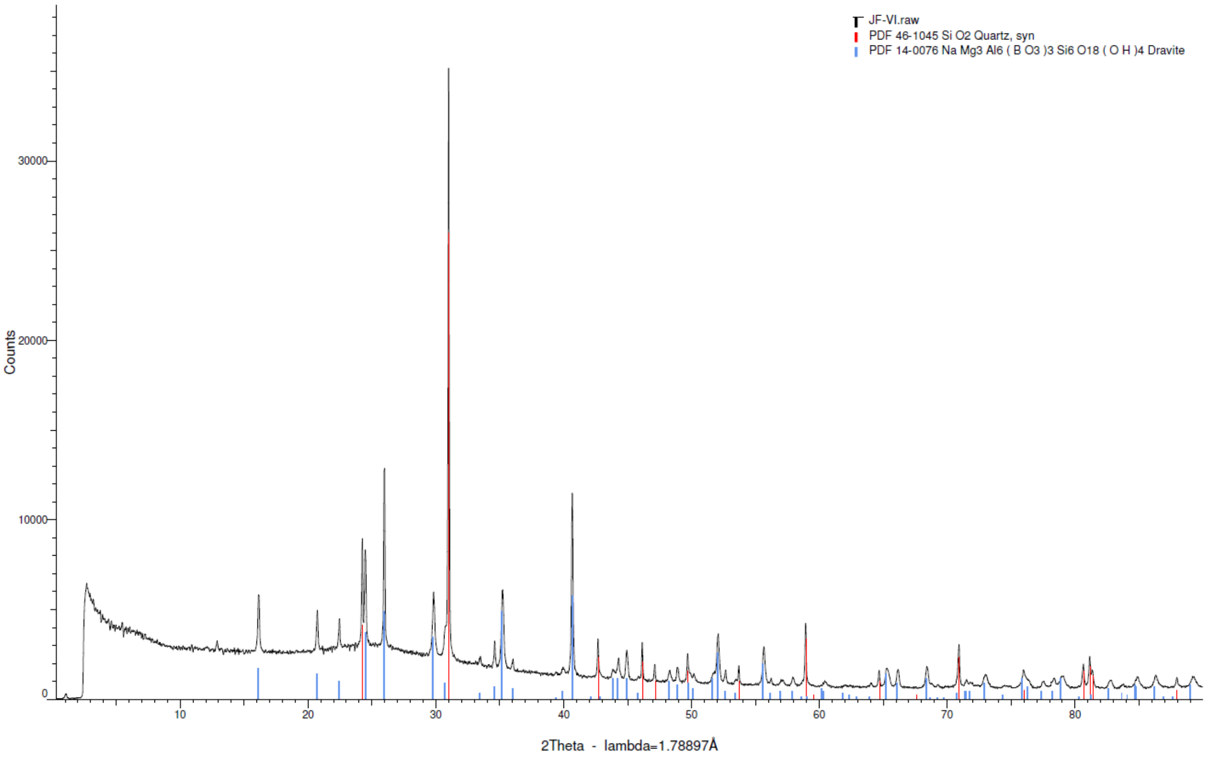

S600-4

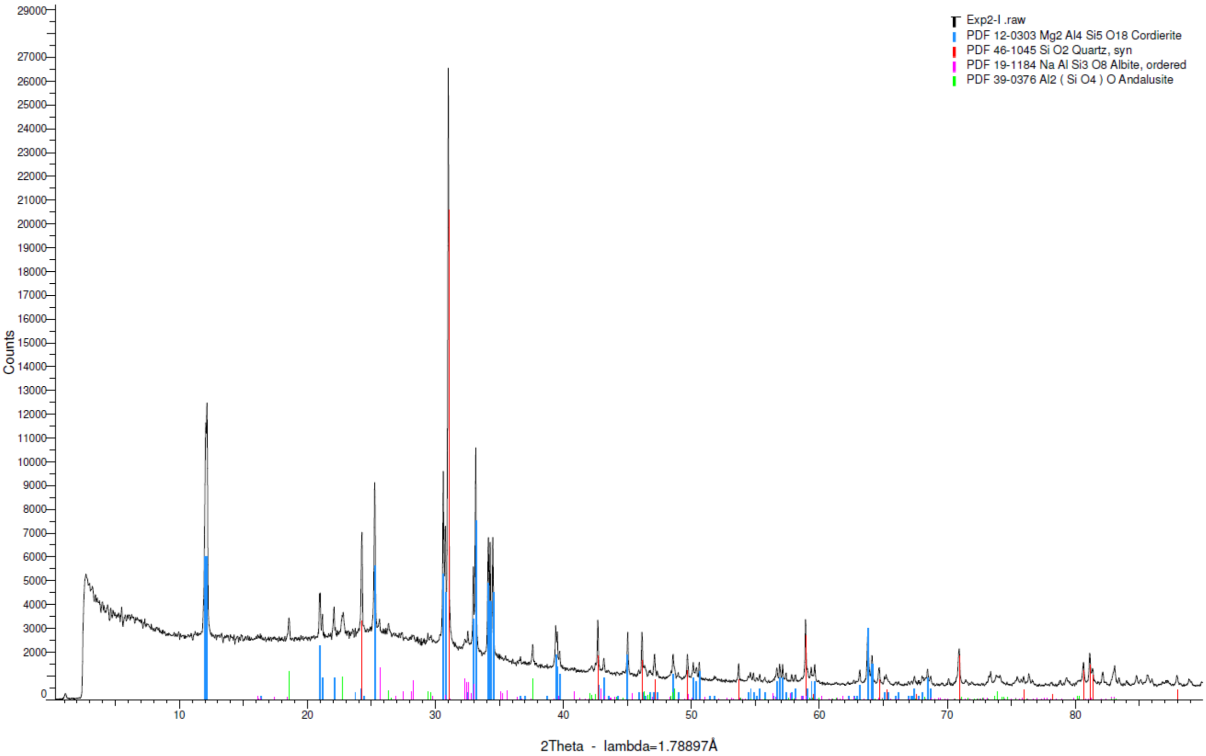
Exp2-I .raw
PDF 12-0303 Mg2 Al4 Si5 O18 Cordierite
PDF 46-1045 Si O2 Quartz, syn
PDF 19-1184 Na Al Si3 O8 Albite, ordered
PDF 39-0376 Al2 (Si O4) O Andalusite
Counts
29000
27000
26000
25000
24000
23000
22000
21000
20000
19000
18000
17000
16000
15000
14000
13000
12000
11000
10000
9000
8000
7000
6000
5000
4000
3000
2000
0
10
20
30
40
50
60
70
80
2Theta - lambda=1.78897Å

S600-6

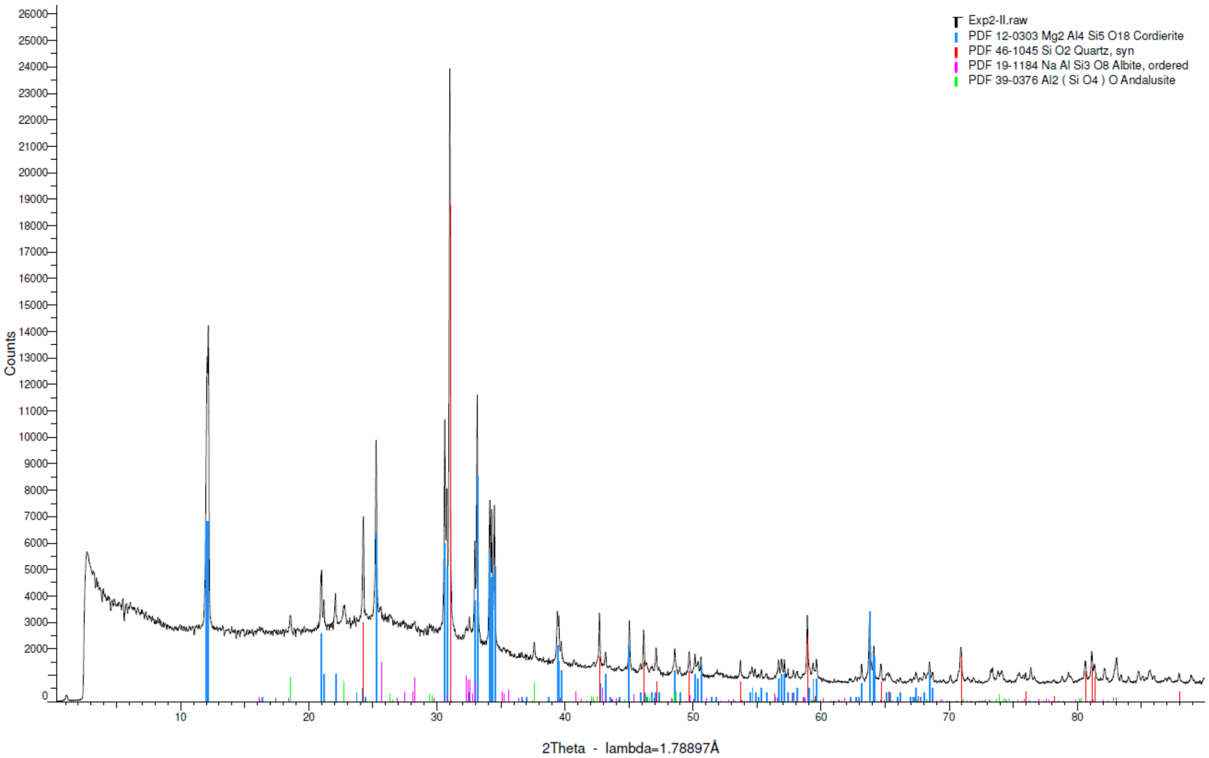
Exp2-II.raw
PDF 12-0303 Mg2 Al4 Si5 O18 Cordierite
PDF 46-1045 Si O2 Quartz, syn
PDF 19-1184 Na Al Si3 O8 Albite, ordered
PDF 39-0376 Al2 (Si O4) O Andalusite
Counts
26000
25000
24000
23000
22000
21000
20000
19000
18000
17000
16000
15000
14000
13000
12000
11000
10000
9000
8000
7000
6000
5000
4000
3000
2000
0
10
20
30
40
50
60
70
80
2Theta - lambda=1.78897Å

S600-6Pt

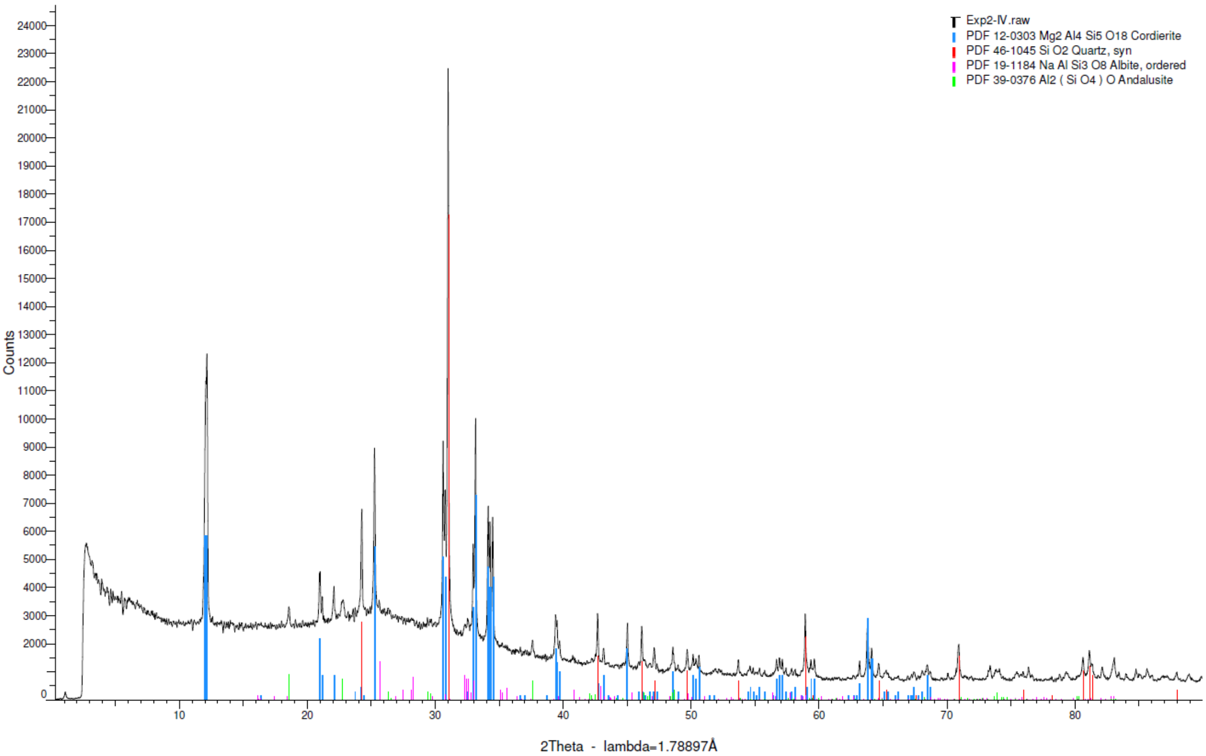

S600-8

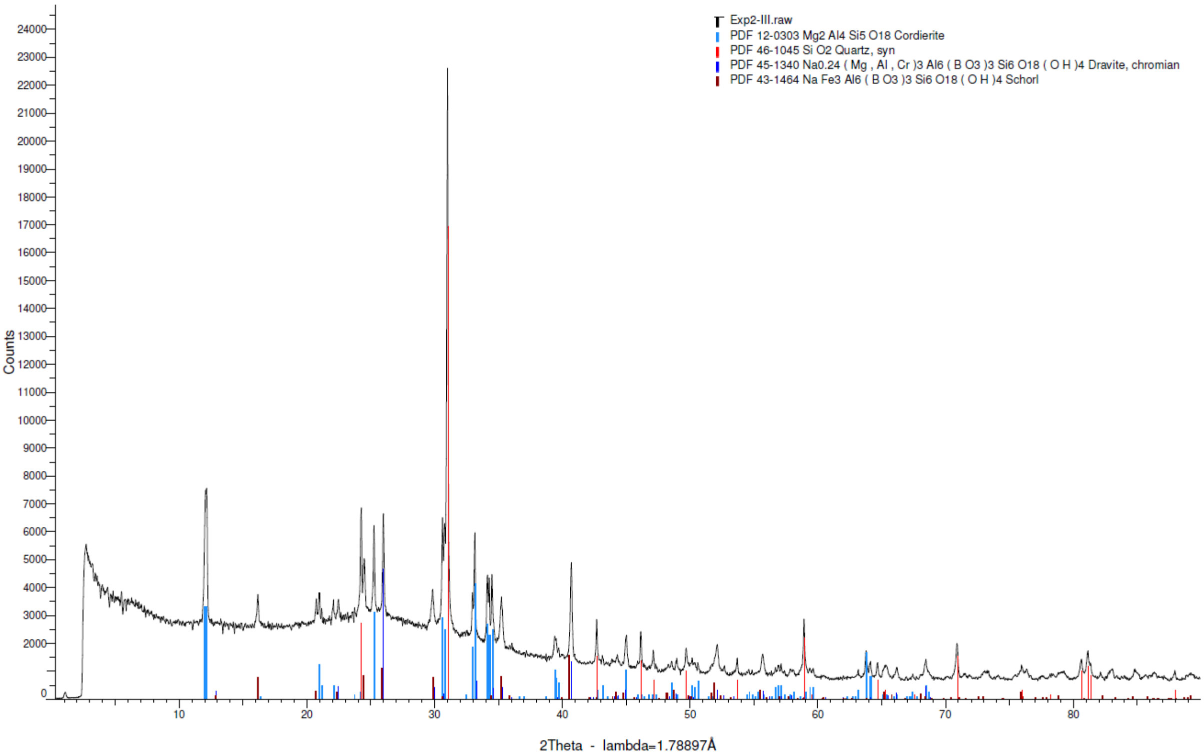

S600-Rev

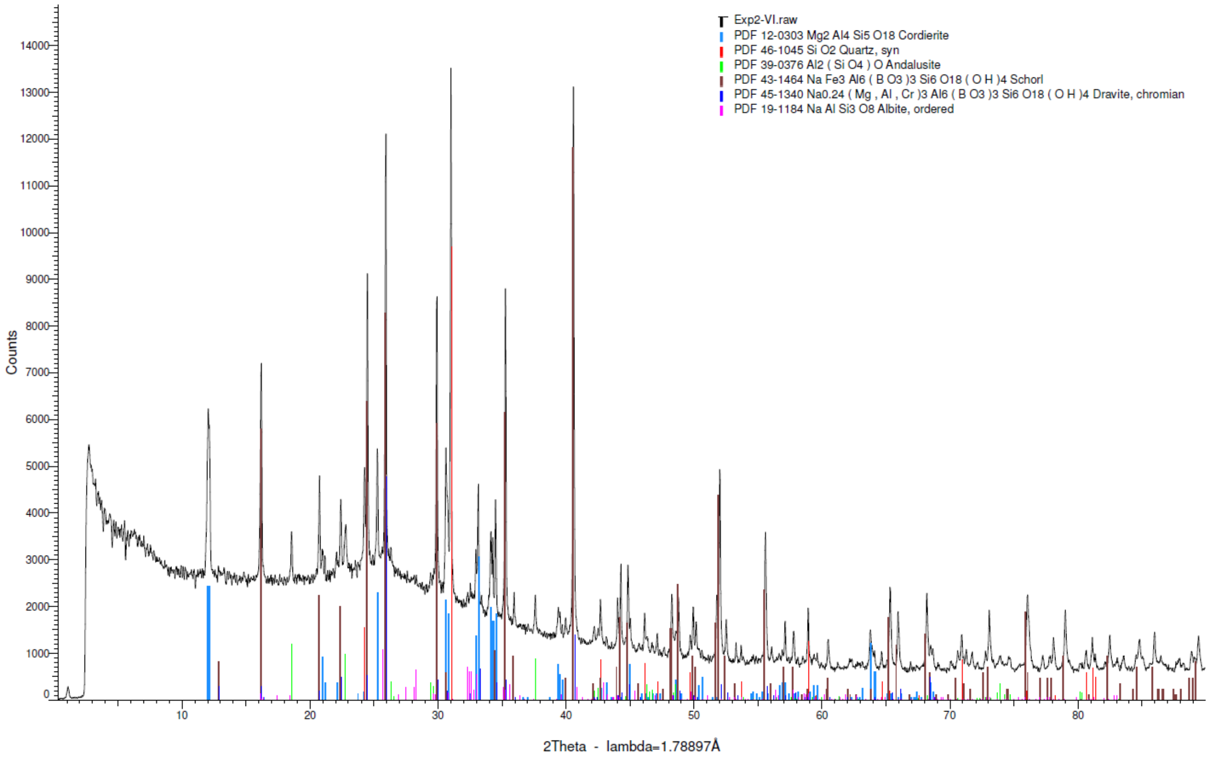

S500-0Pt

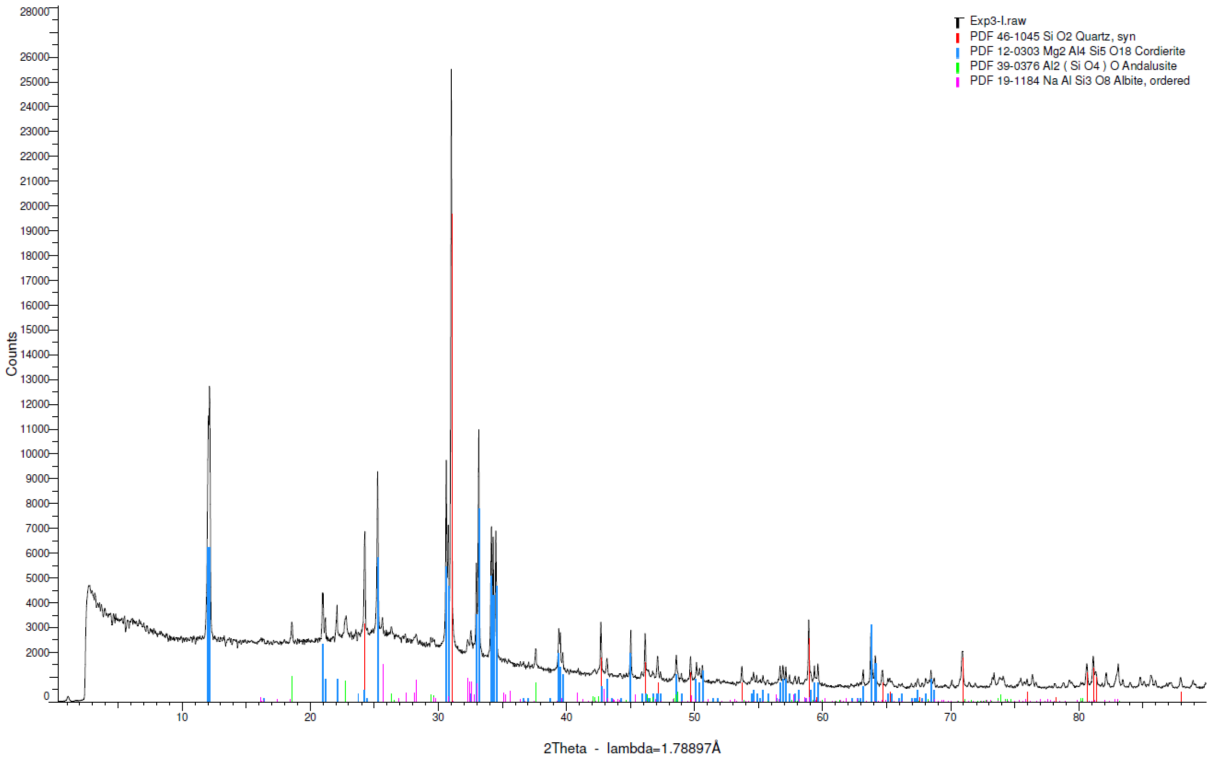

S500-2Pt

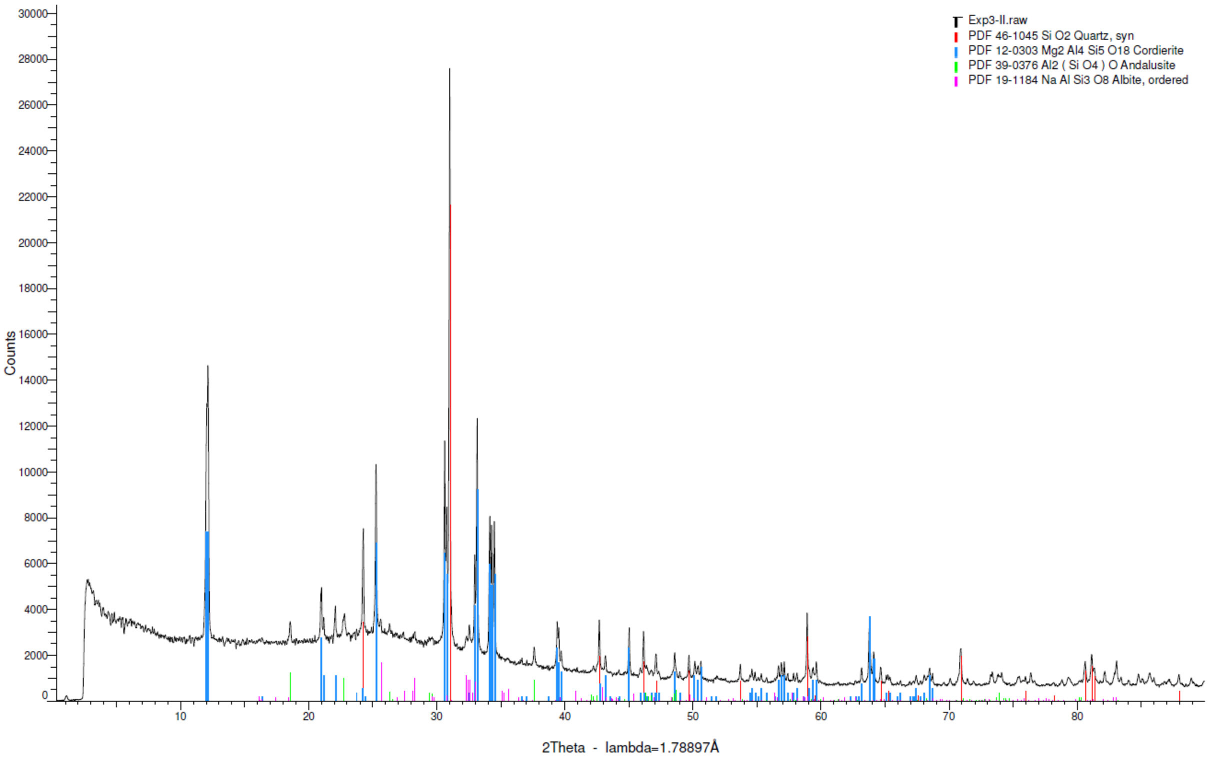

S500-3Pt

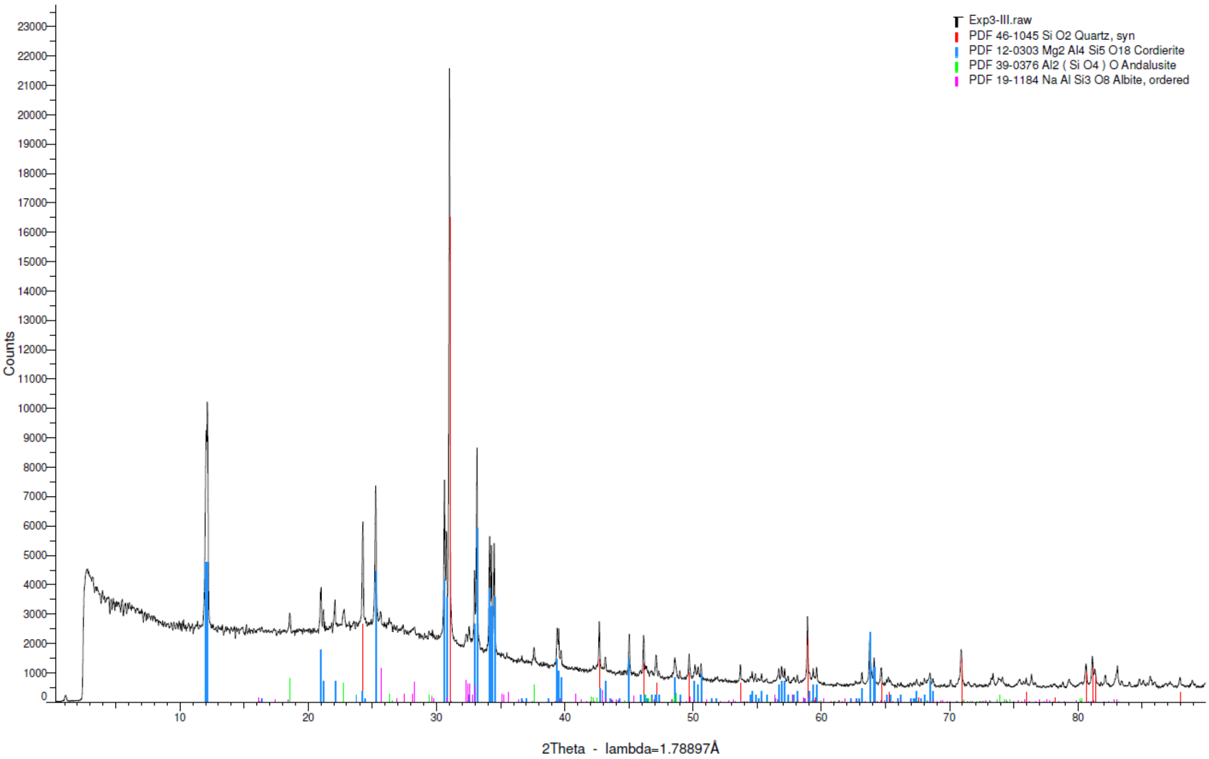

S500-4Pt

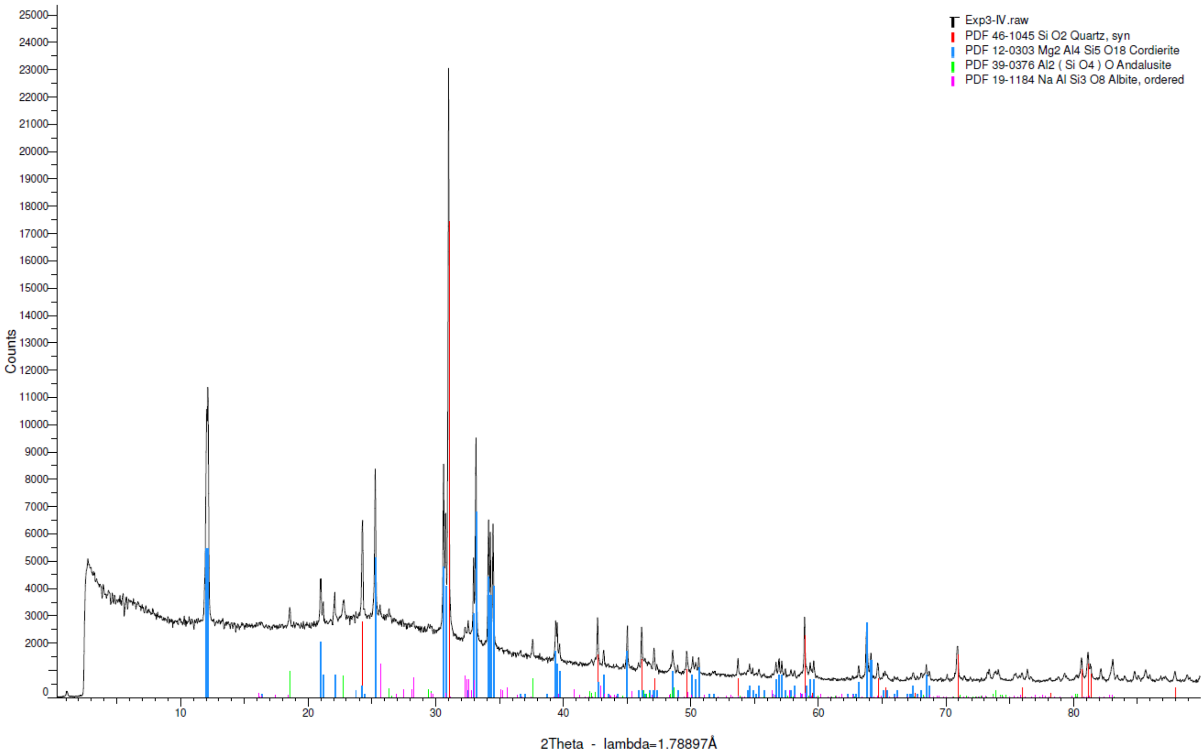

S500-4

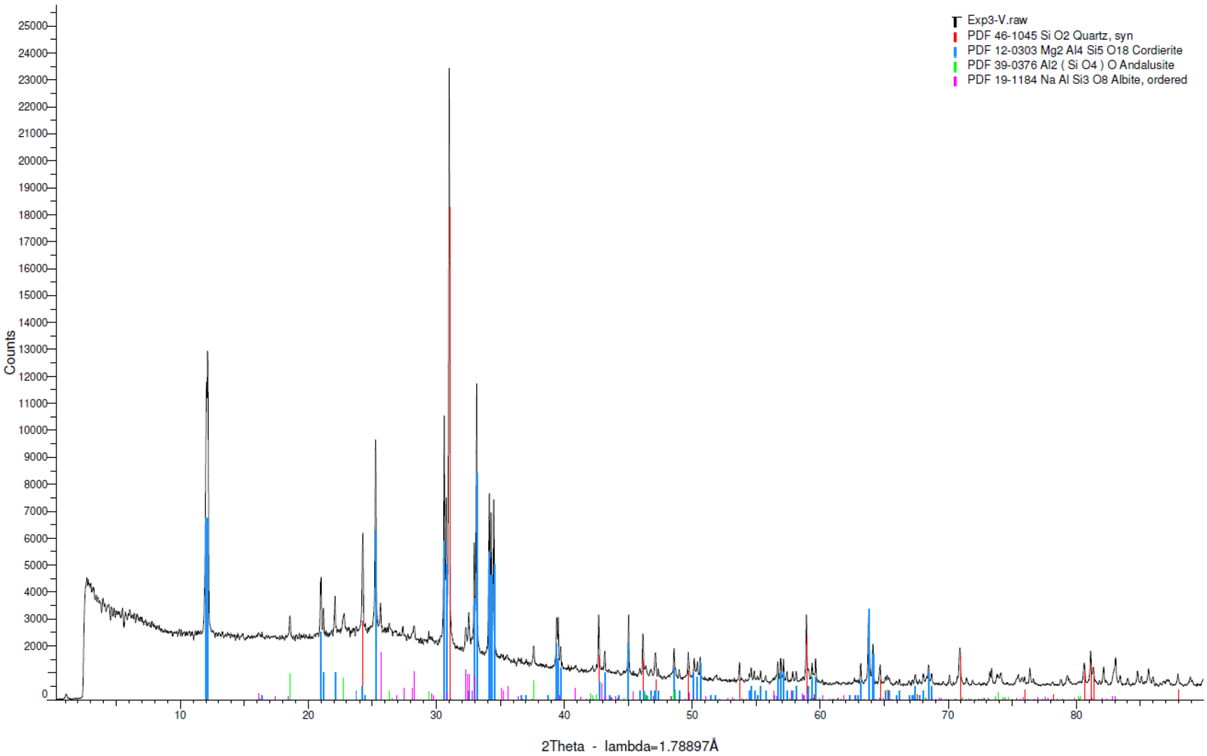

S500-6Pt

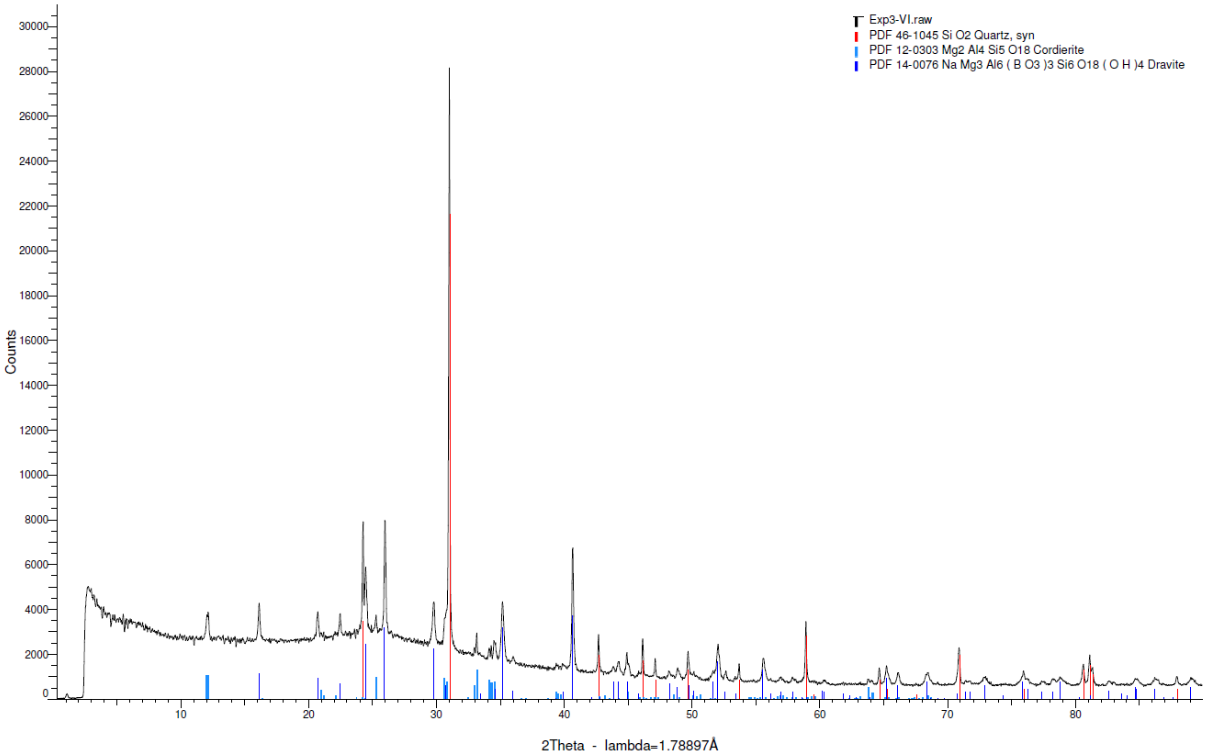

S500-Rev

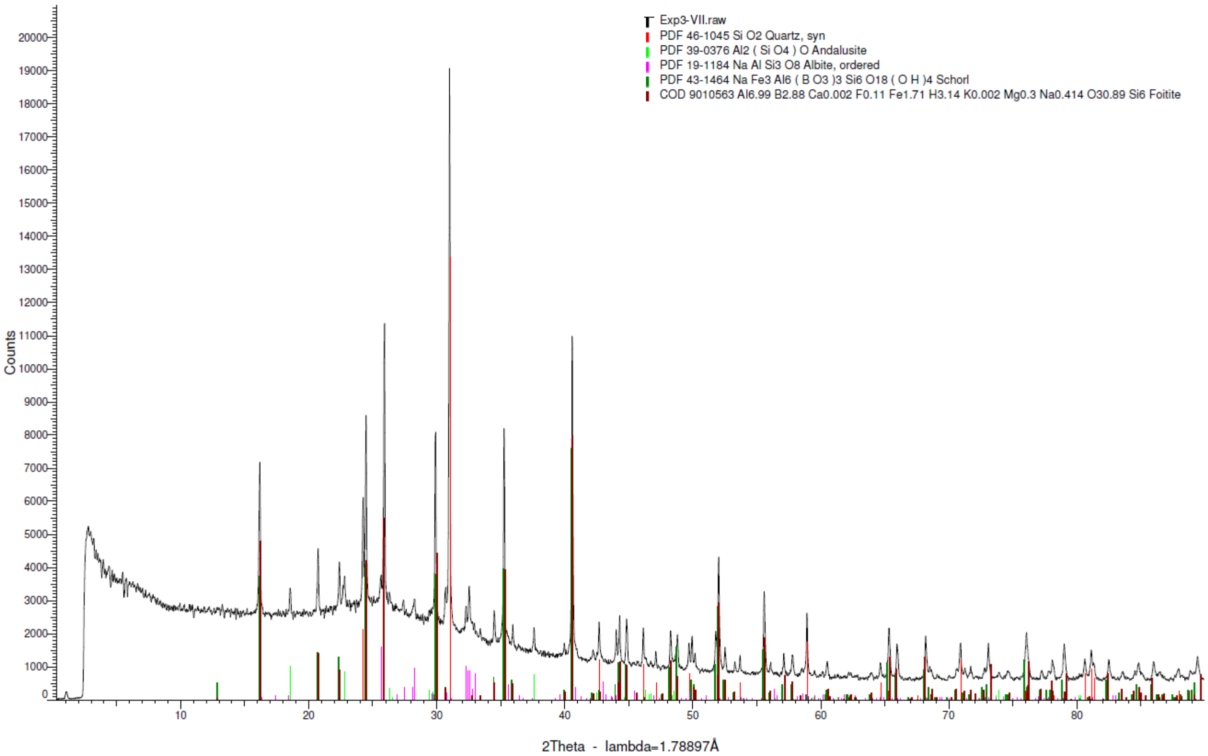

S400-0Pt

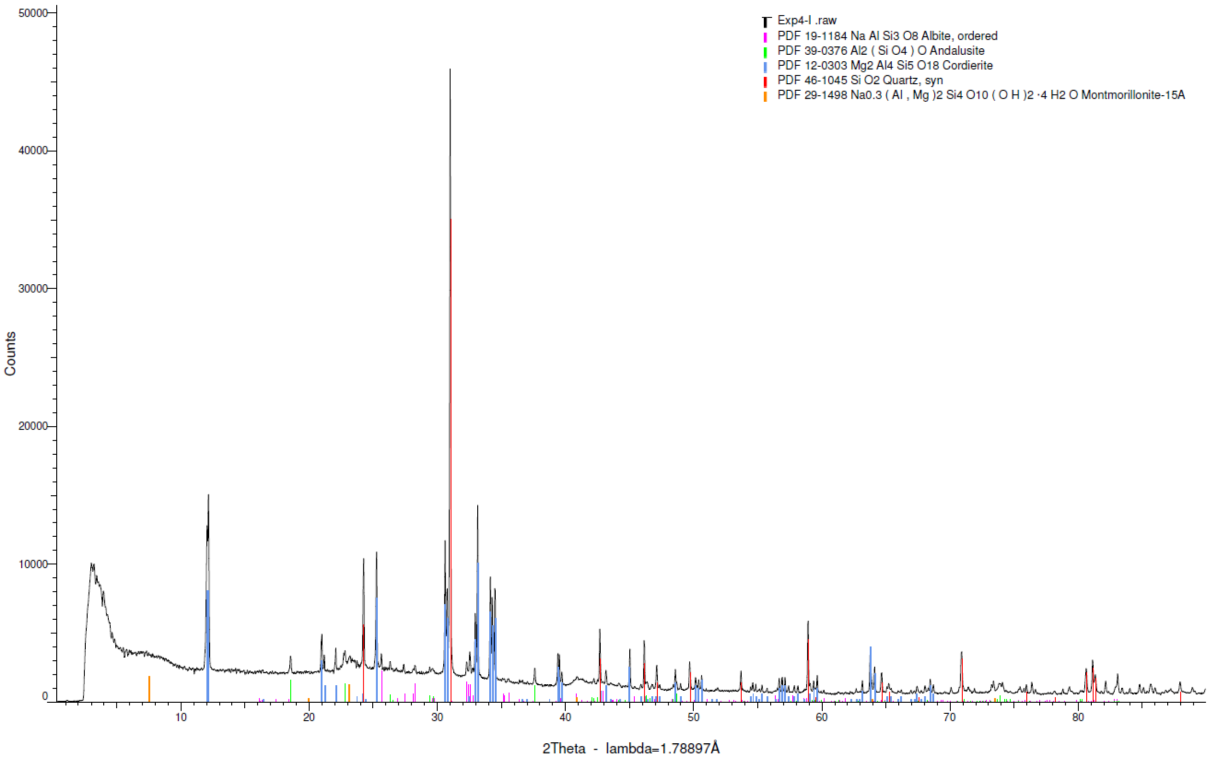

S400-1Pt

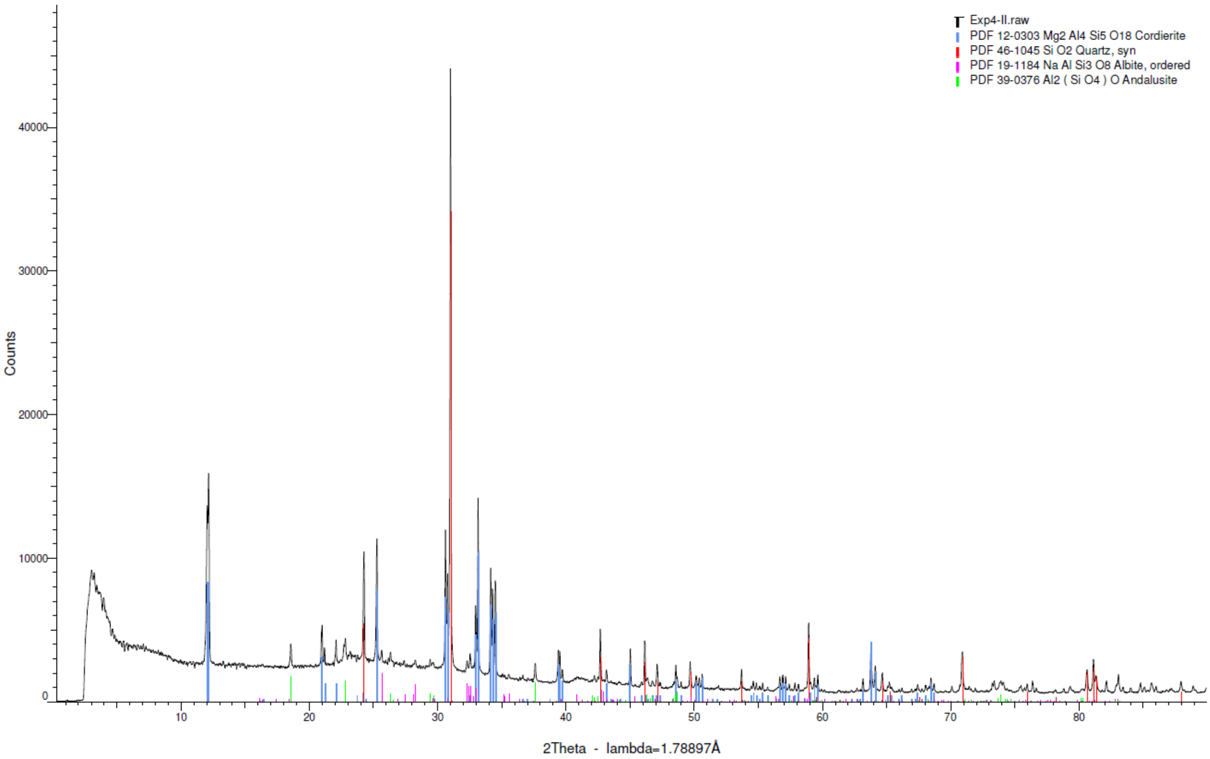

S400-2Pt

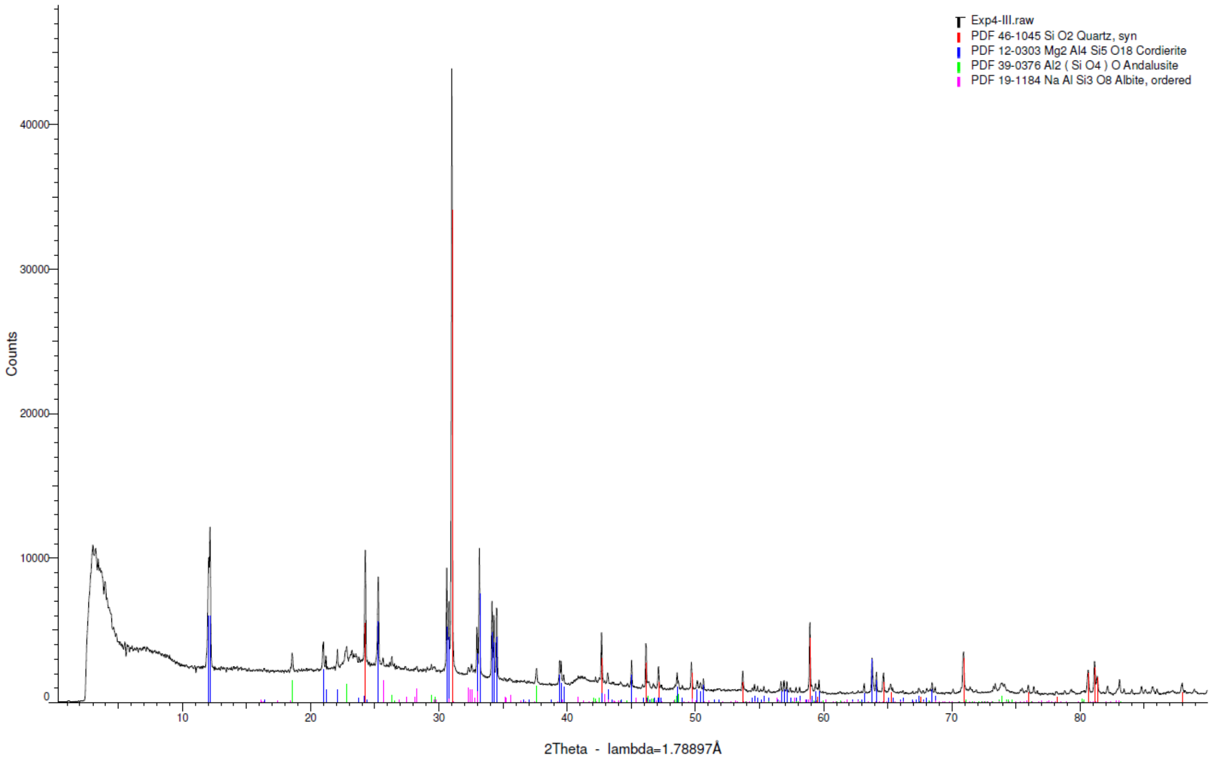

S400-3Pt

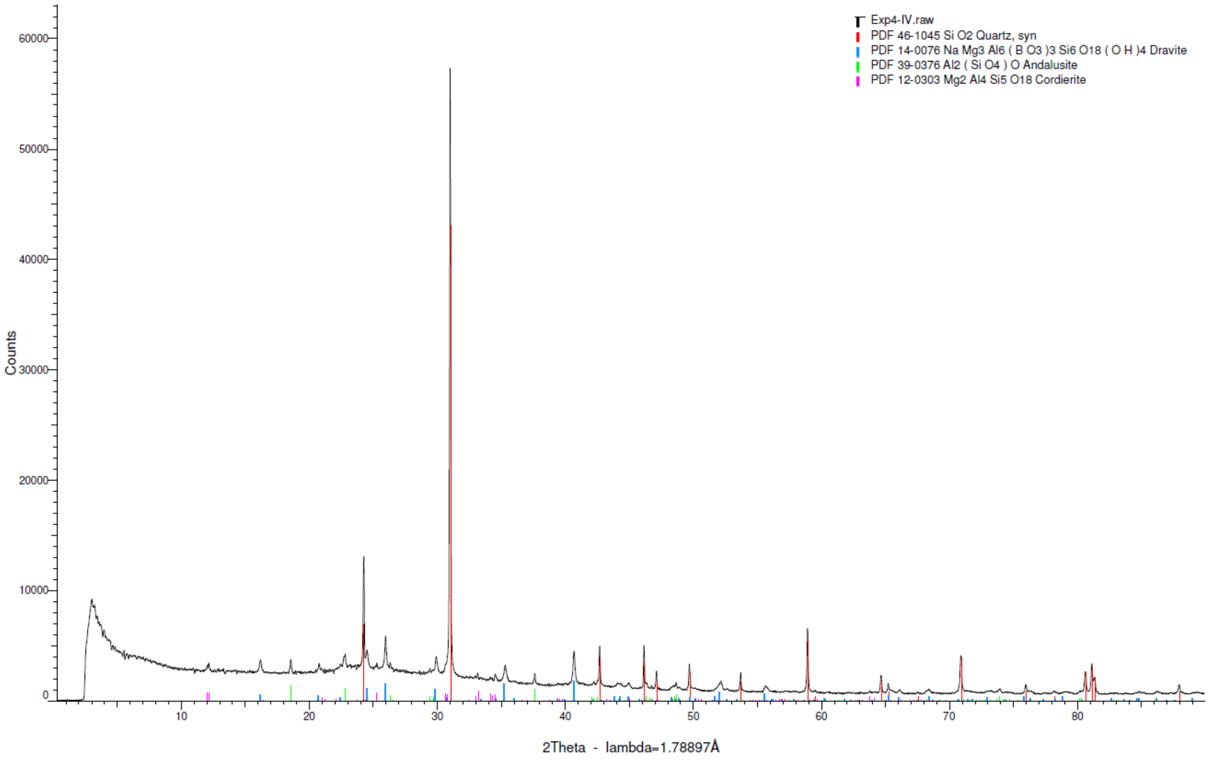

S400-4Pt

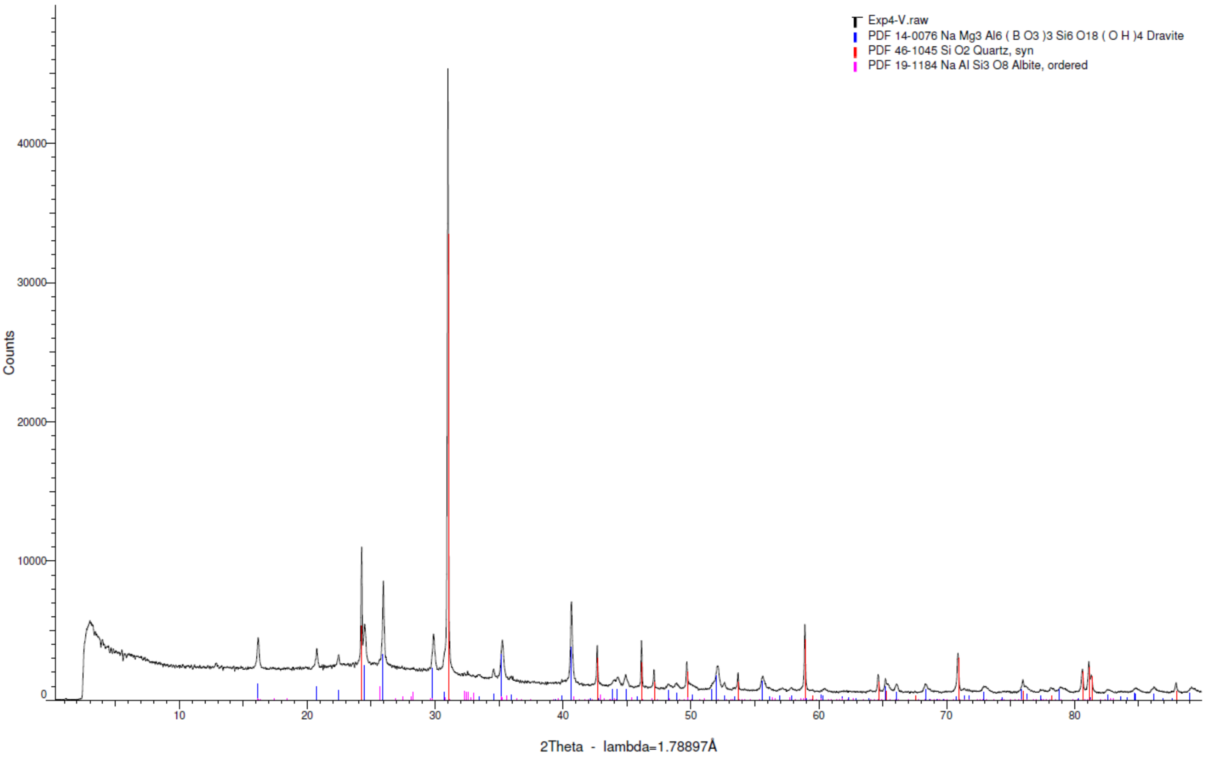

S400-6PtG

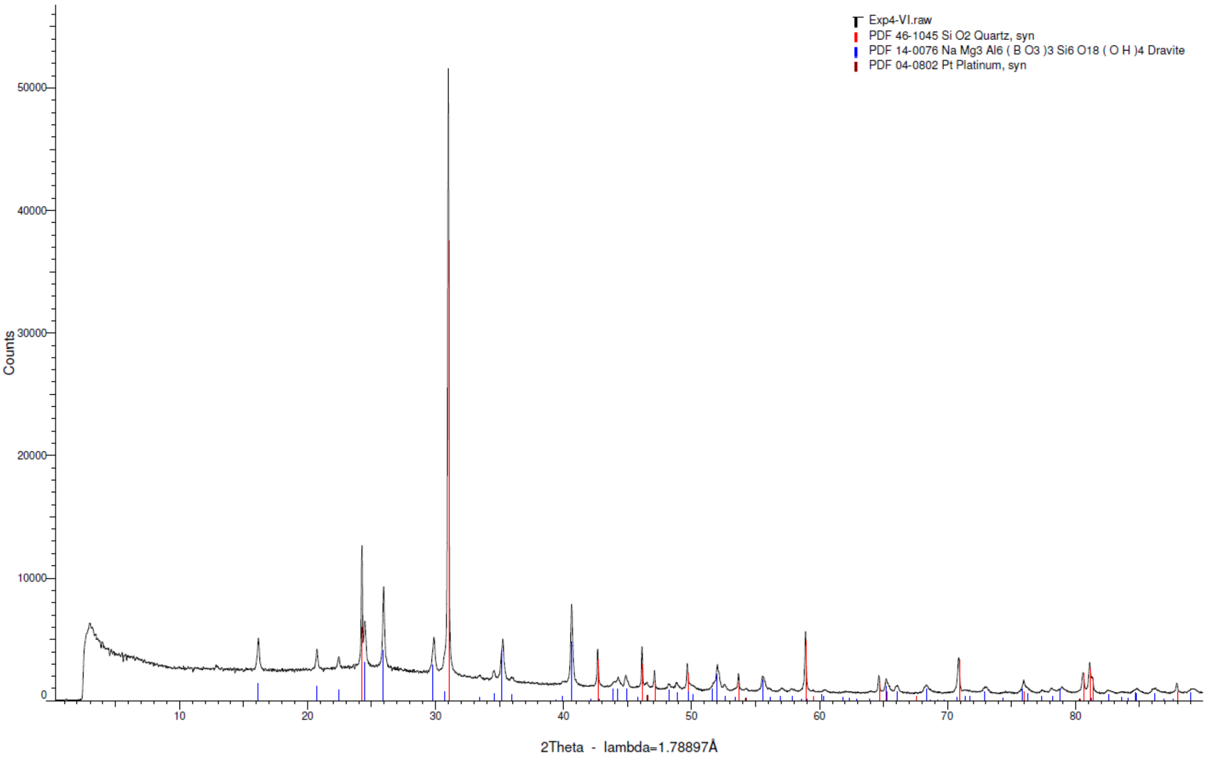

S400-6G

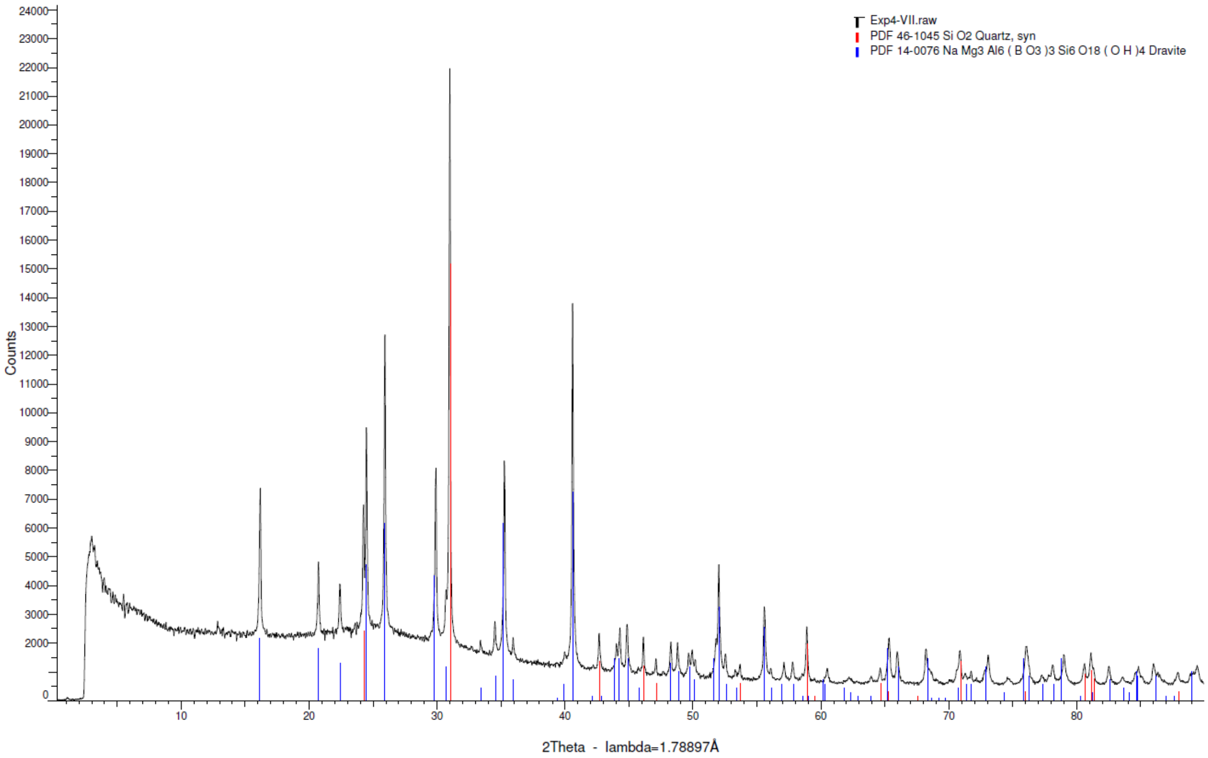
Exp4-VII.raw
PDF 46-1045 Si O2 Quartz, syn
PDF 14-0076 Na Mg3 Al6 (B O3)3 Si6 O18 (O H)4 Dravite
Counts
24000
23000
22000
21000
20000
19000
18000
17000
16000
15000
14000
13000
12000
11000
10000
9000
8000
7000
6000
5000
4000
3000
2000
0
10
20
30
40
50
60
70
80
2Theta - lambda=1.78897Å

SOX-3

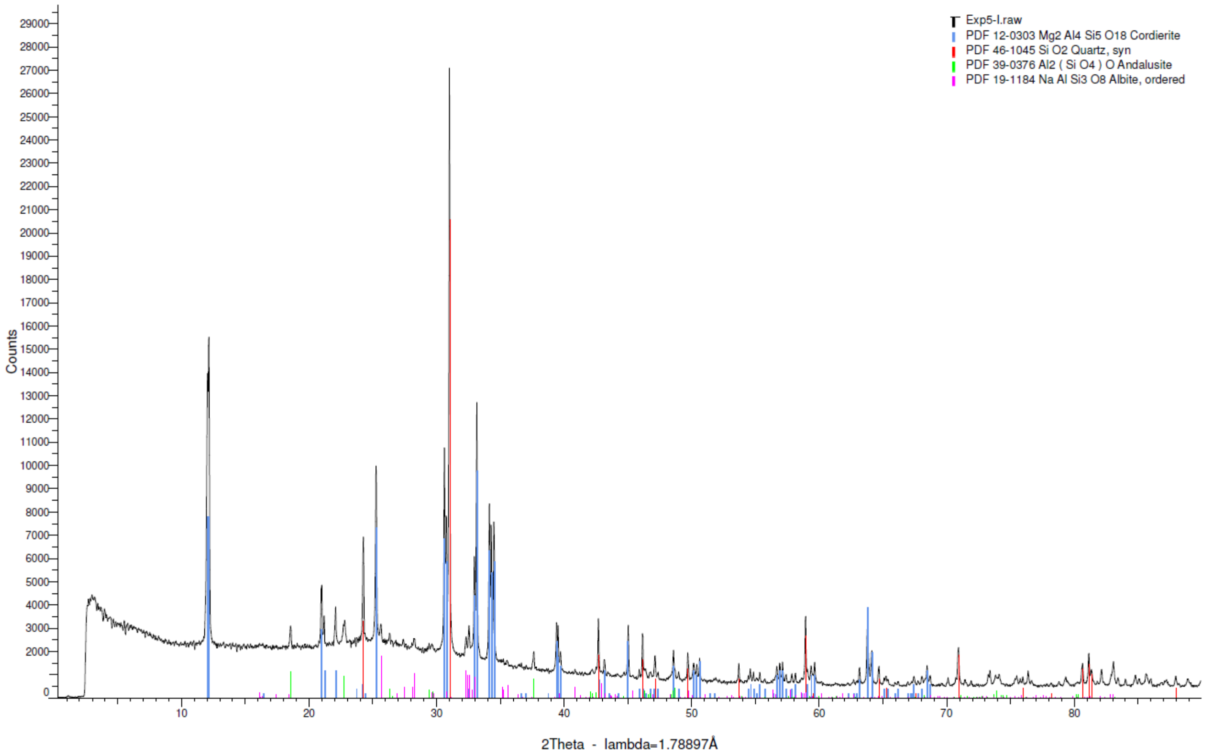
Exp5-I.raw
PDF 12-0303 Mg2 Al4 Si5 O18 Cordierite
PDF 46-1045 Si O2 Quartz, syn
PDF 39-0376 Al2 (Si O4) O Andalusite
PDF 19-1184 Na Al Si3 O8 Albite, ordered
Counts
29000
28000
27000
26000
25000
24000
23000
22000
21000
20000
19000
18000
17000
16000
15000
14000
13000
12000
11000
10000
9000
8000
7000
6000
5000
4000
3000
2000
0
10
20
30
40
50
60
70
80
2Theta - lambda=1.78897Å

SOX-4

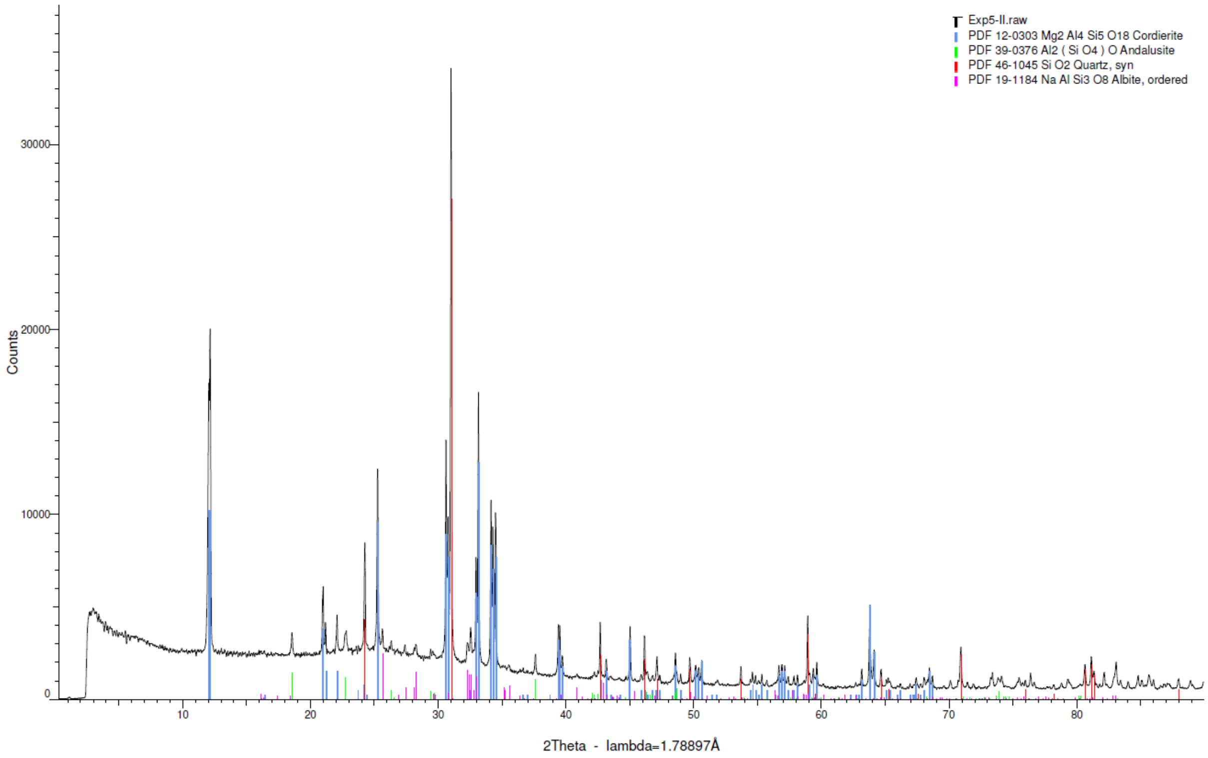
Exp5-II.raw
PDF 12-0303 Mg2 Al4 Si5 O18 Cordierite
PDF 39-0376 Al2 (Si O4) O Andalusite
PDF 46-1045 Si O2 Quartz, syn
PDF 19-1184 Na Al Si3 O8 Albite, ordered
Counts
30000
20000
10000
0
10
20
30
40
50
60
70
80
2Theta - lambda=1.78897Å

SOX-6

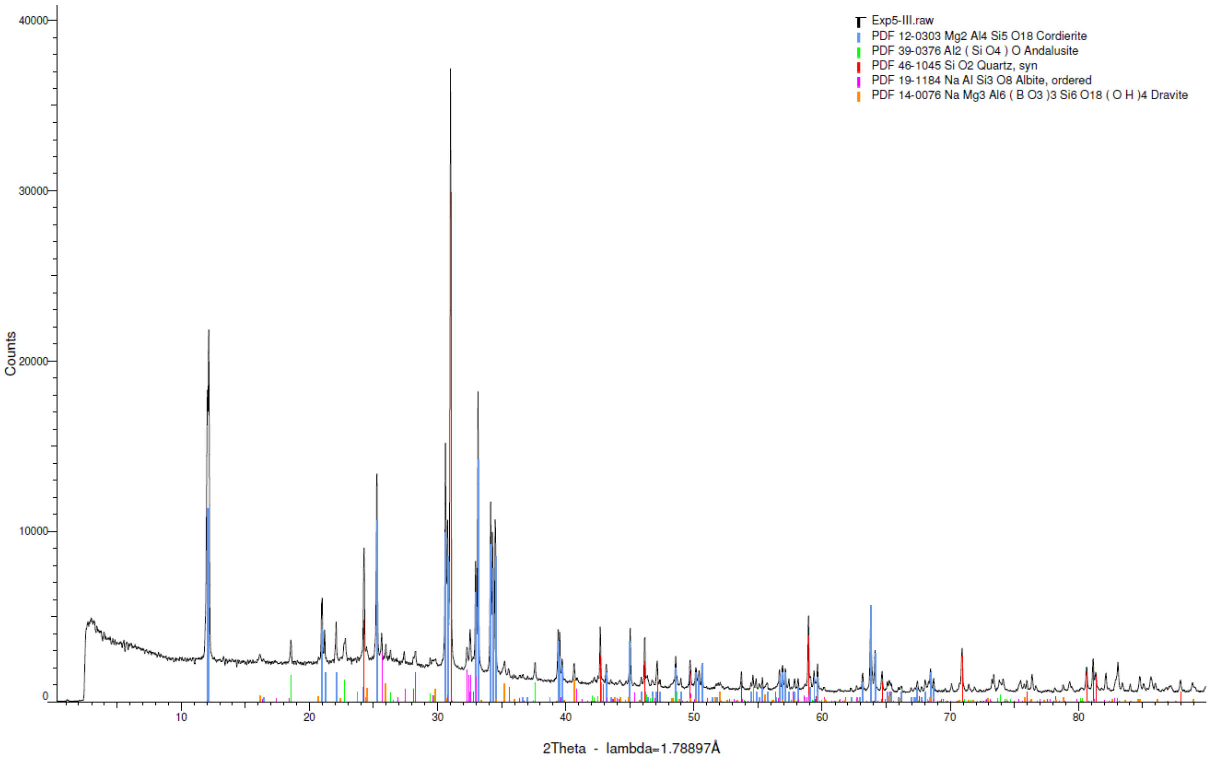
Exp5-III.raw
PDF 12-0303 Mg2 Al4 Si5 O18 Cordierite
PDF 39-0376 Al2 (Si O4) O Andalusite
PDF 46-1045 Si O2 Quartz, syn
PDF 19-1184 Na Al Si3 O8 Albite, ordered
PDF 14-0076 Na Mg3 Al6 (B O3)3 Si6 O18 (O H)4 Dravite
Counts
40000
30000
20000
10000
0
10
20
30
40
50
60
70
80
2Theta - lambda=1.78897Å

SOX-8

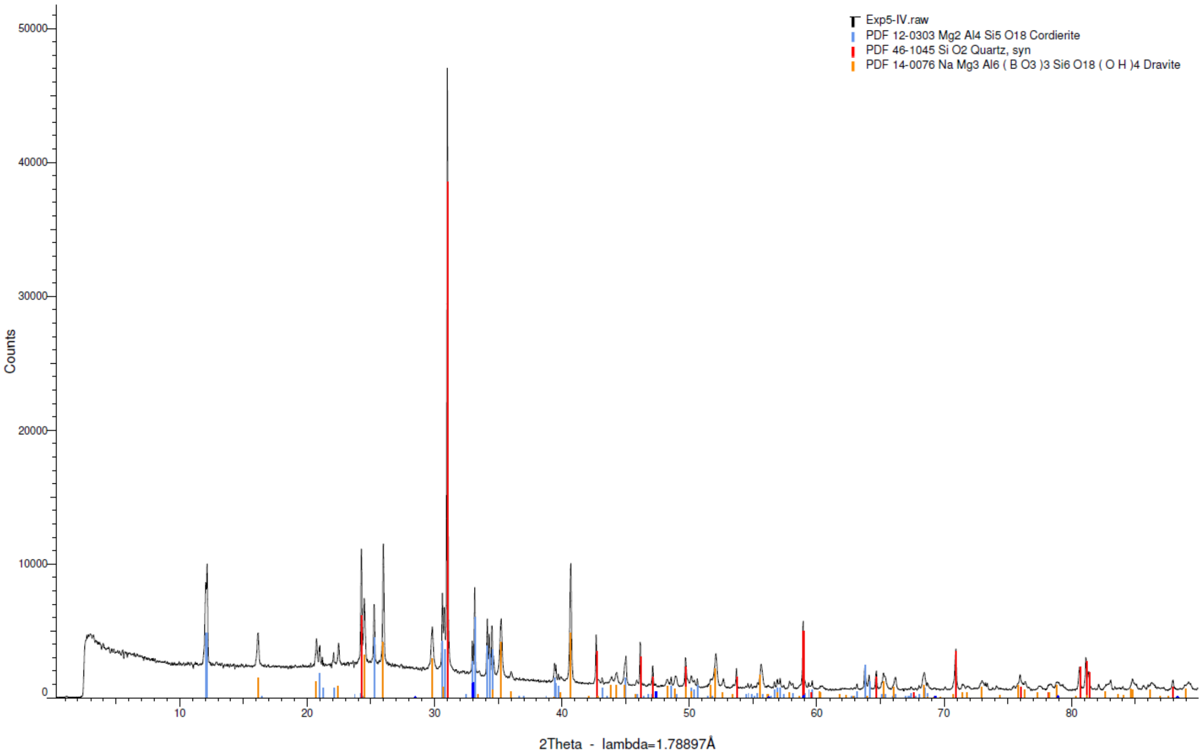
Exp5-IV.raw
PDF 12-0303 Mg2 Al4 Si5 O18 Cordierite
PDF 46-1045 Si O2 Quartz, syn
PDF 14-0076 Na Mg3 Al6 (B O3)3 Si6 O18 (O H)4 Dravite
Counts
50000
40000
30000
20000
10000
0
10
20
30
40
50
60
70
80
2Theta - lambda=1.78897Å

SOX-8G

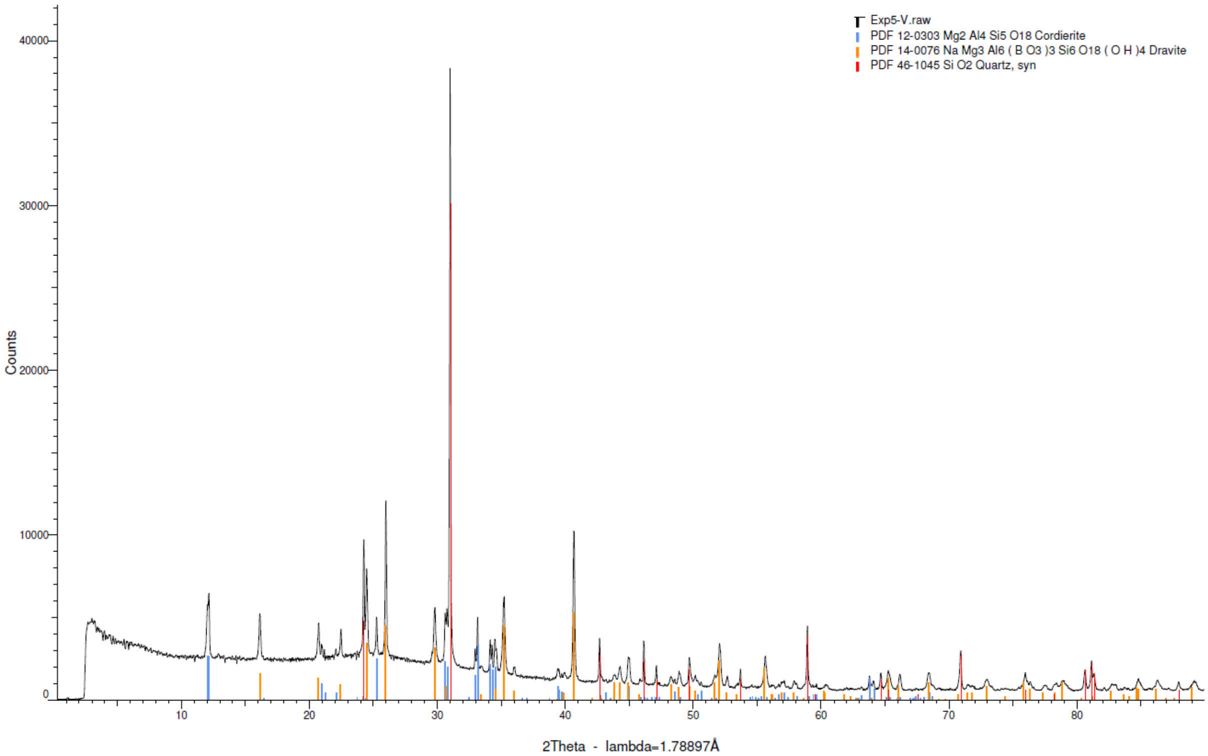
Exp5-V.raw
PDF 12-0303 Mg2 Al4 Si5 O18 Cordierite
PDF 14-0076 Na Mg3 Al6 (B O3)3 Si6 O18 (O H)4 Dravite
PDF 46-1045 Si O2 Quartz, syn
Counts
40000
30000
20000
10000
0
10
20
30
40
50
60
70
80
2Theta - lambda=1.78897Å

Appendix A8

Composition of experimental tourmaline from the cordierite-bearing experiments (Chap II).

Group	Name	SiO_2	TiO_2	Al_2O_3	FeO	MgO	MnO	CaO	Na_2O	K_2O	B_2O_3	H_2O	Total	Site T		Site Z	Site Y					Site X				B	OH^-	Total Al	Infos
														Si	Al	Al	Al	Ti	Fe	Mg	Mn	Ca	Na	K	$[]_X$				
S600-8 _ *IIIa*	2.3_Tur1	36.61	0.28	38.64	2.15	5.67	*b.d.l*	0.78	1.51	*b.d.l*	10.96	3.78	100.37	5.81	0.19	6.00	1.03	0.03	0.29	1.34	0.00	0.13	0.46	0.00	0.40	3.00	4.00	7.22	
	2.3_Tur2	37.61	0.25	38.45	2.08	5.11	*b.d.l*	0.59	1.39	0.10	10.99	3.79	100.43	5.95	0.05	6.00	1.11	0.03	0.27	1.20	0.00	0.10	0.42	0.02	0.45	3.00	4.00	7.16	
	2.3_Tur3	38.29	0.31	39.19	2.04	5.23	*b.d.l*	0.60	1.43	*b.d.l*	11.20	3.86	102.28	5.94	0.06	6.00	1.11	0.04	0.26	1.21	0.00	0.10	0.43	0.00	0.47	3.00	4.00	7.17	
	2.3_Tur4	36.73	0.28	39.40	2.17	6.24	*b.d.l*	0.81	1.63	*b.d.l*	11.15	3.84	102.31	5.73	0.27	6.00	0.97	0.03	0.28	1.45	0.00	0.14	0.49	0.00	0.37	3.00	4.00	7.24	
	2.3_Tur5	36.64	0.21	38.69	2.51	6.73	0.11	0.67	1.80	0.10	11.12	3.83	102.42	5.73	0.27	6.00	0.85	0.02	0.33	1.57	0.01	0.11	0.55	0.02	0.32	3.00	4.00	7.13	
	2.3_Tur6	35.70	0.29	40.58	2.35	5.90	*b.d.l*	1.06	1.55	*b.d.l*	11.14	3.84	102.43	5.57	0.43	6.00	1.04	0.03	0.31	1.37	0.00	0.18	0.47	0.00	0.35	3.00	4.00	7.47	
	2.3_Tur7	36.63	0.42	39.66	2.49	6.50	*b.d.l*	0.82	1.71	0.09	11.24	3.87	103.43	5.67	0.33	6.00	0.90	0.05	0.32	1.50	0.00	0.14	0.51	0.02	0.33	3.00	4.00	7.23	
	2.3_Tur8	34.33	0.33	37.77	2.20	7.05	*b.d.l*	0.81	1.81	*b.d.l*	10.70	3.69	98.79	5.57	0.43	6.00	0.80	0.04	0.30	1.71	0.00	0.14	0.57	0.00	0.29	3.00	4.00	7.23	
	2.3_Tur9	35.51	0.30	38.25	2.26	6.80	*b.d.l*	0.81	1.63	*b.d.l*	10.89	3.76	100.24	5.67	0.33	6.00	0.86	0.04	0.30	1.62	0.00	0.14	0.50	0.00	0.36	3.00	4.00	7.19	
	2.3_Tur10	37.26	0.11	37.36	1.93	7.33	*b.d.l*	0.28	2.08	*b.d.l*	11.04	3.81	101.29	5.87	0.13	6.00	0.80	0.01	0.25	1.72	0.00	0.05	0.63	0.00	0.32	3.00	4.00	6.93	
	2.3_Tur11	35.26	0.22	38.65	2.52	7.14	*b.d.l*	1.01	1.92	*b.d.l*	10.99	3.79	101.51	5.58	0.42	6.00	0.78	0.03	0.33	1.68	0.00	0.17	0.59	0.00	0.24	3.00	4.00	7.21	
	2.3_Tur12	35.07	0.29	38.11	2.21	6.53	*b.d.l*	0.82	1.62	*b.d.l*	10.78	3.72	99.20	5.65	0.35	6.00	0.89	0.04	0.30	1.57	0.00	0.14	0.51	0.00	0.35	3.00	4.00	7.24	
S600-10(G) _ *IV*	1.6_TurOG1	34.50	0.16	37.76	2.97	6.33	*b.d.l*	0.82	1.83	*b.d.l*	10.68	3.68	98.81	5.61	0.39	6.00	0.85	0.02	0.40	1.54	0.00	0.14	0.58	0.00	0.28	3.00	4.00	7.24	
	1.6_TurOG2	35.14	0.17	37.34	2.52	7.01	*b.d.l*	0.43	1.92	*b.d.l*	10.74	3.70	99.00	5.69	0.31	6.00	0.81	0.02	0.34	1.69	0.00	0.07	0.60	0.00	0.32	3.00	4.00	7.12	
	1.6_TurOG3	35.29	0.15	36.08	2.49	7.63	*b.d.l*	0.36	2.20	*b.d.l*	10.68	3.68	98.60	5.74	0.26	6.00	0.66	0.02	0.34	1.85	0.00	0.06	0.69	0.00	0.24	3.00	4.00	6.92	
	1.6_TurOG4	34.11	0.33	38.03	2.55	6.46	*b.d.l*	0.85	1.72	*b.d.l*	10.66	3.68	98.39	5.56	0.44	6.00	0.87	0.04	0.35	1.57	0.00	0.15	0.54	0.00	0.31	3.00	4.00	7.31	
	1.6_TurOG5	35.33	0.32	37.61	2.53	6.78	*b.d.l*	0.67	1.78	*b.d.l*	10.80	3.72	99.60	5.68	0.32	6.00	0.81	0.04	0.34	1.63	0.00	0.11	0.56	0.00	0.33	3.00	4.00	7.13	
	1.6_TurOG6	35.30	0.26	37.74	2.48	6.80	*b.d.l*	0.62	1.85	*b.d.l*	10.81	3.73	99.63	5.68	0.32	6.00	0.83	0.03	0.33	1.63	0.00	0.11	0.58	0.00	0.32	3.00	4.00	7.15	
	1.6_TurOG7	35.42	*b.d.l*	36.63	2.73	7.92	*b.d.l*	0.24	2.41	*b.d.l*	10.80	3.72	99.96	5.70	0.30	6.00	0.64	0.00	0.37	1.90	0.00	0.04	0.75	0.00	0.21	3.00	4.00	6.95	
	1.6_TurOG8	36.66	*b.d.l*	36.86	2.24	6.36	*b.d.l*	0.40	1.81	*b.d.l*	10.78	3.72	98.96	5.91	0.09	6.00	0.91	0.00	0.30	1.53	0.00	0.07	0.57	0.00	0.37	3.00	4.00	7.00	
	1.6_TurOG9	36.35	*b.d.l*	36.50	2.11	6.89	*b.d.l*	0.21	1.93	*b.d.l*	10.74	3.70	98.59	5.88	0.12	6.00	0.85	0.00	0.29	1.66	0.00	0.04	0.61	0.00	0.36	3.00	4.00	6.96	
	1.6_TurOG10	34.85	0.22	37.49	2.25	6.97	*b.d.l*	0.60	1.95	*b.d.l*	10.72	3.70	98.80	5.65	0.35	6.00	0.81	0.03	0.31	1.68	0.00	0.10	0.61	0.00	0.28	3.00	4.00	7.16	
	1.6_TurOG11	34.95	0.20	37.81	2.84	6.75	*b.d.l*	0.70	1.90	*b.d.l*	10.79	3.72	99.78	5.63	0.37	6.00	0.81	0.02	0.38	1.62	0.00	0.12	0.59	0.00	0.28	3.00	4.00	7.18	
	1.6_TurOG12	35.85	0.20	36.92	2.55	7.21	*b.d.l*	0.46	2.11	*b.d.l*	10.83	3.73	99.91	5.75	0.25	6.00	0.73	0.02	0.34	1.73	0.00	0.08	0.66	0.00	0.27	3.00	4.00	6.98	
	1.6_TurOG13	35.08	0.13	37.00	2.36	6.91	*b.d.l*	0.68	1.99	*b.d.l*	10.69	3.69	98.55	5.70	0.30	6.00	0.79	0.02	0.32	1.67	0.00	0.12	0.63	0.00	0.26	3.00	4.00	7.09	
	1.6_TurOG14	36.76	*b.d.l*	37.91	2.14	6.91	*b.d.l*	0.44	1.98	*b.d.l*	11.00	3.79	101.04	5.81	0.19	6.00	0.87	0.00	0.28	1.63	0.00	0.07	0.61	0.00	0.32	3.00	4.00	7.06	
	1.6_TurOG15	36.83	0.13	38.70	2.20	6.69	*b.d.l*	0.45	1.97	*b.d.l*	11.10	3.83	101.92	5.77	0.23	6.00	0.91	0.02	0.29	1.56	0.00	0.08	0.60	0.00	0.33	3.00	4.00	7.14	
	1.6_TurOG16	36.64	*b.d.l*	37.22	2.00	6.90	*b.d.l*	0.28	1.85	0.09	10.87	3.75	99.67	5.86	0.14	6.00	0.88	0.00	0.27	1.64	0.00	0.05	0.57	0.02	0.36	3.00	4.00	7.02	

Group	Name	SiO_2	TiO_2	Al_2O_3	FeO	MgO	MnO	CaO	Na_2O	K_2O	B_2O_3	H_2O	Total	Site T		Site Z	Site Y					Site X				B	OH^-	Total Al	Infos
														Si	Al	Al	Al	Ti	Fe	Mg	Mn	Ca	Na	K	$[]_X$				
S600-10(G) _ *IIIa*	1.5_Turgb1	35.44	0.15	36.70	2.37	6.96	*b.d.l*	0.50	1.87	*b.d.l*	10.69	3.69	98.41	5.76	0.24	6.00	0.79	0.02	0.32	1.69	0.00	0.09	0.59	0.00	0.32	3.00	4.00	7.03	
	1.5_Turgb2	35.05	0.18	37.42	2.29	6.73	*b.d.l*	0.60	1.88	*b.d.l*	10.71	3.69	98.55	5.69	0.31	6.00	0.85	0.02	0.31	1.63	0.00	0.10	0.59	0.00	0.30	3.00	4.00	7.16	
	1.5_Turgb3	32.58	1.27	37.70	4.67	5.29	*b.d.l*	1.32	1.36	*b.d.l*	10.52	3.63	98.37	5.38	0.62	6.00	0.73	0.16	0.65	1.30	0.00	0.23	0.43	0.00	0.33	3.00	4.00	7.34	core
	1.5_Turgb4	34.79	0.27	37.25	2.79	6.51	*b.d.l*	0.80	1.88	*b.d.l*	10.68	3.68	98.67	5.66	0.34	6.00	0.81	0.03	0.38	1.58	0.00	0.14	0.59	0.00	0.27	3.00	4.00	7.14	
	1.5_Turgb5	33.83	0.31	38.58	3.83	5.53	*b.d.l*	1.10	1.56	*b.d.l*	10.67	3.68	99.11	5.51	0.49	6.00	0.91	0.04	0.52	1.34	0.00	0.19	0.49	0.00	0.32	3.00	4.00	7.40	core
	1.5_Turgb6	33.60	1.08	37.73	4.59	5.02	*b.d.l*	1.15	1.55	*b.d.l*	10.61	3.66	99.15	5.50	0.50	6.00	0.79	0.13	0.63	1.23	0.00	0.20	0.49	0.00	0.31	3.00	4.00	7.28	core
	1.5_Turgb7	35.91	*b.d.l*	37.40	2.35	6.83	*b.d.l*	0.38	1.94	*b.d.l*	10.81	3.73	99.47	5.77	0.23	6.00	0.86	0.00	0.32	1.64	0.00	0.07	0.60	0.00	0.33	3.00	4.00	7.09	
	1.5_Turgb8	34.84	0.19	37.24	3.94	6.21	*b.d.l*	0.93	1.66	*b.d.l*	10.71	3.69	99.44	5.66	0.34	6.00	0.78	0.02	0.53	1.50	0.00	0.16	0.52	0.00	0.32	3.00	4.00	7.12	core
	1.5_Turgb9	36.76	0.13	36.42	2.03	7.42	*b.d.l*	0.36	1.94	*b.d.l*	10.86	3.74	99.73	5.88	0.12	6.00	0.75	0.02	0.27	1.77	0.00	0.06	0.60	0.00	0.34	3.00	4.00	6.87	
	1.5_Turgb10	35.35	0.26	37.85	2.62	6.51	*b.d.l*	0.70	1.81	*b.d.l*	10.81	3.73	99.79	5.68	0.32	6.00	0.86	0.03	0.35	1.56	0.00	0.12	0.56	0.00	0.32	3.00	4.00	7.17	
	1.5_Turgb11	36.22	*b.d.l*	37.26	2.33	6.99	*b.d.l*	0.43	1.82	0.09	10.85	3.74	99.85	5.80	0.20	6.00	0.84	0.00	0.31	1.67	0.00	0.07	0.57	0.02	0.34	3.00	4.00	7.03	
	1.5_Turgb12	34.03	0.30	38.49	4.24	5.35	*b.d.l*	1.21	1.49	*b.d.l*	10.70	3.69	99.65	5.53	0.47	6.00	0.90	0.04	0.58	1.30	0.00	0.21	0.47	0.00	0.32	3.00	4.00	7.37	core
	1.6_Turgb1	36.50	0.15	37.43	2.07	6.84	*b.d.l*	0.44	1.85	*b.d.l*	10.90	3.76	99.98	5.82	0.18	6.00	0.86	0.02	0.28	1.63	0.00	0.08	0.57	0.00	0.35	3.00	4.00	7.04	
	1.6_Turgb2	35.68	0.18	37.99	2.52	6.80	*b.d.l*	0.58	1.75	*b.d.l*	10.88	3.75	100.15	5.70	0.30	6.00	0.85	0.02	0.34	1.62	0.00	0.10	0.54	0.00	0.36	3.00	4.00	7.15	
	1.6_Turgb3	35.75	*b.d.l*	38.31	2.76	6.29	*b.d.l*	0.71	1.73	*b.d.l*	10.88	3.75	100.30	5.71	0.29	6.00	0.92	0.00	0.37	1.50	0.00	0.12	0.53	0.00	0.34	3.00	4.00	7.21	
	1.6_Turgb4	35.78	0.16	37.89	2.45	6.94	*b.d.l*	0.56	1.97	*b.d.l*	10.90	3.76	100.48	5.70	0.30	6.00	0.82	0.02	0.33	1.65	0.00	0.09	0.61	0.00	0.30	3.00	4.00	7.12	
	1.6_Turgb5	36.99	0.12	37.23	1.98	7.36	*b.d.l*	0.29	1.89	*b.d.l*	10.98	3.78	100.71	5.86	0.14	6.00	0.80	0.01	0.26	1.74	0.00	0.05	0.58	0.00	0.37	3.00	4.00	6.95	
	1.6_Turgb6	37.22	*b.d.l*	37.30	2.08	6.96	*b.d.l*	0.45	1.85	*b.d.l*	10.98	3.78	100.79	5.89	0.11	6.00	0.85	0.00	0.27	1.64	0.00	0.08	0.57	0.00	0.36	3.00	4.00	6.96	
	1.6_Turgb7	36.72	*b.d.l*	37.28	2.16	7.22	*b.d.l*	0.48	2.02	*b.d.l*	10.95	3.78	100.84	5.83	0.17	6.00	0.80	0.00	0.29	1.71	0.00	0.08	0.62	0.00	0.30	3.00	4.00	6.97	
	1.6_Turgb8	36.20	0.21	37.39	2.45	7.08	*b.d.l*	0.67	2.05	*b.d.l*	10.93	3.77	100.82	5.75	0.25	6.00	0.76	0.03	0.33	1.68	0.00	0.11	0.63	0.00	0.25	3.00	4.00	7.00	
	1.6_Turgb9	37.07	0.14	37.68	2.45	7.29	*b.d.l*	0.50	1.91	*b.d.l*	11.09	3.82	102.01	5.81	0.19	6.00	0.77	0.02	0.32	1.70	0.00	0.08	0.58	0.00	0.33	3.00	4.00	6.96	
S600-10(G) _ *IIIb*	1.5_Turflot1	38.24	*b.d.l*	37.39	1.70	7.31	*b.d.l*	0.13	2.08	*b.d.l*	11.14	3.84	101.97	5.97	0.03	6.00	0.84	0.00	0.22	1.70	0.00	0.02	0.63	0.00	0.35	3.00	4.00	6.87	
	1.5_Turflot2	36.86	0.20	38.80	2.03	7.08	*b.d.l*	0.44	1.91	*b.d.l*	11.15	3.84	102.45	5.75	0.25	6.00	0.87	0.02	0.26	1.64	0.00	0.07	0.58	0.00	0.35	3.00	4.00	7.13	
	1.5_Turflot3	36.24	0.26	39.10	2.20	7.13	*b.d.l*	0.84	1.95	*b.d.l*	11.16	3.85	102.76	5.65	0.35	6.00	0.83	0.03	0.29	1.66	0.00	0.14	0.59	0.00	0.27	3.00	4.00	7.18	
	1.5_Turflot4	36.64	0.27	38.97	2.38	7.27	*b.d.l*	0.84	1.97	*b.d.l*	11.22	3.87	103.51	5.67	0.33	6.00	0.79	0.03	0.31	1.68	0.00	0.14	0.59	0.00	0.27	3.00	4.00	7.11	
	1.5_Turflot5	35.40	0.41	38.81	2.16	6.47	*b.d.l*	1.17	1.60	*b.d.l*	10.95	3.77	100.76	5.62	0.38	6.00	0.89	0.05	0.29	1.53	0.00	0.20	0.49	0.00	0.31	3.00	4.00	7.26	
	1.5_Turflot6	35.85	0.18	37.57	1.98	6.87	*b.d.l*	0.45	1.90	*b.d.l*	10.83	3.73	99.43	5.76	0.24	6.00	0.86	0.02	0.27	1.64	0.00	0.08	0.59	0.00	0.33	3.00	4.00	7.11	
	1.5_Turflot7	36.53	*b.d.l*	37.13	1.82	7.63	*b.d.l*	0.32	2.16	*b.d.l*	10.93	3.77	100.42	5.81	0.19	6.00	0.77	0.00	0.24	1.81	0.00	0.06	0.67	0.00	0.28	3.00	4.00	6.96	
	1.5_Turflot8	36.96	*b.d.l*	35.69	1.99	9.05	*b.d.l*	0.16	2.56	*b.d.l*	10.98	3.79	101.24	5.85	0.15	6.00	0.50	0.00	0.26	2.14	0.00	0.03	0.79	0.00	0.19	3.00	4.00	6.66	
	1.5_Turflot9	35.30	0.39	38.70	3.63	5.86	*b.d.l*	1.10	1.48	*b.d.l*	10.92	3.77	101.19	5.62	0.38	6.00	0.87	0.05	0.48	1.39	0.00	0.19	0.46	0.00	0.36	3.00	4.00	7.26	
	1.5_Turflot10	35.54	0.16	38.04	2.03	7.63	*b.d.l*	0.66	2.06	*b.d.l*	10.95	3.77	100.85	5.64	0.36	6.00	0.76	0.02	0.27	1.81	0.00	0.11	0.63	0.00	0.25	3.00	4.00	7.12	
	1.5_Turflot11	36.25	0.22	39.08	2.23	6.59	*b.d.l*	0.85	1.67	*b.d.l*	11.08	3.82	101.80	5.69	0.31	6.00	0.91	0.03	0.29	1.54	0.00	0.14	0.51	0.00	0.35	3.00	4.00	7.23	
S500-6 _ *IIIa*	8.8_Tur1	36.71	0.14	36.09	2.50	7.61	*b.d.l*	0.43	1.98	0.06	10.87	3.75	100.20	5.87	0.13	6.00	0.67	0.02	0.33	1.81	0.00	0.07	0.61	0.01	0.30	3.00	4.00	6.80	
	8.8_Tur2	37.32	0.11	35.86	2.37	7.58	*b.d.l*	0.30	2.01	0.05	10.91	3.76	100.27	5.95	0.05	6.00	0.68	0.01	0.32	1.80	0.00	0.05	0.62	0.01	0.32	3.00	4.00	6.73	
	8.8_Tur3	37.01	*b.d.l*	36.38	2.15	7.75	*b.d.l*	0.24	2.12	0.05	10.93	3.77	100.43	5.89	0.11	6.00	0.71	0.00	0.29	1.84	0.00	0.04	0.65	0.01	0.30	3.00	4.00	6.82	
	8.8_Tur4	36.94	0.08	36.53	2.20	7.66	*b.d.l*	0.47	1.99	0.06	10.95	3.77	100.66	5.87	0.13	6.00	0.70	0.01	0.29	1.81	0.00	0.08	0.61	0.01	0.29	3.00	4.00	6.84	
	8.8_Tur5	36.77	0.19	37.84	2.89	6.76	*b.d.l*	1.01	1.65	0.04	11.06	3.81	102.11	5.78	0.22	6.00	0.79	0.02	0.38	1.58	0.00	0.17	0.50	0.01	0.32	3.00	4.00	7.01	
	8.8_Tur6	38.19	0.06	36.49	2.26	7.80	*b.d.l*	0.39	2.04	*b.d.l*	11.13	3.84	102.27	5.96	0.04	6.00	0.68	0.01	0.29	1.82	0.00	0.07	0.62	0.00	0.32	3.00	4.00	6.72	
	8.8_Tur7	37.06	0.19	35.75	2.94	6.66	*b.d.l*	1.02	1.49	*b.d.l*	10.82	3.73	99.69	5.95	0.05	6.00	0.72	0.02	0.39	1.59	0.00	0.17	0.47	0.00	0.36	3.00	4.00	6.77	
	8.8_Tur8	36.68	*b.d.l*	35.66	2.41	7.80	0.15	0.36	2.02	*b.d.l*	10.82	3.73	99.72	5.89	0.11	6.00	0.64	0.00	0.32	1.87	0.02	0.06	0.63	0.00	0.31	3.00	4.00	6.75	

Group	Name	SiO_2	TiO_2	Al_2O_3	FeO	MgO	MnO	CaO	Na_2O	K_2O	B_2O_3	H_2O	Total	Site T		Site Z	Site Y					Site X				B	OH^-	Total Al	Infos
														Si	Al	Al	Al	Ti	Fe	Mg	Mn	Ca	Na	K	$[]_X$				
S500-6 _ *IIIa*	8.8_Tur9	36.08	0.08	35.92	2.06	7.59	*b.d.l*	0.31	1.95	*b.d.l*	10.72	3.69	98.45	5.85	0.15	6.00	0.72	0.01	0.28	1.84	0.00	0.05	0.61	0.00	0.33	3.00	4.00	6.87	
	8.8_Tur10	36.06	0.08	36.02	2.59	7.23	*b.d.l*	0.68	1.84	*b.d.l*	10.74	3.70	98.98	5.84	0.16	6.00	0.71	0.01	0.35	1.74	0.00	0.12	0.58	0.00	0.30	3.00	4.00	6.87	
	8.8_Tur11	37.01	0.12	36.55	2.30	7.60	*b.d.l*	0.44	2.00	*b.d.l*	10.96	3.78	100.80	5.87	0.13	6.00	0.70	0.01	0.30	1.80	0.00	0.08	0.61	0.00	0.31	3.00	4.00	6.83	
	8.8_Tur12	37.47	0.12	35.54	2.45	7.45	*b.d.l*	0.44	1.91	0.05	10.89	3.75	100.17	5.98	0.02	6.00	0.67	0.01	0.33	1.77	0.00	0.08	0.59	0.01	0.32	3.00	4.00	6.69	
	8.8_Tur13	37.88	*b.d.l*	36.54	2.34	7.81	*b.d.l*	0.35	2.09	*b.d.l*	11.09	3.82	101.98	5.94	0.06	6.00	0.68	0.00	0.31	1.82	0.00	0.06	0.64	0.00	0.31	3.00	4.00	6.75	
	8.8_Tur14	36.78	0.07	36.47	2.45	7.84	*b.d.l*	0.64	2.03	*b.d.l*	10.96	3.78	101.10	5.83	0.17	6.00	0.65	0.01	0.32	1.85	0.00	0.11	0.62	0.00	0.27	3.00	4.00	6.82	
	8.8_Tur15	36.98	0.10	36.02	2.79	8.02	*b.d.l*	0.49	1.97	0.07	10.97	3.78	101.19	5.86	0.14	6.00	0.59	0.01	0.37	1.90	0.00	0.08	0.61	0.01	0.30	3.00	4.00	6.73	
	8.8_Tur16	37.28	0.05	35.66	1.91	7.93	*b.d.l*	0.21	2.13	0.11	10.89	3.75	100.02	5.95	0.05	6.00	0.66	0.01	0.25	1.89	0.00	0.04	0.66	0.02	0.28	3.00	4.00	6.71	
	8.8_Tur17	36.64	0.15	36.52	2.76	7.54	*b.d.l*	0.69	1.96	*b.d.l*	10.94	3.77	101.02	5.82	0.18	6.00	0.66	0.02	0.37	1.79	0.00	0.12	0.60	0.00	0.28	3.00	4.00	6.84	
S400-6G _ *IV*	4.7_TurOG1	35.88	*b.d.l*	37.20	2.08	6.40	*b.d.l*	1.27	1.18	*b.d.l*	10.74	3.70	98.60	5.81	0.19	6.00	0.91	0.00	0.28	1.55	0.00	0.22	0.37	0.00	0.41	3.00	4.00	7.10	
	4.7_TurOG2	36.28	*b.d.l*	37.18	2.02	6.56	*b.d.l*	1.16	1.26	*b.d.l*	10.80	3.72	99.11	5.84	0.16	6.00	0.89	0.00	0.27	1.57	0.00	0.20	0.39	0.00	0.41	3.00	4.00	7.05	
	4.7_TurOG3	35.92	*b.d.l*	37.31	2.04	6.38	*b.d.l*	1.25	1.14	0.10	10.75	3.71	98.64	5.81	0.19	6.00	0.92	0.00	0.28	1.54	0.00	0.22	0.36	0.02	0.40	3.00	4.00	7.11	
	4.7_TurOG4	36.71	*b.d.l*	37.98	2.05	6.06	*b.d.l*	0.91	1.21	*b.d.l*	10.89	3.75	99.64	5.86	0.14	6.00	1.01	0.00	0.27	1.44	0.00	0.16	0.37	0.00	0.47	3.00	4.00	7.15	
	4.7_TurOG5	36.40	0.11	37.83	1.96	6.64	*b.d.l*	0.97	1.41	*b.d.l*	10.91	3.76	100.01	5.80	0.20	6.00	0.90	0.01	0.26	1.58	0.00	0.17	0.44	0.00	0.40	3.00	4.00	7.10	
	4.7_TurOG6	36.00	*b.d.l*	38.15	1.85	6.64	*b.d.l*	1.17	1.30	*b.d.l*	10.88	3.75	99.92	5.75	0.25	6.00	0.93	0.00	0.25	1.58	0.00	0.20	0.40	0.00	0.40	3.00	4.00	7.18	
	4.7_TurOG7	36.47	*b.d.l*	38.42	1.99	6.64	*b.d.l*	1.03	1.40	*b.d.l*	10.99	3.79	100.82	5.77	0.23	6.00	0.93	0.00	0.26	1.57	0.00	0.17	0.43	0.00	0.40	3.00	4.00	7.16	
	4.7_TurOG8	36.14	*b.d.l*	37.90	2.35	6.68	*b.d.l*	1.02	1.39	*b.d.l*	10.90	3.76	100.21	5.76	0.24	6.00	0.89	0.00	0.31	1.59	0.00	0.17	0.43	0.00	0.39	3.00	4.00	7.12	
	4.7_TurOG9	36.49	*b.d.l*	37.40	2.14	6.58	*b.d.l*	1.00	1.39	0.09	10.87	3.75	99.76	5.84	0.16	6.00	0.89	0.00	0.29	1.57	0.00	0.17	0.43	0.02	0.38	3.00	4.00	7.05	
	4.7_TurOG10	36.72	0.10	38.34	2.20	6.32	*b.d.l*	1.14	1.25	*b.d.l*	11.00	3.79	100.93	5.80	0.20	6.00	0.94	0.01	0.29	1.49	0.00	0.19	0.38	0.00	0.42	3.00	4.00	7.14	
	4.7_TurOG11	36.78	0.16	39.27	2.08	6.63	*b.d.l*	0.98	1.34	*b.d.l*	11.15	3.84	102.29	5.73	0.27	6.00	0.95	0.02	0.27	1.54	0.00	0.16	0.40	0.00	0.43	3.00	4.00	7.21	
	4.7_TurOG12	36.51	*b.d.l*	38.08	2.05	6.57	*b.d.l*	1.25	1.23	*b.d.l*	10.95	3.78	100.60	5.79	0.21	6.00	0.92	0.00	0.27	1.55	0.00	0.21	0.38	0.00	0.41	3.00	4.00	7.12	
	4.7_TurOG13	36.42	*b.d.l*	38.08	2.12	6.29	*b.d.l*	1.43	1.24	*b.d.l*	10.93	3.77	100.29	5.79	0.21	6.00	0.93	0.00	0.28	1.49	0.00	0.24	0.38	0.00	0.37	3.00	4.00	7.14	
	4.7_TurOG14	35.46	0.15	37.41	1.98	6.93	*b.d.l*	0.91	1.39	*b.d.l*	10.75	3.71	98.77	5.73	0.27	6.00	0.86	0.02	0.27	1.67	0.00	0.16	0.43	0.00	0.41	3.00	4.00	7.13	
	4.7_TurOG15	36.04	*b.d.l*	37.80	1.86	7.02	*b.d.l*	0.93	1.40	*b.d.l*	10.87	3.75	99.73	5.76	0.24	6.00	0.88	0.00	0.25	1.67	0.00	0.16	0.43	0.00	0.41	3.00	4.00	7.12	
S400-6G _ *IIIa*	4.7_Tur1	36.37	*b.d.l*	37.18	1.83	6.99	*b.d.l*	0.79	1.42	*b.d.l*	10.83	3.73	99.21	5.84	0.16	6.00	0.87	0.00	0.25	1.67	0.00	0.14	0.44	0.00	0.42	3.00	4.00	7.03	
	4.7_Tur2	38.19	*b.d.l*	35.68	2.00	7.60	*b.d.l*	0.19	1.53	*b.d.l*	10.94	3.77	99.94	6.07	0.00	6.00	0.68	0.00	0.27	1.80	0.00	0.03	0.47	0.00	0.49	3.00	4.00	6.68	
	4.7_Tur3	35.79	*b.d.l*	37.00	2.08	7.35	*b.d.l*	0.84	1.39	*b.d.l*	10.78	3.72	99.02	5.77	0.23	6.00	0.80	0.00	0.28	1.77	0.00	0.14	0.44	0.00	0.42	3.00	4.00	7.03	
	4.7_Tur4	36.59	*b.d.l*	37.83	1.68	7.20	0.16	0.66	1.43	*b.d.l*	10.96	3.78	100.30	5.80	0.20	6.00	0.88	0.00	0.22	1.70	0.02	0.11	0.44	0.00	0.45	3.00	4.00	7.07	
	4.7_Tur5	35.85	*b.d.l*	38.21	1.97	6.71	*b.d.l*	1.07	1.34	*b.d.l*	10.88	3.75	99.81	5.73	0.27	6.00	0.92	0.00	0.26	1.60	0.00	0.18	0.42	0.00	0.40	3.00	4.00	7.20	
	4.7_Tur6	38.02	0.11	36.34	1.92	7.07	*b.d.l*	0.61	1.41	*b.d.l*	10.97	3.78	100.26	6.02	0.00	6.00	0.79	0.01	0.25	1.67	0.00	0.10	0.43	0.00	0.47	3.00	4.00	6.79	
	4.7_Tur7	36.49	*b.d.l*	37.87	2.12	7.01	*b.d.l*	0.78	1.45	*b.d.l*	10.95	3.78	100.65	5.79	0.21	6.00	0.87	0.00	0.28	1.66	0.00	0.13	0.45	0.00	0.42	3.00	4.00	7.08	
	4.7_Tur8	36.84	0.13	36.25	1.84	7.24	*b.d.l*	0.50	1.49	*b.d.l*	10.80	3.72	98.86	5.93	0.07	6.00	0.80	0.02	0.25	1.74	0.00	0.09	0.47	0.00	0.45	3.00	4.00	6.87	
	4.7_Tur9	37.91	*b.d.l*	35.69	2.11	7.42	*b.d.l*	0.40	1.59	*b.d.l*	10.90	3.76	99.91	6.04	0.00	6.00	0.70	0.00	0.28	1.76	0.00	0.07	0.49	0.00	0.44	3.00	4.00	6.70	
	4.7_Tur10	38.66	*b.d.l*	37.02	1.89	7.20	*b.d.l*	0.45	1.44	*b.d.l*	11.13	3.84	101.72	6.04	0.00	6.00	0.81	0.00	0.25	1.67	0.00	0.07	0.43	0.00	0.49	3.00	4.00	6.81	
	4.7_Tur11	35.24	*b.d.l*	37.51	1.91	6.80	*b.d.l*	1.19	1.28	*b.d.l*	10.71	3.69	98.47	5.72	0.28	6.00	0.89	0.00	0.26	1.64	0.00	0.21	0.40	0.00	0.39	3.00	4.00	7.17	
	4.7_Tur12	37.75	*b.d.l*	36.07	1.98	7.73	0.15	0.38	1.45	*b.d.l*	10.95	3.78	100.37	5.99	0.01	6.00	0.74	0.00	0.26	1.83	0.02	0.06	0.45	0.00	0.49	3.00	4.00	6.75	
	4.7_Tur13	37.23	*b.d.l*	36.50	1.98	7.22	*b.d.l*	0.61	1.51	*b.d.l*	10.89	3.75	99.68	5.94	0.06	6.00	0.81	0.00	0.26	1.72	0.00	0.10	0.47	0.00	0.43	3.00	4.00	6.87	
	4.7_Tur14	37.78	0.14	36.98	1.96	7.31	*b.d.l*	0.68	1.42	*b.d.l*	11.05	3.81	101.25	5.94	0.06	6.00	0.80	0.02	0.26	1.71	0.00	0.11	0.43	0.00	0.45	3.00	4.00	6.85	
	4.7_Tur15	37.02	*b.d.l*	36.59	2.04	7.21	*b.d.l*	0.57	1.42	*b.d.l*	10.87	3.75	99.49	5.92	0.08	6.00	0.82	0.00	0.27	1.72	0.00	0.10	0.44	0.00	0.46	3.00	4.00	6.90	
	4.7_Tur16	36.57	*b.d.l*	37.57	1.86	7.06	*b.d.l*	0.77	1.36	*b.d.l*	10.91	3.76	99.94	5.83	0.17	6.00	0.88	0.00	0.25	1.68	0.00	0.13	0.42	0.00	0.45	3.00	4.00	7.05	

Group	Name	SiO_2	TiO_2	Al_2O_3	FeO	MgO	MnO	CaO	Na_2O	K_2O	B_2O_3	H_2O	Total	Site T		Site Z	Site Y					Site X				B	OH^-	Total Al	Infos
														Si	Al	Al	Al	Ti	Fe	Mg	Mn	Ca	Na	K	$[]_X$				
S400-6G _ *IIIa*	4.7_Tur17	37.59	*b.d.l*	35.71	1.99	7.02	*b.d.l*	0.40	1.39	*b.d.l*	10.80	3.72	98.70	6.05	0.00	6.00	0.77	0.00	0.27	1.68	0.00	0.07	0.43	0.00	0.50	3.00	4.00	6.77	
	4.7_Tur18	36.72	*b.d.l*	35.77	2.03	7.08	*b.d.l*	0.56	1.48	*b.d.l*	10.71	3.69	98.40	5.96	0.04	6.00	0.80	0.00	0.28	1.71	0.00	0.10	0.47	0.00	0.44	3.00	4.00	6.84	
	4.7_Tur19	36.02	*b.d.l*	37.25	2.04	6.50	*b.d.l*	1.16	1.35	0.06	10.77	3.71	98.96	5.81	0.19	6.00	0.89	0.00	0.27	1.56	0.00	0.20	0.42	0.01	0.36	3.00	4.00	7.08	
	4.7_Tur20	36.01	*b.d.l*	36.81	2.05	6.83	*b.d.l*	0.87	1.40	*b.d.l*	10.73	3.70	98.48	5.83	0.17	6.00	0.86	0.00	0.28	1.65	0.00	0.15	0.44	0.00	0.41	3.00	4.00	7.02	
	4.7_Tur21	37.21	0.09	36.52	2.05	7.01	*b.d.l*	0.59	1.38	*b.d.l*	10.87	3.75	99.51	5.95	0.05	6.00	0.83	0.01	0.27	1.67	0.00	0.10	0.43	0.00	0.47	3.00	4.00	6.88	
SOX-6 _ I	5.3_Tur1	35.07	0.25	35.53	5.30	6.12	*b.d.l*	0.96	1.74	0.10	10.62	3.66	99.37	5.74	0.26	6.00	0.60	0.03	0.73	1.49	0.00	0.17	0.55	0.02	0.26	3.00	4.00	6.86	
	5.3_Tur2	36.56	0.37	34.84	4.34	5.72	*b.d.l*	0.97	1.32	0.10	10.63	3.66	98.54	5.98	0.02	6.00	0.69	0.04	0.59	1.40	0.00	0.17	0.42	0.02	0.39	3.00	4.00	6.71	
	5.3_Tur3	38.45	0.21	34.39	4.24	7.17	*b.d.l*	0.88	1.64	0.12	10.99	3.79	101.99	6.08	0.00	6.00	0.41	0.03	0.56	1.69	0.00	0.15	0.50	0.02	0.32	3.00	4.00	6.41	
SOX-8(G) _ IIIb	5.4_Turflot1	35.59	0.40	33.89	4.10	7.53	*b.d.l*	0.83	1.92	*b.d.l*	10.58	3.65	98.56	5.85	0.15	6.00	0.41	0.05	0.56	1.85	0.00	0.15	0.61	0.00	0.24	3.00	4.00	6.56	
	5.4_Turflot2	35.54	0.34	35.67	3.31	7.53	*b.d.l*	0.94	1.91	*b.d.l*	10.75	3.71	99.76	5.75	0.25	6.00	0.55	0.04	0.45	1.81	0.00	0.16	0.60	0.00	0.24	3.00	4.00	6.80	
	5.4_Turflot3	38.34	*b.d.l*	34.62	2.54	7.71	*b.d.l*	0.34	2.18	*b.d.l*	10.92	3.77	100.59	6.10	0.00	6.00	0.49	0.00	0.34	1.83	0.00	0.06	0.67	0.00	0.27	3.00	4.00	6.49	
SOX-8(G) _ *IV*	5.5_TurOG1	34.01	0.32	37.13	4.56	5.65	*b.d.l*	0.98	1.62	*b.d.l*	10.57	3.64	98.54	5.59	0.41	6.00	0.79	0.04	0.63	1.39	0.00	0.17	0.52	0.00	0.31	3.00	4.00	7.20	
	5.5_TurOG2	36.28	0.21	36.50	3.28	7.15	*b.d.l*	0.38	2.09	*b.d.l*	10.87	3.75	100.59	5.80	0.20	6.00	0.68	0.03	0.44	1.70	0.00	0.07	0.65	0.00	0.29	3.00	4.00	6.88	
	5.5_TurOG3	35.57	0.19	35.97	2.81	7.32	*b.d.l*	0.43	2.16	*b.d.l*	10.70	3.69	98.91	5.78	0.22	6.00	0.66	0.02	0.38	1.77	0.00	0.08	0.68	0.00	0.25	3.00	4.00	6.89	
	5.5_TurOG4	35.23	0.26	36.55	4.73	6.89	*b.d.l*	0.71	1.85	*b.d.l*	10.80	3.72	100.78	5.67	0.33	6.00	0.60	0.03	0.64	1.65	0.00	0.12	0.58	0.00	0.30	3.00	4.00	6.93	
	5.5_TurOG5	35.41	0.29	37.19	4.49	6.57	*b.d.l*	0.82	1.89	*b.d.l*	10.87	3.75	101.35	5.66	0.34	6.00	0.67	0.03	0.60	1.56	0.00	0.14	0.59	0.00	0.27	3.00	4.00	7.01	
	5.5_TurOG6	35.99	0.21	37.78	3.03	6.98	*b.d.l*	0.56	1.86	*b.d.l*	10.96	3.78	101.28	5.71	0.29	6.00	0.77	0.02	0.40	1.65	0.00	0.10	0.57	0.00	0.33	3.00	4.00	7.06	
	5.5_TurOG7	35.58	0.30	37.12	4.91	6.09	*b.d.l*	0.92	1.69	*b.d.l*	10.86	3.74	101.29	5.70	0.30	6.00	0.70	0.04	0.66	1.45	0.00	0.16	0.52	0.00	0.32	3.00	4.00	7.00	
	5.5_TurOG8	35.71	0.30	37.32	4.10	6.81	*b.d.l*	0.69	1.91	*b.d.l*	10.93	3.77	101.59	5.68	0.32	6.00	0.68	0.04	0.55	1.61	0.00	0.12	0.59	0.00	0.30	3.00	4.00	7.00	
	5.5_TurOG9	34.87	0.49	36.27	6.54	5.21	*b.d.l*	1.00	1.67	*b.d.l*	10.68	3.68	100.52	5.68	0.32	6.00	0.63	0.06	0.89	1.26	0.00	0.17	0.53	0.00	0.30	3.00	4.00	6.96	
	5.5_TurOG10	35.05	0.41	36.80	5.80	5.71	*b.d.l*	0.77	1.70	*b.d.l*	10.76	3.71	100.83	5.66	0.34	6.00	0.67	0.05	0.78	1.38	0.00	0.13	0.53	0.00	0.33	3.00	4.00	7.01	
	5.5_TurOG11	35.04	0.17	36.92	3.16	6.75	*b.d.l*	0.63	1.87	*b.d.l*	10.70	3.69	99.08	5.69	0.31	6.00	0.76	0.02	0.43	1.63	0.00	0.11	0.59	0.00	0.30	3.00	4.00	7.07	
	5.5_TurOG12	35.31	0.15	36.29	3.73	6.36	*b.d.l*	0.78	1.78	*b.d.l*	10.65	3.67	98.80	5.76	0.24	6.00	0.74	0.02	0.51	1.55	0.00	0.14	0.56	0.00	0.30	3.00	4.00	6.98	
	5.5_TurOG13	35.89	0.17	36.62	3.26	7.08	*b.d.l*	0.52	2.08	*b.d.l*	10.83	3.73	100.22	5.76	0.24	6.00	0.69	0.02	0.44	1.69	0.00	0.09	0.65	0.00	0.26	3.00	4.00	6.93	
	5.5_TurOG14	35.76	0.31	36.98	3.25	7.04	*b.d.l*	0.64	1.95	0.09	10.87	3.75	100.63	5.72	0.28	6.00	0.69	0.04	0.43	1.68	0.00	0.11	0.61	0.02	0.27	3.00	4.00	6.97	
	5.5_TurOG15	35.84	0.22	36.72	2.92	7.42	*b.d.l*	0.56	2.10	0.09	10.86	3.74	100.49	5.73	0.27	6.00	0.66	0.03	0.39	1.77	0.00	0.10	0.65	0.02	0.23	3.00	4.00	6.93	
	5.5_TurOG16	36.20	0.19	35.87	2.94	7.01	*b.d.l*	0.42	2.05	*b.d.l*	10.74	3.70	99.31	5.86	0.14	6.00	0.70	0.02	0.40	1.69	0.00	0.07	0.64	0.00	0.28	3.00	4.00	6.84	
	5.5_TurOG17	36.01	0.21	37.33	3.63	6.73	*b.d.l*	0.70	1.89	*b.d.l*	10.92	3.77	101.37	5.73	0.27	6.00	0.73	0.03	0.48	1.60	0.00	0.12	0.58	0.00	0.30	3.00	4.00	7.00	
	5.5_TurOG18	35.56	0.20	36.66	3.35	7.05	*b.d.l*	0.82	1.78	*b.d.l*	10.79	3.72	99.98	5.73	0.27	6.00	0.68	0.02	0.45	1.69	0.00	0.14	0.55	0.00	0.30	3.00	4.00	6.96	
	5.5_TurOG19	36.16	0.31	36.68	3.41	7.11	*b.d.l*	0.79	1.45	*b.d.l*	10.88	3.75	100.57	5.78	0.22	6.00	0.68	0.04	0.46	1.69	0.00	0.14	0.45	0.00	0.41	3.00	4.00	6.91	
	5.5_TurOG20	36.24	*b.d.l*	36.55	2.51	7.44	*b.d.l*	0.59	1.99	0.08	10.85	3.74	100.12	5.81	0.19	6.00	0.71	0.00	0.34	1.78	0.00	0.10	0.62	0.02	0.26	3.00	4.00	6.90	
	5.5_TurOG21	35.56	0.28	36.44	3.91	6.58	*b.d.l*	0.82	1.75	*b.d.l*	10.76	3.71	99.84	5.75	0.25	6.00	0.69	0.03	0.53	1.58	0.00	0.14	0.55	0.00	0.31	3.00	4.00	6.94	
	5.5_TurOG22	34.71	0.20	36.74	4.93	6.48	*b.d.l*	0.93	1.74	*b.d.l*	10.72	3.70	100.23	5.63	0.37	6.00	0.65	0.02	0.67	1.57	0.00	0.16	0.55	0.00	0.29	3.00	4.00	7.02	
	5.5_TurOG23	34.80	0.35	37.39	4.96	5.96	*b.d.l*	0.89	1.83	*b.d.l*	10.78	3.72	100.74	5.61	0.39	6.00	0.71	0.04	0.67	1.43	0.00	0.15	0.57	0.00	0.27	3.00	4.00	7.10	
	5.5_TurOG24	35.60	0.34	36.79	4.25	6.49	*b.d.l*	0.82	1.70	*b.d.l*	10.82	3.73	100.57	5.72	0.28	6.00	0.69	0.04	0.57	1.55	0.00	0.14	0.53	0.00	0.33	3.00	4.00	6.97	
	5.5_TurOG25	36.04	*b.d.l*	36.21	2.52	7.12	*b.d.l*	0.57	1.77	*b.d.l*	10.72	3.70	98.83	5.84	0.16	6.00	0.76	0.00	0.34	1.72	0.00	0.10	0.56	0.00	0.34	3.00	4.00	6.92	
SOX-8(G) _ *IIIa*	5.5_Tur1	36.92	*b.d.l*	37.54	2.80	7.06	*b.d.l*	0.65	2.02	*b.d.l*	11.05	3.81	101.99	5.81	0.19	6.00	0.77	0.00	0.37	1.66	0.00	0.11	0.62	0.00	0.27	3.00	4.00	6.96	
	5.5_Tur2	35.59	0.16	36.80	3.28	7.13	*b.d.l*	0.56	2.09	*b.d.l*	10.82	3.73	100.20	5.72	0.28	6.00	0.69	0.02	0.44	1.71	0.00	0.10	0.65	0.00	0.25	3.00	4.00	6.97	
	5.5_Tur3	36.12	0.15	37.03	2.21	7.39	0.14	0.46	2.16	*b.d.l*	10.89	3.75	100.31	5.77	0.23	6.00	0.73	0.02	0.30	1.76	0.02	0.08	0.67	0.00	0.25	3.00	4.00	6.96	
	5.5_Tur4	35.44	0.28	37.14	4.23	6.66	*b.d.l*	0.91	1.80	*b.d.l*	10.86	3.75	101.09	5.67	0.33	6.00	0.67	0.03	0.57	1.59	0.00	0.16	0.56	0.00	0.28	3.00	4.00	7.00	

Group	**Name**	**SiO_2**	**TiO_2**	**Al_2O_3**	**FeO**	**MgO**	**MnO**	**CaO**	**Na_2O**	**K_2O**	**B_2O_3**	**H_2O**	**Total**	**Site T**		**Site Z**	**Site Y**					**Site X**				**B**	**OH^-**	**Total Al**	**Infos**
														Si	**Al**	**Al**	**Al**	**Ti**	**Fe**	**Mg**	**Mn**	**Ca**	**Na**	**K**	**$[]_X$**				
SOX-8(G) _ *IIIa*	5.5_Tur5	35.72	*b.d.l*	36.48	3.35	6.86	*b.d.l*	0.83	1.78	0.09	10.76	3.71	99.76	5.77	0.23	6.00	0.72	0.00	0.45	1.65	0.00	0.14	0.56	0.02	0.28	3.00	4.00	6.95	
	5.5_Tur6	35.55	0.36	38.31	2.86	6.81	*b.d.l*	0.66	1.81	*b.d.l*	10.95	3.78	101.14	5.64	0.36	6.00	0.81	0.04	0.38	1.61	0.00	0.11	0.56	0.00	0.33	3.00	4.00	7.17	
	5.5_Tur7	35.70	0.32	37.09	3.07	7.18	*b.d.l*	0.69	1.99	*b.d.l*	10.88	3.75	100.70	5.70	0.30	6.00	0.68	0.04	0.41	1.71	0.00	0.12	0.62	0.00	0.27	3.00	4.00	6.98	
	5.5_Tur8	35.34	0.21	37.04	3.68	6.74	*b.d.l*	0.76	1.78	*b.d.l*	10.79	3.72	100.12	5.69	0.31	6.00	0.72	0.02	0.50	1.62	0.00	0.13	0.56	0.00	0.31	3.00	4.00	7.03	
	5.5_Tur9	37.06	*b.d.l*	35.62	2.09	8.09	*b.d.l*	0.21	2.46	*b.d.l*	10.89	3.75	100.28	5.91	0.09	6.00	0.62	0.00	0.28	1.93	0.00	0.04	0.76	0.00	0.20	3.00	4.00	6.70	
	5.5_Tur10	37.81	0.28	35.08	3.23	6.75	*b.d.l*	0.80	1.83	*b.d.l*	10.89	3.75	100.52	6.04	0.00	6.00	0.60	0.03	0.43	1.61	0.00	0.14	0.57	0.00	0.30	3.00	4.00	6.60	
	5.4_Tur1	35.03	0.36	36.66	4.66	6.28	*b.d.l*	0.82	1.75	0.09	10.73	3.70	100.09	5.67	0.33	6.00	0.67	0.04	0.63	1.51	0.00	0.14	0.55	0.02	0.29	3.00	4.00	7.00	
	5.4_Tur2	34.20	0.33	36.93	5.21	6.26	*b.d.l*	0.99	1.64	*b.d.l*	10.68	3.68	99.99	5.57	0.43	6.00	0.65	0.04	0.71	1.52	0.00	0.17	0.52	0.00	0.31	3.00	4.00	7.08	
	5.4_Tur3	35.69	0.24	36.88	2.61	7.08	*b.d.l*	0.64	1.92	*b.d.l*	10.80	3.72	99.66	5.74	0.26	6.00	0.74	0.03	0.35	1.70	0.00	0.11	0.60	0.00	0.29	3.00	4.00	7.00	
	5.4_Tur4	37.44	*b.d.l*	35.82	2.19	8.28	*b.d.l*	0.31	2.23	*b.d.l*	10.99	3.79	101.16	5.92	0.08	6.00	0.60	0.00	0.29	1.95	0.00	0.05	0.68	0.00	0.27	3.00	4.00	6.68	
	5.4_Tur5	35.26	0.18	37.08	3.07	6.82	*b.d.l*	0.70	1.86	0.10	10.76	3.71	99.55	5.70	0.30	6.00	0.75	0.02	0.41	1.64	0.00	0.12	0.58	0.02	0.28	3.00	4.00	7.06	
	5.4_Tur6	35.04	0.28	36.94	4.53	6.39	*b.d.l*	0.89	1.75	*b.d.l*	10.77	3.71	100.43	5.66	0.34	6.00	0.68	0.03	0.61	1.54	0.00	0.15	0.55	0.00	0.30	3.00	4.00	7.03	
	5.4_Tur7	35.83	0.23	37.31	2.79	6.95	*b.d.l*	0.75	2.01	*b.d.l*	10.88	3.75	100.62	5.72	0.28	6.00	0.75	0.03	0.37	1.65	0.00	0.13	0.62	0.00	0.25	3.00	4.00	7.02	
	5.4_Tur8	37.71	0.21	37.85	2.24	7.18	*b.d.l*	0.47	1.80	*b.d.l*	11.17	3.85	102.53	5.87	0.13	6.00	0.81	0.02	0.29	1.66	0.00	0.08	0.54	0.00	0.38	3.00	4.00	6.94	
	5.4_Tur9	37.24	0.17	37.55	2.73	7.17	*b.d.l*	0.64	2.04	*b.d.l*	11.12	3.83	102.53	5.82	0.18	6.00	0.74	0.02	0.36	1.67	0.00	0.11	0.62	0.00	0.27	3.00	4.00	6.92	
	5.4_Tur10	35.40	0.35	36.94	3.77	6.84	*b.d.l*	0.92	1.77	0.08	10.84	3.74	100.64	5.68	0.32	6.00	0.66	0.04	0.51	1.64	0.00	0.16	0.55	0.02	0.28	3.00	4.00	6.98	
	5.4_Tur11	34.98	0.33	37.07	4.72	6.43	0.14	1.02	1.70	*b.d.l*	10.81	3.73	100.92	5.63	0.37	6.00	0.65	0.04	0.63	1.54	0.02	0.18	0.53	0.00	0.29	3.00	4.00	7.02	
	5.4_Tur12	35.10	0.22	36.89	3.70	6.92	*b.d.l*	0.71	1.96	*b.d.l*	10.77	3.71	100.09	5.66	0.34	6.00	0.68	0.03	0.50	1.66	0.00	0.12	0.61	0.00	0.26	3.00	4.00	7.02	
	5.5_Tur11	35.26	*b.d.l*	36.70	3.07	7.08	*b.d.l*	0.58	1.93	*b.d.l*	10.71	3.69	99.23	5.72	0.28	6.00	0.74	0.00	0.42	1.71	0.00	0.10	0.61	0.00	0.29	3.00	4.00	7.02	
	5.5_Tur12	35.68	0.28	36.73	3.83	6.36	*b.d.l*	0.68	1.68	*b.d.l*	10.77	3.71	99.78	5.76	0.24	6.00	0.75	0.03	0.52	1.53	0.00	0.12	0.53	0.00	0.36	3.00	4.00	6.99	
	5.5_Tur13	35.96	0.29	36.38	2.78	6.99	*b.d.l*	0.59	1.75	*b.d.l*	10.76	3.71	99.30	5.81	0.19	6.00	0.73	0.03	0.38	1.68	0.00	0.10	0.55	0.00	0.35	3.00	4.00	6.92	
	5.5_Tur14	36.64	0.16	37.24	2.84	7.15	*b.d.l*	0.45	1.92	*b.d.l*	10.98	3.78	101.20	5.80	0.20	6.00	0.75	0.02	0.38	1.69	0.00	0.08	0.59	0.00	0.33	3.00	4.00	6.95	
	5.5_Tur15	36.15	0.25	36.82	3.44	6.88	*b.d.l*	0.57	1.81	*b.d.l*	10.87	3.75	100.59	5.78	0.22	6.00	0.72	0.03	0.46	1.64	0.00	0.10	0.56	0.00	0.34	3.00	4.00	6.94	
	5.5_Tur16	36.15	0.23	37.53	2.69	7.16	*b.d.l*	0.37	2.07	*b.d.l*	10.95	3.77	100.95	5.74	0.26	6.00	0.76	0.03	0.36	1.69	0.00	0.06	0.64	0.00	0.30	3.00	4.00	7.02	

Appendix A9

Water fugacity and apparent standard Gibbs free energy of B(OH)3 at T and 200 MPa used in the thermodynamic calculations.

P	T	f_{H2O} [a]	$\Delta_{app}G°_{B(OH)3}$ [b] J/mol			
bars	*°C*	*bars*	*Shock et al. (1989)*	*Pokrovski et al. (1995)*	*Akinfiev et al. (2006)*	*Wang et al. (2013)*
2000	300	162.78	-1008593.325	-1019566.743	-1018342.128	-1015887.124
2000	350	271.26	-1018357.734	-1033025.278	-1031621.5	-1028910.995
2000	400	404.88	-1028295.53	-1046983.617	-1045385.872	-1042437.533
2000	450	556.61	-1038627.583	-1061597.701	-1059792.514	-1056637.527
2000	500	719.43	-1049310.548	-1076746.291	-1074718.641	-1071378.429
2000	550	886.31	-1060371.831	-1092383.908	-1090118.481	-1086611.034
2000	600	1050.21	-1071828.794	-1108471.973	-1105953.373	-1102294.172

(a) f_{H2O} values from Burnham et al. (1969). (b) $\Delta_{app}G°_{B(OH)3}$ were calculated by Thermo-ZNS, using the HKF parameters of the corresponding source.

Appendix A10

Calculated $[B_2O_3]_{fluid\_EQ}$ as a function of temperature for the four tourmaline-forming reactions considered (R1, R2, R3, R4, see text) and the two tourmaline thermodynamic datasets used in the calculations (solid lines for Ogorodova et al., 2012 (Ogo_2012) and dashed lines for van Hinsberg and Schumacher, 2007b (H-S_2007)). Experimental brackets of $[B_2O_3]_{fluid\_EQ}$ from this study are shown by solid (tourmaline present) and open (tourmaline absent) symbols. Each graphic was realised by using different HKF parameters set for $B(OH)_3$ (Shock et al. 1989; Pokrovski et al. 1995; Akinfiev et al. 2006; Wang et al. 2013).

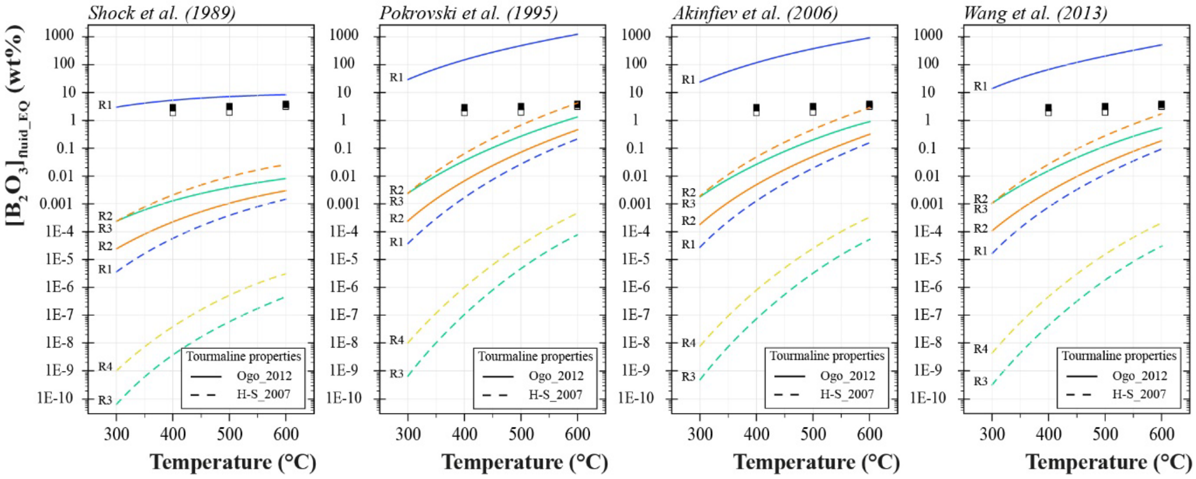

Appendix A11

		$\Delta_f G°$	S°	V°	$Cp(T) = a + bT + cT^{-2} + dT^{-0.5}$				Source
					J/mol.K				
		J/mol	*J/mol.K*	*J/mol*	**a**	**b**	**c**	**d**	
Minerals									
Tourmaline	Dravite	-1.44E+07	643	32.92	1159	8.00E-02	-3.62E+07	0	Ogorodova et al., 2012
	Dravite	-1.46E+07	607.9	32.992	2198	-6.45E-02	9.34E+06	-2.56E+04	van Hinsberg and Schumacher, 2007
	Schorl	-1.35E+07	744	33.07	1030.1	3.51E-01	-2.93E+07	0	Ogorodova et al., 2012
	Schorl	-1.35E+07	692.6	33.07	2215	-4.27E-02	1.08E+07	-2.58E+04	van Hinsberg and Schumacher, 2007
	Magnesiofoitite	-1.43E+07	619	33.2	1134.4	7.83E-02	-3.54E+07	0	Ogorodova et al., 2012
	Magnesiofoitite	-1.46E+07	588.5	33.2	2174	-4.61E-02	8.76E+06	-2.55E+04	van Hinsberg and Schumacher, 2007
	Foitite	-1.38E+07	644.9	33.01	2186	-3.17E-02	9.76E+06	-2.56E+04	van Hinsberg and Schumacher, 2007
Quartz (alpha)		-8.56E+05	41.439	2.269	39.62	4.48E-02	-7.45E+05	0	Thermoddem (Blanc et al., 2012)
Andalusite		-2.43E+06	92.885	5.153	172.85	2.63E-02	-5.19E+06	0	Thermoddem (Blanc et al., 2012)
Cordierite		-8.65E+06	407.2	23.322	531.19	1.95E-01	-1.30E+07	0	Thermoddem (Blanc et al., 2012)
Fe-Cordierite		-7.95E+06	461	23.71	924	0.00E+00	-7.04E+06	-6.44E+03	SUPCRTBL (Zimmer et al., 2016)
Albite (low)		-3.71E+06	207.4	10.007	221.09	1.17E-01	-4.52E+06	0	Thermoddem (Blanc et al., 2012)
Gas									
H_2O		-2.29E+05	188.84	0	27.6	1.37E-02	0	0	Thermoddem (Blanc et al., 2012)

Appendix A12

Starting product	Biotite Core		Rim			K-feldspar	
n	39		9			**23**	
	Mean	*Sd*	*Mean*	*Sd*		*Mean*	*Sd*
SiO_2	35.89	(0.47)	35.17	(0.37)	**SiO_2**	64.26	(0.45)
TiO_2	2.87	(0.09)	3.64	(0.06)	**TiO_2**		
Al_2O_3	15.98	(0.27)	14.49	(0.2)	**Al_2O_3**	18.72	(0.27)
FeO_{total}	17.17	(0.39)	21.72	(0.48)	**FeO_{total}**	0.22	(0.01)
MgO	12.79	(0.21)	9.40	(0.11)	**MgO**	0.05	(0.02)
MnO	0.18	(0.01)	0.29	(0.05)	**MnO**		
CaO	*b.d.l*		*b.d.l*		**CaO**	0.11	(0.02)
Na_2O	0.11	(0.02)	0.10	(0.02)	**Na_2O**	2.34	(0.38)
K_2O	9.49	(0.21)	9.40	(0.08)	**K_2O**	12.86	(0.51)
Cl	*b.d.l*		*b.d.l*		**Cl**		
F	*b.d.l*		*b.d.l*		**F**		
OH [a]	3.92	(0.03)	3.81	(0.03)	**Total**	98.42	
Total	98.99		98.33	(0.71)	**Si**	2.98	(0.01)
Si	2.74	(0.02)	2.76	(0.02)	**Ti**		
Ti	0.17	(0)	0.22	(0)	**Al**	1.02	(0.01)
^{IV}Al	1.26	(0.02)	1.24	(0.02)	**Fe**	0.01	(0)
Fe	1.1	(0.03)	1.43	(0.03)	**Mg**	0	(0)
Mg	1.46	(0.03)	1.1	(0.01)	**Mn**		
Mn	0	(0)	0.02	(0.01)	**Ca**	0.01	(0)
^{VI}Al	0.18	(0.03)	0.11	(0.01)	**Na**	0.21	(0.03)
Ca	1				**K**	0.76	(0.03)
Na	0.02		0.02				
K	0.92	(0.02)	0.94	(0.01)			
Cl							
F							
H	2		2				
Fe/(Fe+Mg)	0.43	(0.01)	0.56	(0.01)			
Al_{Tot}	1.44	(0.02)	1.34	(0.01)			

Appendix A13

Evolution of the alloy phase of the NiO-NiPd sensor as a function of log fO_2 for every run. The dashed line corresponds to the function of Pownceby and O'Neill (1994) linking fO_2 and the X_{Ni} of the sensors at 600°C and 200 MPa. The initial X_{Ni} of both pellets is represented by the dotted lines and their final composition by the square and circle on the dashed line.

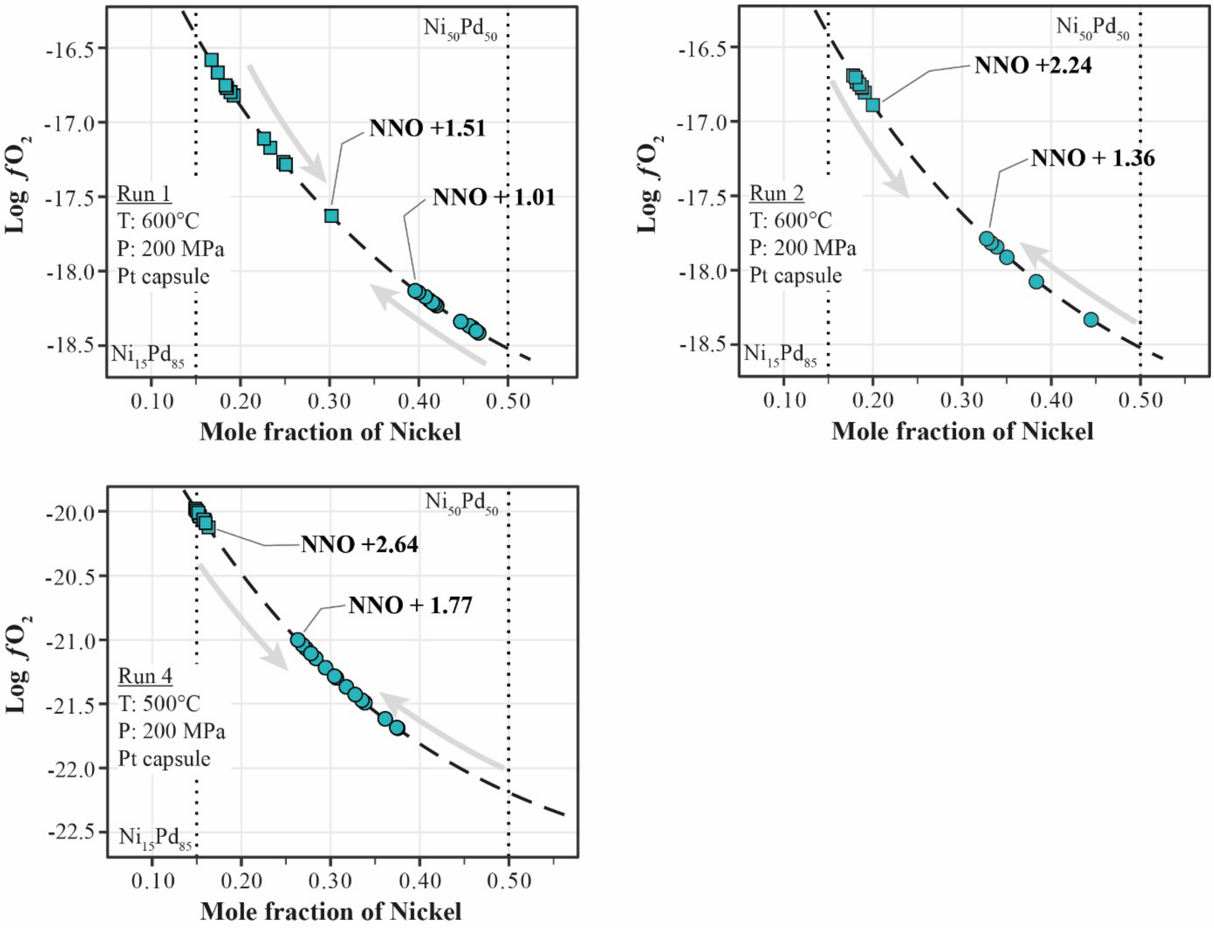

Appendix A14

Onion ring quench phases in B600-3 (left) and S600-4 (right)

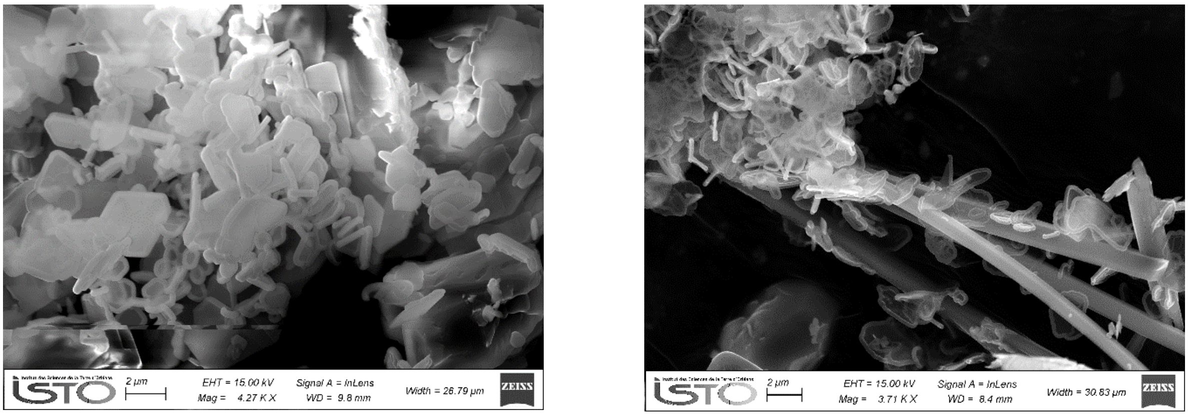

Appendix A15

Composition of experimental tourmaline from the biotite-bearing experiments (Chap III).

Group	**Name**	**SiO$_2$**	**TiO$_2$**	**Al$_2$O$_3$**	**FeO**	**MgO**	**MnO**	**CaO**	**Na$_2$O**	**K$_2$O**	**B$_2$O$_3$**	**H$_2$O**	**Total**	**Site T**		**Site Z**	**Site Y**					**Site X**				**B**	**OH$^-$**	**Total Al**	**Infos**
														Si	**Al**	**Al**	**Al**	**Ti**	**Fe**	**Mg**	**Mn**	**Ca**	**Na**	**K**	**[]$_X$**				
B600-3_III	7.4_Long1-2	35.82	0.81	33.80	8.79	4.92	*b.d.l*	0.40	1.98	*b.d.l*	10.62	3.66	100.89	5.86	0.14	6.00	0.39	0.10	1.20	1.20	0.00	0.07	0.63	0.00	0.30	3.00	4.00	6.52	Core
	7.4_Long1-3	36.56	1.22	33.48	9.29	4.57	*0.16*	0.33	1.76	b.d.l	10.71	3.69	101.79	5.94	0.06	6.00	0.34	0.15	1.26	1.10	0.02	0.06	0.55	0.00	0.39	3.00	4.00	6.41	Core
	7.4_Long1-4	36.18	0.90	33.75	8.48	4.95	*b.d.l*	0.31	1.87	*0.05*	10.64	3.67	100.92	5.91	0.09	6.00	0.40	0.11	1.16	1.21	0.00	0.05	0.59	0.01	0.34	3.00	4.00	6.49	Core
	7.4_Long2-2	36.25	0.57	33.41	8.86	4.52	*b.d.l*	0.27	1.78	*0.05*	10.54	3.63	100.01	5.98	0.02	6.00	0.47	0.07	1.22	1.11	0.00	0.05	0.57	0.01	0.37	3.00	4.00	6.49	Core
	7.4_Long2-3	36.42	0.64	34.21	7.87	5.46	b.d.l	0.28	1.86	0.06	10.72	3.70	101.31	5.90	0.10	6.00	0.44	0.08	1.07	1.32	0.00	0.05	0.58	0.01	0.35	3.00	4.00	6.53	Core
	7.4_Long2-9	36.43	0.55	34.80	7.05	5.29	*0.19*	0.47	1.72	*b.d.l*	10.74	3.70	100.96	5.90	0.10	6.00	0.54	0.07	0.95	1.28	0.03	0.08	0.54	0.00	0.38	3.00	4.00	6.64	Core
	7.4_Ortho1	36.17	0.50	34.42	8.35	4.71	*0.19*	0.31	1.89	b.d.l	10.66	3.68	100.91	5.90	0.10	6.00	0.51	0.06	1.14	1.15	0.03	0.05	0.60	0.00	0.35	3.00	4.00	6.61	Core
	7.4_Ortho2	36.42	1.36	33.40	9.23	4.85	*b.d.l*	0.30	1.87	*b.d.l*	10.71	3.69	101.91	5.91	0.09	6.00	0.29	0.17	1.25	1.17	0.00	0.05	0.59	0.00	0.36	3.00	4.00	6.39	Core
	7.4_Ortho3	36.00	0.80	34.15	8.65	4.92	*b.d.l*	0.34	1.88	*0.07*	10.67	3.68	101.15	5.87	0.13	6.00	0.42	0.10	1.18	1.19	0.00	0.06	0.59	0.01	0.33	3.00	4.00	6.56	Core
	7.4_Ortho4	36.53	0.80	33.38	9.56	4.36	*b.d.l*	0.29	1.76	*0.05*	10.63	3.66	101.11	5.97	0.03	6.00	0.41	0.10	1.31	1.06	0.00	0.05	0.56	0.01	0.38	3.00	4.00	6.43	Core
	7.4_Long1-1	35.14	0.67	36.46	6.87	4.85	*b.d.l*	0.86	1.71	*0.08*	10.74	3.70	101.13	5.69	0.31	6.00	0.64	0.08	0.93	1.17	0.00	0.15	0.54	0.02	0.30	3.00	4.00	6.96	Rim
	7.4_Long1-5	35.00	0.60	35.53	8.18	4.60	*0.22*	1.10	1.59	*0.07*	10.67	3.68	101.24	5.70	0.30	6.00	0.53	0.07	1.11	1.12	0.03	0.19	0.50	0.02	0.29	3.00	4.00	6.82	Rim
	7.4_Long1-6	35.31	0.63	36.12	7.51	4.75	*0.20*	0.78	1.65	*b.d.l*	10.74	3.70	101.42	5.72	0.28	6.00	0.60	0.08	1.02	1.15	0.03	0.14	0.52	0.00	0.35	3.00	4.00	6.89	Rim
	7.4_Long1-7	35.98	0.65	35.43	7.39	5.17	*0.23*	0.89	1.70	*0.05*	10.81	3.72	102.03	5.79	0.21	6.00	0.51	0.08	0.99	1.24	0.03	0.15	0.53	0.01	0.31	3.00	4.00	6.72	Rim
	7.4_Long1-8	35.75	0.60	35.85	7.32	4.87	*b.d.l*	0.90	1.75	*b.d.l*	10.77	3.71	101.55	5.77	0.23	6.00	0.59	0.07	0.99	1.17	0.00	0.16	0.55	0.00	0.30	3.00	4.00	6.82	Rim
	7.4_Long1-9	35.75	0.70	34.49	7.61	5.14	*0.18*	0.92	1.85	*0.06*	10.68	3.68	101.05	5.82	0.18	6.00	0.44	0.09	1.04	1.25	0.02	0.16	0.58	0.01	0.24	3.00	4.00	6.62	Rim
	7.4_Long1-10	36.03	0.75	34.78	8.33	5.38	*b.d.l*	0.75	1.89	*0.08*	10.81	3.73	102.65	5.79	0.21	6.00	0.39	0.09	1.12	1.29	0.00	0.13	0.59	0.02	0.26	3.00	4.00	6.59	Rim
	7.4_Long2-1	35.93	0.69	36.33	6.63	5.14	*b.d.l*	0.66	1.65	*0.07*	10.83	3.73	101.67	5.77	0.23	6.00	0.64	0.08	0.89	1.23	0.00	0.11	0.51	0.01	0.36	3.00	4.00	6.87	Rim
	7.4_Long2-4	35.61	*0.60*	35.75	8.03	4.58	*b.d.l*	0.95	1.68	*0.06*	10.75	3.71	101.79	5.76	0.24	6.00	0.57	0.07	1.09	1.10	0.00	0.16	0.53	0.01	0.30	3.00	4.00	6.81	Rim
	7.4_Long2-5	35.79	*0.54*	35.73	6.93	4.52	*b.d.l*	0.75	1.55	*0.06*	10.67	3.68	100.27	5.83	0.17	6.00	0.69	0.07	0.94	1.10	0.00	0.13	0.49	0.01	0.37	3.00	4.00	6.86	Rim
	7.4_Long2-6	35.60	*0.64*	36.00	8.03	4.99	*b.d.l*	0.99	1.73	*0.07*	10.84	3.74	102.66	5.71	0.29	6.00	0.51	0.08	1.08	1.19	0.00	0.17	0.54	0.01	0.28	3.00	4.00	6.80	Rim
	7.4_Long2-7	35.70	0.63	35.69	7.47	5.03	*b.d.l*	0.79	1.91	*0.06*	10.78	3.71	101.87	5.76	0.24	6.00	0.54	0.08	1.01	1.21	0.00	0.14	0.60	0.01	0.26	3.00	4.00	6.78	Rim
	7.4_Long2-8	36.01	0.60	34.48	7.73	5.18	*0.18*	0.69	1.82	*0.05*	10.70	3.69	101.12	5.85	0.15	6.00	0.46	0.07	1.05	1.25	0.02	0.12	0.57	0.01	0.30	3.00	4.00	6.60	Rim
	7.4_Ortho5	35.31	0.53	34.84	8.39	4.65	*b.d.l*	1.06	1.46	*0.07*	10.61	3.66	100.69	5.79	0.21	6.00	0.51	0.07	1.15	1.13	0.00	0.19	0.46	0.01	0.34	3.00	4.00	6.73	Rim
	7.4_Ortho6	35.12	0.58	35.45	8.34	4.43	*b.d.l*	1.13	1.62	*0.06*	10.65	3.67	101.12	5.73	0.27	6.00	0.54	0.07	1.14	1.08	0.00	0.20	0.51	0.01	0.28	3.00	4.00	6.81	Rim
	7.4_Ortho7	35.51	*0.56*	35.78	7.37	4.61	*b.d.l*	0.93	1.61	*0.05*	10.69	3.69	100.88	5.77	0.23	6.00	0.63	0.07	1.00	1.12	0.00	0.16	0.51	0.01	0.32	3.00	4.00	6.85	Rim
	7.4_Ortho8	35.13	0.55	37.02	7.57	4.61	*b.d.l*	1.03	1.59	*0.05*	10.81	3.73	102.22	5.65	0.35	6.00	0.66	0.07	1.02	1.10	0.00	0.18	0.50	0.01	0.32	3.00	4.00	7.01	Rim
	7.4_Ortho9	35.18	*0.51*	36.61	6.91	4.67	*0.29*	1.08	1.70	0.07	10.76	3.71	101.48	5.68	0.32	6.00	0.65	0.06	0.93	1.12	0.04	0.19	0.53	0.01	0.27	3.00	4.00	6.97	Rim

Group	**Name**	**SiO_2**	**TiO_2**	**Al_2O_3**	**FeO**	**MgO**	**MnO**	**CaO**	**Na_2O**	**K_2O**	**B_2O_3**	**H_2O**	**Total**	**Site T**		**Site Z**	**Site Y**					**Site X**				**B**	**OH^-**	**Total Al**	**Infos**
														Si	**Al**	**Al**	**Al**	**Ti**	**Fe**	**Mg**	**Mn**	**Ca**	**Na**	**K**	**$[]_X$**				
B600-8G_III	7.6_Tur5	34.69	0.65	36.04	8.70	4.51	*b.d.l*	1.31	1.50	*0.10*	10.71	3.69	101.96	5.63	0.37	6.00	0.52	0.08	1.18	1.09	0.00	0.23	0.47	0.02	0.28	3.00	4.00	6.89	Core
	7.6_Tur1	33.05	0.54	36.36	8.42	4.51	*b.d.l*	1.86	1.28	*0.08*	10.52	3.63	100.36	5.46	0.54	6.00	0.54	0.07	1.16	1.11	0.00	0.33	0.41	0.02	0.24	3.00	4.00	7.08	Core
	7.6_Tur2	33.23	0.74	35.51	9.20	4.46	*b.d.l*	1.71	1.38	*0.09*	10.49	3.62	100.53	5.50	0.50	6.00	0.44	0.09	1.27	1.10	0.00	0.30	0.44	0.02	0.23	3.00	4.00	6.93	Core
	7.6_Tur3	34.72	0.63	37.09	8.31	4.44	*b.d.l*	1.57	1.37	*0.08*	10.83	3.73	102.83	5.57	0.43	6.00	0.59	0.08	1.12	1.06	0.00	0.27	0.43	0.02	0.29	3.00	4.00	7.02	Core
	7.6_Tur4	34.32	1.05	35.29	8.45	4.35	*b.d.l*	1.32	1.57	*0.11*	10.58	3.65	100.73	5.64	0.36	6.00	0.47	0.13	1.16	1.07	0.00	0.23	0.50	0.02	0.25	3.00	4.00	6.83	Core
	7.6_Tur5	33.03	1.06	34.75	8.53	4.38	*b.d.l*	1.41	1.48	*0.09*	10.34	3.56	98.69	5.55	0.45	6.00	0.44	0.13	1.20	1.10	0.00	0.25	0.48	0.02	0.25	3.00	4.00	6.88	Core
	7.6_Tur6	32.37	*0.56*	36.26	8.85	4.20	*b.d.l*	1.86	1.17	*0.05*	10.39	3.58	99.35	5.41	0.59	6.00	0.56	0.07	1.24	1.05	0.00	0.33	0.38	0.01	0.28	3.00	4.00	7.15	Core
	7.6_Tur7	31.86	0.58	36.11	9.11	4.12	*b.d.l*	1.92	1.07	*0.05*	10.31	3.55	98.78	5.37	0.63	6.00	0.55	0.07	1.28	1.03	0.00	0.35	0.35	0.01	0.29	3.00	4.00	7.18	Core
	7.6_Tur8	33.41	0.68	35.89	8.92	4.28	*b.d.l*	1.43	1.54	*0.08*	10.51	3.62	100.46	5.52	0.48	6.00	0.52	0.08	1.23	1.06	0.00	0.25	0.49	0.02	0.24	3.00	4.00	6.99	Core
	7.6_Tur9	34.32	0.62	36.74	8.19	4.37	*b.d.l*	0.96	1.72	*0.05*	10.69	3.68	101.48	5.58	0.42	6.00	0.62	0.08	1.11	1.06	0.00	0.17	0.54	0.01	0.28	3.00	4.00	7.04	Core
	7.6_Tur10	33.58	*0.59*	36.37	8.35	4.31	*b.d.l*	1.37	1.59	0.05	10.56	3.64	100.45	5.53	0.47	6.00	0.59	0.07	1.15	1.06	0.00	0.24	0.51	0.01	0.24	3.00	4.00	7.06	Core
	7.6_Tur11	33.93	0.75	36.16	7.95	4.71	*b.d.l*	1.27	1.47	*0.06*	10.60	3.65	100.66	5.56	0.44	6.00	0.55	0.09	1.09	1.15	0.00	0.22	0.47	0.01	0.29	3.00	4.00	6.99	Core
	7.6_Tur12	32.59	0.67	34.22	8.45	4.32	*b.d.l*	1.63	1.37	*0.07*	10.17	3.50	97.09	5.57	0.43	6.00	0.47	0.09	1.21	1.10	0.00	0.30	0.45	0.02	0.23	3.00	4.00	6.89	Core
	7.6_Tur13	32.87	0.68	35.90	8.72	4.37	*b.d.l*	1.66	1.33	*0.06*	10.44	3.60	99.74	5.47	0.53	6.00	0.52	0.09	1.21	1.08	0.00	0.30	0.43	0.01	0.26	3.00	4.00	7.04	Core
	7.6_Tur14C	32.41	*0.68*	36.60	8.58	4.36	*0.21*	1.72	1.26	*0.08*	10.47	3.61	99.97	5.38	0.62	6.00	0.55	0.09	1.19	1.08	0.03	0.31	0.40	0.02	0.27	3.00	4.00	7.16	Core
	7.6_Tur15	34.56	0.72	36.08	8.11	4.51	*b.d.l*	1.08	1.63	*0.10*	10.66	3.68	101.29	5.63	0.37	6.00	0.57	0.09	1.10	1.10	0.00	0.19	0.51	0.02	0.28	3.00	4.00	6.93	Rim
	7.6_Tur16	34.55	0.69	34.40	7.67	4.32	*0.14*	0.88	1.59	*0.11*	10.39	3.58	98.39	5.78	0.22	6.00	0.56	0.09	1.07	1.08	0.02	0.16	0.51	0.02	0.30	3.00	4.00	6.78	Rim
	7.6_Tur17	35.24	*1.08*	36.03	8.46	4.66	*b.d.l*	1.12	1.76	*0.08*	10.84	3.74	103.00	5.65	0.35	6.00	0.46	0.13	1.13	1.11	0.00	0.19	0.55	0.02	0.25	3.00	4.00	6.81	Rim
	7.6_Tur18	34.69	*0.85*	35.19	8.37	4.71	*b.d.l*	1.23	1.47	*0.33*	10.63	3.66	101.27	5.67	0.33	6.00	0.45	0.10	1.14	1.15	0.00	0.22	0.47	0.07	0.25	3.00	4.00	6.78	Rim
	7.6_Tur19	34.25	0.72	33.62	7.65	4.15	*b.d.l*	1.23	1.38	*0.07*	10.24	3.53	96.97	5.82	0.18	6.00	0.54	0.09	1.09	1.05	0.00	0.22	0.45	0.02	0.31	3.00	4.00	6.73	Rim
	7.6_Tur20	35.46	0.64	36.75	8.22	4.45	*b.d.l*	1.11	1.63	*0.05*	10.86	3.75	103.03	5.67	0.33	6.00	0.60	0.08	1.10	1.06	0.00	0.19	0.50	0.01	0.30	3.00	4.00	6.93	Rim
	7.6_Tur21	34.93	*0.70*	35.27	7.76	4.65	*0.15*	0.87	1.73	*0.10*	10.61	3.66	100.42	5.73	0.27	6.00	0.54	0.09	1.06	1.14	0.02	0.15	0.55	0.02	0.28	3.00	4.00	6.81	Rim
	7.6_Tur22	34.71	0.63	33.87	7.76	4.44	*0.17*	0.74	1.80	*0.10*	10.37	3.57	98.17	5.82	0.18	6.00	0.51	0.08	1.09	1.11	0.02	0.13	0.59	0.02	0.26	3.00	4.00	6.69	Rim
	7.6_Tur23	35.34	0.59	35.59	7.35	4.40	*b.d.l*	0.49	1.98	*0.09*	10.62	3.66	100.24	5.78	0.22	6.00	0.65	0.07	1.01	1.07	0.00	0.09	0.63	0.02	0.27	3.00	4.00	6.86	Rim
	7.6_Tur24	34.78	0.61	34.72	7.59	4.31	*b.d.l*	0.58	1.88	*0.07*	10.44	3.60	98.72	5.79	0.21	6.00	0.61	0.08	1.06	1.07	0.00	0.10	0.61	0.01	0.27	3.00	4.00	6.81	Rim
	7.6_Tur25	34.20	0.66	34.83	7.65	4.45	*b.d.l*	0.57	1.91	*0.08*	10.39	3.58	98.49	5.72	0.28	6.00	0.58	0.08	1.07	1.11	0.00	0.10	0.62	0.02	0.26	3.00	4.00	6.86	Rim
	7.6_Tur26	33.16	0.65	34.87	7.71	4.54	*b.d.l*	1.03	1.64	*0.10*	10.28	3.54	97.61	5.61	0.39	6.00	0.55	0.08	1.09	1.14	0.00	0.19	0.54	0.02	0.26	3.00	4.00	6.95	Rim
	7.6_Tur27	36.20	*0.54*	34.20	9.59	4.51	*b.d.l*	0.45	1.66	*b.d.l*	10.68	3.68	101.54	5.89	0.11	6.00	0.45	0.07	1.30	1.09	0.00	0.08	0.53	0.00	0.40	3.00	4.00	6.56	Rim

Group	Name	SiO_2	TiO_2	Al_2O_3	FeO	MgO	MnO	CaO	Na_2O	K_2O	B_2O_3	H_2O	Total	Site T		Site Z	Site Y					Site X				B	OH^-	Total Al	Infos
														Si	Al	Al	Al	Ti	Fe	Mg	Mn	Ca	Na	K	$[]_X$				
B600-8G_III	7.6_Tur28	33.94	*0.67*	35.66	8.18	4.50	*b.d.l*	1.09	1.63	*0.10*	10.52	3.63	100.00	5.61	0.39	6.00	0.55	0.08	1.13	1.11	0.00	0.19	0.52	0.02	0.27	3.00	4.00	6.94	Rim
	7.6_Tur29	35.02	0.63	33.95	7.84	4.32	*b.d.l*	0.30	2.03	*0.09*	10.38	3.58	98.22	5.86	0.14	6.00	0.56	0.08	1.10	1.08	0.00	0.05	0.66	0.02	0.27	3.00	4.00	6.70	Rim
	7.6.2_Tur14R1	34.92	0.69	36.01	7.77	4.51	*0.18*	0.80	1.84	*0.06*	10.68	3.68	101.16	5.68	0.32	6.00	0.58	0.08	1.06	1.09	0.02	0.14	0.58	0.01	0.27	3.00	4.00	6.90	Rim
	7.6.2_Tur14R2	34.82	0.70	36.09	7.99	4.53	*0.15*	0.96	1.73	*0.08*	10.70	3.69	101.43	5.66	0.34	6.00	0.57	0.09	1.09	1.10	0.02	0.17	0.55	0.02	0.27	3.00	4.00	6.91	Rim
B600-8G_IV	7.6_TurOG1	33.39	0.66	35.38	8.36	4.22	*b.d.l*	1.44	1.34	0.09	10.39	3.58	98.99	5.58	0.42	6.00	0.56	0.08	1.17	1.05	0.00	0.26	0.44	0.02	0.29	3.00	4.00	6.97	
	7.6_TurOG2	33.30	0.64	35.62	8.44	4.40	*b.d.l*	1.44	1.42	0.08	10.44	3.60	99.44	5.55	0.45	6.00	0.54	0.08	1.17	1.09	0.00	0.26	0.46	0.02	0.27	3.00	4.00	6.99	
	7.6_TurOG3	31.99	*0.61*	34.76	8.68	4.19	*0.18*	1.75	1.24	0.06	10.15	3.50	97.12	5.48	0.52	6.00	0.49	0.08	1.24	1.07	0.03	0.32	0.41	0.01	0.25	3.00	4.00	7.01	
	7.6_TurOG4	32.42	0.61	36.65	8.83	4.18	*b.d.l*	1.85	1.22	0.06	10.46	3.60	100.03	5.39	0.61	6.00	0.57	0.08	1.23	1.04	0.00	0.33	0.39	0.01	0.26	3.00	4.00	7.18	
	7.6_TurOG5	34.88	0.88	35.48	8.54	4.96	*b.d.l*	1.07	1.61	0.06	10.72	3.69	101.98	5.66	0.34	6.00	0.44	0.11	1.16	1.20	0.00	0.19	0.50	0.01	0.30	3.00	4.00	6.78	
	7.6_TurOG6	34.05	0.61	36.06	8.41	4.29	*b.d.l*	1.39	1.45	*0.06*	10.58	3.65	100.55	5.59	0.41	6.00	0.58	0.07	1.16	1.05	0.00	0.24	0.46	0.01	0.28	3.00	4.00	6.98	
	7.6_TurOG7	33.35	0.63	35.15	7.93	4.17	*b.d.l*	0.99	1.52	*b.d.l*	10.30	3.55	97.75	5.63	0.37	6.00	0.62	0.08	1.12	1.05	0.00	0.18	0.50	0.00	0.32	3.00	4.00	6.99	
	7.6_TurOG8	33.19	*0.61*	35.76	8.58	4.11	b.d.l	1.33	1.36	*0.07*	10.40	3.59	99.10	5.55	0.45	6.00	0.59	0.08	1.20	1.02	0.00	0.24	0.44	0.01	0.31	3.00	4.00	7.04	
	7.6_TurOG9	32.37	0.63	35.62	8.21	4.09	*b.d.l*	1.22	1.58	*0.05*	10.25	3.53	97.68	5.49	0.51	6.00	0.61	0.08	1.16	1.03	0.00	0.22	0.52	0.01	0.25	3.00	4.00	7.12	
	7.6_TurOG10	32.18	0.66	35.12	8.57	4.18	*b.d.l*	1.03	1.65	*0.07*	10.19	3.51	97.24	5.49	0.51	6.00	0.55	0.08	1.22	1.06	0.00	0.19	0.55	0.02	0.25	3.00	4.00	7.06	
	7.6_TurOG11	32.12	0.58	35.59	7.84	4.22	*b.d.l*	1.12	1.59	*b.d.l*	10.19	3.51	96.95	5.48	0.52	6.00	0.64	0.07	1.12	1.07	0.00	0.21	0.53	0.00	0.27	3.00	4.00	7.16	
	7.6_TurOG12	32.10	0.57	35.69	7.99	4.12	*b.d.l*	1.12	1.61	b.d.l	10.20	3.52	97.07	5.47	0.53	6.00	0.64	0.07	1.14	1.05	0.00	0.20	0.53	0.00	0.26	3.00	4.00	7.17	
	7.6_TurOG13	32.29	*0.65*	35.18	8.14	4.33	*b.d.l*	1.15	1.41	*0.07*	10.19	3.51	96.95	5.51	0.49	6.00	0.58	0.08	1.16	1.10	0.00	0.21	0.46	0.02	0.31	3.00	4.00	7.07	
	7.6_TurOG14	32.60	0.62	35.07	7.93	4.17	*b.d.l*	1.10	1.67	*b.d.l*	10.20	3.52	96.96	5.56	0.44	6.00	0.60	0.08	1.13	1.06	0.00	0.20	0.55	0.00	0.25	3.00	4.00	7.04	
	7.6_TurOG15	31.67	0.67	35.12	8.66	4.15	*b.d.l*	1.12	1.60	0.05	10.12	3.49	96.77	5.44	0.56	6.00	0.55	0.09	1.24	1.06	0.00	0.21	0.53	0.01	0.25	3.00	4.00	7.11	
	7.6_TurOG16	32.37	0.61	35.10	8.65	4.09	*b.d.l*	1.16	1.59	0.06	10.21	3.52	97.41	5.51	0.49	6.00	0.56	0.08	1.23	1.04	0.00	0.21	0.53	0.01	0.25	3.00	4.00	7.05	
	7.6_TurOG17	34.04	0.64	36.22	8.09	4.38	*b.d.l*	1.16	1.65	*0.06*	10.59	3.65	100.50	5.59	0.41	6.00	0.60	0.08	1.11	1.07	0.00	0.20	0.53	0.01	0.26	3.00	4.00	7.01	
	7.6_TurOG18	35.16	*0.60*	36.50	7.57	4.31	*0.17*	1.03	1.60	*0.08*	10.74	3.70	101.47	5.69	0.31	6.00	0.65	0.07	1.02	1.04	0.02	0.18	0.50	0.02	0.30	3.00	4.00	6.96	
	7.6_TurOG19	33.80	*0.57*	35.53	8.06	4.25	*b.d.l*	1.23	1.56	*b.d.l*	10.44	3.60	99.07	5.63	0.37	6.00	0.60	0.07	1.12	1.05	0.00	0.22	0.50	0.00	0.28	3.00	4.00	6.97	
	7.6_TurOG20	34.74	*0.61*	36.24	7.83	4.23	*b.d.l*	1.14	1.56	b.d.l	10.64	3.67	100.72	5.67	0.33	6.00	0.65	0.07	1.07	1.03	0.00	0.20	0.49	0.00	0.31	3.00	4.00	6.97	
	7.6_TurOG21	34.69	*0.60*	33.88	7.55	4.08	*b.d.l*	0.92	1.59	*0.11*	10.30	3.55	97.42	5.85	0.15	6.00	0.59	0.08	1.06	1.03	0.00	0.17	0.52	0.02	0.29	3.00	4.00	6.74	
	7.6_TurOG22	35.69	0.64	36.69	7.99	4.29	*b.d.l*	0.93	1.66	*b.d.l*	10.85	3.74	102.60	5.72	0.28	6.00	0.65	0.08	1.07	1.03	0.00	0.16	0.51	0.00	0.33	3.00	4.00	6.93	
	7.6_TurOG23	34.81	*0.60*	35.88	7.50	4.20	*b.d.l*	1.11	1.55	*b.d.l*	10.58	3.65	100.02	5.72	0.28	6.00	0.66	0.07	1.03	1.03	0.00	0.20	0.49	0.00	0.31	3.00	4.00	6.94	
	7.6_TurOG24	34.35	*0.62*	36.51	8.33	4.30	*b.d.l*	1.13	1.59	*0.05*	10.67	3.68	101.36	5.60	0.40	6.00	0.61	0.08	1.14	1.04	0.00	0.20	0.50	0.01	0.29	3.00	4.00	7.01	

Group	Name	SiO_2	TiO_2	Al_2O_3	FeO	MgO	MnO	CaO	Na_2O	K_2O	B_2O_3	H_2O	Total	Site T		Site Z	Site Y					Site X				B	OH^-	Total Al	Infos
														Si	Al	Al	Al	Ti	Fe	Mg	Mn	Ca	Na	K	[]X				
B600-8G_IV	7.6_TurOG25	34.47	*0.56*	35.84	7.89	4.28	*b.d.l*	1.11	1.68	*b.d.l*	10.56	3.64	100.17	5.67	0.33	6.00	0.62	0.07	1.08	1.05	0.00	0.20	0.54	0.00	0.27	3.00	4.00	6.95	
	7.6_TurOG26	34.77	*0.69*	36.86	8.48	4.34	*b.d.l*	1.11	1.68	b.d.l	10.79	3.72	102.58	5.60	0.40	6.00	0.60	0.08	1.14	1.04	0.00	0.19	0.52	0.00	0.28	3.00	4.00	7.00	
	7.6_TurOG27	34.31	0.64	35.79	8.67	4.25	*0.22*	1.07	1.72	*0.08*	10.61	3.66	101.02	5.62	0.38	6.00	0.54	0.08	1.19	1.04	0.03	0.19	0.55	0.02	0.25	3.00	4.00	6.91	
	7.6_TurOG28	35.01	0.70	35.21	8.46	4.43	*b.d.l*	0.89	1.76	*0.08*	10.62	3.66	100.94	5.73	0.27	6.00	0.52	0.09	1.16	1.08	0.00	0.16	0.56	0.02	0.27	3.00	4.00	6.79	
	7.6_TurOG29	34.17	*0.63*	36.16	7.71	4.13	*0.15*	1.20	1.60	*0.05*	10.56	3.64	100.02	5.63	0.37	6.00	0.64	0.08	1.06	1.01	0.02	0.21	0.51	0.01	0.27	3.00	4.00	7.02	
	7.6_TurOG30	35.61	*0.61*	35.60	7.97	5.16	*b.d.l*	0.69	1.80	*b.d.l*	10.78	3.71	102.08	5.74	0.26	6.00	0.51	0.07	1.07	1.24	0.00	0.12	0.56	0.00	0.32	3.00	4.00	6.77	
	7.6_TurOG31	34.67	0.61	36.17	7.75	4.37	*b.d.l*	0.95	1.64	*0.06*	10.63	3.66	100.59	5.67	0.33	6.00	0.64	0.07	1.06	1.06	0.00	0.17	0.52	0.01	0.30	3.00	4.00	6.97	
B600-10_III	9.5_Core1	33.39	*0.72*	34.90	8.39	4.73	*b.d.l*	1.80	1.36	*0.08*	10.42	3.59	99.51	5.57	0.43	6.00	0.43	0.09	1.17	1.18	0.00	0.32	0.44	0.02	0.22	3.00	4.00	6.86	Core
	9.5_Core2	32.84	*0.66*	35.73	9.06	4.26	*b.d.l*	1.81	1.29	*0.07*	10.43	3.59	99.89	5.47	0.53	6.00	0.49	0.08	1.26	1.06	0.00	0.32	0.42	0.02	0.24	3.00	4.00	7.02	Core
	9.5_Core3	33.05	*0.57*	35.76	8.93	4.52	*b.d.l*	1.71	1.25	*0.08*	10.46	3.61	99.96	5.49	0.51	6.00	0.49	0.07	1.24	1.12	0.00	0.31	0.40	0.02	0.28	3.00	4.00	7.00	Core
	9.5_Core4	33.27	*0.68*	36.43	8.35	4.53	*0.13*	1.17	1.58	*0.07*	10.55	3.64	100.41	5.48	0.52	6.00	0.56	0.08	1.15	1.11	0.02	0.21	0.50	0.01	0.28	3.00	4.00	7.08	Core
	9.5_Core5	35.13	*0.66*	35.43	7.87	4.24	b.d.l	1.38	1.31	*0.18*	10.62	3.66	100.52	5.75	0.25	6.00	0.59	0.08	1.08	1.03	0.00	0.24	0.42	0.04	0.30	3.00	4.00	6.84	Core
	9.5_Core6	33.92	*0.69*	35.74	8.41	4.50	*b.d.l*	1.34	1.56	*0.08*	10.56	3.64	100.53	5.59	0.41	6.00	0.52	0.09	1.16	1.10	0.00	0.24	0.50	0.02	0.25	3.00	4.00	6.94	Core
	9.5_Core7	33.71	0.68	35.34	8.67	4.67	*0.22*	1.24	1.71	*0.09*	10.53	3.63	100.49	5.57	0.43	6.00	0.44	0.08	1.20	1.15	0.03	0.22	0.55	0.02	0.21	3.00	4.00	6.88	Core
	9.5_Core8	33.43	*0.64*	36.46	8.07	4.58	*0.21*	1.70	1.46	*0.08*	10.59	3.65	100.89	5.48	0.52	6.00	0.53	0.08	1.11	1.12	0.03	0.30	0.47	0.02	0.22	3.00	4.00	7.05	Core
	9.5_Core9	34.45	0.68	36.29	8.23	4.49	*b.d.l*	1.29	1.55	*0.09*	10.68	3.68	101.54	5.60	0.40	6.00	0.56	0.08	1.12	1.09	0.00	0.23	0.49	0.02	0.27	3.00	4.00	6.96	Core
	9.5_Core10	35.47	*0.77*	36.55	7.54	4.50	*b.d.l*	1.07	1.65	*0.09*	10.82	3.73	102.25	5.70	0.30	6.00	0.62	0.09	1.01	1.08	0.00	0.18	0.51	0.02	0.28	3.00	4.00	6.92	Core
	9.5_Core11	33.87	*0.55*	36.61	8.76	4.51	*0.23*	1.94	1.20	*0.09*	10.70	3.69	102.15	5.50	0.50	6.00	0.51	0.07	1.19	1.09	0.03	0.34	0.38	0.02	0.27	3.00	4.00	7.01	Core
	9.5_Rim1	33.90	*0.71*	33.93	8.44	4.57	*b.d.l*	1.08	1.65	*0.10*	10.33	3.56	98.33	5.71	0.29	6.00	0.44	0.09	1.19	1.15	0.00	0.19	0.54	0.02	0.25	3.00	4.00	6.73	Rim
	9.5_Rim2	35.08	*0.62*	34.21	7.35	4.28	b.d.l	0.92	1.83	*0.14*	10.43	3.59	98.61	5.85	0.15	6.00	0.57	0.08	1.02	1.06	0.00	0.16	0.59	0.03	0.22	3.00	4.00	6.72	Rim
	9.5_Rim3	34.95	*0.82*	33.70	8.44	4.31	*b.d.l*	0.62	1.87	*0.10*	10.41	3.59	98.89	5.83	0.17	6.00	0.47	0.10	1.18	1.07	0.00	0.11	0.61	0.02	0.26	3.00	4.00	6.63	Rim
	9.5_Rim4	34.99	0.77	34.07	8.39	4.26	*b.d.l*	0.64	1.69	*0.11*	10.44	3.60	99.08	5.83	0.17	6.00	0.51	0.10	1.17	1.06	0.00	0.12	0.54	0.02	0.32	3.00	4.00	6.69	Rim
	9.5_Rim5	34.88	*0.67*	34.20	8.20	4.50	*b.d.l*	0.90	1.67	*0.12*	10.46	3.61	99.23	5.79	0.21	6.00	0.49	0.08	1.14	1.11	0.00	0.16	0.54	0.03	0.27	3.00	4.00	6.70	Rim
	9.5_Rim6	35.94	*0.76*	34.52	7.13	4.28	*b.d.l*	0.86	1.61	*0.14*	10.57	3.64	99.47	5.91	0.09	6.00	0.60	0.09	0.98	1.05	0.00	0.15	0.51	0.03	0.31	3.00	4.00	6.69	Rim
	9.5_Rim7	35.28	*0.72*	34.17	7.90	4.55	*b.d.l*	0.65	1.92	*0.11*	10.51	3.62	99.57	5.84	0.16	6.00	0.50	0.09	1.09	1.12	0.00	0.11	0.62	0.02	0.25	3.00	4.00	6.66	Rim
	9.5_Rim8	34.78	*0.61*	35.27	7.29	4.58	*b.d.l*	1.15	1.63	*0.11*	10.55	3.64	99.74	5.73	0.27	6.00	0.58	0.08	1.01	1.13	0.00	0.20	0.52	0.02	0.25	3.00	4.00	6.85	Rim
	9.5_Rim9	36.38	*0.56*	34.30	6.39	5.94	*b.d.l*	0.42	1.97	0.05	10.70	3.69	100.41	5.91	0.09	6.00	0.48	0.07	0.87	1.44	0.00	0.07	0.62	0.01	0.30	3.00	4.00	6.57	Rim
	9.5_Rim10	36.56	*0.52*	34.73	6.83	5.43	*b.d.l*	0.59	1.44	*0.06*	10.73	3.70	100.67	5.92	0.08	6.00	0.56	0.06	0.93	1.31	0.00	0.10	0.45	0.01	0.43	3.00	4.00	6.63	Rim

Group	Name	SiO_2	TiO_2	Al_2O_3	FeO	MgO	MnO	CaO	Na_2O	K_2O	B_2O_3	H_2O	Total	Site T		Site Z	Site Y					Site X				B	OH^-	Total Al	Infos
														Si	Al	Al	Al	Ti	Fe	Mg	Mn	Ca	Na	K	$[]_X$				
B600-10_III	9.5_Rim11	34.36	0.73	35.41	8.13	4.97	*b.d.l*	1.08	1.63	*0.10*	10.60	3.65	100.80	5.63	0.37	6.00	0.48	0.09	1.12	1.22	0.00	0.19	0.52	0.02	0.27	3.00	4.00	6.84	Rim
	9.5_Rim12	36.25	0.67	35.04	8.09	4.42	*0.15*	0.79	1.74	0.12	10.75	3.71	101.73	5.86	0.14	6.00	0.54	0.08	1.09	1.06	0.02	0.14	0.55	0.02	0.29	3.00	4.00	6.68	Rim
	9.5_Rim13	35.36	0.66	36.06	7.96	4.52	*b.d.l*	1.13	1.64	0.10	10.76	3.71	101.93	5.71	0.29	6.00	0.57	0.08	1.08	1.09	0.00	0.20	0.51	0.02	0.27	3.00	4.00	6.86	Rim
B500-8G_III	8.6_Turgb1	34.13	0.30	35.68	7.33	4.28	*b.d.l*	1.18	1.48	0.10	10.43	3.60	98.65	5.69	0.31	6.00	0.69	0.04	1.02	1.06	0.00	0.21	0.48	0.02	0.29	3.00	4.00	7.01	Asso.
	8.6_Turgb2	36.13	0.64	34.97	9.51	4.13	*b.d.l*	0.40	1.77	*0.07*	10.74	3.70	102.06	5.85	0.15	6.00	0.52	0.08	1.29	1.00	0.00	0.07	0.55	0.01	0.36	3.00	4.00	6.67	Asso.
	8.6_Turgb3	35.14	0.33	35.99	7.85	4.43	*b.d.l*	1.38	1.38	*0.15*	10.68	3.68	101.05	5.72	0.28	6.00	0.63	0.04	1.07	1.08	0.00	0.24	0.44	0.03	0.29	3.00	4.00	6.90	Asso.
	8.6_Turgb4	34.97	*0.39*	35.40	8.42	4.23	*b.d.l*	1.43	1.30	*0.12*	10.59	3.65	100.59	5.74	0.26	6.00	0.58	0.05	1.15	1.03	0.00	0.25	0.41	0.03	0.31	3.00	4.00	6.85	Asso.
	8.6_Turgb5	35.19	0.49	35.09	8.41	4.14	*b.d.l*	1.08	1.56	*0.11*	10.58	3.65	100.32	5.78	0.22	6.00	0.58	0.06	1.16	1.01	0.00	0.19	0.50	0.02	0.29	3.00	4.00	6.80	Asso.
	8.6_Turgb6	33.78	0.34	35.25	7.70	4.32	*b.d.l*	1.24	1.47	*0.08*	10.36	3.57	98.12	5.67	0.33	6.00	0.63	0.04	1.08	1.08	0.00	0.22	0.48	0.02	0.28	3.00	4.00	6.97	Asso.
	8.6_Turgb7	34.60	0.40	34.96	7.76	3.88	*b.d.l*	1.06	1.36	*0.13*	10.39	3.58	98.23	5.79	0.21	6.00	0.68	0.05	1.09	0.97	0.00	0.19	0.44	0.03	0.34	3.00	4.00	6.89	Asso.
	8.6_Turgb8	35.48	0.50	34.68	7.61	3.96	*0.18*	1.10	1.33	*0.44*	10.51	3.62	99.47	5.87	0.13	6.00	0.62	0.06	1.05	0.98	0.03	0.19	0.43	0.09	0.29	3.00	4.00	6.76	Asso.
	8.6_Turgb9	35.56	0.26	34.77	7.74	3.87	*b.d.l*	1.14	1.29	*0.13*	10.48	3.61	98.97	5.90	0.10	6.00	0.69	0.03	1.07	0.96	0.00	0.20	0.41	0.03	0.36	3.00	4.00	6.79	Asso.
	8.6_Turgb10	35.73	0.30	36.96	7.37	4.28	*b.d.l*	1.36	1.37	*0.05*	10.83	3.73	102.03	5.74	0.26	6.00	0.73	0.04	0.99	1.02	0.00	0.23	0.43	0.01	0.33	3.00	4.00	6.99	Asso.
	8.6_Flot1	35.16	0.34	35.41	8.08	4.36	*b.d.l*	1.31	1.44	*0.06*	10.61	3.66	100.58	5.76	0.24	6.00	0.60	0.04	1.11	1.06	0.00	0.23	0.46	0.01	0.30	3.00	4.00	6.84	Isol.
	8.6_Flot2	34.98	0.34	36.37	7.96	4.28	*b.d.l*	1.30	1.40	*b.d.l*	10.68	3.68	101.10	5.69	0.31	6.00	0.67	0.04	1.08	1.04	0.00	0.23	0.44	0.00	0.33	3.00	4.00	6.98	Isol.
	8.6_Flot3	36.40	0.37	35.17	8.08	4.25	*0.15*	1.38	1.38	*0.06*	10.76	3.71	101.72	5.88	0.12	6.00	0.58	0.05	1.09	1.02	0.02	0.24	0.43	0.01	0.31	3.00	4.00	6.70	Isol.
	8.6_Flot4	34.61	0.33	36.20	8.08	4.42	*b.d.l*	1.30	1.53	*b.d.l*	10.64	3.67	101.00	5.66	0.34	6.00	0.63	0.04	1.10	1.08	0.00	0.23	0.49	0.00	0.29	3.00	4.00	6.97	Isol.
	8.6_Flot5	35.67	0.34	36.85	8.49	4.32	*b.d.l*	1.52	1.19	*0.05*	10.88	3.75	103.14	5.70	0.30	6.00	0.64	0.04	1.13	1.03	0.00	0.26	0.37	0.01	0.36	3.00	4.00	6.94	Isol.
	8.6_Flot6	34.46	0.27	36.07	7.95	4.48	*b.d.l*	1.64	1.39	*0.04*	10.61	3.66	100.67	5.65	0.35	6.00	0.61	0.03	1.09	1.09	0.00	0.29	0.44	0.01	0.26	3.00	4.00	6.96	Isol.
	8.6_Flot7	35.86	0.70	34.79	####	3.61	*b.d.l*	0.30	1.71	*0.04*	10.68	3.68	102.11	5.84	0.16	6.00	0.51	0.09	1.44	0.87	0.00	0.05	0.54	0.01	0.40	3.00	4.00	6.67	Isol.
	8.6_Flot8	34.87	0.36	36.56	7.91	4.31	*b.d.l*	1.37	1.45	b.d.l	10.70	3.69	101.28	5.66	0.34	6.00	0.66	0.04	1.07	1.04	0.00	0.24	0.46	0.00	0.30	3.00	4.00	7.00	Isol.
B500-8G_IV	8.6_OG1	35.45	0.28	36.05	9.00	3.85	*b.d.l*	1.71	1.14	b.d.l	10.73	3.70	101.99	5.74	0.26	6.00	0.62	0.03	1.22	0.93	0.00	0.30	0.36	0.00	0.35	3.00	4.00	6.88	
	8.6_OG2	35.83	0.26	37.90	8.09	4.03	*b.d.l*	1.53	1.32	*b.d.l*	10.98	3.78	103.75	5.67	0.33	6.00	0.75	0.03	1.07	0.95	0.00	0.26	0.41	0.00	0.34	3.00	4.00	7.07	
	8.6_OG3	35.40	0.29	37.82	8.07	4.06	*b.d.l*	1.57	1.21	*b.d.l*	10.91	3.76	103.13	5.64	0.36	6.00	0.74	0.03	1.08	0.96	0.00	0.27	0.37	0.00	0.36	3.00	4.00	7.10	
	8.6_OG4	34.93	0.29	37.16	8.21	3.95	*b.d.l*	1.28	1.35	*b.d.l*	10.74	3.70	101.72	5.65	0.35	6.00	0.74	0.04	1.11	0.95	0.00	0.22	0.42	0.00	0.35	3.00	4.00	7.09	
	8.6_OG5	35.29	0.27	37.48	8.10	3.92	*b.d.l*	1.37	1.31	*b.d.l*	10.83	3.73	102.35	5.67	0.33	6.00	0.76	0.03	1.09	0.94	0.00	0.24	0.41	0.00	0.36	3.00	4.00	7.09	
	8.6_OG6	35.40	*0.26*	37.07	8.22	3.88	*b.d.l*	1.41	1.19	b.d.l	10.79	3.72	102.08	5.70	0.30	6.00	0.74	0.03	1.11	0.93	0.00	0.24	0.37	0.00	0.39	3.00	4.00	7.04	
	8.6_OG7	35.48	0.28	37.54	8.04	4.02	*b.d.l*	1.49	1.28	*b.d.l*	10.88	3.75	102.89	5.67	0.33	6.00	0.74	0.03	1.07	0.96	0.00	0.26	0.40	0.00	0.35	3.00	4.00	7.07	

Group	**Name**	**SiO_2**	**TiO_2**	**Al_2O_3**	**FeO**	**MgO**	**MnO**	**CaO**	**Na_2O**	**K_2O**	**B_2O_3**	**H_2O**	**Total**	**Site T**		**Site Z**	**Site Y**					**Site X**				**B**	**OH^-**	**Total Al**	**Infos**
														Si	**Al**	**Al**	**Al**	**Ti**	**Fe**	**Mg**	**Mn**	**Ca**	**Na**	**K**	**$[]_X$**				
B500-8G_IV	8.6_OG8	35.28	0.28	37.37	8.25	3.84	*0.17*	1.35	1.37	*0.09*	10.83	3.73	102.54	5.66	0.34	6.00	0.73	0.03	1.11	0.92	0.02	0.23	0.43	0.02	0.33	3.00	4.00	7.07	
	8.6_OG9	35.88	0.33	38.27	7.74	3.85	*b.d.l*	1.38	1.21	*0.07*	10.98	3.79	103.59	5.68	0.32	6.00	0.82	0.04	1.02	0.91	0.00	0.23	0.37	0.01	0.38	3.00	4.00	7.14	
	8.6_OG10	34.48	0.26	36.77	7.58	4.10	*b.d.l*	1.54	1.20	*0.07*	10.62	3.66	100.36	5.64	0.36	6.00	0.74	0.03	1.04	1.00	0.00	0.27	0.38	0.02	0.33	3.00	4.00	7.09	
	8.6_OG11	35.99	*0.25*	37.87	7.86	3.91	*b.d.l*	1.43	1.22	*0.05*	10.96	3.78	103.34	5.71	0.29	6.00	0.79	0.03	1.04	0.93	0.00	0.24	0.37	0.01	0.37	3.00	4.00	7.08	

Appendix A16

Illustrated workflow for the construction of the porosity map.

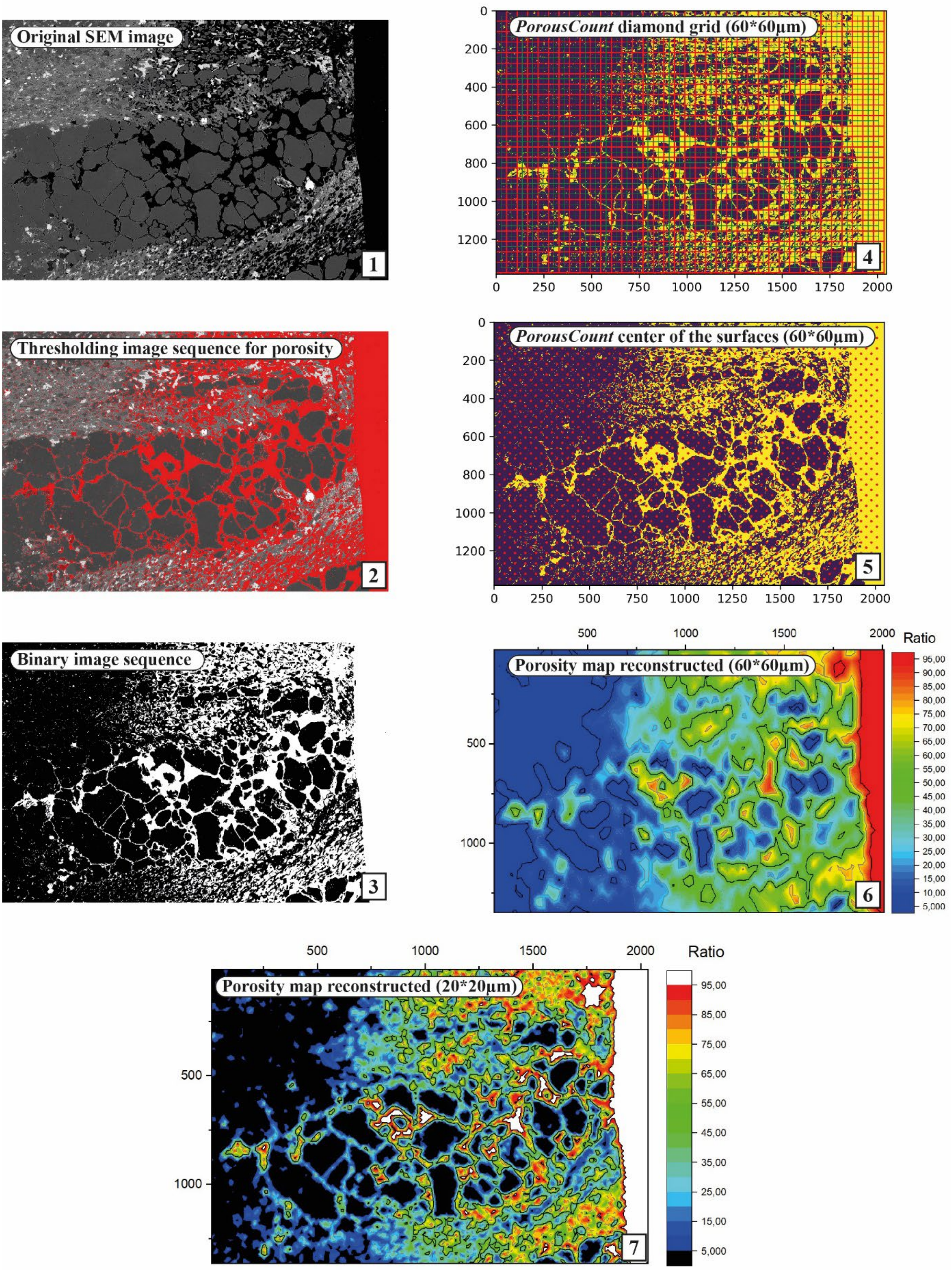

Appendix A17

This spotted schist core stayed at 400°C and 450 bars during 22h in the autoclave without any circulation of fluid in it. Upon observation, it appears that the carbonate spots are all altered on their rim, showing a clear reaction front between the original siderite and quartz and neoformed fayalite. The olivine crystallises as a porous material, in replacement of the siderite and extents its growth into the porosity left by the quartz. At 400°C, fayalite oxide composition add up to 100% and shows no trace of alteration.

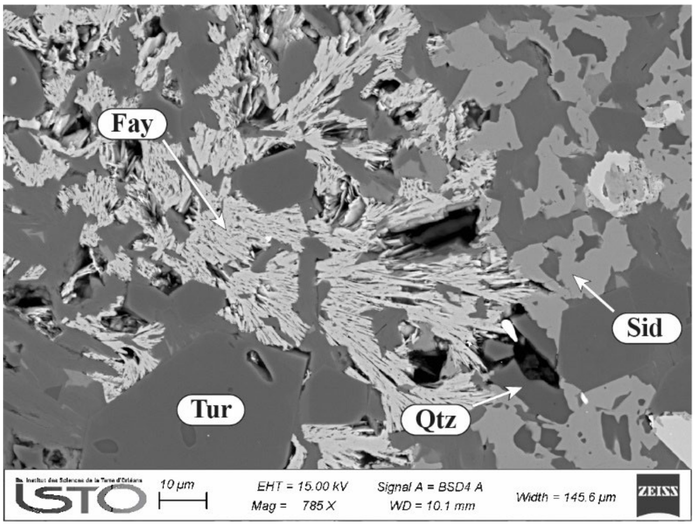

Appendix A18

Mineral	Biotite								Muscovite							
Texture	Matrix						Quartz spots and veins		Matrix						Quartz spots and veins	
	Subhedral		Altered		Rim				Subhedral		Altered		Rim			
n	14		18		8		21		18		21		14		12	
SiO_2	35.54	(1.59)	35.06	(0.93)	37.99	(2.9)	36.05	(1.22)	45.78	(0.67)	46.33	(0.79)	47.84	(0.96)	46.62	(0.84)
TiO_2	1.19	(0.12)	1.17	(0.07)	0.87	(0.38)	1.33	(0.15)	0.6	(0.56)	0.54	(0.14)	0.4	(0.17)	0.44	(0.09)
Al_2O_3	18.85	(0.97)	18.9	(0.71)	16.86	(2)	18.6	(0.69)	33.75	(0.74)	32.44	(1.06)	28.37	(2.96)	32.01	(2.54)
FeO_{total}	23.4	(1.47)	23.72	(1.05)	19.52	(4.18)	22.66	(1.29)	1.98	(0.42)	2.19	(0.46)	3.73	(0.99)	2.78	(1.29)
MgO	5.88	(0.66)	5.91	(0.6)	8.28	(2.46)	6.26	(0.44)	1.13	(0.22)	1.64	(0.36)	3.01	(0.97)	1.75	(0.82)
MnO	0.27	(0.08)	0.25	(0.06)	0.27	(0.05)	0.29	(0.07)	0.23	(0.02)	*b.d.l*		0.26		0.24	(0)
CaO	0.05		*b.d.l*		*b.d.l*		*b.d.l*		0.06		*b.d.l*		*b.d.l*		0.05	
Na_2O	0.07	(0.01)	0.07	(0.03)	0.06	(0.01)	0.1	(0.03)	0.65	(0.13)	0.48	(0.13)	0.26	(0.17)	0.49	(0.2)
K_2O	9.48	(0.22)	9.49	(0.2)	9.65	(0.32)	9.48	(0.15)	10.19	(0.33)	10.31	(0.35)	10.54	(0.47)	10.44	(0.45)
Cl	0.05	(0.01)	0.06	(0.01)	0.05		0.05	(0.01)	*b.d.l*		*b.d.l*		*b.d.l*		*b.d.l*	
F	1.14	(0.67)	1.44	(0.1)	2.79	(1.79)	1.52	(0.42)	1	(0.13)	1.02	(0.17)	2.22	(0.8)	1.13	(0.33)
OH^a	3.63	(0)	3.73	(0)	2.54	(0)	3.24	(0)	4.3	(0.22)	4.3	(0.23)	3.79	(0.66)	4.12	(0.3)
Total	99.59	(0.93)	100.33	(1.13)	98.74	(0.64)	99.67	(0.94)	99.43		99.57		100.04		100.18	
Si	2.79	(0.12)	2.76	(0.06)	2.95	(0.18)	2.82	(0.07)	3.1	(0.04)	3.14	(0.03)	3.27	(0.08)	3.15	(0.06)
Ti	0.07	(0.01)	0.07	(0)	0.05	(0.02)	0.08	(0.01)	0.03	(0.03)	0.03	(0.01)	0.02	(0.01)	0.02	(0)
^{IV}Al	1.21	(0.12)	1.24	(0.06)	1.05	(0.18)	1.18	(0.07)	0.9	(0.04)	0.86	(0.03)	0.73	(0.08)	0.85	(0.06)
Fe	1.53	(0.1)	1.56	(0.07)	1.27	(0.29)	1.48	(0.1)	0.11	(0.02)	0.12	(0.03)	0.21	(0.06)	0.16	(0.07)
Mg	0.69	(0.07)	0.69	(0.07)	0.95	(0.27)	0.73	(0.05)	0.11	(0.02)	0.17	(0.04)	0.31	(0.1)	0.18	(0.08)
Mn	0.02	(0.01)	0.02	(0)	0.02	(0)	0.02	(0)	0	(0.01)	0	(0)	0	(0.01)	0.01	(0.01)
^{VI}Al	0.53	(0.06)	0.51	(0.03)	0.49	(0.07)	0.53	(0.05)	1.79	(0.05)	1.74	(0.05)	1.55	(0.13)	1.71	(0.13)
Ca	0								0						0	
Na	0.01	(0)	0.01	(0)	0.01	(0)	0.01	(0)	0.08	(0.02)	0.06	(0.02)	0.03	(0.02)	0.06	(0.03)
K	0.95	(0.02)	0.95	(0.02)	0.96	(0.02)	0.95	(0.02)	0.88	(0.03)	0.89	(0.03)	0.92	(0.05)	0.9	(0.04)
Cl	0.01	(0)	0.01	(0)	0.01	(0)	0.01	(0)								
F	0.29	(0.16)	0.36	(0.02)	0.68	(0.43)	0.37	(0.1)	0.21	(0.03)	0.22	(0.04)	0.48	(0.18)	0.24	(0.07)
H	1.7		1.63		1.31		1.62		1.94	(0.1)	1.95	(0.1)	1.72	(0.28)	1.86	(0.13)
Al_{Tot}	1.74	(0.09)	1.75	(0.07)	1.55	(0.21)	1.71	(0.06)	2.69	(0.05)	2.59	(0.07)	2.28	(0.21)	2.55	(0.19)

Mineral	Carbonate					
Texture	Spots					
	Core		Rim		Veins	
n	13		19		6	
SiO_2	0.78	(0.89)	0.93	(1.01)	0.97	(0.75)
TiO_2	0.39	(0.44)	0.11	(0.02)	0.26	(0.18)
Al_2O_3	0.56	(0.59)	0.81	(0.7)	0.55	(0.41)
FeO_{total}	44.64	(3.86)	51.06	(4.06)	56.58	(2.51)
MgO	3	(0.33)	3.71	(0.48)	3.24	(1.3)
MnO	11.5	(3.43)	4.85	(3.68)	0.32	(0.06)
CaO	0.05	(0.01)	0.05		0.14	(0.13)
Na_2O	*b.d.l.*		0.06		0.07	
K_2O	0.24	(0.25)	0.2	(0.19)	0.25	(0.15)
Cl	*b.d.l.*		*b.d.l.*		*b.d.l.*	
F	*b.d.l.*		*b.d.l.*		*b.d.l.*	
$CO_3{}^a$	36.57	(0)	37.36	(0)	37.44	(0)
Total	96.82	(0)	98.07	(0)	99.59	(0)
Si	0.01	(0.02)	0.02	(0.02)	0.02	(0.01)
Ti	0.01	(0.01)	0	(0)	0	(0)
Al	0.01	(0.01)	0.02	(0.01)	0.01	(0.01)
Fe	0.7	(0.07)	0.79	(0.06)	0.85	(0.06)
Mg	0.08	(0.01)	0.1	(0.01)	0.09	(0.03)
Mn	0.18	(0.05)	0.08	(0.06)	0	(0)
Ca	0	(0)	0		0	
Na			0		0	
K	0.01	(0.01)	0	(0)	0.01	(0)
Cl						
F						
C	1	(0)	1	(0)	1	(0)

						Tourmaline						
Zonation	**Core 1**		**Core 2**		**Interm.**		**Rim 1**		**Rim 2**		**Late**	
n	16		9		25		26		27		17	
SiO_2	36.72	(0.54)	36.49	(0.51)	36.49	(0.4)	36.97	(0.35)	36.66	(0.54)	35.72	(0.79)
TiO_2	0.54	(0.21)	0.74	(0.16)	0.61	(0.14)	0.39	(0.17)	0.64	(0.09)	0.62	(0.11)
Al_2O_3	33.63	(0.62)	32.73	(0.64)	34.09	(0.54)	34.69	(0.52)	33.77	(0.6)	32.23	(1.06)
FeO	8.19	(0.59)	8.67	(0.41)	7.93	(0.56)	7.89	(0.37)	8.15	(0.41)	9.67	(0.86)
MgO	5.53	(0.26)	5.84	(0.24)	5.45	(0.24)	4.94	(0.38)	5.46	(0.19)	5.19	(0.42)
MnO			0.22				0.14	(0.01)			0.17	(0.02)
CaO	0.32	(0.16)	0.24	(0.21)	0.23	(0.1)	0.16	(0.09)	0.16	(0.09)	0.12	(0.04)
Na_2O	1.78	(0.05)	2.04	(0.14)	1.91	(0.12)	1.62	(0.14)	2.03	(0.09)	2.31	(0.23)
K_2O	0.04	(0.01)			0.06	(0.01)	0.05	(0.01)	0.07	(0.03)	0.08	(0.02)
B_2O_3[b]	10.70		10.66		10.73		10.74		10.70		10.49	
H_2O[c]	3.69		3.68		3.70		3.70		3.69		3.56	
Total	101.14		101.31		101.20		101.29		101.33		100.16	
Site T												
Si	5.96	(0.07)	5.95	(0.07)	5.92	(0.03)	5.98	(0.05)	5.94	(0.05)	5.93	(0.03)
Al	0.05	(0.05)	0.05	(0.06)	0.08	(0.03)	0.03	(0.03)	0.06	(0.05)	0.07	(0.03)
Site Z												
Al	6.00		6.00		6.00		6.00		6.00		6.00	
Site Y												
Al	0.39	(0.07)	0.24	(0.08)	0.44	(0.07)	0.58	(0.08)	0.39	(0.06)	0.24	(0.12)
Ti	0.07	(0.03)	0.09	(0.02)	0.07	(0.02)	0.05	(0.02)	0.08	(0.01)	0.08	(0.01)
Fe	1.11	(0.08)	1.18	(0.06)	1.08	(0.08)	1.07	(0.05)	1.10	(0.06)	1.34	(0.13)
Mg	1.34	(0.06)	1.42	(0.05)	1.32	(0.05)	1.19	(0.09)	1.32	(0.05)	1.29	(0.11)
Mn	0.00	(0)	0.00	(0.01)	0.00	(0)	0.00	(0.01)	0.00	(0)	0.00	(0.01)
Site X												
Ca	0.05	(0.03)	0.04	(0.04)	0.04	(0.02)	0.02	(0.02)	0.03	(0.02)	0.02	(0.01)
Na	0.56	(0.02)	0.64	(0.04)	0.60	(0.04)	0.51	(0.04)	0.64	(0.03)	0.74	(0.08)
K	0.00	(0)	0.00	(0)	0.00	(0)	0.00	(0.01)	0.01	(0.01)	0.01	(0.01)
$[]_X$	0.39	(0.03)	0.31	(0.04)	0.36	(0.03)	0.46	(0.05)	0.33	(0.03)	0.23	(0.09)
B	3		3		3		3		3		3	
OH-	4		4		4		4		4		4	
Total Al	6.44	(0.1)	6.29	(0.12)	6.52	(0.08)	6.61	(0.08)	6.45	(0.09)	6.3	(0.12)
Fe/(Fe+Mg	0.45	(0.03)	0.45	(0.02)	0.45	(0.02)	0.47	(0.03)	0.46	(0.02)	0.51	(0.04)

Appendix A19

Composition of natural biotite from the spotted schist of Panasqueira.

Mineral	Name	SiO_2	TiO_2	Al_2O_3	FeO_{tot}	MgO	MnO	CaO	Na_2O	K_2O	Cl	F	H_2O	Total	Si	Al^{IV}	Al^{VI}	Ti	Fe^{2+}	Mg	Mn	Ca	Na	K	Cl	F	OH^-	Total Al	Infos
Biotite	STP4_Bt1	34.39	0.96	19.54	24.51	5.25	*b.d.l.*	*b.d.l.*	*b.d.l.*	9.62	0.05	*b.d.l.*	3.79	100.38	2.72	1.28	0.54	0.06	1.62	0.62	0.00	0.00	0.00	0.97	0.01	0.00	1.99	1.82	Subhedral
	STP4_Bt2	36.38	1.08	17.57	22.61	6.84	0.27	*b.d.l.*	0.06	9.53	*b.d.l.*	*b.d.l.*	3.84	99.11	2.84	1.16	0.46	0.06	1.48	0.80	0.02	0.00	0.01	0.95	0.00	0.00	2.00	1.62	Subhedral
	STP4_Bt3	35.98	1.23	18.68	23.84	6.11	0.25	*b.d.l.*	*b.d.l.*	9.69	0.07	*b.d.l.*	3.88	99.85	2.78	1.22	0.48	0.07	1.54	0.70	0.02	0.00	0.00	0.96	0.01	0.00	1.99	1.70	Subhedral
	STP4_Bt4	35.16	1.30	19.75	24.20	5.41	*b.d.l.*	0.05	0.07	9.24	0.06	*b.d.l.*	3.85	99.94	2.73	1.27	0.54	0.08	1.57	0.63	0.00	0.00	0.01	0.92	0.01	0.00	1.99	1.81	Subhedral
	STP4_Bt5	34.97	1.38	19.26	23.26	6.17	0.42	*b.d.l.*	*b.d.l.*	9.76	*b.d.l.*	*b.d.l.*	3.85	100.08	2.72	1.28	0.49	0.08	1.51	0.72	0.03	0.00	0.00	0.97	0.00	0.00	2.00	1.77	Subhedral
	STP4_Bt6	34.12	1.18	19.46	24.34	5.50	*b.d.l.*	*b.d.l.*	*b.d.l.*	9.40	*b.d.l.*	*b.d.l.*	3.78	98.65	2.70	1.30	0.52	0.07	1.61	0.65	0.00	0.00	0.00	0.95	0.00	0.00	2.00	1.82	Subhedral
	STP2_Bt1	35.29	1.13	19.12	23.36	5.92	0.23	*b.d.l.*	*b.d.l.*	9.11	0.05	*b.d.l.*	3.82	100.85	2.76	1.24	0.53	0.07	1.53	0.69	0.02	0.00	0.00	0.91	0.01	0.00	1.99	1.77	Subhedral
	STP2_Bt2	35.43	1.30	19.58	23.24	5.68	*b.d.l.*	*b.d.l.*	0.08	9.52	0.07	*b.d.l.*	3.85	101.15	2.75	1.25	0.55	0.08	1.51	0.66	0.00	0.00	0.01	0.94	0.01	0.00	1.99	1.79	Subhedral
	STP2_Bt3	34.76	1.16	18.94	23.69	6.04	*b.d.l.*	*b.d.l.*	0.07	9.59	*b.d.l.*	*b.d.l.*	3.81	100.61	2.74	1.26	0.49	0.07	1.56	0.71	0.00	0.00	0.01	0.96	0.00	0.00	2.00	1.76	Subhedral
	STP0_Bt1	34.98	1.22	19.12	24.29	5.31	0.18	*b.d.l.*	0.07	9.63	0.04	0.81	3.39	99.03	2.77	1.23	0.56	0.07	1.61	0.63	0.01	0.00	0.01	0.97	0.20	0.00	1.99	1.78	Subhedral
	STP0_Bt2	36.51	1.10	17.35	21.61	7.22	0.25	*b.d.l.*	0.06	9.58	*b.d.l.*	1.87	2.94	98.50	2.86	1.14	0.46	0.06	1.41	0.84	0.02	0.00	0.01	0.96	0.46	0.00	2.00	1.60	Subhedral
	STP0_Bt3	34.38	1.37	19.61	24.10	5.38	*b.d.l.*	*b.d.l.*	0.08	9.67	0.04	0.60	3.49	98.85	2.72	1.28	0.55	0.08	1.60	0.64	0.00	0.00	0.01	0.98	0.15	0.00	2.00	1.83	Subhedral
	STP0_Bt4	34.82	1.10	19.30	25.27	4.94	*b.d.l.*	*b.d.l.*	*b.d.l.*	9.21	*b.d.l.*	0.57	3.54	98.90	2.74	1.26	0.53	0.06	1.66	0.58	0.00	0.00	0.00	0.93	0.14	0.00	2.00	1.79	Subhedral
	STP0_Bt5	40.46	1.24	16.63	19.34	6.58	*b.d.l.*	*b.d.l.*	*b.d.l.*	9.13	0.05	1.86	2.95	98.39	3.16	0.84	0.69	0.07	1.26	0.77	0.00	0.00	0.00	0.91	0.46	0.00	1.99	1.53	Subhedral
	STP4_BtAlt1	34.79	1.25	19.46	24.82	5.40	0.19	*b.d.l.*	*b.d.l.*	9.53	*b.d.l.*	*b.d.l.*	3.84	101.70	2.72	1.28	0.51	0.07	1.62	0.63	0.01	0.00	0.00	0.95	0.00	0.00	2.00	1.79	Altered
	STP4_BtAlt2	34.10	1.27	18.95	24.40	5.64	0.30	*b.d.l.*	*b.d.l.*	9.06	*b.d.l.*	*b.d.l.*	3.77	100.01	2.71	1.29	0.48	0.08	1.62	0.67	0.02	0.00	0.00	0.92	0.00	0.00	2.00	1.77	Altered
	STP4_BtAlt3	34.23	1.16	19.96	25.05	5.23	*b.d.l.*	*b.d.l.*	*b.d.l.*	9.53	0.05	*b.d.l.*	3.82	101.56	2.68	1.32	0.53	0.07	1.64	0.61	0.00	0.00	0.00	0.95	0.01	0.00	1.99	1.84	Altered
	STP4_BtAlt4	33.94	1.19	18.89	24.49	5.73	*b.d.l.*	*b.d.l.*	0.06	9.59	0.06	*b.d.l.*	3.77	100.48	2.70	1.30	0.47	0.07	1.63	0.68	0.00	0.00	0.01	0.97	0.01	0.00	1.99	1.77	Altered
	STP4_BtAlt5	34.34	1.16	18.89	23.92	5.80	*b.d.l.*	*b.d.l.*	*b.d.l.*	9.33	0.05	*b.d.l.*	3.77	100.40	2.73	1.27	0.50	0.07	1.59	0.69	0.00	0.00	0.00	0.95	0.01	0.00	1.99	1.77	Altered
	STP4_BtAlt6	36.24	1.05	18.02	23.40	6.69	*b.d.l.*	*b.d.l.*	*b.d.l.*	9.69	*b.d.l.*	*b.d.l.*	3.86	101.94	2.81	1.19	0.46	0.06	1.52	0.77	0.00	0.00	0.00	0.96	0.00	0.00	2.00	1.65	Altered
	STP4_BtAlt7	35.72	1.05	18.33	22.14	6.82	0.22	*b.d.l.*	0.06	9.21	*b.d.l.*	*b.d.l.*	3.82	100.28	2.80	1.20	0.50	0.06	1.45	0.80	0.01	0.00	0.01	0.92	0.00	0.00	2.00	1.69	Altered
	STP4_BtAlt8	36.48	1.16	17.69	22.28	7.01	0.38	*b.d.l.*	*b.d.l.*	9.67	0.05	*b.d.l.*	3.86	99.68	2.83	1.17	0.46	0.07	1.45	0.81	0.02	0.00	0.00	0.96	0.01	0.00	1.99	1.62	Altered
	STP4_BtAlt9	34.89	1.26	18.84	24.45	5.49	*b.d.l.*	*b.d.l.*	*b.d.l.*	9.61	0.04	*b.d.l.*	3.81	98.49	2.75	1.25	0.49	0.07	1.61	0.64	0.00	0.00	0.00	0.96	0.01	0.00	1.99	1.75	Altered
	STP2_BtAlt1	34.49	1.22	19.52	23.13	5.64	0.24	*b.d.l.*	0.13	9.19	0.08	*b.d.l.*	3.79	99.35	2.72	1.28	0.54	0.07	1.53	0.66	0.02	0.00	0.02	0.93	0.01	0.00	1.99	1.82	Altered
	STP2_BtAlt2	34.99	1.10	19.57	23.31	5.55	0.23	*b.d.l.*	*b.d.l.*	9.73	*b.d.l.*	*b.d.l.*	3.82	100.71	2.74	1.26	0.55	0.07	1.53	0.65	0.01	0.00	0.00	0.97	0.00	0.00	2.00	1.81	Altered
	STP2_BtAlt3	34.94	1.18	18.94	23.98	5.58	0.25	*b.d.l.*	*b.d.l.*	9.68	0.05	*b.d.l.*	3.81	100.90	2.75	1.25	0.50	0.07	1.58	0.65	0.02	0.00	0.00	0.97	0.01	0.00	1.99	1.75	Altered
	STP2_BtAlt4	34.51	1.28	19.93	23.30	5.42	*b.d.l.*	*b.d.l.*	0.06	9.44	0.06	*b.d.l.*	3.81	100.38	2.72	1.28	0.56	0.08	1.53	0.64	0.00	0.00	0.01	0.95	0.01	0.00	1.99	1.85	Altered
	STP2_BtAlt5	35.42	1.13	18.84	23.58	5.90	*b.d.l.*	*b.d.l.*	0.06	9.62	*b.d.l.*	*b.d.l.*	3.83	101.21	2.77	1.23	0.51	0.07	1.54	0.69	0.00	0.00	0.01	0.96	0.00	0.00	2.00	1.74	Altered

Mineral	**Name**	**SiO_2**	**TiO_2**	**Al_2O_3**	**FeO_{tot}**	**MgO**	**MnO**	**CaO**	**Na_2O**	**K_2O**	**Cl**	**F**	**H_2O**	**Total**	**Si**	**Al^{IV}**	**Al^{VI}**	**Ti**	**Fe^{2+}**	**Mg**	**Mn**	**Ca**	**Na**	**K**	**Cl**	**F**	**OH^-**	**Total Al**	**Infos**
Biotite	STP2_BtAlt6	36.04	1.18	18.33	23.52	6.42	*b.d.l.*	*b.d.l.*	0.09	9.45	0.06	*b.d.l.*	3.86	101.86	2.80	1.20	0.48	0.07	1.53	0.74	0.00	0.00	0.01	0.94	0.01	0.00	1.99	1.68	Altered
	STP0_BtAlt1	33.56	1.08	19.87	26.13	5.02	*b.d.l.*	*b.d.l.*	*b.d.l.*	9.43	*b.d.l.*	*b.d.l.*	3.79	99.27	2.65	1.35	0.50	0.06	1.73	0.59	0.00	0.00	0.00	0.95	0.00		2.00	1.85	Altered
	STP0_BtAlt2	36.89	1.10	18.22	22.29	6.68	0.26	*b.d.l.*	0.06	9.66	0.05	1.51	3.09	99.81	2.89	1.11	0.58	0.06	1.46	0.78	0.02	0.00	0.01	0.97	0.37		1.99	1.68	Altered
	STP0_BtAlt3	35.48	1.15	17.93	22.78	6.46	0.19	*b.d.l.*	0.06	9.32	0.06	1.37	3.07	97.89	2.85	1.15	0.54	0.07	1.53	0.77	0.01	0.00	0.01	0.95	0.35		1.99	1.70	Altered
	STP0_BtR1	34.98	1.32	18.51	24.94	5.75	*b.d.l.*	*b.d.l.*	*b.d.l.*	9.55	*b.d.l.*	0.90	3.39	99.41	2.74	1.26	0.46	0.08	1.64	0.67	0.00	0.00	0.00	0.96	0.22		2.00	1.71	Rim
	STP0_BtR2	37.16	1.11	17.75	21.82	6.83	0.21	*b.d.l.*	0.07	9.43	*b.d.l.*	1.95	2.94	99.31	2.88	1.12	0.50	0.06	1.41	0.79	0.01	0.00	0.01	0.93	0.48		2.00	1.62	Rim
	STP0_BtR3	39.80	0.58	16.14	16.38	9.33	0.30	*b.d.l.*	*b.d.l.*	9.68	*b.d.l.*	4.00	2.00	98.29	3.06	0.94	0.52	0.03	1.05	1.07	0.02	0.00	0.00	0.95	0.97		2.00	1.46	Rim
	STP0_BtR4	40.78	0.52	15.40	14.68	10.57	*b.d.l.*	*b.d.l.*	*b.d.l.*	10.23	*b.d.l.*	4.74	1.68	98.74	3.11	0.89	0.50	0.03	0.94	1.20	0.00	0.00	0.00	1.00	1.14		2.00	1.39	Rim
	STP0_BtR5	41.05	0.38	15.60	16.02	9.73	0.31	*b.d.l.*	0.05	9.75	*b.d.l.*	4.30	1.90	99.09	3.12	0.88	0.52	0.02	1.02	1.10	0.02	0.00	0.01	0.95	1.03		2.00	1.40	Rim
	STP0_BtR6	33.62	1.18	19.67	24.52	5.21	*b.d.l.*	*b.d.l.*	*b.d.l.*	9.15	*b.d.l.*	0.40	3.57	97.43	2.68	1.32	0.53	0.07	1.64	0.62	0.00	0.00	0.00	0.93	0.10		2.00	1.85	Rim
	STP0_BtR7	40.47	0.65	13.61	16.03	12.00	*b.d.l.*	*b.d.l.*	*b.d.l.*	9.84	*b.d.l.*	4.57	1.75	99.03	3.10	0.90	0.33	0.04	1.03	1.37	0.00	0.00	0.00	0.96	1.11		2.00	1.23	Rim
	STP0_BtR8	36.09	1.26	18.23	21.80	6.83	*b.d.l.*	*b.d.l.*	0.07	9.56	0.05	1.47	3.06	98.61	2.87	1.13	0.57	0.08	1.45	0.81	0.00	0.00	0.01	0.97	0.37		1.99	1.71	Rim
	STP2_Btvein1	34.86	1.04	18.60	24.05	6.05	0.30	*b.d.l.*	*b.d.l.*	9.24	0.08	*b.d.l.*	3.80	100.75	2.75	1.25	0.48	0.06	1.59	0.71	0.02	0.00	0.00	0.93	0.01	0.00	1.99	1.73	Vein
	STP2_Btvein2	34.67	1.23	19.72	24.77	5.59	*b.d.l.*	*b.d.l.*	0.08	9.37	0.06	*b.d.l.*	3.84	101.89	2.70	1.30	0.51	0.07	1.61	0.65	0.00	0.00	0.01	0.93	0.01	0.00	1.99	1.81	Vein
	STP2_Btvein3	34.39	1.12	18.75	23.97	5.89	*b.d.l.*	*b.d.l.*	*b.d.l.*	9.38	0.05	*b.d.l.*	3.77	100.07	2.73	1.27	0.49	0.07	1.59	0.70	0.00	0.00	0.00	0.95	0.01	0.00	1.99	1.76	Vein
	STP2_Btvein4	34.55	1.11	18.52	24.51	6.13	*b.d.l.*	*b.d.l.*	*b.d.l.*	9.43	*b.d.l.*	*b.d.l.*	3.79	100.69	2.73	1.27	0.46	0.07	1.62	0.72	0.00	0.00	0.00	0.95	0.00	0.00	2.00	1.72	Vein
	STP0_Btvein1	36.24	1.35	17.95	22.14	6.69	0.19	*b.d.l.*	0.11	9.56	0.05	1.58	3.02	98.88	2.88	1.12	0.56	0.08	1.47	0.79	0.01	0.00	0.02	0.97	0.40		1.99	1.68	Vein
	STP0_Btvein2	36.97	1.33	18.04	20.90	6.75	0.31	*b.d.l.*	0.09	9.46	*b.d.l.*	1.76	3.03	98.66	2.87	1.13	0.52	0.08	1.36	0.78	0.02	0.00	0.01	0.94	0.43		2.00	1.65	Vein
	STP0_Btvein3	36.25	1.33	18.18	21.94	6.53	0.34	*b.d.l.*	0.10	9.29	*b.d.l.*	1.63	3.07	98.68	2.83	1.17	0.50	0.08	1.43	0.76	0.02	0.00	0.02	0.92	0.40		2.00	1.67	Vein
	STP0_Btvein4	35.73	1.49	19.20	22.32	6.34	0.35	*b.d.l.*	0.13	9.78	0.06	1.20	3.24	99.84	2.80	1.20	0.57	0.09	1.46	0.74	0.02	0.00	0.02	0.98	0.30		1.99	1.77	Vein
	STP0_Btvein5	34.73	1.36	19.14	24.38	5.53	0.20	*b.d.l.*	*b.d.l.*	9.46	*b.d.l.*	0.72	3.47	99.07	2.73	1.27	0.50	0.08	1.60	0.65	0.01	0.00	0.00	0.95	0.18		2.00	1.77	Vein
	STP0_Btvein6	35.64	1.51	19.43	23.15	5.89	0.37	*b.d.l.*	0.13	9.28	0.07	1.11	3.28	99.86	2.79	1.21	0.58	0.09	1.52	0.69	0.02	0.00	0.02	0.93	0.28		1.99	1.79	Vein
	STP0_Btvein7	35.57	1.48	19.26	22.52	5.73	0.25	*b.d.l.*	0.09	9.57	0.04	1.12	3.26	98.87	2.81	1.19	0.60	0.09	1.49	0.67	0.02	0.00	0.01	0.96	0.28		1.99	1.79	Vein
	STP1_Btvein1	36.14	1.52	18.47	22.65	6.28	*b.d.l.*	*b.d.l.*	0.10	9.46	0.04	1.51	3.06	99.41	2.86	1.14	0.58	0.09	1.50	0.74	0.00	0.00	0.02	0.95	0.38		1.99	1.72	Vein
	STP1_Btvein2	36.05	1.46	18.41	22.44	6.49	0.39	*b.d.l.*	0.06	9.70	*b.d.l.*	1.60	3.11	99.75	2.80	1.20	0.48	0.09	1.46	0.75	0.03	0.00	0.01	0.96	0.39		2.00	1.68	Vein
	STP1_Btvein3	35.93	1.43	17.95	21.65	6.66	0.27	*b.d.l.*	*b.d.l.*	9.54	0.05	1.44	3.06	98.00	2.87	1.13	0.56	0.09	1.45	0.79	0.02	0.00	0.00	0.97	0.36		1.99	1.69	Vein
	STP1_Btvein4	36.15	1.37	17.85	23.00	6.53	*b.d.l.*	*b.d.l.*	*b.d.l.*	9.50	0.05	1.48	3.06	99.19	2.87	1.13	0.54	0.08	1.53	0.77	0.00	0.00	0.00	0.96	0.37		1.99	1.67	Vein
	STP1_Btvein5	36.84	1.42	18.52	21.89	6.30	0.32	*b.d.l.*	0.10	9.57	0.05	1.67	3.01	99.69	2.89	1.11	0.61	0.08	1.44	0.74	0.02	0.00	0.02	0.96	0.42		1.99	1.71	Vein

Mineral	**Name**	**SiO_2**	**TiO_2**	**Al_2O_3**	**FeO_{tot}**	**MgO**	**MnO**	**CaO**	**Na_2O**	**K_2O**	**Cl**	**F**	**H_2O**	**Total**	**Si**	**Al^{IV}**	**Al^{VI}**	**Ti**	**Fe^{2+}**	**Mg**	**Mn**	**Ca**	**Na**	**K**	**Cl**	**F**	**OH^-**	**Total Al**	**Infos**
Biotite	STP1_Btvein6	35.66	1.40	18.16	23.01	6.46	*b.d.l.*	*b.d.l.*	*b.d.l.*	9.67	*b.d.l.*	1.60	3.07	99.19	2.79	1.21	0.47	0.08	1.51	0.75	0.00	0.00	0.00	0.97	0.40		2.00	1.67	Vein
	STP0_Btvein8	38.92	1.45	19.20	20.64	6.14	0.26	*b.d.l.*	0.14	9.20	*b.d.l.*	1.75	3.16	100.89	2.92	1.08	0.62	0.08	1.29	0.69	0.02	0.00	0.02	0.88	0.42		2.00	1.70	Vein
	STP0_Btvein9	36.45	1.35	19.77	23.20	5.76	*b.d.l.*	*b.d.l.*	*b.d.l.*	9.60	*b.d.l.*	1.34	3.29	100.91	2.78	1.22	0.56	0.08	1.48	0.66	0.00	0.00	0.00	0.94	0.32		2.00	1.78	Vein
	STP0_Btvein10	36.34	1.14	18.49	22.87	6.41	*b.d.l.*	*b.d.l.*	*b.d.l.*	9.57	*b.d.l.*	1.53	3.14	99.64	2.82	1.18	0.51	0.07	1.48	0.74	0.00	0.00	0.00	0.95	0.37		2.00	1.69	Vein
	STP0_Btvein11	39.02	1.07	17.00	19.77	7.34	0.16	*b.d.l.*	0.05	9.37	*b.d.l.*	2.75	2.60	99.15	2.99	1.01	0.53	0.06	1.27	0.84	0.01	0.00	0.01	0.92	0.67		2.00	1.54	Vein

Appendix A20

Composition of natural white micas from the spotted schist of Panasqueira.

Mineral	Name	SiO_2	TiO_2	Al_2O_3	FeO_{tot}	MgO	MnO	CaO	Na_2O	K_2O	Cl	F	H_2O	Total	Si	Al^{IV}	Al^{VI}	Ti	Fe^{2+}	Mg	Mn	Ca	Na	K	Cl	F	OH^-	Total Al	Infos
White micas	STP0_Ms1	44.00	2.57	33.03	3.06	1.05	*b.d.l.*	*b.d.l.*	0.62	10.08	*b.d.l.*	0.85	3.99	99.23	3.00	1.00	1.65	0.13	0.17	0.11	0.00	0.00	0.08	0.88	0.00	0.18	1.82	2.65	Subhedral
	STP2_Ms1	45.18	1.11	34.37	1.81	1.22	*b.d.l.*	0.06	0.61	10.18	*b.d.l.*	*b.d.l.*	4.45	100.36	3.04	0.96	1.77	0.06	0.10	0.12	0.00	0.00	0.08	0.87	0.00	0.00	2.00	2.73	Subhedral
	STP0_Ms2	45.49	0.32	34.34	2.02	1.09	*b.d.l.*	*b.d.l.*	0.71	10.44	*b.d.l.*	0.88	4.02	99.37	3.07	0.93	1.81	0.02	0.11	0.11	0.00	0.00	0.09	0.90	0.00	0.19	1.81	2.73	Subhedral
	STP4_Ms1	44.77	1.13	33.22	1.55	1.12	*b.d.l.*	*b.d.l.*	0.68	10.26	*b.d.l.*	*b.d.l.*	4.36	97.97	3.08	0.92	1.76	0.06	0.09	0.11	0.00	0.00	0.09	0.90	0.00	0.00	2.00	2.69	Subhedral
	STP0_Ms3	45.25	0.44	33.83	2.21	1.33	*b.d.l.*	*b.d.l.*	0.61	9.94	*b.d.l.*	1.10	3.89	98.70	3.08	0.92	1.79	0.02	0.13	0.14	0.00	0.00	0.08	0.86	0.00	0.24	1.76	2.71	Subhedral
	STP4_Ms2	46.32	0.61	34.39	2.07	1.27	*b.d.l.*	*b.d.l.*	0.31	10.94	*b.d.l.*	*b.d.l.*	4.50	101.49	3.08	0.92	1.78	0.03	0.12	0.13	0.00	0.00	0.04	0.93	0.00	0.00	2.00	2.70	Subhedral
	STP4_Ms3	45.89	0.32	34.30	2.14	0.96	*b.d.l.*	*b.d.l.*	0.73	10.40	*b.d.l.*	*b.d.l.*	4.45	100.03	3.09	0.91	1.81	0.02	0.12	0.10	0.00	0.00	0.10	0.89	0.00	0.00	2.00	2.72	Subhedral
	STP4_Ms4	46.17	0.24	34.90	1.48	0.80	*b.d.l.*	*b.d.l.*	0.82	10.01	*b.d.l.*	*b.d.l.*	4.47	99.69	3.10	0.90	1.86	0.01	0.08	0.08	0.00	0.00	0.11	0.86	0.00	0.00	2.00	2.76	Subhedral
	STP4_Ms5	45.58	0.32	34.08	1.63	0.90	*b.d.l.*	*b.d.l.*	0.77	10.20	*b.d.l.*	*b.d.l.*	4.41	98.49	3.10	0.90	1.83	0.02	0.09	0.09	0.00	0.00	0.10	0.88	0.00	0.00	2.00	2.73	Subhedral
	STP4_Ms6	45.75	0.36	33.92	1.96	0.94	*b.d.l.*	*b.d.l.*	0.76	10.14	*b.d.l.*	*b.d.l.*	4.42	99.04	3.10	0.90	1.81	0.02	0.11	0.09	0.00	0.00	0.10	0.88	0.00	0.00	2.00	2.71	Subhedral
	STP0_Ms4	45.79	0.16	33.64	2.26	1.26	*b.d.l.*	*b.d.l.*	0.63	10.34	*b.d.l.*	1.03	3.93	99.17	3.10	0.90	1.79	0.01	0.13	0.13	0.00	0.00	0.08	0.89	0.00	0.22	1.78	2.69	Subhedral
	STP0_Ms5	46.51	0.65	33.57	2.17	1.34	*b.d.l.*	*b.d.l.*	0.68	10.37	*b.d.l.*	1.14	3.94	100.37	3.11	0.89	1.76	0.03	0.12	0.13	0.00	0.00	0.09	0.88	0.00	0.24	1.76	2.65	Subhedral
	STP4_Ms7	46.30	0.51	33.95	1.64	1.11	*b.d.l.*	*b.d.l.*	0.72	10.16	*b.d.l.*	*b.d.l.*	4.46	99.82	3.11	0.89	1.80	0.03	0.09	0.11	0.00	0.00	0.09	0.87	0.00	0.00	2.00	2.69	Subhedral
	STP2_Ms2	45.86	0.71	33.69	1.83	1.16	*b.d.l.*	*b.d.l.*	0.43	9.31	*b.d.l.*	*b.d.l.*	4.41	98.74	3.11	0.89	1.81	0.04	0.10	0.12	0.00	0.00	0.06	0.81	0.00	0.00	2.00	2.70	Subhedral
	STP4_Ms8	45.97	0.23	34.26	1.24	0.93	*b.d.l.*	*b.d.l.*	0.69	10.01	*b.d.l.*	*b.d.l.*	4.42	98.78	3.12	0.88	1.85	0.01	0.07	0.09	0.00	0.00	0.09	0.87	0.00	0.00	2.00	2.74	Subhedral
	STP4_Ms9	46.21	0.30	33.40	2.02	1.01	0.22	*b.d.l.*	0.75	10.00	*b.d.l.*	*b.d.l.*	4.42	99.27	3.13	0.87	1.80	0.02	0.11	0.10	0.01	0.00	0.10	0.86	0.00	0.00	2.00	2.67	Subhedral
	STP4_Ms10	46.18	0.33	33.14	1.89	1.20	*b.d.l.*	*b.d.l.*	0.68	10.11	*b.d.l.*	*b.d.l.*	4.41	99.08	3.14	0.86	1.79	0.02	0.11	0.12	0.00	0.00	0.09	0.88	0.00	0.00	2.00	2.65	Subhedral
	STP4_Ms11	46.84	0.54	31.55	2.60	1.74	0.25	*b.d.l.*	0.41	10.54	*b.d.l.*	*b.d.l.*	4.42	100.18	3.17	0.83	1.69	0.03	0.15	0.18	0.01	0.00	0.05	0.91	0.00	0.00	2.00	2.52	Subhedral
	STP0_MsAlt1	44.96	0.66	32.75	2.20	1.44	*b.d.l.*	*b.d.l.*	0.60	10.52	*b.d.l.*	1.03	3.87	98.09	3.09	0.91	1.74	0.03	0.13	0.15	0.00	0.00	0.08	0.92	0.00	0.22	1.78	2.65	Altered
	STP1_MsAlt1	45.45	0.49	34.03	1.58	0.96	*b.d.l.*	*b.d.l.*	0.72	10.33	*b.d.l.*	0.78	4.04	98.45	3.09	0.91	1.82	0.02	0.09	0.10	0.00	0.00	0.10	0.90	0.00	0.17	1.83	2.73	Altered
	STP4_MsAlt1	46.30	0.51	33.96	1.84	1.35	*b.d.l.*	*b.d.l.*	0.65	10.41	*b.d.l.*	*b.d.l.*	4.47	100.75	3.10	0.90	1.78	0.03	0.10	0.13	0.00	0.00	0.08	0.89	0.00	0.00	2.00	2.68	Altered
	STP1_MsAlt2	46.38	0.35	34.05	1.63	1.16	*b.d.l.*	*b.d.l.*	0.70	10.38	*b.d.l.*	0.95	4.01	99.67	3.11	0.89	1.81	0.02	0.09	0.12	0.00	0.00	0.09	0.89	0.00	0.20	1.80	2.69	Altered
	STP2_MsAlt1	45.62	0.48	32.90	2.02	1.69	*b.d.l.*	*b.d.l.*	0.31	10.11	*b.d.l.*	*b.d.l.*	4.39	98.53	3.12	0.88	1.76	0.02	0.12	0.17	0.00	0.00	0.04	0.88	0.00	0.00	2.00	2.65	Altered
	STP4_MsAlt2	46.89	0.32	33.80	1.93	1.56	*b.d.l.*	*b.d.l.*	0.37	10.53	*b.d.l.*	*b.d.l.*	4.49	101.39	3.13	0.87	1.78	0.02	0.11	0.15	0.00	0.00	0.05	0.90	0.00	0.00	2.00	2.66	Altered
	STP4_MsAlt3	46.31	0.66	32.73	1.97	1.39	*b.d.l.*	*b.d.l.*	0.53	10.28	*b.d.l.*	*b.d.l.*	4.42	99.46	3.14	0.86	1.75	0.03	0.11	0.14	0.00	0.00	0.07	0.89	0.00	0.00	2.00	2.61	Altered
	STP2_MsAlt2	46.49	0.71	32.39	2.17	1.80	*b.d.l.*	*b.d.l.*	0.45	10.41	*b.d.l.*	*b.d.l.*	4.44	100.70	3.14	0.86	1.72	0.04	0.12	0.18	0.00	0.00	0.06	0.90	0.00	0.00	2.00	2.58	Altered
	STP4_MsAlt4	45.53	0.57	31.95	1.99	1.46	*b.d.l.*	*b.d.l.*	0.52	10.34	*b.d.l.*	*b.d.l.*	4.34	98.27	3.14	0.86	1.74	0.03	0.11	0.15	0.00	0.00	0.07	0.91	0.00	0.00	2.00	2.60	Altered
	STP4_MsAlt5	46.04	0.78	32.03	2.15	1.63	*b.d.l.*	*b.d.l.*	0.51	9.98	*b.d.l.*	*b.d.l.*	4.38	98.62	3.15	0.85	1.73	0.04	0.12	0.17	0.00	0.00	0.07	0.87	0.00	0.00	2.00	2.58	Altered

Mineral	Name	SiO_2	TiO_2	Al_2O_3	FeO_{tot}	MgO	MnO	CaO	Na_2O	K_2O	Cl	F	H_2O	Total	Si	Al^{IV}	Al^{VI}	Ti	Fe^{2+}	Mg	Mn	Ca	Na	K	Cl	F	OH^-	Total Al	Infos
White micas	STP2_MsAlt3	44.83	0.41	29.93	3.43	2.41	*b.d.l.*	*b.d.l.*	0.30	10.39	*b.d.l.*	*b.d.l.*	4.26	97.91	3.15	0.85	1.63	0.02	0.20	0.25	0.00	0.00	0.04	0.93	0.00	0.00	2.00	2.48	Altered
	STP0_MsAlt2	46.09	0.55	31.69	2.62	1.66	*b.d.l.*	*b.d.l.*	0.39	10.75	*b.d.l.*	1.23	3.80	98.79	3.15	0.85	1.70	0.03	0.15	0.17	0.00	0.00	0.05	0.94	0.00	0.27	1.73	2.55	Altered
	STP0_MsAlt3	46.50	0.52	32.56	1.95	1.46	*b.d.l.*	*b.d.l.*	0.48	10.52	*b.d.l.*	1.11	3.89	99.05	3.15	0.85	1.75	0.03	0.11	0.15	0.00	0.00	0.06	0.91	0.00	0.24	1.76	2.60	Altered
	STP4_MsAlt6	46.49	0.66	32.54	1.85	1.43	*b.d.l.*	*b.d.l.*	0.52	10.22	*b.d.l.*	*b.d.l.*	4.42	99.25	3.15	0.85	1.75	0.03	0.11	0.14	0.00	0.00	0.07	0.88	0.00	0.00	2.00	2.60	Altered
	STP4_MsAlt7	45.98	0.48	30.97	2.82	2.22	*b.d.l.*	*b.d.l.*	0.29	10.62	*b.d.l.*	*b.d.l.*	4.36	99.23	3.16	0.84	1.67	0.03	0.16	0.23	0.00	0.00	0.04	0.93	0.00	0.00	2.00	2.51	Altered
	STP4_MsAlt8	46.47	0.47	31.97	2.31	1.63	*b.d.l.*	*b.d.l.*	0.60	10.44	*b.d.l.*	*b.d.l.*	4.41	99.27	3.16	0.84	1.72	0.02	0.13	0.16	0.00	0.00	0.08	0.91	0.00	0.00	2.00	2.56	Altered
	STP2_MsAlt4	47.30	0.60	32.85	2.21	1.64	*b.d.l.*	*b.d.l.*	0.47	9.54	*b.d.l.*	*b.d.l.*	4.48	100.42	3.16	0.84	1.75	0.03	0.12	0.16	0.00	0.00	0.06	0.81	0.00	0.00	2.00	2.59	Altered
	STP2_MsAlt5	47.73	0.31	32.91	2.40	1.77	*b.d.l.*	*b.d.l.*	0.36	10.49	*b.d.l.*	*b.d.l.*	4.52	102.09	3.17	0.83	1.74	0.02	0.13	0.17	0.00	0.00	0.05	0.89	0.00	0.00	2.00	2.57	Altered
	STP4_MsAlt9	46.97	0.31	30.87	2.99	2.39	*b.d.l.*	*b.d.l.*	0.42	10.90	*b.d.l.*	*b.d.l.*	4.42	101.37	3.18	0.82	1.65	0.02	0.17	0.24	0.00	0.00	0.05	0.94	0.00	0.00	2.00	2.46	Altered
	STP4_MsAlt10	46.91	0.73	31.95	1.70	1.73	*b.d.l.*	*b.d.l.*	0.42	9.85	*b.d.l.*	*b.d.l.*	4.41	99.13	3.18	0.82	1.74	0.04	0.10	0.17	0.00	0.00	0.06	0.85	0.00	0.00	2.00	2.56	Altered
	STP2_MsAlt6	47.72	0.67	32.50	2.16	1.58	*b.d.l.*	*b.d.l.*	0.40	9.55	*b.d.l.*	*b.d.l.*	4.48	100.48	3.19	0.81	1.75	0.03	0.12	0.16	0.00	0.00	0.05	0.81	0.00	0.00	2.00	2.56	Altered
	STP2_MsR1	48.66	0.57	31.79	2.89	1.89	*b.d.l.*	*b.d.l.*	0.26	9.25	*b.d.l.*	*b.d.l.*	4.51	100.89	3.23	0.77	1.72	0.03	0.16	0.19	0.00	0.00	0.03	0.78	0.00	0.00	2.00	2.49	Rim
	STP4_MsR1	48.08	0.30	28.26	4.84	3.12	*b.d.l.*	*b.d.l.*	0.21	10.39	*b.d.l.*	*b.d.l.*	4.41	101.21	3.26	0.74	1.52	0.02	0.27	0.32	0.00	0.00	0.03	0.90	0.00	0.00	2.00	2.26	Rim
	STP4_MsR2	48.12	0.44	28.21	4.57	2.88	*b.d.l.*	*b.d.l.*	0.26	10.51	*b.d.l.*	*b.d.l.*	4.41	101.56	3.27	0.73	1.53	0.02	0.26	0.29	0.00	0.00	0.03	0.91	0.00	0.00	2.00	2.26	Rim
	STP4_MsR3	48.26	0.47	28.81	3.18	2.66	*b.d.l.*	*b.d.l.*	0.33	10.31	*b.d.l.*	*b.d.l.*	4.40	100.20	3.28	0.72	1.59	0.02	0.18	0.27	0.00	0.00	0.04	0.90	0.00	0.00	2.00	2.31	Rim
	STP2_MsR2	48.74	0.22	28.02	3.79	3.51	*b.d.l.*	*b.d.l.*	0.20	11.00	*b.d.l.*	*b.d.l.*	4.44	102.37	3.29	0.71	1.52	0.01	0.21	0.35	0.00	0.00	0.03	0.95	0.00	0.00	2.00	2.23	Rim
	STP2_MsR3	48.19	0.63	26.54	4.48	3.55	*b.d.l.*	*b.d.l.*	0.10	10.91	*b.d.l.*	*b.d.l.*	4.37	100.83	3.31	0.69	1.45	0.03	0.26	0.36	0.00	0.00	0.01	0.95	0.00	0.00	2.00	2.15	Rim
	STP0_MsR1	47.47	0.17	25.63	4.58	3.70	*b.d.l.*	*b.d.l.*	0.13	11.13	*b.d.l.*	2.87	2.92	98.60	3.32	0.68	1.44	0.01	0.27	0.39	0.00	0.00	0.02	0.99	0.00	0.64	1.36	2.11	Rim
	STP0_MsR2	49.03	0.32	25.49	4.88	3.91	0.26	*b.d.l.*	0.10	10.72	*b.d.l.*	2.86	3.02	100.59	3.36	0.64	1.41	0.02	0.28	0.40	0.01	0.00	0.01	0.94	0.00	0.62	1.38	2.06	Rim
	STP0_MsR3	46.34	0.63	33.13	2.01	1.55	*b.d.l.*	*b.d.l.*	0.59	10.55	*b.d.l.*	1.31	3.83	99.93	3.12	0.88	1.75	0.03	0.11	0.16	0.00	0.00	0.08	0.91	0.00	0.28	1.72	2.63	Rim
	STP0_MsR4	46.26	0.16	32.92	2.11	1.86	*b.d.l.*	*b.d.l.*	0.66	10.10	*b.d.l.*	1.35	3.79	99.22	3.13	0.87	1.75	0.01	0.12	0.19	0.00	0.00	0.09	0.87	0.00	0.29	1.71	2.62	Rim
	STP0_MsR5	46.68	0.36	29.65	2.92	2.57	*b.d.l.*	*b.d.l.*	0.31	10.58	*b.d.l.*	1.46	3.66	98.19	3.22	0.78	1.62	0.02	0.17	0.26	0.00	0.00	0.04	0.93	0.00	0.32	1.68	2.41	Rim
	STP0_MsR6	47.04	0.54	29.46	3.33	2.41	*b.d.l.*	*b.d.l.*	0.25	10.87	*b.d.l.*	1.97	3.44	99.31	3.22	0.78	1.60	0.03	0.19	0.25	0.00	0.00	0.03	0.95	0.00	0.43	1.57	2.38	Rim
	STP0_MsR7	47.79	0.30	26.72	4.09	3.33	*b.d.l.*	*b.d.l.*	0.20	10.81	*b.d.l.*	2.59	3.10	99.05	3.31	0.69	1.49	0.02	0.24	0.34	0.00	0.00	0.03	0.96	0.00	0.57	1.43	2.18	Rim
	STP0_MsR8	49.13	0.57	22.57	4.59	5.22	*b.d.l.*	*b.d.l.*	0.06	10.41	*b.d.l.*	3.35	2.70	98.60	3.43	0.57	1.29	0.03	0.27	0.54	0.00	0.00	0.01	0.93	0.00	0.74	1.26	1.86	Rim
	STP0_MsVein1	44.95	0.27	35.07	1.42	0.77	*b.d.l.*	*b.d.l.*	0.79	10.63	*b.d.l.*	0.91	3.99	98.78	3.05	0.95	1.85	0.01	0.08	0.08	0.00	0.00	0.10	0.92	0.00	0.19	1.81	2.80	Vein
	STP1_MsVein1	45.38	0.45	33.74	1.80	1.21	*b.d.l.*	*b.d.l.*	0.76	10.36	*b.d.l.*	0.99	3.93	98.63	3.09	0.91	1.79	0.02	0.10	0.12	0.00	0.00	0.10	0.90	0.00	0.21	1.79	2.70	Vein
	STP1_MsVein2	46.27	0.34	34.18	1.48	1.06	*b.d.l.*	*b.d.l.*	0.62	10.50	*b.d.l.*	0.99	3.99	99.47	3.11	0.89	1.82	0.02	0.08	0.11	0.00	0.00	0.08	0.90	0.00	0.21	1.79	2.71	Vein

Mineral	**Name**	**SiO_2**	**TiO_2**	**Al_2O_3**	**FeO_{tot}**	**MgO**	**MnO**	**CaO**	**Na_2O**	**K_2O**	**Cl**	**F**	**H_2O**	**Total**	**Si**	**Al^{IV}**	**Al^{VI}**	**Ti**	**Fe^{2+}**	**Mg**	**Mn**	**Ca**	**Na**	**K**	**Cl**	**F**	**OH^-**	**Total Al**	**Infos**
White micas	STP0_MsVein2	46.24	0.44	33.73	1.78	1.07	*b.d.l.*	*b.d.l.*	0.74	10.60	*b.d.l.*	0.83	4.06	99.53	3.11	0.89	1.79	0.02	0.10	0.11	0.00	0.00	0.10	0.91	0.00	0.18	1.82	2.68	Vein
	STP1_MsVein3	46.42	0.48	32.98	2.52	1.47	*b.d.l.*	*b.d.l.*	0.55	10.51	*b.d.l.*	1.12	3.92	100.02	3.12	0.88	1.74	0.02	0.14	0.15	0.00	0.00	0.07	0.90	0.00	0.24	1.76	2.62	Vein
	STP2_MsVein1	47.07	0.52	32.72	2.94	1.68	*b.d.l.*	*b.d.l.*	0.42	10.34	*b.d.l.*	*b.d.l.*	4.49	101.41	3.14	0.86	1.72	0.03	0.16	0.17	0.00	0.00	0.05	0.88	0.00	0.00	2.00	2.58	Vein
	STP2_MsVein2	47.40	0.45	33.66	2.35	1.33	*b.d.l.*	*b.d.l.*	0.37	9.11	*b.d.l.*	*b.d.l.*	4.50	100.35	3.16	0.84	1.80	0.02	0.13	0.13	0.00	0.00	0.05	0.77	0.00	0.00	2.00	2.64	Vein
	STP1_MsVein4	46.55	0.57	31.90	2.37	1.54	*b.d.l.*	*b.d.l.*	0.50	10.65	*b.d.l.*	1.31	3.79	99.24	3.16	0.84	1.72	0.03	0.13	0.16	0.00	0.00	0.07	0.92	0.00	0.28	1.72	2.55	Vein
	STP2_MsVein3	46.69	0.46	29.52	4.19	2.64	*b.d.l.*	*b.d.l.*	0.26	10.59	*b.d.l.*	*b.d.l.*	4.38	101.45	3.20	0.80	1.58	0.02	0.24	0.27	0.00	0.00	0.03	0.92	0.00	0.00	2.00	2.38	Vein
	STP1_MsVein5	47.55	0.52	30.68	2.96	2.24	*b.d.l.*	*b.d.l.*	0.45	10.80	*b.d.l.*	1.79	3.60	100.59	3.20	0.80	1.64	0.03	0.17	0.22	0.00	0.00	0.06	0.93	0.00	0.38	1.62	2.44	Vein
	STP2_MsVein4	47.43	0.40	29.83	3.70	2.46	0.23	*b.d.l.*	0.24	10.32	*b.d.l.*	*b.d.l.*	4.41	100.83	3.22	0.78	1.61	0.02	0.21	0.25	0.01	0.00	0.03	0.89	0.00	0.00	2.00	2.39	Vein
	STP2_MsVein5	47.50	0.34	26.18	5.85	3.60	0.24	0.05	0.21	10.89	*b.d.l.*	*b.d.l.*	4.34	101.90	3.28	0.72	1.41	0.02	0.34	0.37	0.01	0.00	0.03	0.96	0.00	0.00	2.00	2.13	Vein

Appendix A21

Composition of natural carbonates from the spotted schist of Panasqueira.

Mineral	Name	SiO_2	TiO_2	Al_2O_3	FeO_{tot}	MgO	MnO	CaO	Na_2O	K_2O	Cl	F	CO_2	Total	Si	Ti	Al	Fe^{2+}	Mg	Mn	Ca	Na	K	Cl	F	C	Infos
Carbonates	STP2_Carb1	0.12	*b.d.l.*	*b.d.l.*	41.16	2.83	14.84	*b.d.l.*	*b.d.l.*	0.12	*b.d.l.*	*b.d.l.*	37.74	96.91	0.00	0.00	0.00	0.67	0.08	0.25	0.00	0.00	0.00	0.00	0.00	1.00	Core
	STP4_Carb1	2.41	0.70	1.43	39.66	2.60	14.47	*b.d.l.*	*b.d.l.*	0.74	*b.d.l.*	*b.d.l.*	42.61	104.68	0.04	0.01	0.03	0.67	0.08	0.25	0.00	0.00	0.02	0.00	0.00	1.00	Core
	STP4_Carb2	0.20	*b.d.l.*	0.19	40.90	2.71	14.18	*b.d.l.*	*b.d.l.*	*b.d.l.*	*b.d.l.*	*b.d.l.*	37.35	95.61	0.00	0.00	0.00	0.68	0.08	0.24	0.00	0.00	0.00	0.00	0.00	1.00	Core
	STP2_Carb2	*b.d.l.*	*b.d.l.*	*b.d.l.*	41.91	2.66	14.01	0.05	*b.d.l.*	*b.d.l.*	*b.d.l.*	*b.d.l.*	37.31	96.05	0.00	0.00	0.00	0.69	0.08	0.23	0.00	0.00	0.00	0.00	0.00	1.00	Core
	STP4_Carb3	1.16	*b.d.l.*	*b.d.l.*	43.92	2.80	13.59	*b.d.l.*	*b.d.l.*	*b.d.l.*	*b.d.l.*	*b.d.l.*	40.09	101.65	0.02	0.00	0.00	0.70	0.08	0.22	0.00	0.00	0.00	0.00	0.00	1.00	Core
	STP2_Carb3	1.33	0.08	0.47	42.06	2.91	13.54	0.06	*b.d.l.*	0.39	*b.d.l.*	*b.d.l.*	40.21	101.10	0.02	0.00	0.01	0.69	0.09	0.22	0.00	0.00	0.01	0.00	0.00	1.00	Core
	STP4_Carb4	0.06	*b.d.l.*	*b.d.l.*	44.49	2.87	12.69	*b.d.l.*	*b.d.l.*	0.12	*b.d.l.*	*b.d.l.*	38.40	98.75	0.00	0.00	0.00	0.71	0.08	0.21	0.00	0.00	0.00	0.00	0.00	1.00	Core
	STP2_Carb4	2.30	*b.d.l.*	*b.d.l.*	42.67	2.86	12.14	*b.d.l.*	*b.d.l.*	*b.d.l.*	*b.d.l.*	*b.d.l.*	40.16	100.19	0.04	0.00	0.00	0.71	0.08	0.20	0.00	0.00	0.00	0.00	0.00	1.00	Core
	STP2_Carb5	*b.d.l.*	*b.d.l.*	*b.d.l.*	45.97	3.09	11.96	*b.d.l.*	*b.d.l.*	0.07	*b.d.l.*	*b.d.l.*	38.99	100.18	0.00	0.00	0.00	0.72	0.09	0.19	0.00	0.00	0.00	0.00	0.00	1.00	Core
	STP2_Carb6	0.12	*b.d.l.*	*b.d.l.*	48.29	3.17	8.86	*b.d.l.*	*b.d.l.*	0.06	*b.d.l.*	*b.d.l.*	38.75	99.32	0.00	0.00	0.00	0.77	0.09	0.14	0.00	0.00	0.00	0.00	0.00	1.00	Core
	STP2_Carb7	0.54	*b.d.l.*	0.17	47.28	3.28	8.16	0.04	*b.d.l.*	0.20	*b.d.l.*	*b.d.l.*	38.73	98.41	0.01	0.00	0.00	0.77	0.10	0.13	0.00	0.00	0.00	0.00	0.00	1.00	Core
	STP2_Carb8	0.11	*b.d.l.*	*b.d.l.*	49.23	3.44	7.43	*b.d.l.*	*b.d.l.*	*b.d.l.*	*b.d.l.*	*b.d.l.*	38.69	99.01	0.00	0.00	0.00	0.78	0.10	0.12	0.00	0.00	0.00	0.00	0.00	1.00	Core
	STP2_Carb9	0.18	*b.d.l.*	*b.d.l.*	52.75	3.72	3.57	*b.d.l.*	*b.d.l.*	*b.d.l.*	*b.d.l.*	*b.d.l.*	38.86	99.15	0.00	0.00	0.00	0.84	0.11	0.06	0.00	0.00	0.00	0.00	0.00	1.00	Core
	STP2_Carb10	0.54	*b.d.l.*	0.08	45.34	3.10	10.25	*b.d.l.*	*b.d.l.*	0.23	*b.d.l.*	*b.d.l.*	38.51	98.13	0.01	0.00	0.00	0.74	0.09	0.17	0.00	0.00	0.01	0.00	0.00	1.00	Rim
	STP2_Carb11	2.64	*b.d.l.*	1.86	43.94	2.86	10.03	*b.d.l.*	*b.d.l.*	0.62	*b.d.l.*	*b.d.l.*	42.83	104.90	0.05	0.00	0.04	0.74	0.09	0.17	0.00	0.00	0.01	0.00	0.00	1.00	Rim
	STP2_Carb12	*b.d.l.*	*b.d.l.*	*b.d.l.*	47.02	3.21	9.55	*b.d.l.*	*b.d.l.*	*b.d.l.*	*b.d.l.*	*b.d.l.*	38.23	98.23	0.00	0.00	0.00	0.75	0.09	0.15	0.00	0.00	0.00	0.00	0.00	1.00	Rim
	STP2_Carb13	0.12	*b.d.l.*	*b.d.l.*	47.53	3.27	8.82	*b.d.l.*	*b.d.l.*	*b.d.l.*	*b.d.l.*	*b.d.l.*	38.32	98.19	0.00	0.00	0.00	0.76	0.09	0.14	0.00	0.00	0.00	0.00	0.00	1.00	Rim
	STP2_Carb14	0.32	*b.d.l.*	*b.d.l.*	47.26	3.20	8.65	0.05	0.06	*b.d.l.*	*b.d.l.*	*b.d.l.*	38.35	98.00	0.01	0.00	0.00	0.77	0.09	0.14	0.00	0.00	0.00	0.00	0.00	1.00	Rim
	STP2_Carb15	*b.d.l.*	*b.d.l.*	*b.d.l.*	47.51	3.28	7.86	*b.d.l.*	*b.d.l.*	0.10	*b.d.l.*	*b.d.l.*	37.60	96.50	0.00	0.00	0.00	0.77	0.10	0.13	0.00	0.00	0.00	0.00	0.00	1.00	Rim
	STP2_Carb16	0.65	0.12	0.63	47.71	3.61	7.59	*b.d.l.*	*b.d.l.*	0.15	*b.d.l.*	*b.d.l.*	39.85	100.34	0.01	0.00	0.01	0.77	0.10	0.12	0.00	0.00	0.00	0.00	0.00	1.00	Rim
	STP2_Carb17	*b.d.l.*	*b.d.l.*	0.06	47.61	3.99	7.40	*b.d.l.*	*b.d.l.*	*b.d.l.*	*b.d.l.*	*b.d.l.*	38.20	97.33	0.00	0.00	0.00	0.77	0.11	0.12	0.00	0.00	0.00	0.00	0.00	1.00	Rim
	STP4_Carb5	*b.d.l.*	0.12	*b.d.l.*	52.76	3.49	4.69	*b.d.l.*	*b.d.l.*	*b.d.l.*	*b.d.l.*	*b.d.l.*	39.17	100.44	0.00	0.00	0.00	0.83	0.10	0.07	0.00	0.00	0.00	0.00	0.00	1.00	Rim
	STP4_Carb6	1.13	*b.d.l.*	0.94	50.63	3.46	4.64	*b.d.l.*	*b.d.l.*	0.20	*b.d.l.*	*b.d.l.*	40.63	101.72	0.02	0.00	0.02	0.82	0.10	0.08	0.00	0.00	0.00	0.00	0.00	1.00	Rim
	STP4_Carb7	0.06	*b.d.l.*	*b.d.l.*	53.20	3.78	3.37	*b.d.l.*	*b.d.l.*	*b.d.l.*	*b.d.l.*	*b.d.l.*	38.88	99.43	0.00	0.00	0.00	0.84	0.11	0.05	0.00	0.00	0.00	0.00	0.00	1.00	Rim
	STP2_Carb17	*b.d.l.*	*b.d.l.*	*b.d.l.*	54.80	3.95	1.86	*b.d.l.*	*b.d.l.*	*b.d.l.*	*b.d.l.*	*b.d.l.*	39.03	99.79	0.00	0.00	0.00	0.86	0.11	0.03	0.00	0.00	0.00	0.00	0.00	1.00	Rim
	STP2_Carb18	*b.d.l.*	*b.d.l.*	*b.d.l.*	54.91	4.27	1.64	*b.d.l.*	*b.d.l.*	*b.d.l.*	*b.d.l.*	*b.d.l.*	39.32	100.30	0.00	0.00	0.00	0.86	0.12	0.03	0.00	0.00	0.00	0.00	0.00	1.00	Rim
	STP2_Carb19	*b.d.l.*	*b.d.l.*	*b.d.l.*	54.47	4.10	1.48	*b.d.l.*	*b.d.l.*	*b.d.l.*	*b.d.l.*	*b.d.l.*	38.75	98.86	0.00	0.00	0.00	0.86	0.12	0.02	0.00	0.00	0.00	0.00	0.00	1.00	Rim
	STP4_Carb8	2.29	0.08	1.30	53.31	4.53	1.20	*b.d.l.*	*b.d.l.*	0.44	*b.d.l.*	*b.d.l.*	43.68	106.87	0.04	0.00	0.03	0.85	0.13	0.02	0.00	0.00	0.01	0.00	0.00	1.00	Rim

Mineral	**Name**	**SiO_2**	**TiO_2**	**Al_2O_3**	**FeO_{tot}**	**MgO**	**MnO**	**CaO**	**Na_2O**	**K_2O**	**Cl**	**F**	**CO_2**	**Total**	**Si**	**Ti**	**Al**	**Fe^{2+}**	**Mg**	**Mn**	**Ca**	**Na**	**K**	**Cl**	**F**	**C**	**Infos**
Carbonates	STP2_Carb20	0.47	*b.d.l.*	*b.d.l.*	55.59	4.27	0.95	*b.d.l.*	*b.d.l.*	0.05	*b.d.l.*	*b.d.l.*	40.02	101.36	0.01	0.00	0.00	0.87	0.12	0.02	0.00	0.00	0.00	0.00	0.00	1.00	Rim
	STP2_Carb21	0.14	*b.d.l.*	*b.d.l.*	55.80	3.95	0.94	*b.d.l.*	*b.d.l.*	0.08	*b.d.l.*	*b.d.l.*	39.31	100.29	0.00	0.00	0.00	0.87	0.11	0.01	0.00	0.00	0.00	0.00	0.00	1.00	Rim
	STP2_Carb22	0.20	*b.d.l.*	*b.d.l.*	55.95	4.10	0.67	*b.d.l.*	*b.d.l.*	0.06	*b.d.l.*	*b.d.l.*	39.48	100.57	0.00	0.00	0.00	0.87	0.11	0.01	0.00	0.00	0.00	0.00	0.00	1.00	Rim
	STP2_Carb23	2.67	*b.d.l.*	*b.d.l.*	54.83	4.14	0.59	*b.d.l.*	*b.d.l.*	0.10	*b.d.l.*	*b.d.l.*	42.43	104.91	0.05	0.00	0.00	0.87	0.12	0.01	0.00	0.00	0.00	0.00	0.00	1.00	Rim
	STP0_Carb1	0.40	*b.d.l.*	0.17	58.39	2.40	0.37	0.08	*b.d.l.*	0.11	*b.d.l.*	*b.d.l.*	39.54	101.53	0.01	0.00	0.00	0.93	0.07	0.01	0.00	0.00	0.00	0.00	0.00	1.00	Vein
	STP0_Carb2	1.83	*b.d.l.*	0.78	52.04	5.51	0.36	0.36	*b.d.l.*	0.42	*b.d.l.*	*b.d.l.*	42.28	103.62	0.03	0.00	0.02	0.84	0.16	0.01	0.01	0.00	0.01	0.00	0.00	1.00	Vein
	STP4_Carb9	0.55	0.39	0.34	58.15	2.51	0.34	0.06	*b.d.l.*	0.18	*b.d.l.*	*b.d.l.*	40.37	102.96	0.01	0.01	0.01	0.92	0.07	0.01	0.00	0.00	0.00	0.00	0.00	1.00	Vein
	STP4_Carb10	0.13	*b.d.l.*	0.07	58.13	3.85	0.32	*b.d.l.*	*b.d.l.*	*b.d.l.*	*b.d.l.*	*b.d.l.*	40.28	102.90	0.00	0.00	0.00	0.89	0.11	0.01	0.00	0.00	0.00	0.00	0.00	1.00	Vein
	STP0_Carb3	1.00	0.14	0.85	57.57	1.97	0.30	0.08	0.07	0.15	*b.d.l.*	*b.d.l.*	40.49	102.60	0.02	0.00	0.02	0.94	0.06	0.01	0.00	0.00	0.00	0.00	0.00	1.00	Vein
	STP0_Carb4	1.90	*b.d.l.*	1.07	55.21	3.23	0.20	0.11	*b.d.l.*	0.42	*b.d.l.*	*b.d.l.*	41.93	104.12	0.03	0.00	0.02	0.90	0.09	0.00	0.00	0.00	0.01	0.00	0.00	1.00	Vein

Appendix A22

Composition of natural tourmalines from the spotted schist of Panasqueira.

Group	Name	SiO_2	TiO_2	Al_2O_3	FeO	MgO	MnO	CaO	Na_2O	K_2O	F	B_2O_3	H_2O	Total	Site T		Site Z	Site Y					Site X				F	B	OH^-	Total Al	Infos
															Si	Al	Al	Al	Ti	Fe	Mg	Mn	Ca	Na	K	$[]_X$					
Tourmaline	STP0_TurC1	36.00	0.73	33.71	8.27	5.49	*b.d.l.*	0.34	1.85	*b.d.l.*	*b.d.l.*	10.64	3.67	100.70	5.88	0.12	6.00	0.37	0.09	1.13	1.34	0.00	0.06	0.59	0.00	0.35	0.00	3.00	4.00	6.49	Core1
	STP0_TurC2	35.82	0.50	33.23	7.90	5.81	*b.d.l.*	0.51	1.77	0.04	*b.d.l.*	10.55	3.64	99.76	5.90	0.10	6.00	0.35	0.06	1.09	1.43	0.00	0.09	0.57	0.01	0.34	0.00	3.00	4.00	6.45	Core1
	STP0_TurC3	36.48	0.37	33.39	9.24	5.49	*b.d.l.*	0.13	1.79	*b.d.l.*	*b.d.l.*	10.67	3.68	101.24	5.94	0.06	6.00	0.36	0.05	1.26	1.33	0.00	0.02	0.57	0.00	0.41	0.00	3.00	4.00	6.41	Core1
	STP0_TurC4	36.89	0.48	32.94	8.60	5.25	*b.d.l.*	*b.d.l.*	1.79	*b.d.l.*	*b.d.l.*	10.61	3.66	100.22	6.05	0.00	6.00	0.36	0.06	1.18	1.28	0.00	0.00	0.57	0.00	0.43	0.00	3.00	4.00	6.36	Core1
	STP0_TurC5	37.32	0.52	33.66	7.47	5.69	*b.d.l.*	0.28	1.74	*b.d.l.*	*b.d.l.*	10.76	3.71	101.16	6.03	0.00	6.00	0.41	0.06	1.01	1.37	0.00	0.05	0.54	0.00	0.41	0.00	3.00	4.00	6.41	Core1
	STP0_TurC6	36.96	0.78	32.53	9.01	5.38	*b.d.l.*	0.45	1.72	*b.d.l.*	*b.d.l.*	10.66	3.68	101.19	6.02	0.00	6.00	0.25	0.10	1.23	1.31	0.00	0.08	0.54	0.00	0.38	0.00	3.00	4.00	6.25	Core1
	STP0_TurC7	37.65	0.27	32.94	8.70	5.36	*b.d.l.*	0.05	1.84	*b.d.l.*	*b.d.l.*	10.72	3.69	101.21	6.11	0.00	6.00	0.30	0.03	1.18	1.30	0.00	0.01	0.58	0.00	0.41	0.00	3.00	4.00	6.30	Core1
	STP0_TurC8	36.84	0.41	34.49	7.56	5.53	*b.d.l.*	0.34	1.77	*b.d.l.*	*b.d.l.*	10.78	3.71	101.42	5.94	0.06	6.00	0.50	0.05	1.02	1.33	0.00	0.06	0.55	0.00	0.39	0.00	3.00	4.00	6.56	Core1
	STP0_TurC9	36.17	0.37	34.51	7.70	5.85	*b.d.l.*	0.39	1.78	*b.d.l.*	*b.d.l.*	10.73	3.70	101.19	5.86	0.14	6.00	0.45	0.04	1.04	1.41	0.00	0.07	0.56	0.00	0.37	0.00	3.00	4.00	6.59	Core1
	STP0_TurC10	36.84	0.94	33.39	7.85	5.62	*b.d.l.*	0.30	1.72	0.03	*b.d.l.*	10.72	3.69	101.10	5.97	0.03	6.00	0.36	0.11	1.06	1.36	0.00	0.05	0.54	0.01	0.40	0.00	3.00	4.00	6.38	Core1
	STP0_TurC11	36.32	0.86	33.57	8.07	5.82	*b.d.l.*	0.55	1.74	*b.d.l.*	*b.d.l.*	10.71	3.69	101.34	5.89	0.11	6.00	0.31	0.11	1.09	1.41	0.00	0.10	0.55	0.00	0.36	0.00	3.00	4.00	6.42	Core1
	STP0_TurC12	37.14	0.28	34.77	8.16	5.10	*b.d.l.*	0.28	1.72	*b.d.l.*	*b.d.l.*	10.82	3.73	102.00	5.96	0.04	6.00	0.54	0.03	1.10	1.22	0.00	0.05	0.53	0.00	0.42	0.00	3.00	4.00	6.58	Core1
	STP4_TurC1	36.99	0.51	33.27	7.57	5.75	*b.d.l.*	0.54	1.75	*b.d.l.*	*b.d.l.*	10.69	3.69	100.74	6.01	0.00	6.00	0.37	0.06	1.03	1.39	0.00	0.09	0.55	0.00	0.35	0.00	3.00	4.00	6.37	Core1
	STP4_TurC2	37.03	0.70	33.97	7.49	5.90	*b.d.l.*	0.41	1.87	0.04	*b.d.l.*	10.82	3.73	101.96	5.95	0.05	6.00	0.38	0.08	1.01	1.41	0.00	0.07	0.58	0.01	0.34	0.00	3.00	4.00	6.43	Core1
	STP4_TurC3	37.21	0.38	33.53	8.96	5.23	*b.d.l.*	0.06	1.80	0.05	*b.d.l.*	10.74	3.70	101.67	6.02	0.00	6.00	0.39	0.05	1.21	1.26	0.00	0.01	0.57	0.01	0.41	0.00	3.00	4.00	6.39	Core1
	STP2_TurC1	35.92	0.60	34.12	8.46	5.13	*b.d.l.*	0.15	1.80	*b.d.l.*	*b.d.l.*	10.62	3.66	100.45	5.88	0.12	6.00	0.46	0.07	1.16	1.25	0.00	0.03	0.57	0.00	0.40	0.00	3.00	4.00	6.58	Core1
	STP0_TurC13	35.56	0.67	32.75	8.73	5.94	*b.d.l.*	0.29	1.98	*b.d.l.*	*b.d.l.*	10.53	3.63	100.09	5.87	0.13	6.00	0.24	0.08	1.21	1.46	0.00	0.05	0.63	0.00	0.32	0.00	3.00	4.00	6.37	Core2
	STP0_TurC14	36.37	0.86	32.21	9.17	5.63	*b.d.l.*	0.07	1.83	*b.d.l.*	*b.d.l.*	10.56	3.64	100.35	5.99	0.01	6.00	0.23	0.11	1.26	1.38	0.00	0.01	0.58	0.00	0.40	0.00	3.00	4.00	6.25	Core2
	STP0_TurC15	36.82	0.59	32.82	8.95	5.90	*b.d.l.*	0.07	2.15	*b.d.l.*	*b.d.l.*	10.71	3.69	101.70	5.97	0.03	6.00	0.25	0.07	1.21	1.43	0.00	0.01	0.68	0.00	0.31	0.00	3.00	4.00	6.28	Core2
	STP0_TurC16	37.03	1.01	31.78	9.04	5.83	*b.d.l.*	0.07	2.15	*b.d.l.*	*b.d.l.*	10.65	3.67	101.25	6.04	0.00	6.00	0.11	0.12	1.23	1.42	0.00	0.01	0.68	0.00	0.31	0.00	3.00	4.00	6.11	Core2
	STP0_TurC17	36.05	0.81	33.87	8.13	6.08	0.22	0.57	1.85	*b.d.l.*	*b.d.l.*	10.76	3.71	102.03	5.82	0.18	6.00	0.27	0.10	1.10	1.46	0.03	0.10	0.58	0.00	0.32	0.00	3.00	4.00	6.45	Core2
	STP0_TurC18	36.93	0.56	32.68	8.63	6.11	*b.d.l.*	0.29	2.08	*b.d.l.*	*b.d.l.*	10.72	3.70	101.69	5.99	0.01	6.00	0.23	0.07	1.17	1.48	0.00	0.05	0.65	0.00	0.30	0.00	3.00	4.00	6.24	Core2
	STP0_TurC19	36.52	0.53	33.25	8.12	5.85	*b.d.l.*	0.58	1.94	*b.d.l.*	0.01	10.69	3.68	101.16	5.94	0.06	6.00	0.31	0.06	1.10	1.42	0.00	0.10	0.61	0.00	0.29	0.01	3.00	3.99	6.37	Core2
	STP0_TurC20	37.03	0.88	32.10	8.99	5.90	*b.d.l.*	0.12	2.19	*b.d.l.*	*b.d.l.*	10.69	3.69	101.59	6.02	0.00	6.00	0.15	0.11	1.22	1.43	0.00	0.02	0.69	0.00	0.29	0.00	3.00	4.00	6.15	Core2
	STP2_TurC2	36.12	0.73	33.13	8.23	5.33	*b.d.l.*	0.09	2.17	*b.d.l.*	*b.d.l.*	10.57	3.64	100.01	5.94	0.06	6.00	0.37	0.09	1.13	1.31	0.00	0.02	0.69	0.00	0.29	0.00	3.00	4.00	6.42	Core2
	STP0_TurInt1	35.71	0.59	34.32	7.93	5.09	*b.d.l.*	0.19	1.75	0.06	*b.d.l.*	10.58	3.65	99.85	5.87	0.13	6.00	0.51	0.07	1.09	1.25	0.00	0.03	0.56	0.01	0.40	0.00	3.00	4.00	6.65	Interm
	STP0_TurInt2	35.72	0.62	32.26	9.52	5.28	*b.d.l.*	0.11	2.05	0.07	*b.d.l.*	10.46	3.60	99.69	5.94	0.06	6.00	0.26	0.08	1.32	1.31	0.00	0.02	0.66	0.02	0.30	0.00	3.00	4.00	6.32	Interm
	STP0_TurInt3	36.07	0.66	33.79	8.74	5.34	*b.d.l.*	0.09	2.04	*b.d.l.*	*b.d.l.*	10.66	3.67	101.07	5.88	0.12	6.00	0.38	0.08	1.19	1.30	0.00	0.02	0.65	0.00	0.34	0.00	3.00	4.00	6.50	Interm

Group	Name	SiO_2	TiO_2	Al_2O_3	FeO	MgO	MnO	CaO	Na_2O	K_2O	F	B_2O_3	H_2O	Total	Site T		Site Z	Site Y					Site X				F	B	OH^-	Total Al	Infos
															Si	Al	Al	Al	Ti	Fe	Mg	Mn	Ca	Na	K	$[]_X$					
Tourmaline	STP0_TurInt4	36.80	0.67	33.96	7.96	5.48	*b.d.l.*	0.16	2.07	*b.d.l.*	*b.d.l.*	10.76	3.71	101.57	5.95	0.05	6.00	0.41	0.08	1.07	1.32	0.00	0.03	0.65	0.00	0.32	0.00	3.00	4.00	6.47	Interm
	STP0_TurInt5	36.40	0.72	33.55	8.16	5.55	*b.d.l.*	0.20	2.16	*b.d.l.*	*b.d.l.*	10.69	3.68	101.12	5.92	0.08	6.00	0.35	0.09	1.11	1.35	0.00	0.03	0.68	0.00	0.29	0.00	3.00	4.00	6.43	Interm
	STP0_TurInt6	36.15	0.68	33.76	8.82	5.41	*b.d.l.*	0.21	2.11	*b.d.l.*	*b.d.l.*	10.69	3.69	101.53	5.88	0.12	6.00	0.34	0.08	1.20	1.31	0.00	0.04	0.66	0.00	0.30	0.00	3.00	4.00	6.47	Interm
	STP0_TurInt7	36.28	0.50	34.87	7.83	5.32	*b.d.l.*	0.26	1.79	*b.d.l.*	*b.d.l.*	10.74	3.70	101.30	5.87	0.13	6.00	0.52	0.06	1.06	1.28	0.00	0.04	0.56	0.00	0.39	0.00	3.00	4.00	6.65	Interm
	STP0_TurInt8	36.94	0.74	34.91	7.53	5.45	*b.d.l.*	0.19	1.88	*b.d.l.*	*b.d.l.*	10.87	3.75	102.26	5.91	0.09	6.00	0.49	0.09	1.01	1.30	0.00	0.03	0.58	0.00	0.38	0.00	3.00	4.00	6.58	Interm
	STP0_TurInt9	36.35	0.67	34.26	8.09	5.27	*b.d.l.*	0.20	1.81	*b.d.l.*	*b.d.l.*	10.70	3.69	101.04	5.90	0.10	6.00	0.46	0.08	1.10	1.28	0.00	0.03	0.57	0.00	0.39	0.00	3.00	4.00	6.56	Interm
	STP0_TurInt10	36.35	0.67	34.19	8.31	5.33	*b.d.l.*	0.16	2.00	*b.d.l.*	*b.d.l.*	10.72	3.70	101.42	5.89	0.11	6.00	0.42	0.08	1.13	1.29	0.00	0.03	0.63	0.00	0.34	0.00	3.00	4.00	6.53	Interm
	STP0_TurInt11	37.07	0.66	34.26	8.57	5.48	*b.d.l.*	0.12	1.96	*b.d.l.*	*b.d.l.*	10.86	3.74	102.73	5.93	0.07	6.00	0.40	0.08	1.15	1.31	0.00	0.02	0.61	0.00	0.37	0.00	3.00	4.00	6.46	Interm
	STP0_TurInt12	36.64	0.35	34.46	7.78	5.71	*b.d.l.*	0.27	1.80	*b.d.l.*	*b.d.l.*	10.77	3.71	101.51	5.91	0.09	6.00	0.47	0.04	1.05	1.37	0.00	0.05	0.56	0.00	0.39	0.00	3.00	4.00	6.56	Interm
	STP0_TurInt13	36.62	0.94	34.42	7.09	5.26	*b.d.l.*	0.16	1.71	0.06	*b.d.l.*	10.72	3.70	100.68	5.94	0.06	6.00	0.51	0.11	0.96	1.27	0.00	0.03	0.54	0.01	0.42	0.00	3.00	4.00	6.58	Interm
	STP0_TurInt14	36.36	0.60	33.72	6.93	5.87	*b.d.l.*	0.46	1.77	*b.d.l.*	*b.d.l.*	10.64	3.67	100.02	5.94	0.06	6.00	0.43	0.07	0.95	1.43	0.00	0.08	0.56	0.00	0.36	0.00	3.00	4.00	6.49	Interm
	STP0_TurInt15	36.35	0.36	34.52	7.67	5.42	*b.d.l.*	0.39	1.96	*b.d.l.*	*b.d.l.*	10.72	3.69	101.07	5.89	0.11	6.00	0.49	0.04	1.04	1.31	0.00	0.07	0.62	0.00	0.32	0.00	3.00	4.00	6.60	Interm
	STP0_TurInt16	36.76	0.68	34.26	7.90	5.34	*b.d.l.*	0.18	1.88	*b.d.l.*	*b.d.l.*	10.76	3.71	101.47	5.94	0.06	6.00	0.46	0.08	1.07	1.29	0.00	0.03	0.59	0.00	0.38	0.00	3.00	4.00	6.52	Interm
	STP0_TurInt17	36.90	0.43	34.16	7.90	6.06	*b.d.l.*	0.38	1.93	*b.d.l.*	*b.d.l.*	10.84	3.74	102.32	5.92	0.08	6.00	0.38	0.05	1.06	1.45	0.00	0.06	0.60	0.00	0.34	0.00	3.00	4.00	6.46	Interm
	STP0_TurInt18	37.43	0.64	34.14	7.40	6.04	*b.d.l.*	0.45	1.82	*b.d.l.*	*b.d.l.*	10.90	3.76	102.57	5.97	0.03	6.00	0.39	0.08	0.99	1.43	0.00	0.08	0.56	0.00	0.36	0.00	3.00	4.00	6.42	Interm
	STP0_TurInt19	36.26	0.64	34.48	7.43	5.48	*b.d.l.*	0.29	1.86	*b.d.l.*	*b.d.l.*	10.71	3.69	100.84	5.89	0.11	6.00	0.48	0.08	1.01	1.33	0.00	0.05	0.58	0.00	0.36	0.00	3.00	4.00	6.60	Interm
	STP4_TurInt1	36.88	0.36	34.61	7.39	5.41	*b.d.l.*	0.30	1.89	*b.d.l.*	*b.d.l.*	10.77	3.71	101.32	5.95	0.05	6.00	0.53	0.04	1.00	1.30	0.00	0.05	0.59	0.00	0.36	0.00	3.00	4.00	6.58	Interm
	STP4_TurInt2	36.53	0.69	33.61	7.88	5.34	*b.d.l.*	0.21	1.82	*b.d.l.*	*b.d.l.*	10.64	3.67	100.39	5.96	0.04	6.00	0.43	0.08	1.08	1.30	0.00	0.04	0.58	0.00	0.39	0.00	3.00	4.00	6.47	Interm
	STP4_TurInt3	36.56	0.66	33.49	7.99	5.27	*b.d.l.*	0.16	1.94	*b.d.l.*	*b.d.l.*	10.64	3.67	100.38	5.97	0.03	6.00	0.43	0.08	1.09	1.28	0.00	0.03	0.61	0.00	0.36	0.00	3.00	4.00	6.45	Interm
	STP2_TurInt1	36.40	0.42	34.15	7.68	5.23	*b.d.l.*	0.23	1.85	*b.d.l.*	*b.d.l.*	10.65	3.67	100.27	5.94	0.06	6.00	0.51	0.05	1.05	1.27	0.00	0.04	0.58	0.00	0.38	0.00	3.00	4.00	6.57	Interm
	STP2_TurInt2	36.18	0.65	33.78	7.68	5.53	*b.d.l.*	0.19	1.91	*b.d.l.*	*b.d.l.*	10.63	3.66	100.20	5.92	0.08	6.00	0.43	0.08	1.05	1.35	0.00	0.03	0.61	0.00	0.36	0.00	3.00	4.00	6.51	Interm
	STP2_TurInt3	36.64	0.62	34.35	8.00	5.22	*b.d.l.*	0.14	1.97	*b.d.l.*	*b.d.l.*	10.75	3.70	101.40	5.93	0.07	6.00	0.47	0.08	1.08	1.26	0.00	0.02	0.62	0.00	0.36	0.00	3.00	4.00	6.55	Interm
	STP0_TurR1	36.98	0.49	33.85	7.92	5.18	*b.d.l.*	0.38	1.54	*b.d.l.*	*b.d.l.*	10.70	3.69	100.72	6.01	0.00	6.00	0.48	0.06	1.08	1.25	0.00	0.07	0.49	0.00	0.45	0.00	3.00	4.00	6.48	Rim1
	STP0_TurR2	37.01	0.30	33.55	7.77	5.42	*b.d.l.*	0.26	1.55	0.05	*b.d.l.*	10.65	3.67	100.23	6.04	0.00	6.00	0.45	0.04	1.06	1.32	0.00	0.04	0.49	0.01	0.46	0.00	3.00	4.00	6.45	Rim1
	STP0_TurR3	37.24	0.23	34.31	7.42	5.25	*b.d.l.*	0.21	1.48	0.04	*b.d.l.*	10.73	3.70	100.61	6.03	0.00	6.00	0.55	0.03	1.01	1.27	0.00	0.04	0.46	0.01	0.49	0.00	3.00	4.00	6.55	Rim1
	STP0_TurR4	36.74	0.35	34.42	7.64	5.17	*b.d.l.*	0.18	1.78	*b.d.l.*	*b.d.l.*	10.70	3.69	100.66	5.97	0.03	6.00	0.55	0.04	1.04	1.25	0.00	0.03	0.56	0.00	0.41	0.00	3.00	4.00	6.59	Rim1
	STP0_TurR5	36.62	0.24	34.94	7.81	4.44	*b.d.l.*	*b.d.l.*	1.46	0.04	*b.d.l.*	10.64	3.67	99.87	5.98	0.02	6.00	0.71	0.03	1.07	1.08	0.00	0.00	0.46	0.01	0.53	0.00	3.00	4.00	6.73	Rim1
	STP0_TurR6	36.97	0.27	34.79	8.20	4.39	*b.d.l.*	*b.d.l.*	1.60	*b.d.l.*	*b.d.l.*	10.70	3.69	100.59	6.01	0.00	6.00	0.66	0.03	1.11	1.06	0.00	0.00	0.50	0.00	0.50	0.00	3.00	4.00	6.66	Rim1

Group	Name	SiO_2	TiO_2	Al_2O_3	FeO	MgO	MnO	CaO	Na_2O	K_2O	F	B_2O_3	H_2O	Total	Site T		Site Z	Site Y					Site X				F	B	OH^-	Total Al	Infos
															Si	Al	Al	Al	Ti	Fe	Mg	Mn	Ca	Na	K	$[]_X$					
Tourmaline	STP0_TurR7	36.47	0.36	34.87	8.40	4.82	*b.d.l.*	0.10	1.56	*b.d.l.*	*b.d.l.*	10.71	3.69	100.97	5.92	0.08	6.00	0.59	0.04	1.14	1.17	0.00	0.02	0.49	0.00	0.49	0.00	3.00	4.00	6.67	Rim1
	STP0_TurR8	36.86	0.37	34.55	8.68	4.66	*b.d.l.*	*b.d.l.*	1.73	*b.d.l.*	*b.d.l.*	10.73	3.70	101.28	5.97	0.03	6.00	0.57	0.05	1.18	1.13	0.00	0.00	0.54	0.00	0.46	0.00	3.00	4.00	6.60	Rim1
	STP0_TurR9	37.51	0.22	35.22	7.83	5.13	0.13	0.10	1.35	*b.d.l.*	*b.d.l.*	10.88	3.75	102.13	5.99	0.01	6.00	0.63	0.03	1.05	1.22	0.02	0.02	0.42	0.00	0.57	0.00	3.00	4.00	6.63	Rim1
	STP0_TurR10	36.96	0.14	35.45	7.51	4.98	*b.d.l.*	0.18	1.40	*b.d.l.*	*b.d.l.*	10.79	3.72	101.12	5.96	0.04	6.00	0.69	0.02	1.01	1.20	0.00	0.03	0.44	0.00	0.53	0.00	3.00	4.00	6.73	Rim1
	STP0_TurR11	36.21	0.29	34.65	7.37	5.36	*b.d.l.*	0.31	1.69	*b.d.l.*	*b.d.l.*	10.66	3.67	100.22	5.90	0.10	6.00	0.56	0.04	1.00	1.30	0.00	0.05	0.54	0.00	0.41	0.00	3.00	4.00	6.66	Rim1
	STP0_TurR12	36.89	0.58	34.18	7.41	5.40	*b.d.l.*	0.20	1.50	*b.d.l.*	*b.d.l.*	10.71	3.69	100.58	5.99	0.01	6.00	0.52	0.07	1.01	1.31	0.00	0.04	0.47	0.00	0.49	0.00	3.00	4.00	6.54	Rim1
	STP0_TurR13	36.81	0.50	35.60	7.53	4.96	*b.d.l.*	0.07	1.66	*b.d.l.*	*b.d.l.*	10.83	3.73	101.69	5.91	0.09	6.00	0.64	0.06	1.01	1.19	0.00	0.01	0.52	0.00	0.47	0.00	3.00	4.00	6.73	Rim1
	STP0_TurR14	36.88	0.34	35.09	8.06	4.88	*b.d.l.*	0.09	1.55	0.05	*b.d.l.*	10.78	3.72	101.44	5.95	0.05	6.00	0.61	0.04	1.09	1.17	0.00	0.02	0.48	0.01	0.49	0.00	3.00	4.00	6.67	Rim1
	STP0_TurR15	37.41	0.21	35.87	8.12	4.30	*b.d.l.*	0.06	1.56	*b.d.l.*	*b.d.l.*	10.88	3.75	102.14	5.98	0.02	6.00	0.73	0.03	1.08	1.02	0.00	0.01	0.48	0.00	0.51	0.00	3.00	4.00	6.76	Rim1
	STP4_TurR1	37.33	0.22	34.94	7.82	4.40	*b.d.l.*	0.07	1.50	*b.d.l.*	*b.d.l.*	10.74	3.70	100.72	6.04	0.00	6.00	0.66	0.03	1.06	1.06	0.00	0.01	0.47	0.00	0.52	0.00	3.00	4.00	6.66	Rim1
	STP4_TurR2	37.72	0.29	34.76	8.16	4.42	0.15	0.05	1.49	*b.d.l.*	*b.d.l.*	10.81	3.73	101.57	6.07	0.00	6.00	0.59	0.03	1.10	1.06	0.02	0.01	0.46	0.00	0.53	0.00	3.00	4.00	6.59	Rim1
	STP4_TurR3	37.31	0.29	34.66	7.83	4.40	*b.d.l.*	0.08	1.67	0.05	*b.d.l.*	10.73	3.70	100.73	6.05	0.00	6.00	0.62	0.04	1.06	1.06	0.00	0.01	0.53	0.01	0.45	0.00	3.00	4.00	6.62	Rim1
	STP4_TurR4	36.81	0.45	34.39	8.16	5.08	*b.d.l.*	0.15	1.82	0.04	*b.d.l.*	10.74	3.70	101.33	5.96	0.04	6.00	0.51	0.05	1.10	1.22	0.00	0.03	0.57	0.01	0.40	0.00	3.00	4.00	6.56	Rim1
	STP4_TurR5	37.15	0.33	34.51	7.97	4.60	*b.d.l.*	0.07	1.55	0.06	*b.d.l.*	10.71	3.69	100.64	6.03	0.00	6.00	0.60	0.04	1.08	1.11	0.00	0.01	0.49	0.01	0.49	0.00	3.00	4.00	6.60	Rim1
	STP2_TurR1	36.77	0.30	35.04	8.50	4.92	*b.d.l.*	0.07	1.61	*b.d.l.*	*b.d.l.*	10.78	3.72	101.71	5.93	0.07	6.00	0.58	0.04	1.15	1.18	0.00	0.01	0.50	0.00	0.49	0.00	3.00	4.00	6.65	Rim1
	STP4_TurR6	36.67	0.80	34.41	7.52	5.12	*b.d.l.*	0.16	1.75	*b.d.l.*	*b.d.l.*	10.73	3.70	100.87	5.94	0.06	6.00	0.52	0.10	1.02	1.24	0.00	0.03	0.55	0.00	0.42	0.00	3.00	4.00	6.57	Rim1
	STP4_TurR7	37.39	0.56	34.35	7.31	5.50	*b.d.l.*	0.22	1.88	0.07	*b.d.l.*	10.84	3.74	101.86	6.00	0.00	6.00	0.49	0.07	0.98	1.31	0.00	0.04	0.59	0.01	0.36	0.00	3.00	4.00	6.49	Rim1
	STP4_TurR8	36.51	0.71	34.12	8.03	5.09	*b.d.l.*	0.23	1.80	*b.d.l.*	*b.d.l.*	10.69	3.69	100.88	5.94	0.06	6.00	0.47	0.09	1.09	1.23	0.00	0.04	0.57	0.00	0.39	0.00	3.00	4.00	6.54	Rim1
	STP4_TurR9	37.01	0.62	34.42	8.42	5.24	*b.d.l.*	0.18	1.85	*b.d.l.*	*b.d.l.*	10.83	3.73	102.30	5.94	0.06	6.00	0.45	0.08	1.13	1.25	0.00	0.03	0.58	0.00	0.39	0.00	3.00	4.00	6.51	Rim1
	STP4_TurR10	36.92	0.59	34.91	7.67	5.33	*b.d.l.*	0.31	1.71	0.05	*b.d.l.*	10.84	3.74	102.07	5.92	0.08	6.00	0.52	0.07	1.03	1.27	0.00	0.05	0.53	0.01	0.41	0.00	3.00	4.00	6.60	Rim1
	STP0_TurR16	36.37	0.59	32.52	9.01	5.47	*b.d.l.*	0.11	2.18	0.05	0.01	10.57	3.65	100.52	5.98	0.02	6.00	0.28	0.07	1.24	1.34	0.00	0.02	0.69	0.01	0.28	0.01	3.00	4.00	6.30	Rim2
	STP0_TurR17	36.73	0.73	32.18	8.65	5.74	*b.d.l.*	0.45	1.91	*b.d.l.*	0.03	10.61	3.66	100.70	6.02	0.00	6.00	0.21	0.09	1.19	1.40	0.00	0.08	0.61	0.00	0.31	0.02	3.00	4.00	6.21	Rim2
	STP0_TurR18	37.08	0.49	33.54	7.41	5.75	*b.d.l.*	0.50	2.02	0.04	*b.d.l.*	10.75	3.70	101.28	6.00	0.00	6.00	0.39	0.06	1.00	1.39	0.00	0.09	0.63	0.01	0.27	0.00	3.00	4.00	6.39	Rim2
	STP0_TurR19	37.24	0.63	34.44	8.42	5.23	*b.d.l.*	0.12	2.02	*b.d.l.*	*b.d.l.*	10.87	3.75	102.72	5.95	0.05	6.00	0.44	0.08	1.13	1.25	0.00	0.02	0.63	0.00	0.35	0.00	3.00	4.00	6.49	Rim2
	STP0_TurR20	36.61	0.65	33.89	8.08	5.44	*b.d.l.*	0.17	1.92	0.04	*b.d.l.*	10.72	3.69	101.23	5.94	0.06	6.00	0.42	0.08	1.10	1.32	0.00	0.03	0.60	0.01	0.36	0.00	3.00	4.00	6.48	Rim2
	STP0_TurR21	36.44	0.55	33.63	8.32	5.63	*b.d.l.*	0.15	2.08	0.05	*b.d.l.*	10.69	3.69	101.22	5.92	0.08	6.00	0.37	0.07	1.13	1.36	0.00	0.03	0.66	0.01	0.31	0.00	3.00	4.00	6.44	Rim2
	STP0_TurR22	36.71	0.57	34.56	7.82	5.38	*b.d.l.*	0.12	1.93	*b.d.l.*	*b.d.l.*	10.78	3.72	101.58	5.92	0.08	6.00	0.49	0.07	1.05	1.29	0.00	0.02	0.60	0.00	0.38	0.00	3.00	4.00	6.57	Rim2
	STP0_TurR23	36.26	0.64	33.78	8.27	5.55	*b.d.l.*	0.16	2.00	*b.d.l.*	*b.d.l.*	10.68	3.68	100.99	5.90	0.10	6.00	0.39	0.08	1.13	1.35	0.00	0.03	0.63	0.00	0.34	0.00	3.00	4.00	6.48	Rim2

Group	Name	SiO_2	TiO_2	Al_2O_3	FeO	MgO	MnO	CaO	Na_2O	K_2O	F	B_2O_3	H_2O	Total	Site T		Site Z	Site Y					Site X				F	B	OH^-	Total Al	Infos
															Si	Al	Al	Al	Ti	Fe	Mg	Mn	Ca	Na	K	[]X					
Tourmaline	STP0_TurR24	35.75	0.59	34.50	8.04	5.35	*b.d.l.*	0.15	2.02	*b.d.l.*	*b.d.l.*	10.65	3.67	100.72	5.83	0.17	6.00	0.46	0.07	1.10	1.30	0.00	0.03	0.64	0.00	0.34	0.00	3.00	4.00	6.63	Rim2
	STP0_TurR25	35.53	0.73	33.83	7.58	5.56	*b.d.l.*	0.20	2.10	*b.d.l.*	*b.d.l.*	10.56	3.64	99.73	5.85	0.15	6.00	0.41	0.09	1.04	1.36	0.00	0.03	0.67	0.00	0.29	0.00	3.00	4.00	6.56	Rim2
	STP0_TurR26	36.27	0.81	33.86	8.16	5.66	*b.d.l.*	0.17	2.01	*b.d.l.*	*b.d.l.*	10.71	3.69	101.35	5.88	0.12	6.00	0.36	0.10	1.11	1.37	0.00	0.03	0.63	0.00	0.34	0.00	3.00	4.00	6.47	Rim2
	STP0_TurR27	36.59	0.71	33.59	7.66	5.48	*b.d.l.*	0.16	1.94	*b.d.l.*	*b.d.l.*	10.66	3.67	100.45	5.97	0.03	6.00	0.42	0.09	1.04	1.33	0.00	0.03	0.61	0.00	0.36	0.00	3.00	4.00	6.46	Rim2
	STP0_TurR28	35.63	0.71	33.46	7.68	5.60	*b.d.l.*	0.16	2.06	*b.d.l.*	*b.d.l.*	10.53	3.63	99.44	5.88	0.12	6.00	0.39	0.09	1.06	1.38	0.00	0.03	0.66	0.00	0.31	0.00	3.00	4.00	6.51	Rim2
	STP0_TurR29	36.96	0.72	33.95	8.36	5.67	*b.d.l.*	0.16	2.06	*b.d.l.*	*b.d.l.*	10.83	3.73	102.45	5.93	0.07	6.00	0.35	0.09	1.12	1.36	0.00	0.03	0.64	0.00	0.33	0.00	3.00	4.00	6.42	Rim2
	STP0_TurR30	36.64	0.84	33.88	8.33	5.41	*b.d.l.*	0.17	2.05	*b.d.l.*	*b.d.l.*	10.76	3.71	101.77	5.92	0.08	6.00	0.37	0.10	1.13	1.30	0.00	0.03	0.64	0.00	0.33	0.00	3.00	4.00	6.45	Rim2
	STP0_TurR31	36.89	0.65	34.76	8.23	5.32	*b.d.l.*	0.15	1.87	*b.d.l.*	*b.d.l.*	10.85	3.74	102.46	5.91	0.09	6.00	0.47	0.08	1.10	1.27	0.00	0.03	0.58	0.00	0.39	0.00	3.00	4.00	6.56	Rim2
	STP4_TurR11	36.39	0.69	33.02	8.62	5.50	*b.d.l.*	0.09	2.19	0.06	*b.d.l.*	10.63	3.66	100.85	5.95	0.05	6.00	0.31	0.09	1.18	1.34	0.00	0.02	0.69	0.01	0.28	0.00	3.00	4.00	6.36	Rim2
	STP4_TurR12	36.77	0.59	33.54	8.57	5.24	*b.d.l.*	0.11	1.97	0.06	*b.d.l.*	10.69	3.69	101.22	5.98	0.02	6.00	0.40	0.07	1.17	1.27	0.00	0.02	0.62	0.01	0.35	0.00	3.00	4.00	6.42	Rim2
	STP4_TurR13	36.55	0.76	33.80	8.10	5.34	*b.d.l.*	0.14	1.97	0.06	*b.d.l.*	10.70	3.69	101.10	5.94	0.06	6.00	0.41	0.09	1.10	1.29	0.00	0.02	0.62	0.01	0.35	0.00	3.00	4.00	6.47	Rim2
	STP4_TurR14	37.24	0.57	34.25	8.29	4.97	*b.d.l.*	0.10	1.92	0.07	*b.d.l.*	10.80	3.72	101.93	5.99	0.01	6.00	0.49	0.07	1.12	1.19	0.00	0.02	0.60	0.01	0.37	0.00	3.00	4.00	6.50	Rim2
	STP4_TurR15	37.13	0.59	32.88	8.71	5.36	*b.d.l.*	0.15	2.13	0.07	*b.d.l.*	10.70	3.69	101.40	6.03	0.00	6.00	0.30	0.07	1.18	1.30	0.00	0.03	0.67	0.01	0.29	0.00	3.00	4.00	6.30	Rim2
	STP2_TurR2	36.81	0.53	33.98	8.23	5.39	*b.d.l.*	0.11	2.07	0.10	*b.d.l.*	10.76	3.71	101.69	5.95	0.05	6.00	0.42	0.06	1.11	1.30	0.00	0.02	0.65	0.02	0.31	0.00	3.00	4.00	6.47	Rim2
	STP2_TurR3	37.78	0.60	34.13	7.78	5.61	*b.d.l.*	0.12	2.19	0.13	*b.d.l.*	10.93	3.77	103.03	6.01	0.00	6.00	0.40	0.07	1.03	1.33	0.00	0.02	0.68	0.03	0.28	0.00	3.00	4.00	6.40	Rim2
	STP2_TurR4	37.00	0.63	34.42	7.60	5.45	*b.d.l.*	0.16	2.04	*b.d.l.*	*b.d.l.*	10.81	3.73	101.84	5.95	0.05	6.00	0.47	0.08	1.02	1.30	0.00	0.03	0.63	0.00	0.34	0.00	3.00	4.00	6.52	Rim2
	STP2_TurR5	37.09	0.66	33.93	7.52	5.75	*b.d.l.*	0.18	2.15	*b.d.l.*	*b.d.l.*	10.81	3.72	101.82	5.97	0.03	6.00	0.40	0.08	1.01	1.38	0.00	0.03	0.67	0.00	0.30	0.00	3.00	4.00	6.43	Rim2
	STP2_TurR6	35.90	0.48	33.74	7.97	5.41	*b.d.l.*	0.11	2.05	*b.d.l.*	*b.d.l.*	10.57	3.64	99.86	5.90	0.10	6.00	0.44	0.06	1.10	1.32	0.00	0.02	0.65	0.00	0.33	0.00	3.00	4.00	6.54	Rim2
	STP2_TurR7	37.37	0.63	33.80	8.58	5.10	*b.d.l.*	0.09	2.07	0.07	*b.d.l.*	10.81	3.73	102.24	6.01	0.00	6.00	0.41	0.08	1.15	1.22	0.00	0.02	0.64	0.01	0.32	0.00	3.00	4.00	6.41	Rim2
	STP0_TurLate1	35.97	0.52	31.94	10.63	4.92	*b.d.l.*	0.13	2.20	0.06	0.23	10.48	3.61	100.68	5.97	0.03	6.00	0.21	0.07	1.47	1.22	0.00	0.02	0.71	0.01	0.26	0.12	3.00	4.00	6.24	Late
	STP0_TurLate2	34.63	0.46	30.80	10.39	5.02	*b.d.l.*	0.05	2.47	0.07	0.35	10.15	3.50	97.88	5.93	0.07	6.00	0.15	0.06	1.49	1.28	0.00	0.01	0.82	0.01	0.16	0.19	3.00	4.00	6.22	Late
	STP0_TurLate3	35.40	0.46	30.68	10.84	5.30	*b.d.l.*	*b.d.l.*	2.75	0.06	0.35	10.31	3.56	99.71	5.96	0.04	6.00	0.06	0.06	1.53	1.33	0.00	0.00	0.90	0.01	0.09	0.19	3.00	4.00	6.09	Late
	STP0_TurLate4	35.95	0.51	31.58	10.74	5.14	*b.d.l.*	0.12	2.33	*b.d.l.*	0.20	10.47	3.61	100.64	5.97	0.03	6.00	0.15	0.06	1.49	1.27	0.00	0.02	0.75	0.00	0.23	0.10	3.00	4.00	6.18	Late
	STP0_TurLate5	35.55	0.74	32.25	10.15	4.90	0.19	0.16	2.11	*b.d.l.*	0.16	10.46	3.60	100.27	5.91	0.09	6.00	0.23	0.09	1.41	1.21	0.03	0.03	0.68	0.00	0.29	0.08	3.00	4.00	6.32	Late
	STP0_TurLate6	34.81	0.75	31.14	9.58	5.59	*b.d.l.*	0.13	2.55	0.11	0.07	10.27	3.54	98.55	5.89	0.11	6.00	0.10	0.10	1.36	1.41	0.00	0.02	0.83	0.02	0.12	0.04	3.00	4.00	6.21	Late
	STP0_TurLate7	36.57	0.69	32.66	10.03	5.46	*b.d.l.*	0.11	2.31	*b.d.l.*	*b.d.l.*	10.70	3.69	102.22	5.94	0.06	6.00	0.20	0.08	1.36	1.32	0.00	0.02	0.73	0.00	0.25	0.00	3.00	4.00	6.25	Late
	STP0_TurLate8	36.59	0.64	33.86	8.82	5.36	*b.d.l.*	0.11	2.07	*b.d.l.*	*b.d.l.*	10.75	3.70	101.89	5.92	0.08	6.00	0.37	0.08	1.19	1.29	0.00	0.02	0.65	0.00	0.33	0.00	3.00	4.00	6.45	Late
	STP0_TurLate9	35.70	0.87	32.56	10.55	4.95	0.15	0.11	2.16	*b.d.l.*	*b.d.l.*	10.56	3.64	101.25	5.88	0.12	6.00	0.20	0.11	1.45	1.21	0.02	0.02	0.69	0.00	0.29	0.00	3.00	4.00	6.32	Late

Group	Name	SiO_2	TiO_2	Al_2O_3	FeO	MgO	MnO	CaO	Na_2O	K_2O	F	B_2O_3	H_2O	Total	Site T		Site Z	Site Y					Site X				F	B	OH^-	Total Al	Infos
															Si	**Al**	**Al**	**Al**	**Ti**	**Fe**	**Mg**	**Mn**	**Ca**	**Na**	**K**	**[]x**					
Tourmaline	STP0_TurLate1	36.34	0.66	33.83	9.12	4.57	*b.d.l.*	0.10	1.97	*b.d.l.*	*b.d.l.*	10.64	3.67	100.87	5.94	0.06	6.00	0.45	0.08	1.25	1.11	0.00	0.02	0.62	0.00	0.36	0.00	3.00	4.00	6.52	Late
	STP0_TurLate11	36.23	0.50	33.64	9.98	4.24	*b.d.l.*	0.10	2.03	*b.d.l.*	*b.d.l.*	10.60	3.65	100.96	5.94	0.06	6.00	0.44	0.06	1.37	1.04	0.00	0.02	0.64	0.00	0.34	0.00	3.00	4.00	6.50	Late
	STP2_TurLate1	34.33	0.57	31.52	9.45	4.98	*b.d.l.*	0.14	2.26	0.09	*b.d.l.*	10.14	3.50	96.98	5.88	0.12	6.00	0.25	0.07	1.35	1.27	0.00	0.03	0.75	0.02	0.20	0.00	3.00	4.00	6.37	Late
	STP2_TurLate2	34.83	0.62	31.59	8.26	5.94	*b.d.l.*	0.08	2.54	0.08	*b.d.l.*	10.27	3.54	97.75	5.89	0.11	6.00	0.19	0.08	1.17	1.50	0.00	0.01	0.83	0.02	0.14	0.00	3.00	4.00	6.30	Late
	STP2_TurLate3	36.67	0.65	33.00	8.84	5.36	*b.d.l.*	0.09	2.23	0.08	*b.d.l.*	10.67	3.68	101.26	5.98	0.02	6.00	0.31	0.08	1.20	1.30	0.00	0.02	0.70	0.02	0.26	0.00	3.00	4.00	6.34	Late
	STP2_TurLate4	34.82	0.65	30.93	10.02	5.60	*b.d.l.*	0.16	2.71	*b.d.l.*	*b.d.l.*	10.28	3.54	98.72	5.89	0.11	6.00	0.06	0.08	1.42	1.41	0.00	0.03	0.89	0.00	0.08	0.00	3.00	4.00	6.17	Late
	STP2_TurLate5	36.43	0.63	33.05	8.49	5.28	*b.d.l.*	0.08	2.27	*b.d.l.*	*b.d.l.*	10.61	3.66	100.49	5.97	0.03	6.00	0.35	0.08	1.16	1.29	0.00	0.01	0.72	0.00	0.26	0.00	3.00	4.00	6.38	Late
	STP2_TurLate6	36.45	0.66	32.87	8.53	5.65	*b.d.l.*	0.21	2.26	*b.d.l.*	*b.d.l.*	10.64	3.67	100.94	5.96	0.04	6.00	0.28	0.08	1.17	1.38	0.00	0.04	0.71	0.00	0.25	0.00	3.00	4.00	6.33	Late

Appendix A23

Cathodoluminescence observations of beryl and kaolinite respectively in the centre of the high porosity zone and inside the quartz veins.

The yellow dots do not correspond to a mineral, they have been observed all over the sample, even in the epoxy resin, outside the sample.

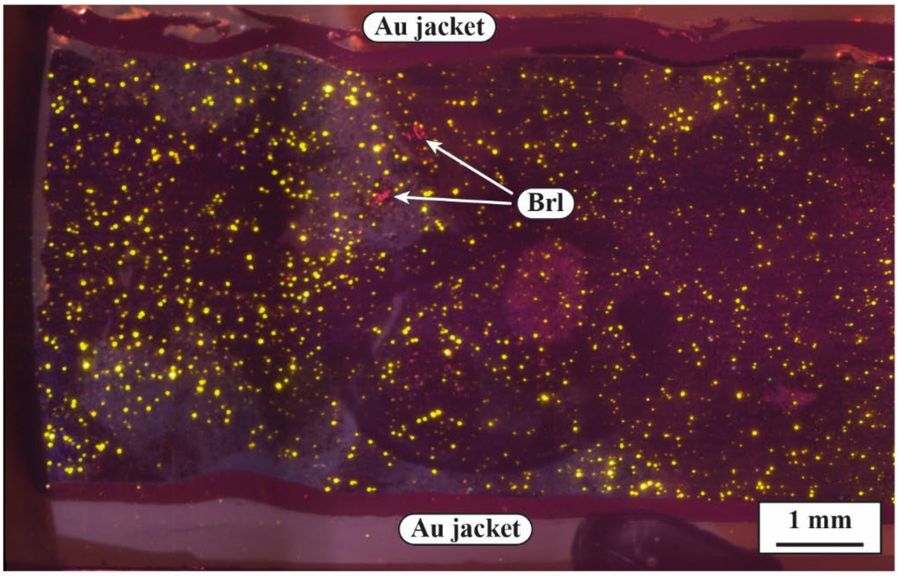

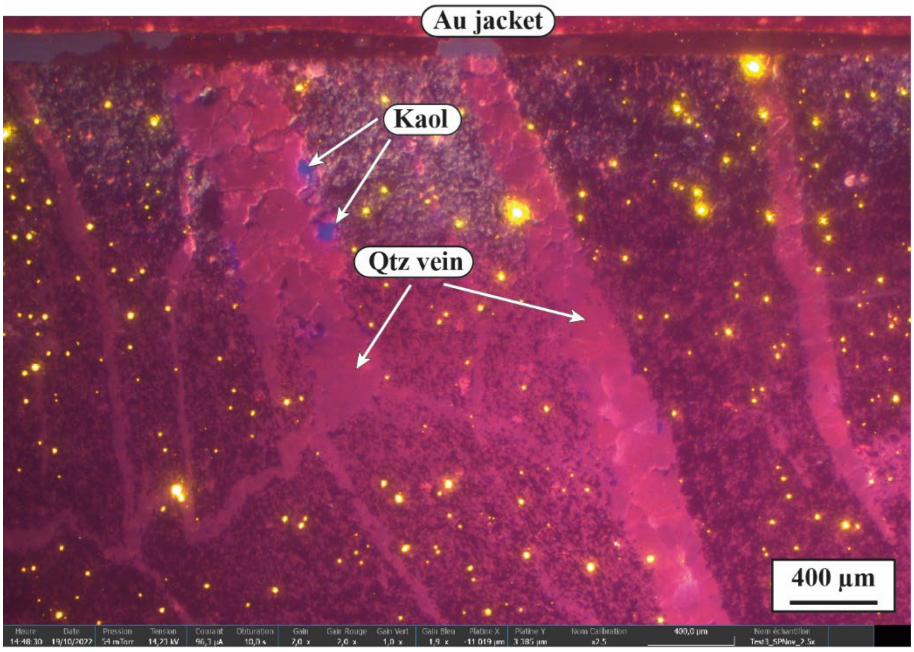

Appendix A24

Composition of experimental fayalite from the reacted core of spotted schist.

Mineral	**Name**	**SiO_2**	**TiO_2**	**Al_2O_3**	**FeO_{tot}**	**MgO**	**MnO**	**CaO**	**Na_2O**	**K_2O**	**Cl**	**F**	**Total**	**Si**	**Ti**	**Al**	**Fe^{2+}**	**Mg**	**Mn**	**Ca**	**Na**	**K**	**Cl**	**F**	**Fay%**	**Tph%**	**Fst%**
Fayalite	SPNov_Fay1	25.46	*b.d.l.*	0.88	56.98	1.89	7.45	*b.d.l.*	*b.d.l.*	0.16	*b.d.l.*	*b.d.l.*	92.85	0.93	0.00	0.04	1.74	0.10	0.23	0.00	0.00	0.01	0.00	0.00	83.92	11.11	4.97
	SPNov_Fay2	24.26	0.05	*b.d.l.*	58.81	3.27	6.58	*b.d.l.*	*b.d.l.*	0.06	*b.d.l.*	*b.d.l.*	93.04	0.90	0.00	0.00	1.82	0.18	0.21	0.00	0.00	0.00	0.00	0.00	82.48	9.35	8.17
	SPNov_Fay3	13.95	0.09	1.13	75.15	0.22	2.38	0.07	0.10	0.12	*b.d.l.*	*b.d.l.*	93.22	0.58	0.00	0.06	2.63	0.01	0.08	0.00	0.01	0.01	0.00	0.00	96.41	3.10	0.50
	SPNov_Fay4	24.84	*b.d.l.*	*b.d.l.*	57.99	2.41	7.93	*b.d.l.*	*b.d.l.*	*b.d.l.*	*b.d.l.*	*b.d.l.*	93.23	0.92	0.00	0.00	1.79	0.13	0.25	0.00	0.00	0.00	0.00	0.00	82.46	11.42	6.12
	SPNov_Fay5	25.16	*b.d.l.*	*b.d.l.*	51.89	2.71	13.59	*b.d.l.*	*b.d.l.*	0.10	*b.d.l.*	*b.d.l.*	93.51	0.92	0.00	0.00	1.59	0.15	0.42	0.00	0.00	0.00	0.00	0.00	73.61	19.53	6.86
	SPNov_Fay6	24.95	0.79	*b.d.l.*	55.87	2.42	9.99	*b.d.l.*	*b.d.l.*	*b.d.l.*	*b.d.l.*	*b.d.l.*	94.07	0.91	0.02	0.00	1.70	0.13	0.31	0.00	0.00	0.00	0.00	0.00	79.46	14.40	6.14
	SPNov_Fay7	25.42	*b.d.l.*	0.89	55.62	2.29	9.66	*b.d.l.*	*b.d.l.*	0.35	*b.d.l.*	*b.d.l.*	94.28	0.92	0.00	0.04	1.68	0.12	0.30	0.00	0.00	0.02	0.00	0.00	80.04	14.08	5.88
	SPNov_Fay8	23.97	*b.d.l.*	*b.d.l.*	63.86	2.99	3.69	*b.d.l.*	*b.d.l.*	*b.d.l.*	*b.d.l.*	*b.d.l.*	94.57	0.88	0.00	0.00	1.96	0.16	0.11	0.00	0.00	0.00	0.00	0.00	87.57	5.13	7.30
	SPNov_Fay9	24.17	*b.d.l.*	*b.d.l.*	64.89	3.08	2.29	*b.d.l.*	*b.d.l.*	0.07	*b.d.l.*	*b.d.l.*	94.58	0.89	0.00	0.00	1.99	0.17	0.07	0.00	0.00	0.00	0.00	0.00	89.25	3.19	7.55
	SPNov_Fay10	26.66	*b.d.l.*	*b.d.l.*	58.00	0.82	9.01	*b.d.l.*	*b.d.l.*	*b.d.l.*	*b.d.l.*	*b.d.l.*	94.59	0.96	0.00	0.00	1.75	0.04	0.28	0.00	0.00	0.00	0.00	0.00	84.57	13.31	2.12
	SPNov_Fay11	23.61	*b.d.l.*	0.15	64.34	2.52	3.95	*b.d.l.*	*b.d.l.*	*b.d.l.*	*b.d.l.*	*b.d.l.*	94.65	0.87	0.00	0.01	1.99	0.14	0.12	0.00	0.00	0.00	0.00	0.00	88.34	5.50	6.16
	SPNov_Fay12	26.30	0.06	*b.d.l.*	61.51	0.71	6.13	*b.d.l.*	*b.d.l.*	*b.d.l.*	*b.d.l.*	*b.d.l.*	94.73	0.95	0.00	0.00	1.86	0.04	0.19	0.00	0.00	0.00	0.00	0.00	89.16	9.01	1.84
	SPNov_Fay13	26.41	0.09	*b.d.l.*	58.82	0.79	8.67	*b.d.l.*	*b.d.l.*	*b.d.l.*	*b.d.l.*	*b.d.l.*	94.84	0.95	0.00	0.00	1.78	0.04	0.27	0.00	0.00	0.00	0.00	0.00	85.24	12.72	2.04
	SPNov_Fay14	25.88	0.06	*b.d.l.*	56.55	3.47	9.21	*b.d.l.*	*b.d.l.*	*b.d.l.*	*b.d.l.*	*b.d.l.*	95.23	0.92	0.00	0.00	1.69	0.18	0.28	0.00	0.00	0.00	0.00	0.00	78.47	12.94	8.59
	SPNov_Fay15	26.67	0.06	0.13	49.64	2.18	16.64	*b.d.l.*	*b.d.l.*	*b.d.l.*	*b.d.l.*	*b.d.l.*	95.36	0.95	0.00	0.01	1.48	0.12	0.50	0.00	0.00	0.00	0.00	0.00	70.52	23.95	5.53
	SPNov_Fay16	24.76	*b.d.l.*	*b.d.l.*	61.75	2.69	6.16	*b.d.l.*	*b.d.l.*	0.06	*b.d.l.*	*b.d.l.*	95.44	0.90	0.00	0.00	1.87	0.15	0.19	0.00	0.00	0.00	0.00	0.00	84.83	8.57	6.60
	SPNov_Fay17	26.91	0.06	0.07	59.82	0.90	7.68	*b.d.l.*	*b.d.l.*	*b.d.l.*	*b.d.l.*	*b.d.l.*	95.50	0.96	0.00	0.00	1.79	0.05	0.23	0.00	0.00	0.00	0.00	0.00	86.43	11.25	2.32
	SPNov_Fay18	26.29	*b.d.l.*	*b.d.l.*	62.80	2.94	3.38	*b.d.l.*	*b.d.l.*	*b.d.l.*	*b.d.l.*	*b.d.l.*	95.51	0.94	0.00	0.00	1.87	0.16	0.10	0.00	0.00	0.00	0.00	0.00	87.89	4.79	7.32
	SPNov_Fay19	24.77	*b.d.l.*	*b.d.l.*	65.02	2.99	2.62	*b.d.l.*	*b.d.l.*	*b.d.l.*	*b.d.l.*	*b.d.l.*	95.57	0.90	0.00	0.00	1.97	0.16	0.08	0.00	0.00	0.00	0.00	0.00	89.06	3.64	7.30
	SPNov_Fay20	24.24	*b.d.l.*	0.09	61.60	2.44	7.34	*b.d.l.*	*b.d.l.*	*b.d.l.*	*b.d.l.*	*b.d.l.*	95.83	0.88	0.00	0.00	1.87	0.13	0.23	0.00	0.00	0.00	0.00	0.00	83.93	10.13	5.94
	SPNov_Fay21	26.08	*b.d.l.*	0.07	60.62	0.58	8.67	*b.d.l.*	*b.d.l.*	*b.d.l.*	*b.d.l.*	*b.d.l.*	96.05	0.94	0.00	0.00	1.82	0.03	0.26	0.00	0.00	0.00	0.00	0.00	86.07	12.47	1.46
	SPNov_Fay22	27.86	*b.d.l.*	0.11	62.57	0.83	5.26	*b.d.l.*	*b.d.l.*	0.10	*b.d.l.*	*b.d.l.*	96.72	0.98	0.00	0.00	1.84	0.04	0.16	0.00	0.00	0.00	0.00	0.00	90.20	7.68	2.12

Appendix A25

Composition of experimental fibrous mineral from the reacted core of spotted schist.

Mineral	Name	SiO_2	TiO_2	Al_2O_3	FeO_{tot}	MgO	MnO	CaO	Na_2O	K_2O	Cl	F	Total	Infos
New Phases	SPNov_New1	24.90	0.30	19.06	25.62	8.38	1.60	0.11	*b.d.l.*	0.76	*b.d.l.*	*b.d.l.*	80.73	Fib. Min.
	SPNov_New2	14.14	1.35	15.78	41.59	7.15	0.61	0.10	*b.d.l.*	*b.d.l.*	*b.d.l.*	*b.d.l.*	80.80	Fib. Min.
	SPNov_New3	3.48	*b.d.l.*	76.59	*b.d.l.*	0.82	*b.d.l.*	*b.d.l.*	0.04	*b.d.l.*	*b.d.l.*	*b.d.l.*	80.96	Fib. Min.
	SPNov_New4	24.41	0.09	22.82	24.48	8.29	1.12	0.08	*b.d.l.*	0.05	0.04	*b.d.l.*	81.42	Fib. Min.
	SPNov_New5	25.68	*b.d.l.*	19.56	29.22	5.25	1.45	0.13	0.12	0.06	*b.d.l.*	*b.d.l.*	81.50	Fib. Min.
	SPNov_New6	25.23	0.05	21.35	26.04	7.77	1.60	*b.d.l.*	0.11	*b.d.l.*	*b.d.l.*	*b.d.l.*	82.22	Fib. Min.
	SPNov_New7	30.83	*b.d.l.*	25.27	16.77	8.58	0.92	0.07	0.09	0.07	0.07	*b.d.l.*	82.72	Fib. Min.
	SPNov_New8	22.95	0.08	22.91	26.66	8.19	1.82	0.05	*b.d.l.*	*b.d.l.*	0.04	*b.d.l.*	82.73	Fib. Min.
	SPNov_New9	27.02	*b.d.l.*	22.19	26.09	5.78	1.32	0.11	0.18	0.11	0.07	*b.d.l.*	82.86	Fib. Min.
	SPNov_New10	33.41	0.06	15.48	30.75	1.12	1.89	0.24	*b.d.l.*	0.09	0.09	*b.d.l.*	83.13	Fib. Min.
	SPNov_New11	27.42	*b.d.l.*	13.95	36.47	3.12	1.97	0.10	0.14	0.09	*b.d.l.*	*b.d.l.*	83.35	Fib. Min.
	SPNov_New12	31.19	*b.d.l.*	18.48	26.85	4.61	1.17	0.33	0.18	0.37	0.25	*b.d.l.*	83.43	Fib. Min.
	SPNov_New13	26.98	*b.d.l.*	22.36	23.11	9.61	1.14	*b.d.l.*	0.14	0.10	*b.d.l.*	*b.d.l.*	83.52	Fib. Min.
	SPNov_New14	27.75	0.07	18.37	27.47	8.08	1.51	0.18	0.19	0.05	*b.d.l.*	*b.d.l.*	83.68	Fib. Min.
	SPNov_New15	27.27	*b.d.l.*	23.84	23.19	8.57	0.99	0.10	0.08	*b.d.l.*	*b.d.l.*	*b.d.l.*	84.15	Fib. Min.
	SPNov_New16	26.20	*b.d.l.*	18.94	31.10	6.75	0.97	0.12	*b.d.l.*	0.25	*b.d.l.*	*b.d.l.*	84.41	Fib. Min.
	SPNov_New17	25.66	*b.d.l.*	20.16	31.06	6.28	1.26	0.07	*b.d.l.*	0.06	*b.d.l.*	*b.d.l.*	84.64	Fib. Min.
	SPNov_New18	28.05	0.19	16.15	32.44	6.31	1.12	0.18	0.29	0.09	*b.d.l.*	*b.d.l.*	84.84	Fib. Min.
	SPNov_New19	28.94	0.15	17.14	29.24	7.30	2.01	0.16	0.17	0.05	0.04	*b.d.l.*	85.20	Fib. Min.
	SPNov_New20	28.72	0.06	22.45	27.15	5.22	1.48	0.10	0.13	0.06	*b.d.l.*	*b.d.l.*	85.39	Fib. Min.
	SPNov_New21	28.36	*b.d.l.*	15.63	34.83	3.65	2.12	0.17	0.10	0.59	*b.d.l.*	*b.d.l.*	85.45	Fib. Min.
	SPNov_New22	26.34	*b.d.l.*	21.78	27.95	7.86	1.70	*b.d.l.*	0.06	*b.d.l.*	*b.d.l.*	*b.d.l.*	85.73	Fib. Min.
	SPNov_New23	30.53	*b.d.l.*	19.60	30.36	4.17	1.07	0.14	0.09	0.05	*b.d.l.*	*b.d.l.*	86.04	Fib. Min.
	SPNov_New24	26.66	*b.d.l.*	18.49	34.73	3.85	2.67	0.08	0.08	0.05	*b.d.l.*	*b.d.l.*	86.62	Fib. Min.
	SPNov_New25	27.14	*b.d.l.*	17.74	33.64	4.88	2.95	0.10	0.09	0.07	*b.d.l.*	*b.d.l.*	86.64	Fib. Min.
	SPNov_New26	29.87	*b.d.l.*	18.37	32.55	4.50	1.22	0.13	*b.d.l.*	0.04	*b.d.l.*	*b.d.l.*	86.73	Fib. Min.
	SPNov_New27	26.55	0.88	26.83	23.15	8.03	1.10	0.11	0.13	0.05	*b.d.l.*	*b.d.l.*	86.84	Fib. Min.
	SPNov_New28	27.39	0.06	19.60	29.92	7.63	2.10	0.06	*b.d.l.*	0.07	*b.d.l.*	*b.d.l.*	86.86	Fib. Min.

Mineral	Name	SiO_2	TiO_2	Al_2O_3	FeO_{tot}	MgO	MnO	CaO	Na_2O	K_2O	Cl	F	Total	Infos
New Phases	SPNov_New29	39.41	0.20	21.09	16.98	4.40	0.58	0.09	0.11	4.10	0.03	*b.d.l.*	87.00	Fib. Min.
	SPNov_New30	25.99	0.07	18.92	33.60	4.88	3.07	*b.d.l.*	0.07	0.49	*b.d.l.*	*b.d.l.*	87.13	Fib. Min.
	SPNov_New31	27.02	*b.d.l.*	20.76	31.44	6.65	1.05	0.11	*b.d.l.*	0.08	*b.d.l.*	*b.d.l.*	87.15	Fib. Min.
	SPNov_New32	27.21	*b.d.l.*	19.33	34.48	4.68	1.30	0.12	0.09	0.11	*b.d.l.*	*b.d.l.*	87.35	Fib. Min.
	SPNov_New33	27.97	0.08	19.26	32.25	6.81	0.95	0.15	*b.d.l.*	*b.d.l.*	*b.d.l.*	*b.d.l.*	87.53	Fib. Min.
	SPNov_New34	27.17	*b.d.l.*	19.64	31.45	7.64	1.30	0.09	0.07	0.20	*b.d.l.*	*b.d.l.*	87.60	Fib. Min.
	SPNov_New35	27.84	0.65	25.46	23.03	8.90	0.98	0.08	0.17	0.58	*b.d.l.*	*b.d.l.*	87.68	Fib. Min.
	SPNov_New36	29.93	*b.d.l.*	17.71	34.55	3.96	1.27	0.19	0.06	*b.d.l.*	*b.d.l.*	*b.d.l.*	87.71	Fib. Min.
	SPNov_New37	33.79	*b.d.l.*	16.41	28.13	4.52	1.39	0.13	0.10	3.25	*b.d.l.*	*b.d.l.*	87.74	Fib. Min.
	SPNov_New38	26.90	*b.d.l.*	20.45	34.02	3.31	2.92	0.06	*b.d.l.*	*b.d.l.*	*b.d.l.*	*b.d.l.*	87.75	Fib. Min.
	SPNov_New39	26.78	0.06	18.63	35.84	5.03	1.37	0.08	*b.d.l.*	0.06	*b.d.l.*	*b.d.l.*	87.86	Fib. Min.
	SPNov_New40	29.15	*b.d.l.*	18.88	34.39	4.55	1.30	0.12	*b.d.l.*	*b.d.l.*	*b.d.l.*	*b.d.l.*	88.47	Fib. Min.
	SPNov_New41	29.84	0.06	21.65	27.72	6.32	1.30	0.05	0.07	1.46	*b.d.l.*	*b.d.l.*	88.49	Fib. Min.
	SPNov_New42	27.09	0.06	17.81	35.96	4.12	3.14	0.08	0.16	0.08	*b.d.l.*	*b.d.l.*	88.50	Fib. Min.
	SPNov_New43	31.41	*b.d.l.*	19.76	30.16	5.64	1.16	0.11	0.11	0.14	*b.d.l.*	*b.d.l.*	88.51	Fib. Min.
	SPNov_New44	27.71	0.08	19.08	34.33	3.93	3.11	0.11	0.18	0.07	*b.d.l.*	*b.d.l.*	88.60	Fib. Min.
	SPNov_New45	27.09	0.07	18.43	34.87	4.52	2.90	0.06	0.12	0.61	*b.d.l.*	*b.d.l.*	88.68	Fib. Min.
	SPNov_New46	28.50	*b.d.l.*	19.04	35.40	4.36	1.19	0.12	*b.d.l.*	*b.d.l.*	*b.d.l.*	*b.d.l.*	88.71	Fib. Min.
	SPNov_New47	26.98	0.13	19.57	33.31	6.66	1.88	0.09	0.07	0.09	*b.d.l.*	*b.d.l.*	88.77	Fib. Min.
	SPNov_New48	26.70	*b.d.l.*	19.97	34.46	3.95	3.48	0.05	0.07	0.08	*b.d.l.*	*b.d.l.*	88.81	Fib. Min.
	SPNov_New49	29.88	*b.d.l.*	20.60	32.15	4.97	1.03	0.15	*b.d.l.*	*b.d.l.*	*b.d.l.*	*b.d.l.*	88.85	Fib. Min.
	SPNov_New50	32.53	0.18	24.04	25.75	4.97	0.54	0.22	0.54	0.08	*b.d.l.*	*b.d.l.*	88.88	Fib. Min.
	SPNov_New51	28.19	0.07	17.86	34.54	4.41	3.01	0.06	0.12	0.85	*b.d.l.*	*b.d.l.*	89.11	Fib. Min.
	SPNov_New52	27.66	*b.d.l.*	21.89	31.27	6.49	1.28	0.09	0.17	0.27	*b.d.l.*	*b.d.l.*	89.17	Fib. Min.
	SPNov_New53	28.64	0.08	18.65	34.72	5.68	0.87	0.07	*b.d.l.*	0.42	*b.d.l.*	*b.d.l.*	89.18	Fib. Min.
	SPNov_New54	30.51	*b.d.l.*	16.07	36.64	3.42	2.55	0.21	0.14	0.09	*b.d.l.*	*b.d.l.*	89.67	Fib. Min.
	SPNov_New55	30.64	0.10	23.16	27.16	5.57	1.25	0.07	0.16	1.87	*b.d.l.*	*b.d.l.*	89.99	Fib. Min.
	SPNov_New56	31.68	0.28	19.01	26.90	8.18	1.23	0.05	0.10	2.91	*b.d.l.*	*b.d.l.*	90.34	Fib. Min.

Mineral	**Name**	**SiO_2**	**TiO_2**	**Al_2O_3**	**FeO_{tot}**	**MgO**	**MnO**	**CaO**	**Na_2O**	**K_2O**	**Cl**	**F**	**Total**	**Infos**
New Phases	SPNov_New56	31.27	*b.d.l.*	21.43	31.65	4.68	1.06	0.14	*b.d.l.*	0.12	*b.d.l.*	*b.d.l.*	90.45	Fib. Min.
	SPNov_New57	29.58	0.06	23.96	25.89	7.48	1.20	0.07	0.11	0.25	*b.d.l.*	*b.d.l.*	88.61	Ms. Og.
	SPNov_New58	33.40	0.22	26.42	15.92	5.88	0.84	*b.d.l.*	0.13	3.78	*b.d.l.*	*b.d.l.*	86.66	Ms. Og.
	SPNov_New59	46.20	0.10	26.09	5.25	4.01	*b.d.l.*	*b.d.l.*	0.09	5.91	*b.d.l.*	1.94	89.74	Ms. Og.
	SPNov_New60	37.16	0.27	26.55	16.76	4.92	0.97	*b.d.l.*	0.08	5.93	*b.d.l.*	*b.d.l.*	92.65	Ms. Og.
	SPNov_New61	40.63	0.55	32.36	4.51	3.10	0.10	0.07	1.05	6.38	*b.d.l.*	0.66	89.43	Ms. Og.
	SPNov_New62	29.40	0.14	26.12	22.38	7.16	0.81	*b.d.l.*	*b.d.l.*	2.93	*b.d.l.*	*b.d.l.*	88.97	Ms. Og.
	SPNov_New63	25.79	*b.d.l.*	17.53	35.83	4.94	1.20	0.06	*b.d.l.*	0.06	*b.d.l.*	*b.d.l.*	85.47	Bt. Og.
	SPNov_New64	21.97	1.11	22.68	23.79	12.58	0.48	*b.d.l.*	*b.d.l.*	0.11	*b.d.l.*	*b.d.l.*	82.76	Bt. Og.
	SPNov_New65	30.16	1.28	30.86	16.79	6.09	0.51	0.28	0.70	0.11	*b.d.l.*	*b.d.l.*	86.79	Bt. Og.
	SPNov_New66	19.14	0.54	20.96	29.19	11.71	0.47	0.12	*b.d.l.*	0.16	0.05	*b.d.l.*	82.35	Bt. Og.
	SPNov_New67	22.53	2.17	24.18	20.93	12.59	0.60	*b.d.l.*	*b.d.l.*	0.40	*b.d.l.*	*b.d.l.*	83.45	Bt. Og.
	SPNov_New68	22.66	0.20	24.28	22.20	11.84	0.56	*b.d.l.*	*b.d.l.*	0.47	*b.d.l.*	*b.d.l.*	82.27	Bt. Og.
	SPNov_New69	24.35	0.34	23.22	25.11	11.45	0.64	0.08	*b.d.l.*	0.75	*b.d.l.*	*b.d.l.*	85.95	Bt. Og.
	SPNov_New70	24.22	0.42	22.25	24.84	7.90	0.71	*b.d.l.*	*b.d.l.*	0.86	*b.d.l.*	*b.d.l.*	81.22	Bt. Og.
	SPNov_New71	31.66	0.18	19.25	27.93	7.50	1.08	0.07	0.12	3.13	*b.d.l.*	*b.d.l.*	90.95	Bt. Og.
	SPNov_New72	30.41	0.92	18.96	28.46	5.00	1.36	*b.d.l.*	*b.d.l.*	4.83	*b.d.l.*	*b.d.l.*	90.02	Bt. Og.
	SPNov_New73	33.00	0.62	17.79	21.59	5.38	0.50	0.05	0.06	5.76	0.07	0.45	85.28	Bt. Og.
	SPNov_New74	29.81	0.91	18.22	22.91	7.35	0.38	*b.d.l.*	*b.d.l.*	5.91	0.06	*b.d.l.*	85.59	Bt. Og.
	SPNov_New75	31.75	0.99	17.70	23.50	6.41	0.33	0.06	*b.d.l.*	7.07	*b.d.l.*	0.51	88.38	Bt. Og.
	SPNov_New76	36.96	0.59	15.56	19.21	9.51	0.66	*b.d.l.*	*b.d.l.*	7.28	*b.d.l.*	3.08	92.91	Bt. Og.
	SPNov_New77	36.45	1.05	19.19	23.34	6.16	0.34	*b.d.l.*	0.06	7.76	*b.d.l.*	0.90	95.30	Bt. Og.
	SPNov_New78	31.79	1.19	16.68	23.98	6.14	*b.d.l.*	*b.d.l.*	0.13	8.22	0.07	0.48	88.80	Bt. Og.
	SPNov_New79	25.64	0.44	20.41	25.16	7.32	0.41	*b.d.l.*	*b.d.l.*	2.65	0.07	*b.d.l.*	82.13	Bt. Og.
	SPNov_New80	25.96	0.62	24.04	28.15	8.46	0.69	*b.d.l.*	*b.d.l.*	0.98	*b.d.l.*	*b.d.l.*	88.93	Bt. Og.
	SPNov_New81	28.86	0.87	19.93	23.28	6.46	0.37	*b.d.l.*	*b.d.l.*	4.71	0.05	*b.d.l.*	84.81	Bt. Og.

Appendix A26

Sample name	Elapsed time (h)	Al	B	Co	Mn	Ni	Zn	Ti	Br	Ca	K	Fe	Mg	Na	$SiO_{2(aq)}$	Cl	C_{min}
		(µg/L)								*(mg/L)*							
Starting Solution Oct	0	414	7667214	*b.d.l.*	1.75	*b.d.l.*	7.07	*b.d.l.*	*b.d.l.*	*b.d.l.*	0.6	*b.d.l.*	*b.d.l.*	1.2	*b.d.l.*	*b.d.l.*	*b.d.l.*
Starting Solution Nov	829	304	7198904	*b.d.l.*	1.97	1.13	18.9	*b.d.l.*	*b.d.l.*	*b.d.l.*	0.8	*b.d.l.*	*b.d.l.*	2.1	*b.d.l.*	*b.d.l.*	*b.d.l.*
Prelevement 1	40	320	1773734	3.91	79.6	242	798	*b.d.l.*	*b.d.l.*	0.8	3.4	0.225	*b.d.l.*	29	84.6	34.9	*b.d.l.*
Prelevement 2	60	2620	6852087	2.86	267	186	327	*b.d.l.*	*b.d.l.*	0.8	7.1	0.876	0.7	21.8	164	27.2	*b.d.l.*
Prelevement 3	154	3617	7192949	2.78	194	172	318	*b.d.l.*	*b.d.l.*	0.6	9.8	1.25	*b.d.l.*	28.2	349	37.6	*b.d.l.*
Prelevement 4	180	2935	6344001	1.84	137	113	225	*b.d.l.*	*b.d.l.*	0.5	9.4	0.681	*b.d.l.*	18.7	319	22.2	*b.d.l.*
Prelevement 5	203	2882	6276389	1.36	109	81.4	174	*b.d.l.*	*b.d.l.*	*b.d.l.*	9.5	0.645	*b.d.l.*	15.8	316	18.7	*b.d.l.*
Prelevement 6	228	2819	6134981	1.16	113	71.1	176	*b.d.l.*	*b.d.l.*	*b.d.l.*	9.6	0.613	*b.d.l.*	14.1	328	16.5	*b.d.l.*
Prelevement 7	298	3930	7529687	1.13	130	71.8	183	*b.d.l.*	*b.d.l.*	*b.d.l.*	11.7	0.837	*b.d.l.*	14.1	402	16.3	*b.d.l.*
Prelevement 8	322	2724	5632235	0.866	92.1	48.9	128	*b.d.l.*	*b.d.l.*	*b.d.l.*	9.8	0.49	*b.d.l.*	10.2	313	10.5	*b.d.l.*
Prelevement 9	347	3020	5819980	0.911	92.6	48	117	*b.d.l.*	*b.d.l.*	*b.d.l.*	10.2	0.492	*b.d.l.*	9.6	315	9.9	*b.d.l.*
Prelevement 10	379	4411	6537863	0.739	94.8	45.3	99.5	*b.d.l.*	*b.d.l.*	*b.d.l.*	28	0.57	*b.d.l.*	8.8	326	9.3	*b.d.l.*
Prelevement 11	402	3098	5958386	0.707	82.8	38.9	83.7	*b.d.l.*	*b.d.l.*	*b.d.l.*	10.5	0.46	*b.d.l.*	7.5	292	8	*b.d.l.*
Prelevement 12	466	4084	6992898	0.733	89.7	43.1	93.4	*b.d.l.*	*b.d.l.*	*b.d.l.*	12.9	0.63	*b.d.l.*	7.9	367	8.6	*b.d.l.*
Prelevement 13	490	3035	5432992	0.594	67.4	32.9	77.2	*b.d.l.*	*b.d.l.*	*b.d.l.*	10.7	0.421	*b.d.l.*	6.1	296	5.9	*b.d.l.*
Prelevement 14	515	3018	5880145	0.555	64.3	32.1	70.7	*b.d.l.*	*b.d.l.*	*b.d.l.*	10.8	0.43	*b.d.l.*	5.8	296	5.6	*b.d.l.*
Prelevement 15	570	5636	7120825	0.591	78.6	39.7	75.2	*b.d.l.*	*b.d.l.*	*b.d.l.*	13.1	0.54	*b.d.l.*	6.1	347	5.9	*b.d.l.*
Prelevement 16	635	4580	7674657	0.57	88.6	35.6	78.3	*b.d.l.*	*b.d.l.*	*b.d.l.*	14.4	0.53	*b.d.l.*	5.7	352	5.4	*b.d.l.*
Prelevement 17	663	3637	6402493	*b.d.l.*	64.3	24.2	64.9	*b.d.l.*	*b.d.l.*	*b.d.l.*	12.5	0.36	*b.d.l.*	4.6	287	4	*b.d.l.*
Prelevement 18	687	3290	6186954	*b.d.l.*	53.1	21.5	60.7	*b.d.l.*	*b.d.l.*	*b.d.l.*	11.8	0.33	*b.d.l.*	4.2	269	3.6	*b.d.l.*
Prelevement 19	711	3236	5765495	*b.d.l.*	45.2	19.1	57.8	*b.d.l.*	*b.d.l.*	*b.d.l.*	11.6	0.31	*b.d.l.*	4	270	3.3	*b.d.l.*
Prelevement 20	739	3297	5687277	*b.d.l.*	46	24.8	64.4	*b.d.l.*	*b.d.l.*	*b.d.l.*	12.3	0.33	*b.d.l.*	4.1	287	3.4	*b.d.l.*
Prelevement 21	803	3944	6768678	0.532	45	23.4	79.4	*b.d.l.*	*b.d.l.*	*b.d.l.*	14.4	0.44	*b.d.l.*	4.4	355	3.7	*b.d.l.*
Prelevement 22	829	2631	4774822	*b.d.l.*	32.3	19.3	63.8	*b.d.l.*	*b.d.l.*	*b.d.l.*	11.7	0.28	*b.d.l.*	3.7	274	2.7	*b.d.l.*
Prelevement 23	856	2624	4790614	*b.d.l.*	29.3	14.9	55.7	*b.d.l.*	*b.d.l.*	*b.d.l.*	11.7	0.253	*b.d.l.*	3.1	264	2	*b.d.l.*
Prelevement 24	877	1049	2547417	*b.d.l.*	13.6	8.23	63.5	*b.d.l.*	*b.d.l.*	*b.d.l.*	7.6	0.025	*b.d.l.*	2.1	163	0.9	*b.d.l.*

Chemical analysis for samples from the reactive percolation experiment (raw data).

Sample name	Elapsed time (h)	Al	B	Co	Mn	Ni	Zn	Ti	Br	Ca	K	Fe	Mg	Na	$SiO_{2(aq)}$	Cl	C_{min}
		(mol/L)															
Starting Solution Oct	0	1.53E-05	6.89E-01		3.19E-08		1.08E-07				1.53E-05			5.22E-05			
Starting Solution Nov	829	1.13E-05	6.76E-01		3.59E-08	1.92E-08	2.89E-07				2.05E-05			9.13E-05			
Prelevement 1	40	1.77E-05	2.44E-01	9.87E-08	2.16E-06	6.13E-06	1.82E-05			2.97E-05	1.29E-04	6.00E-06		1.88E-03	2.10E-03	1.47E-03	
Prelevement 2	60	1.09E-04	7.15E-01	5.47E-08	5.48E-06	3.57E-06	5.64E-06			2.25E-05	2.05E-04	1.77E-05	3.25E-05	1.07E-03	3.08E-03	8.65E-04	
Prelevement 3	154	1.44E-04	7.14E-01	5.06E-08	3.79E-06	3.14E-06	5.22E-06			1.61E-05	2.69E-04	2.40E-05		1.32E-03	6.23E-03	1.14E-03	
Prelevement 4	180	1.39E-04	7.49E-01	3.98E-08	3.18E-06	2.45E-06	4.39E-06			1.59E-05	3.07E-04	1.56E-05		1.04E-03	6.77E-03	7.99E-04	
Prelevement 5	203	1.41E-04	7.66E-01	3.05E-08	2.62E-06	1.83E-06	3.51E-06				3.21E-04	1.52E-05		9.07E-04	6.94E-03	6.96E-04	
Prelevement 6	228	1.38E-04	7.49E-01	2.60E-08	2.71E-06	1.60E-06	3.55E-06				3.24E-04	1.45E-05		8.09E-04	7.20E-03	6.14E-04	
Prelevement 7	298	1.62E-04	7.76E-01	2.14E-08	2.63E-06	1.36E-06	3.12E-06				3.33E-04	1.67E-05		6.83E-04	7.45E-03	5.12E-04	
Prelevement 8	322	1.31E-04	6.76E-01	1.91E-08	2.17E-06	1.08E-06	2.54E-06				3.25E-04	1.14E-05		5.76E-04	6.76E-03	3.84E-04	
Prelevement 9	347	1.59E-04	7.65E-01	2.20E-08	2.39E-06	1.16E-06	2.54E-06				3.71E-04	1.25E-05		5.93E-04	7.45E-03	3.97E-04	
Prelevement 10	379	2.00E-04	7.40E-01	1.53E-08	2.11E-06	9.44E-07	1.86E-06				8.76E-04	1.25E-05		4.68E-04	6.63E-03	3.21E-04	
Prelevement 11	402	1.49E-04	7.15E-01	1.56E-08	1.96E-06	8.60E-07	1.66E-06				3.48E-04	1.07E-05		4.23E-04	6.31E-03	2.93E-04	
Prelevement 12	466	1.70E-04	7.28E-01	1.40E-08	1.84E-06	8.27E-07	1.61E-06				3.72E-04	1.27E-05		3.87E-04	6.88E-03	2.73E-04	
Prelevement 13	490	1.46E-04	6.54E-01	1.31E-08	1.60E-06	7.29E-07	1.54E-06				3.56E-04	9.80E-06		3.45E-04	6.41E-03	2.16E-04	
Prelevement 14	515	1.43E-04	6.97E-01	1.21E-08	1.50E-06	7.01E-07	1.39E-06				3.54E-04	9.86E-06		3.23E-04	6.31E-03	2.02E-04	
Prelevement 15	570	2.36E-04	7.45E-01	1.13E-08	1.62E-06	7.65E-07	1.30E-06				3.79E-04	1.09E-05		3.00E-04	6.53E-03	1.88E-04	
Prelevement 16	635	1.90E-04	7.93E-01	1.08E-08	1.80E-06	6.77E-07	1.34E-06				4.11E-04	1.06E-05		2.77E-04	6.54E-03	1.70E-04	
Prelevement 17	663	1.67E-04	7.33E-01		1.45E-06	5.10E-07	1.23E-06				3.95E-04	7.97E-06		2.47E-04	5.91E-03	1.40E-04	
Prelevement 18	687	1.58E-04	7.42E-01		1.25E-06	4.75E-07	1.20E-06				3.91E-04	7.66E-06		2.37E-04	5.80E-03	1.32E-04	
Prelevement 19	711	1.58E-04	7.01E-01		1.08E-06	4.27E-07	1.16E-06				3.90E-04	7.29E-06		2.29E-04	5.90E-03	1.22E-04	
Prelevement 20	739	1.58E-04	6.80E-01		1.08E-06	5.46E-07	1.27E-06				4.07E-04	7.64E-06		2.31E-04	6.18E-03	1.24E-04	
Prelevement 21	803	1.71E-04	7.33E-01	1.06E-08	9.59E-07	4.66E-07	1.42E-06				4.31E-04	9.22E-06		2.24E-04	6.91E-03	1.22E-04	
Prelevement 22	829	1.33E-04	6.01E-01		8.00E-07	4.48E-07	1.33E-06				4.07E-04	6.82E-06		2.19E-04	6.21E-03	1.04E-04	
Prelevement 23	856	1.34E-04	6.10E-01		7.34E-07	3.49E-07	1.17E-06				4.12E-04	6.23E-06		1.86E-04	6.05E-03	7.76E-05	
Prelevement 24	877	7.39E-05	4.48E-01		4.70E-07	2.66E-07	1.85E-06				3.69E-04	8.50E-07		1.74E-04	5.15E-03	4.82E-05	

Chemical analysis for samples from the reactive percolation experiment (corrected data).

Julien FORT

Tourmalinisation des systèmes hydrothermaux périgranitiques : approche expérimentale du champ de stabilité et des dynamiques des processus métasomatiques dans les systèmes borosilicatés

La formation des gisements hydrothermaux dépend essentiellement des propriétés physico-chimiques du fluide et de la roche encaissante et des couplages et rétroactions thermiques, hydrauliques, mécaniques et chimiques qui en résultent. L'observation des altérations associées aux minéralisations ne permettent qu'une estimation parcellaire de ces phénomènes complexes. Les simulations numériques sont donc extrêmement utiles pour évaluer ces couplages, soit en modélisant l'écoulement des fluides et le transfert de chaleur, soit en modélisant les équilibres thermodynamiques entre les fluides et les minéraux. Des progrès récents ont permis de combiner ces deux types de simulations et les résultats soulignent qu'en modifiant les propriétés pétrophysiques de la roche hôte, l'altération constitue une force motrice à la fois physique et chimique lors de la formation des gisements. Un tel développement nécessite (i) une bonne implémentation de l'altération dans les simulations d'équilibre an batch et (ii) des lois quantitatives décrivant l'effet de l'altération sur la perméabilité de la roche. Cette thèse se concentre sur la tourmaline, un minéral emblématique et omniprésent de la transition magmatique/hydrothermale, présent dans les altérations depuis le stade tardif de la cristallisation magmatique jusqu'au métasomatisme à basse température. Cependant, le manque de données calibrant la stabilité de la tourmaline est un obstacle à son utilisation dans la modélisation thermodynamique. Les objectifs sont donc (i) de fournir de nouvelles contraintes expérimentales sur $[B_2O_3]_{fluid\_EQ}$, la concentration en bore du fluide à l'équilibre avec la tourmaline, (ii) d'évaluer la qualité actuelle de l'implémentation de la tourmaline dans les modèles thermodynamiques, et (iii) d'étudier les dynamiques du métasomatisme du bore dans un environnement périgranitique, via une expérience de percolation réactive. Les résultats obtenus par expérimentation en batch à 600, 500 et 400°C (200 MPa, en condition modérément oxydante) montrent que les équilibres tourmaline-cordiérite et tourmaline-biotite nécessitent un $[B_2O_3]_{fluide}$ compris entre 8 et 1 wt%. Les expériences réalisées sur les mêmes assemblages mais avec une chimie des fluides variable (pH et concentration en chlorure alcalin) montrent une réduction du $[B_2O_3]_{fluid\_EQ}$ ainsi que d'importantes modifications de texture et de composition. Ces gammes de concentrations en bore sont cohérentes avec les contraintes de composition des fluides hydrothermaux naturels et des magmas peralumineux. La comparaison entre les résultats expérimentaux et les calculs thermodynamiques du $[B_2O_3]_{fluid\_EQ}$ soulignent les limitations des simulations numériques, liées à l'absence de modèle de solution solide pour les tourmalines complexes. L'expérience de percolation réactive a été réalisée en infiltrant une saumure de $B(OH)_3$ dans un micaschiste tacheté à 300°C et 30 MPa pendant 6 semaines. L'organisation globale des altérations est interprétée comme le résultat d'une interaction entre la minéralogie locale et la vitesse du fluide, allant d'un lessivage intense dans les zones à fort débit à des pseudomorphose dans les zones à faible débit.

Mots clés : Systèmes hydrothermaux, Interactions fluide/roche, Pétrophysique, Expérimentation, Modélisation thermodynamique, Ressources minérales

Tourmalinisation of perigranitic hydrothermal systems: experimental approach to the stability field and dynamics of metasomatic processes in borosilicate systems

The formation of hydrothermal deposits depends essentially on the physico-chemical properties of the fluid and the surrounding rocks, and the resulting thermal, hydraulic, mechanical and chemical couplings and feedback. Observation of alteration associated with mineralisation provides only a fragmentary estimate of these complex phenomena. Numerical simulations are therefore extremely useful for assessing these couplings, either by modelling fluid flow and heat transfer, or by modelling thermodynamic equilibria between fluid and minerals. Recent advances allowed the combination of those two kinds of simulations and the results highlight that by modifying the petrophysics properties of the host rock, alteration constitute both a physical and chemical driving force during the ore deposit formation. Such development requires (i) a good implementation of the alteration in batch equilibrium simulation and (ii) quantitative laws describing the effect of the alteration on the permeability of the rock. This PhD focus on the tourmaline, an emblematic ubiquitous mineral of the magmatic/hydrothermal transition, present in the alterations from the late stage of magmatic crystallisation to the low temperature metasomatism. However, the lack of calibrating data on tourmaline stability is a barrier to its use in thermodynamic modelling. Thus, the objectives are (i) to provide new experimental constraints on $[B_2O_3]_{fluid\_EQ}$, the boron concentration of the fluid at equilibrium with tourmaline (ii) to assess the actual quality of tourmaline implementation in thermodynamic models, and (iii) to study the dynamic of boron metasomatism in perigranitic environment, through reactive percolation experiment. The results obtained by batch experimentation at 600, 500 and 400°C (200 MPa, under moderately oxidising condition) show that the tourmaline-cordierite and tourmaline-biotite equilibria require a $[B_2O_3]_{fluid}$ ranging between 8 and 1 wt%. Experiments performed on the same assemblages but with varying fluid chemistry (pH and alkali chloride concentration) show a reduction of the $[B_2O_3]_{fluid\_EQ}$ along with important textural and compositional modifications. Those boron concentration ranges required to form tourmaline are consistent with compositional constraints from natural hydrothermal fluids and peraluminous melts. Comparison between experimental results and thermodynamic calculations of $[B_2O_3]_{fluid\_EQ}$ highlights the limitations of numerical simulations, due to the lack of solution model for chemically complex tourmalines. The reactive percolation experiment was performed by infiltrating a $B(OH)_3$ brine into a spotted micaschist at 300°C and 30 MPa for 6 weeks. The global organisation of the alterations are interpreted as the result of an interplay between the local mineralogy and the fluid velocity ranging from intense leaching in the high-flow zones and pseudomorphism in the low-flow zones.

Keywords : Hydrothermal systems, fluid/rock interaction, Petrophysic, Experimentation, Thermodynamic modelling, Economic geology

Institut des Sciences de
la Terre d'Orléans
1A rue de la Férollerie
45100 Orléans